

# Investigation of atmospheric aerosols and cloud condensation nuclei under pristine and polluted conditions

Dissertation

zur Erlangung des Grades eines  
'Doctor rerum naturalium (Dr. rer. nat.)' der Fachbereiche:  
08 - Physik, Mathematik und Informatik,  
09 - Chemie, Pharmazie und Geowissenschaften,  
10 - Biologie,  
Universitätsmedizin

verfasst und vorgelegt von

Mira Pöhlker  
(geb. Krüger)

geboren am 30. Mai 1988  
in Gießen

Max Planck Graduate Center  
mit der Johannes Gutenberg-Universität Mainz  
angefertigt am Max-Planck-Institut für Chemie

Mainz, 2017



I hereby declare that I wrote the dissertation submitted without any unauthorized external assistance and used only sources acknowledged in the work. All textual passages, which are appropriated verbatim or paraphrased from published and unpublished texts as well as all information obtained from oral sources, are duly indicated and listed in accordance with bibliographical rules. In carrying out this research, I complied with the rules of standard scientific practice as formulated in the statutes of Johannes Gutenberg-University Mainz to insure standard scientific practice.

Mainz, 19. November 2017, Mira Pöhlker (née Krüger)



# Abstract

The interactions and effects of aerosols and clouds are among the largest uncertainties in the assessment and modeling of climate change. Due to the increasing human influence on planet Earth, remote locations that allow to probe pristine air approximating pre-industrial conditions are becoming progressively rare. Such conditions are, however, of particular scientific interest for understanding climate and global environmental change. This dissertation investigates the properties and interactions of aerosols serving as cloud condensation nuclei (CCN) under pristine and polluted conditions by aircraft and ground-based measurements.

At the Amazon Tall Tower Observatory (ATTO), a robust experimental setup was developed and used to obtain the first size-resolved CCN measurements spanning a full seasonal cycle in the Amazonian rainforest. The unique data set comprises annual and seasonal averages of aerosol and CCN parameters as well as characteristic case studies including present-day pristine conditions, biomass burning aerosols, and long range transport effects. A novel parameterization of CCN efficiency spectra and concentrations as a function of water vapor supersaturation was developed for efficient representation of aerosol and CCN properties in model studies. This approach enhances the efficiency, accuracy, and reliability with which CCN concentrations can be taken into account in process models and large-scale models of clouds and precipitation, the atmosphere and climate. The parametrization shall serve as a basis for detailed microphysical studies on the formation and properties of clouds and precipitation in the Amazon region. The CCN observations at the ATTO site were also used to evaluate a new method to retrieve CCN concentrations from satellite data.

Within the ACRIDICON project (Aerosol, Cloud, Precipitation, and Radiation Interactions and Dynamics of Convective Cloud Systems), aerosol-cloud interactions were investigated during two collaborative measurement campaigns. During the ACRIDICON-Zugspitze campaign, cloud supersaturations were derived from both aerosol size distribution and size-resolved CCN measurements. An instrument package for airborne measurements of CCN and aerosol properties was developed and implemented on the research aircraft HALO to probe the vertical structure and evolution of convective clouds in the Amazon Basin during the ACRIDICON-CHUVA campaign. The results indicate that new particle formation occurs in the outflow of deep convective clouds, which seems to be an important source of aerosol particles and CCN in the boundary layer and may be the dominant process of secondary particle formation in the pre-industrial atmosphere.



# Zusammenfassung

Die Wechselwirkungen von Aerosolen und Wolken stellen eine der größten Unsicherheiten im Verständnis des Klimawandels und in entsprechenden Modellstudien dar. Durch den zunehmenden Einfluss menschlicher Aktivitäten auf das Erdsystem werden entlegene Orte mit Reinluftbedingungen, die einer vorindustriellen Atmosphäre ähneln, immer seltener. Diese sind jedoch von besonderer wissenschaftlicher Relevanz, um das Ausmaß anthropogener Klima- und Umweltveränderungen zu quantifizieren. Die vorliegende Dissertation untersucht die Eigenschaften und Wechselwirkungen von Aerosolpartikeln, die als Wolkenkondensationskeime (CCN) dienen können, durch flugzeug- und bodengestützte Messungen in reiner und verschmutzter Luft.

Für größen aufgelöste CCN-Untersuchungen am Amazon Tall Tower Observatory (ATTO) wurde ein robustes Messsystem entwickelt, mit welchem erstmalig ein kompletter saisonaler Zyklus im Amazonas-Regenwald aufgenommen wurde. Dieser einzigartige Datensatz beinhaltet Jahresmittelwerte und saisonale Kenngrößen der Aerosol- und CCN-Eigenschaften sowie charakteristische Fallstudien zu Reinluftbedingungen, Aerosolen aus Biomasse- bzw. Waldbränden und den Effekten atmosphärischer Langstreckentransporte. Zur effizienten Beschreibung von Aerosol- und CCN-Eigenschaften in Modellstudien wurde eine neuartige Parametrisierung der CCN-Effizienzspektren und -Konzentrationen als Funktion der Wasserdampfübersättigung entwickelt. Dieser Ansatz erhöht die Effizienz, Genauigkeit und Reproduzierbarkeit, mit welcher CCN-Konzentrationen in Prozessmodellen sowie in großskaligen Modellen von Wolken, Niederschlagsbildung, der Atmosphäre und des Klimas berücksichtigt werden können. Die Parametrisierung soll als Grundlage für detaillierte mikrophysikalische Studien zur Entstehung und den Eigenschaften von Wolken und Niederschlag in der Amazonasregion dienen. Die CCN-Messergebnisse von ATTO wurden auch zur Evaluierung einer neuen Methode für die Bestimmung von CCN-Konzentrationen aus Satelliten-Daten eingesetzt.

Im Rahmen des ACRIDICON-Projektes (Aerosol, Cloud, Precipitation, and Radiation Interactions and Dynamics of Convective Cloud Systems) wurden die Wechselwirkungen zwischen Aerosolen und Wolken in zwei kooperativen Messkampagnen untersucht. Während der ACRIDICON-Zugspitze-Kampagne wurden Wolkenübersättigungen sowohl aus Aerosolgrößenverteilungen als auch aus größen aufgelösten CCN-Messungen abgeleitet. Ein Instrumentenpaket für flugzeuggestützte Messungen von CCN- und Aerosoleigenschaften wurde entwickelt und im Forschungsflugzeug HALO installiert, um die vertikale Struktur und die Entwicklung von konvektiven Wolken im Amazonasbecken während der ACRIDICON-CHUVA-Kampagne zu untersuchen. Die Ergebnisse lassen darauf schließen, dass Partikelneubildung im Ausfluss hochreichender konvektiver Wolken stattfindet, was eine wichtige Quelle für Aerosolpartikel und CCN in der atmosphärischen Grenzschicht darstellt. Weiterhin könnte dieser Prozess eine dominante Rolle in der sekundären Partikelneubildung der vorindustriellen Atmosphäre gespielt haben.



# Table of Contents

<b>Abstract</b>		<b>iii</b>
<b>Zusammenfassung</b>		<b>v</b>
<b>1 Introduction and motivation</b>		<b>1</b>
1.1	Atmospheric aerosol properties and interactions	1
1.2	Aerosols and clouds over the Amazon rainforest	4
1.3	Research objectives	5
1.3.1	ATTO project	5
1.3.2	ACRIDICON project	5
<b>2 Results and conclusions</b>		<b>6</b>
2.1	Individual studies	6
2.1.1	Long-term characterization of cloud condensation nuclei at the ATTO site and new model parametrization for CCN prediction	6
2.1.2	Comparison of pristine, biomass burning, and long-range transport conditions at the ATTO site	6
2.1.3	Aerosol nucleation in the upper troposphere over the Amazon during the ACRIDICON-CHUVA campaign	7
2.1.4	Assessment of cloud supersaturation during the ACRIDICON-Zugspitze campaign	7
2.1.5	Satellite retrieval of CCN concentrations	7
2.2	Summary and outlook	8
<b>3 References</b>		<b>9</b>
<b>Appendix A List of related publications and presentations</b>		<b>12</b>
<b>Appendix B Selected publications</b>		<b>17</b>
B1	Pöhlker et al., Atmos. Chem. Phys., 2016	19
B2	Pöhlker et al., Atmos. Chem. Phys. Discuss., 2017	53
B3	Andreae et al., Atmos. Chem. Phys. Discuss., 2017	115
B4	Krüger et al., Atmos. Meas. Tech., 2014	217
B5	Rosenfeld et al., Proc. Natl. Acad. Sci. USA, 2016	233



## Chapter 1

# Introduction and motivation

## 1.1 Atmospheric aerosol properties and interactions

Human activities have become a driving force that changes many characteristics of our planet and environment on local, regional, and global scales. To emphasize that this “anthropogenic force” is of a geohistorical dimension, Paul Crutzen has coined the term *Anthropocene*, as a geological epoch humankind has recently entered (Crutzen, 2002; Steffen et al., 2011; Pöschl and Shiraiwa, 2015; Reinmuth-Selzle et al., 2017). The present study belongs to the wide field of Earth system science, aiming to provide a better understanding of the anthropogenic effects on the Earth system by investigating the past and current state of the atmosphere as well as assessing future scenarios of atmospheric changes and related consequences.

Atmospheric aerosols originate from natural and anthropogenic sources and comprise a diverse mixture of different particle classes, such as mineral and soil dust, sea spray, soot and other combustion residues, biogenic particles, and many others (Pöschl, 2005). In the atmosphere, aerosols undergo a complex and dynamic life cycle, which changes their properties and atmospheric influence as illustrated in Figure 1. They play an important role in atmospheric physics and chemistry as well as public health (Pöschl and Shiraiwa, 2015). Besides their influence on the Earth’s radiative budget via absorption and scattering of solar radiation (so-called direct effect), aerosols act as cloud condensation nuclei (CCN) in the formation of cloud droplets and as ice nuclei (IN) in the formation of ice crystals (so-called indirect effect) (Satheesh and Moorthy, 2005; Andreae and Rosenfeld, 2008; Hoose and Möhler, 2012).

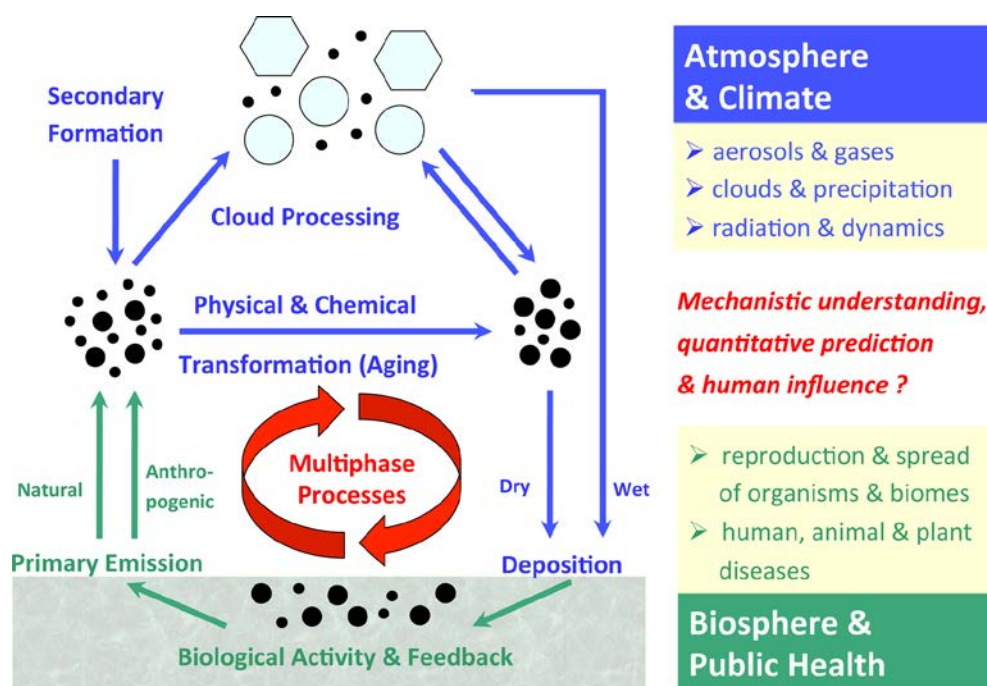


Figure 1. Illustration of the life cycle of atmospheric aerosols (i.e., sources, processing, deposition), emphasizing their atmospheric and biospheric relevance. Adopted from Pöschl and Shiraiwa (2015).

Aerosol-cloud-precipitation interactions are a key factor in the Earth atmosphere and climate system (e.g., Andreae and Rosenfeld, 2008; Tao et al., 2012; Rosenfeld et al., 2014; Bony et al., 2015; Seinfeld et al., 2016). Thus, sound scientific knowledge on the life cycle and the highly dynamic properties of clouds is of significant importance for our understanding of atmospheric cycling and climate change. Aerosol particles, in their role as CCN, represent one of the key factors in the formation and development of clouds and precipitation (Solomon et al., 2007).

Which particles act as CCN depends on the water vapor supersaturation,  $S$ , in the atmosphere, as well as the aerosol particle size and chemical composition (e.g., Dusek et al., 2006; Rose et al., 2010). The relationship between these parameters is described by the Köhler theory: The equilibrium water vapor pressure over strongly curved small droplets is much higher than the water vapor pressure over a flat surface (so-called Kelvin effect). Accordingly, comparatively high water vapor pressures – means supersaturated conditions – are necessary to form stable small droplets. Particularly, homogeneous droplet nucleation requires  $S$  levels of several hundred percent (Andreae and Rosenfeld, 2008). Heterogeneous droplet nucleation onto aerosol particles in the atmospherically most relevant size range takes place at much lower  $S$  levels around 1 %. The vapor pressure over an aqueous solution is lower in comparison to pure water (so-called Raoult effect), which enhances the importance of partly or even fully soluble particles in CCN activation (Pöschl et al., 2009). The water uptake of aerosol particles can be described very efficiently by the hygroscopicity parameter  $\kappa$  (Petters and Kreidenweis, 2007). For atmospheric particles, the  $\kappa$  values are typically in the range of 0.01 to 1, with large values representing a high ability to take up water (Andreae and Rosenfeld, 2008; Su et al., 2010).

With respect to microphysical processes in cloud formation and development, the number concentration of CCN,  $N_{CCN}(S)$ , as a function of  $S$  plays a key role, while  $S$  is predominantly determined by the updraft velocity,  $w$ , of the adiabatically rising air parcel at the cloud base. Depending on  $N_{CCN}(S)$  and  $S$ , a certain number of cloud droplets,  $N_d$ , is formed at the cloud base. Upon further cloud development and rising air masses, the initial droplets grow by condensation of water vapor, which can be observed as changes in the cloud drop size distribution (DSD). Thus, the DSD is a function of thermodynamic parameters (i.e.,  $w$ ), aerosol conditions (i.e.,  $N_{CCN}(S)$ ), and the cloud evolution (i.e., the cloud depth  $H$ ). Important bulk DSD properties are, in particular,  $N_d$  and the effective droplet radius  $r_e$  (Rosenfeld et al., 2014). For  $r_e > 11 \mu\text{m}$ , the probability of droplet collision and coalescence processes become significant and warm rain formation is initiated (Cecchini et al., 2017a, Cecchini et al., 2017b). For larger  $H$ , cold rain formation plays an increasingly important role, following ice formation in the presence of IN (Rosenfeld et al., 2008).

It is well documented that changing aerosol regimes, ranging from pristine to highly polluted states, influence the microphysical basis of the development of clouds and precipitation (e.g., Roberts et al., 2003; Andreae et al., 2004; Reutter et al., 2009). Specifically, pollution-induced changes, such as increased  $N_d$  with a corresponding decrease of average droplet size, intense competition for water vapor and, thus, a deceleration of drop growth rates, suppression of supersaturated conditions, reduced coalescence of smaller droplets, increased  $H$  as well as an invigoration of cloud dynamics and rain, are well documented (e.g., Koren et al., 2004; Freud et al., 2008; Koren et al., 2012). The aerosol influence on the cloud's microphysical basis alters the macrophysical cloud properties as well. Figure 2 illustrates how a man-made increase in  $N_{CCN}(S)$  causes an enhanced  $N_d$  and shifts the DSD to smaller droplets, which in turn strongly increase the cloud albedo (Carslaw et al., 2013). Note that the cloud albedo plays a critical role in the Earth radiative budget and, thus, man-made

changes of the cloud albedo constitutes one of the largest uncertainties in our current understanding of the changing climate system (Bony et al., 2015). Importantly, Figure 2 emphasizes the relationships between anthropogenic emissions,  $N_{CCN}(S)$ ,  $N_d$ , cloud albedo, and radiative forcing. With increasing anthropogenic emissions, the cloud albedo and the radiative forcing converge towards saturated conditions, which correspond to present-day (PD) pollution levels. This means, in turn, that the highest sensitivity of the relationships can be found towards clean, pristine conditions as an approximation a pre-industrial (PI) state. This further implies that a reduction of the large uncertainty in our understanding and modelling attempts of the impact of aerosol changes on cloud albedo and climate requires a better understanding of a PI aerosol state. The occurrence of pristine episodes, which approximate a PI state, is becoming increasingly rare in the PD atmosphere. Only certain marine regions and very few continental places nowadays still allow an observation of PI episodes (Hamilton et al., 2014).

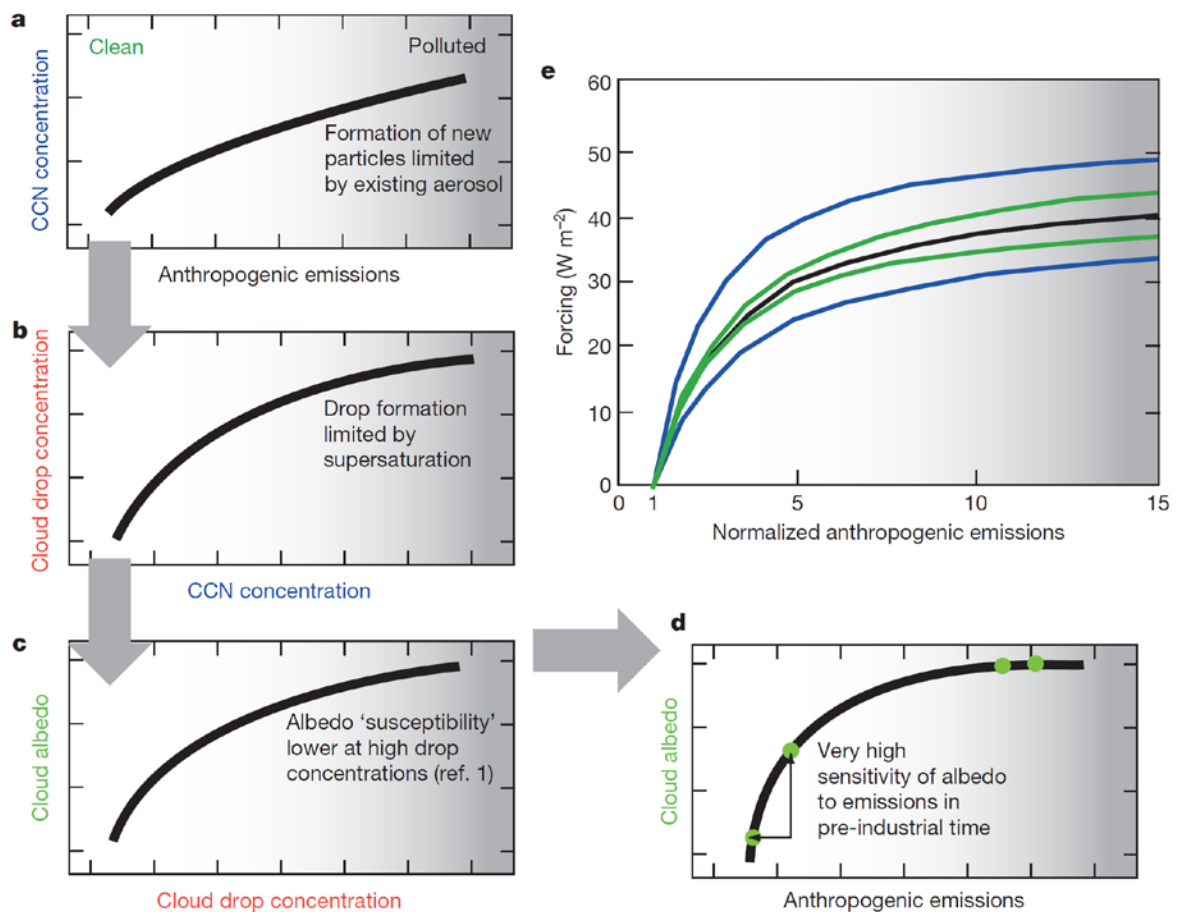


**Figure 2.** Schematics to explain the relationship between,  $N_{CCN}(S)$ ,  $N_d$ , and cloud albedo and the impact of natural emissions for the forcing uncertainty. Figure adopted from Carslaw et al. (2013).

## 1.2 Aerosols and clouds over the Amazon rainforest

The Amazon rainforest represents an ecosystem of global importance, which is subject to substantial man-made perturbations (Lenton et al., 2008; Davidson et al., 2012). The atmosphere over the rainforest ecosystem in the Amazon Basin represents an ‘outdoor laboratory’ of particular interest for atmospheric and climate research since it oscillates between a very clean wet season and a highly polluted dry season state (Martin et al., 2010; Andreae et al., 2015). The wet season provides one of the globally rare chances to observe pristine and, thus, approximately PI episodes in a vegetated continental environment (Andreae, 2007; Andreae et al., 2015). During this time of the year, the aerosol particle population, the cloud field, and the hydrological cycle of the Amazonian rain forest are mainly influenced by biogenic emissions of gases and aerosol particles as well as their atmospheric processing in combination with high absolute humidity and strong solar radiation (Martin et al. 2010). The main processes in this biogeochemical reactor, in which biogenic aerosols act as CCN and IN and, thus, influence the formation of clouds and precipitation, are illustrated in Figure 3 (Pöschl et al., 2010). This is in stark contrast to the dry season conditions, which are influenced by intense man-made pollution (e.g., Artaxo et al., 2013). Several studies have reported clear indications for pollution-related changes in cloud properties and precipitation patterns in the Amazon region (Davidson et al., 2012). However, numerous open questions regarding the cloud microphysical processes under pristine vs. strongly polluted condition remain. Thus, detailed aerosol and CCN observations under pristine conditions, as an approximation of a PI state, will enhance our understanding of the anthropogenic impact of the Earth atmosphere, in general, as well as the vulnerable Amazon region, in particular (Carslaw et al. 2013).

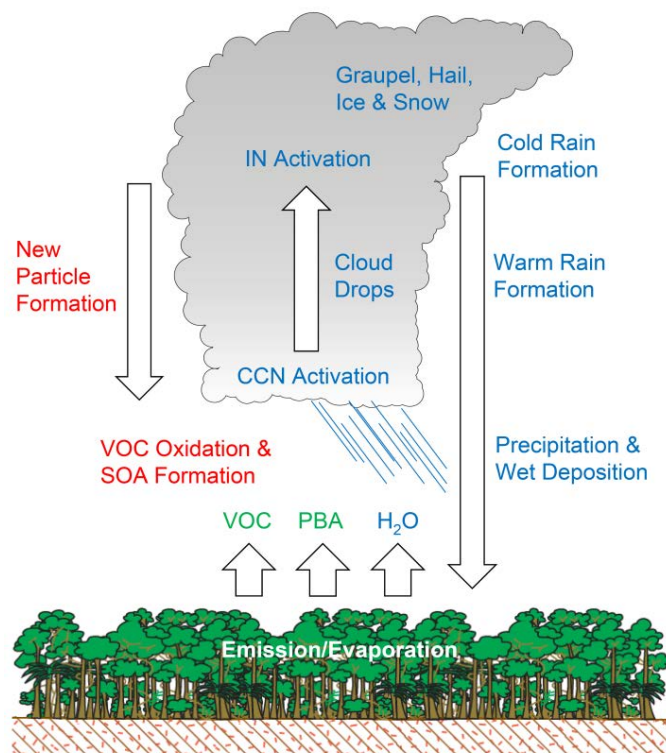


Figure 3. Cloud and biogenic aerosol cycle in the pristine Amazonian atmosphere. Figure adopted from Pöschl et al. (2010).

### 1.3 Research objectives

This thesis focusses on the aerosol-cloud-precipitation interactions in the globally important Amazon region by means of aerosol and CCN analyses in the context of two international and large-scale field experiments: First, the continuous and in-depth atmospheric observations at the Amazon Tall Tower Observatory (ATTO) site and, second, the aircraft measurements in the Amazon Basin as well as complementary mountain top measurements in Europe in the context of the ACRIDICON project.

#### 1.3.1 ATTO project

The ATTO site has been established as a long-term research station in an untouched rainforest region in the central Amazon Basin (for details see Andreae et al., 2015). Besides a broad set of meteorological, ecological, and trace gas observations, a comprehensive and detailed aerosol analysis is being conducted at the ATTO site. Improving our understanding of the aerosol-cloud-precipitation interaction as a function of pristine vs. highly polluted conditions represents one of the scientific core projects at the ATTO site. In 2014 and 2015, the ATTO site was part of the international GoAmazon2014/5 campaign, which took place at several sites in and around the city of Manaus (Martin et al., 2016; 2017). In the context of this thesis, systematic aerosol and CCN observations have been conducted as part of the ATTO and GoAmazon2014/5 research. This thesis summarizes the key results and conclusions.

#### 1.3.2 ACRIDICON project

The ACRIDICON project has combined research on aerosol-cloud-precipitation-radiation interactions as well as dynamics of convective and orographic cloud systems in the context of two field experiments: (i) The ACRIDICON-CHUVA campaign focused on tropical deep convective clouds in the Amazon Basin, in unique combination with the continuous ATTO research (Machado et al., 2014; Wendisch et al., 2016). For these observations, the high altitude long-range (HALO) aircraft has been used to study aerosol and cloud microphysics in detailed cloud profiling maneuvers during September 2014. For the aircraft observation, an aerosol and CCN instrument package has been designed and developed, which was operated successfully on board of HALO during ACRIDICON-CHUVA. (ii) Previous to the ACRIDICON-CHUVA experiments, the ACRIDICON-Zugspitze campaign was conducted at the mountain top station Schneefernerhaus in September 2012, focusing on orographic clouds. Here, size-resolved aerosol and CCN measurements were conducted.

## Chapter 2

# Results and conclusions

## 2.1 Individual studies

### 2.1.1 Long-term characterization of cloud condensation nuclei at the ATTO site and new model parametrization for CCN prediction

This study presents the first systematic analysis of aerosol and CCN key parameters in the Amazon region (i.e., at the ATTO site), spanning a full seasonal cycle and, thus, providing a detailed climatology of CCN properties. The key findings of the study are (i) the pronounced dependence of  $N_{CCN}(S)$  on the total aerosol number concentration,  $N_{CN}$ , ranging from clean wet season to polluted dry season conditions, (ii) the remarkable temporal stability of the  $\kappa$  levels without pronounced seasonal and diurnal trends, indicating the predominance of organic aerosols, and (iii) the clearly distinct properties of the Aitken vs. accumulation mode aerosol populations, presumably as a function of atmospheric aerosols processing. Based on this systematic aerosol and CCN characterization, different CCN parametrization schemes were tested and compared to represent the CCN key features in modelling studies. Moreover, a novel parametrization strategy using CCN efficiency spectra and concentrations as a functions of  $S$  was developed, allowing accurate CCN predictions based on a small set of input parameters. For details see Appendix B.1, Pöhlker et al., Atmos. Chem. Phys., 2016.

### 2.1.2 Comparison of pristine, biomass burning, and long-range transport conditions at the ATTO site

This study is based on Pöhlker et al. 2016 and presents the variability of aerosol and CCN key parameters, resolving aerosol advection and transformation processes. Particularly, the analysis focusses on the following four case studies, which present the most characteristic states of the Amazonian atmosphere: (i) present-day pristine periods, being characterized by the absence of detectable anthropogenic pollution aerosols, (ii) long-range transport of African aerosols, bringing a mixture of biomass burning smoke, Saharan dust and Atlantic sea spray, (iii) the influence of a pronounced, aged biomass burning plume from deforestation fires in Southern Brazil, and (iv) a superposition of nearby fires and the plume of an African volcanic eruption. For the case studies, the characteristic  $N_{CN}$ ,  $N_{CCN}(S)$ , and  $\kappa$  size distributions were extracted, which reveal distinctly different aerosol populations. Moreover, the CCN efficiency spectra – as CCN signatures of the contrasting case studies – were obtained as predestinated input data for dedicated modelling studies. Moreover, the CCN efficiency spectra help to understand the specific response of the contrasting aerosol populations to varying supersaturation regime. For details see Appendix B.2, Pöhlker et al., Atmos. Chem. Phys. Discuss., 2017.

### 2.1.3 Aerosol nucleation in the upper troposphere over the Amazon during the ACRIDICON-CHUVA campaign

During the ACRIDICON-CHUVA campaign, remarkably high  $N_{\text{CN}}$  levels were observed in the upper troposphere (UT), exceeding  $N_{\text{CN}}$  levels in the planetary boundary layer (BL) by one or two orders of magnitude. Convective transport of BL aerosols into the UT could be ruled out due to characteristic difference in the particle's size range and chemical composition. A strong enhancement of small particles (<90 nm diameter) in convective outflows suggest that new particle formation takes place in the UT, followed by frequent downward transport of these particles in the BL. These newly formed particles, however, grow into a CCN-relevant size and, thus, enhance  $N_{\text{CCN}}$  in the UT as well. This process may also explain the origin and nature of newly formed particles in the pristine and, thus, PI, atmosphere. My contributions to this study were the development, certification, and operation of the CCN and aerosol instrument package on board of the HALO aircraft as well as the analysis and interpretation of CCN profiles and related data. For details see Appendix B.3., Andreae, et al., Atmos. Chem. Phys. Discuss. 2017.

### 2.1.4 Assessment of cloud supersaturation during the ACRIDICON-Zugspitze campaign

During the ACRIDICON-Zugspitze campaign, a new method has been developed to use, measured aerosol and CCN size distributions to estimate effective water vapor supersaturation levels inside clouds. The CCN based method has the advantage that it does not require specific knowledge or assumptions about aerosol properties. During the evolution of a cloud, the air masses are exposed to different  $S$  levels. This study presents a method to distinguish between the lower and upper bounds ( $S_{\text{low}}$ ,  $S_{\text{high}}$ ) and the average value ( $S_{\text{avg}}$ ) of peak supersaturation, encountered by the particles in the cloud. For the investigated cloud event, the following supersaturation levels were derived  $S_{\text{low}} \approx 0.07\text{-}0.25\%$ ,  $S_{\text{high}} \approx 0.86\text{-}1.31\%$ , and  $S_{\text{avg}} \approx 0.42\text{-}0.68\%$ . For details see Appendix B.4., Krüger, et al., Atmos. Meas. Tech. 2012.

### 2.1.5 Satellite retrieval of CCN concentrations

To assess the impact of aerosols on cloud radiative properties on global scales, a simultaneous satellite retrieval of the updraft velocities,  $w$ , and  $N_{\text{CCN}}(S)$  at cloud based is required. In a new approach,  $w$  and  $N_{\text{CCN}}(S)$  were obtained from an operational polar orbiting weather satellite. This study presents the evaluation of the  $N_{\text{CCN}}(S)$  calculated based on satellite data by comparing the results with ground based CCN measurements from three locations, including the ATTO site. The satellite-derived CCN results are consistent with the ground based CCN measurements with an accuracy of  $\pm 30\%$ . My contributions to this study were the measurement and analysis of the CCN data from the ATTO site as well as the evaluation and uncertainty analysis of satellite-derived vs. in-situ measured CCN concentrations. For details see Appendix B.5., Rosenfeld, et al., Proc. Natl. Acad. Sci. USA, 2016.

## 2.2 Summary and outlook

The main results and focal points of this dissertation can be summarized as follows:

- (i) At the Amazon Tall Tower Observatory (ATTO), a robust experimental setup was developed and operated to obtain a unique data set of annual and seasonal averages of the aerosol and CCN properties. Characteristic case studies were performed to characterize different atmospheric conditions including biomass burning influence, long range transported effects, and a present-day pristine state approximating pre-industrial conditions. The CCN observations at the ATTO site were used to evaluate a new method to retrieve CCN concentrations from satellite data.
- (ii) A novel parameterization of CCN efficiency spectra and concentrations as a function of water vapor supersaturation was developed. It enhances the efficiency, accuracy, and reliability with which CCN concentrations can be taken into account in process models and large-scale models of clouds and precipitation, the atmosphere and climate.
- (iii) During the ACRIDICON-Zugspitze campaign, cloud supersaturations were derived from both aerosol size distribution and size-resolved CCN measurements.
- (iv) For the ACRIDICON-CHUVA campaign with the HALO aircraft, an instrument package for airborne CCN and aerosol measurements was designed, developed, and operated during research flights in the Amazon Basin. The analysis of the vertical structure and evolution of convective clouds provided unprecedented insights into new particle formation in the upper troposphere. This process appears to be an important source of aerosols and CCN in the rainforest boundary layer, which links the aircraft results to the ground-based ATTO observations.

Furthermore, long-term size-resolved aerosol and CCN measurements at a remote marine location at the Atlantic coast of Barbados were started within this PhD study. The analysis and interpretation of the aerosol and CCN properties in connection to the cloud properties measured at the Barbados Cloud Observatory will further advance the understanding of aerosol-cloud interactions in a marine environment (green vs. blue ocean). The instrument setup, which has been developed for the ACRIDICON-CHUVA project, was also successfully operated during the EMeRGe-EU campaign (*Effect of Megacities on the Transport and Transformation of Pollutants on the Regional to Global Scales*) targeting European megacity plumes in July 2017. The companion campaign EMeRGe-Asia will target Asian megacities and is scheduled for 2018.

The research performed in the context of this PhD study has resulted in three first author papers and contributed to 18 further studies, which have been published or are currently undergoing peer review in international scientific journals.

# References

- Andreae, M. O., Acevedo, O. C., Araùjo, A., Artaxo, P., Barbosa, C. G. G., Barbosa, H. M. J., Brito, J., Carbone, S., Chi, X., Cintra, B. B. L., da Silva, N. F., Dias, N. L., Dias-Júnior, C. Q., Ditas, F., Ditz, R., Godoi, A. F. L., Godoi, R. H. M., Heimann, M., Hoffmann, T., Kesselmeier, J., Könemann, T., Krüger, M. L., Lavric, J. V., Manzi, A. O., Moran-Zuloaga, D., Nölscher, A. C., Santos Nogueira, D., Piedade, M. T. F., Pöhlker, C., Pöschl, U., Rizzo, L. V., Ro, C. U., Ruckteschler, N., Sá, L. D. A., Sá, M. D. O., Sales, C. B., Santos, R. M. N. D., Saturno, J., Schöngart, J., Sörgel, M., de Souza, C. M., de Souza, R. A. F., Su, H., Targhetta, N., Tóta, J., Trebs, I., Trumbore, S., van Eijck, A., Walter, D., Wang, Z., Weber, B., Williams, J., Winderlich, J., Wittmann, F., Wolff, S., and Yáñez-Serrano, A. M.: The Amazon Tall Tower Observatory (ATTO): overview of pilot measurements on ecosystem ecology, meteorology, trace gases, and aerosols, *Atmos. Chem. Phys.*, 15, 10723-10776, 10.5194/acp-15-10723-2015, 2015.
- Andreae, M. O., and Rosenfeld, D.: Aerosol-cloud-precipitation interactions. Part 1. The nature and sources of cloud-active aerosols, *Earth-Sci. Rev.*, 89, 13-41, 10.1016/j.earscirev.2008.03.001, 2008.
- Andreae, M. O.: Aerosols before pollution, *Science*, 315, 50-51, 10.1126/science.1136529, 2007.
- Andreae, M. O., Rosenfeld, D., Artaxo, P., Costa, A. A., Frank, G. P., Longo, K. M., and Silva-Dias, M. A. F.: Smoking rain clouds over the Amazon, *Science*, 303, 1337-1342, 10.1126/science.1092779, 2004.
- Artaxo, P., Rizzo, L. V., Brito, J. F., Barbosa, H. M. J., Arana, A., Sena, E. T., Cirino, G. G., Bastos, W., Martin, S. T., and Andreae, M. O.: Atmospheric aerosols in Amazonia and land use change: from natural biogenic to biomass burning conditions, *Faraday Discuss.*, 165, 203-235, 10.1039/c3fd00052d, 2013
- Bony, S., Stevens, B., Frierson, D. M. W., Jakob, C., Kageyama, M., Pincus, R., Shepherd, T. G., Sherwood, S. C., Siebesma, A. P., Sobel, A. H., Watanabe, M., and Webb, M. J.: Clouds, circulation and climate sensitivity, *Nature Geoscience*, 8, 261-268, 10.1038/ngeo2398, 2015.
- Carslaw, K. S., Lee, L. A., Reddington, C. L., Pringle, K. J., Rap, A., Forster, P. M., Mann, G. W., Spracklen, D. V., Woodhouse, M. T., Regayre, L. A., and Pierce, J. R.: Large contribution of natural aerosols to uncertainty in indirect forcing, *Nature*, 503, 67-+, 10.1038/nature12674, 2013.
- Cecchini, M. A., Machado, L. A. T., Andreae, M. O., Martin, S. T., Albrecht, R. I., Artaxo, P., Barbosa, H. M. J., Borrmann, S., Fütterer, D., Jurkat, T., Mahnke, C., Minikin, A., Molleker, S., Pöhlker, M. L., Pöschl, U., Rosenfeld, D., Voigt, C., Wenzierl, B., and Wendisch, M.: Sensitivities of Amazonian clouds to aerosols and updraft speed, *Atmos. Chem. Phys.*, 17, 10037-10050, <https://doi.org/10.5194/acp-17-10037-2017>, 2017a.
- Cecchini, M. A., Machado, L. A. T., Wendisch, M., Costa, A., Krämer, M., Andreae, M. O., Afchine, A., Albrecht, R. I., Artaxo, P., Borrmann, S., Fütterer, D., Klimach, T., Mahnke, C., Martin, S. T., Minikin, A., Molleker, S., Pardo, L. H., Pöhlker, C., Pöhlker, M. L., Pöschl, U., Rosenfeld, D., and Weinzierl, B.: Illustration of microphysical processes in Amazonian deep convective clouds in the Gamma phase space: Introduction and potential applications, *Atmos. Chem. Phys. Discuss.*, 2017, 1-49, 10.5194/acp-2017-185, 2017b
- Crutzen, P. J.: Geology of mankind, *Nature*, 415, 23-23, 10.1038/415023a, 2002.
- Davidson, E. A., de Araujo, A. C., Artaxo, P., Balch, J. K., Brown, I. F., Bustamante, M. M. C., Coe, M. T., DeFries, R. S., Keller, M., Longo, M., Munger, J. W., Schroeder, W., Soares-Filho, B. S., Souza, C. M., Jr., and Wofsy, S. C.: The Amazon basin in transition, *Nature*, 481, 321-328, 10.1038/nature10717, 2012.
- Dusek, U., Frank, G. P., Hildebrandt, L., Curtius, J., Schneider, J., Walter, S., Chand, D., Drewnick, F., Hings, S., Jung, D., Borrmann, S., and Andreae, M. O.: Size matters more than chemistry for cloud-nucleating ability of aerosol particles, *Science*, 312, 1375-1378, 10.1126/science.1125261, 2006.
- Freud, E., Rosenfeld, D., Andreae, M. O., Costa, A. A., and Artaxo, P.: Robust relations between CCN and the vertical evolution of cloud drop size distribution in deep convective clouds, *Atmospheric Chemistry and Physics*, 8, 1661-1675, 2008.
- Hamilton, D. S., Lee, L. A., Pringle, K. J., Reddington, C. L., Spracklen, D. V., and Carslaw, K. S.: Occurrence of pristine aerosol environments on a polluted planet, *Proceedings of the National Academy of Sciences of the United States of America*, 111, 18466-18471, 10.1073/pnas.1415440111, 2014.
- Hoose, C., and Möhler, O.: Heterogeneous ice nucleation on atmospheric aerosols: a review of results from laboratory experiments, *Atmospheric Chemistry and Physics*, 12, 9817-9854, 10.5194/acp-12-9817-2012, 2012.
- Koren, I., Altaratz, O., Remer, L. A., Feingold, G., Martins, J. V., and Heiblum, R. H.: Aerosol-induced intensification of rain from the tropics to the mid-latitudes, *Nature Geoscience*, 5, 118-122, 10.1038/ngeo1364, 2012.

- Koren, I., Kaufman, Y. J., Remer, L. A., and Martins, J. V.: Measurement of the effect of Amazon smoke on inhibition of cloud formation, *Science*, 303, 1342-1345, 10.1126/science.1089424, 2004.
- Lenton, T. M., Held, H., Kriegler, E., Hall, J. W., Lucht, W., Rahmstorf, S., and Schellnhuber, H. J.: Tipping elements in the Earth's 55 climate system, *Proceedings of the National Academy of Sciences*, 105, 1786-1793, 10.1073/pnas.0705414105, 2008.
- Machado, L. A. T., Dias, M. A. F. S., Morales, C., Fisch, G., Vila, D., Albrecht, R., Goodman, S. J., Calheiros, A. J. P., Biscaro, T., Kummerow, C., Cohen, J., Fitzjarrald, D., Nascimento, E. L., Sakamoto, M. S., Cunningham, C., Chaboureaud, J.-P., Petersen, W. A., 5 Adams, D. K., Baldini, L., Angelis, C. F., Sapucci, L. F., Salio, P., Barbosa, H. M. J., Landolfo, E., Souza, R. A. F., Blakeslee, R. J., Bailey, J., Freitas, S., Lima, W. F. A., and Tokay, A.: The Chuva Project: How Does Convection Vary across Brazil?, *Bulletin of the American Meteorological Society*, 95, 1365-1380, doi:10.1175/BAMS-D-13-00084.1, 2014.
- Martin, S. T., Artaxo, P., Machado, L., Manzi, A. O., Souza, R. A. F., Schumacher, C., Wang, J., Biscaro, T., Brito, J., Calheiros, A., Jardine, K., Medeiros, A., Portela, B., Sá, S. S. d., Adachi, K., Aiken, A. C., Albrecht, R., Alexander, L., Andreae, M. O., Barbosa, H. M. J., Buseck, P., Chand, D., Comstock, J. M., Day, D. A., Dubey, M., Fan, J., Fast, J., Fisch, G., Fortner, E., Giangrande, S., Gilles, M., Goldstein, A. H., Guenther, A., Hubbe, J., Jensen, M., Jimenez, J. L., Keutsch, F. N., Kim, S., Kuang, C., Laskin, A., McKinney, K., Mei, F., Miller, M., Nascimento, R., Pauliquevis, T., Pekour, M., Peres, J., Petäjä, T., Pöhlker, C., Pöschl, U., Rizzo, L., Schmid, 25 B., Shilling, J. E., Dias, M. A. S., Smith, J. N., Tomlinson, J. M., Tóta, J., and Wendisch, M.: The Green Ocean Amazon Experiment (GoAmazon2014/5) Observes Pollution Affecting Gases, Aerosols, Clouds, and Rainfall over the Rain Forest, *Bulletin of the American Meteorological Society*, 98, 981-997, 10.1175/bams-d-15-00221.1, 2017.
- Martin, S. T., Artaxo, P., Machado, L. A. T., Manzi, A. O., Souza, R. A. F., Schumacher, C., Wang, J., Andreae, M. O., Barbosa, H. M. J., Fan, J., Fisch, G., Goldstein, A. H., Guenther, A., Jimenez, J. L., Pöschl, U., Silva Dias, M. A., Smith, J. N., and Wendisch, M.: Introduction: Observations and Modeling of the Green Ocean Amazon (GoAmazon2014/5), *Atmos. Chem. Phys.*, 16, 4785-4797, 10.5194/acp-16-4785-2016, 2016.
- Martin, S. T., Andreae, M. O., Artaxo, P., Baumgardner, D., Chen, Q., Goldstein, A. H., Guenther, A., Heald, C. L., Mayol-Bracero, O. L., McMurry, P. H., Pauliquevis, T., Poschl, U., Prather, K. A., Roberts, G. C., Saleska, S. R., Dias, M. A. S., Spracklen, D. V., Swietlicki, E., and Trebs, I.: Sources and properties of Amazonian aerosol particles, *Rev. Geophys.*, 48, RG2002, 10.1029/2008rg000280, 2010.
- Petters, M. D., and Kreidenweis, S. M.: A single parameter representation of hygroscopic growth and cloud condensation nucleus activity, *Atmospheric Chemistry and Physics*, 7, 1961-1971, 2007.
- Pöschl, U., and Shiraiwa, M.: Multiphase Chemistry at the Atmosphere-Biosphere Interface Influencing Climate and Public Health in the Anthropocene, *Chemical Reviews*, 115, 4440-4475, 10.1021/cr500487s, 2015.
- Pöschl, U., Martin, S. T., Sinha, B., Chen, Q., Gunthe, S. S., Huffman, J. A., Borrmann, S., Farmer, D. K., Garland, R. M., Helas, G., Jimenez, J. L., King, S. M., Manzi, A., Mikhailov, E., Pauliquevis, T., Petters, M. D., Prenni, A. J., Roldin, P., Rose, D., Schneider, J., Su, H., Zorn, S. R., Artaxo, P., and Andreae, M. O.: Rainforest Aerosols as Biogenic Nuclei of Clouds and Precipitation in the Amazon, *Science*, 329, 1513-1516, 10.1126/science.1191056, 2010.
- Pöschl, U., Rose, D., and Andreae, M. O.: Climatologies of Cloud-related Aerosols. Part 2: Particle Hygroscopicity and Cloud Condensation Nucleus Activity, in: *Clouds in the Perturbed Climate System: Their Relationship to Energy Balance, Atmospheric Dynamics, and Precipitation*, edited by: Heintzenberg, J., and Charlson, R. J., MIT Press, Cambridge, 58 - 72, 2009.
- Pöschl, U.: Atmospheric aerosols: Composition, transformation, climate and health effects, *Angewandte Chemie-International Edition*, 44, 7520-7540, 10.1002/anie.200501122, 2005.
- Reinmuth-Selzle, K., Kampf, C. J., Lucas, K., Lang-Yona, N., Frohlich-Nowoisky, J., Shiraiwa, M., Lakey, P. S. J., Lai, S. C., Liu, F. B., Kunert, A. T., Ziegler, K., Shen, F. X., Sgarbanti, R., Weber, B., Bellinghausen, I., Saloga, J., Weller, M. G., Duschl, A., Schuppan, D., and Poschl, U.: Air Pollution and Climate Change Effects on Allergies in the Anthropocene: Abundance, Interaction, and Modification of Allergens and Adjuvants, *Environmental Science & Technology*, 51, 4119-4141, 10.1021/acs.est.6b04908, 2017.
- Roberts, G. C., Nenes, A., Seinfeld, J. H., and Andreae, M. O.: Impact of biomass burning on cloud properties in the Amazon Basin, *Journal of Geophysical Research-Atmospheres*, 108, 10.1029/2001jd000985, 2003.
- Rose, D., Nowak, A., Achtert, P., Wiedensohler, A., Hu, M., Shao, M., Zhang, Y., Andreae, M. O., and Poschl, U.: Cloud condensation nuclei in polluted air and biomass burning smoke near the mega-city Guangzhou, China - Part 1: Size-resolved measurements and implications for the modeling of aerosol particle hygroscopicity and CCN activity, *Atmospheric Chemistry and Physics*, 10, 3365-3383, 2010.

- Rosenfeld, D., Andreae, M. O., Asmi, A., Chin, M., de Leeuw, G., Donovan, D. P., Kahn, R., Kinne, S., Kivekas, N., Kulmala, M., Lau, W., Schmidt, K. S., Suni, T., Wagner, T., Wild, M., and Quaas, J.: Global observations of aerosol-cloud-precipitation-climate interactions, *Rev. Geophys.*, 52, 750-808, 10.1002/2013rg000441, 2014.
- Rosenfeld, D., Lohmann, U., Raga, G. B., O'Dowd, C. D., Kulmala, M., Fuzzi, S., Reissell, A., and Andreae, M. O.: Flood or drought: How do aerosols affect precipitation?, *Science*, 321, 1309-1313, 10.1126/science.1160606, 2008.
- Reutter, P., Su, H., Trentmann, J., Simmel, M., Rose, D., Gunthe, S. S., Wernli, H., Andreae, M. O., and Pöschl, U.: Aerosol- and updraft-limited regimes of cloud droplet formation: influence of particle number, size and hygroscopicity on the activation of cloud condensation nuclei (CCN), *Atmos. Chem. Phys.*, 9, 7067-7080, 10.5194/acp-9-7067-2009, 2009.
- Satheesh, S. K., and Moorthy, K. K.: Radiative effects of natural aerosols: A review, *Atmospheric Environment*, 39, 2089-2110, 2005.
- Seinfeld, J. H., Bretherton, C., Carslaw, K. S., Coe, H., DeMott, P. J., Dunlea, E. J., Feingold, G., Ghan, S., Guenther, A. B., Kahn, R., Kraucunas, I., Kreidenweis, S. M., Molina, M. J., Nenes, A., Penner, J. E., Prather, K. A., Ramanathan, V., Ramaswamy, V., Rasch, P. J., Ravishankara, A. R., Rosenfeld, D., Stephens, G., and Wood, R.: Improving our fundamental understanding of the role of aerosol-cloud interactions in the climate system, *Proceedings of the National Academy of Sciences of the United States of America*, 113, 5781-5790, 10.1073/pnas.1514043113, 2016.
- Solomon, S., Qin, D., Manning, Z., Chen, Z., Marquis, M., Avery, K. B., Tignor, M., and Miller, H. L. E.: IPCC 4th Assessment Report, Cambridge Univ. Press, Cambridge, 2007.
- Steffen, W., Grinevald, J., Crutzen, P., and McNeill, J.: The Anthropocene: conceptual and historical perspectives, *Philosophical Transactions of the Royal Society a-Mathematical Physical and Engineering Sciences*, 369, 842-867, 10.1098/rsta.2010.0327, 2011.
- Su, H., Rose, D., Cheng, Y. F., Gunthe, S. S., Massling, A., Stock, M., Wiedensohler, A., Andreae, M. O., and Pöschl, U.: Hygroscopicity distribution concept for measurement data analysis and modeling of aerosol particle mixing state with regard to hygroscopic growth and CCN activation, *Atmos. Chem. Phys.*, 10, 7489-7503, 10.5194/acp-10-7489-2010, 2010.
- Tao, W. K., Chen, J. P., Li, Z. Q., Wang, C., and Zhang, C. D.: Impact of aerosols on convective clouds and precipitation, *Rev. Geophys.*, 50, 10.1029/2011rg000369, 2012.
- Wendisch, M., Pöschl, U., Andreae, M. O., Machado, L. A. T., Albrecht, R., Schlager, H., Rosenfeld, D., Martin, S. T., Abdelmonem, 40 A., Afchine, A., Araújo, A., Artaxo, P., Aufmhoff, H., Barbosa, H. M. J., Borrmann, S., Braga, R., Buchholz, B., Cecchini, M. A., Costa, A., Curtius, J., Dollner, M., Dorf, M., Dreiling, V., Ebert, V., Ehrlich, A., Ewald, F., Fisch, G., Fix, A., Frank, F., Fütterer, D., Heckl, C., Heidelberg, F., Hüneke, T., Jäkel, E., Järvinen, E., Jurkat, T., Kanter, S., Kästner, U., Kenntner, M., Kesselmeier, J., Klimach, T., Knecht, M., Kohl, R., Kölling, T., Krämer, M., Krüger, M., Krisna, T. C., Lavric, J. V., Longo, K., Mahnke, C., Manzi, A. O., Mayer, B., Mertes, S., Minikin, A., Molleker, S., Münch, S., Nillius, B., Pfeilsticker, K., Pöhlker, C., Roiger, A., Rose, D., 45 Rosenow, D., Sauer, D., Schnaiter, M., Schneider, J., Schulz, C., Souza, R. A. F. d., Spanu, A., Stock, P., Vila, D., Voigt, C., Walser, A., Walter, D., Weigel, R., Weinzierl, B., Werner, F., Yamasoe, M. A., Ziereis, H., Zinner, T., and Zöger, M.: The ACRIDICON-CHUVA campaign: Studying tropical deep convective clouds and precipitation over Amazonia using the new German research aircraft HALO, *Bulletin of the American Meteorological Society*, 0, null, doi:10.1175/BAMS-D-14-00255.1, 2016.

## Appendix A

### List of related publications and presentations

#### Peer-reviewed publications and manuscripts currently in review

- 21 Saturno, J., Holanda, B. A., Pöhlker, C., Ditas, F., Wang, Q., Morán-Zuloaga, D., Brito, J., Carbone, S., Cheng, Y., Chi, X., Ditas, J., Hoffmann, T., Hrabě de Angelis, I., Könemann, T., Lavrič, J. V., Ma, N., Ming, J., Paulsen, H., Pöhlker, M. L., Rizzo, L. V., Schlag, P., Su, H., Walter, D., Wolff, S., Zhang, Y., Artaxo, P., Pöschl, U. and Andreae, M. O.: Black and brown carbon over central Amazonia: Long-term aerosol measurements at the ATTO site, **Atmos. Chem. Phys. Discuss.**, submitted, 2017.
- 20 Moran-Zuloaga, D., Ditas, F., Walter, D., Saturno, J., Brito, J., Carbone, S., Chi, X., Hrabě de Angelis, I., Baars, H., Godoi, R. H. M., Heese, B., Holanda, B. A., Lavrič, J. V., Martin, S. T., Ming, J., Pöhlker, M. L., Ruckteschler, N., Su, H., Wang, Y., Wang, Q., Wang, Z., Weber, B., Wolff, S., Artaxo, P., Pöschl, U., Andreae, M. O. and Pöhlker, C.: Long-term study on coarse mode aerosols in the Amazon rain forest with the frequent intrusion of Saharan dust plumes, **Atmos. Chem. Phys. Discuss.**, submitted, 2017.
- 19 Machado, L. A. T., Calheiros, A. J. P., Biscaro, T., Giangrande, S., Silva Dias, M. A. F., Cecchini, M. A., Albrecht, R., Andreae, M. O., Araujo, W. F., Artaxo, P., Borrmann, S., Braga, R., Burleyson, C., Eichholz, C. W., Fan, J., Feng, Z., Fisch, G. F., Jensen, M. P., Martin, S. T., Pöschl, U., Pöhlker, C., Pöhlker, M. L., Ribaud, J. F., Rosenfeld, D., Saraiva, J. M. B., Schumacher, C., Thalman, R., Walter, D., and Wendisch, M.: Overview: Precipitation Characteristics and Sensitivities to the Environmental Conditions during GoAmazon2014/5 and ACRIDICON-CHUVA, **Atmos. Chem. Phys. Discuss.**, 2017, 1-41, 10.5194/acp-2017-990, 2017.
- 18 Pöhlker, M. L., Ditas, F., Saturno, J., Klimach, T., Hrabě de Angelis, I., Araújo, A., Brito, J., Carbone, S., Cheng, Y., Chi, X., Ditz, R., Gunthe, S. S., Kandler, K., Kesselmeier, J., Könemann, T., Lavrič, J. V., Martin, S. T., Mikhailov, E., Moran-Zuloaga, D., Rizzo, L. V., Rose, D., Su, H., Thalman, R., Walter, D., Wang, J., Wolff, S., Barbosa, H. M. J., Artaxo, P., Andreae, M. O., Pöschl, U., and Pöhlker, C.: Long-term observations of cloud condensation nuclei in the Amazon rain forest – Part 2: Variability and characteristic differences under near-pristine, biomass burning, and long-range transport conditions, **Atmos. Chem. Phys. Discuss.**, 2017, 1-51, 10.5194/acp-2017-847, 2017.
- 17 Cecchini, M. A., Machado, L. A. T., Andreae, M. O., Martin, S. T., Albrecht, R. I., Artaxo, P., Barbosa, H. M. J., Borrmann, S., Fütterer, D., Jurkat, T., Mahnke, C., Minikin, A., Mollenker, S., Pöhlker, M. L., Pöschl, U., Rosenfeld, D., Voigt, C., Wenzierl, B., and Wendisch, M.: Sensitivities of Amazonian clouds to aerosols and updraft speed, **Atmos. Chem. Phys.**, 17, 10037-10050, 10.5194/acp-17-10037-2017.

- 16 Schmale, J., Henning, S., Decesari, S., Henzing, B., Keskinen, H., Paramonov, M., Sellegri, K., Ovadnevaite, J., Pöhlker, M. L., Brito, J., Bougiatioti, A., Kristensson, A., Kalivitis, N., Stavroulas, I., Carbone, S., Jefferson, A., Park, M., Schlag, P., Iwamoto, Y., Aalto, P., Äijälä, M., Bukowiecki, N., Ehn, M., Frank, G., Fröhlich, R., Frumau, A., Herrmann, E., Herrmann, H., Holzinger, R., Kos, G., Kulmala, M., Mihalopoulos, N., Nenes, A., O'Dowd, C., Petäjä, T., Picard, D., Pöhlker, C., Pöschl, U., Poulain, L., Prévôt, A. S. H., Swietlicki, E., Andreae, M. O., Artaxo, P., Wiedensohler, A., Ogren, J., Matsuki, A., Yum, S. S., Stratmann, F., Baltensperger, U., and Gysel, M.: What do we learn from long-term cloud condensation nuclei number concentration, particle number size distribution, and chemical composition measurements at regionally representative observatories?, **Atmos. Chem. Phys. Discuss.**, 2017, 1-51, 10.5194/acp-2017-798, 2017.
- 15 Andreae, M. O., Afchine, A., Albrecht, R., Holanda, B. A., Artaxo, P., Barbosa, H. M. J., Bormann, S., Cecchini, M. A., Costa, A., Dollner, M., Fütterer, D., Järvinen, E., Jurkat, T., Klimach, T., Konemann, T., Knote, C., Krämer, M., Krisna, T., Machado, L. A. T., Mertes, S., Minikin, A., Pöhlker, C., Pöhlker, M. L., Pöschl, U., Rosenfeld, D., Sauer, D., Schlager, H., Schnaiter, M., Schneider, J., Schulz, C., Spanu, A., Sperling, V. B., Voigt, C., Walser, A., Wang, J., Weinzierl, B., Wendisch, M., and Ziereis, H.: Aerosol characteristics and particle production in the upper troposphere over the Amazon Basin, **Atmos. Chem. Phys. Discuss.**, 2017, 1-95, 10.5194/acp-2017-694, 2017.
- 14 Cecchini, M. A., Machado, L. A. T., Wendisch, M., Costa, A., Krämer, M., Andreae, M. O., Afchine, A., Albrecht, R. I., Artaxo, P., Bormann, S., Fütterer, D., Klimach, T., Mahnke, C., Martin, S. T., Minikin, A., Molleker, S., Pardo, L. H., Pöhlker, C., Pöhlker, M. L., Pöschl, U., Rosenfeld, D., and Weinzierl, B.: Illustration of microphysical processes in Amazonian deep convective clouds in the Gamma phase space: Introduction and potential applications, **Atmos. Chem. Phys.**, 2017, 1-49, 10.5194/acp-2017-185, 2017.
- 13 Thalman, R., de Sá, S. S., Palm, B. B., Barbosa, H. M. J., Pöhlker, M. L., Alexander, M. L., Brito, J., Carbone, S., Castillo, P., Day, D. A., Kuang, C., Manzi, A., Ng, N. L., Sedlacek Iii, A. J., Souza, R., Springston, S., Watson, T., Pöhlker, C., Pöschl, U., Andreae, M. O., Artaxo, P., Jimenez, J. L., Martin, S. T., and Wang, J.: CCN activity and organic hygroscopicity of aerosols downwind of an urban region in central Amazonia: seasonal and diel variations and impact of anthropogenic emissions, **Atmos. Chem. Phys.**, 17, 11779-11801, 10.5194/acp-17-11779-2017, 2017.
- 12 Braga, R. C., Rosenfeld, D., Weigel, R., Jurkat, T., Andreae, M. O., Wendisch, M., Pöhlker, M. L., Klimach, T., Pöschl, U., Pöhlker, C., Voigt, C., Mahnke, C., Bormann, S., Albrecht, R. I., Molleker, S., Vila, D. A., Machado, L. A. T., and Artaxo, P.: Comparing calculated microphysical properties of tropical convective clouds at cloud base with measurements during the ACRIDICON-CHUVA campaign, **Atmos. Chem. Phys.**, 17, 7365-7386, 2017.

- 11 Saturno, J., Pöhlker, C., Massabò, D., Brito, J., Carbone, S., Cheng, Y., Chi, X., Ditas, F., Hrabě de Angelis, I., Morán-Zuloaga, D., Pöhlker, M. L., Rizzo, L. V., Walter, D., Wang, Q., Artaxo, P., Prati, P., and Andreae, M. O.: Comparison of different Aethalometer correction schemes and a reference multi-wavelength absorption technique for ambient aerosol data, **Atmos. Meas. Tech.**, 10, 2837-2850, 10.5194/amt-10-2837-2017, 2017.
- 10 Pöhlker, M. L., Pöhlker, C., Ditas, F., Klimach, T., Hrabě de Angelis, I., Araújo, A., Brito, J., Carbone, S., Cheng, Y., Chi, X., Ditz, R., Gunthe, S. S., Kesselmeier, J., Könemann, T., Lavrič, J. V., Martin, S. T., Mikhailov, E., Moran-Zuloaga, D., Rose, D., Saturno, J., Su, H., Thalman, R., Walter, D., Wang, J., Wolff, S., Barbosa, H. M. J., Artaxo, P., Andreae, M. O., and Pöschl, U.: Long-term observations of cloud condensation nuclei in the Amazon rain forest – Part 1: Aerosol size distribution, hygroscopicity, and new model parametrizations for CCN prediction, **Atmos. Chem. Phys.**, 16, 15709-15740, 10.5194/acp-16-15709-2016, 2016.
- 9 Wang, J., Krejci, R., Giangrande, S., Kuang, C., Barbosa, H. M. J., Brito, J., Carbone, S., Chi, X., Comstock, J., Ditas, F., Lavric, J., Manninen, H. E., Mei, F., Moran-Zuloaga, D., Pöhlker, C., Pöhlker, M. L., Saturno, J., Schmid, B., Souza, R. A. F., Springston, S. R., Tomlinson, J. M., Toto, T., Walte, D., Wimmer, D., Smith, J. N., Kulmala, M., Machado, L. A. T., Artaxo, P., Andreae, M. O., Petäjä, T., and Martin, S. T.: Vertical transport during rainfall sustains aerosol concentration in Amazon boundary layer, **Nature**, 2016.
- 8 Wendisch, M., Pöschl, U., Andreae, M. O., Machado, L. A. T., Albrecht, R., Schlager, H., Rosenfeld, D., Martin, S. T., Abdelmonem, A., Afchine, A., Araújo, A., Artaxo, P., Aufmhoff, H., Barbosa, H. M. J., Borrmann, S., Braga, R., Buchholz, B., Cecchini, M. A., Costa, A., Curtius, J., Dollner, M., Dorf, M., Dreiling, V., Ebert, V., Ehrlich, A., Ewald, F., Fisch, G., Fix, A., Frank, F., Fütterer, D., Heckl, C., Heidelberg, F., Hüneke, T., Jäkel, E., Järvinen, E., Jurkat, T., Kanter, S., Kästner, U., Kenntner, M., Kesselmeier, J., Klimach, T., Knecht, M., Kohl, R., Kölling, T., Krämer, M., Krüger, M., Krisna, T. C., Lavric, J. V., Longo, K., Mahnke, C., Manzi, A. O., Mayer, B., Mertes, S., Minikin, A., Molleker, S., Münch, S., Nillius, B., Pfeilsticker, K., Pöhlker, C., Roiger, A., Rose, D., Rosenow, D., Sauer, D., Schnaiter, M., Schneider, J., Schulz, C., Souza, R. A. F. d., Spanu, A., Stock, P., Vila, D., Voigt, C., Walser, A., Walter, D., Weigel, R., Weinzierl, B., Werner, F., Yamasoe, M. A., Ziereis, H., Zinner, T., and Zöger, M.: The ACRIDICON-CHUVA campaign: Studying tropical deep convective clouds and precipitation over Amazonia using the new German research aircraft HALO, **Bulletin of the American Meteorological Society**, 0, null, doi:10.1175/BAMS-D-14-00255.1, 2016.
- 7 Rosenfeld, D., Zheng, Y., Hashimshoni, E., Pöhlker, M. L., Jefferson, A., Pöhlker, C., Yu, X., Zhu, Y., Liu, G., Yue, Z., Fischman, B., Li, Z., Giguzin, D., Goren, T., Artaxo, P., Barbosa, H. M. J., Pöschl, U., and Andreae, M. O.: Satellite retrieval of cloud condensation nuclei concentrations by using clouds as CCN chambers, **Proceedings of the National Academy of Sciences**, 113, 5828-5834, 10.1073/pnas.1514044113, 2016.

- 6 Vogel, A. L., Schneider, J., Müller-Tautges, C., Phillips, G. J., Pöhlker, M. L., Rose, D., Zuth, C., Makkonen, U., Hakola, H., Crowley, J. N., Andreae, M. O., Pöschl, U., and Hoffmann, T.: Aerosol Chemistry Resolved by Mass Spectrometry: Linking Field Measurements of Cloud Condensation Nuclei Activity to Organic Aerosol Composition, **Environmental Science & Technology**, 10.1021/acs.est.6b01675, 2016.
- 5 Su, H., Cheng, Y., Ma, N., Wang, Z., Wang, X., Pöhlker, M. L., Nillius, B., Wiedensohler, A., and Pöschl, U.: A broad supersaturation scanning (BS2) approach for rapid measurement of aerosol particle hygroscopicity and cloud condensation nuclei activity, *Atmos. Meas. Tech.*, 9, 5183-5192, 10.5194/amt-9-5183-2016, 2016.
- 4 Andreae, M. O., Acevedo, O. C., Araùjo, A., Artaxo, P., Barbosa, C. G. G., Barbosa, H. M. J., Brito, J., Carbone, S., Chi, X., Cintra, B. B. L., da Silva, N. F., Dias, N. L., Dias-Júnior, C. Q., Ditas, F., Ditz, R., Godoi, A. F. L., Godoi, R. H. M., Heimann, M., Hoffmann, T., Kesselmeier, J., Könemann, T., Krüger, M. L., Lavric, J. V., Manzi, A. O., Lopes, A. P., Martins, D. L., Mikhailov, E. F., Moran-Zuloaga, D., Nelson, B. W., Nölscher, A. C., Santos Nogueira, D., Piedade, M. T. F., Pöhlker, C., Pöschl, U., Quesada, C. A., Rizzo, L. V., Ro, C. U., Ruckteschler, N., Sá, L. D. A., de Oliveira Sá, M., Sales, C. B., dos Santos, R. M. N., Saturno, J., Schöngart, J., Sörgel, M., de Souza, C. M., de Souza, R. A. F., Su, H., Targhetta, N., Tóta, J., Trebs, I., Trumbore, S., van Eijck, A., Walter, D., Wang, Z., Weber, B., Williams, J., Winderlich, J., Wittmann, F., Wolff, S., and Yáñez-Serrano, A. M.: The Amazon Tall Tower Observatory (ATTO): overview of pilot measurements on ecosystem ecology, meteorology, trace gases, and aerosols, **Atmos. Chem. Phys.**, 15, 10723-10776, 10.5194/acp-15-10723-2015, 2015.
- 3 Mikhailov, E. F., Mironov, G. N., Pöhlker, C., Chi, X., Krüger, M. L., Shiraiwa, M., Förster, J. D., Pöschl, U., Vlasenko, S. S., Ryshkevich, T. I., Weigand, M., Kilcoyne, A. L. D., and Andreae, M. O.: Chemical composition, microstructure, and hygroscopic properties of aerosol particles at the Zotino Tall Tower Observatory (ZOTTO), Siberia, during a summer campaign, **Atmos. Chem. Phys.**, 15, 8847-8869, 10.5194/acp-15-8847-2015, 2015.
- 2 Pöhlker, C., Saturno, J., Krüger, M. L., Förster, J.-D., Weigand, M., Wiedemann, K. T., Bechtel, M., Artaxo, P., and Andreae, M. O.: Efflorescence upon humidification? X-ray microspectroscopic in situ observation of changes in aerosol microstructure and phase state upon hydration, **Geophysical Research Letters**, 41, 3681-3689, 10.1002/2014GL059409, 2014.
- 1 Krüger, M. L., Mertes, S., Klimach, T., Cheng, Y. F., Su, H., Schneider, J., Andreae, M. O., Pöschl, U., and Rose, D.: Assessment of cloud supersaturation by size-resolved aerosol particle and cloud condensation nuclei (CCN) measurements, **Atmos. Meas. Tech.**, 7, 2615-2629, 10.5194/amt-7-2615-2014, 2014.

## Selected oral presentations

DMT User Group Workshop, Boulder, CO, USA, Nov **2012**

*Calibration of a cloud condensation nuclei counter (CCNC)*

Visit of University of Denver, Denver, CO, USA, Jun **2013**

*Investigation of atmospheric aerosol and cloud condensation nuclei*

European Aerosol Conference, Prague, Czech Republic, Sep **2013**

*Assessment of cloud supersaturation by cloud condensation nuclei (CCN) measurements*

GoAmazon2014/5 conference, Harvard University, Cambridge, MA, USA, May **2015**

*Cloud condensation nuclei (CCN) & single particle soot photometer (SP2) measurements during the ACRIDICON-CHUVA campaign & at T0a*

European Aerosol Conference, Milano, Italy, Sep **2015**

*Aircraft and ground-based measurements of cloud condensation nuclei (CCN) in and over the tropical rain forest of Amazonia*

ACRIDICON-CHUVA workshop, Mainz, Germany, Oct **2016**

*Vertical distribution and cloud interaction of cloud condensation nuclei*

1st HALO symposium, Oberpfaffenhofen, Germany, Mar **2017**

*Cloud interaction of Cloud Condensation Nuclei and Black Carbon Aerosol Particles*

MPGC seminar, Mainz, Germany, May **2017**

*Cloud Condensation Nuclei in the Central Amazon and in Barbados*

## Selected poster presentations

IMPRS autumn school, Dresden, Germany, November **2012**

*Cloud Condensation Nuclei (CCN) measurements during ACRIDICON-Zugspitze Campaign 2012*

INUIT summer school, Braunfels, Germany, Sep. **2013**

*Preliminary results of microspectroscopy on ice residuals*

EGU General Assembly, Vienna, Austria, Apr. **2014**

*Assessment of cloud supersaturation*

ACRIDICON-CHUVA workshop, Sao Jose dos Campos, Brazil May **2014**

*Cloud condensation nuclei (CCN) measurements during ACRIDICON-CHUVA*

Heareus seminar, Bad Honnef, Germany, March **2017**

*Cloud Interaction of Cloud Condensation Nuclei in the Amazon Basin during ACRIDICON-CHUVA*

EGU General Assembly, Vienna, Austria, April **2017**

*Long-Term Observations of Aerosol and Cloud Condensation Nuclei Concentrations in Barbados*

## Appendix B

### Selected publications

- B1. Pöhlker, M. L., Pöhlker, C., Ditas, F., Klimach, T., Hrabě de Angelis, I., Araújo, A., Brito, J., Carbone, S., Cheng, Y., Chi, X., Ditz, R., Gunthe, S. S., Kesselmeier, J., Könemann, T., Lavrič, J. V., Martin, S. T., Mikhailov, E., Moran-Zuloaga, D., Rose, D., Saturno, J., Su, H., Thalman, R., Walter, D., Wang, J., Wolff, S., Barbosa, H. M. J., Artaxo, P., Andreae, M. O., and Pöschl, U.: Long-term observations of cloud condensation nuclei in the Amazon rain forest – Part 1: Aerosol size distribution, hygroscopicity, and new model parametrizations for CCN prediction, **Atmos. Chem. Phys.**, 16, 15709-15740, 10.5194/acp-16-15709-2016, 2016.
- B2. Pöhlker, M. L., Ditas, F., Saturno, J., Klimach, T., Hrabě de Angelis, I., Araújo, A., Brito, J., Carbone, S., Cheng, Y., Chi, X., Ditz, R., Gunthe, S. S., Kandler, K., Kesselmeier, J., Könemann, T., Lavrič, J. V., Martin, S. T., Mikhailov, E., Moran-Zuloaga, D., Rizzo, L. V., Rose, D., Su, H., Thalman, R., Walter, D., Wang, J., Wolff, S., Barbosa, H. M. J., Artaxo, P., Andreae, M. O., Pöschl, U., and Pöhlker, C.: Long-term observations of cloud condensation nuclei in the Amazon rain forest – Part 2: Variability and characteristic differences under near-pristine, biomass burning, and long-range transport conditions, **Atmos. Chem. Phys. Discuss.**, 2017, 1-51, 10.5194/acp-2017-847, 2017.
- B3. Andreae, M. O., Afchine, A., Albrecht, R., Holanda, B. A., Artaxo, P., Barbosa, H. M. J., Bormann, S., Cecchini, M. A., Costa, A., Dollner, M., Fütterer, D., Järvinen, E., Jurkat, T., Klimach, T., Könemann, T., Knöche, C., Krämer, M., Krishna, T., Machado, L. A. T., Mertes, S., Minikin, A., Pöhlker, C., Pöhlker, M. L., Pöschl, U., Rosenfeld, D., Sauer, D., Schlager, H., Schnaiter, M., Schneider, J., Schulz, C., Spanu, A., Sperling, V. B., Voigt, C., Walser, A., Wang, J., Weinzierl, B., Wendisch, M., and Ziereis, H.: Aerosol characteristics and particle production in the upper troposphere over the Amazon Basin, **Atmos. Chem. Phys. Discuss.**, 2017, 1-95, 10.5194/acp-2017-694, 2017.
- B4. Krüger, M. L., Mertes, S., Klimach, T., Cheng, Y. F., Su, H., Schneider, J., Andreae, M. O., Pöschl, U., and Rose, D.: Assessment of cloud supersaturation by size-resolved aerosol particle and cloud condensation nuclei (CCN) measurements, **Atmos. Meas. Tech.**, 7, 2615-2629, 10.5194/amt-7-2615-2014, 2014.
- B5. Rosenfeld, D., Zheng, Y., Hashimshoni, E., Pöhlker, M. L., Jefferson, A., Pöhlker, C., Yu, X., Zhu, Y., Liu, G., Yue, Z., Fischman, B., Li, Z., Giguzin, D., Goren, T., Artaxo, P., Barbosa, H. M. J., Pöschl, U., and Andreae, M. O.: Satellite retrieval of cloud condensation nuclei concentrations by using clouds as CCN chambers, **Proceedings of the National Academy of Sciences**, 113, 5828-5834, 10.1073/pnas.1514044113, 2016.



## B1. Pöhlker et al. Atmos. Chem. Phys., 2016

### Long-term observations of cloud condensation nuclei in the Amazon rain forest – Part 1: Aerosol size distribution, hygroscopicity, and new model parametrizations for CCN

Mira L. Pöhlker<sup>1</sup>, Christopher Pöhlker<sup>1</sup>, Florian Ditas<sup>1</sup>, Thomas Klimach<sup>1</sup>, Isabella Hrabec de Angelis<sup>1</sup>, Alessandro Araújo<sup>2</sup>, Joel Brito<sup>3,a</sup>, Samara Carbone<sup>3,b</sup>, Yafang Cheng<sup>1</sup>, Xuguang Chi<sup>1,c</sup>, Reiner Ditz<sup>1</sup>, Sachin S. Gunthe<sup>4</sup>, Jürgen Kesselmeier<sup>1</sup>, Tobias Könemann<sup>1</sup>, Jošt V. Lavrič<sup>5</sup>, Scot T. Martin<sup>6</sup>, Eugene Mikhailov<sup>7</sup>, Daniel Moran-Zuloaga<sup>1</sup>, Diana Rose<sup>8</sup>, Jorge Saturno<sup>1</sup>, Hang Su<sup>1</sup>, Ryan Thalman<sup>9,d</sup>, David Walter<sup>1</sup>, JianWang<sup>9</sup>, StefanWolff<sup>1,10</sup>, Henrique M. J. Barbosa<sup>3</sup>, Paulo Artaxo<sup>3</sup>, Meinrat O. Andreae<sup>1,11</sup>, and Ulrich Pöschl<sup>1</sup>

<sup>1</sup> *Multiphase Chemistry and Biogeochemistry Departments, Max Planck Institute for Chemistry, Mainz, Germany*

<sup>2</sup> *Empresa Brasileira de Pesquisa Agropecuária (EMBRAPA), Belém, PA, Brazil*

<sup>3</sup> *Institute of Physics, University of São Paulo, São Paulo, Brazil*

<sup>4</sup> *EWRE Division, Department of Civil Engineering, Indian Institute of Technology Madras, Chennai, India*

<sup>5</sup> *Department of Biogeochemical Systems, Max Planck Institute for Biogeochemistry, Jena, Germany*

<sup>6</sup> *School of Engineering and Applied Sciences, Harvard University, Cambridge, MA, USA*

<sup>7</sup> *St. Petersburg State University, 7/9 Universitetskaya nab, St. Petersburg, Russia*

<sup>8</sup> *Institute for Atmospheric and Environmental Research, Goethe University Frankfurt am Main, Frankfurt, Germany*

<sup>9</sup> *Biological, Environmental & Climate Sciences Department, Brookhaven National Laboratory, Upton, NY, USA*

<sup>10</sup> *Instituto Nacional de Pesquisas da Amazonia (INPA), Manaus, Brazil*

<sup>11</sup> *Scripps Institution of Oceanography, University of California San Diego, La Jolla, CA, USA*

<sup>a</sup> *now at: Laboratory for Meteorological Physics, University Blaise Pascal, Clermont-Ferrand, France*

<sup>b</sup> *now at: Federal University of Uberlândia, Uberlândia-MG, Brazil*

<sup>c</sup> *now at: Institute for Climate and Global Change Research, Nanjing University, Nanjing, China*

<sup>d</sup> *now at: Department of Chemistry, Snow College, Richfield, UT, USA*



# Long-term observations of cloud condensation nuclei in the Amazon rain forest – Part 1: Aerosol size distribution, hygroscopicity, and new model parametrizations for CCN prediction

Mira L. Pöhlker<sup>1</sup>, Christopher Pöhlker<sup>1</sup>, Florian Ditas<sup>1</sup>, Thomas Klimach<sup>1</sup>, Isabella Hrabe de Angelis<sup>1</sup>, Alessandro Araújo<sup>2</sup>, Joel Brito<sup>3,a</sup>, Samara Carbone<sup>3,b</sup>, Yafang Cheng<sup>1</sup>, Xuguang Chi<sup>1,c</sup>, Reiner Ditzl<sup>1</sup>, Sachin S. Gunthe<sup>4</sup>, Jürgen Kesselmeier<sup>1</sup>, Tobias Könemann<sup>1</sup>, Jošt V. Lavrič<sup>5</sup>, Scot T. Martin<sup>6</sup>, Eugene Mikhailov<sup>7</sup>, Daniel Moran-Zuloaga<sup>1</sup>, Diana Rose<sup>8</sup>, Jorge Saturno<sup>1</sup>, Hang Su<sup>1</sup>, Ryan Thalman<sup>9,d</sup>, David Walter<sup>1</sup>, Jian Wang<sup>9</sup>, Stefan Wolff<sup>1,10</sup>, Henrique M. J. Barbosa<sup>3</sup>, Paulo Artaxo<sup>3</sup>, Meinrat O. Andreae<sup>1,11</sup>, and Ulrich Pöschl<sup>1</sup>

<sup>1</sup>Multiphase Chemistry and Biogeochemistry Departments, Max Planck Institute for Chemistry, 55020 Mainz, Germany

<sup>2</sup>Empresa Brasileira de Pesquisa Agropecuária (EMBRAPA), Trav. Dr. Enéas Pinheiro, Belém, PA, 66095-100, Brazil

<sup>3</sup>Institute of Physics, University of São Paulo, São Paulo, 05508-900, Brazil

<sup>4</sup>EWRE Division, Department of Civil Engineering, Indian Institute of Technology Madras, Chennai 600036, India

<sup>5</sup>Department of Biogeochemical Systems, Max Planck Institute for Biogeochemistry, 07701 Jena, Germany

<sup>6</sup>School of Engineering and Applied Sciences, Harvard University, Cambridge, MA 02138, USA

<sup>7</sup>St. Petersburg State University, 7/9 Universitetskaya nab, St. Petersburg, 199034, Russia

<sup>8</sup>Institute for Atmospheric and Environmental Research, Goethe University Frankfurt am Main, 60438 Frankfurt, Germany

<sup>9</sup>Biological, Environmental & Climate Sciences Department, Brookhaven National Laboratory, Upton, NY 11973, USA

<sup>10</sup>Instituto Nacional de Pesquisas da Amazonia (INPA), Manaus, 69083-000, Brazil

<sup>11</sup>Scripps Institution of Oceanography, University of California San Diego, La Jolla, CA 92037, USA

<sup>a</sup>now at: Laboratory for Meteorological Physics, University Blaise Pascal, Clermont-Ferrand, France

<sup>b</sup>now at: Federal University of Uberlândia, Uberlândia-MG, 38408-100, Brazil

<sup>c</sup>now at: Institute for Climate and Global Change Research & School of Atmospheric Sciences, Nanjing University, Nanjing, 210093, China

<sup>d</sup>now at: Department of Chemistry, Snow College, Richfield, UT 84701, USA

Correspondence to: Mira L. Pöhlker (m.pohlker@mpic.de)

Received: 16 June 2016 – Published in Atmos. Chem. Phys. Discuss.: 23 June 2016

Revised: 18 October 2016 – Accepted: 7 November 2016 – Published: 20 December 2016

**Abstract.** Size-resolved long-term measurements of atmospheric aerosol and cloud condensation nuclei (CCN) concentrations and hygroscopicity were conducted at the remote Amazon Tall Tower Observatory (ATTO) in the central Amazon Basin over a 1-year period and full seasonal cycle (March 2014–February 2015). The measurements provide a climatology of CCN properties characteristic of a remote central Amazonian rain forest site.

The CCN measurements were continuously cycled through 10 levels of supersaturation ( $S = 0.11$  to  $1.10\%$ ) and span the aerosol particle size range from 20 to 245 nm. The mean critical diameters of CCN activation range from

43 nm at  $S = 1.10\%$  to 172 nm at  $S = 0.11\%$ . The particle hygroscopicity exhibits a pronounced size dependence with lower values for the Aitken mode ( $\kappa_{\text{Ait}} = 0.14 \pm 0.03$ ), higher values for the accumulation mode ( $\kappa_{\text{Acc}} = 0.22 \pm 0.05$ ), and an overall mean value of  $\kappa_{\text{mean}} = 0.17 \pm 0.06$ , consistent with high fractions of organic aerosol.

The hygroscopicity parameter,  $\kappa$ , exhibits remarkably little temporal variability: no pronounced diurnal cycles, only weak seasonal trends, and few short-term variations during long-range transport events. In contrast, the CCN number concentrations exhibit a pronounced seasonal cycle, tracking the pollution-related seasonality in total aerosol concentra-

tion. We find that the variability in the CCN concentrations in the central Amazon is mostly driven by aerosol particle number concentration and size distribution, while variations in aerosol hygroscopicity and chemical composition matter only during a few episodes.

For modeling purposes, we compare different approaches of predicting CCN number concentration and present a novel parametrization, which allows accurate CCN predictions based on a small set of input data.

## 1 Introduction

### 1.1 Atmospheric aerosols and clouds

In our current understanding of the Earth's climate system and its man-made perturbation, the multiscale and feedback-rich life cycles of clouds represent one of the largest uncertainties (Boucher et al., 2013; Stevens et al., 2016). Accordingly, the adequate and robust representation of cloud properties is an Achilles' heel in climate modeling efforts (Bony et al., 2015). Atmospheric aerosols are a key ingredient in the life cycle of clouds (known as aerosol indirect effect) as they affect their formation, development, and properties by acting as cloud condensation nuclei (CCN) and ice nuclei (IN) (Lohmann and Feichter, 2005; Rosenfeld et al., 2008). Aerosol particles can originate from various natural and anthropogenic sources and span wide ranges of concentration, particle size, composition, as well as chemical and physical properties (Pöschl, 2005). Their activation into cloud droplets depends on their size, composition, and mixing state as well as the water vapor supersaturation (e.g., Köhler, 1936; Dusek et al., 2006; McFiggans et al., 2006; Andreae and Rosenfeld, 2008; Su et al., 2010). The microphysical link between clouds and aerosol has been the subject of manifold and long-term research efforts. On one hand, the cycling of CCN as well as their relationship to the aerosol population has been studied in a variety of field experiments worldwide (e.g., Gunthe et al., 2009; Rose et al., 2010; Jurányi et al., 2011; Paramonov et al., 2015). On the other hand, the knowledge obtained from the growing body of field data has been translated into different parametrization strategies that represent the cloud–aerosol microphysical processes in modeling studies (e.g., Nenes and Seinfeld, 2003; Petters and Kreidenweis, 2007; Su et al., 2010; Deng et al., 2013; Mikhailov et al., 2013).

### 1.2 Amazon rain forest and its hydrological cycle

The Amazon rain forest is a unique and important ecosystem for various reasons such as its high density and diversity of life, its role as major carbon storage, and its large recycling rate of energy and water in the Earth's hydrological cycle (Brienen et al., 2015; Gloor et al., 2015; Olivares et al., 2015; Yáñez-Serrano et al., 2015). In times of global change,

the man-made disturbance and pressure on this ecosystem have strongly increased and have started a transition of the Amazon into an uncharted future (Davidson et al., 2012; Lawrence and Vandecar, 2015). In the context of atmospheric composition, the Amazon is unique since it represents one of the last terrestrial locations worldwide that allows – at least for part of the year – to investigate an relatively undisturbed state of the atmosphere in the absence of major anthropogenic pollution (Roberts et al., 2001; Andreae, 2007; Andreae et al., 2012; Hamilton et al., 2014).

Overall, the troposphere over the Amazon is defined by the alternation of a relatively clean wet season and a polluted dry season, as outlined in more detail in previous studies (e.g., Martin et al., 2010b; Andreae et al., 2012, 2015; Mishra et al., 2015). In this paper, we use the following classification of the Amazonian seasons<sup>1</sup>: (i) the wet season typically spans February to May and shows the cleanest atmospheric state, (ii) the transition period from wet to dry season typically spans June and July, (iii) the dry season months August to November show the highest pollution levels, and (iv) the transition period from dry to wet season spans December and January (Andreae et al., 2015; Moran-Zuloaga et al., 2017).

A lively discussed aspect of the Amazonian hydrological cycle is the potential impact of changing aerosol regimes, which oscillate between polluted and pristine extremes, on the development of clouds and precipitation (e.g., Roberts et al., 2003; Andreae et al., 2004; Rosenfeld et al., 2008). A variety of pollution-induced changes in cloud properties, such as increased cloud drop concentrations with a corresponding decrease of their average size, intense competition for water vapor, and thus a deceleration of drop growth rates, suppression of supersaturation, reduced coalescence of smaller droplets, increased cloud depths as well as an invigoration of cloud dynamics and rain, are well documented (e.g., Koren et al., 2004, 2012; Freud et al., 2008).

Overall, the aforementioned observations indicate that increasing aerosol concentrations can have substantial impacts on spatial and temporal rainfall patterns in the Amazon (e.g., Martins et al., 2009a; Reutter et al., 2009). In view of the globally increasing pollution levels and the ongoing deforestation in the Amazon, pollution-triggered perturbations of the hydrological cycle are discussed as potential major threats to the Amazonian ecosystem, its forest structure, stability, and integrity (e.g., Coe et al., 2013; Junk, 2013).

<sup>1</sup>The Amazonian seasons are mostly defined meteorologically with respect to precipitation data (Fu et al., 2001; Fernandes et al., 2015). Note that in this study we use a slightly different definition of the seasons in the central Amazon based on meteorological and aerosol data to emphasize the seasonality in aerosol sources and prevalence. For example, the “meteorological wet season” typically has its core period in February (maximum in precipitation), whereas the “pollution-defined wet season” has its core period in April/May (e.g., minimum in carbon monoxide (CO) and black carbon (BC) concentrations) (Andreae et al., 2015).

### 1.3 Previous CCN measurements in the Amazon

Ground-based and airborne CCN measurements have been conducted in a number of field campaigns in the Amazon Basin as outlined below in chronological order, constituting the baseline and context for the present study.

**1998:** Roberts and coworkers (Roberts et al., 2001; Roberts et al., 2002) conducted the first CCN measurements in the Amazon in the context of the LBA/CLAIRE-98 campaign (ground-based, Balbina site, March and April 1998) and pointed out that under clean conditions the CCN concentration  $N_{\text{CCN}}(S)$  (at a certain supersaturation  $S$ ) in the “green ocean” Amazon is surprisingly similar to conditions in the maritime “blue ocean” atmosphere. Regarding the low natural  $N_{\text{CCN}}(S)$ , which is dominated by mostly organic particles, they further suggested that cloud and precipitation properties may react sensitively to pollution-induced increases of the total aerosol load.

**1999:** In the context of the LBA-EUSTACH campaign in 1999, ground-based CCN measurements at three different sites in the Amazon Basin were conducted (Andreae et al., 2002; Roberts et al., 2003). This was the first study on CCN properties and cloud dynamics under the influence of strong biomass burning emissions in the Amazon.

**2001:** In the follow-up study LBA/CLAIRE-2001 in July 2001, ground-based (Balbina site) and airborne measurements (around Manaus) were conducted. For the ground-based study, Rissler et al. (2004) combined a hygroscopicity tandem differential mobility analyzer (HTDMA) with CCN measurements, focusing on the CCN-relevant water-soluble fraction in the particles, and provided a CCN closure and parametrization for model approaches. In addition, an airborne analysis of the aerosol and CCN properties was conducted, focusing on the contrast between the Amazonian background air and the Manaus plume (Kuhn et al., 2010).

**2002:** Subsequently, in the course of the LBA-SMOCC-2002 campaign in southern Brazil during major biomass burning episodes (Rondônia state, September and October 2002), ground-based and airborne CCN measurements were performed (Vestin et al., 2007; Martins et al., 2009b). A major finding of this study was that the CCN efficiency of natural biogenic and man-made pyrogenic (cloud-processed) aerosols is surprisingly similar (Andreae et al., 2004). Furthermore,  $N_{\text{CCN}}(0.5\%)$  was found as a valuable predictor for the required cloud depth of warm rain formation, which is an important property for cloud dynamics (Freud et al., 2008).

**2008:** During the AMAZE-08 campaign (ground-based, ZF2 site, February and March 2008), the first size-

resolved CCN measurements in the Amazon were conducted (Gunthe et al., 2009; Martin et al., 2010a). These studies report that aerosol particles in the Aitken and accumulation modes, which represent the CCN-relevant size range, predominantly contain organic constituents and thus have comparably low hygroscopicity levels. The observed hygroscopicity parameter  $\kappa$  ranges between 0.1 and 0.2, which corresponds to the typical hygroscopicity of secondary organic aerosol (SOA) (Andreae and Rosenfeld, 2008).

**2010/11:** During several short observational periods, Almeida et al. (2014) measured total CCN concentrations around the city of Fortaleza in northeast Brazil. The selected measurement locations receive wind from changing directions. Accordingly, the response of the CCN population to marine, urban, and rural air masses was investigated.

**2013:** Recently, Whitehead et al. (2016) reported results from further short-term, size-resolved CCN and HTDMA measurements that were conducted north of Manaus (ground-based, ZF2 site, July 2013) as part of the Brazil–UK network for investigation of Amazonian atmospheric composition and impacts on climate (BUNIAACIC) project. The results of this study agree well with Gunthe et al. (2009).

**2014/15:** As part of the international field campaign observation and modeling of the green ocean Amazon (GoAmazon2014/5), size-resolved CCN measurements were conducted at three sites in and around Manaus: the Amazon Tall Tower Observatory (ATTO) site (T0a, pristine rain forest), which is discussed in the present study, the T2 site (in Manaus, urban environment), and the T3 site (rural site in the Manaus plume) (Martin et al., 2016; Thalman et al., 2017). All three size-resolved CCN measurements in the context of GoAmazon2014/5 took place in close collaboration. Moreover, CCN measurements were conducted onboard the G-1 aircraft during the GoAmazon2014/5 intensive observation periods IOP1 and IOP2 (Martin et al., 2016).

**2014:** Furthermore, as part of the German–Brazilian ACRIDICON (Wendisch et al., 2016) and CHUVA (Machado et al., 2014) projects, airborne CCN measurements were made over the entire Amazon Basin (September 2014). The results of this study are currently being analyzed for an upcoming publication and represent an ideal complement to the long-term data of the present study.

In addition to the aforementioned CCN measurements, some further studies relied on HTDMA measurements to probe the aerosol hygroscopicity and particle growth factors below 100 % relative humidity (RH), which can be used

to extrapolate the CCN activity in supersaturation regimes (Zhou et al., 2002; Rissler et al., 2006).

#### 1.4 Aims and scope of this study

All of the previously published CCN measurements in the Amazon have been conducted over relatively short time periods of up to several weeks. In addition, size-resolved CCN measurements are still sparse in the Amazon region. In this study, we present the first continuous, long-term, and size-resolved CCN data set from the Amazon Basin, which spans a full seasonal cycle and therefore represents the CCN properties during contrasting seasonal conditions.

The focus of this study is on presenting major trends and characteristics of the CCN population in the Amazon Basin. Thus, our study contributes to a global inventory of CCN properties, representing this unique and climatically important ecosystem. We extract key CCN properties and parameters that help to include CCN predictions in the Amazon region into future modeling studies. Based on our data set, different parametrization strategies for CCN prediction are compared and discussed. Moreover, we present a novel and generalized CCN parametrization, which allows efficient modeling of CCN concentrations based on a minimal set of basic aerosol properties.

This paper represents part 1 of a comprehensive analysis of the CCN cycling in the central Amazon. It covers the overall trends and presents annually averaged CCN parameters as well as characteristic differences in the CCN population between the Amazonian seasons. A companion paper (Part 2) provides in-depth analyses of particularly interesting events through short-term case studies and aims for a more emission- and process-related understanding of the CCN variability (M. L. Pöhlker et al., 2017a).

## 2 Methods

### 2.1 Measurement site and period

The measurements reported in this study were conducted at the ATTO site (02°08.602' S, 59°00.033' W; 130 m a.s.l.), which is located in an untouched rain forest area in the central Amazon, about 150 km northeast of the city of Manaus, Brazil. An overview of the atmospheric, geographic, and ecological conditions at the ATTO site has been published recently by Andreae et al. (2015), where a detailed description of the aerosol setup for the long-term measurements can be found. The instrumentation for CCN measurements is part of a broad aerosol measurement setup, which also covers aerosol size and concentration, absorptivity, scattering, fluorescence, as well as chemical composition (Andreae et al., 2015). The aerosol inlet is located at a height of 60 m, which is about 30 m above the forest canopy. The sample air is dried by silica gel diffusion dryers at the main inlet, which keeps the RH below 40 %. For the CCN setup, a second diffusion

dryer decreases the RH even further to < 20 %, which ensures reliable hygroscopicity measurements.

The CCN measurements are ongoing since the end of March 2014. This study covers the measurement period from the end of March 2014 to February 2015, representing almost a full seasonal cycle. Also, the measurement period overlaps with the international large-scale field campaign GoAmazon2014/5 that was conducted in and around the city of Manaus from 1 January 2014 through 31 December 2015. During GoAmazon2014/5, comprehensive CCN measurements were conducted at different sites (see Sect. 1.3) (Martin et al., 2016). The ATTO site served as a clean background (T0a) site during GoAmazon2014/5. Furthermore, the measurement period of this study encompasses the German–Brazilian ACRIDICON-CHUVA field measurement campaign in September 2014 (Machado et al., 2014; Wendisch et al., 2016), where (non-size-resolved) CCN measurements at multiple supersaturation levels were performed onboard the high-altitude and long-range research aircraft (HALO) flying over the Amazon Basin.

### 2.2 Size-resolved CCN measurements

The number concentration of CCN was measured with a continuous-flow streamwise thermal gradient CCN counter (CCNC, model CCN-100, DMT, Boulder, CO, USA) (Roberts and Nenes, 2005; Rose et al., 2008b). The inlet flow rate of the CCNC was 0.5 L min<sup>-1</sup> with a sheath-to-aerosol flow ratio of 11. The water pump was operated at a rate of 4 mL h<sup>-1</sup> corresponding to the CCNC setting of “low” liquid flow. The supersaturation ( $S$ ) of the CCNC was cycled through 10 different  $S$  values between 0.11 and 1.10 % (see Table 1), which are defined by controlled temperature gradients inside the CCNC column. Particles with a critical supersaturation ( $S_c$ )  $\leq S$  in the column are activated and form water droplets. Droplets with diameters  $\geq 1 \mu\text{m}$  are detected by an optical particle counter (OPC) at the exit of the column.

Size-resolved CCN activation curves (for nomenclature, see Sect. 2.3) were measured based on the concept of Frank et al. (2006), following the procedures in Rose et al. (2008a) and Krüger et al. (2014) by combining the CCNC with a differential mobility analyzer (DMA, model M, Grimm Aerosol Technik, Ainring, Germany). The DMA was operated with a sheath-to-aerosol flow ratio of 5. The DMA selects particles with a certain diameter ( $D$ ) in the size range of 20 to 245 nm (sequence of  $D$  value has been optimized for every  $S$ ), which are then passed into the two instruments: (i) the CCNC system and (ii) a condensation particle counter (CPC, model 5412, Grimm Aerosol Technik), which measures the number concentration of aerosol particles with selected  $D$  ( $N_{\text{CN}}(D)$ ), while the CCNC measures the number concentration of CCN with selected  $D$  for the given  $S$  ( $N_{\text{CCN}}(S, D)$ ). The cycle through a full CCN activation curve ( $N_{\text{CCN}}(S, D)/N_{\text{CN}}(D)$ ) for one  $S$  level took  $\sim 28$  min, including  $\sim 40$  s equilibration time for every new  $D$ , and  $\sim 2$  min equilibration time

**Table 1.** Characteristic CCN parameters as a function of the supersaturation  $S$ , averaged over the entire measurement period: midpoint activation diameter  $D_a(S)$ , hygroscopicity parameter  $\kappa(S, D_a)$ , width of CCN activation curve  $\sigma(S)$ , heterogeneity parameter  $\sigma(S)/D_a(S)$ , maximum activated fraction  $\text{MAF}(S)$ , CCN number concentration  $N_{\text{CCN}}(S)$ , total particle concentration ( $> 10$  nm)  $N_{\text{CN},10}$ , CCN efficiencies  $N_{\text{CCN}}(S)/N_{\text{CN},10}$ , and number of data points  $n$ .  $S$  is shown as set value  $\pm$  the experimentally derived deviation in  $S$ . All other values are given as arithmetic mean  $\pm 1$  standard deviation. All values are provided for ambient conditions (temperature  $\sim 28^\circ\text{C}$ ; pressure  $\sim 100$  kPa).

$S$ (%)	$D_a(S)$ (nm)	$\kappa(S, D_a)$	$\sigma(S)$ (nm)	$\sigma(S)/D_a(S)$	$\text{MAF}(S)$	$N_{\text{CCN}}(S)$ ( $\text{cm}^{-3}$ )	$N_{\text{CN},10}$ ( $\text{cm}^{-3}$ )	$N_{\text{CCN}}(S)/N_{\text{CN},10}$	$n$
$0.11 \pm 0.01$	$172 \pm 12$	$0.22 \pm 0.05$	$45 \pm 11$	$0.26 \pm 0.06$	$0.93 \pm 0.10$	$275 \pm 219$	$1100 \pm 776$	$0.24 \pm 0.10$	1071
$0.15 \pm 0.02$	$136 \pm 10$	$0.22 \pm 0.05$	$42 \pm 10$	$0.31 \pm 0.06$	$0.97 \pm 0.05$	$457 \pm 384$	$1093 \pm 770$	$0.39 \pm 0.13$	1086
$0.20 \pm 0.02$	$117 \pm 9$	$0.21 \pm 0.05$	$35 \pm 10$	$0.30 \pm 0.07$	$0.98 \pm 0.04$	$571 \pm 482$	$1096 \pm 775$	$0.48 \pm 0.15$	1087
$0.24 \pm 0.03$	$105 \pm 8$	$0.19 \pm 0.05$	$29 \pm 8$	$0.28 \pm 0.07$	$0.99 \pm 0.04$	$652 \pm 550$	$1098 \pm 778$	$0.55 \pm 0.16$	1078
$0.29 \pm 0.03$	$98 \pm 7$	$0.17 \pm 0.04$	$27 \pm 8$	$0.27 \pm 0.08$	$1.01 \pm 0.05$	$719 \pm 601$	$1103 \pm 784$	$0.60 \pm 0.17$	1069
$0.47 \pm 0.04$	$77 \pm 5$	$0.13 \pm 0.03$	$17 \pm 6$	$0.22 \pm 0.07$	$1.03 \pm 0.04$	$883 \pm 744$	$1101 \pm 799$	$0.74 \pm 0.18$	1008
$0.61 \pm 0.06$	$63 \pm 4$	$0.14 \pm 0.03$	$15 \pm 5$	$0.23 \pm 0.07$	$0.97 \pm 0.03$	$900 \pm 719$	$1089 \pm 791$	$0.78 \pm 0.14$	922
$0.74 \pm 0.08$	$57 \pm 4$	$0.13 \pm 0.03$	$14 \pm 6$	$0.24 \pm 0.09$	$0.96 \pm 0.03$	$941 \pm 730$	$1108 \pm 809$	$0.82 \pm 0.12$	984
$0.92 \pm 0.11$	$49 \pm 4$	$0.13 \pm 0.03$	$12 \pm 6$	$0.24 \pm 0.11$	$0.96 \pm 0.04$	$987 \pm 742$	$1117 \pm 814$	$0.86 \pm 0.10$	995
$1.10 \pm 0.08$	$43 \pm 3$	$0.13 \pm 0.03$	$11 \pm 5$	$0.25 \pm 0.10$	$0.95 \pm 0.03$	$1013 \pm 747$	$1120 \pm 792$	$0.88 \pm 0.08$	952

for every new  $S$  level. The completion of a full measurement cycle comprising CCN activation curves for 12–13  $D$  values (number of  $D$  depends on  $S$ ) and 10 different  $S$  levels took  $\sim 4.5$  h. The entire CCN system (including the CCNC, DMA, and CPC) was controlled by a dedicated LabVIEW (National Instruments, Munich, Germany) routine.

The  $S$  levels of the CCNC system were calibrated periodically (March, May, and September 2014) using ammonium sulfate ( $(\text{NH}_4)_2\text{SO}_4$ , Sigma Aldrich, St. Louis, MO, USA) particles generated in an aerosol nebulizer (TSI Inc., Shoreview, MN, USA). The calibration procedure was conducted according to Rose et al. (2008b). All three calibrations gave consistent results and thus confirmed that the  $S$  cycling in the CCNC was very stable and reliable throughout the entire measurement period.

All concentration data presented here are given for ambient conditions. During the entire measurement period, no significant fluctuations in temperature ( $\sim 28^\circ\text{C}$ ) and pressure ( $\sim 100$  kPa) were observed in the air-conditioned laboratory container.

### 2.3 Data analysis, error analysis, and nomenclature of CCN key parameters

The theoretical background and related CCN analysis procedures are comprehensively described elsewhere (Petters and Kreidenweis, 2007; Rose et al., 2008a). For the present study, the following corrections were applied to the data set. (i) The CCN activation curves were corrected for systematic deviations in the counting efficiency of the CCNC and CPC according to Rose et al. (2010). (ii) Usually, the double-charge correction of the CCN activation curve is conducted according to Frank et al. (2006). For this study, we developed the following alternative approach, which reconstructs the CCN efficiency curves based on data from an independent scanning mobility particle sizer (SMPS, TSI model

3080 with CPC 3772 operating with standard TSI software) at the ATTO site. The activation curve for every  $D$  can be described by the following equation:

$$\frac{\sum_i N_{\text{CCN}}(S, D_i)}{\sum_i N_{\text{CN}}(D_i)} = \frac{\sum_i f(D_i) \cdot s(D_i) \cdot a(S, D_i)}{\sum_i f(D_i) \cdot s(D_i)}. \quad (1)$$

The index  $i$  represents the charge of the particles (typically  $1 \leq i \leq 4$ ). The left side of the equation is the measured (non-corrected) ratio of CCN to condensation nuclei (CN) for one selected  $D$  and  $S$ . The parameter  $s(D_i)$  is the multi-charge-corrected particle number size distribution inverted from the SMPS measurements at  $D_i$  with its different charge states. The parameter  $f(D_i)$  is the corresponding fraction of particles with the charge  $i$ . The function  $a(S, D_i)$  accounts for the activated fraction of  $s(D_i)$  at a given supersaturation  $S$ . We describe  $a(S, D_i)$  as a cumulative Gaussian function. Using a nonlinear least-squares fit method (Levenberg–Marquardt) together with the knowledge of  $s(D_i)$  and  $f(D_i)$ , the parameters of the function  $a(S, D_i)$  can be optimized to get an optimal fit of the measured CCN activation curve for a given  $S$ . The function  $a(S, D)$  is the cumulative Gaussian function after the fit, which describes the multi-charge-corrected CCN activation curve and has been used as a basis for the further analysis. Because the information on multiple charged particles also contributes to the fit results, this approach is superior to previously used methods, where this information is neglected. Based on  $a(S, D)$ , the critical diameter ( $D_a(S)$ , where 50 % of the particles are activated) is used to retrieve the effective hygroscopicity parameter ( $\kappa(S, D_a)$ ) according to the  $\kappa$ -Köhler model (Petters and Kreidenweis, 2007). A detailed description of the calculation can be found in Petters and Kreidenweis (2007), Rose et al. (2010), and Mikhailov et al. (2009).

The CCN size distribution ( $N_{CCN}(S, D)$ ) was calculated by

$$N_{CCN}(S, D) = s(D) \cdot a(S, D). \quad (2)$$

In this equation,  $s(D)$  represents the particle number size distribution of the SMPS at  $D$  ( $10 \leq D \leq 450$  nm).

The CCN efficiencies ( $N_{CCN}(S)/N_{CN,10}$ ; for nomenclature, see end of Sect. 2.3) have been calculated based on the integral concentration of CN with lower size cutoff  $D_{cut} = 10$  nm ( $N_{CN,10}$ )<sup>2</sup> and CCN ( $N_{CCN}(S)$ ) as

$$\frac{N_{CCN}(S)}{N_{CN,10}} = \frac{\int_D N_{CCN}(S, D) \cdot dD}{\int_D s(D) \cdot dD}. \quad (3)$$

In addition to  $D_a(S)$ , the maximum activated fraction (MAF( $S$ )) can be obtained from  $a(S, D)$ . MAF( $S$ ) typically equals unity, except for completely hydrophobic particles (i.e., fresh soot). The third parameter that can be derived from  $a(S, D)$  is the width of the CCN activation curve  $\sigma(S)$ , which strongly depends on  $D_a(S)$ . The ratio between  $\sigma(S)$  and  $D_a(S)$  ( $\sigma(S)/D_a(S)$ ) is called heterogeneity parameter and can be used as an indicator for the chemical and geometric diversity of the aerosol particles.

The error in  $S$  was calculated based on the uncertainty according to the commonly used calibration procedure (Rose et al., 2008b). Overall, the error  $\Delta S$  of  $S$  equals approximately 10%; however, in the following analysis, we have used the specific  $\Delta S$  values for every  $S$  (see Table 1). The uncertainty of the selected  $D$  of the DMA ( $\Delta D$ ) was obtained as the mean width of the Gaussian fit of polystyrene latex (PSL) beads and equals 5.3 nm. For  $N_{CCN}(S, D)$  and  $N_{CN}(D)$ , the standard error of the counting statistic was used. By Gaussian error propagation we determined  $\Delta(N_{CCN}(S, D)/N_{CN}(D))$  and then repeated the data analysis for the upper and lower bounds  $(1 \pm \Delta) \times (N_{CCN}(D, S)/N_{CN}(D))$ . The resulting relative errors of the values  $N_{CCN}(S)$ ,  $N_{CN,10}$ , and  $N_{CCN}(S)/N_{CN,10}$  do not depend on  $S$  and equal 6%. The errors of  $D_a(S)$  and  $\kappa(S, D_a)$  depend on  $S$  and can be described as

$$\Delta D_a(S) = D_a(S) \cdot (S \cdot 0.07 + 0.03) \quad (4)$$

$$\Delta \kappa(S, D_a) = \kappa(S, D_a) \cdot (S \cdot 0.17 + 0.10). \quad (5)$$

Throughout this study, we observed a slight systematic deviation of the results for the supersaturation  $S = 0.47\%$ . This effect can be seen, for example, in MAF(0.47%) values exceeding unity in Fig. 1 and  $N_{CCN}(0.47\%, D)/N_{CN}(D)$  values exceeding unity in Fig. 5. The effect persists even after applying all aforementioned corrections to the data and is most pronounced during the dry season. Yet, since we did not find any evidence of these data being erroneous, we decided to keep them in the study.

<sup>2</sup>Note that  $N_{CN,10}$  usually corresponds to the total CPC-detectable aerosol particle number concentration for the characteristic size distribution at the ATTO site because the particle population in the nucleation-mode range (i.e., < 10 nm) is negligibly small.

The use of certain terms in the context of CCN measurements is not uniform in the literature. For clarity, we summarize the key parameters and terms applied in this study as follows: (i) the value  $N_{CCN}(S, D)/N_{CN}(D)$  is called CCN activated fraction, while (ii)  $N_{CCN}(S, D)/N_{CN}(D)$  plotted against  $D$  is called CCN activation curve; (iii)  $N_{CCN}(S)$  plotted against  $S$  is called CCN spectrum; (iv)  $N_{CCN}(S)/N_{CN, D_{cut}}$  at a certain  $S$  level is called CCN efficiency; (v)  $N_{CCN}(S)/N_{CN, D_{cut}}$  plotted against  $S$  is called CCN efficiency spectrum.

## 2.4 Aerosol mass spectrometry

In addition to the CCN measurements, aerosol chemical speciation monitor (ACSM, Aerodyne Research Inc., Billerica, MA, USA) measurements are being performed at the ATTO site (Andreae et al., 2015). The ACSM routinely characterizes nonrefractory submicron aerosol species such as organics, nitrate, sulfate, ammonium, and chloride (Ng et al., 2011). Particles are focused by an aerodynamic lens system into a narrow particle beam, which is transmitted through three successive vacuum chambers. In the third chamber, the particle beam is directed into a hot tungsten oven (600 °C) where the particles are flash vaporized, ionized with a 70 eV electron impact ionizer, and detected with a quadrupole mass spectrometer. In this study, a time resolution of 30 min was used. The measurements provide a total mass concentration of the chemical composition of the aerosol particles. Further details about the ACSM can be found in Ng et al. (2011).

## 2.5 Carbon monoxide measurements

Carbon monoxide (CO) measurements are conducted continuously at the ATTO site using a G1302 analyzer (Picarro Inc. Santa Clara, CA, USA). The experimental setup from the point of view of functioning and performance is a duplication of the system described in Winderlich et al. (2010).

## 3 Results and discussion

### 3.1 Time series of CCN parameters for the entire measurement period

Over the entire measurement period from 25 March 2014 to 5 February 2015 we recorded size-resolved CCN activation curves at 10 different levels of water vapor supersaturation  $S$  with an overall time resolution of approximately 4.5 h. A total of 10 253 CCN activation curves were fitted and analyzed to obtain parameters of CCN activity as detailed above (Sect. 2.3). Table 1 serves as a central reference in the course of this study and summarizes the annual mean values and standard deviations of the following key parameters, resolved by  $S$ :  $D_a(S)$ ,  $\kappa(S, D_a)$ ,  $\sigma(S)$ ,  $\sigma(S)/D_a(S)$ , MAF( $S$ ),  $N_{CCN}(S)$ ,  $N_{CN,10}$ , and  $N_{CCN}(S)/N_{CN,10}$ . In Fig. 1, some of these CCN key parameters are presented as time se-

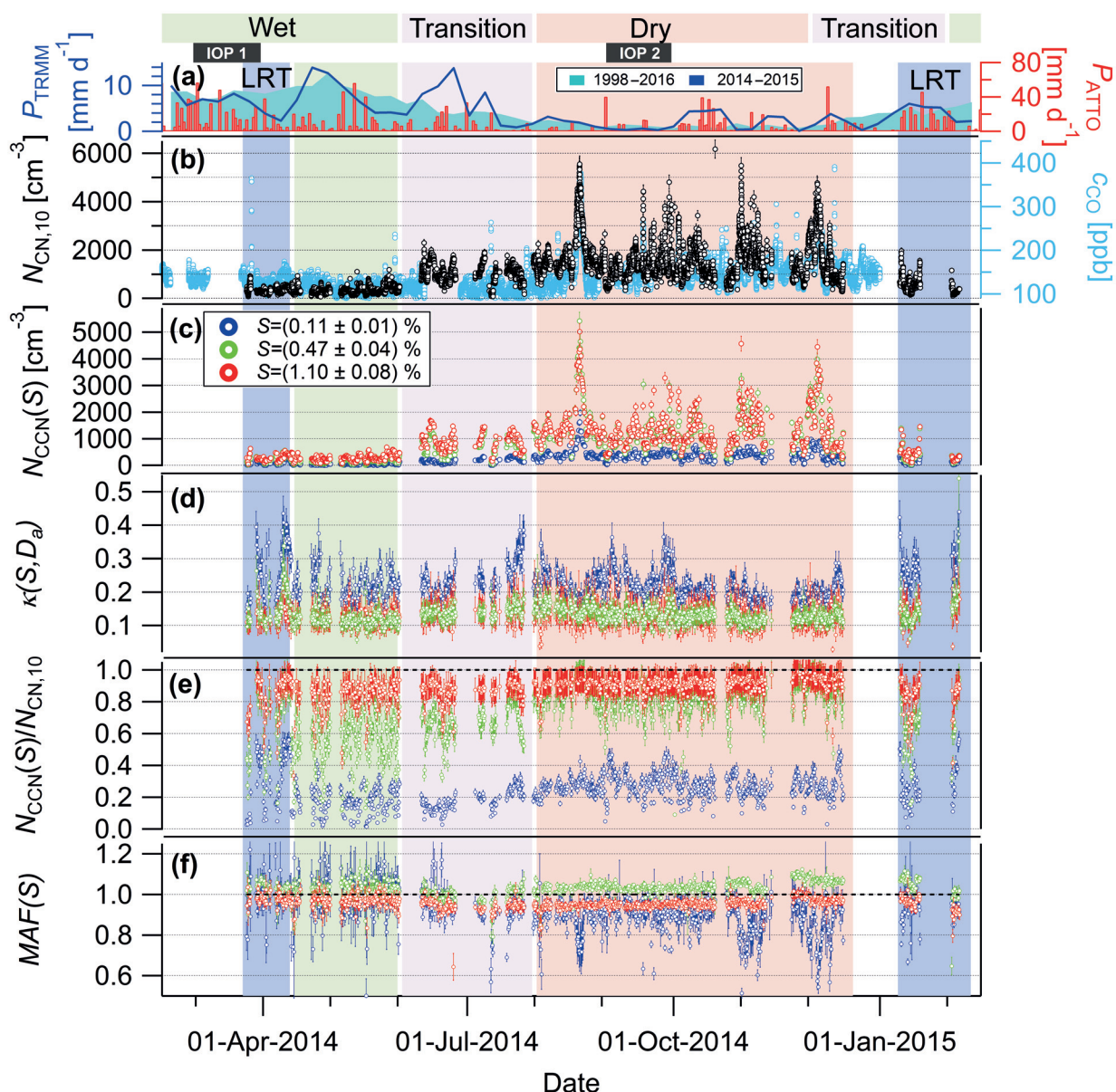


**Figure 1.** Seasonal trends in time series of precipitation rate  $P$ , total aerosol concentration  $N_{\text{CN},10}$ , carbon monoxide mole fraction ( $c_{\text{CO}}$ ), and CCN key parameters for three selected supersaturations  $S$  for the entire measurement period (shown in original time resolution). (a) Precipitation rates from tropical rainfall measuring mission (TRMM)  $P_{\text{TRMM}}$  and in situ measurements at the ATTO site  $P_{\text{ATTO}}$ . The  $P_{\text{TRMM}}$  seasonal cycles are derived from an area upwind of the ATTO site ( $59.5^\circ \text{W}$ ,  $2.4^\circ \text{N}$ ,  $54.0^\circ \text{W}$ ,  $3.5^\circ \text{S}$ ), covering a long-term period from 1 January 1998 to 30 June 2016 (aqua shading), and the period of the CCN measurements from 1 March 2014 to 28 February 2015 (blue line). (b) Time series of pollution tracers  $N_{\text{CN},10}$  and  $c_{\text{CO}}$ . (c) CCN concentrations  $N_{\text{CCN}}(S)$ , (d) hygroscopicity parameter  $\kappa(S, D_a)$ , (e) CCN efficiencies  $N_{\text{CCN}}(S)/N_{\text{CN},10}$ , and (f) maximum activated fraction  $\text{MAF}(S)$ . Three different types of shading represent (i) the seasonality in the Amazon atmosphere according to Andreae et al. (2015) (wet vs. dry seasons with transition periods, illustrated at the top of the graph), (ii) periods of IOP1 and IOP2 during GoAmazon2014/5, (iii) seasonal periods of interest in context of the present study as defined in Sect. 3.3 (shading in background of time series).

ries over the entire measurement period to provide a general overview of their temporal evolution and variability. Concentration time series of the pollution tracers  $N_{\text{CN},10}$  and CO are added to illustrate the pollution seasonality at the ATTO site.

Figure 1a presents precipitation data from satellite and in situ measurements at the ATTO site to illustrate the meteorological seasonality for the measurement period. The precipitation rates in the Amazon Basin can show pronounced

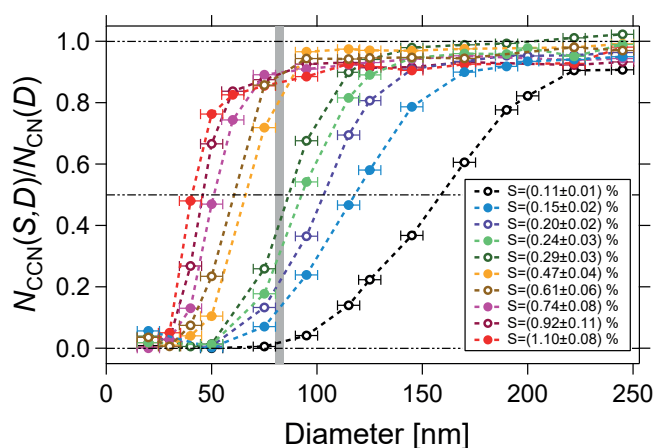
anomalies due to teleconnections with the Atlantic and/or Pacific sea surface temperatures (SSTs) (Fu et al., 2001; Fernandes et al., 2015). The most prominent example here is the El Niño–Southern Oscillation (ENSO) and its various impacts on the Amazonian ecosystem (e.g., Asner et al., 2000; Ronchail et al., 2002). For the measurement period, the Oceanic Niño Index (ONI) ranged between  $-0.4$  and  $0.6$  °C, confirming that only towards the end of the measurement period a slightly positive anomaly was observed.<sup>3</sup> In Fig. 1a, satellite data from the tropical rainfall measurement mission (TRMM) are presented for the area around the ATTO site. The TRMM data are provided for an extended time period (January 1998 until June 2016) and, for comparison, for the CCN measurement period (March 2014 until February 2015). This comparison shows that the 2014/15 precipitation rates do not deviate substantially from the 18-year average data, and thus further confirms that the measurement period can be regarded as a typical year with typical seasons and no pronounced hydrological anomalies.

Figure 1b displays the characteristic seasonal cycle in  $N_{\text{CN},10}$  and the CO mole fraction ( $c_{\text{CO}}$ ). Both pollution tracers reach their maxima during the dry season ( $N_{\text{CN},10} = 1400 \pm 710 \text{ cm}^{-3}$ ;  $c_{\text{CO}} = 144 \pm 45 \text{ ppb}$ ), whereas the lowest values are observed during the wet season ( $N_{\text{CN},10} = 285 \pm 131 \text{ cm}^{-3}$ ;  $c_{\text{CO}} = 117 \pm 12 \text{ ppb}$ ) (given as mean  $\pm 1$  standard deviation). An obvious feature of the dry season months is the occurrence of rather short and strong peaks (reaching up to  $N_{\text{CN},10} = \sim 5000 \text{ cm}^{-3}$ ;  $c_{\text{CO}} = \sim 400 \text{ ppb}$ ) on top of elevated background pollution levels. The pronounced peaks originate from biomass burning plumes, which impact the ATTO site for comparatively short periods (a few hours up to several days). Selected events are discussed in detail in M. L. Pöhlker et al. (2017a). Figure 1c shows that  $N_{\text{CCN}}(S)$  follows the same overall trends. A rather close correlation between  $N_{\text{CCN}}(S)$  and  $N_{\text{CN},10}$  as well as  $N_{\text{CCN}}(S)$  and  $c_{\text{CO}}$  can be observed, as pointed out in previous studies (Andreae, 2009; Kuhn et al., 2010). Figure 1d displays the  $\kappa(S, D_a)$  time series for three exemplary  $S$  levels. It shows that the  $\kappa(S, D_a)$  values, which provide indirect information of the particles' chemical composition, are remarkably stable throughout the year (see also standard deviations of  $\kappa(S, D_a)$  in Table 1). This illustrates that the dry season maximum in  $N_{\text{CCN}}(S)$  is mainly related to the overall increase in  $N_{\text{CN},10}$ , and not to substantial variations in aerosol composition and therefore  $\kappa(S, D_a)$ . The levels of the three  $\kappa(S, D_a)$  time series, with their corresponding  $D_a(S)$ , provide a first indication that  $\kappa(S, D_a)$  shows a clear size dependence, as further discussed in Sect. 3.2. The pro-

nounced (but rather rare) “spikes” in  $\kappa(S, D_a)$  (i.e., in April and August) as well as various other specific events in this time series are analyzed in detail in the companion Part 2 paper (M. L. Pöhlker et al., 2017a). Figure 1e gives an overview of the CCN efficiencies  $N_{\text{CCN}}(S)/N_{\text{CN},10}$  (for three  $S$  levels) and its seasonal trends. This representation shows continuously high fractions of cloud-active particles for higher  $S$  (e.g.,  $N_{\text{CCN}}(1.10\%)/N_{\text{CN},10} > 0.9$ ) throughout the entire measurement period with almost no seasonality. For intermediate  $S$ , such as 0.47 %, the values of  $N_{\text{CCN}}(0.47\%)/N_{\text{CN},10}$  range from 0.6 to 0.9 and reveal a noticeable seasonal cycle, with the highest levels during the dry season. Furthermore,  $N_{\text{CCN}}(0.11\%)/N_{\text{CN},10}$  is mostly below 0.4, with clear seasonal trends. These observations can be explained by the characteristic aerosol size distribution at the ATTO site (Andreae et al., 2015), which (i) is dominated by particles in the Aitken (annually averaged peak  $D_{\text{Ait}}$  at  $\sim 70 \text{ nm}$ ) and accumulation modes (annually averaged peak  $D_{\text{Acc}}$  at  $\sim 150 \text{ nm}$ ), (ii) shows a sparse occurrence of nucleation-mode particles ( $< 30 \text{ nm}$ ), and (iii) reveals a clear seasonality in the relative abundance of Aitken and accumulation modes (see Sect. 3.3 and Fig. 6). Thus, the higher dry season abundance of accumulation-mode particles, which are more prone to act as CCN, results in higher  $N_{\text{CCN}}(S)/N_{\text{CN},10}$  levels, particularly at lower  $S$ .

Analogous  $N_{\text{CCN}}(S)/N_{\text{CN}}$  results from other continental background sites have been published previously: for example, Levin et al. (2012) reported  $N_{\text{CCN}}(0.97\%)/N_{\text{CN}} = 0.4\text{--}0.7$ ,  $N_{\text{CCN}}(0.56\%)/N_{\text{CN}} = 0.25\text{--}0.5$ , and  $N_{\text{CCN}}(0.14\%)/N_{\text{CN}} < 0.15$  for a semi-arid Rocky Mountain site. Jurányi et al. (2011) reported  $N_{\text{CCN}}(1.18\%)/N_{\text{CN},16} = 0.6\text{--}0.9$ ,  $N_{\text{CCN}}(0.47\%)/N_{\text{CN},16} = 0.2\text{--}0.6$ , and  $N_{\text{CCN}}(0.12\%)/N_{\text{CN},16} < 0.25$  for the high alpine Jungfraujoch site. At both locations, the CCN efficiencies tend to be lower than the corresponding results at the ATTO site, which can be explained by the frequent occurrence of new particle formation (NPF) and the related abundance of ultrafine particles (with sizes well below  $D_a(S)$ ) at these sites (Boulon et al., 2010; Ortega et al., 2014). The activated fractions at the Rocky Mountain and Jungfraujoch sites have a stronger seasonality than those at ATTO, probably inversely related to the seasonal cycle in NPF. Overall, we state that the activated fractions in the central Amazon, due to the absence of significant ultrafine particle ( $< 30 \text{ nm}$ ) populations, tend to be constantly higher than in other continental background locations (Paramonov et al., 2015). The absence of “classical” NPF (Kulmala et al., 2004) and the corresponding lack of ultrafine particles is a unique property of the Amazon atmosphere resulting in the uniquely high CCN efficiencies. A systematic study on the abundance, properties, and seasonality of the sparse nucleation-mode bursts in the central Amazon is the subject of an upcoming study.

<sup>3</sup>For the ONI data and specific information on the reference area and time frame, refer to National Oceanic and Atmospheric Administration (NOAA)/National Weather Service, 2016. Historical El Niño/La Niña episodes (1950–present) are available at [http://www.cpc.ncep.noaa.gov/products/analysis\\_monitoring/ensostuff/ensoyears.shtml](http://www.cpc.ncep.noaa.gov/products/analysis_monitoring/ensostuff/ensoyears.shtml) (last access: 1 October 2016).



**Figure 2.** CCN activation curves for all measured  $S$  levels ( $S=0.11$ – $1.10$  %), averaged over the entire measurement period. Data points represent arithmetic mean values. For  $N_{CCN}(S,D)/N_{CN}(D)$ , the standard error is plotted, which is very small (due to the large number of scans with comparatively small variability) and therefore not perceptible in this representation. For the diameter,  $D$ , the error bars represent the experimental error as specified in Sect. 2.3. The grey vertical band represents the position of the Hoppel minimum (including error range) for the annual mean number size distribution (compare to Fig. 3). Dashed lines provide visual orientation and indicate 0, 50, and 100 % activation. The value at 50 % activation is used for calculation of the hygroscopicity parameter  $\kappa(S,D_a)$ . The lines connecting the data points merely serve as visual orientation.

The  $MAF(S)$  time series in Fig. 1f represents a valuable additional parameter to determine the abundance of “poor” CCN (i.e., aerosol particles that are not activated into CCN within the tested  $S$  range). For higher  $S$  (i.e.,  $S > 0.11$  %),  $MAF(S)$  is close to unity over the whole year. In contrast,  $MAF(0.11$  %) fluctuates around unity during the wet season months; however, it drops below unity during the biomass-burning-impacted dry season and subsequent transition period. For some episodes,  $MAF(S)$  shows very pronounced dips, as further discussed in the Part 2 study (M. L. Pöhlker et al., 2017a).

### 3.2 Annual means of CCN activation curves and hygroscopicity parameter

Figure 2 displays the annual mean CCN activation curves for all  $S$  levels. Thus, it represents an overall characterization of the particle activation behavior, which means that for decreasing  $S$  levels the activation diameter,  $D_a(S)$ , increases. In other words, every  $S$  corresponds to a certain (and to some extent typical)  $D_a(S)$  range, where particles start to become activated (see Table 1). As an example, relatively high  $S$  conditions (0.47–1.10 %) yield substantial activation already in the Aitken-mode range, while low  $S$  levels (0.11–0.29 %) correspond to activation of larger particles, mostly in the ac-

cumulation mode. Note that  $S$  levels in convective clouds rarely exceed 1.0 %, but that in the presence of precipitation higher  $S$  values are possible (Cotton and Anthes, 1989). The step from the activation curves at  $S=0.47$  % to  $S=0.29$  % relates to the position of the characteristic Hoppel minimum (at 97 nm for the annual mean size distribution; see Table 2) between Aitken and accumulation mode in the bimodal size distribution. Thus, the step to  $S=0.47$  % represents the onset of significant activation in the Aitken-mode size range.

A different representation of these observations is displayed in Fig. 3, which shows the bimodally fitted (bimodal logarithmic normal distribution,  $R^2=0.99$ ) annual mean  $N_{CN}(D)$  size distribution. In this annual average representation, the Aitken-mode maximum is located at  $D_{Ait}=69 \pm 1$  nm, the accumulation-mode maximum at  $D_{Acc}=149 \pm 2$  nm, and both are separated by the Hoppel minimum (compare to Table 2) (Hoppel et al., 1996). Furthermore, Fig. 3 clearly shows that different  $\kappa(S,D_a)$  values are retrieved for the Aitken ( $\kappa_{Ait}=0.14 \pm 0.03$ ) vs. the accumulation-mode size range ( $\kappa_{Acc}=0.22 \pm 0.03$ ). This indicates that Aitken- and accumulation-mode particles have different hygroscopicities and thus different chemical compositions. In this case, Aitken-mode particles tend to be more predominantly organic (close to  $\kappa=0.1$ ) than the accumulation-mode particles, which tend to contain more inorganic species (i.e., ammonium, sulfates, potassium) (Prenni et al., 2007; Gunthe et al., 2009; Wex et al., 2009; C. Pöhlker et al., 2012). The enhanced hygroscopicity in the accumulation mode is a well-documented observation for various locations worldwide, which is thought to result from the cloud processing history of this aerosol size fraction (e.g., Paramonov et al., 2013, 2015). For the Amazon Basin, our observed size dependence of  $\kappa(S,D_a)$  agrees well with the values reported by Gunthe et al. (2009) and Whitehead et al. (2016).

The arithmetic mean hygroscopicity parameter at the ATTO site for all sizes ( $43 \text{ nm} < D_a < 172 \text{ nm}$ ) and for the entire measurement period is  $\kappa_{mean}=0.17 \pm 0.06$ . For comparison, Gunthe et al. (2009) reported  $\kappa_{mean}=0.16 \pm 0.06$  (for the early wet season 2008). The observed standard deviation is rather small, which reflects the low variability of  $\kappa_{mean}$  throughout the year (see Fig. 1b).

No perceptible diurnal trend in  $\kappa_{mean}$  is present in the annually averaged data. This is because the ATTO site is not (strongly) influenced by aerosol compositional changes that follow pronounced diurnal cycles (i.e., input of anthropogenic emissions). A consequence of this finding is that the overall hygroscopicity of the aerosol at the ATTO site (as a representative measurement station of the central Amazon) is well represented in model studies by using  $\kappa_{mean}=0.17 \pm 0.06$  (see also Sect. 3.5.4). Previous long-term CCN observations from alpine, semi-arid, and boreal background sites have similarly shown that diurnal cycles in  $\kappa(S,D_a)$  (or the related  $D_a(S)$ ) tend to be rather small or even

**Table 2.** Properties (position  $x_0$ , integral number concentration  $N_{\text{CN}}$ , width  $\sigma$ ) of Aitken and accumulation modes from the double log-normal fit (compare to  $R^2$ ) of the total particle size distributions. Values are given as annual means and subdivided into seasonal periods of interest as specified in Sect. 3.3 (compare also to Fig. 6). In addition, values for the position of the Hoppel minimum  $D_{\text{H}}$  as well as estimated average peak supersaturation in cloud  $S_{\text{cloud}}(D_{\text{H}}, \kappa)$  are listed. The errors represent the uncertainty of the fit parameters. The error in  $S_{\text{cloud}}(D_{\text{H}}, \kappa)$  is the experimentally derived error in  $S$ .

Season	Mode	$N_{\text{CN}}$ ( $\text{cm}^{-3}$ )	$\kappa$	$x_0$ (nm)	$\sigma$	$R^2$	$D_{\text{H}}$ (nm)	$S_{\text{cloud}}(D_{\text{H}}, \kappa)$ (%)
Year	Aitken	$397 \pm 31$	$0.13 \pm 0.03$	$69 \pm 1$	$0.44 \pm 0.02$	0.99	$97 \pm 2$	$0.29 \pm 0.03$
	accumulation	$906 \pm 29$	$0.22 \pm 0.05$	$149 \pm 2$	$0.57 \pm 0.01$			
LRT	Aitken	$231 \pm 8$	$0.14 \pm 0.04$	$67 \pm 1$	$0.63 \pm 0.01$	0.99	$109 \pm 2$	$0.23 \pm 0.02$
	accumulation	$232 \pm 10$	$0.28 \pm 0.08$	$172 \pm 1$	$0.51 \pm 0.01$			
Wet	Aitken	$246 \pm 9$	$0.13 \pm 0.02$	$70 \pm 1$	$0.53 \pm 0.01$	0.99	$112 \pm 2$	$0.22 \pm 0.02$
	accumulation	$145 \pm 8$	$0.21 \pm 0.05$	$170 \pm 2$	$0.42 \pm 0.01$			
Transition	Aitken	$405 \pm 24$	$0.14 \pm 0.02$	$65 \pm 1$	$0.42 \pm 0.01$	0.99	$92 \pm 2$	$0.34 \pm 0.03$
	accumulation	$668 \pm 24$	$0.24 \pm 0.04$	$135 \pm 1$	$0.53 \pm 0.01$			
Dry	Aitken	$483 \pm 49$	$0.13 \pm 0.03$	$71 \pm 2$	$0.42 \pm 0.03$	0.99	$97 \pm 2$	$0.29 \pm 0.03$
	accumulation	$1349 \pm 47$	$0.21 \pm 0.04$	$150 \pm 2$	$0.58 \pm 0.01$			

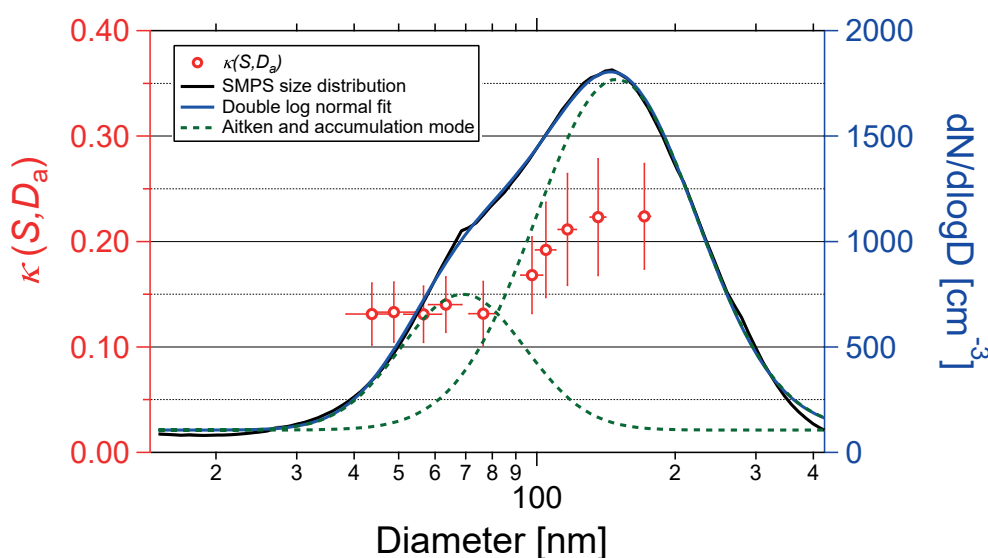


**Figure 3.** Size dependence of the hygroscopicity parameter  $\kappa(S, D_a)$  averaged over the entire measurement period. Values of  $\kappa(S, D_a)$  for every  $S$  level are plotted against their corresponding midpoint activation diameter  $D_a(S)$  (left axis). For  $\kappa(S, D_a)$ , the error bars represent 1 standard deviation. For  $D_a(S)$ , the experimentally derived error is shown. In addition, the average number size distribution for the entire measurement period is shown (right axis). Dashed green lines represent the average Aitken and accumulation modes. The standard error of the number size distribution is indicated as grey shading, which is very small and therefore hardly perceptible in this representation due to the large number of scans with comparatively small variability. Distinctly different  $\kappa(S, D_a)$  levels can be observed for the Aitken and accumulation modes with lower variability in the Aitken than in the accumulation mode.

absent (Jurányi et al., 2011; Levin et al., 2012; Paramonov et al., 2013).

Figure 4 combines the annually averaged size distributions of  $N_{\text{CN}}(D)$  as well as  $N_{\text{CCN}}(S, D)$  for all  $S$  levels. These curves result from multiplying the  $N_{\text{CN}}(D)$  size distribution with the CCN activation curves in Fig. 2 and clearly visualize the inverse relationship of  $D_a(S)$  and  $S$ . Following the

previous discussion of Fig. 2,  $S$  ranging between 0.11 and 0.29 % mostly activates accumulation-mode particles, while  $S$  ranging between 0.47 and 1.10 % activates the accumulation mode plus a substantial fraction of Aitken-mode particles. For the highest supersaturation ( $S = 1.10$  %) that was used in this study, almost the entire  $N_{\text{CN}}(D)$  size distribution is being activated into CCN, which (regarding the very

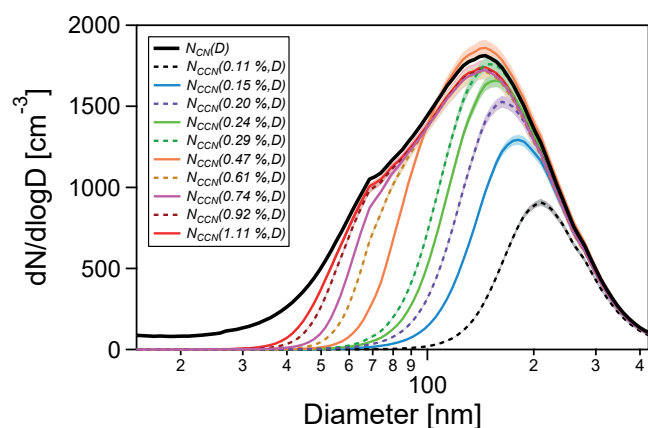


**Figure 4.** Number size distributions of total aerosol particles,  $N_{CN}(D)$ , and of cloud condensation nuclei,  $N_{CCN}(S, D)$ , at all 10 supersaturation levels ( $S = 0.11$ – $1.10$  %) averaged over the entire measurement period. The  $N_{CCN}(S, D)$  size distributions were calculated by multiplying the average  $N_{CN}(D)$  size distributions (in Fig. 3) with the average CCN activation curves in (Fig. 2).

sparse occurrence of particles  $< 30$  nm) explains the high  $N_{CCN}(1.10\%)/N_{CN,10}$  levels in Fig. 1d.

### 3.3 Seasonal differences in CCN properties at the ATTO site

Within the seasonal periods in the central Amazon as defined in Sect. 1.2, we have subdivided the annual data set into the following four periods of interest, which represent the contrasting aerosol conditions and/or sources. (a) The first half of the wet seasons 2014 and 2015 received substantial amounts of long-range transport (LRT) aerosol: mostly African dust, biomass smoke, and fossil fuel emissions (Ansmann et al., 2009; Salvador et al., 2016). Here, the corresponding period of interest will be called LRT season and covers 24 March to 13 April 2014 and 9 January to 10 February 2015. (b) In the late wet season 2014, all pollution indicators approached background conditions. Thus, the period from 13 April to 31 May 2014 will be treated as the clean wet season in this study. (c) The months June to July represent the transition period from wet to dry season and will be called “transition wet to dry”. (d) The period of interest that covers the dry season with frequent intrusion of biomass burning smoke ranges from August to December 2014.

Figure 5 shows the CCN activation curves for all  $S$  levels, subdivided into the four seasonal periods of interest. Although the plots for the individual seasons appear to differ only subtly, e.g., in  $D_a(S)$  position and curve width, there is one major difference: the variable shape of the activation curve for the smallest  $S = 0.11$  %. Particularly, the behavior of  $MAF(0.11\%)$  shows clear seasonal differences. It reaches unity during the wet season, whereas it levels off below unity for the LRT, transition, and particularly for the

dry season periods. The fraction of non-activated particles with  $D \leq 245$  nm at  $S = 0.11$  % is  $\sim 10$  % during the transition period and  $\sim 20$  % during the dry season. Interestingly, this effect is only observed for  $S = 0.11$  %, whereas  $MAF(> 0.11\%)$  reaches unity throughout the entire year. An explanation for this observation could be the intrusion of relatively fresh biomass burning aerosol plumes during the transition period and dry season, which contain a fraction of comparatively inefficient CCN. Soot is probably a main candidate here; however, fresh soot should also significantly reduce the  $MAF(S)$  for higher  $S$  levels (Rose et al., 2010). Thus, we speculate that probably “semi-aged” soot particles may be an explanation for the observed activation behavior.

Figure 6 corresponds to Fig. 3 and subdivides the annual mean  $\kappa(S, D_a)$  size distribution ( $\kappa(S, D_a)$  plotted against all measured  $D_a(S)$ ) as well as the annual mean  $N_{CN}(D)$  size distribution into their seasonal counterparts. The particle size distributions were fitted with a bimodal logarithmic normal distribution and the corresponding results are listed in detail in Table 2. The differences in the characteristic size distributions for the individual seasons clearly emerge: in addition to the strong variations in total particle number concentration (see Fig. 1), the accumulation mode overwhelms the Aitken mode during the dry season, while accumulation and Aitken modes occur at comparable strength under wet season conditions. In other words, during the dry season, Aitken-mode particles account on average for about 26 % of the total aerosol population ( $N_{CN,Ait} = 483 \pm 49$  cm $^{-3}$  vs.  $N_{CN,Acc} = 1349 \pm 47$  cm $^{-3}$ ), whereas during the wet season, the Aitken mode accounts for about 62 % ( $N_{CN,Ait} = 246 \pm 9$  cm $^{-3}$  vs.  $N_{CN,Acc} = 145 \pm 8$  cm $^{-3}$ ) (see Table 2). The size distribution of the transition period from wet to dry season represents an intermediate state between the wet and dry season “extremes”. Furthermore, the comparison between wet season conditions with and without LRT influence reveals comparable distributions. However, a slight increase in the accumulation mode during LRT conditions indicates the presence of dust, smoke, pollution, and aged sea spray on top of the biogenic aerosol population during pristine periods (M. L. Pöhlker et al., 2017a).

The Hoppel minimum  $D_H$  (Hoppel et al., 1996) between the Aitken and accumulation modes<sup>4</sup> also shows seasonal variations with its largest values around 110 nm in the wet season and its smallest values around 95 nm in the dry season (compare to Fig. 5 and Table 2). Following Krüger et al. (2014), the observed  $D_H$  can be used to determine an effective average cloud peak supersaturation  $S_{cloud}(D_H, \kappa)$ .

<sup>4</sup>The position of  $D_H$  was determined as the intersection of the fitted and normalized modes (monomodal fits for Aitken and accumulation mode were normalized to equal area). The normalization is necessary for a precise localization of  $D_H$  because large differences in Aitken- and accumulation-mode strength (e.g., for the dry season conditions) cause biased  $D_H$  as the intersection of both modes is shifted towards the smaller mode.

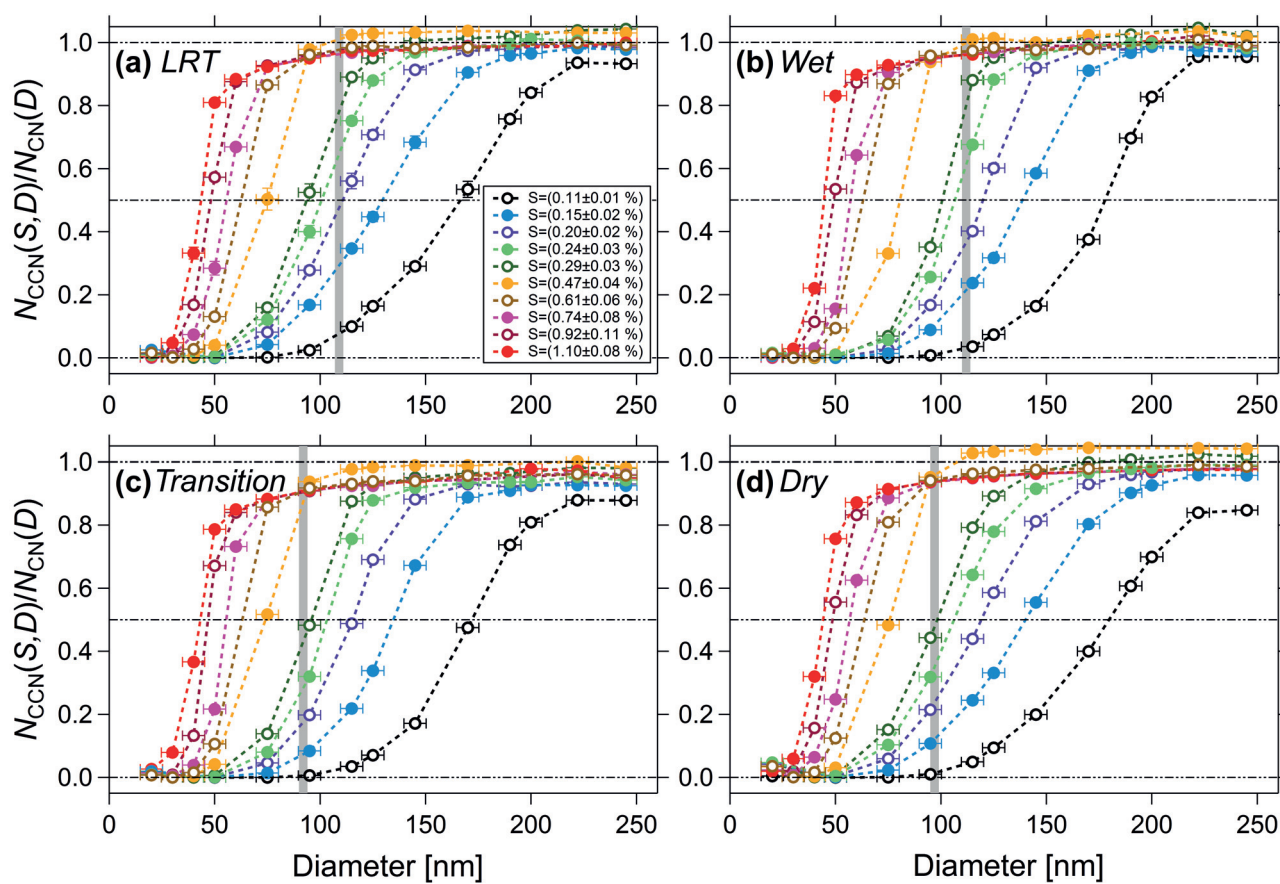


**Figure 5.** CCN activation curves for all measured  $S$  levels ( $S = 0.11$ – $1.10$  %), subdivided into seasonal periods of interest as specified in Sect. 3.3. Data points represent arithmetic mean values. For  $N_{\text{CCN}}(S, D)/N_{\text{CN}}(D)$ , the standard error is plotted, which is very small (due to the large number of scans with comparatively small variability) and therefore not perceptible in this representation. For the diameter,  $D$ , the error bars represent the experimental error as specified in Sect. 2.3. The grey vertical bands represent the (seasonal) position of the Hoppel minima (including error range; compare to Table 2). Dashed horizontal lines provide visual orientation and indicate 0, 50, and 100 % activation. The 50 % activation diameter is used for calculation of the hygroscopicity parameter  $\kappa(S, D_a)$ . The lines connecting the data points merely serve as visual orientation.

Cloud development and dynamics are highly complex processes in which aerosol particles are activated at different supersaturations. In the context of this study,  $S_{\text{cloud}}(D_{\text{H}}, \kappa)$  is used as a mean cloud supersaturation and serves as an overall reference value; however, it does not reflect the complex development of  $S$  inside a cloud. Based on our data,  $S_{\text{cloud}}(D_{\text{H}}, \kappa)$  is estimated as a value around 0.29 % during dry season conditions and around 0.22 % during wet season conditions (Table 2). This indicates that  $S_{\text{cloud}}(D_{\text{H}}, \kappa)$  levels tend to be noticeable lower during wet season cloud development compared to the dry season scenario. A plausible cause for the comparatively small  $D_{\text{H}}$  and high  $S_{\text{cloud}}(D_{\text{H}}, \kappa)$  in the dry season could be invigorated updraft regimes in the convective clouds. This invigoration could be caused by the stronger solar heating during the dry season and/or the increased aerosol load under biomass-burning-impacted conditions, as suggested previously (Andreae et al., 2004; Rosenfeld et al., 2008). As outlined in Sect. 1.1, aerosol particle

size, concentration, and hygroscopicity as well as cloud supersaturation represent key parameters for a detailed understanding of cloud properties. Figure 6 provides reference values for all these parameters, resolved by seasons and thus provides comprehensive insight into the Amazonian cloud properties.

Comparing the seasonal  $\kappa(S, D_a)$  size distributions in Fig. 6, it is obvious that the (seasonally averaged)  $\kappa_{\text{Ait}}$  values in the Aitken-mode size range are surprisingly stable between 0.13 and 0.14 throughout the whole year. This indicates that the Aitken-mode aerosol population was persistently dominated by almost pure organic particles throughout the seasons. In contrast, noticeable seasonal differences were observed for (seasonally averaged)  $\kappa_{\text{Acc}}$  values in the accumulation-mode size range, with mean values ranging from around 0.21 to 0.28. This indicates that the accumulation mode also comprises high contents of organic materials, however, with elevated amounts of inorganic ingredi-

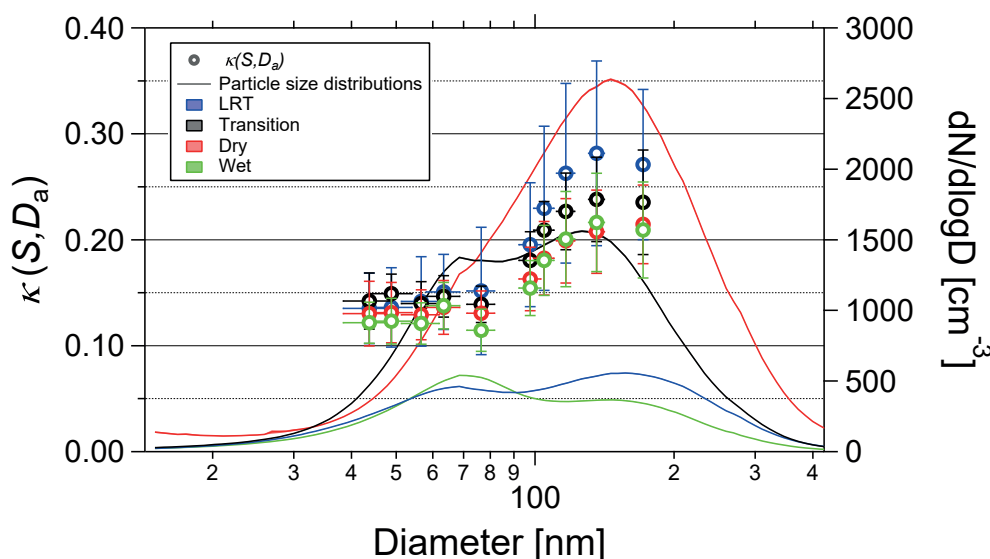


**Figure 6.** Size dependence of the hygroscopicity parameter  $\kappa(S, D_a)$  subdivided into seasonal periods of interest (color coding) as specified in Sect. 3.3. Values of  $\kappa(S, D_a)$  for every  $S$  level are plotted against their corresponding midpoint activation diameter  $D_a(S)$  (left axis). For  $\kappa(S, D_a)$ , the error bars represent 1 standard deviation. For  $D_a(S)$ , the experimentally derived error is shown. In addition, the average number size distributions for the seasonal periods of interest are shown (right axis). The standard error of the number size distributions is indicated as shading, which is very small and therefore hardly perceptible in this representation due to the large number of scans with comparatively small variability. A clear size dependence and seasonal trends in  $\kappa(S, D_a)$  levels can be observed. The averaged number size distributions show very pronounced seasonal differences.

ents (i.e., sulfate, ammonium, and potassium). In the size range around  $D_H$ , which separates the (apparently) chemically distinct aerosol populations of Aitken and accumulation modes, a step-like increase in  $\kappa(S, D_a)$  is observed. The highest seasonally averaged  $\kappa(S, D_a)$  values (up to 0.28) are observed during intrusion of dust, marine sulfate, and sea-salt-rich LRT plumes. Note that short-term peaks in  $\kappa(S, D_a)$  can be even higher; see case studies in Part 2 (M. L. Pöhlker et al., 2017a). In the absence of LRT, the  $\kappa_{Acc}$  values are also rather stable for most of the year and range between 0.21 and 0.24. Overall, a remarkable observation is the high similarity between the wet and dry season  $\kappa(S, D_a)$  size distributions, while many other aerosol parameters undergo substantial seasonal variations (Andreae et al., 2015).

The  $\kappa(S, D_a)$  levels reported here agree well with the corresponding results in the previous Amazonian CCN studies by Gunthe et al. (2009) and Whitehead et al. (2016), which range between 0.1 and 0.4, with a mean around  $0.16 \pm 0.06$ . In a wider context, our results also agree well with previous long-term measurements at other continental background locations (i.e., alpine, semi-arid, and boreal sites) (Jurányi et al., 2011; Levin et al., 2012; Paramonov et al., 2013; Mikhailov et al., 2015). Comparing these four sites with each other, the following observations can be made. (i)  $\kappa_{Ait}$  tends to be smaller than  $\kappa_{Acc}$  at all four background locations. (ii) At the alpine, semi-arid, and boreal sites,  $\kappa(S, D_a)$  undergoes a rather gradual increase from the Aitken- to the accumulation-mode size range (Paramonov et al., 2013,

and references therein), whereas this increase appears to be steeper (step-like) in the Amazon. This can clearly be seen in the present study (e.g., Fig. 3) as well as in Gunthe et al. (2009) and Whitehead et al. (2016). (iii) Particularly in the vegetated environments (i.e., tropical, boreal, and semi-arid forests),  $\kappa_{Ait}$  mostly ranges between 0.1 and 0.2, suggesting that the Aitken-mode particles predominantly comprise organic constituents. Furthermore,  $\kappa_{Ait}$  shows a remarkably small seasonality for these locations. (iv) The  $\kappa_{Acc}$  levels show a much wider variability throughout the seasons for all locations.

Figure 7 presents the diurnal cycles in  $\kappa_{mean}$  for the four seasonal periods of interest. No perceptible diurnal trends in  $\kappa_{mean}$  can be observed for any of the seasons. The only observable difference is an increased variability of  $\kappa_{mean}$  during the LRT season (see error bars in Fig. 7a). This can be explained by the episodic character of LRT intrusions, which causes an “alternating pattern” of clean periods with background conditions and periods of elevated concentrations of LRT aerosol (M. L. Pöhlker et al., 2017a). For comparison, the diurnal cycles in  $N_{CN}$  concentration have been added to Fig. 7, which confirm the absence of strong diurnal variations in the aerosol population.

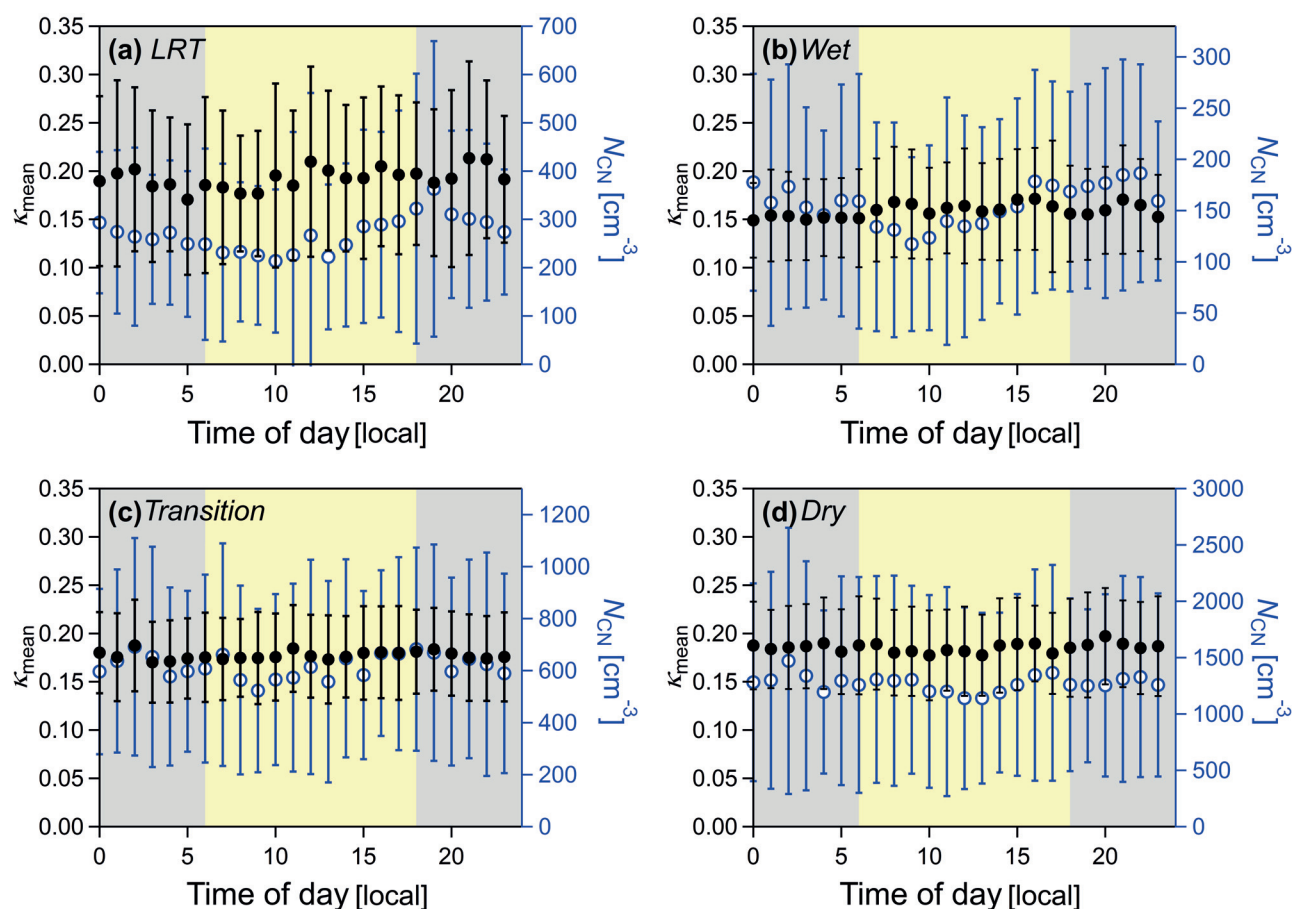


**Figure 7.** Diurnal cycles in hygroscopicity parameter,  $\kappa_{\text{mean}}$ , and total aerosol number concentration,  $N_{\text{CN}}$ , subdivided into seasonal periods of interest as specified in Sect. 3.3. No diurnal trend is detectable throughout the year. Note that the range of 1 standard deviation of  $\kappa_{\text{mean}}$  around the mean is surprisingly small given that long seasonal time periods and data from all  $S$  levels have been averaged. The only perceptible difference is a larger scattering during a period with LRT influence (a). Grey and yellow shading indicate night and day.

### 3.4 Aerosol chemical composition and effective hygroscopicity

Continuous ACSM measurements are being conducted at the ATTO site since March 2014, providing online and non-size-resolved information on the chemical composition of the non-refractory aerosol (Andreae et al., 2015). Here, we compare the ACSM data on the aerosol's chemical composition with the CCNC-derived  $\kappa(S, D_a)$  values. This analysis focuses on the dry season months, when ACSM and CCNC were operated in parallel.<sup>5</sup> Note that the ACSM covers a size range from 75 to 650 nm (Ng et al., 2010), while the size-resolved CCN measurements provide information only up to particle sizes of about 170 nm. Since the ACSM records the size-integrated masses of defined chemical species (organics,

<sup>5</sup>Although the ACSM measurements were started in March 2014, instrumental issues during the initial months caused some uncertainty for the corresponding data. Thus, for this study, we focus only on the data period August to December 2014, when the instrumental issues were resolved.

nitrate, sulfate, ammonium, and chloride), the results tend to be dominated by the fraction of larger particles with comparatively high masses (i.e., in the accumulation-mode size range) and are influenced less by the fraction of small particles with comparatively low masses (i.e., in the Aitken-mode size range). Thus, in order to increase the comparability between ACSM and CCNC, we have chosen the lowest  $S$  level ( $S = 0.11 \pm 0.01\%$ ), which represents the largest measured  $D_a(S)$  ( $D_a(S) = 172 \pm 12$  nm).

In Fig. 8, the  $\kappa(0.11\%, D_a)$  values are plotted against the ACSM-derived organic mass fraction ( $f_{\text{org}}$ ). The data were fitted with (i) a linear fit and (ii) a bivariate regression according to Cantrell (2008). A linear fit approach was used by Gunthe et al. (2009) to determine the effective hygroscopicity parameters  $\kappa_{\text{org}} = 0.1$  of biogenic Amazonian SOA ( $f_{\text{org}} = 1$ ) and  $\kappa_{\text{inorg}} = 0.6$  for the inorganic fraction ( $f_{\text{org}} = 0$ ). For the present data set, the same procedure results in an acceptable coefficient of determination ( $R^2 = 0.66$ ). We estimated the effective hygroscopicity parameters  $\kappa_{\text{org}} = 0.12 \pm 0.01$  and  $\kappa_{\text{inorg}} = 0.61 \pm 0.01$  based

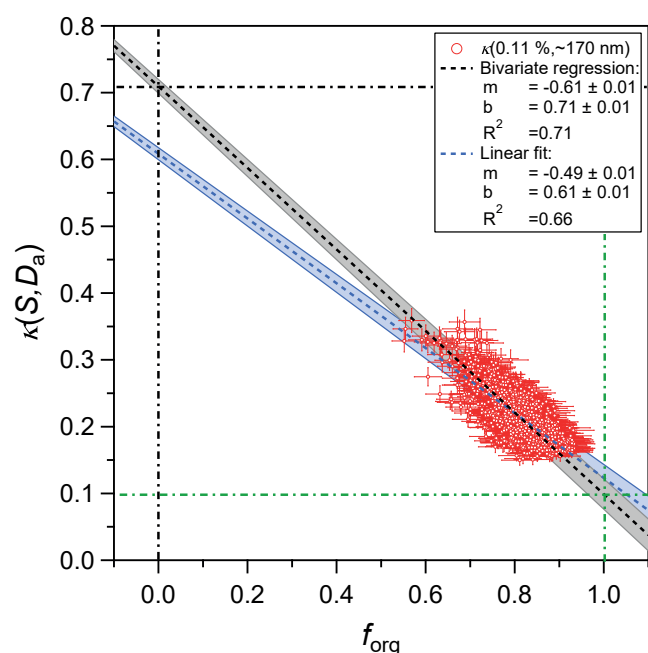


**Figure 8.** Correlation between  $\kappa(0.11\%, \sim 170\text{ nm})$  and the organic mass fraction,  $f_{\text{org}}$ , determined by the ACSM during the dry season months. The data were fitted by a linear and a bivariate regression fit. Shading of the fit lines shows the standard error of the fit. The error bars of the data markers represent the experimental error, which is estimated as 5% for  $f_{\text{org}}$  and 10% for  $\kappa(0.11\%, \sim 170\text{ nm})$ .

on the linear fit and extrapolation to  $f_{\text{org}} = 1$  and  $f_{\text{org}} = 0$ , respectively. This is in good agreement with previous studies (King et al., 2007; Engelhart et al., 2008; Gunthe et al., 2009; Rose et al., 2011). However, a drawback of the linear fitting approach is the fact that swapping  $f_{\text{org}}$  and  $\kappa(0.11\%, D_a)$  on the axes will change the results.

Therefore, we also applied the bivariate regression fit, which takes into account that both parameters,  $f_{\text{org}}$  and  $\kappa(0.11\%, D_a)$ , have an experimental error. For the bivariate regression, an error of 5% in  $f_{\text{org}}$  and an error of 10% in  $\kappa(0.11\%, D_a)$  were used. A coefficient of determination of  $R^2 = 0.71$  was obtained for the bivariate regression, which is slightly better than for the linear fit. Based on the bivariate regression, we estimated effective hygroscopicity parameters  $\kappa_{\text{org}} = 0.10 \pm 0.01$  and  $\kappa_{\text{inorg}} = 0.71 \pm 0.01$  for the organic and inorganic fractions, respectively.

### 3.5 CCN parametrizations and prediction of CCN number concentrations

Cloud-resolving models at all scales – spanning from large eddy simulations (LESs) to global climate models (GCMs) – require simple and efficient parametrizations of the complex microphysical basis to adequately reflect the spatiotemporal CCN cycling (Cohard et al., 1998; Andreae, 2009). Previously, several different approaches to predict CCN concen-

trations have been suggested (Andreae, 2009; Gunthe et al., 2009; Rose et al., 2010; Deng et al., 2013). Any parametrization strategy seeks, on one hand, an efficient combination of a minimal set of input data and, on the other hand, a good representation of the atmospheric CCN population.

The detailed analysis in this study has shown that the CCN population in the central Amazon is mainly defined by comparatively stable  $\kappa(S, D_a)$  levels, due to the predominance of organic aerosol particles, and rather pronounced seasonal trends in aerosol number size distribution. Particularly, the remarkably stable  $\kappa(S, D_a)$  values suggest that the Amazonian CCN cycling can be parametrized rather precisely for efficient prediction of CCN concentrations. In the following paragraphs, we apply the following CCN parametrization strategies to the present data set and explore their strengths and limitations:

- CCN prediction based on the correlation between  $N_{\text{CCN}}(0.4\%)$  and  $N_{\text{CN}}$ , called the  $\Delta N_{\text{CCN}}(0.4\%)/\Delta N_{\text{CN}}$  parametrization here;
- CCN prediction based on the correlation between  $N_{\text{CCN}}(S)$  and  $c_{\text{CO}}$ , called the  $\Delta N_{\text{CCN}}(S)/\Delta c_{\text{CO}}$  parametrization here;
- CCN prediction based on analytical fit functions of experimentally obtained CCN spectra, called CCN spectra parametrization;
- CCN prediction based on the  $\kappa$ -Köhler model, called  $\kappa$ -Köhler parametrization; and
- CCN prediction based on a novel and effective parametrization built on CCN efficiency spectra, called CCN efficiency spectra parametrization.

The prediction accuracy for the individual strategies is summarized in Table 3.

#### 3.5.1 $\Delta N_{\text{CCN}}(0.4\%)/\Delta N_{\text{CN}}$ parametrization

Andreae (2009) analyzed CCN data sets from several contrasting field sites worldwide and found significant relationships between the satellite-retrieved aerosol optical thickness (AOT) and the corresponding  $N_{\text{CCN}}(0.4\%)$  levels as well as between the total aerosol number concentration  $N_{\text{CN}}$  and  $N_{\text{CCN}}(0.4\%)$ . The obtained ratio  $N_{\text{CCN}}(0.4\%)/N_{\text{CN}} = 0.36 \pm 0.14$  – in other words, the globally averaged CCN efficiency at  $S = 0.4\%$  – can be used to predict CCN concentrations. The corresponding results for the present data set are displayed in Fig. 9a and show a surprisingly tight correlation, given that a globally obtained  $N_{\text{CCN}}(0.4\%)/N_{\text{CN}}$  ratio has been used. However, Fig. 9a also shows a systematic underestimation of the predicted CCN concentration  $N_{\text{CCN,p}}(0.4\%)$ , which can be explained by the comparatively high activated fractions in the Amazon (e.g.,  $N_{\text{CCN}}(0.47\%)/N_{\text{CN},10}$  ranging from 0.6 to 0.9;

S (%)	$\Delta N_{CCN}(S)/\Delta N_{CN}$		$\Delta N_{CCN}(S)/\Delta c_{CO}$		Fits of CCN spectra						Erf fit of CCN efficiency spectra											
	bias	dev	bias	dev	Twomey power-law fit		Erf fit		$\kappa$ -Köhler		Annual average		Resolved by seasons									
					annual	seasonal	annual	seasonal	annual	seasonal	annual	seasonal	annual	seasonal								
0.11 ± 0.01	–	–	1.48	1.75	4.68	4.75	1.50	1.57	2.54	2.81	0.61	0.89	0.18	0.22	0.64	0.74	0.24	0.44	0.39	0.53	0.14	0.36
0.15 ± 0.02	–	–	0.50	1.21	2.78	2.99	0.71	0.92	2.42	2.69	0.62	0.85	0.07	0.11	0.27	0.47	0.10	0.32	0.15	0.36	0.04	0.27
0.20 ± 0.02	–	–	2.84	2.96	2.46	2.75	0.59	0.85	2.60	2.86	0.70	0.91	0.11	0.13	0.22	0.43	0.13	0.30	0.14	0.33	0.08	0.24
0.24 ± 0.03	–	–	1.78	1.98	1.93	2.26	0.45	0.74	2.24	2.50	0.64	0.84	0.09	0.10	0.16	0.37	0.12	0.25	0.12	0.28	0.09	0.20
0.29 ± 0.03	–	–	2.19	2.33	1.74	2.09	0.40	0.71	2.12	2.39	0.62	0.82	0.14	0.14	0.22	0.42	0.14	0.25	0.17	0.32	0.11	0.20
0.40	–0.41	0.47	–	–	–	–	–	–	–	–	–	–	–	–	–	–	–	–	–	–	–	–
0.47 ± 0.04	–	–	1.33	1.54	1.36	1.73	0.33	0.63	1.70	1.93	0.50	0.71	0.04	0.06	0.09	0.26	0.07	0.16	0.08	0.20	0.06	0.12
0.61 ± 0.06	–	–	1.02	1.15	1.23	1.55	0.36	0.61	1.47	1.73	0.47	0.67	0.08	0.09	0.08	0.18	0.05	0.09	0.08	0.15	0.05	0.08
0.74 ± 0.08	–	–	1.50	1.59	1.22	1.51	0.40	0.62	1.37	1.63	0.44	0.64	0.09	0.10	0.09	0.16	0.04	0.06	0.09	0.14	0.04	0.06
0.92 ± 0.11	–	–	1.11	1.28	1.15	1.42	0.45	0.63	1.18	1.44	0.40	0.60	0.08	0.08	0.05	0.10	0.01	0.03	0.05	0.09	0.01	0.04
1.10 ± 0.08	–	–	1.12	1.25	1.11	1.35	0.48	0.64	1.05	1.31	0.35	0.57	0.08	0.08	0.04	0.08	–0.01	0.04	0.05	0.08	–0.01	0.05
All	–	–	1.50	1.73	2.00	2.27	0.57	0.80	1.89	2.15	0.54	0.75	0.10	0.11	0.19	0.33	0.10	0.20	0.14	0.25	0.06	0.17

**Table 3.** Characteristic deviation between observed and predicted CCN number concentrations –  $N_{CCN}(S)$  and  $N_{CCN,p}(S)$  – based on different parametrization schemes, according to Rose et al. (2008). For every parametrization scheme and resolved by  $S$ , the following information is provided: (i) arithmetic mean values of the relative bias  $\Delta_{bias} N_{CCN}(S) = (N_{CCN,p}(S) - N_{CCN}(S))/N_{CCN}(S)$  and (ii) of the total relative deviation  $\Delta_{dev} N_{CCN}(S) = |N_{CCN,p}(S) - N_{CCN}(S)|/N_{CCN}(S)$ .

see Fig. 1). Activated fractions in other locations worldwide tend to be lower due to the (more persistent) abundance of nucleation-mode particles, as discussed in Sect. 3.1.

In Sect. 3.5.5, we will show that our novel parametrization is an extension of this approach: the  $N_{CCN}(0.4\%)/N_{CN}$  parametrization refers to a globally averaged CCN efficiency at one specific  $S$ , while the CCN efficiency spectra parametrization is based on an analytical description of CCN efficiencies across the entire (relevant)  $S$  range and has been determined specifically for the central Amazon.

### 3.5.2 $\Delta N_{CCN}(S)/\Delta c_{CO}$ parametrization

Experimentally obtained excess  $N_{CCN}(S)$  to excess  $c_{CO}$  ratios can be used to calculate  $N_{CCN,p}(S)$ . Kuhn et al. (2010) determined  $\Delta N_{CCN}(0.6\%)/\Delta c_{CO} = \sim 26 \text{ cm}^{-3} \text{ ppb}^{-1}$  for biomass burning plumes and  $\Delta N_{CCN}(0.6\%)/\Delta c_{CO} = \sim 49 \text{ cm}^{-3} \text{ ppb}^{-1}$  for urban emissions in the area around Manaus, Brazil. Lawson et al. (2015) investigated biomass burning emissions in Australia and found  $\Delta N_{CCN}(0.5\%)/\Delta c_{CO} = 9.4 \text{ cm}^{-3} \text{ ppb}^{-1}$ . In the context of the present study, we have calculated  $\Delta N_{CCN}(S)/\Delta c_{CO}$  for a strong biomass burning event in August 2014. This event and its impact on the CCN population is the subject of a detailed discussion in the companion Part 2 paper (M. L. Pöhlker et al., 2017a). Here, we use the  $\Delta N_{CCN}(S)/\Delta c_{CO}$  ratios from the companion paper to obtain a CCN prediction. The observed  $\Delta N_{CCN}(S)/\Delta c_{CO}$  ratios range between  $6.7 \pm 0.5 \text{ cm}^{-3} \text{ ppb}^{-1}$  (for  $S = 0.11\%$ ) and values around  $18.0 \pm 1.3 \text{ cm}^{-3} \text{ ppb}^{-1}$  (for higher  $S$ ) (see summary in Table 4). Since biomass burning is the dominant source of pollution in the central Amazon, these biomass-burning-related  $\Delta N_{CCN}(S)/\Delta c_{CO}$  ratios in Table 4 were used to calculate  $N_{CCN,p}(S)$  for the present data set. The corresponding results in Fig. 9b show a reasonable correlation for highly polluted conditions ( $N_{CN} > 2000 \text{ cm}^{-3}$ ) and a poor correlation for cleaner states ( $N_{CN} < 2000 \text{ cm}^{-3}$ ). This behavior can be explained by the fact that the high concentrations in CCN and CO originate from frequent biomass burning plumes during the Amazonian dry season (see Fig. 1). Thus, they can be assigned to the same sources with rather defined  $\Delta N_{CCN}(S)/\Delta c_{CO}$  ratios (Andreae et al., 2012). During the contrasting cleaner periods, CN and CO originate from a variety of different sources, which are often not related and therefore explain the poor correlation for clean to semi-polluted conditions. Overall, Fig. 9b indicates that the quality of CO-based CCN prediction is rather poor, due to the complex interplay of different sources. The overall deviation between  $N_{CCN,p}(S)$  and  $N_{CCN}(S)$  for this approach is about 170% (Table 3).

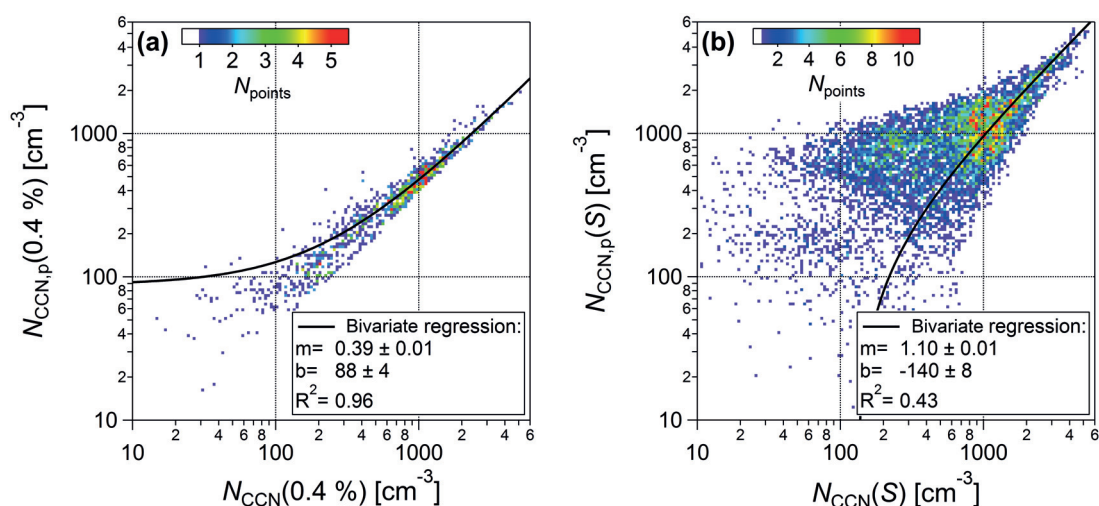


**Figure 9.** Predicted vs. measured CCN number concentrations calculated from (a) observed ratio  $N_{\text{CCN}}(0.4\%)/N_{\text{CN}}=0.36$  in Andreae (2009) and (b) observed (biomass-burning-related) excess CCN to excess CO ratios in M. L. Pöhlker et al. (2017a). The color code shows the number of data points falling into the pixel area, following Jurányi et al. (2011). The black line represents a bivariate regression fit of the data.

**Table 4.** Excess  $N_{\text{CCN}}(S)$  to excess  $c_{\text{CO}}$  ratios  $\Delta N_{\text{CCN}}(S)/\Delta c_{\text{CO}}$  for the individual  $S$  levels during peak period of the strong biomass burning event in August 2014. This event is analyzed in detail through a case study in the companion Part 2 paper (M. L. Pöhlker et al., 2017a). The values  $\Delta N_{\text{CCN}}(S)/\Delta c_{\text{CO}}$  were obtained from bivariate regression fit of scatterplots between  $N_{\text{CCN}}(S)$  and  $c_{\text{CO}}$  for individual  $S$  levels (Andreae et al., 2012). The parameter  $N_{\text{CCN}}(S)$  in this table represents the  $y$  axis intercept of the linear regression of  $N_{\text{CCN}}$  vs.  $c_{\text{CO}}$  at  $c_{\text{CO}} = 0$  ppb and is, therefore, negative (see M. L. Pöhlker et al., 2017a).

$S$ (%)	$\Delta N_{\text{CCN}}(S)/\Delta c_{\text{CO}}(\text{cm}^{-3} \text{ ppb}^{-1})$	$N_{\text{CCN}}(S) (\text{cm}^{-3})$	$R^2$
$0.11 \pm 0.01$	$6.7 \pm 0.5$	$-603 \pm 125$	0.86
$0.15 \pm 0.02$	$13.6 \pm 1.4$	$-1447 \pm 354$	0.68
$0.20 \pm 0.02$	$14.3 \pm 0.8$	$-1128 \pm 208$	0.90
$0.24 \pm 0.03$	$16.8 \pm 1.0$	$-1460 \pm 261$	0.86
$0.29 \pm 0.03$	$17.4 \pm 1.3$	$-1378 \pm 296$	0.83
$0.47 \pm 0.04$	$20.1 \pm 1.7$	$-1675 \pm 425$	0.84
$0.61 \pm 0.06$	$17.9 \pm 1.3$	$-1206 \pm 332$	0.88
$0.74 \pm 0.08$	$16.5 \pm 1.3$	$-933 \pm 329$	0.88
$0.92 \pm 0.11$	$18.1 \pm 1.4$	$-1265 \pm 355$	0.85
$1.10 \pm 0.08$	$17.5 \pm 1.3$	$-1096 \pm 328$	0.87

### 3.5.3 Classical and improved CCN spectra parametrization

The total number of particles that are activated at a given  $S$  is regarded as one of the central parameters in cloud formation and evolution (Andreae and Rosenfeld, 2008). Thus, CCN spectra ( $N_{\text{CCN}}(S)$  plotted against  $S$ ) are a widely and frequently used representation in various studies to summarize the observed  $N_{\text{CCN}}(S)$  values over the cloud-relevant  $S$  range for a given time period and location (Twomey and Wojciechowski, 1969; Roberts et al., 2002; Rissler et al., 2004; Freud et al., 2008; Gunthe et al., 2009; Martins et al., 2009b). Different analytical fit functions of the experimental CCN spectra have been proposed and are used as parametrization schemes for  $N_{\text{CCN}}(S)$  in modeling studies (e.g., Cohard et

al., 1998; Khain et al., 2000; Pinsky et al., 2012; Deng et al., 2013).

In the context of the present study, the annual mean Amazonian CCN spectrum is shown in Fig. 10. As an analytical representation of the experimental data, we have used Twomey's empirically found (classical) power-law fit function (Twomey, 1959):

$$N_{\text{CCN}}(S) = N_{\text{CCN}}(1\%) \cdot \left(\frac{S}{1\%}\right)^k, \quad (6)$$

which yields a reasonable coefficient of determination of  $R^2 = 0.88$  (Fig. 10a). Besides the annual mean spectrum, we also conducted a Twomey fit for the seasonally resolved CCN spectra (not shown) and summarized the resulting fit parameters in Table 5. The obtained fit parameters (e.g., for the an-

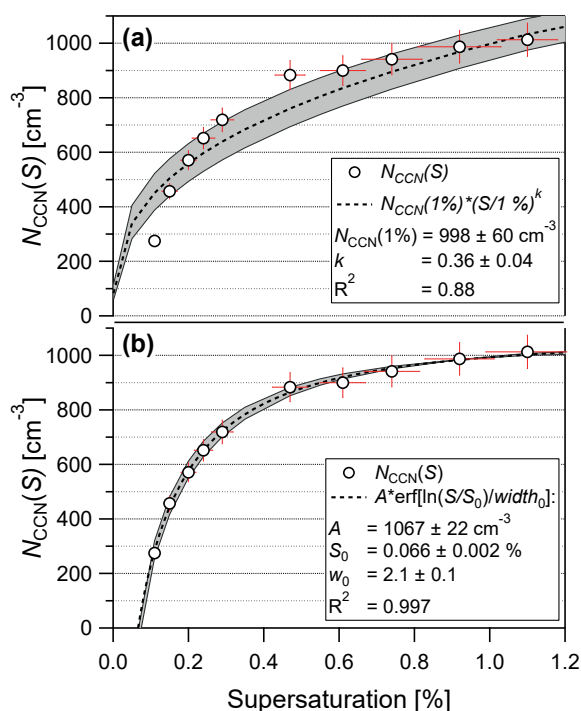


**Figure 10.** CCN spectrum (circular markers) averaged over the entire measurement period and fitted with the classical Twomey power-law fit (a) and an alternative error function fit (b). Error bars at the markers represent the measurement error in  $S$  and standard error in  $N_{CCN}(S)$ . The dashed line is a fit function with grey shading as uncertainty of the fit.

**Table 5.** Twomey fit parameters describing CCN spectra  $N_{CCN}(S)$  vs.  $S$  as parametrization input data (compare to Figs. 10 and 11a, c). Fit parameters are provided for annually averaged CCN spectra and resolved by seasons.

Time period	$N_{CCN}(1\%)$ ( $\text{cm}^{-3}$ )	$k$	$R^2$
Annual	$998 \pm 60$	$0.36 \pm 0.04$	0.88
Wet season	$289 \pm 7$	$0.57 \pm 0.03$	0.98
LRT period	$378 \pm 9$	$0.38 \pm 0.03$	0.94
Transition	$970 \pm 40$	$0.49 \pm 0.05$	0.94
Dry season	$1469 \pm 78$	$0.36 \pm 0.06$	0.86

nual mean CCN spectrum)  $N_{CCN}(1\%) = 998 \text{ cm}^{-3}$  (sometimes also called  $c$ ) and  $k = 0.36$  agree with results from previous measurements that are summarized by Martins et al. (2009b). The power-law function has become a widely used parametrization due to its simplicity (Cohard et al., 1998). However, because it is based on strong assumptions and not related to the physical basis of the fitted data, it has certain drawbacks, such as the poor representation of  $N_{CCN}(S)$  at small  $S$  (i.e.,  $< 0.2\%$ ), as well as the fact that for larger  $S$  (i.e.,  $> 1.2\%$ ) it does not converge against  $N_{CN}$ , which is, for physical reasons, the upper limit.

**Table 6.** Erf fit parameters describing CCN spectra  $N_{CCN}(S)$  vs.  $S$  as parametrization input data (compare to Figs. 10 and 11b, d). Fit parameters are provided for annually averaged CCN spectra and resolved by seasons.

Time period	$A$ ( $\text{cm}^{-3}$ )	$S_0$ (%)	$w_0$	$R^2$
Annual	$1067 \pm 22$	$0.07 \pm 0.01$	$2.1 \pm 0.1$	0.99
Wet season	$340 \pm 30$	$0.08 \pm 0.01$	$2.9 \pm 0.2$	0.97
LRT period	$532 \pm 72$	$0.04 \pm 0.01$	$4.5 \pm 1.0$	0.98
Transition	$1180 \pm 37$	$0.07 \pm 0.01$	$3.0 \pm 0.2$	0.99
Dry season	$1430 \pm 24$	$0.07 \pm 0.01$	$1.8 \pm 0.1$	0.99

As an alternative, an error function fit – which is used in this context for the first time – represents the data much better (Fig. 10b). The proposed error function (erf)

$$N_{CCN}(S) = A \cdot \text{erf}\left(\frac{\ln\left(\frac{S}{S_0}\right)}{w_0}\right) \quad (7)$$

is related to the physical basis of the fitted data and yields a high coefficient of determination ( $R^2 = 0.997$ ). Mathematically, this erf represents an integration of a log-normal  $N_{CN}(D)$  size distribution. Analogously, the  $N_{CCN}(D)$  spectrum represents the cumulative distribution of the relative  $N_{CN}(D)$  distribution (compare to Fig. 4). A double-erf fit would be even more appropriate for the bimodal Amazon  $N_{CN}(D)$  distribution (compare to Fig. 6 and discussion in Sect. 3.5.5). However, the single-erf fit proposed above proved to be (already) a very good analytical representation as underlined by the high coefficient of determination ( $R^2 > 0.99$ ). The erf fit reflects the physically expected saturation behavior of aerosol activation for high  $S$  and thus converges against a limit of  $A = 1067 \pm 22 \text{ cm}^{-3}$ , which matches well with the mean total number concentration of  $N_{CN,10} = 1097 \pm 66 \text{ cm}^{-3}$ . The erf fit (if not forced through the origin) transects the abscissa at  $S_0 = 0.066\%$ . Therefore, the erf fit cannot describe the CCN activation behavior for low  $S$  ( $\leq 0.07\%$ ), which is also an experimentally unaccessible  $S$  range. For this approach, we also summarized the corresponding fit parameters for the annual mean CCN spectrum and the seasonally resolved cases in Table 6.

Figure 11a and b show the corresponding  $N_{CCN,p}(S)$  vs.  $N_{CCN}(S)$  scatterplots based on the annual mean CCN spectrum using the Twomey and erf fits.<sup>6</sup> In general, parametrizations based on CCN spectra yield a mean state based on average concentrations (see fit parameters in Fig. 10 as well as Tables 5 and 6) and ignore the temporal variability of the aerosol abundance (Martins et al., 2009a; Rose et al., 2010; Jurányi et al., 2011). Upon closer inspection, Table 3 shows that the erf fit allows somewhat better predictions (e.g., deviation of power-law fit about 227 % vs. 215 % for erf fit

<sup>6</sup>The horizontal lines in the scatterplots result from the fact that constant  $N_{CCN,p}(S)$  values are obtained for the different  $S$  levels.

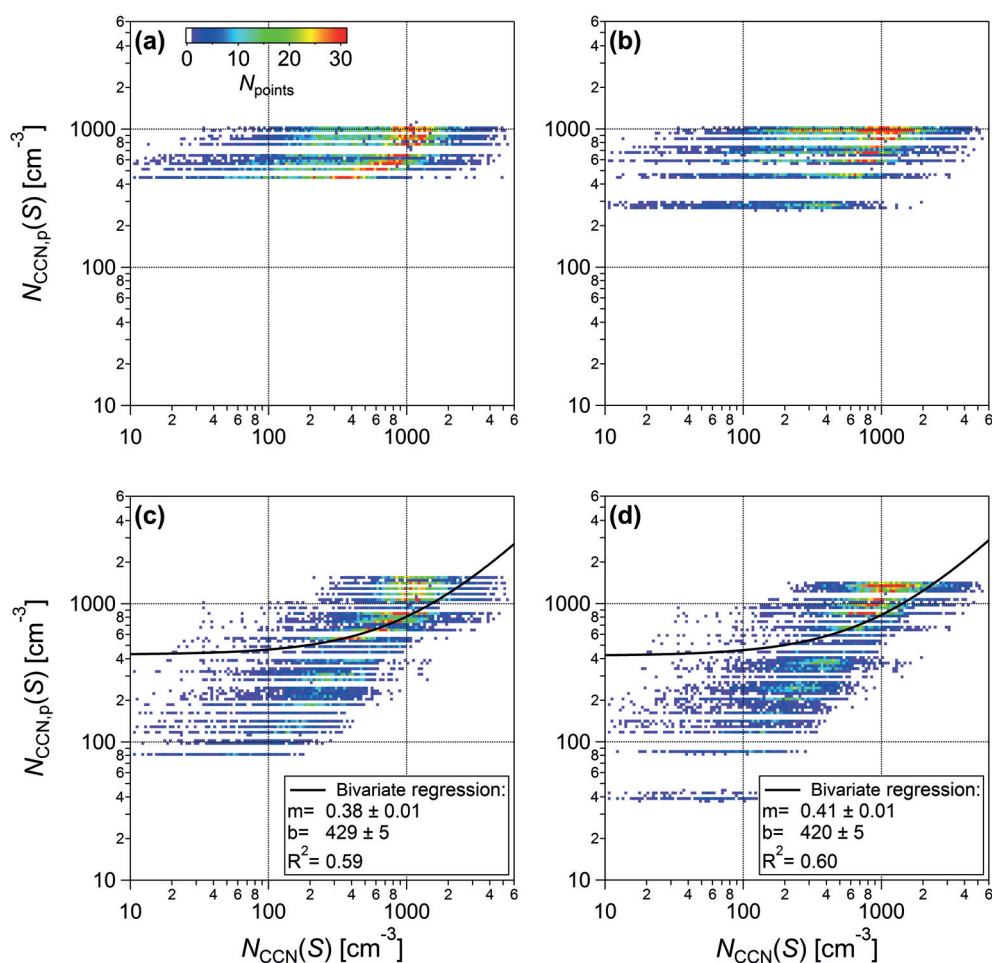


**Figure 11.** Predicted vs. measured CCN number concentrations based on the classical Twomey power-law fit (a, c) and an alternative error function fit (b, d). The top row (a, b) represents the annually averaged cases, whereas the bottom row (c, d) represents parametrizations based on seasonally resolved CCN spectra. Both predictions are based exclusively on the corresponding average fit functions (i.e., the annually averaged CCN spectra in Fig. 10 and seasonally averaged CCN spectra, as specified in Tables 5 and 6) without considering time-resolved aerosol parameters. The color code shows the number of data points falling into the pixel area, following Jurányi et al. (2011). Predicted and measured CCN concentrations deviate significantly, showing the inherent limitations of the CCN spectra approach. For the annually averaged data (a, b), no meaningful bivariate regression fit could be obtained.

in the case of annual mean and 80 % vs. 75 % for the seasonally resolved case), which can be explained by the fact that the erf fit represents the experimental data more appropriately (compare to Fig. 10). Overall, however, the power-law fit and the erf fit approaches give rather poor correlations due to the missing representation of the aerosol's temporal variability. This is particularly obvious for the annual mean case, since the total aerosol abundance varies significantly between wet and dry season conditions. Accordingly, the CCN spectra parametrization, which operates with constants, predictably underestimates the dry season conditions and overestimates the wet season conditions. In addition to the analytical fit approaches for the annual mean spectrum (Fig. 11a and b), we conducted an analogous CCN prediction based on seasonally resolved CCN spectra (Fig. 11c and

d). The prediction accuracy clearly improves (e.g., deviation of erf fit for annual mean case equals 215 % vs. 75 % for seasonally resolved case; see Table 3). Figure 11 illustrates that the prediction accuracy of parametrizations that rely on analytical fit functions of CCN spectra (i.e., Twomey, erf, and related functions) improves with decreasing variability of the aerosol population (e.g., for shorter periods with less variable aerosol properties). However, the missing representation of the aerosol's temporal variability remains an inherent limitation of the CCN spectra parametrization. It can be concluded that this parametrization requires a minimum of aerosol input data (i.e., only the parameters of the corresponding fit function), which explains its wide use in various modeling studies. However, Fig. 11 and Table 3 show that this simplicity is clearly at the expense of the prediction accuracy.

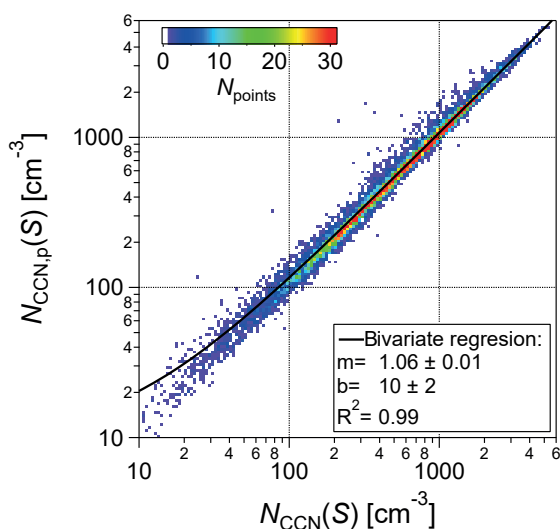


**Figure 12.** Predicted vs. measured CCN number concentrations using the  $\kappa$ -Köhler model approach. This approach requires the following time-resolved aerosol input data: (i) time-resolved aerosol size spectra spanning the CCN-relevant range (e.g., SMPS) and (ii) annual average  $\kappa$  values for the Aitken and accumulation size range ( $\kappa_{\text{Ait}} = 0.14$  and  $\kappa_{\text{Acc}} = 0.22$ ). The color code shows the number of data points falling into the pixel area, following Jurányi et al. (2011). The black line represents a bivariate regression fit of the data.

### 3.5.4 $\kappa$ -Köhler parametrization

The  $\kappa$ -Köhler model approach has been used in previous studies and gave good CCN predictions (e.g., Gunthe et al., 2009; Rose et al., 2010). For the present data set, the  $N_{\text{CCN},p}(S)$  concentrations were calculated according to Rose et al. (2010).<sup>7</sup> Here, the annually averaged values  $\kappa_{\text{Ait}} = 0.14$  and  $\kappa_{\text{Acc}} = 0.22$  were used for the CCN prediction, since they accurately represent the stable  $\kappa$  levels in the central Amazon. Figure 12 shows the corresponding  $N_{\text{CCN},p}(S)$  vs.  $N_{\text{CCN}}(S)$  scatterplot, in which the areas with the highest density of data points precisely follow the one-to-one line. Table 3 underlines this good agreement, as the observed deviation of around 10 % between  $N_{\text{CCN},p}(S)$  and  $N_{\text{CCN}}(S)$  is the smallest among all tested parametrizations. Accordingly, the  $\kappa$ -Köhler model approach turns out to be a very accurate parametrization. However, it requires a time series of  $N_{\text{CN}}$  size distributions as input data and is therefore the most “data demanding” strategy in this regard.

### 3.5.5 CCN efficiency spectra parametrization

It has to be kept in mind that CCN spectra strongly depend on the total aerosol concentration and thus predominantly reflect

<sup>7</sup>Briefly, for every SMPS scan, the  $N_{\text{CN}}$  size distribution has been integrated above the critical diameter  $D_a$ , in which  $D_a$  has been obtained based on a given  $\kappa$  and  $S$ .

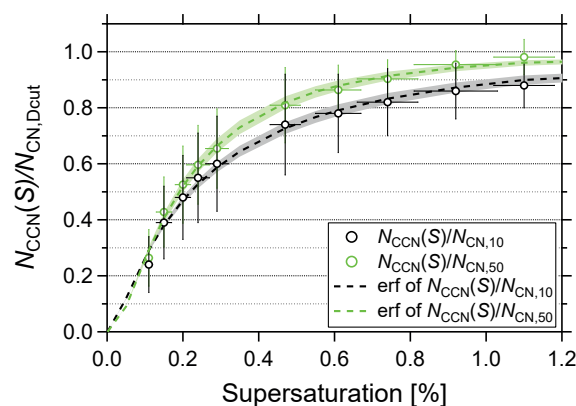


**Figure 13.** CCN efficiency spectra averaged over the entire measurement period for the reference concentrations,  $N_{\text{CN},10}$  and  $N_{\text{CN},50}$ . The fit functions are error function fits (the dashed line with shading represents the uncertainty of the fit). The error bars at the markers represent the measurement error in  $S$  and 1 standard deviation (not the standard error as in Fig. 10) in  $N_{\text{CCN}}(S)/N_{\text{CN},D_{\text{cut}}}$ .

the specific (temporary) aerosol population during the period of the study. The shape of CCN spectra provides some information on the aerosol activation behavior as a function of  $S$ . However, the strong variability in the total aerosol abundance makes it difficult to compare the CCN efficiency behavior between different locations and/or periods of interest with specific (e.g., seasonal) conditions. For the present data set, Fig. 13 shows annually averaged CCN efficiency spectra ( $N_{\text{CCN}}(S)/N_{\text{CN},D_{\text{cut}}}$  plotted against  $S$ ) for two different reference aerosol concentrations  $N_{\text{CN},10}$  and  $N_{\text{CN},50}$ .<sup>8</sup> The corresponding fit parameters are summarized in Table 7. The CCN efficiency spectra are independent of the total aerosol load and instead reflect the fraction of activated particles for the relevant  $S$  range. Here, we also use an erf fit,

$$\frac{N_{\text{CCN}}(S)}{N_{\text{CN},D_{\text{cut}}}} = \frac{1}{2} + \frac{1}{2} \cdot \text{erf} \left( \frac{\ln \left( \frac{S}{S_1} \right)}{w_1} \right), \quad (8)$$

to describe the data for the same reasons as outlined in Sect. 3.5.3. The fits yield high coefficients of determination ( $R^2 = 0.99$ ). Per definition,  $N_{\text{CCN}}(S)/N_{\text{CN},D_{\text{cut}}}$  spans from zero to unity. Therefore, the offset  $y_0$  of the function as well as the pre-factor  $A$  have been set to 0.5. For the atmospherically relevant  $S$  range – typically  $S < 0.6\%$  (see Andreae, 2009) – aerosol sizes around 50–60 nm are considered the onset of the CCN size range (see also Fig. 4). Accordingly, if  $D_{\text{cut}}$  is chosen close to this activation threshold, the corresponding  $N_{\text{CCN}}(S)/N_{\text{CN},D_{\text{cut}}}$  approaches unity, which can be seen in Fig. 13. The free variable  $S_1$  (e.g.,  $S_1 = 0.22 \pm 0.01\%$  for  $N_{\text{CN},10}$  and  $S_1 = 0.19 \pm 0.01\%$  for  $N_{\text{CN},50}$ ) represents the

<sup>8</sup>The use of aerosol number concentrations with  $D_{\text{cut}} = 50$  nm has been suggested by Paramonov et al. (2015) as a reference value to ensure comparability of CCN efficiencies from different studies.

**Table 7.** Erf fit parameters describing CCN efficiency spectra  $N_{CCN}(S)/N_{CN,D_{cut}}$  vs.  $S$  as model input data (compare to Figs. 13 and 14). Fit parameters are provided for (i) annually averaged efficiency spectra with five different aerosol number reference concentrations  $N_{CN,D_{cut}}$  and (ii) resolved by seasons for  $N_{CN,10}$  and  $N_{CN,50}$ .

$N_{CN,D_{cut}}$	Time period	$S_1$ (%)	$w_1$	$R^2$
$N_{CN,10}$	Annual	$0.22 \pm 0.01$	$1.78 \pm 0.08$	0.99
$N_{CN,20}$		$0.22 \pm 0.01$	$1.78 \pm 0.08$	0.99
$N_{CN,30}$		$0.22 \pm 0.01$	$1.72 \pm 0.07$	0.99
$N_{CN,50}$		$0.19 \pm 0.01$	$1.41 \pm 0.05$	0.99
$N_{CN,10}$	Wet season	$0.35 \pm 0.01$	$1.80 \pm 0.06$	0.99
	LRT period	$0.22 \pm 0.01$	$2.39 \pm 0.10$	0.98
	Transition	$0.28 \pm 0.01$	$1.70 \pm 0.05$	0.99
	Dry season	$0.18 \pm 0.01$	$1.57 \pm 0.11$	0.98
$N_{CN,50}$	Wet season	$0.26 \pm 0.01$	$1.37 \pm 0.12$	0.99
	LRT period	$0.17 \pm 0.01$	$1.58 \pm 0.10$	0.99
	Transition	$0.23 \pm 0.01$	$1.38 \pm 0.04$	0.99
	Dry season	$0.17 \pm 0.01$	$1.31 \pm 0.06$	0.92

$S$  value where half of the aerosol particles are activated into cloud droplets. A monodisperse aerosol with a defined composition would yield a steep step-like CCN efficiency spectrum, while the complex Amazonian aerosol results in a wide and rather smooth “step”. In other words, the width of the erf fit (here  $w_1 = 1.78 \pm 0.08$  for  $N_{CN,10}$  and  $w_1 = 1.41 \pm 0.05$  for  $N_{CN,50}$ ) is an (indirect) measure for the diversity (i.e., size and composition) of the aerosol population.

Figure 14 shows a direct comparison of the CCN efficiency spectra resolved by seasonal periods of interest (compare also to Sect. 3.3), which reveals characteristic differences in the curve’s shape (i.e., its “steepness”). The corresponding fit parameters are summarized in Table 7. A good numeric indicator for the differences in “steepness” is the fit parameter  $S_1$ , which specifies the 50 % activation supersaturation of the total aerosol population. The largest contrast in shape and  $S_1$  can be seen between the dry and wet season scenario: during the dry season, the CCN efficiency increases steeply with  $S$ , and  $S_1$  is reached at 0.18 % for  $N_{CN,10}$ , whereas during the wet season, the increase of the CCN efficiency is rather gradual and  $S_1$  is reached only at 0.35 % for  $N_{CN,10}$ . The transition period represents (once more) an intermediate state between the dry and wet season extremes ( $S_1 = 0.28$  % for  $N_{CN,10}$ ). For transition period conditions, Kuhn et al. (2010) reported  $N_{CCN}(0.6\%)/N_{CN} = 0.66 \pm 0.15$ , which is in good agreement with Fig. 14c ( $N_{CCN}(0.61\%)/N_{CN,10} = 0.72 \pm 0.10$ ).

The observed differences among the CCN efficiency spectra in Fig. 14 reflect some of the major trends in the aerosol seasonality in Amazonia. A closer look at Fig. 6 helps to understand those. Overall, the key parameters in the CCN activation behavior are (primarily) the aerosol number size

distribution and, in a secondary role, the particles’ chemical composition, represented by  $\kappa(S, D_a)$  (Dusek et al., 2006). Thus, the seasonally averaged number size distributions and the seasonally averaged  $\kappa(S, D_a)$  size distribution in Fig. 6 have to be considered to explain the different shapes in Fig. 14. Focusing on the contrasting wet and dry season plots, it can be stated that (i) while the  $\kappa(S, D_a)$  size distributions for wet and dry seasons appear to be very similar (same size trend and same values), the number size distributions (i.e., the ratio of Aitken and accumulation modes) differ substantially. (ii) With increasing  $S$ , the diameter  $D_a(S)$  decreases and is shifted from the accumulation-mode towards the Aitken-mode size range. (iii) Thus, under dry season conditions, comparatively small  $S$  levels ( $S = 0.11$ – $0.2$  %) can already activate most particles of the pronounced accumulation mode. (iv) In contrast, under wet season conditions, while the same  $S$  levels still activate the accumulation-mode particles, the comparatively strong Aitken mode remains unactivated. This means that the ratio of Aitken- and accumulation-mode particles ( $N_{CN,Ait}/N_{CN,Acc}(\text{wet}) = 1.7$ ;  $N_{CN,Ait}/N_{CN,Acc}(\text{dry}) = 0.4$ ; compare to Table 2) determines the activated fraction as a function of  $S$  and thus also the steepness of the CCN efficiency spectra in Fig. 14.

While size appears as the dominant parameter in the CCN activation behavior, in certain cases variability in chemical composition also matters (Dusek et al., 2006). In Fig. 14, this can be seen for the wet season cases with and without LRT influence: in the presence of LRT aerosol, the 50 % activation occurs already at  $S_1 = 0.22$  % for  $N_{CN,10}$ , which is much closer to the dry ( $S_1 = 0.18$  % for  $N_{CN,10}$ ) than to the wet season ( $S_1 = 0.35$  % for  $N_{CN,10}$ ) behavior. While Fig. 6 shows that the number size distributions for both cases are similar, the observed difference in Fig. 14 can be explained by the deviations in the corresponding  $\kappa(S, D_a)$  size distributions. In other words, the elevated  $\kappa(S, D_a)$  levels during the intrusion of LRT aerosols allows the activation of particle sizes that remain inactivated at the lower  $\kappa(S, D_a)$  levels in the absence of LRT aerosol. Therefore, the differences in chemical composition can explain the decreased  $S_1$  in these cases.

In Fig. 14, single-erf fits have been used as analytical descriptions of the CCN efficiency spectra. Overall, this approach provides a good representation of the experimental data (see high coefficients of determination in Table 5). However, the single-erf fit is merely an approximation, assuming that the aerosol size distribution is monomodal. This is a valid assumption for the dry season (see Fig. 6) and corresponds to a good agreement between fit and data points in Fig. 14d. In contrast, the wet season shows pronounced and prevailing bimodal size distributions (see Fig. 6), which corresponds to a clear discrepancy between the fit and data points in Fig. 14b (i.e., for  $S > 0.3$  %). For a bimodal size distribution, a double-erf fit is the physically more appropriate description (see also discussion in Sect. 3.5.3). Figure 15 illustrates the contrast between a single- and a double-erf fit

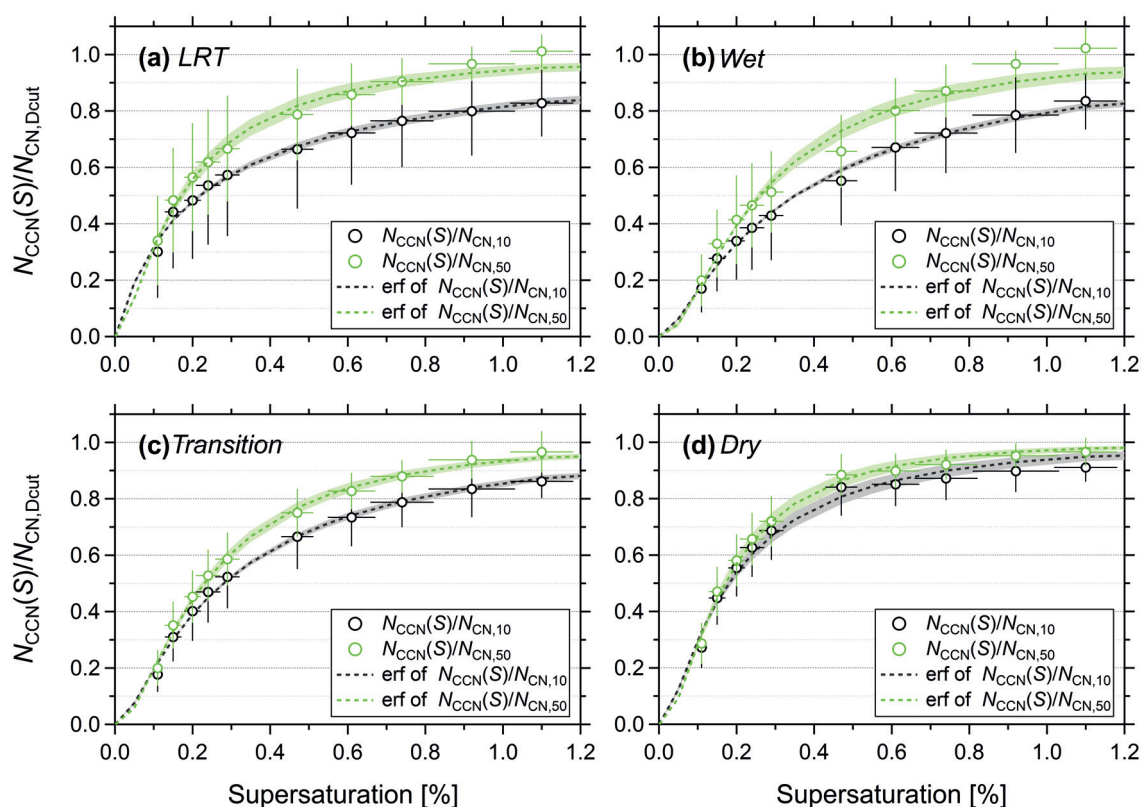


**Figure 14.** CCN efficiency spectra averaged over the entire measurement period for reference concentrations,  $N_{\text{CCN},10}$  and  $N_{\text{CCN},50}$ , and subdivided into seasonal periods of interest as specified in Sect. 3.3. The fit functions are error function fits (the dashed line with shading represents the uncertainty of the fit). The error bars at the markers represent the measurement error in  $S$  and 1 standard deviation (not the standard error, as in Fig. 10) in  $N_{\text{CCN}}(S)/N_{\text{CCN},D_{\text{cut}}}$ .

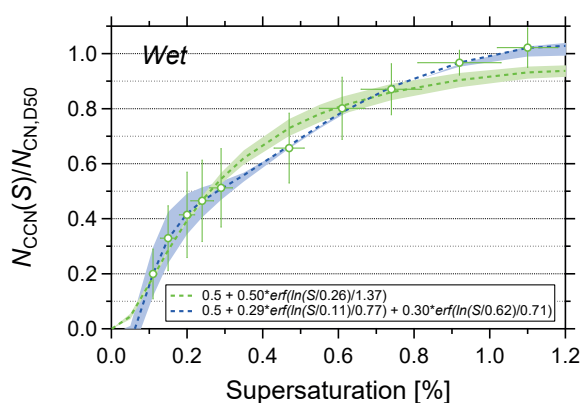


**Figure 15.** CCN efficiency spectrum for the wet season scenario (Fig. 14b) with  $N_{\text{CCN},50}$  as reference concentration. The experimental data have been fitted with single- and double-erf fits (dashed lines with shading as uncertainty of the fits). The error bars at the markers represent the measurement error in  $S$  and 1 standard deviation in  $N_{\text{CCN}}(S)/N_{\text{CCN},50}$ .

of the wet season CCN efficiency spectrum for  $N_{\text{CCN},50}$ . As expected, the double-erf fit is clearly a better representation of the data across the entire  $S$  range. However, in the context of this study, the double-erf fit of CCN spectra merely serves as proof of concept. It will be discussed in more detail in a follow-up study (M. L. Pöhlker et al., 2017b). Thus, in the context of the following CCN parametrization, we will work exclusively with the single-erf fit approach for the following reasons: (i) the single-erf fit represents the simpler parametrization scheme (two fit parameters instead of six) and (ii) the difference in the CCN prediction accuracy of single- vs. double-erf fit turns out to be insignificant.

Figure 16 explores the applicability of the CCN efficiency spectra parametrization (single-erf fits) to calculate CCN concentrations. The following four modifications of the parametrization scheme are compared: annually averaged CCN efficiency spectra with (i)  $D_{\text{cut}} = 10$  nm and (ii)  $D_{\text{cut}} = 50$  nm (compare to Fig. 13) as well as seasonally resolved CCN efficiency spectra with (iii)  $D_{\text{cut}} = 10$  nm, and (iv)  $D_{\text{cut}} = 50$  nm (compare to Fig. 14). All cases in Fig. 16 show rather tight correlations, which prove the high prediction accuracy of the CCN efficiency spectra parametrization. The corresponding deviations between  $N_{\text{CCN}}(S)$  and

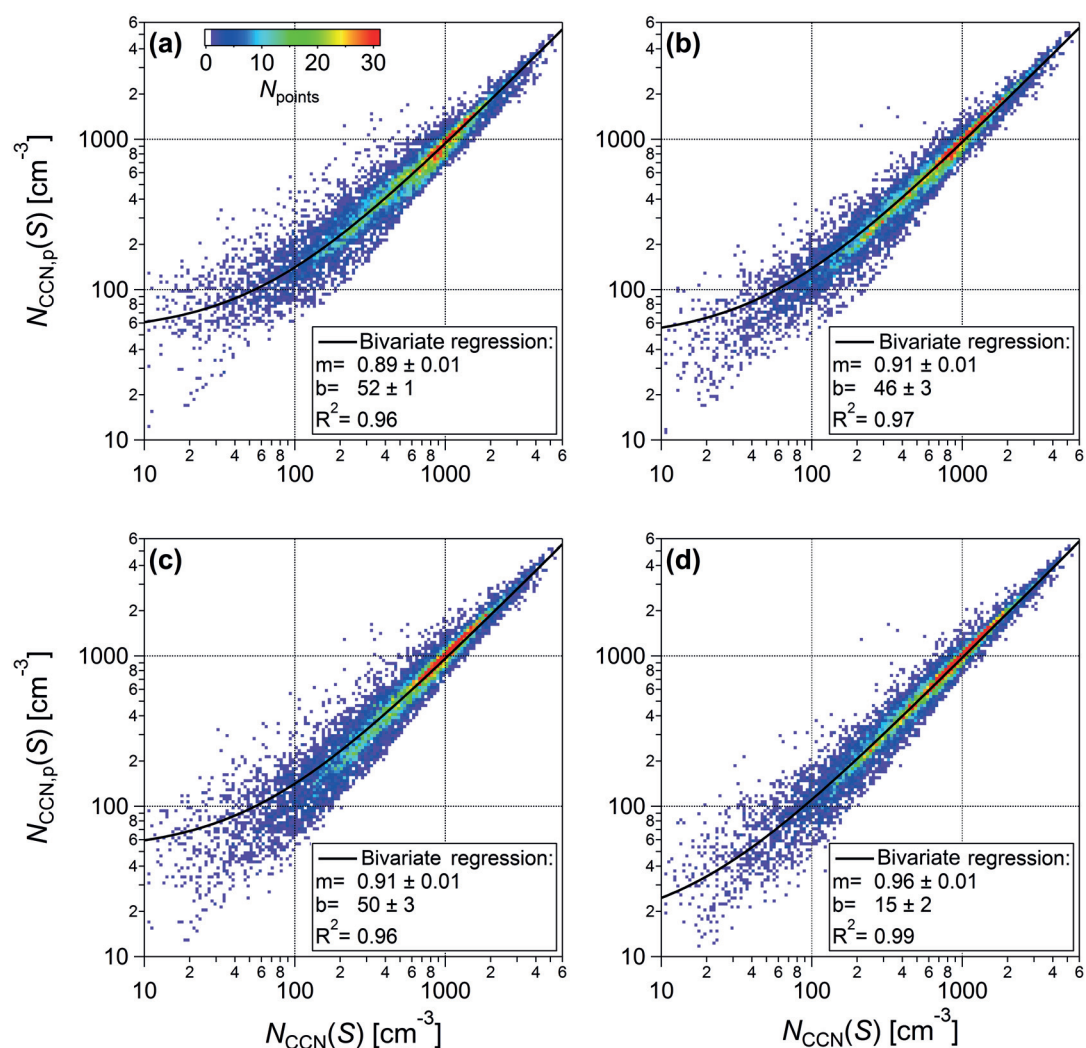


**Figure 16.** Predicted vs. measured CCN number concentrations, based on our novel parametrization using time-resolved aerosol number concentrations and average error function fits of CCN efficiency spectra. The panels show the following four variations of the parametrization: (a) erf fit of the annually averaged  $N_{CCN}(S)/N_{CN,10}$  vs.  $S$  efficiency plot, (b) erf fit of the annually averaged  $N_{CCN}(S)/N_{CN,50}$  vs.  $S$  efficiency plot, (c) erf fits of the  $N_{CCN}(S)/N_{CN,10}$  vs.  $S$  efficiency plot, resolved by seasons, and (d) erf fits of the  $N_{CCN}(S)/N_{CN,50}$  vs.  $S$  efficiency plot, resolved by seasons. This approach requires the following as input data: (i) a time series of total aerosol concentration (e.g.,  $N_{CN,10}$  from a CPC measurement or  $N_{CN,50}$  as model output) and (ii) the parameters of the erf fit (e.g., as provided in Table 7). The color code shows the number of data points falling into the pixel area, following Jurányi et al. (2011). The black line represents a bivariate regression fit of the data.

$N_{CCN,p}(S)$  are summarized in Table 3. The comparison confirms that the cases with  $D_{\text{cut}} = 50$  nm perform better than  $D_{\text{cut}} = 10$  nm. Moreover, the seasonally resolved cases show higher prediction accuracies than the annually averaged scenarios. Thus, the highest deviation of 33 % is observed for the case of Fig. 16a and the lowest deviation (and therefore best performance) with 17 % for the case of Fig. 16d (see Table 3).

In a way, the CCN efficiency spectra parametrization represents a “compromise” between the previously introduced parametrization strategies: it operates with a comparatively small set of input data and still provides good prediction ac-

curacies. The input data require the fit parameters  $S_1$  and  $w_1$  of the single-erf fit, which reflects the “shape” of the fit functions. This part conveys the specific CCN activation behavior of the given aerosol population (e.g., the wet season scenario). In addition, a time series of  $N_{CN,D_{\text{cut}}}$  is required, which accounts for the temporal variability of the aerosol population. The new parametrization approach is currently extended and applied to further data sets worldwide (M. L. Pöhlker et al., 2017b).

#### 4 Conclusions

Size-resolved CCN measurements have been conducted at the remote ATTO site in the central Amazon, spanning a full seasonal cycle from March 2014 to February 2015. These measurements represent the first long-term study on CCN concentrations and hygroscopicity in this unique and globally important ecosystem. The reported measurements span the aerosol size range of 20–245 nm and therefore cover the Aitken and accumulation modes, which dominate the aerosol burden in the Amazon throughout the year (Andreae et al., 2015). The supersaturation in the CCN counter was cycled through 10 levels from  $S = 0.11\%$  to  $S = 1.10\%$ . Overall, this study presents an in-depth analysis of the key CCN parameters, based on a continuous sequence of more than 10 000 CCN activation curves with a temporal resolution of 4.5 h and therefore allows a detailed analysis of the CCN cycling in the central Amazon Basin.

The Amazonian atmosphere reveals a characteristic bimodal aerosol size distribution, which is dominated by pronounced Aitken and accumulation modes ( $D_{\text{Ait}} \sim 70$  nm vs.  $D_{\text{Acc}} \sim 150$  nm) as well as the sparse occurrence of nucleation-mode particles ( $< 30$  nm). This size distribution closely relates to the observed CCN properties, as its entire size range – and thus the majority of particles – fall into the CCN-active range. Accumulation-mode particles are CCN active at supersaturations between 0.11 and 0.29%, while supersaturations between 0.47 and 1.10% activate both the Aitken and accumulation modes. The absence of nucleation-mode particles further explains the high activated fractions  $N_{\text{CCN}}(S)/N_{\text{CN},10}$  that were observed throughout all seasons, with  $N_{\text{CCN}}(0.11\%)/N_{\text{CN},10}$  reaching up to 0.4 and  $N_{\text{CCN}}(1.10\%)/N_{\text{CN},10}$  constantly exceeding 0.9. These values are substantially higher than corresponding activated fractions at other continental background sites worldwide (Jurányi et al., 2011; Levin et al., 2012; Paramonov et al., 2013). Overall, the CCN concentrations  $N_{\text{CCN}}(S)$  for all  $S$  levels closely follow the pronounced pollution-related seasonal cycle in  $N_{\text{CN}}$  that is typical for the Amazon region.

The hygroscopicity parameter  $\kappa(S, D_a)$ , which reflects the chemical composition of the particles, appears to be remarkably stable throughout the entire measurement period with only a weak seasonal cycle and no perceptible diurnal trends. Numerically, the  $\kappa(S, D_a)$  values lie within a rather narrow range from 0.1 to 0.3 for most of the time. The mean hygroscopicity averaged over the entire period and size range and its corresponding standard deviation is  $\kappa_{\text{mean}} = 0.17 \pm 0.06$ . In terms of particle size,  $\kappa(S, D_a)$  reveals a clear size dependence with lower values for the Aitken mode ( $\kappa_{\text{Ait}} = 0.14 \pm 0.03$ ) and elevated levels in the accumulation-mode range ( $\kappa_{\text{Acc}} = 0.22 \pm 0.05$ ). Previous studies showed that the Amazonian aerosol population is dominated by organic aerosols throughout the seasons (Talbot et al., 1988, 1990; Graham et al., 2003; Gunthe et al., 2009; Martin et al., 2010b; Chen et al., 2015). The comparatively low  $\kappa(S, D_a)$  values in

this study underline this observation. However, the observed difference between  $\kappa_{\text{Ait}}$  and  $\kappa_{\text{Acc}}$  shows that the Aitken mode is almost purely organic (close to  $\kappa = 0.1$ ), while the accumulation mode is somewhat enriched in inorganic constituents.

Focusing on seasonal differences, substantial changes in the aerosol concentrations and the shape of the size distribution have been observed. During the (clean) wet season, equally strong Aitken and accumulation modes were observed, while during the (polluted) dry season the accumulation mode overwhelms the Aitken mode. The transition periods represent intermediate states between these extremes. Interestingly, the strong seasonal variability in aerosol abundance and sources does not correspond to noticeable changes in  $\kappa(S, D_a)$ . In other words,  $\kappa_{\text{Ait}}$  and  $\kappa_{\text{Acc}}$  are almost identical for dry and wet season conditions. The only seasonal period where  $\kappa(S, D_a)$  deviates from its typical range is the LRT season when out-of-basin dust, marine sulfate, and sea salt are transported into the Amazon Basin. During this period, a significant increase in  $\kappa_{\text{Acc}}$  up to 0.28 is observed. In summary, the seasonally averaged CCN populations (represented by the CCN efficiency spectra) are mostly defined by particle size (i.e., shape of aerosol size distribution). The only episodes when (besides size) chemical variability also matters are the LRT periods with their enhanced  $\kappa(S, D_a)$  values.

Based on the CCN key parameters that have been obtained in the present study, we show that the CCN population over Amazonia can be modeled very effectively. Different approaches to infer a CCN concentration from basic aerosol parameters have been compared and it turns out that a remarkably good correlation between modeled and measured data can be obtained based on continuous SMPS time series as well as the annually averaged  $\kappa_{\text{Ait}}$  and  $\kappa_{\text{acc}}$  values from this study. Alternatively, CCN concentration can effectively be calculated based on our novel parametrization, which is based on fitted CCN efficiency spectra and continuous time series of total aerosol number concentrations. These efficient approaches to infer the Amazonian CCN population are expected to help improve future modeling studies.

#### 5 Data availability

The CCN data of this study has been deposited as a Supplement. The data is provided in NASA Ames format (see British Atmospheric Data Centre (BADC), 2008). For specific data requests or detailed information on the deposited data, please refer to the corresponding author [m.pohlker@mpic.de](mailto:m.pohlker@mpic.de).

## Appendix A

Table A1. List of symbols.

Symbol	Quantity and unit
$A$	CN number concentration derived from erf fit of CCN spectra, $\text{cm}^{-3}$
$a(S, D_i)$	cumulative Gaussian fit of multi-charge CCN activation fraction at a given $D$ and $S$
$a(S, D)$	cumulative Gaussian fit of CCN activation fraction at a given $S$
$c_{\text{CO}}$	CO mole fraction, ppb
$D$	mobility equivalent particle diameter, nm
$D_a(S)$	midpoint activation diameter determined from CCN activation curve, nm
$D_{\text{Ait}}$	position of Aitken-mode maximum, nm
$D_{\text{Acc}}$	position of accumulation-mode maximum, nm
$D_{\text{cut}}$	lower cutoff diameter in aerosol number reference concentration $N_{\text{CN}, D_{\text{cut}}}$ , nm
$D_{\text{H}}$	position of Hoppel minimum, nm
$f(D_i)$	multiple-charged fraction at a given $D$
$f_{\text{org}}$	organic mass fraction
$f_{\text{inorg}}$	inorganic mass fraction
$I$	number of charges
$\kappa$	hygroscopicity parameter
$\kappa(S, D_a)$	hygroscopicity parameter determined from CCN activation curve
$\kappa_{\text{Acc}}$	mean hygroscopicity parameter for accumulation-mode particles
$\kappa_{\text{Ait}}$	mean hygroscopicity parameter for Aitken-mode particles
$\kappa_{\text{mean}}$	mean hygroscopicity parameter for all measured $S$
$\text{MAF}(S)$	maximum activated fraction determined by CCN activation curve
$N$	number of data points
$N_{\text{CCN}}(S)$	CCN number concentration at a given $S$ , $\text{cm}^{-3}$
$N_{\text{CCN,p}}(S)$	predicted CCN number concentration at a given $S$ , $\text{cm}^{-3}$
$N_{\text{CCN}}(S, D_a)$	CCN number concentration determined from CCN activation curve, $\text{cm}^{-3}$
$N_{\text{CCN}}(S, D)/N_{\text{CN}}(D)$	CCN activation fraction
$N_{\text{CCN}}(S)/N_{\text{CN}, D_{\text{cut}}}$	CCN efficiency for aerosol reference concentration $N_{\text{CN}, D_{\text{cut}}}$
$N_{\text{CN}, D_{\text{cut}}}$	aerosol number reference concentration ( $> D_{\text{cut}}$ ), $\text{cm}^{-3}$
$N_{\text{CN}, 10}$	aerosol number reference concentration ( $> 10$ nm), $\text{cm}^{-3}$
$N_{\text{CN}, 50}$	aerosol number reference concentration ( $> 50$ nm), $\text{cm}^{-3}$
$N_{\text{CN, Acc}}$	CN number concentration for accumulation-mode particles, $\text{cm}^{-3}$
$N_{\text{CN, Ait}}$	CN number concentration for Aitken-mode particles, $\text{cm}^{-3}$
$P_{\text{ATTO}}$	precipitation rate at ATTO site, $\text{mm day}^{-1}$
$P_{\text{TRMM}}$	precipitation rate from TRMM mission, $\text{mm day}^{-1}$
$S$	water vapor supersaturation, %
$S_c$	critical supersaturation for CCN activation, %
$S_{\text{cloud}}(D_{\text{H}}, \kappa)$	average cloud peak supersaturation, %
$s(D)$	SMPS size distribution, $\text{cm}^{-3}$
$s(D_i)$	multi-charge size distribution of $D$ , $\text{cm}^{-3}$
$S_0$	abscissa transect of erf fit of CCN spectra, %
$S_1$	midpoint activation supersaturation determined from CCN efficiency spectra, %
$w_0$	width of erf fit of CCN spectra
$w_1$	width of erf fit of CCN efficiency spectra
$x_0$	position of mobility equivalent particle diameter, nm
$\sigma$	width of log-normal fit of Aitken and accumulation modes
$\sigma(S)$	width of CCN activation curve, nm
$\sigma(S)/D_a(S)$	heterogeneity parameter

**Table A2.** List of abbreviations.

Abbreviation	Description
ACSM	aerosol chemical speciation monitor
AOT	aerosol optical thickness
ATTO	Amazon Tall Tower Observatory
ACRIDICON	aerosol, cloud, precipitation, and radiation interactions and dynamics of convective cloud systems
BUNIAACIC	Brazil–UK network for investigation of Amazonian atmospheric composition and impacts on climate
BC	black carbon
CCN	cloud condensation nuclei
CCNC	cloud condensation nuclei counter
CN	condensation nuclei
CHUVA	cloud processes of the main precipitation systems in Brazil: a contribution to cloud resolving modeling and to the GPMs (global precipitation measurements)
CPC	condensation particle counter
CO	carbon monoxide
DMA	differential mobility analyzer
ENSO	El Niño–Southern Oscillation
Erf	log-normal error function
GCMs	global climate models
GoAmazon14/5	green ocean Amazon 2014/5
HALO	high-altitude and long-range research aircraft
HTDMA	hygroscopicity tandem differential mobility analyzer
IN	ice nuclei
IOP	intensive observation period
LES	large eddy simulation
LRT	long-range transport
NPF	new particle formation
ONI	Oceanic Niño Index
OPC	optical particle counter
PSL	polystyrene latex
RH	relative humidity
SE	standard error
SMPS	scanning mobility particle sizer
SOA	secondary organic aerosol
SST	sea surface temperature
TRMM	tropical rainfall measuring mission
UTC	coordinated universal time

The Supplement related to this article is available online at doi:10.5194/acp-16-15709-2016-supplement.

**Acknowledgements.** This work has been supported by the Max Planck Society (MPG) and the Max Planck Graduate Center with the Johannes Gutenberg University Mainz (MPGC). For the operation of the ATTO site, we acknowledge the support by the German Federal Ministry of Education and Research (BMBF contract 01LB1001A) and the Brazilian Ministério da Ciência, Tecnologia e Inovação (MCTI/FINEP contract 01.11.01248.00) and the Amazon State University (UEA), FAPEAM, LBA/INPA and SDS/CEUC/RDS-Uatumã, and the St. Petersburg state University, Russia (project 11.37.220.2016) as well as the EU FP7 project BACCHUS (project no. 603445). This paper contains results of research conducted under the Technical/Scientific Cooperation Agreement between the National Institute for Amazonian Research, the State University of Amazonas, and the Max Planck Gesellschaft e.V.; the opinions expressed are the entire responsibility of the authors and not of the participating institutions. We highly acknowledge the support by the Instituto Nacional de Pesquisas da Amazônia (INPA). We would like to especially thank all the people involved in the technical, logistical, and scientific support of the ATTO project, in particular Matthias Sörgel, Thomas Disper, Andrew Crozier, Uwe Schulz, Steffen Schmidt, Antonio Ocimar Manzi, Alcides Camargo Ribeiro, Hermes Braga Xavier, Elton Mendes da Silva, Nagib Alberto de Castro Souza, Adi Vasconcelos Brandão, Amaury Rodrigues Pereira, Antonio Huxley Melo Nascimento, Thiago de Lima Xavier, Josué Ferreira de Souza, Roberta Pereira de Souza, Bruno Takeshi, and Wallace Rabelo Costa. Further, we thank the GoAmazon2014/5 team for the fruitful collaboration and discussions. We acknowledge technical support by the DMT and Grimm Aerosol Technik teams in the course of the experiments. Moreover, we thank Qiaoqiao Wang, Bettina Weber, Nina Ruckteschler, Bruna Amorim Holanda, Kathrin Reinmuth-Selzle, J. Alex Huffman, Ramon Braga, and Daniel Rosenfeld for support and stimulating discussions.

The article processing charges for this open-access publication were covered by the Max Planck Society.

Edited by: G. Fisch

Reviewed by: two anonymous referees

## References

- Almeida, G. P., Borrmann, S., and Leal Junior, J. B. V.: Cloud condensation nuclei (CCN) concentration in the Brazilian northeast semi-arid region: the influence of local circulation, *Meteorol. Atmos. Phys.*, 125, 159–176, doi:10.1007/s00703-014-0329-1, 2014.
- Andreae, M. O.: Aerosols before pollution, *Science*, 315, 50–51, doi:10.1126/science.1136529, 2007.
- Andreae, M. O.: Correlation between cloud condensation nuclei concentration and aerosol optical thickness in remote and polluted regions, *Atmos. Chem. Phys.*, 9, 543–556, doi:10.5194/acp-9-543-2009, 2009.
- Andreae, M. O. and Rosenfeld, D.: Aerosol-cloud-precipitation interactions. Part 1. The nature and sources of cloud-active aerosols, *Earth-Sci. Rev.*, 89, 13–41, doi:10.1016/j.earscirev.2008.03.001, 2008.
- Andreae, M. O., Artaxo, P., Brandao, C., Carswell, F. E., Ciccioli, P., da Costa, A. L., Culf, A. D., Esteves, J. L., Gash, J. H. C., Grace, J., Kabat, P., Lelieveld, J., Malhi, Y., Manzi, A. O., Meixner, F. X., Nobre, A. D., Nobre, C., Ruivo, M., Silva-Dias, M. A., Stefani, P., Valentini, R., von Jouanne, J., and Waterloo, M. J.: Biogeochemical cycling of carbon, water, energy, trace gases, and aerosols in Amazonia: The LBA-EUSTACH experiments, *J. Geophys. Res.-Atmos.*, 107, LBA 33-1–BA 33-25 doi:10.1029/2001jd000524, 2002.
- Andreae, M. O., Artaxo, P., Beck, V., Bela, M., Freitas, S., Gerbig, C., Longo, K., Munger, J. W., Wiedemann, K. T., and Wofsy, S. C.: Carbon monoxide and related trace gases and aerosols over the Amazon Basin during the wet and dry seasons, *Atmos. Chem. Phys.*, 12, 6041–6065, doi:10.5194/acp-12-6041-2012, 2012.
- Andreae, M. O., Rosenfeld, D., Artaxo, P., Costa, A. A., Frank, G. P., Longo, K. M., and Silva-Dias, M. A. F.: Smoking rain clouds over the Amazon, *Science*, 303, 1337–1342, doi:10.1126/science.1092779, 2004.
- Andreae, M. O., Acevedo, O. C., Araújo, A., Artaxo, P., Barbosa, C. G. G., Barbosa, H. M. J., Brito, J., Carbone, S., Chi, X., Cintra, B. B. L., da Silva, N. F., Dias, N. L., Dias-Júnior, C. Q., Ditas, F., Ditz, R., Godoi, A. F. L., Godoi, R. H. M., Heimann, M., Hoffmann, T., Kesselmeier, J., Könemann, T., Krüger, M. L., Lavric, J. V., Manzi, A. O., Lopes, A. P., Martins, D. L., Mikhailov, E. F., Moran-Zuloaga, D., Nelson, B. W., Nölscher, A. C., Santos Nogueira, D., Piedade, M. T. F., Pöhlker, C., Pöschl, U., Quesada, C. A., Rizzo, L. V., Ro, C.-U., Ruckteschler, N., Sá, L. D. A., de Oliveira Sá, M., Sales, C. B., dos Santos, R. M. N., Saturno, J., Schöngart, J., Sörgel, M., de Souza, C. M., de Souza, R. A. F., Su, H., Targheta, N., Tóta, J., Trebs, I., Trumbore, S., van Eijck, A., Walter, D., Wang, Z., Weber, B., Williams, J., Winderlich, J., Wittmann, F., Wolff, S., and Yáñez-Serrano, A. M.: The Amazon Tall Tower Observatory (ATTO): overview of pilot measurements on ecosystem ecology, meteorology, trace gases, and aerosols, *Atmos. Chem. Phys.*, 15, 10723–10776, doi:10.5194/acp-15-10723-2015, 2015.
- Ansmann, A., Baars, H., Tesche, M., Müller, D., Althausen, D., Engelmann, R., Pauliquevis, T., and Artaxo, P.: Dust and smoke transport from Africa to South America: Lidar profiling over Cape Verde and the Amazon rainforest, *Geophys. Res. Lett.*, 36, L11802, doi:10.1029/2009gl0137923, 2009.
- Asner, G. P., Townsend, A. R., and Braswell, B. H.: Satellite observation of El Niño effects on Amazon forest phenology and productivity, *Geophys. Res. Lett.*, 27, 981–984, doi:10.1029/1999gl011113, 2000.
- Bony, S., Stevens, B., Frierson, D. M. W., Jakob, C., Kageyama, M., Pincus, R., Shepherd, T. G., Sherwood, S. C., Siebesma, A. P., Sobel, A. H., Watanabe, M., and Webb, M. J.: Clouds, circulation and climate sensitivity, *Nat. Geosci.*, 8, 261–268, doi:10.1038/ngeo2398, 2015.
- Boucher, O., Randall, D., Artaxo, P., Bretherton, C., Feingold, G., Forster, P., Kerminen, V. M., Kondo, Y., Liao, H., Lohmann, U., Rasch, P., Satheesh, S. K., Sherwood, S. B., S., and Zhang, X. Y.: Clouds and Aerosols, Cambridge, United Kingdom and New York, NY, US, 571–658, 2013.

- Boulon, J., Sellegrì, K., Venzac, H., Picard, D., Weingartner, E., Wehrle, G., Collaud Coen, M., Büttiker, R., Flückiger, E., Baltensperger, U., and Laj, P.: New particle formation and ultrafine charged aerosol climatology at a high altitude site in the Alps (Jungfraujoch, 3580 m a.s.l., Switzerland), *Atmos. Chem. Phys.*, 10, 9333–9349, doi:10.5194/acp-10-9333-2010, 2010.
- Brienen, R. J. W., Phillips, O. L., Feldpausch, T. R., Gloor, E., Baker, T. R., Lloyd, J., Lopez-Gonzalez, G., Monteagudo-Mendoza, A., Malhi, Y., Lewis, S. L., Martinez, R. V., Alexiades, M., Davila, E. A., Alvarez-Loayza, P., Andrade, A., Aragao, L., Araujo-Murakami, A., Arets, E., Arroyo, L., Aymard, G. A., Banki, O. S., Baraloto, C., Barroso, J., Bonal, D., Boot, R. G. A., Camargo, J. L. C., Castilho, C. V., Chama, V., Chao, K. J., Chave, J., Comiskey, J. A., Valverde, F. C., da Costa, L., de Oliveira, E. A., Di Fiore, A., Erwin, T. L., Fauset, S., Forsthofer, M., Galbraith, D. R., Grahame, E. S., Groot, N., Herault, B., Higuchi, N., Coronado, E. N. H., Keeling, H., Killeen, T. J., Laurance, W. F., Laurance, S., Licona, J., Magnussen, W. E., Marimon, B. S., Marimon, B. H., Mendoza, C., Neill, D. A., Nogueira, E. M., Nunez, P., Camacho, N. C. P., Parada, A., Pardo-Molina, G., Peacock, J., Pena-Claros, M., Pickavance, G. C., Pitman, N. C. A., Poorter, L., Prieto, A., Quesada, C. A., Ramirez, F., Ramirez-Angulo, H., Restrepo, Z., Roopsind, A., Rudas, A., Salomao, R. P., Schwarz, M., Silva, N., Silva-Espejo, J. E., Silveira, M., Stropp, J., Talbot, J., ter Steege, H., Teran-Aguilar, J., Terborgh, J., Thomas-Caesar, R., Toledo, M., Torello-Raventos, M., Umetsu, R. K., Van der Heijden, G. M. F., Van der Hout, P., Vieira, I. C. G., Vieira, S. A., Vilanova, E., Vos, V. A., and Zagt, R. J.: Long-term decline of the Amazon carbon sink, *Nature*, 519, p. 344, doi:10.1038/nature14283, 2015.
- British Atmospheric Data Centre (BADC): NASA Ames Format for Data Exchange, available at: <http://cedadocs.badc.rl.ac.uk/73/4/index.html> (last access: 19 December 2016), 2008.
- Cantrell, C. A.: Technical Note: Review of methods for linear least-squares fitting of data and application to atmospheric chemistry problems, *Atmos. Chem. Phys.*, 8, 5477–5487, doi:10.5194/acp-8-5477-2008, 2008.
- Chen, Q., Farmer, D. K., Rizzo, L. V., Pauliquevis, T., Kuwata, M., Karl, T. G., Guenther, A., Allan, J. D., Coe, H., Andreae, M. O., Pöschl, U., Jimenez, J. L., Artaxo, P., and Martin, S. T.: Submicron particle mass concentrations and sources in the Amazonian wet season (AMAZE-08), *Atmos. Chem. Phys.*, 15, 3687–3701, doi:10.5194/acp-15-3687-2015, 2015.
- Coe, M. T., Marthews, T. R., Costa, M. H., Galbraith, D. R., Greenglass, N. L., Imbuzeiro, H. M. A., Levine, N. M., Malhi, Y., Moorcroft, P. R., Muza, M. N., Powell, T. L., Saleska, S. R., Solorzano, L. A., and Wang, J.: Deforestation and climate feedbacks threaten the ecological integrity of south-eastern Amazonia, *Philos. T. Roy. Soc. B*, 368, 1–9, doi:10.1098/rstb.2012.0155, 2013.
- Cohard, J. M., Pinty, J. P., and Bedos, C.: Extending Twomey's analytical estimate of nucleated cloud droplet concentrations from CCN spectra, *J. Atmos. Sci.*, 55, 3348–3357, doi:10.1175/1520-0469(1998)055<3348:etsaeco>2.0.co;2, 1998.
- Cotton, W. R. and Anthes, R. A.: *Storm and cloud dynamics*, San Diego, Academic Press, 833 pp., 1989.
- Davidson, E. A., de Araujo, A. C., Artaxo, P., Balch, J. K., Brown, I. F., Bustamante, M. M. C., Coe, M. T., DeFries, R. S., Keller, M., Longo, M., Munger, J. W., Schroeder, W., Soares-Filho, B. S., Souza Jr., C. M., and Wofsy, S. C.: The Amazon basin in transition, *Nature*, 481, 321–328, doi:10.1038/nature10717, 2012.
- Deng, Z. Z., Zhao, C. S., Ma, N., Ran, L., Zhou, G. Q., Lu, D. R., and Zhou, X. J.: An examination of parameterizations for the CCN number concentration based on in situ measurements of aerosol activation properties in the North China Plain, *Atmos. Chem. Phys.*, 13, 6227–6237, doi:10.5194/acp-13-6227-2013, 2013.
- Dusek, U., Frank, G. P., Hildebrandt, L., Curtius, J., Schneider, J., Walter, S., Chand, D., Drewnick, F., Hings, S., Jung, D., Borrmann, S., and Andreae, M. O.: Size matters more than chemistry for cloud-nucleating ability of aerosol particles, *Science*, 312, 1375–1378, doi:10.1126/science.1125261, 2006.
- Engelhart, G. J., Asa-Awuku, A., Nenes, A., and Pandis, S. N.: CCN activity and droplet growth kinetics of fresh and aged monoterpene secondary organic aerosol, *Atmos. Chem. Phys.*, 8, 3937–3949, doi:10.5194/acp-8-3937-2008, 2008.
- Fernandes, K., Giannini, A., Verchot, L., Baethgen, W., and Pinedo-Vasquez, M.: Decadal covariability of Atlantic SSTs and western Amazon dry-season hydroclimate in observations and CMIP5 simulations, *Geophys. Res. Lett.*, 42, 6793–6801, doi:10.1002/2015gl063911, 2015.
- Frank, G. P., Dusek, U., and Andreae, M. O.: Technical note: A method for measuring size-resolved CCN in the atmosphere, *Atmos. Chem. Phys. Discuss.*, 6, 4879–4895, doi:10.5194/acpd-6-4879-2006, 2006.
- Freud, E., Rosenfeld, D., Andreae, M. O., Costa, A. A., and Artaxo, P.: Robust relations between CCN and the vertical evolution of cloud drop size distribution in deep convective clouds, *Atmos. Chem. Phys.*, 8, 1661–1675, doi:10.5194/acp-8-1661-2008, 2008.
- Fu, R., Dickinson, R. E., Chen, M. X., and Wang, H.: How do tropical sea surface temperatures influence the seasonal distribution of precipitation in the equatorial Amazon?, *J. Climate*, 14, 4003–4026, doi:10.1175/1520-0442(2001)014<4003:hdtstst>2.0.co;2, 2001.
- Gloor, M., Barichivich, J., Ziv, G., Brienen, R., Schongart, J., Peylin, P., Cintra, B. B. L., Feldpausch, T., Phillips, O., and Baker, J.: Recent Amazon climate as background for possible ongoing and future changes of Amazon humid forests, *Global Biogeochem. Cy.*, 29, 1384–1399, doi:10.1002/2014gb005080, 2015.
- Graham, B., Guyon, P., Maenhaut, W., Taylor, P. E., Ebert, M., Matthias-Maser, S., Mayol-Bracero, O. L., Godoi, R. H. M., Artaxo, P., Meixner, F. X., Moura, M. A. L., Rocha, C., Van Grieken, R., Glovsky, M. M., Flagan, R. C., and Andreae, M. O.: Composition and diurnal variability of the natural Amazonian aerosol, *J. Geophys. Res.-Atmos.*, 108, 4765, doi:10.1029/2003jd004049, 2003.
- Gunthe, S. S., King, S. M., Rose, D., Chen, Q., Roldin, P., Farmer, D. K., Jimenez, J. L., Artaxo, P., Andreae, M. O., Martin, S. T., and Pöschl, U.: Cloud condensation nuclei in pristine tropical rainforest air of Amazonia: size-resolved measurements and modeling of atmospheric aerosol composition and CCN activity, *Atmos. Chem. Phys.*, 9, 7551–7575, doi:10.5194/acp-9-7551-2009, 2009.
- Hamilton, D. S., Lee, L. A., Pringle, K. J., Reddington, C. L., Spracklen, D. V., and Carslaw, K. S.: Occurrence of pristine

- aerosol environments on a polluted planet, *P. Natl. Acad. Sci. USA*, 111, 18466–18471, doi:10.1073/pnas.1415440111, 2014.
- Hoppel, W. A., Frick, G. M., and Fitzgerald, J. W.: Deducing droplet concentration and supersaturation in marine boundary layer clouds from surface aerosol measurements, *J. Geophys. Res.-Atmos.*, 101, 26553–26565, doi:10.1029/96jd02243, 1996.
- Junk, W. J.: Current state of knowledge regarding South America wetlands and their future under global climate change, *Aquat. Sci.*, 75, 113–131, doi:10.1007/s00027-012-0253-8, 2013.
- Jurányi, Z., Gysel, M., Weingartner, E., Bukowiecki, N., Kammermann, L., and Baltensperger, U.: A 17 month climatology of the cloud condensation nuclei number concentration at the high alpine site Jungfraujoch, *J. Geophys. Res.-Atmos.*, 116, D10204, doi:10.1029/2010JD015199, 2011.
- Khain, A., Ovchinnikov, M., Pinsky, M., Pokrovsky, A., and Krugliak, H.: Notes on the state-of-the-art numerical modeling of cloud microphysics, *Atmos. Res.*, 55, 159–224, doi:10.1016/s0169-8095(00)00064-8, 2000.
- King, S. M., Rosenoern, T., Shilling, J. E., Chen, Q., and Martin, S. T.: Cloud condensation nucleus activity of secondary organic aerosol particles mixed with sulfate, *Geophys. Res. Lett.*, 34, 2007GL030390, doi:10.1029/2007GL030390, 2007.
- Köhler, H.: The nucleus in and the growth of hygroscopic droplets, *T. Faraday Soc.*, 32, 1152–1161, doi:10.1039/tf9363201152, 1936.
- Koren, I., Kaufman, Y. J., Remer, L. A., and Martins, J. V.: Measurement of the effect of Amazon smoke on inhibition of cloud formation, *Science*, 303, 1342–1345, doi:10.1126/science.1089424, 2004.
- Koren, I., Altaratz, O., Remer, L. A., Feingold, G., Martins, J. V., and Heiblum, R. H.: Aerosol-induced intensification of rain from the tropics to the mid-latitudes, *Nat. Geosci.*, 5, 118–122, doi:10.1038/ngeo1364, 2012.
- Krüger, M. L., Mertes, S., Klimach, T., Cheng, Y. F., Su, H., Schneider, J., Andreae, M. O., Pöschl, U., and Rose, D.: Assessment of cloud supersaturation by size-resolved aerosol particle and cloud condensation nuclei (CCN) measurements, *Atmos. Meas. Tech.*, 7, 2615–2629, doi:10.5194/amt-7-2615-2014, 2014.
- Kuhn, U., Ganzeveld, L., Thielmann, A., Dindorf, T., Schebeske, G., Welling, M., Sciare, J., Roberts, G., Meixner, F. X., Kesselmeier, J., Lelieveld, J., Kolle, O., Ciccioli, P., Lloyd, J., Trentmann, J., Artaxo, P., and Andreae, M. O.: Impact of Manaus City on the Amazon Green Ocean atmosphere: ozone production, precursor sensitivity and aerosol load, *Atmos. Chem. Phys.*, 10, 9251–9282, doi:10.5194/acp-10-9251-2010, 2010.
- Kulmala, M., Vehkamäki, H., Petaja, T., Dal Maso, M., Lauri, A., Kerminen, V. M., Birmili, W., and McMurry, P. H.: Formation and growth rates of ultrafine atmospheric particles: a review of observations, *J. Aerosol Sci.*, 35, 143–176, doi:10.1016/j.jaerosci.2003.10.003, 2004.
- Lawrence, D. and Vandecar, K.: Effects of tropical deforestation on climate and agriculture, *Nature Climate Change*, 5, 27–36, doi:10.1038/nclimate2430, 2015.
- Lawson, S. J., Keywood, M. D., Galbally, I. E., Gras, J. L., Caine, J. M., Cope, M. E., Krummel, P. B., Fraser, P. J., Steele, L. P., Bentley, S. T., Meyer, C. P., Ristovski, Z., and Goldstein, A. H.: Biomass burning emissions of trace gases and particles in marine air at Cape Grim, Tasmania, *Atmos. Chem. Phys.*, 15, 13393–13411, doi:10.5194/acp-15-13393-2015, 2015.
- Levin, E. J. T., Prenni, A. J., Petters, M. D., Kreidenweis, S. M., Sullivan, R. C., Atwood, S. A., Ortega, J., DeMott, P. J., and Smith, J. N.: An annual cycle of size-resolved aerosol hygroscopicity at a forested site in Colorado, *J. Geophys. Res.-Atmos.*, 117, D06201, doi:10.1029/2011JD016854, 2012.
- Lohmann, U. and Feichter, J.: Global indirect aerosol effects: a review, *Atmos. Chem. Phys.*, 5, 715–737, doi:10.5194/acp-5-715-2005, 2005.
- Machado, L. A. T., Silva Dias, M. A. F., Morales, C., Fisch, G., Vila, D., Albrecht, R., Goodman, S. J., Calheiros, A. J. P., Biscaro, T., Kummerow, C., Cohen, J., Fitzjarrald, D., Nascimento, E. L., Sakamoto, M. S., Cunningham, C., Chaboureau, J.-P., Petersen, W. A., Adams, D. K., Baldini, L., Angelis, C. F., Sapucci, L. F., Salio, P., Barbosa, H. M. J., Landulfo, E., Souza, R. A. F., Blakeslee, R. J., Bailey, J., Freitas, S., Lima, W. F. A., and Tokay, A.: THE CHUVA PROJECT How Does Convection Vary across Brazil?, *B. Am. Meteorol. Soc.*, 95, 1365–1380, doi:10.1175/bams-d-13-00084.1, 2014.
- Martin, S. T., Andreae, M. O., Althausen, D., Artaxo, P., Baars, H., Borrmann, S., Chen, Q., Farmer, D. K., Guenther, A., Gunthe, S. S., Jimenez, J. L., Karl, T., Longo, K., Manzi, A., Müller, T., Pauliquevis, T., Petters, M. D., Prenni, A. J., Pöschl, U., Rizzo, L. V., Schneider, J., Smith, J. N., Swietlicki, E., Tota, J., Wang, J., Wiedensohler, A., and Zorn, S. R.: An overview of the Amazonian Aerosol Characterization Experiment 2008 (AMAZE-08), *Atmos. Chem. Phys.*, 10, 11415–11438, doi:10.5194/acp-10-11415-2010, 2010a.
- Martin, S. T., Andreae, M. O., Artaxo, P., Baumgardner, D., Chen, Q., Goldstein, A. H., Guenther, A., Heald, C. L., Mayol-Bracero, O. L., McMurry, P. H., Pauliquevis, T., Pöschl, U., Prather, K. A., Roberts, G. C., Saleska, S. R., Dias, M. A. S., Spracklen, D. V., Swietlicki, E., and Trebs, I.: Sources and properties of Amazonian aerosol particles, *Rev. Geophys.*, 48, RG2002, doi:10.1029/2008rg000280, 2010b.
- Martin, S. T., Artaxo, P., Machado, L. A. T., Manzi, A. O., Souza, R. A. F., Schumacher, C., Wang, J., Andreae, M. O., Barbosa, H. M. J., Fan, J., Fisch, G., Goldstein, A. H., Guenther, A., Jimenez, J. L., Pöschl, U., Silva Dias, M. A., Smith, J. N., and Wendisch, M.: Introduction: Observations and Modeling of the Green Ocean Amazon (GoAmazon2014/5), *Atmos. Chem. Phys.*, 16, 4785–4797, doi:10.5194/acp-16-4785-2016, 2016.
- Martins, J. A., Dias, M., and Goncalves, F. L. T.: Impact of biomass burning aerosols on precipitation in the Amazon: A modeling case study, *J. Geophys. Res.-Atmos.*, 114, 83–93, doi:10.1029/2007jd009587, 2009a.
- Martins, J. A., Goncalves, F. L. T., Morales, C. A., Fisch, G. F., Pinheiro, F. G. M., Leal, J. B. V., Jr., Oliveira, C. J., Silva, E. M., Oliveira, J. C. P., Costa, A. A., and Silva Dias, M. A. F.: Cloud condensation nuclei from biomass burning during the Amazonian dry-to-wet transition season, *Meteorol. Atmos. Phys.*, 104, 83–93, doi:10.1007/s00703-009-0019-6, 2009b.
- McFiggans, G., Artaxo, P., Baltensperger, U., Coe, H., Facchini, M. C., Feingold, G., Fuzzi, S., Gysel, M., Laaksonen, A., Lohmann, U., Mentel, T. F., Murphy, D. M., O’Dowd, C. D., Snider, J. R., and Weingartner, E.: The effect of physical and chemical aerosol properties on warm cloud droplet activation, *Atmos. Chem. Phys.*, 6, 2593–2649, doi:10.5194/acp-6-2593-2006, 2006.
- Mikhailov, E., Vlasenko, S., Martin, S. T., Koop, T., and Pöschl, U.: Amorphous and crystalline aerosol particles interacting with

- water vapor: conceptual framework and experimental evidence for restructuring, phase transitions and kinetic limitations, *Atmos. Chem. Phys.*, 9, 9491–9522, doi:10.5194/acp-9-9491-2009, 2009.
- Mikhailov, E., Vlasenko, S., Rose, D., and Pöschl, U.: Mass-based hygroscopicity parameter interaction model and measurement of atmospheric aerosol water uptake, *Atmos. Chem. Phys.*, 13, 717–740, doi:10.5194/acp-13-717-2013, 2013.
- Mikhailov, E. F., Mironov, G. N., Pöhlker, C., Chi, X., Krüger, M. L., Shiraiwa, M., Förster, J.-D., Pöschl, U., Vlasenko, S. S., Ryskhovich, T. I., Weigand, M., Kilcoyne, A. L. D., and Andreae, M. O.: Chemical composition, microstructure, and hygroscopic properties of aerosol particles at the Zotino Tall Tower Observatory (ZOTTO), Siberia, during a summer campaign, *Atmos. Chem. Phys.*, 15, 8847–8869, doi:10.5194/acp-15-8847-2015, 2015.
- Mishra, A. K., Lehahn, Y., Rudich, Y., and Koren, I.: Co-variability of smoke and fire in the Amazon basin, *Atmos. Environ.*, 109, 97–104, doi:10.1016/j.atmosenv.2015.03.007, 2015.
- Moran-Zuloaga, D., Ditas, F., Walter, D., Araùjo, A., Brito, J., Carbone, S., Chi, X., Hrabe de Angelis, I., Lavric, J. V., Ming, J., Pöhlker, M. L., Ruckteschler, N., Saturno, J., Wang, Y., Wang, Q., Weber, B., Wolff, S., Artaxo, P., Andreae, M. O., and Pöhlker, C.: Coarse mode aerosols in the Amazon rainforest, *Atmos. Chem. Phys. Discuss.*, in preparation, 2017.
- Nenes, A. and Seinfeld, J. H.: Parameterization of cloud droplet formation in global climate models, *J. Geophys. Res.-Atmos.*, 108, AAC 7-1–ACC 7-14, doi:10.1029/2002jd002911, 2003.
- Ng, N. L., Canagaratna, M. R., Zhang, Q., Jimenez, J. L., Tian, J., Ulbrich, I. M., Kroll, J. H., Docherty, K. S., Chhabra, P. S., Bahreini, R., Murphy, S. M., Seinfeld, J. H., Hildebrandt, L., Donahue, N. M., DeCarlo, P. F., Lanz, V. A., Prévôt, A. S. H., Dinar, E., Rudich, Y., and Worsnop, D. R.: Organic aerosol components observed in Northern Hemispheric datasets from Aerosol Mass Spectrometry, *Atmos. Chem. Phys.*, 10, 4625–4641, doi:10.5194/acp-10-4625-2010, 2010.
- Ng, N. L., Herndon, S. C., Trimborn, A., Canagaratna, M. R., Croteau, P. L., Onasch, T. B., Sueper, D., Worsnop, D. R., Zhang, Q., Sun, Y. L., and Jayne, J. T.: An Aerosol Chemical Speciation Monitor (ACSM) for Routine Monitoring of the Composition and Mass Concentrations of Ambient Aerosol, *Aerosol Sci. Tech.*, 45, 780–794, doi:10.1080/02786826.2011.560211, 2011.
- Olivares, I., Svenning, J. C., van Bodegom, P. M., and Balslev, H.: Effects of Warming and Drought on the Vegetation and Plant Diversity in the Amazon Basin, *Bot. Rev.*, 81, 42–69, doi:10.1007/s12229-014-9149-8, 2015.
- Ortega, J., Turnipseed, A., Guenther, A. B., Karl, T. G., Day, D. A., Gochis, D., Huffman, J. A., Prenni, A. J., Levin, E. J. T., Kreidenweis, S. M., DeMott, P. J., Tobo, Y., Patton, E. G., Hodzic, A., Cui, Y. Y., Harley, P. C., Hornbrook, R. S., Apel, E. C., Monson, R. K., Eller, A. S. D., Greenberg, J. P., Barth, M. C., Campuzano-Jost, P., Palm, B. B., Jimenez, J. L., Aiken, A. C., Dubey, M. K., Geron, C., Offenberg, J., Ryan, M. G., Fornwalt, P. J., Pryor, S. C., Keutsch, F. N., DiGangi, J. P., Chan, A. W. H., Goldstein, A. H., Wolfe, G. M., Kim, S., Kaser, L., Schnitzhofer, R., Hansel, A., Cantrell, C. A., Mauldin, R. L., and Smith, J. N.: Overview of the Manitou Experimental Forest Observatory: site description and selected science results from 2008 to 2013, *Atmos. Chem. Phys.*, 14, 6345–6367, doi:10.5194/acp-14-6345-2014, 2014.
- Paramonov, M., Aalto, P. P., Asmi, A., Prisle, N., Kerminen, V.-M., Kulmala, M., and Petäjä, T.: The analysis of size-segregated cloud condensation nuclei counter (CCNC) data and its implications for cloud droplet activation, *Atmos. Chem. Phys.*, 13, 10285–10301, doi:10.5194/acp-13-10285-2013, 2013.
- Paramonov, M., Kerminen, V.-M., Gysel, M., Aalto, P. P., Andreae, M. O., Asmi, E., Baltensperger, U., Bougiatioti, A., Brus, D., Frank, G. P., Good, N., Gunthe, S. S., Hao, L., Irwin, M., Jaatinen, A., Jurányi, Z., King, S. M., Kortelainen, A., Kristensson, A., Lihavainen, H., Kulmala, M., Lohmann, U., Martin, S. T., McFiggans, G., Mihalopoulos, N., Nenes, A., O'Dowd, C. D., Ovadnevaite, J., Petäjä, T., Pöschl, U., Roberts, G. C., Rose, D., Svenningsson, B., Swietlicki, E., Weingartner, E., Whitehead, J., Wiedensohler, A., Wittbom, C., and Sierau, B.: A synthesis of cloud condensation nuclei counter (CCNC) measurements within the EUCAARI network, *Atmos. Chem. Phys.*, 15, 12211–12229, doi:10.5194/acp-15-12211-2015, 2015.
- Petters, M. D. and Kreidenweis, S. M.: A single parameter representation of hygroscopic growth and cloud condensation nucleus activity, *Atmos. Chem. Phys.*, 7, 1961–1971, doi:10.5194/acp-7-1961-2007, 2007.
- Pinsky, M., Khain, A., Mazin, I., and Korolev, A.: Analytical estimation of droplet concentration at cloud base, *J. Geophys. Res.-Atmos.*, 117, D18211, doi:10.1029/2012jd017753, 2012.
- Pöhlker, C., Wiedemann, K. T., Sinha, B., Shiraiwa, M., Gunthe, S. S., Smith, M., Su, H., Artaxo, P., Chen, Q., Cheng, Y. F., Elbert, W., Gilles, M. K., Kilcoyne, A. L. D., Moffet, R. C., Weigand, M., Martin, S. T., Pöschl, U., and Andreae, M. O.: Biogenic Potassium Salt Particles as Seeds for Secondary Organic Aerosol in the Amazon, *Science*, 337, 1075–1078, doi:10.1126/science.1223264, 2012.
- Pöhlker, M. L., Pöhlker, C., Ditas, F., Klimach, T., Hrabe de Angelis, I., Araujo, A., Brito, J., Carbone, S., Chi, X., Cheng, Y., Ditz, R., Gunthe, S. S., Kesselmeier, J., Könemann, T., Lavric, J. V., Martin, S. T., Moran, D., Rose, D., Saturno, J., Su, H., Thalman, R., Walter, D., Wang, J., Wolff, S., Barbosa, H. M. J., Artaxo, P., Andreae, M. O., and Pöschl, U.: Long-term observations of cloud condensation nuclei in the Amazon rain forest – Part 2: Near-pristine episodes, ultrafine particle bursts, biomass burning and long range transport events, in preparation, 2017a.
- Pöhlker, M. L., Rose, D., Pöhlker, C., Klimach, T., Hrabe de Angelis, I., Ditas, F., Cheng, Y., Gunthe, S. S., Su, H., Andreae, M. O., and Pöschl, U.: Parameterizations for model predictions of cloud condensation nuclei (CCN) concentration and hygroscopicity from tropical to polar environments, in preparation, 2017b.
- Pöschl, U.: Atmospheric aerosols: Composition, transformation, climate and health effects, *Angew. Chem.-Int. Edit.*, 44, 7520–7540, doi:10.1002/anie.200501122, 2005.
- Prenni, A. J., Petters, M. D., Kreidenweis, S. M., DeMott, P. J., and Ziemann, P. J.: Cloud droplet activation of secondary organic aerosol, *J. Geophys. Res.-Atmos.*, 112, 402–405, doi:10.1029/2006jd007963, 2007.
- Reutter, P., Su, H., Trentmann, J., Simmel, M., Rose, D., Gunthe, S. S., Wernli, H., Andreae, M. O., and Pöschl, U.: Aerosol- and updraft-limited regimes of cloud droplet formation: influence of particle number, size and hygroscopicity on the activation of cloud condensation nuclei (CCN), *Atmos. Chem. Phys.*, 9, 7067–7080, doi:10.5194/acp-9-7067-2009, 2009.

- Rissler, J., Swietlicki, E., Zhou, J., Roberts, G., Andreae, M. O., Gatti, L. V., and Artaxo, P.: Physical properties of the sub-micrometer aerosol over the Amazon rain forest during the wet-to-dry season transition – comparison of modeled and measured CCN concentrations, *Atmos. Chem. Phys.*, 4, 2119–2143, doi:10.5194/acp-4-2119-2004, 2004.
- Rissler, J., Vestin, A., Swietlicki, E., Fisch, G., Zhou, J., Artaxo, P., and Andreae, M. O.: Size distribution and hygroscopic properties of aerosol particles from dry-season biomass burning in Amazonia, *Atmos. Chem. Phys.*, 6, 471–491, doi:10.5194/acp-6-471-2006, 2006.
- Roberts, G. C. and Nenes, A.: A continuous-flow stream-wise thermal-gradient CCN chamber for atmospheric measurements, *Aerosol Sci. Technol.*, 39, 206–221, doi:10.1080/027868290913988, 2005.
- Roberts, G. C., Artaxo, P., Zhou, J. C., Swietlicki, E., and Andreae, M. O.: Sensitivity of CCN spectra on chemical and physical properties of aerosol: A case study from the Amazon Basin, *J. Geophys. Res.-Atmos.*, 107, LBA 37-1–LBA 37-18 doi:10.1029/2001jd000583, 2002.
- Roberts, G. C., Nenes, A., Seinfeld, J. H., and Andreae, M. O.: Impact of biomass burning on cloud properties in the Amazon Basin, *J. Geophys. Res.-Atmos.*, 108, ACC 9-1–ACC 9-19, doi:10.1029/2001jd000985, 2003.
- Roberts, M. C., Andreae, M. O., Zhou, J. C., and Artaxo, P.: Cloud condensation nuclei in the Amazon Basin: “Marine” conditions over a continent?, *Geophys. Res. Lett.*, 28, 2807–2810, 2001.
- Ronchail, J., Cochonneau, G., Molinier, M., Guyot, J. L., Chaves, A. G. D., Guimaraes, V., and de Oliveira, E.: Interannual rainfall variability in the Amazon basin and sea-surface temperatures in the equatorial Pacific and the tropical Atlantic Oceans, *Int. J. Climatol.*, 22, 1663–1686, doi:10.1002/joc.815, 2002.
- Rose, D., Gunthe, S. S., Mikhailov, E., Frank, G. P., Dusek, U., Andreae, M. O., and Pöschl, U.: Calibration and measurement uncertainties of a continuous-flow cloud condensation nuclei counter (DMT-CCNC): CCN activation of ammonium sulfate and sodium chloride aerosol particles in theory and experiment, *Atmos. Chem. Phys.*, 8, 1153–1179, doi:10.5194/acp-8-1153-2008, 2008a.
- Rose, D., Gunthe, S. S., Mikhailov, E., Frank, G. P., Dusek, U., Andreae, M. O., and Pöschl, U.: Calibration and measurement uncertainties of a continuous-flow cloud condensation nuclei counter (DMT-CCNC): CCN activation of ammonium sulfate and sodium chloride aerosol particles in theory and experiment, *Atmos. Chem. Phys.*, 8, 1153–1179, doi:10.5194/acp-8-1153-2008, 2008b.
- Rose, D., Nowak, A., Achtert, P., Wiedensohler, A., Hu, M., Shao, M., Zhang, Y., Andreae, M. O., and Pöschl, U.: Cloud condensation nuclei in polluted air and biomass burning smoke near the mega-city Guangzhou, China – Part 1: Size-resolved measurements and implications for the modeling of aerosol particle hygroscopicity and CCN activity, *Atmos. Chem. Phys.*, 10, 3365–3383, doi:10.5194/acp-10-3365-2010, 2010.
- Rose, D., Gunthe, S. S., Su, H., Garland, R. M., Yang, H., Berghof, M., Cheng, Y. F., Wehner, B., Achtert, P., Nowak, A., Wiedensohler, A., Takegawa, N., Kondo, Y., Hu, M., Zhang, Y., Andreae, M. O., and Pöschl, U.: Cloud condensation nuclei in polluted air and biomass burning smoke near the mega-city Guangzhou, China – Part 2: Size-resolved aerosol chemical composition, diurnal cycles, and externally mixed weakly CCN-active soot particles, *Atmos. Chem. Phys.*, 11, 2817–2836, doi:10.5194/acp-11-2817-2011, 2011.
- Rosenfeld, D., Lohmann, U., Raga, G. B., O’Dowd, C. D., Kulmala, M., Fuzzi, S., Reissell, A., and Andreae, M. O.: Flood or drought: How do aerosols affect precipitation?, *Science*, 321, 1309–1313, doi:10.1126/science.1160606, 2008.
- Salvador, P., Almeida, S. M., Cardoso, J., Almeida-Silva, M., Nunes, T., Cerqueira, M., Alves, C., Reis, M. A., Chaves, P. C., Artífiano, B., and Pio, C.: Composition and origin of PM<sub>10</sub> in Cape Verde: Characterization of long-range transport episodes, *Atmos. Environ.*, 127, 326–339, doi:10.1016/j.atmosenv.2015.12.057, 2016.
- Stevens, B., Farrell, D., Hirsch, L., Jansen, F., Nuijens, L., Serikov, I., Brüggemann, B., Forde, M., Linne, H., Lonitz, K., and Prospero, J. M.: The Barbados Cloud Observatory – Anchoring Investigations of Clouds and Circulation on the Edge of the ITCZ, *B. Am. Meteorol. Soc.*, 0, 787–801, doi:10.1175/BAMS-D-14-00247.1, 2016.
- Su, H., Rose, D., Cheng, Y. F., Gunthe, S. S., Massling, A., Stock, M., Wiedensohler, A., Andreae, M. O., and Pöschl, U.: Hygroscopicity distribution concept for measurement data analysis and modeling of aerosol particle mixing state with regard to hygroscopic growth and CCN activation, *Atmos. Chem. Phys.*, 10, 7489–7503, doi:10.5194/acp-10-7489-2010, 2010.
- Talbot, R. W., Andreae, M. O., Andreae, T. W., and Harriss, R. C.: Regional aerosol chemistry of the Amazon basin during the dry season, *J. Geophys. Res.-Atmos.*, 93, 1499–1508, doi:10.1029/JD093iD02p01499, 1988.
- Talbot, R. W., Andreae, M. O., Berresheim, H., Artaxo, P., Garstang, M., Harriss, R. C., Beecher, K. M., and Li, S. M.: Aerosol chemistry during the wet season in central Amazonia – the influence of long-range transport, *J. Geophys. Res.-Atmos.*, 95, 16955–16969, doi:10.1029/JD095iD10p16955, 1990.
- Thalman, R., de Sá, S. S., Palm, B. B., Barbosa, H. M. J., Plker, M. L., Alexander, M. L., Carbone, S., Day, D. A., Kuang, C., Manzi, A. O., Ng, N. L., Sedlacek, A., Souza, R. A. F., Springston, S., Watson, T., Pöhlker, C., Pöschl, U., Andreae, M. O., Artaxo, P., Jimenez, J. L., Martin, S. T., and Wang, J.: CCN activity and organic hygroscopicity of Amazonian aerosols – seasonal and diel variations and impact of anthropogenic emissions, in preparation, 2017.
- Twomey, S.: The nuclei of natural cloud formation—part II: The supersaturation in natural clouds and the variation of cloud droplet concentration, *Geofis Pura e Appl.*, 43, 243–249, 1959.
- Twomey, S. and Wojciechowski, T. A.: Observations of the geographical variation of cloud nuclei, *J. Atmos. Sci.*, 26, 684–688, 1969.
- Vestin, A., Rissler, J., Swietlicki, E., Frank, G. P., and Andreae, M. O.: Cloud-nucleating properties of the Amazonian biomass burning aerosol: Cloud condensation nuclei measurements and modeling, *J. Geophys. Res.-Atmos.*, 112, D14201, doi:10.1029/2006jd8104, 2007.
- Wendisch, M., Pöschl, U., Andreae, M. O., Machado, L. A. T., Albrecht, R., Schlager, H., Rosenfeld, D., Martin, S. T., Abdelmonem, A., Afchine, A., Araùjo, A., Artaxo, P., Aufmhoff, H., Barbosa, H. M. J., Borrmann, S., Braga, R., Buchholz, B., Cecchini, M. A., Costa, A., Curtius, J., Dollner, M., Dorf, M., Dreiling, V., Ebert, V., Ehrlich, A., Ewald, F., Fisch, G., Fix, A., Frank,

- F., Fütterer, D., Heckl, C., Heidelberg, F., Hüneke, T., Jäkel, E., Järvinen, E., Jurkat, T., Kanter, S., Kästner, U., Kenntner, M., Kesselmeier, J., Klimach, T., Knecht, M., Kohl, R., Kölling, T., Krämer, M., Krüger, M., Krisna, T. C., Lavric, J. V., Longo, K., Mahnke, C., Manzi, A. O., Mayer, B., Mertes, S., Minikin, A., Mollenker, S., Münch, S., Nillius, B., Pfeilsticker, K., Pöhlker, C., Roiger, A., Rose, D., Rosenow, D., Sauer, D., Schnaiter, M., Schneider, J., Schulz, C., de Souza, R. A. F., Spanu, A., Stock, P., Vila, D., Voigt, C., Walser, A., Walter, D., Weigel, R., Weinzierl, B., Werner, F., Yamasoe, M. A., Ziereis, H., Zinner, T., and Zöger, M.: ACRIDICON-CHUVA Campaign: Studying Tropical Deep Convective Clouds and Precipitation over Amazonia Using the New German Research Aircraft HALO, *B. Am. Meteorol. Soc.*, 97, 1885–1908, doi:10.1175/bams-d-14-00255.1, 2016.
- Wex, H., Petters, M. D., Carrico, C. M., Hallbauer, E., Massling, A., McMeeking, G. R., Poulain, L., Wu, Z., Kreidenweis, S. M., and Stratmann, F.: Towards closing the gap between hygroscopic growth and activation for secondary organic aerosol: Part 1 – Evidence from measurements, *Atmos. Chem. Phys.*, 9, 3987–3997, doi:10.5194/acp-9-3987-2009, 2009.
- Whitehead, J. D., Darbyshire, E., Brito, J., Barbosa, H. M. J., Crawford, I., Stern, R., Gallagher, M. W., Kaye, P. H., Allan, J. D., Coe, H., Artaxo, P., and McFiggans, G.: Biogenic cloud nuclei in the central Amazon during the transition from wet to dry season, *Atmos. Chem. Phys.*, 16, 9727–9743, doi:10.5194/acp-16-9727-2016, 2016.
- Winderlich, J., Chen, H., Gerbig, C., Seifert, T., Kolle, O., Lavric, J. V., Kaiser, C., Höfer, A., and Heimann, M.: Continuous low-maintenance CO<sub>2</sub>/CH<sub>4</sub>/H<sub>2</sub>O measurements at the Zotino Tall Tower Observatory (ZOTTO) in Central Siberia, *Atmos. Meas. Tech.*, 3, 1113–1128, doi:10.5194/amt-3-1113-2010, 2010.
- Yáñez-Serrano, A. M., Nölscher, A. C., Williams, J., Wolff, S., Alves, E., Martins, G. A., Bourtsoukidis, E., Brito, J., Jardine, K., Artaxo, P., and Kesselmeier, J.: Diel and seasonal changes of biogenic volatile organic compounds within and above an Amazonian rainforest, *Atmos. Chem. Phys.*, 15, 3359–3378, doi:10.5194/acp-15-3359-2015, 2015.
- Zhou, J., Swietlicki, E., Hansson, H. C., and Artaxo, P.: Submicrometer aerosol particle size distribution and hygroscopic growth measured in the Amazon rain forest during the wet season, *J. Geophys. Res.*, 107, 8055, doi:10.1029/2000jd000203, 2002.



**Long-term observations of cloud condensation nuclei in the Amazon rain forest – Part 2:  
Variability and characteristic differences under near-pristine, biomass burning,  
and long-range transport conditions**

Mira L. Pöhlker<sup>1</sup>, Florian Ditas<sup>1</sup>, Jorge Saturno<sup>1</sup>, Thomas Klimach<sup>1</sup>, Isabella Hrabě de Angelis<sup>1</sup>,  
Alessandro Araujo<sup>2</sup>, Joel Brito<sup>3a</sup>, Samara Carbone<sup>3b</sup>, Yafang Cheng<sup>1</sup>, Xuguang Chi<sup>1,c</sup>, Reiner Ditz<sup>1</sup>,  
Sachin S. Gunthe<sup>4</sup>, Konrad Kandler<sup>5</sup>, Jürgen Kesselmeier<sup>1</sup>, Tobias Könemann<sup>1</sup>, Jošt V. Lavrič<sup>6</sup>,  
Scot T. Martin<sup>7,8</sup>, Eugene Mikhailov<sup>9</sup>, Daniel Moran-Zuloaga<sup>1</sup>, Luciana V. Rizzo<sup>10</sup>, Diana Rose<sup>11</sup>, Hang Su<sup>1</sup>,  
Ryan Thalman<sup>12,d</sup>, David Walter<sup>1</sup>, Jian Wang<sup>12</sup>, Stefan Wolff<sup>1</sup>, Henrique M. J. Barbosa<sup>3</sup>, Paulo Artaxo<sup>2</sup>,  
Meinrat O. Andreae<sup>1,13</sup>, Ulrich Pöschl<sup>1</sup> and Christopher Pöhlker<sup>1</sup>

<sup>1</sup> *Multiphase Chemistry and Biogeochemistry Departments, Max Planck Institute for Chemistry, Mainz, Germany*

<sup>2</sup> *Empresa Brasileira de Pesquisa Agropecuária (EMBRAPA), Belém, PA, Brazil*

<sup>3</sup> *Institute of Physics, University of São Paulo, São Paulo, Brazil*

<sup>4</sup> *EWRE Division, Department of Civil Engineering, Indian Institute of Technology Madras, Chennai, India*

<sup>5</sup> *Institut für Angewandte Geowissenschaften, Technische Universität Darmstadt, Germany*

<sup>6</sup> *Department of Biogeochemical Systems, Max Planck Institute for Biogeochemistry, Jena, Germany*

<sup>7</sup> *School of Engineering and Applied Sciences, Harvard University, Cambridge, MA, USA*

<sup>8</sup> *John A. Paulson School of Engineering and Applied Sciences, Harvard University, Cambridge, MA, USA*

<sup>9</sup> *St. Petersburg State University, 7/9 Universitetskaya nab, St. Petersburg, Russia*

<sup>10</sup> *Instituto de Ciências Ambientais, Químicas e Farmacêuticas, Universidade Federal de São Paulo, SP, Brazil*

<sup>11</sup> *Institut für Atmosphäre und Umwelt, Goethe Universität, Frankfurt, Germany*

<sup>12</sup> *Biological, Environmental & Climate Sciences Department, Brookhaven National Laboratory, Upton, NY, USA*

<sup>13</sup> *Scripps Institution of Oceanography, University of California San Diego, La Jolla, CA, USA*

<sup>a</sup> *now at Laboratoire de Météorologie Physique, Université Clermont Auvergne, Aubière, France*

<sup>b</sup> *now at Federal University of Uberlandia*

<sup>c</sup> *Institute for Climate and Global Change Research, Nanjing University, Nanjing, China*

<sup>d</sup> *now at Department of Chemistry, Snow College, Richfield, UT, USA*



## Long-term observations of cloud condensation nuclei in the Amazon rain forest – Part 2: Variability and characteristic differences under near-pristine, biomass burning, and long-range transport conditions

Mira L. Pöhlker<sup>1</sup>, Florian Ditas<sup>1</sup>, Jorge Saturno<sup>1</sup>, Thomas Klimach<sup>1</sup>, Isabella Hrabě de Angelis<sup>1</sup>, Alessandro Araújo<sup>2</sup>, Joel Brito<sup>3a</sup>, Samara Carbone<sup>3b</sup>, Yafang Cheng<sup>1</sup>, Xuguang Chi<sup>1c</sup>, Reiner Ditz<sup>1</sup>, Sachin S. Gunthe<sup>4</sup>, Konrad Kandler<sup>5</sup>, Jürgen Kesselmeier<sup>1</sup>, Tobias Könemann<sup>1</sup>, Jošt V. Lavrič<sup>6</sup>, Scot T. Martin<sup>7,8</sup>, Eugene Mikhailov<sup>9</sup>, Daniel Moran-Zuloaga<sup>1</sup>, Luciana V. Rizzo<sup>10</sup>, Diana Rose<sup>11</sup>, Hang Su<sup>1</sup>, Ryan Thalman<sup>12,d</sup>, David Walter<sup>1</sup>, Jian Wang<sup>12</sup>, Stefan Wolff<sup>1</sup>, Henrique M. J. Barbosa<sup>3</sup>, Paulo Artaxo<sup>2</sup>, Meinrat O. Andreae<sup>1,13</sup>, Ulrich Pöschl<sup>1</sup> and Christopher Pöhlker<sup>1</sup>

<sup>1</sup>*Multiphase Chemistry and Biogeochemistry Departments, Max Planck Institute for Chemistry, 55020 Mainz, Germany.*

<sup>2</sup>*Instituto Nacional de Pesquisas da Amazonia (INPA), Manaus-AM, CEP 69083-000 Brazil.*

<sup>3</sup>*Institute of Physics, University of São Paulo, São Paulo 05508-900, Brazil.*

<sup>4</sup>*EWRE Division, Department of Civil Engineering, Indian Institute of Technology Madras, Chennai 600036, India.*

<sup>5</sup>*Institut für Angewandte Geowissenschaften, Technische Universität Darmstadt, Germany.*

<sup>6</sup>*Department of Biogeochemical Systems, Max Planck Institute for Biogeochemistry, 07701 Jena, Germany.*

<sup>7</sup>*John A. Paulson School of Engineering and Applied Sciences, Harvard University, Cambridge, MA, USA.*

<sup>8</sup>*Department of Earth and Planetary Sciences, Harvard University, Cambridge, MA, USA.*

<sup>9</sup>*St. Petersburg State University, 7/9 Universitetskaya nab, St. Petersburg, 199034, Russia.*

<sup>10</sup>*Instituto de Ciências Ambientais, Químicas e Farmacêuticas, Universidade Federal de São Paulo (UNIFESP), Diadema, SP, Brazil.*

<sup>11</sup>*Institut für Atmosphäre und Umwelt, Goethe Universität, 60438 Frankfurt, Germany.*

<sup>12</sup>*Biological, Environmental & Climate Sciences Department, Brookhaven National Laboratory, Upton, NY 11973-5000, USA.*

<sup>13</sup>*Scripps Institution of Oceanography, University of California San Diego, La Jolla, CA 92037, USA.*

<sup>a</sup> *now at Laboratoire de Météorologie Physique, Université Clermont Auvergne, Aubière, France.*

<sup>b</sup> *now at Institute of Agrarian Sciences, Federal University of Uberlândia, Uberlândia, Minas Gerais, Brazil.*

<sup>c</sup> *now at Institute for Climate and Global Change Research & School of Atmospheric Sciences, Nanjing University, Nanjing, 210093, China.*

<sup>d</sup> *now at Department of Chemistry, Snow College, Richfield, UT, USA.*

Correspondence to: M. Pöhlker ([m.pohlker@mpic.de](mailto:m.pohlker@mpic.de)) and C. Pöhlker ([c.pohlker@mpic.de](mailto:c.pohlker@mpic.de))



## Abstract

Size-resolved measurements of atmospheric aerosol and cloud condensation nuclei (CCN) concentrations and hygroscopicity were conducted at the remote Amazon Tall Tower Observatory (ATTO) in the central Amazon Basin over a full seasonal cycle (Mar 2014 - Feb 2015). In a companion part 1 paper, we presented an in-depth  
5 CCN characterization based on annually as well as seasonally averaged time intervals and discuss different parametrization strategies to represent the Amazonian CCN cycling in modelling studies (M. Pöhlker et. al. 2016b). The present part 2 study analyzes the aerosol and CCN variability in original time resolution and, thus, resolves aerosol advection and transformation for the following case studies, which represent the most characteristic states of the Amazonian atmosphere:

- 10 (1) Near-pristine (NP) conditions, defined as the absence of detectable black carbon ( $< 0.01 \mu\text{g m}^{-3}$ ), showed their highest occurrence (up to 30 %) in the wet season (i.e., Mar - May). On average, the NP episodes are characterized by a bimodal aerosol size distribution (strong Aitken mode:  $D_{\text{Ait}} = 70 \text{ nm}$ ,  $N_{\text{Ait}} = \sim 200 \text{ cm}^{-3}$  vs. weaker accumulation mode:  $D_{\text{acc}} = 170 \text{ nm}$ ,  $N_{\text{acc}} = \sim 60 \text{ cm}^{-3}$ ), a mostly organic particle composition, and relatively low hygroscopicity levels ( $\kappa_{\text{Ait}} = 0.12$  vs.  $\kappa_{\text{acc}} = 0.18$ ). The NP CCN efficiency spectrum shows that  
15 the CCN population is sensitive to changes in supersaturation ( $S$ ) over a wide  $S$  range.
- (2) Long-range transport (LRT) conditions frequently mix Saharan dust, African combustion smoke, and sea spray aerosols into the Amazonian wet season atmosphere. The LRT episodes (i.e., Feb - Apr) are characterized by an accumulation mode dominated size distribution ( $D_{\text{Ait}} = 80 \text{ nm}$ ,  $N_{\text{Ait}} = 120 \text{ cm}^{-3}$  vs.  $D_{\text{acc}} = 180 \text{ nm}$ ,  $N_{\text{acc}} = 300 \text{ cm}^{-3}$ ), a clearly increased abundance of dust and salt compounds, and relatively high hygroscopicity levels ( $\kappa_{\text{Ait}} = 0.18$ ,  $\kappa_{\text{acc}} = 0.34$ ). The LRT CCN efficiency spectrum shows that the CCN population is  
20 highly sensitive to changes in  $S$  in the low  $S$  regime.
- (3) Biomass burning (BB) conditions dominate the Amazonian dry season. A selected characteristic BB episode shows a very strong accumulation mode ( $D_{\text{Ait}} = 70 \text{ nm}$ ,  $N_{\text{Ait}} = \sim 140 \text{ cm}^{-3}$  vs.  $D_{\text{acc}} = 170 \text{ nm}$ ,  $N_{\text{acc}} = \sim 3400 \text{ cm}^{-3}$ ), particles with very high organic fractions ( $>90 \%$ ), and correspondingly low hygroscopicity levels ( $\kappa_{\text{Ait}} =$   
25  $0.14$ ,  $\kappa_{\text{acc}} = 0.17$ ). The BB CCN efficiency spectrum shows that the CCN population is highly sensitive to changes in  $S$  in the low  $S$  regime.
- (4) Mixed pollution conditions show the superposition of African (i.e., volcanic) and Amazonian (i.e., biomass  
30 burning) aerosol emissions during the dry season. The African aerosols showed a broad monomodal distribution ( $D = 130 \text{ nm}$ ,  $N = \sim 1300 \text{ cm}^{-3}$ ), with very high sulfate fractions (20 %), and correspondingly high hygroscopicity ( $\kappa_{\text{Ait}} = 0.14$ ,  $\kappa_{\text{acc}} = 0.22$ ). This was superimposed by fresh smoke from nearby fires with one strong mode ( $D = 113 \text{ nm}$ ,  $N_{\text{acc}} = \sim 2800 \text{ cm}^{-3}$ ), an organic-dominated aerosol, and sharply decreased hygroscopicity ( $\kappa_{\text{Ait}} = 0.10$ ,  $\kappa_{\text{acc}} = 0.20$ ). These conditions underline the rapidly changing pollution regimes with clear impacts on the aerosol and CCN properties.

Overall, this study provides detailed insights into the CCN cycling in relation to aerosol-cloud interaction in the  
35 vulnerable and climate-relevant Amazon region. The detailed analysis of aerosol and CCN key properties and particularly the extracted CCN efficiency spectra with the associated fit parameters provide a basis for an in-depth analysis of aerosol-cloud interaction in the Amazon and beyond.



## 1 Introduction

Clouds are a key factor in the Earth's atmosphere and climate system (Bony et al., 2015). Thus, sound scientific knowledge on the life cycle and highly dynamic properties of clouds is of significant importance for our understanding of atmospheric cycling and climate change (Seinfeld et al., 2016). A number of recent overview studies summarize the various facets of aerosol-cloud-precipitation-climate interactions in a detailed and comprehensive way (e.g., Andreae and Rosenfeld, 2008; Tao et al., 2012; Rosenfeld et al., 2014).

The Amazon Basin and its unique rain forest ecosystem are fundamentally shaped by the intense and large-scale (re)circulation of water between biosphere and atmosphere. Accordingly, the life cycle of shallow and deep convective clouds in the Amazon has been subject of numerous previous studies (e.g., Andreae et al., 2004; Freud et al., 2008; Rosenfeld et al., 2016b; Wendisch et al., 2016; Braga et al., 2017). In particular, the extent of anthropogenic influence on cloud lifecycle through continuous land use change and combustion-related aerosol emissions has been actively debated (Roberts et al., 2003; Davidson et al., 2012; Goncalves et al., 2015). It is well established that the properties and dynamics of clouds can be fundamentally altered by changing cloud condensation nuclei (CCN) regimes, which are a fraction of the total (tropospheric) aerosol population (Rosenfeld et al., 2008; Reutter et al., 2009).

In terms of microphysical processes in cloud formation and development, the number concentration of CCN,  $N_{CCN}(S)$ , and the peak water vapor supersaturation,  $S$ , at the cloud base play a key role. Here,  $S$  is predominantly determined by the updraft velocity,  $w_b$ , of the adiabatically rising air parcel at the cloud base. Depending on  $N_{CCN}(S)$  and  $S$ , a certain number of cloud droplets at the cloud base,  $N_{db}$ , is formed (Rosenfeld et al., 2016b). In the Amazon Basin,  $N_{db}$  ranges around few hundred particles per cubic centimeter for clean and between 1000 and 2000  $\text{cm}^{-3}$  for polluted conditions (Rosenfeld et al., 2016a; Braga et al., 2017). Upon cloud development and rising air masses, the initial droplets grow by condensation of water vapor, which can be observed as changes in the cloud drop size distribution (DSD). Thus, the DSD is a function of thermodynamic parameters (i.e., the updraft velocity  $w$ ), aerosol conditions (i.e.,  $N_{CCN}(S)$ ), and the cloud evolution (i.e., the cloud depth  $H$ ). Important bulk DSD properties are, in particular the droplet number concentration,  $N_a$ , and the effective droplet radius  $r_e$ . For  $r_e > 11 \mu\text{m}$ , the probability of droplet collision and coalescence processes increases to significant levels and warm rain formation is initiated (Cecchini et al., 2017b).

A detailed analysis of the properties and variability of the Amazonian CCN population is a prerequisite for the understanding of cloud cycling in this region. However, the CCN data from the Basin is still sparse. Therefore, we conducted a systematic characterization of the trends and properties of the central Amazonian CCN population at the Amazon tall tower observatory (ATTO) site. The first half of this study has been published recently as part 1 (M. Pöhlker et al., 2016). The present manuscript represents part 2 of this endeavor and focuses on the variability and properties of periods that are characteristic for the Amazonian atmosphere.

### 1.1 Brief summary of companion part 1 paper

The part 1 paper (M. Pöhlker et al., 2016) focuses on the multi-month trends in the Amazonian CCN population by presenting data from a full seasonal cycle. In particular, it presents annually averages of the key CCN parameters, a detailed analysis of the specific seasonal as well as diurnal trends and a systematic analysis of different CCN parametrization schemes to represent the Amazonian CCN cycling in modeling studies.

The major findings of part 1 can be summarized as follows: (i) The CCN population in the central Amazon is predominantly defined by the overall aerosol concentration as well as the shape of the characteristic bimodal



aerosol size distribution in the CCN-relevant size range. Accordingly, a key property that has to be taken into account for the interpretation of the CCN results is the relative proportion of the Aitken and accumulation modes (mode maxima at  $D_{\text{Ait}} \sim 70$  nm and  $D_{\text{Acc}} \sim 150$  nm). (ii) The hygroscopicity parameters,  $\kappa(S, D_a)$ , of the two modes were found to be remarkably stable for most of the observation period ( $\kappa_{\text{Ait}} = 0.14 \pm 0.03$  vs.  $\kappa_{\text{Acc}} = 0.22 \pm 0.05$ ) with only weak seasonal and no diel variability. Accordingly, we concluded in part 1 that the shape of the aerosol size distribution is the predominant factor, whereas  $\kappa(S, D_a)$  is only of secondary importance for the variability in the Amazonian CCN population, in agreement with previous studies. (iii) Furthermore, part 1 summarizes the CCN key parameters that allow an efficient modeling of the Amazonian CCN population. The prediction of CCN concentrations is particularly reliable when time series of total aerosol concentration and/or the aerosol size distribution are available. The data and parametrization schemes in part 1 will improve the representation of the Amazonian CCN cycling in future modeling studies.

As a particularly helpful concept, we emphasized CCN efficiency spectra, which can be regarded as ‘CCN signatures’ for a particular aerosol population, by describing their behavior for the atmospherically most relevant  $S$  range. Here, a rather simple analytical expression (i.e., a single- or double-error function fits) suffice to represent the essence of the CCN-relevant properties of an aerosol population, which includes the characteristic shape of the aerosol size distribution and the  $\kappa(S, D_a)$  size dependence. Furthermore, the CCN efficiency spectra are independent of the total aerosol number concentration (in contrast to CCN spectra) and, thus, can flexibly be scaled to the concentration range of interest to obtain CCN concentrations at a certain  $S$  level. Finally and beyond their potential use in models as CCN parametrization, the shape of the CCN efficiency spectra is very instructive to visualize the specific behavior of contrasting aerosol population in cloud formation. This aspect will be one focal point of the present study.

## 1.2 Aims and scope of this study

To complete the analysis started in part 1, this manuscript analyzes the CCN variability in original time resolution ( $\sim 4.5$  h), which is sufficient to resolve its short-term variability in relation to air mass changes as well as aerosol emission and transformation processes. In the present work, we will zoom into the long-term CCN data set in two steps: First, we discuss the aerosol and CCN variability for two contrasting 2-months periods that characterize the *pollution minimum* and *maximum* in relation to complementary, trace gas, and aerosol parameters. Second, we will analyze four case studies with a length of a few days that represent the following particularly interesting and characteristic events/conditions in the central Amazon region: (i) the cleanest observed episodes, which can be regarded as a near-pristine atmospheric state, (ii) long-range transport (LRT) aerosol advection during the wet season, which typically brings Saharan dust, African combustion aerosols, as well as marine aerosol particles, (iii) advection of biomass burning smoke from large deforestation fires in southeast Basin after few days of atmospheric processing, and (iv) prevalence of mixed pollution from African LRT and local fires, representing a frequent pollution scenario at the ATTO site. In summary, the overall purpose of this study is to link the measured CCN abundance and properties with the characteristic emissions and transformation processes that govern the Amazonian aerosol population. With the CCN parametrization strategies, developed in part 1, we provide a basis for efficient CCN prediction under characteristic aerosol and CCN conditions in the Amazon Basin.



## 2 Experimental section

### 2.1 Aerosol and trace gas measurements at the ATTO site

The present study is mostly based on *in situ* measurements at the remote ATTO site, which has been described in detail by Andreae et al. (2015). Further relevant information regarding the site, the measurement period, and the aerosol and trace gas instrumentation can be found in the part 1 paper by M. Pöhlker et al. (2016). Note that the time frame of the present analysis including the four in-depth case studies overlapped with the two intensive observation periods (IOPs) of international Green Ocean Amazon 2014/5 (GoAmazon2014/5) campaign (Martin et al., 2016a; 2016b). Specific details on the measurements of equivalent black carbon ( $BC_e$ ) mass concentrations,  $M_{BC_e}$ , with the multi-angle absorption photometer (MAAP) can be found in Saturno et al. (2016; 2017b). Specific details on the measurements of the mole fraction of carbon monoxide (CO),  $c_{CO}$ , with a G1302 analyzer (Picarro Inc. Santa Clara, CA, USA) can be found in Winderlich et al. (2010).

Details on the aerosol chemical speciation monitor (ACSM, Aerodyne Research Inc., Billerica, MA, USA) measurements, which provide online information on the mass concentrations,  $M_{species}$ , of organics (OA), sulfate ( $SO_4^{2-}$ ), nitrate ( $NO_3^-$ ), ammonium ( $NH_4^+$ ), and chloride ( $Cl^-$ ), can be found in Ng et al. (2011). A detailed description of the long-term operation of the ACSM at the ATTO site can be found in Carbone et al. (2017). For selected case study and seasonal time frames, we calculated the mean values of  $M_{species}$  as well as corresponding mass fractions,  $f_{species}$ , according to

$$f_{species} = \frac{M_{species}}{M_{OA} + M_{SO_4} + M_{NH_4} + M_{NO_3} + M_{Cl}}$$

Furthermore, predicted hygroscopicity parameters,  $\kappa_p$ , were calculated based on the ACSM results according to Gunthe et al. (2009) by

$$\kappa_p = f_{OA} \cdot 0.1 + (1 - f_{OA}) \cdot 0.6$$

However, it has to be noted that  $M_{NH_4}$  ranged below its detection limit ( $0.248 \mu\text{g m}^{-3}$ ) during the clean Amazon wet season months, making the obtained results unreliable (the questionable periods are marked in Table 3, which is discussed later in this study). For these periods with questionable results,  $M_{NH_4}$  was omitted in the calculation of the mass fractions

$$f_{species} = \frac{M_{species}}{M_{OA} + M_{SO_4} + M_{NO_3} + M_{Cl}}$$

which has to be kept in mind in the interpretation of the results. Similarly, also  $\kappa_p$  was calculated with  $M_{NH_4}$  being omitted. The nominal size range of the ACSM spans from 75 to 650 nm and the measurements are conducted size-integrated. Accordingly, the ACSM results tend to be dominated by larger particles with relatively high masses, which makes the  $M_{species}$  results more representative for the accumulation mode composition. Accordingly, the calculated  $\kappa_p$  was compared to the hygroscopicity parameter for the lowest measured  $S$  level,  $\kappa(0.11\%)$ , corresponding with the largest measured critical diameter  $D_c$  ( $\sim 170$  nm).

### 2.2 CCN measurements and data analysis

A detailed description of the operation of the CCN counter (CCNC) and the subsequent data analysis can be found in the companion paper (M. Pöhlker et al., 2016), which is the basis for the present study. For further CCN-relevant information, we refer the reader to Rose et al. (2008) and Krüger et al. (2014). The CCN efficiency spectra parameterization as introduced in part 1 plays a key role in the present manuscript. The single-error function (erf) fit (mode = 1) is represented by the following function



$$\frac{N_{CCN}(S)}{N_{CN,10}} = v_1 + a_1 \cdot \operatorname{erf} \left( \frac{\ln \frac{S}{S_1}}{w_1} \right)$$

with  $v_1$  as offset,  $a_1$  as prefactor,  $S_1$  as the supersaturation, at which half of the maximum activated fraction (MAF) of the aerosol particles acts as CCN (e.g., 50 % for  $v_1 = 0.5$ ), and  $w_1$  as the width of the erf fit. To simplify the fitting procedure,  $a_1 = 0.5$  was assumed. Further,  $v_1 = 0.5$  can be used as an input parameter in most cases. The combination,  $a_1 = 0.5$  and  $v_1 = 0.5$ , yields convergence of the erf against unity, corresponding with an activation of all particles as CCN at high  $S$ , which is adequate in most cases. Analogously, the double-erf fit (mode = 2) is represented by the function

$$\frac{N_{CCN}(S)}{N_{CN,10}} = v_1 + a_1 \cdot \operatorname{erf} \left( \frac{\ln \frac{S}{S_1}}{w_1} \right) + a_2 \cdot \operatorname{erf} \left( \frac{\ln \frac{S}{S_2}}{w_2} \right)$$

with the index 1 and 2 specifying the variables for both modes. To simplify the fitting procedure,  $a_1 = 0.5$  and  $v_1 = 0.5$  was assumed.

Another important aspect is worth mentioning: In part 1 we tested different reference aerosol number concentrations,  $N_{CN,Deut}$  (e.g.,  $N_{CN,10}$  and  $N_{CN,50}$ ), for the CCN efficiency spectra parametrization. In this study, we use only one reference concentration for clarity – namely  $N_{CN,10}$ . The choice of  $N_{CN,10}$  can be explained by the fact that it is experimentally rather easily accessible (e.g., via condensation particle counter, CPC, measurements), whereas reference concentrations such as  $N_{CN,50}$  require more elaborated experimental setups (e.g., scanning mobility particle sizer, SMPS, data).

### 2.3 Definition of near-pristine periods

Biomass and fossil fuel combustion have been the primary sources of pollution aerosols in the Amazon region. Since combustion processes are always associated with the emission of black carbon (BC), the MAAP-derived  $BC_c$  serves as a primary marker for the presence of pollution aerosols in this study. Accordingly, we identified the cleanest aerosol conditions observed, which are called *near-pristine* periods throughout this study, as the absence of detectable  $BC_c$ . Petzold and Schönlinner (2004) determined the detection limit of the MAAP “as the minimum resolvable absorbance” by considering “the variability of blank filter optical properties”. The detection limit corresponds with the resulting mean absorbance of the blank filter + 3 times the standard deviation (std) resulting in an absorption coefficient of  $0.132 \text{ Mm}^{-1}$  for 30-min averages. The  $M_{BC_c}$  was calculated by using mass absorption cross sections (MAC) retrieved by fitting MAAP absorption coefficients at 637 nm and single particle soot photometer (SP2) rBC mass measurements during the different seasons as explained in Saturno et al. (2017). Using the MAC values measured at the ATTO site (MAC for the wet season:  $11.4 \pm 1.2 \text{ m}^2 \text{ g}^{-1}$ ; MAC for the dry season:  $12.3 \pm 1.3 \text{ m}^2 \text{ g}^{-1}$ ), the conversion to  $M_{BC_c}$  corresponds to  $0.011 - 0.012 \mu\text{g m}^{-3}$ . Note that this threshold would be higher if a “traditional” MAC value of  $6.6 \text{ m}^2 \text{ g}^{-1}$  were used to calculate  $M_{BC_c}$  ( $\sim 0.019 \mu\text{g m}^{-3}$ ). Here, we selected a threshold concentration of  $M_{BC_c}^* = 0.01 \mu\text{g m}^{-3}$ , when the ATTO-specific MAC values are taken into account. Accordingly, near-pristine periods fulfill the criterion  $M_{BC_c} < M_{BC_c}^*$  for  $\geq 6$  h (after applying a 5-point running average to the 1 h  $M_{BC_c}$  data).



#### 2.4 Backward trajectories

The systematic back trajectory (BT) analysis and classification in this study has been adopted from C. Pöhlker et al. (2017), where an in-depth description of the procedure can be found. Briefly: The BT analysis is based on the hybrid single particle Lagrangian integrated trajectory model (HYSPLIT, NOAA-ARL) with meteorological input data from the global data assimilation system (GDAS1) (Draxler and Hess, 1998). Three-day BTs have been calculated every 1 h with a start height of 1000 m at the ATTO site for the time period of 1 Jan 2008 until 30 June 2016. A sensitivity test confirmed that start heights of the HYSPLIT back trajectories at 200 and 1000 m gave very similar results. Accordingly, the chosen start height at 1000 m appears to be a good representation of the origin of the boundary layer air masses. Subsequently, the resulting ensemble of 74,496 individual BTs has been classified into 15 clusters with k-means cluster analysis (CA). The supplement Fig. S1 shows a map of the north-eastern Amazon Basin with the ATTO site and the mean track of the 15 BT clusters. It illustrates that the air masses arrive almost exclusively in a rather narrow easterly wind sector (between 45° and 120°). Within this sector, four BT subgroups can be identified: (i) a northeasterly (NE) track including the clusters NE1, NE2, and NE3, shown in bluish colors; (ii) an east-northeasterly (ENE) track including the clusters ENE1, ENE2, ENE3, and ENE4, shown in greenish colors; (iii) an easterly (E) track including the clusters E1, E2, E3, and E4, shown in reddish colors; and (iv) a group of ‘inland’ trajectories in east-southeasterly (ESE) directions including clusters ESE1, ESE2, and ESE3 as well as one cluster towards the south-west (i.e., SW1). For a detailed characterization of the region, which is covered by the BTs and represents the ATTO site footprint with the trace gas, aerosol, and CCN sources that are presumably most relevant for the long-term observation at the ATTO site, we refer the reader to C. Pöhlker et al. (2017).

#### 2.5 Satellite data and analysis

The satellite data products used in this study were obtained from the NASA Giovanni web interface (<http://giovanni.gsfc.nasa.gov/>, last access 26 May 2017), developed and maintained by the NASA Goddard Earth Sciences Data and Information Services Center (GES DISC) (Acker and Leptoukh, 2007). The following satellite products have been used:

- Cloud top temperature data (AIRX3STD\_v006 product) from the atmospheric infrared sounder (AIRS) instruments on board of the satellites Terra (data included from 24 Feb 2002 to 30 Jun 2016) and Aqua (data included from 04 Jul 2002 to 30 Jun 2016) satellites. For the corresponding time series in this study, the Aqua and Terra data were averaged per day for a representative region.
- Cloud cover data is obtained by the moderate resolution imaging spectroradiometers (MODIS) on board of the Terra (included data from 24 Feb 2002 to 30 Jun 2016) and Aqua (included data from 04 Jul 2002 to 30 Jun 2016) satellites. The obtained Aqua and Terra time series were averaged. Note that cloud cover strongly depends on the spatial resolution of the instrument as outlined in King et al. (2013).
- Cloud droplet effective radius,  $r_e$ , is calculated from the products measured from the MODIS instrument on board of Terra (included data from 24 Feb 2002 to 30 Jun 2016) and Aqua (included data from 04 Jul 2002 to 30 Jun 2016) satellites. Since  $r_e$  varies with vertical cloud development and total CCN abundance, we filtered the  $r_e$  data by cloud top temperature (King et al., 2013).
- Precipitation rate data,  $P_{\text{TRMM}}$ , from the tropical rainfall measuring mission (TRMM). The TRMM\_3B42\_Daily\_v7 product has been used for the time period 01 Jan 1998 until 30 Jun 2016.



The satellite data were used as time series of area averaged data products within a region of interest around the ATTO site ( $ROI_{ATTO}$ :  $59.5^\circ$  W to  $54^\circ$  W and  $3.5^\circ$  S to  $2.4^\circ$  N) as specified in Fig. S1.

## 2.6 Seasonal cycles of remote sensing and in situ data

5 To provide an overall picture of the seasonal cycle of selected aerosol and meteorological parameters representative for the ATTO region, various data sets were combined in Fig. 1. Remote sensing data products were used in the time frames outlined above. For  $M_{BCe}$ ,  $c_{CO}$ , and  $N_{CN,10}$ , 4–6 years of ATTO site measurements were available. Additionally,  $M_{BCe}$  data measured at the ZF2 site, located 40 km NW of Manaus, were used to reflect the conditions back to 2008 (e.g., Martin et al., 2010a). In terms of sources and conditions, the ATTO and ZF2 sites are  
10 comparable (C. Pöhlker et al., 2017). The  $c_{CO}$  data include ATTO site measurements from 2012 to 2017.

## 2.7 Aerosol sampling and scanning electron microscopy with x-ray spectroscopy

Aerosol samples for electron micro-spectroscopy were collected by impaction. A home-made single stage impactor (flow rate = 1–1.5 lpm; and nominal cut-off  $D_{cut} = \sim 500$  nm) was used for collection. The collection efficiency below  $D_{cut}$  decreases steeply, however, a certain fraction of particles in this size range is still collected.  
15 Moreover, a fraction of very small particles is additionally collected via diffusive deposition and therefore available for the microscopic analysis. Aerosol particles were deposited onto silicon nitride substrates ( $Si_3N_4$ , membrane width 500  $\mu m$ , membrane thicknesses 100 or 150 nm, Silson Ltd., Northampton, UK). Afterwards samples were stored in airtight containers at  $-20^\circ C$  immediately after sampling.

20 Without further treatment like sputter-coating, particles were analyzed in a high-resolution scanning electron microscope (SEM; FEI Quanta 200F, FEI, Eindhoven, The Netherlands). An acceleration voltage of 12.5 kV with a spot size of approximately 3 nm was used. X-ray emission was analyzed with an energy-dispersive X-ray analysis (EDX; Edax Genesis, Edax Inc.). The system is able to record characteristic X-ray emissions for all elements with  $Z > 5$ . Obviously, in the present work Si could not be quantified due to the silicon substrate (Kandler  
25 et al., 2011).

## 3 Results and discussion

### 3.1 Aerosol and cloud microphysical seasonality in the Amazon

Prior to the in-depth analysis of the aerosol and CCN cycling for characteristic case studies, this section provides  
30 an overview of the aerosol and cloud microphysical seasonality, representing the precipitation cycle in the ATTO region. The pollution markers  $c_{CO}$  and  $M_{BCe}$  in Fig. 1a show a pronounced seasonal cycle with a prevalence of clean conditions in the wet season vs. the biomass burning-related pollution maximum in the dry season (Andreae et al., 2015). The annual minimum in  $M_{BCe}$  levels occurred at the end of April (with a weekly  $M_{BCe}$  means of  $\sim 0.03 \mu g m^{-3}$ ), whereas its highest concentrations were observed in August and September (with a  
35 weekly  $M_{BCe}$  means of  $\sim 0.40 \mu g m^{-3}$ ). The seasonal cycle of  $c_{CO}$  shows a temporal shift of about 1 month with its minimum in the beginning of June (with a weekly  $c_{CO}$  means  $\sim 100$  ppb) and largest values from October to December (with a weekly  $c_{CO}$  means  $\sim 200$  ppb). The phase shift between the  $c_{CO}$  and  $M_{BCe}$  seasonality can be explained by the complex spatiotemporal interplay of combustion-related BC and CO sources, aerosol wet scavenging, as well as alternating advection of Northern vs. Southern hemispheric (NH vs. SH) air masses (Martin et al.,  
40 2010b; Andreae et al., 2012; 2015). Similar to the  $M_{BCe}$  trends, the total aerosol particle concentration  $N_{CN,10}$  tracks the seasonality in biomass burning activities (in South America and Africa) with lowest concentrations in



March and April ( $N_{CN,10}$  weekly means  $\sim 200\text{--}300\text{ cm}^{-3}$ ) and highest values between August and November ( $N_{CN,10}$  weekly means from 1000 to 2000  $\text{cm}^{-3}$ ) as shown in Fig 1b. The CCN concentration at a supersaturation of 0.5 %,  $N_{CCN}(0.5\%)$ , which was calculated based on long-term SMPS data and the  $\kappa$ -Köhler parametrization as outlined in our part 1 paper, mostly tracked the seasonal trends in  $N_{CN,10}$ . Its minimum around Mar and April showed weekly mean  $N_{CCN}(0.5\%)$  values around 200  $\text{cm}^{-3}$ , whereas the maximum showed values between 1000 and 2000  $\text{cm}^{-3}$ .

Figure 1c shows the seasonal cycles of two different precipitation related data products: First, the  $P_{TRMM}$  data, representing the area-averaged precipitation rate in the ROI<sub>ATTO</sub> (see Fig. S1). The  $P_{TRMM}$  data reveals a rather broad wet season precipitation maximum from March to May (defining the wet season from a meteorological perspective). The smallest precipitation rates are observed from September to November. Second, the  $P_{BT}$  data represents the cumulative precipitation along the BTs arriving at the ATTO site (for details see C. Pöhlker et al., 2017). Thus,  $P_{BT}$  represents a measure for the extent of rain-related aerosol scavenging – particularly of long-range transport aerosols – upon air mass transport to the ATTO site. A pronounced maximum in  $P_{BT}$  and the related scavenging is observed for the months April and May, which coincides with the minimum in aerosol parameters (i.e.,  $M_{BCc}$  and  $N_{CN}$ ) (see also Moran-Zuloaga et al., 2017).

Figure 1d shows the seasonal cycles in cloud fraction and cloud top temperature for the ROI<sub>ATTO</sub>. Both are predominantly influenced by the position of the intertropical convergence zone (ITCZ) with its belt of extended deep convective cloud systems and strong precipitation. According to Fig. 1d, the densest cloud cover and deepest convection (represented by lowest cloud top temperature) occurs upon northwards passage of the ITCZ in the middle of the wet season (i.e., March and April) as well as upon southwards passage of the ITCZ at the end of the dry season (around November). The maximum in deep convection in March and April – expectedly – corresponds with the peak in  $P_{TRMM}$ . A global picture of the spatiotemporal trends in cloud microphysical properties can be found in King et al. (2013).

Figure 1e presents the satellite-derived effective radius  $r_e$  of liquid cloud droplets that links the seasonality in aerosol and cloud properties. The  $r_e$  data have been filtered by cloud top temperature to discriminate the different  $r_e$  growth states in different heights of the convective clouds. It is well established that increased CCN loads entail an influence on cloud properties, which typically results in corresponding decrease in droplet diameter (e.g., Freud et al., 2008; Stevens and Feingold, 2009). Figure 1e underlines this trend by means of a pronounced seasonality in  $r_e$  with its maximum during clean wet season conditions (i.e., April and May) and its minimum during the polluted months in the dry season (i.e., August to November). The detailed understanding of the impact of the CCN loading on the cloud microphysical properties, however, is the subject of ongoing studies.

The trends in Fig. 1 provide a coherent picture of the aerosol, cloud, and precipitation seasonality as well as their corresponding linkages. The following sections will zoom into this overall picture by presenting detailed aerosol and CCN data from characteristic wet and dry season conditions of the year 2014. The corresponding months that are discussed in greater detail (April and May in Fig. 2 and August and September in Fig. 4) are highlight in Fig. 1 by a background shading to embed the corresponding observations into this overall picture.

### 3.2 Aerosol and CCN time series for representative wet season conditions

During Amazonian wet season (February to May), the influence of local and regional anthropogenic pollution (i.e., from biomass and fossil fuel burning) decreases to a minimum and simultaneous strong precipitation causes efficient aerosol scavenging (see Fig. 1). The combination of both effects constitutes a comparatively clean state



of the Amazonian atmosphere (Martin et al., 2010b; Andreae et al., 2015). During this time of the year, biogenic aerosols from the surrounding rain forest ecosystem, such as secondary organic aerosol (SOA) from the oxidation of biogenic volatile organic compounds (BVOC) as well as primary biological aerosol particles (PBAP), prevail (Pöschl et al., 2010; Huffman et al., 2012; Yanez-Serrano et al., 2015). However, the regionally and biogenically dominated background state of the atmosphere is frequently perturbed by the episodic advection of long-range transport (LRT) aerosols from Africa in air masses that bypass the major rain fields and, therefore, ‘survive’ the intense scavenging (Moran-Zuloaga et al., 2017). The frequent intrusion of LRT aerosols is a characteristic feature during the Amazonian wet season and represents a strong and important impact on the Amazonian ecosystem (e.g., Chen et al., 2009; Bristow et al., 2010; Baars et al., 2011; Abouchami et al., 2013; Yu et al., 2015; Rizzolo et al., 2016). These LRT plumes mostly comprise a complex mixture of Saharan dust, African biomass burning smoke, and marine aerosols from the transatlantic air passage (e.g., Talbot et al., 1990; Swap et al., 1992; Glaser et al., 2015).

The 2-months period in Fig. 2 can be regarded as representative for typical wet season conditions in the ATTO region as it includes both scenarios: periods with the prevalence of the local (biogenic) background aerosol and episodes under the influence of LRT plumes, as well as intermediate states. In general, the wet season 2014 showed ‘average hydrological conditions’ without significant precipitation anomalies within the ROI<sub>ATTO</sub>, which is in stark contrast to 2015/16 with its pronounced El Niño influence and an associated negative precipitation anomaly (see C. Pöhlker et al., 2017; Saturno et al., 2017b). Furthermore, the pollution tracers,  $N_{CN}$ ,  $M_{BCe}$ , and  $c_{CO}$ , showed comparatively low values with concentrations around  $N_{CN} = 330 \pm 130 \text{ cm}^{-3}$ ,  $M_{BCe} = 0.03 \pm 0.05 \mu\text{g m}^{-3}$ , and  $c_{CO} = 110 \pm 10 \text{ ppb}$  (given as mean  $\pm 1$  std for entire time period in Fig. 2) in agreement with previous studies (Andreae et al., 2012; Artaxo et al., 2013; Andreae et al., 2015). In terms of atmospheric circulation, the first half of the 2-month time frame was dominated by back trajectory arrivals from the north-east (blue and green BT clusters, see Fig. 2a and Fig. S1), whereas during the second half the dominant wind direction shifted towards easterly directions (orange and red BT clusters, see Fig. 2a and Fig. S1) (compare Andreae et al., 2015; Moran-Zuloaga et al., 2017). This gradual swing of the dominant wind direction from NH to SH relates to the northwards movement of the ITCZ.

Three episodes with detectable LRT influence occurred during the selected time period in Fig. 2 and have been called *LRT1*, *LRT2*, and *LRT3* in the context of this study (see Table 1). These episodes have been defined according to Moran-Zuloaga et al. (2017).<sup>1</sup> The question to what extent the Amazonian wet season approximates a pristine and pre-industrial state, which is unaffected by human activities, has been actively debated over the last years (Andreae, 2007; Martin et al., 2010b; Hamilton et al., 2014). Although the wet season is free from major pollution influence, there is evidently a persistent background pollution in varying states of dilution. Andreae et al. (2012) argued in this context that the “atmospheric state and processes in the Amazon Basin cannot be understood without the consideration of pollutant inputs by long-range transport”. This is particularly true for gaseous compounds (e.g., CO), however, also a certain fraction of advected pollution aerosols may endure the intense wet deposition and reach the ATTO site. This statement is supported by Fig. 2, which shows comparably clean con-

<sup>1</sup> Moran-Zuloaga et al. (2017) showed that seven moderate to major LRT events occurred in the wet season 2014. Three of these seven LRT episodes overlap with the present CCN data and are called *LRT1*, *LRT2*, and *LRT3* in the context of this study. According to the nomenclature in Moran-Zuloaga et al. (2017), these events correspond to 2014\_5, 2014\_6, and 2014\_7.



ditions (mean  $M_{\text{BCe}} \pm 1 \text{ std}$ :  $0.013 \pm 0.013 \mu\text{g m}^{-3}$ ) for the extended period from 14 April until end of May. However, a closer inspection of the data shows several  $M_{\text{BCe}}$  peaks (some even exceeding  $0.1 \mu\text{g m}^{-3}$ ) that indicate the influence of diluted pollution plumes. Although (highly) diluted, these plumes impact the CCN population, as discussed in Sect. 3.4.

5 In order to shed light on this important aspect, we quantified the relative abundance of very clean periods in the ATTO region, which are called *near-pristine* (NP) in this study (see details in Sect. 2.3). A statistical overview of the relative fraction of near-pristine episodes for the years 2012 to 2017 is shown in Fig. 3. It shows that near-pristine conditions typically occur from March to May with their highest abundance around late April and early May when weekly frequencies of occurrence reach up to 30 % or more. Note that the near-pristine episodes  
10 in 2014 mostly occurred in April and May, which is in good agreement with the multi-year trends. The individual near-pristine episodes in 2014 are represented as grey vertical shading in Fig. 2. Their frequency of occurrence clearly increased towards the end of the wet season, inversely related to the frequency of occurrence of the LRT events, which mostly occurred towards the beginning of the wet season (Moran-Zuloaga et al., 2017). For a detailed analysis in Sect. 3.4, we selected three of the longer (i.e., multi-day) near-pristine periods, which are  
15 highlighted as *NP1*, *NP2*, and *NP3* in Fig. 2.

The following general picture emerges for the CCN parameters: The time series of the  $\kappa(S, D_a)$  size distributions in Fig. 2d clearly illustrates the different  $\kappa(S, D_a)$  of Aitken and accumulation modes as discussed in our part 1 study (M. Pöhlker et al., 2016). Overall,  $\kappa(S, D_a)$  shows a clear variability for low  $S$ , representing the accumulation mode, and rather stable values for higher  $S$ , representing the Aitken mode (see Fig. 2h). The occurrence of  
20 the LRT plumes stands out clearly by causing a significant enhancement of  $\kappa(S, D_a)$  with  $\kappa_{\text{Acc}}$  reaching 0.4 and  $\kappa_{\text{Ait}}$  reaching 0.25 (see Fig. 2d and h). Moreover, the LRT events are also associated with increased  $N_{\text{CCN}}(S)$  and  $N_{\text{CCN}}(S)/N_{\text{CN}}$  values (Fig. 2g and i). Note that the occurrence of the LRT events precisely coincides with the minima in  $P_{\text{BT}}$ , and, thus, ‘windows’ in aerosol scavenging (compare Moran-Zuloaga et al., 2017).

For the extended and comparatively clean period from 14 April until end of May, the SMPS contour plot  
25 (Fig. 2c) reveals equally strong Aitken and accumulation modes as well as a ‘patchy’ appearance, due to frequent rainfall causing (local) aerosol scavenging. As outlined in our part 1 study, the aerosol abundance in the particle size range  $>40 \text{ nm}$  predominantly defined the measured CCN population (M. Pöhlker et al., 2016). Accordingly, the  $N_{\text{CCN}}(S)$  and  $N_{\text{CCN}}(S)/N_{\text{CN}}$  time series directly track the SMPS-derived patchy pattern. The low  $S$  levels – i.e.,  $N_{\text{CCN}}(0.11 \%)$  – which do not activate Aitken mode particles, closely followed the accumulation mode concentration,  $N_{\text{acc}}$ , time series, whereas the higher  $S$  levels (i.e.,  $N_{\text{CCN}}(1.10 \%)$ ), which also activated particles in the Aitken mode, closely tracked  $N_{\text{CN},10}$  ( $= N_{\text{Ait}} + N_{\text{acc}}$ ). Two of the subsequent case studies will focus in more detail of  
30 the specific CCN properties of the *NP* (Sect. 3.4) and *LRT* (Sect. 3.5) cases (see also Table 1).

### 3.3 Aerosol and CCN time series for representative dry season conditions

35 During the dry season (August to November), the central Amazon is under continuous influence of pronounced anthropogenic pollution. The predominant type is biomass burning smoke from deforestation fires, which coined the term “biomass burning season” (Freud et al., 2008). In addition, various urban and industrial emission sources in eastern and southern Brazil as well as southern Africa may also contribute by hard-to-define quantities (e.g., Andreae et al., 1994; Saturno et al., 2017b). The minimum in precipitation rates and, thus, in aerosol scavenging fosters the distribution of pollution aerosols over large areas by extending their atmospheric lifetime (see  
40 Fig. 1).



Figure 4 represents the dry season pendant of Fig. 2 and shows the corresponding time series for a characteristic dry season period from 01 August until 30 September 2014. The BT clusters in Fig. 4a show that easterly and southeasterly BTs prevailed, since the ITCZ was located north of the ATTO site. The BT clusters, which are most characteristic for the dry season, approached the Amazon River delta from the southern Atlantic and then follow the river in western direction towards the ATTO site (red and orange clusters, see Fig. S1). These ‘dry season river BTs’ are subject of more detailed discussion in the case study in Sect. 3.7. For certain episodes, the wind swings further to southeasterly directions and brings air masses from inland directions (black, brown, and grey BT clusters, see Fig. S1). These ‘dry season inland BTs’ are further discussed in the case study in Sect. 3.6.

In contrast to the wet season, the accumulation mode clearly dominates the size distribution, which explains the increased CCN efficiencies, particularly at low  $S$  (Fig. 4c and i). The frequent ‘pulses’ in the accumulation mode concentration can be attributed to (aged) biomass burning plumes, which impact the ATTO site episodically (typically for few days) (see Freitas et al., 2005). The  $M_{BCe}$ ,  $N_{CN}$ , and  $c_{CO}$  levels were typical for dry season conditions in the NE Amazon Basin with  $M_{BCe} = 0.55 \pm 0.35 \mu\text{g m}^{-3}$ ,  $N_{CN} = 1520 \pm 780 \text{ cm}^{-3}$  and  $c_{CO} = 140 \pm 50 \text{ ppb}$  (given as mean  $\pm 1$  std for the time period in Fig. 4) (e.g., Rissler et al., 2004; Andreae et al., 2012; Artaxo et al., 2013; Andreae et al., 2015; Saturno et al., 2017b).

The most obvious event in Fig. 4 is the advection of a strong biomass burning (BB) plume from 17 to 23 August 2014 (the highest pollution levels that were observed during the entire CCN measurement period). This event can be recognized by means of strong pulses in  $N_{Acc}$ ,  $M_{BCe}$ , and  $c_{CO}$  as well as a dip in  $\kappa(S, D_a)$ . The ACSM-derived organic-to-sulfate ratio confirms that the biomass burning pulse comprised a predominantly organic aerosol. In general, the measured  $\kappa(S, D_a)$  levels respond inversely to the organic-to-sulfate ratio, confirming previous studies, which stated that organic matter and sulfate constituents are mostly defining the aerosol’s hygroscopicity in the Amazon (Roberts et al., 2002; Gunthe et al., 2009). The major biomass burning plume in Aug 2014 is subject of the detailed case study *BB* in Sect. 3.6.

Beside this major biomass burning plume, several shorter pulses, which were supposedly also caused by up-wind fires, were observed throughout the dry season period and their frequency of occurrence increased towards the end (i.e., after 12 Sep). Phenomenologically, the major and minor biomass burning plumes were similar as they exhibit peaks in  $N_{CN}$ ,  $M_{BCe}$ , and  $c_{CO}$  and simultaneous dips in  $\kappa(S, D_a)$  and the organic-to-sulfate ratio. The second half of September comprised interesting conditions with comparatively high sulfate concentrations and a sequence of short biomass burning plumes. Thus, this period is influenced by a mixture of different (pollution) aerosol populations from African long-range transport and regional South American sources. A detailed description of the case study *MixPol* can be found on the in Sect. 3.7.

Similar to the wet season, different  $\kappa(S, D_a)$  levels for the Aitken and accumulation modes as well as comparably low  $\kappa(S, D_a)$  variability over time ( $\kappa_{Ait} = 0.14 \pm 0.03$  vs.  $\kappa_{Acc} = 0.23 \pm 0.04$ , covering the entire time period in Fig. 4d and h) were observed. The  $MAF(S)$  values tend to reach unity, except for  $MAF(0.11 \%)$  under the influence of biomass burning smoke (i.e., for the smaller and major smoke plumes).

#### 3.4 Case study *NP* on near-pristine conditions

Aerosol-cloud interactions remain to be the largest uncertainty in global climate models and a better understanding of a preindustrial atmospheric state would help considerably to reduce this uncertainty (Carslaw et al., 2013; Seinfeld et al., 2016). Since the Amazonian wet season provides the rare chance to analyze episodes of very



clean *continental* conditions<sup>2</sup>, this case study extracts the characteristic aerosol and CCN properties and trends during the near-pristine periods as defined in Sect. 2.3 (compare also Table 1). Along these lines, Fig. 5 zooms into three selected episodes – called *NP1*, *NP2*, and *NP3* as highlighted in Fig. 2 – and combines meteorological, aerosol, and CCN time series for a detailed analysis.

5 The meteorological parameters in Fig. 5a, b, and c illustrate typical wet season conditions: (i) a rather high degree of cloudiness, which can be seen by means of the strong cloud-related dimming of the incoming short-wave radiation,  $SW_{in}$ , (ii) frequent local ( $P_{ATTO}$ ) and regional ( $P_{TRMM}$ ) rain events, (iii) a comparatively stable northeasterly wind direction, which is consistent with the BT analysis in Fig. 2, (iv) a rather constant wind speed,  $U$ , for most of the time, which was getting more vigorous during rain events, (v) high relative humidity (RH) conditions, being inversely related to  $SW_{in}$  and reaching saturation during the nights, and (vi) a characteristic time series of the equivalent potential temperature,  $\theta_e$ , which tracked the daily onset of solar heating (see simultaneous increase of  $SW_{in}$  and  $\theta_e$ ) and further provides valuable information on vertical atmospheric mixing, particularly in connection with rain events. Specifically, sudden drops in  $\theta_e$  indicate a downward transport of air masses from upper tropospheric layers, which occurred frequently with the onset of strong rain (for more details see Wang et al., 2016).

15 The corresponding aerosol cycling is shown as aerosol number size distribution ( $dN/d\log D$ ) contour plot in Fig. 5d. Under near-pristine conditions (i.e., grey shading) we found a dominant Aitken mode and a comparatively weak accumulation mode as reported previously (e.g., Andreae et al., 2015; M. Pöhlker et al., 2016). Moreover, the Aitken and accumulation modes reveal a patchy and discontinuous abundance with rather sudden concentration increases and drops. These observations can be explained by a combination of different effects and processes: *First*, the strong and persistent (mostly combustion-related) sources of accumulation mode aerosol particles, which are responsible for the continuous and dominant accumulation mode in the dry season, were absent.

20 *Second*, the frequent rain events acted as an efficient aerosol removal mechanism via aerosol rain-out (i.e., particle activation into cloud/rain droplets) and wash-out (i.e., particle collection by falling droplets below clouds). The wash-out efficiency is slightly higher (~ factor 1.5) for Aitken than accumulation mode particles (Wang et al., 2010; Zikova and Zdimal, 2016). In contrast, the rain-out efficiency, corresponding to CCN activation, is typically much higher for accumulation than Aitken mode particles (M. Pöhlker et al., 2016). Accordingly, the rain pulses strongly modulated the aerosol's abundance via sudden and efficient deposition, which is visible in Fig. 5d as characteristic 'notches' in the aerosol contour plot. The notches represent the (removed) part of the aerosol size fraction that was activated as CCN into cloud droplets. Illustrative examples can be found during days with strong rain showers, such as 27 April, 05 May, and 06 May. Note that the 'depth of the notches', corresponding to the smallest activated particles, could in principle be used to estimate the  $S$  levels during the corresponding events (compare procedure in Krüger et al., 2014). Further note in this context that besides depletion of the accumulation relative to the Aitken mode, aerosol activation and *cloud processing* are known to also foster the opposite effect: The growth of Aitken mode particles into the accumulation mode via formation of aqueous phase reaction products (i.e., sulfate and aqueous phase SOA) in the cloud droplets, followed by droplet

<sup>2</sup> Note that this refers only to very clean continental conditions within the wet season hydrological regime. Very clean conditions within the dry season hydrological regime, which may differ substantially from the wet season scenario due to a contrasting (micro)meteorology, are not experimentally accessible due to the persistent character of the combustion-related aerosols and trace gases.



re-evaporation and deposition of the newly formed compounds onto the particles (e.g., Ervens, 2015; Farmer et al., 2015). Possibly, during 07 May, cloud processing was responsible for the formation of a rather strong accumulation mode from an existing Aitken mode population (Fig. 5).

As a *third* process, the Aitken mode population in the rain forest boundary layer (BL) was frequently replenished by pulse-like appearance of particles with diameters <50 nm. These events are supposed to be rain-related downward transport of air masses from an upper troposphere (UT) particle pool and the subsequent growth of the injected fine particles (Wang et al., 2016; Andreae et al., 2017). Remarkably, the combination of all these effects results in a comparatively constant total particle abundance  $N_{\text{CN}}$  across the rain showers, due to compensating effects of accumulation mode particle losses and simultaneous increases in Aitken mode abundance (see details in Wang et al., 2016). The rain-related downward transport of fine UT particles and their subsequent growth – presumably by the condensation of low-volatility vapors – is a characteristic feature of the Amazonian wet season. At least three pronounced examples for this process are included in the time frame of Fig. 5 (i.e., 27/28 April, 04/05 May, and 16/17 May). After their injection into the forests BL, the fine particles (initial diameters between 20 and 50 nm for the events in Fig. 5) reveal a “banana-like” growth into the Aitken mode size range (~70 nm) in the course of about 12–24 h. For the events in Fig. 5, we calculated an initial, and thus maximum, growth rate of 0.6 to 6 nm h<sup>-1</sup>, which agrees well with the 1 to 6 nm h<sup>-1</sup>, as reported by Kulmala et al. (2004) for tropical regions as well as the reported 5 nm h<sup>-1</sup> in Zhou et al. (2002) for an Amazonian site. Note that these ‘Amazonian bananas’ differ from the classical new particle formation (NPF) that has been reported for various continental sites (i.e., in Northern temperate regions) (Kulmala et al., 2004), since number concentrations are lower by orders of magnitude and their nucleation and initial growth does not occur in the BL, but in the UT (Ekman et al., 2008; Engstrom et al., 2008; Pöschl et al., 2010; Andreae et al., 2017). Accordingly, the UT particle population that is frequently injected into the BL is already aged to a certain extent and, thus, presumably reflects chemical processes different from the atmospheric chemistry in the BL. The physicochemical details of the UT nucleation and growth are still largely unknown and subject of ongoing research (e.g., Andreae et al., 2017).

The CCN properties during near-pristine conditions are represented by time series of  $\kappa(S, D_a)$  size distributions (Fig. 5d) and  $N_{\text{CCN}}(S)$  for two selected  $S$  (Fig. 5e). The temporal pattern of the  $\kappa(S, D_a)$  size distributions, which provides indications of the aerosol particles’ chemical composition, reflects the ‘pattern’ of the underlying  $dN/d\log D$  contour plot. Consistent with our observations in part 1 (M. Pöhlker et al., 2016), the accumulation mode reveals higher  $\kappa(S, D_a)$  levels than the Aitken mode, likely due to chemical aging through cloud processing and a related increase in hygroscopicity (Farmer et al., 2015). The lowest  $\kappa(S, D_a)$  levels were observed for the ‘Amazonian bananas’ (see Fig. 5d). Both, the accumulation and Aitken mode  $\kappa(S, D_a)$  levels show a variability that tracks the Aitken and accumulation mode abundance. Note that  $N_{\text{CCN}}(0.5\%)$  and particularly  $N_{\text{CCN}}(0.2\%)$  show pronounced increases during periods with increased  $M_{\text{BCE}}$  levels (e.g., 25 April, 05 May, and 17 May). This underlines the remarkable impact of diluted pollution on the CCN population in an aerosol limited regime according to Reutter et al. (2009).

Figure 6a and b summarize the average aerosol and CCN key properties under near-pristine conditions. Figure 6a shows the characteristic average  $N_{\text{CN}}(D)$  size distribution with a pronounced bimodal appearance, comprising a dominant Aitken mode ( $D_{\text{Ait}} = 67 \pm 1$  nm,  $N_{\text{Ait}} = \sim 200$  cm<sup>-3</sup>) and a comparatively weak accumulation mode ( $D_{\text{acc}} = 171 \pm 2$  nm,  $N_{\text{acc}} = \sim 60$  cm<sup>-3</sup>) (see Table 2). This bimodal shape mode is typical for clean Amazonian conditions as reported previously (e.g., Gunthe et al., 2009) and notably resembles aerosol size distributions during marine background conditions (e.g., Atwood et al., 2017). The corresponding  $N_{\text{CCN}}(S, D)$  size distributions



for all  $S$  levels show that for  $S < 0.3$  % mostly accumulation mode particles were activated, whereas for  $S > 0.3$  % the Aitken mode particles also acted as CCN. Furthermore, Fig. 6a shows the average  $\kappa(S, D_a)$  size dependence with a characteristic step-wise increase of  $\kappa(S, D_a)$  towards larger  $D$ . The Aitken mode  $\kappa(S, D_a)$  levels are rather low and sharply defined (mean  $\pm$  std:  $0.12 \pm 0.01$ ), whereas the accumulation mode  $\kappa(S, D_a)$  levels are slightly higher ( $0.18 \pm 0.02$ ). The results suggest that the Aitken mode particles, which are frequently injected into the BL via downward transport from the UT, mostly comprised organic matter. This observation agrees well with recent results showing that “the UT particles consist predominantly of organic material, with minor amounts of nitrate and very small fractions of sulfate” (Andreae et al., 2017). The hygroscopicity of organic material,  $\kappa_{\text{org}}$ , is typically assumed as  $\sim 0.10$ , however can vary substantially (close to 0 up to 0.3) as a function of the organic material and its oxygen-to-carbon (O:C) ratio (Jimenez et al., 2009; Thalman et al., 2017). The  $\kappa(S, D_a)$  levels of the accumulation mode similarly indicate the presence of predominantly organic particles, however with somewhat more inorganic constituents than in the Aitken mode. This is consistent with the corresponding ACSM results in Table 3, underlining that organic matter accounts for most of the mass (89 %), whereas nitrate (4 %) and sulfate (6 %) add only small contributions. Note that  $M_{\text{NH}_4}$  ranged below detection limit for NP conditions and its contributions was omitted in the calculation of the mass fractions accordingly (see Sect. 2.1). A predicted average hygroscopicity parameter,  $\kappa_p$ , of  $0.16 \pm 0.05$  was calculated based on the ACSM results – excluding the questionable  $M_{\text{NH}_4}$  – and agrees with the measured value of  $\kappa(0.11 \text{ \%}) = 0.19 \pm 0.05$  (Table 3).

Figure 6b displays the CCN efficiency spectrum for near-pristine conditions, which can be regarded as *CCN signature* of the corresponding aerosol population (for details refer to the companion part 1 paper). The pronounced bimodal particle size distribution with its characteristic Hoppel minimum and the step-wise increase of  $\kappa(S, D_a)$  (see Fig. 6a) result in a weak plateau at about  $S = 0.4$  %, which required to apply a double-erf fit. For comparison, we also applied a single-erf fit. Expectedly, the double-erf fit is the better representation of the experimental data, although the single-erf fit also covers the data reasonably well, since the plateau is not particularly pronounced. However, a closer look reveals differences between the single- vs. double-erf fits for small and large  $S$ . In the small  $S$  range ( $< 0.1$  %), the double-erf fit indicates that the NP aerosol particles start acting as CCN only above a minimum threshold at about  $S = 0.06$  %. One possible physical explanation of this behavior could be the absence of suitable CCN in the size range of several hundred nanometers, which are indeed comparatively sparse under NP conditions according to Fig. 5. However, this size range was not covered directly by our CCN measurements, making it hard to draw solid conclusions. In the large  $S$  range ( $> 1$  %), the spectrum has not reached full activation yet and keeps increasing. Since the double-erf fit describes the data more accurately than the single-erf fit, its extrapolation for  $S > 1.2$  % is likely more accurate and suggests that ‘full’ activation ( $\sim 90$  %) is reached at  $S \sim 1.7$  %. A CCN efficiency spectrum, representing very clean “green ocean” conditions at another Amazonian site from previous measurements<sup>3</sup>, has been added to Fig. 6b for comparison and show very good agreement with our results (Roberts et al., 2001; Andreae et al., 2004).

The CCN efficiency spectra represent an instructive tool to visualize characteristic differences in the behavior of certain (contrasting) aerosol populations in cloud formation. Of particular relevance is the slope of the CCN efficiency spectra,  $d(N_{\text{CCN}}(S)/N_{\text{CN},10})/dS$  as the sensitivity of the activated CCN fraction of a given aerosol

<sup>3</sup> Data is taken from the CLAIRE 1998 campaign (28 March to 15 April 1998), conducted close to the village of Balbina, northeast of Manaus, Brazil.



population within a given  $S$  range to changes in supersaturation,  $\Delta S$ . Accordingly, high  $d(N_{\text{CCN}}(S)/N_{\text{CN},10})/dS$  levels indicate a regime, in which already subtle a  $\Delta S$  has relatively strong effects on the  $N_{\text{CCN}}(S)$  and, thus,  $N_d$  concentrations (assuming constant  $N_{\text{CN},10}$ ), whereas low  $d(N_{\text{CCN}}(S)/N_{\text{CN},10})/dS$  levels indicate a regime that is characterized by rather stable  $N_{\text{CCN}}(S)$  and  $N_d$  concentrations, even upon large  $\Delta S$ . This perception of CCN efficiency spectra stands in certain analogy to a concept introduced by Reutter et al. (2009), which classifies the sensitivity of  $N_d$  concentrations in response to changes in  $N_{\text{CN}}$  and  $w_b$ . This results in three distinct regimes: (i) an *aerosol-limited* regime, which is characterized by high  $S_{\text{max}}$  ( $>0.5\%$ ), a high  $w_b/N_{\text{CN}}$  ratio, high activated fractions  $N_d/N_{\text{CN}}$ , and a linear relationship between  $N_{\text{CN}}$  and  $N_d$ ; (ii) an *updraft-limited* regime, which is characterized by rather low  $S_{\text{max}}$  ( $<0.2\%$ ), a low  $w_b/N_{\text{CN}}$  ratio, low activated fractions  $N_d/N_{\text{CN}}$ , and a linear relationship between  $w_b$  and  $N_d$ ; and (iii) a *transitional* regime with intermediate states and non-linear dependencies of  $N_d$  on  $N_{\text{CN}}$  and  $w_b$ . Note that the concept by Reutter et al. has been developed for the conditions of pyro-convective clouds and, thus, represents an extreme case, which has to be kept in mind in the subsequent comparison with the CCN efficiency spectra.<sup>4</sup> Based on Reutter et al., NP conditions with the associated low aerosol concentrations ( $N_{\text{CN},10} = 270 \pm 100 \text{ cm}^{-3}$ , Table 4) can be characterized as aerosol-limited, due to the overall low abundance of potential CCN. However, the CCN efficiency spectrum in Fig. 6b suggests that the NP aerosol population *also* has a certain sensitivity to  $w_b$ , since changes in updraft velocity  $\Delta w_b$  – and the associated  $\Delta S$  (even for  $S > 1\%$ ) – largely modulate the activated fraction  $N_{\text{CCN}}(S)/N_{\text{CN},10}$ . In this sense, the NP CCN efficiency spectrum has a very characteristic shape and differs clearly from the other case studies, as it keeps increasing over a wide  $S$  range with a somewhat larger slope for  $S < 0.3\%$  and a slightly decreasing slope for  $S > 0.3\%$ . Accordingly, the NP case appears to be aerosol- and updraft-sensitive, which makes the corresponding aerosol-cloud interaction highly dynamic. For more quantitative insights, modelling runs according to Reutter et al. based on the characteristic NP bimodal  $N_{\text{CN}}(D)$  size distribution in Fig. 6a (in contrast to the monomodal accumulation mode, taken into account for the pyro-convective conditions) as well as adjusted  $N_{\text{CN}}$  and  $w_b$  ranges are required.

### 25 3.5 Case study LRT on Saharan dust influence

The African continent is of significant importance for the Amazonian atmospheric composition as it represents a major source of desert dust and pollution aerosols (e.g., Swap et al., 1992; Andreae et al., 1994; Yu et al., 2015; Rizzolo et al., 2016). A systematic overview of the properties and relevance of LRT plume arrival in the ATTO region during the Amazonian wet season can be found in Moran-Zuloaga et al. (2017). Furthermore, a general characterization of the CCN population's response to LRT conditions can be found in our part 1 paper (M. Pöhlker et al., 2016). Based on these previous studies, the present paper analyzes the characteristic impact of LRT plumes on the CCN population in detail.

The characteristic impact of LRT plumes on the aerosol and CCN data can already be seen in Fig. 2 by means of the episodes *LRT1*, *LRT2*, and *LRT3*. For a detailed analysis, the *LRT3* episode – as a particularly instructive example – has been chosen and is represented in Fig. 7 by selected meteorological, aerosol, and CCN

<sup>4</sup> The cloud parcel modelling by Reutter et al. (2009) was conducted for the specific case of pyro-convective conditions, developing over strong fires. Accordingly, a typical (monomodal) biomass burning aerosol size distribution with an accumulation mode maximum at 120 nm was used. In this sense, the study is bound to rather specific and extreme conditions. However, Reutter et al. state that the “key features of the three regimes of CCN activation (...) are not specific for young biomass burning aerosols and pyro-convective conditions but likely to apply also for other types of aerosols and meteorological conditions”.



time series.<sup>5</sup> The layout of Fig. 7 is identical to the corresponding figures of the other case studies for clarity and comparability. Note that the advected dust plumes typically cause substantial increases in both, the coarse mode, which plays a secondary role here, and the accumulation mode, which explains their relevance for the CCN cycling (Moran-Zuloaga et al., 2017). The LRT influence is clearly visible in Fig. 7 by means of increases in  $M_{BCc}$  (due to the LRT plume's smoke component), the accumulation mode abundance in the  $dN/d\log D$  contour plot, the concentrations  $N_{CN}$  and  $N_{CCN}(S)$  as well as in  $\kappa(S, D_a)$ .

The plume's influence on the ATTO site lasted for about four days with its onset on 09 April ~12:00 and its end on 13 April ~12:00, which is in good agreement with the corresponding remote sensing data in Moran-Zuloaga et al. (2017). During these four days, meteorology determined the variability of the LRT aerosol in the rain forest BL via air mass advection (i.e., wind speed and direction), rain-related scavenging (i.e.,  $P_{ATTO}$  and  $P_{TRMM}$ ), and convective mixing (i.e., represented by  $SW_{in}$  as a proxy). Throughout the *LRT3* period, the dominant wind direction was mostly NE to E, which is characteristic for wet season conditions (compare Fig. 2). Note that the BTs arriving from the NE are particularly prone to bring dust-laden air into the ATTO region (Moran-Zuloaga et al., 2017). Furthermore, only few (major) rain events and related aerosol scavenging occurred during this time, which is a further prerequisite for efficient LRT transport. The arrival of the *LRT3* plume during afternoon hours of 09 April occurred via convective downward mixing of the aerosol into the forest BL (see simultaneous increases in  $SW_{in}$ ,  $\theta_e$ , and the accumulation mode in  $dN/d\log D$ ) and its influence lasted until 13 April, when the concentration time series decreased gradually. Note that the advected LRT plumes are transported into the ATTO region as compact and stratified aerosol layers up to altitudes of 2-3 km (Moran-Zuloaga et al., 2017). Aerosol concentrations were highest during the afternoon hours on 09, 10 and 11 April, when convection (see  $SW_{in}$ ) is most efficient in mixing the aerosols downward into the BL. Furthermore, a sudden rain-related air mass change lasting for about 12 h (see wind direction and  $\theta_e$  changes) in the end of 09 April/beginning of 10 April was associated with a simultaneous drop in LRT aerosol concentrations. The CCN population responded noticeably to the injection of the LRT pulses, which can be seen in  $N_{CCN}(S)$ ,  $N_{CCN}(S)/N_{CN,10}$ , and  $\kappa(S, D_a)$  in Fig. 2. Figure 7 displays the  $N_{CCN}(0.2\%)$  and  $N_{CCN}(0.5\%)$  time series, which show a two- to threefold increase upon LRT aerosol intrusion. Moreover, the  $\kappa(S, D_a)$  data can be used as an indirect measure for the aerosol chemical composition, which primarily reflects the average ratio of organic vs. inorganic constituents in the particles. In Fig. 7d, the occurrence of elevated  $\kappa(S, D_a)$  levels coincides exactly with the variability in  $dN/d\log D$ . For this particular event,  $\kappa_{Acc}$  increased from ~0.3 to ~0.4, whereas  $\kappa_{Ait}$  increased from ~0.15 to ~0.25.

Figure 6c summarizes the characteristic  $N_{CN}(D)$  and  $N_{CCN}(S, D)$  size distributions as well as the size dependence of  $\kappa(S, D_a)$  during LRT influence. In general, the comparison of Fig. 6a and c contrasts the characteristic LRT vs. NP conditions and emphasizes that the intrusion of African LRT plumes into the wet season BL has significant influence on the aerosol and CCN population. Specifically, the accumulation mode under LRT conditions ( $D_{acc} = 178 \pm 2$  nm,  $N_{acc} = \sim 300$  cm<sup>-3</sup>) is about 5 times enhanced in comparison to the NP episodes. The Aitken mode ( $D_{ait} = 77 \pm 2$  nm,  $N_{ait} = \sim 120$  cm<sup>-3</sup>), which appears in the LRT  $N_{CN}(D)$  distribution only as a shoulder, shows comparable absolute strength as under NP conditions (see Table 2). The  $N_{CCN}(S, D)$  size distributions show that supersaturations  $S \leq 0.3\%$  activate particles mostly in the accumulation mode range, whereas  $S > 0.3\%$  starts activating the Aitken mode population. The  $\kappa(S, D_a)$  size distribution shows  $\kappa_{Acc}$  reaching rather high levels

<sup>5</sup> Note that the *LRT3* event has also been chosen for in-depth case study analysis in Moran-Zuloaga et al. (2017), where it is called 2014\_7. Accordingly, a number of additional aspects and observations concerning the *LRT3* event, which are not explicitly discussed in this work, can be found there.



up to 0.40 ( $\kappa_{Acc} = 0.34 \pm 0.04$ ) and  $\kappa_{Ait}$  with values up to 0.2 ( $\kappa_{Ait} = 0.18 \pm 0.02$ ). In comparison to the NP conditions,  $\kappa_{Acc}$  was clearly enhanced due to the presence of aged, internally mixed and salt-rich particles (see discussion in subsequent section). In contrast, the  $\kappa_{Ait}$  levels were only slightly higher than during the NP periods, probably due to a broader accumulation mode base, which reached into the Aitken mode range. Note that the relative increase in  $\kappa(S, D_a)$  for the contrasting LRT and NP conditions is large enough to exert an influence on the CCN population, which is an exceptional case throughout the Amazonian seasons, since the  $\kappa(S, D_a)$  levels for most of the year vary within a rather narrow range (0.1 to 0.2) (see part 1 paper).

The African LRT plumes that frequently impact the Amazon Basin during the wet season comprise a complex mixture of different aerosols components, including (i) a fraction of Saharan dust (mostly  $>1 \mu\text{m}$ ), (ii) biomass burning aerosols from fires in the Sahel region (mostly in the accumulation mode), and (iii) marine aerosols from the plume's transatlantic passage (in coarse and accumulation modes) (Andreae et al., 1986; Talbot et al., 1990; Swap et al., 1992). Fresh soot and uncoated dust particles typically have low hygroscopicities, whereas sea salt particles (i.e., NaCl and sulfates) represent comparatively efficient CCN. The LRT plumes encounter a rather long atmospheric journey – about 10 days according to Gläser et al. (2015) – which is associated with strong atmospheric processing and typically results in complex internally mixed particles (see Andreae et al., 1986). The resulting mixtures of dust and salt as well as coated soot particles, as commonly found in the dust plumes, readily act as CCN at realistic  $S$  levels ( $<1\%$ ) (Andreae and Rosenfeld, 2008).

Table 3 summarizes the ACSM results on aerosol chemical composition during LRT influence.<sup>6</sup> Note that the ACSM only measures the non-refractory fraction of the particle mass and, thus, does not detect a large fractions of the dust and salt constituents. During LRT conditions and with respect to the non-refractory part, organic mass dominated the particle composition (73 %), with minor nitrate contributions (3 %) and larger fractions of ammonium (12 %)<sup>7</sup> and sulfate (10 %). Furthermore, a sea salt-related increase in detected chloride mass (4 %) relative to the NP state was observed. Based on the ACSM results, a predicted  $\kappa_p$ , of  $0.24 \pm 0.16$  was obtained, which agrees reasonably well with the measured hygroscopicity level  $\kappa(0.11\%) = 0.35 \pm 0.04$ . Accordingly, the observed elevated fractions of sulfate and ammonium were responsible for part of the increase in  $\kappa(S, D_a)$ . The remaining difference between  $\kappa_p$  and  $\kappa(0.11\%)$  can likely be explained by further refractory inorganics that were not covered by the ACSM. As an illustration of the complex mixing state of the African LRT aerosol population, Fig. S2 and S3 provide selected SEM-EDX data from a characteristic LRT aerosol sample. Note that these results merely serve as a *qualitative example* here, whereas a quantitative microspectroscopic analysis of LRT samples is subject of ongoing work. The observed particles' morphology underlines the influence of atmospheric processing and shows a high degree of internal mixing. Chemically, the EDX maps show dust particles, sulfate salts, as well as a rather large abundance of NaCl particles.

Figure 6d displays the characteristic CCN efficiency spectrum for the LRT conditions, which – expectedly – shows a rather steep increase at low  $S$  due to two effects pointing in the same direction: an enhanced accumulation mode and the presence of rather 'good' CCN with comparatively high  $\kappa(S, D_a)$  levels. This large initial slope

<sup>6</sup> ACSM data was available from Aug 2014 to Sep 2016. Accordingly, the ACSM time frame does not cover the *LRT1*, *LRT2*, and *LRT3* events, which are discussed in detail in this work. Instead, we analyzed the ACSM data for 12 comparable LRT episodes in 2015 and 2016 according to Moran-Zuloaga et al. (2017) (see also Table 1).

<sup>7</sup> Ammonium mass concentrations are only slightly above detection limit and, thus, the results have to be considered carefully.



corresponds with a very small value for the characteristic variable  $S_1 = 0.09\%$ , which shows that at comparatively low  $S$  (lowest  $S_1$  among all analyzed cases) already 50 % of the aerosol population were activated as CCN (Table 4). At  $S$  levels around 0.3 % already ~80 % of the aerosols acted as CCN, ‘full’ activation (90%) is already reached for  $S = \sim 0.5\%$ . At higher  $S$  (i.e.,  $> 0.9\%$ ) the efficiency spectrum approaches unity. This is in stark contrast to the near-pristine CCN efficiency spectrum in Fig. 6b, where 50 % of the particles were activated at significantly higher  $S$  around 0.5 %, whereas ‘full’ activation (90%) was hardly reached at high  $S$  around 1.7 %. Thus, the LRT episodes show a pronounced sensitivity to  $\Delta S$  only in the low  $S$  regime, in contrast to the near pristine case with a sensitivity to  $\Delta S$  spanning across a wide  $S$  range. With the characteristic shape of the CCN efficiency spectrum (i.e., rather strong accumulation mode) and the low aerosol concentrations ( $N_{\text{CN},10} = 440 \pm 100 \text{ cm}^{-3}$ , Table 4) taken into account, the LRT episodes appear to be aerosol-limited according to Reutter et al. (2009).

### 3.6 Case study *BB* on biomass burning smoke

During the dry season, the ATTO site is frequently influenced by smoke from biomass burning (BB) activities in different regions of the Amazon forest (Freitas et al., 2005; Andreae et al., 2012; 2015; C. Pöhlker et al., 2017). As a characteristic example, the case study *BB* focuses on the strong biomass burning plume that was observed at the ATTO site in the middle of August 2014. During this event, pollution aerosol and trace gas concentrations reached their annual maxima with  $N_{\text{CN},10}$  peaking at  $5000 \text{ cm}^{-3}$ ,  $c_{\text{CO}}$  at 350 ppb, and  $M_{\text{BCc}}$  reaching up to  $2.5 \mu\text{g m}^{-3}$ , as shown in Fig. 4. Selected meteorological, aerosol, and CCN time series of the event are shown in Fig. 8. This case study provides the fortunate opportunity to analyze the CCN properties of *aged smoke* from a rather defined large-scale BB plume in the Amazon region.

Figure 8 shows that the influence of biomass burning smoke on the ATTO site lasted for about 6 days (17 to 23 August) with a rather gradual onset and decay. In terms of meteorology, this period was characterized by mostly cloud-free conditions (see  $\text{SW}_{\text{in}}$ ) without precipitation, comparatively low RH levels, and some variability in wind direction. Note that during the presence of this major smoke plume, an atmospheric dimming in the ATTO region could be recognized (i.e., compare  $\text{SW}_{\text{in}}$  maxima for the seven consecutive days). The signature of the smoke aerosol particles can very clearly be seen in the  $dN/d\log D$  contour plot,  $N_{\text{CN}}$ , as well as  $M_{\text{BCc}}$ . In terms of particle size, the pronounced increase mostly occurred in the accumulation mode, which appears to be comparatively broad for this specific event. The CCN concentrations – e.g.,  $N_{\text{CCN}(0.2\%)}$  and  $N_{\text{CCN}(0.5\%)}$  – track the relative increase in total aerosol abundance and show a 4 to 5-fold increase as well. At the same time, the presence of the pyrogenic aerosols correspond to a clear drop in aerosol hygroscopicity in both, the Aitken ( $\Delta\kappa_{\text{Ait}} \approx -0.05$ ) and accumulation modes ( $\Delta\kappa_{\text{Acc}} \approx -0.1$ ) (see overlay of  $\kappa(S, D_a)$  size distributions and the  $dN/d\log D$  contour plot in Fig. 8d). This drop in  $\kappa(S, D_a)$  is associated with a high organic-to-sulfate,  $\text{OA}/\text{SO}_4^{2-}$ , ratio (Fig. 8f), reflecting the dominant role of organic constituents in biomass burning particles as documented in previous studies (Fuzzi et al., 2007; Artaxo et al., 2013; Latham et al., 2013).

Geographically, the location of the fires and, thus, the origin of the strong biomass burning plume could be found by means of a combination of BTs and satellite data products as shown in Fig. S4 (Draxler and Hess, 1998; Acker and Leptoukh, 2007; Justice et al., 2011). The strong pollution at the ATTO site resulted from the presence of intense fires in the southern Amazon and a temporary ‘swing’ of the BT track over the fire locations. During the dry season, the BTs mostly belong to the E and ESE clusters (see Fig. S1 and 4). For the period before and after the biomass burning plume, the BT track follows a ‘coastal path’ and enters the continent in the



region of the Amazon River delta (about 0° N 50° W). Subsequently, the air masses ‘follow’ the Amazon River in western directions to the ATTO site. During the peak period of the *BB* event the BTs deviate from the ‘coastal path’ and follow an ‘inland path’ across the southeast of Brazil (see Fig. S4a and Fig. 4). At about 7° S and 55° W, the BTs intersect a region with strong fire activities, which are clearly visible in satellite products such as

5 NO<sub>2</sub> total column measurements. These fires are localized along the Cuiabá-Santarém highway (BR-163). This highway corridor is known as a region of intense logging and burning of primary forest and its conversion to cattle pasture (Nepstad et al., 2002; Fearnside, 2007; C. Pöhlker et al., 2017). The transport time of the smoke from the fires to the ATTO site is about 2-3 days (given by the BTs), which provides a reference for the residence time and aging of the aerosol particles in the atmosphere. The satellite image in Fig. S4b shows the smoke plume that

10 originated in the BR-163 region and traveled northwestwards. It clearly impacts the area around Manaus and the ATTO site precisely during the ‘event days’ in August.

For further characterization of the *BB* case study, we calculated a ratio of excess  $N_{\text{CN},10}$  to excess  $c_{\text{CO}}$  ( $\Delta N_{\text{CN},10}/\Delta c_{\text{CO}}$ ) for the event of  $17.9 \pm 0.7 \text{ cm}^{-3} \text{ ppb}^{-1}$  (see Fig. S5a), which agrees well with the typical range for a variety of vegetation fires ( $30 \pm 15 \text{ cm}^{-3} \text{ ppb}^{-1}$ ), in contrast to much higher  $\Delta N_{\text{CN},10}/\Delta c_{\text{CO}}$  levels for urban

15 ( $100 - 300 \text{ cm}^{-3} \text{ ppb}^{-1}$ ) and power plant emissions (up to  $900 \text{ cm}^{-3} \text{ ppb}^{-1}$ ) (Janhaell et al., 2010; Kuhn et al., 2010; Andreae et al., 2012). Furthermore, the ratios of excess  $N_{\text{CCN}}(S)$  to excess  $c_{\text{CO}}$ ,  $\Delta N_{\text{CCN}}(S)/\Delta c_{\text{CO}}$ , for the individual  $S$  levels range between  $6.7 \pm 0.5 \text{ cm}^{-3} \text{ ppb}^{-1}$  for the lowest  $S = 0.11 \%$  and values around  $18.0 \pm 1.3 \text{ cm}^{-3} \text{ ppb}^{-1}$  for higher  $S$  (see Table S1 and Fig. S5b). The  $\Delta N_{\text{CCN}}(S)/\Delta c_{\text{CO}}$  ratios converge against  $\Delta N_{\text{CN}}/\Delta c_{\text{CO}}$  already for comparably small  $S$  (i.e.,  $> 0.24 \%$ ), which can be explained by the fact that small  $S$  already activate a substantial fraction of the pronounced (mostly pyrogenic) accumulation mode (see discussion below). Kuhn et al. (2010) reported  $\Delta N_{\text{CCN}}(0.6\%)/\Delta c_{\text{CO}}$  ratios around  $26 \text{ cm}^{-3} \text{ ppb}^{-1}$  for biomass burning plumes and around  $49 \text{ cm}^{-3} \text{ ppb}^{-1}$  for urban plumes, which is consistent with our observations. The obtained  $\Delta N_{\text{CCN}}(S)/\Delta c_{\text{CO}}$  ratios were utilized in a dedicated CCN parameterization scheme in our part 1 study (M. Pöhlker et al., 2016).

Figure 6e summarizes the corresponding  $N_{\text{CN}}$  and  $N_{\text{CCN}}(S)$  size distributions as well as the size dependence of  $\kappa(S, D_a)$  for the *BB* case study. It shows a very strong accumulation mode  $D_{\text{acc}} = 167 \pm 1 \text{ nm}$ ,  $N_{\text{acc}} = \sim 3400 \text{ cm}^{-3}$ , ‘swamping’ the Aitken mode  $D_{\text{ait}} = 70 \pm 1 \text{ nm}$ ,  $N_{\text{ait}} = \sim 140 \text{ cm}^{-3}$  almost completely, giving the entire distribution a monomodal appearance. It can be seen that already comparatively low  $S$  levels activate substantial fractions of the *BB* particle population. For  $S < 0.5 \%$  almost the entire aerosol population is activated as CCN. The averaged  $\kappa(S, D_a)$  levels are rather low for both, the Aitken and accumulation modes ( $\kappa_{\text{ait}} = 0.14 \pm 0.01$  and

25  $\kappa_{\text{acc}} = 0.17 \pm 0.02$ ), in which  $\kappa_{\text{acc}}$  belongs to the lowest values found in the accumulation mode size range throughout the entire study. The low  $\kappa(S, D_a)$  levels can be explained by the fact that pyrogenic aerosols predominantly contain organic constituents and rather low levels of inorganic species. The ACSM results during the *BB* period emphasize the predominant mass fraction of organics (91 %) as well as the minor contribution by nitrate (2 %), ammonium (3 %), and sulfate (4 %) (Table 3). The predicted  $\kappa_p$  of  $0.14 \pm 0.02$  agrees reasonably well

30 with the measurement result  $\kappa(0.10 \%) = 0.18 \pm 0.01$ .

Figure 6f displays the characteristic CCN efficiency spectrum for the *BB* period, which levels out clearly below unity. The grey line shows the erf fit treated to go from zero to one, which obviously does not match the data points for large  $S$ . The red line is an erf fit of the data where the plateau is an open fit parameter.<sup>8</sup> This erf fit

<sup>8</sup> The single erf fit with the pre-defined variable  $v_1 = 0.5$  and  $a_1 = 0.5$ , which is an inappropriate representation of the experimental data, has been included here for consistency, since the assumption that the activated fraction reaches 100 % worked well for all other case studies.



matches the data points very well and the fit parameters as presented in Table 4 reveal the plateau at 93 %. Physically, this indicates the presence of an externally mixed aerosol population with 7 % of the particles being hydrophobic (e.g., fresh soot) and not acting as CCN in the measured  $S$  range. The slope of the efficiency spectrum shows a steep increase for  $S < 0.4$  %, however, below  $S \sim 0.05$  % no significant fraction of the particles can be activated. Since this region is not covered by direct CCN measurements, this might be related to a large amount of accumulation mode particles with a low hygroscopicity. According to these findings, the  $\Delta S$  sensitive range is rather small, spanning from  $\sim 0.05$  % to  $\sim 0.4$  %. According to Reutter et al. (2009), the *BB* case study conditions with the large number of available CCN (e.g.,  $N_{\text{CCN}(0.47\%)} > 4000 \text{ cm}^{-3}$ ) fall into the updraft-limited regime.

Generally, the large aerosol load, its optical properties, and its ability to serve as CCN might already influence cloud properties and stratification of the thermodynamic profile of the atmosphere at both, local and regional scales (Cecchini et al., 2017a). As mentioned above, the incoming solar radiation was dimmed compared to the days before and after this *BB* event. Furthermore, the cloud fraction decreased, which might result from stabilizing the atmosphere due to increased absorption of solar radiation in and above the boundary layer (Koren et al., 2004; Rosenfeld et al., 2008; Rosario et al., 2013). A detailed investigation of the direct radiative forcing and the modification of cloud properties by aerosol particles in the Amazon rain forest are clearly beyond the scope of this study. Nevertheless, the results shown here may serve as input for dedicated regional climate simulations.

### 3.7 Case study *MixPol* on the complexity of the dry season aerosol population

This *MixPol* case study, which represents a scenario of *mixed pollution*, focusses on a 7-day period in September 2014 with an exceptionally low  $\text{OA}/\text{SO}_4^{2-}$  mass ratio of about 3 (Table 3). Previous studies pointed out that the dry season atmosphere in the Amazon is typically dominated by smoke emissions from deforestation fires in the Basin (Freud et al., 2008; Artaxo et al., 2013). This is widely correct, however, upon deeper inspection the picture becomes more complex, since the contributions of further anthropogenic pollution types (i.e., fossil fuel combustion, industry etc.) as well as natural sources (i.e., marine aerosol, biogenic emissions) to the dry season aerosol population have to be taken into account (C. Pöhlker et al., 2017; Saturno et al., 2017b). The significance of these additional non-biomass burning-related sources has not yet been quantified conclusively. Accordingly, the purpose of this case study is to shed exemplary light on the complexity of the dry season aerosol population by means of the present *MixPol* case study period. This analysis will underline and discuss the mixture of superimposed aerosol types, the comparatively high variability of aerosol key parameters, and the characteristic differences between long-range transport perturbed dry season conditions and superimposed regional emission pulses. Ultimately, these observations are discussed in the light of the related CCN cycling.

Meteorologically, the time frame of *MixPol* was mostly cloud-free (see daily profile in  $\text{SW}_{\text{in}}$ ) and without precipitation (see  $P_{\text{TRMM}}$  and  $P_{\text{ATTO}}$ ) as well as characterized by rather stable wind conditions (Fig. 9). With respect to the aerosol and CCN parameters, the relevant time series, such as  $N_{\text{CN}}$ ,  $M_{\text{BCe}}$ ,  $N_{\text{CCN}}(S)$ , show a comparatively high variability. Specifically, the  $dN/d\log D$  contour plot shows an alternating pattern: On one hand and marked by a grey shading, rather extended periods with comparably low aerosol concentrations (around  $1000 \text{ cm}^{-3}$ ) and high  $\kappa(S, D_a)$  values (up to 0.35) can be observed. The  $\kappa(S, D_a)$  levels reaching  $\sim 0.35$  are among the highest in the entire dry season 2014 (compare Fig. 4). On the other hand and marked by a purple shading, these conditions are interrupted by several *pulses* with strongly enhanced aerosol concentrations (up to  $5000 \text{ cm}^{-3}$ ) as well as substantially lower  $\kappa(S, D_a)$  values (around 0.1). The changes in  $\kappa(S, D_a)$  occur with simultaneous



changes in the aerosol chemical composition: Slight increases of the  $OA/SO_4^{2-}$  ratio indicates that the pulses comprise organic-rich aerosol (purple shading, called *low*  $\kappa$  conditions), whereas the lower  $OA/SO_4^{2-}$  aerosol is comparatively rich in sulfate (grey shading, called *high*  $\kappa$  conditions).

5 A combination of BTs and satellite data during the *MixPol* period shows that all BTs follow an easterly direction along the Amazon River (Fig. S6), which is the most frequent scenario during the dry season as outlined in a recent study (C. Pöhlker et al., 2017). The same study also shows that during this period, the shores of the Amazon River can be regarded as the core region of the ATTO site footprint, where BT densities are highest. Accordingly, all aerosol and trace gas sources in these areas are of primary importance for the ATTO region. For instance, this is true for a deforestation hotspot in the area around the cities Oriximina and Obidos as well as a  
10 variety of anthropogenic sources (i.e., industry, power plants, cities, shipping) (compare Fig. S6 and C. Pöhlker et al., 2017). During the *MixPol* time frame, several (smaller) deforestation fires were observed within the fetch of the corresponding BTs (Fig. S6). These fires, which mostly burnt for less than a day according to satellite observation, are likely responsible for the ‘low  $\kappa(S, D_a)$  and increased  $OA/SO_4^{2-}$  pulses’ within the *MixPol* period. Thus, the pulses can be considered as the advection of near-by biomass burning plumes into the ATTO region.  
15 According to the BT data, the smoke experienced a transport and aging time of 12–18 h. Thus, the smoke plumes during *MixPol* are fresher than during the *BB* case study, which experienced atmospheric aging for 2–3 days. Interestingly, this difference in aging could potentially be related to differences in the corresponding  $\kappa(S, D_a)$  values with fresh smoke during *MixPol* showing a lower hygroscopicity ( $\kappa_{Ait, MixPol} = \sim 0.10$ ,  $\kappa_{Acc, MixPol} = \sim 0.14$ ) and the aged smoke showing higher values  
20 ( $\kappa_{Ait, BB} = \sim 0.14$ ,  $\kappa_{Acc, BB} = \sim 0.17$ ).

Besides the rather short biomass burning smoke pulses, the sulfate-rich background aerosols must have originated from other sources, since the relative sulfate contents in biomass burning smoke are typically below 6–7 %, which can be seen for instance by means of the *BB* case in Table 3 (see also Fuzzi et al., 2007; Gunthe et al., 2009). Several anthropogenic sources within the ATTO site footprint, such as industrial emissions, power  
25 plants, and/or ship traffic on the Amazon River could potentially be responsible for the sulfate emissions. Furthermore, the sulfate-rich aerosol could be imported from African sources, such as oilrigs and related activities in the Gulf of Guinea. For the particularly high sulfate contents during *MixPol*, Saturno et al. (2017a) provided evidence that volcanic activities (i.e., Nyiragongo and Nyamuragira volcanoes in Eastern Congo) had an important influence here. Furthermore, Fioletov et al. (2016) indicated that these African volcanoes are major sulfur dioxide,  $SO_2$ , sources, even on a global scale, and, thus candidates for  $SO_2$  and sulfate export towards the Amazon  
30 Basin. Generally, the background aerosol population during *MixPol* can be considered as a mixture of aged aerosols from Africa and South America, which are mixed and processed in the transport air masses *en route*. While a quantification of the individual contributions is far beyond the scope of this paper, it illustrates the complexity of the dry season aerosol population with potential biomass burning, urban, industrial, and volcanic contributions.  
35

Figure 6g and h summarize the  $N_{CN}(D)$ ,  $N_{CCN}(S, D)$ , and  $\kappa(S, D_a)$  size distributions during *MixPol*, separately for the biomass burning pulses (*low*  $\kappa$  with increased  $OA/SO_4^{2-} \approx 4$ ) and LRT pollution (*high*  $\kappa$  with lower  $OA/SO_4^{2-} \approx 3$ ). In both cases, the size distributions show a broad monomodal distribution, which did not allow a stable double log-normal mode fitting of Aitken and accumulation modes (see Table 2). This mode is centered at  
40  $\sim 135$  nm for the (aged) LRT sulfate-rich aerosol, whereas the relatively fresh biomass burning smoke shows a modal diameter of  $\sim 113$  nm, in agreement with  $\sim 100$  nm for fresh biomass burning smoke reported by Andreae



et al. (2004). The corresponding  $N_{CCN}(S,D)$  size distributions show similar shapes, however, substantial absolute differences in CCN concentration occurred. Furthermore, clear differences are also observed for the average  $\kappa(S,D_a)$  size distributions: During the *high*  $\kappa$  conditions,  $\kappa(S,D_a)$  shows a pronounced size dependence. The average hygroscopicity parameter  $<100$  nm is rather size independent ( $\kappa_{<100\text{nm}} = 0.14 \pm 0.01$ ). Instead, the average  $\kappa_{>100\text{nm}}$  increases with  $D$  up to 0.26 (on average:  $\kappa_{>100\text{nm}} = 0.22 \pm 0.03$ ). According to the shape of the  $\kappa(S,D_a)$  size distribution in Fig. 6g, it can be assumed that the aerosol hygroscopicity was even higher for  $D$  larger than the covered size range here (i.e.,  $>170$  nm). During the dry season, the highest  $\kappa(S,D_a)$  levels for accumulation mode particles were observed during the peak abundance of sulfate at the ATTO site. The hygroscopicity during the *low*  $\kappa$  pulses shows generally lower values and weaker size dependence for particles smaller than 150 nm. The average  $\kappa_{<150\text{nm}} = 0.10 \pm 0.01$  was even smaller than during *BB* and *NP* cases and represents one of the lowest values measured during the entire observation period. For larger particles (e.g.,  $>150$  nm)  $\kappa(S,D_a)$  strongly increased towards values comparable to those during the *high*  $\kappa$  events indicating that both ‘events’ are rather superimposed than alternating (on average:  $\kappa_{>150\text{nm}} = 0.20 \pm 0.04$ ).

Figure 6i shows the CCN efficiency spectra for the two *MixPol* states. The slope for the *high*  $\kappa$  state is significantly steeper compared to the slope of the *low*  $\kappa$  pulses. The  $S_1$  level of 50 % activation (0.16 %) for the sulfate-rich aerosol population is clearly lower than during the short biomass burning pulses (0.28 %). This rather large difference can be explained by the smaller modal diameter of the *low*  $\kappa$  relative to the *high*  $\kappa$  case. Furthermore,  $\kappa$  is significantly decreased for the biomass burning pulses, which are dominated by organic constituents. However, note that the absolute CCN concentration given by  $N_{CCN}$  is – while being less hygroscopic – significantly higher for the organic-rich periods (for  $S > 0.07$  %).

In general, the *MixPol* case study emphasizes the following aspects: (i) The dry season aerosols that arrive at the ATTO site can be rather complex mixtures of superimposed emissions from different sources with contrasting chemical properties. (ii) The properties of the aerosol and CCN population can change rather suddenly and substantially (see  $N_{CN}$  and  $N_{CCN}(S)$  changes by factor of 3–4 within few hours). Similarly, the aerosol hygroscopicity can vary rather strongly from the lowest value observed in the entire study ( $\sim 0.1$ ) to values around 0.35 and higher, which belong to the largest values observed here during the dry season. These quickly and substantially changing aerosol regimes will presumably also impact the cloud conditions during dry season. (iii) Finally, the Amazonian aerosol and CCN population can be substantially perturbed by emissions from sources (i.e., volcanoes in the Eastern Congo) that are remarkably far away from the ATTO site ( $\sim 10,000$  km) (Saturno et al., 2017a). This emphasizes very clearly that intercontinental influences have to be considered carefully in the analysis of the Amazonian atmospheric composition.

### 3.8 Overview of CCN efficiency spectra

CCN efficiency spectra represent an effective strategy to summarize the CCN properties of a certain aerosol population and, thus, can be regarded as *CCN signatures*. This last section provides a synoptic overview of the CCN efficiency spectra of all analyzed conditions by combining the case study-specific spectra from the present work with the seasonally averaged spectra from the companion part 1 study as well as spectra from a previous study (Andreae et al., 2004). The direct comparison allows to extract characteristic similarities, differences and trends, which could be linked to a concluding discussion on aerosol-cloud-interactions. Figure 10a combines all relevant spectra for a wide  $S$  range. For clarity throughout the discussion, we subdivided the  $S$  range according to Reutter et al. (2009) into a low  $S$  ( $S < 0.2$  %), a high  $S$  ( $S > 0.5$  %), and an intermediate  $S$  ( $0.2\% < S < 0.5\%$ ) regime.



Furthermore, we marked the range, in which average peak supersaturations at cloud base,  $S_{\text{cloud}}(D_{\text{H}}, \kappa)$ , in the ATTO region are expected. The  $S_{\text{cloud}}(D_{\text{H}}, \kappa)$  results were obtained according to Krüger et al. (2014) and can be found in our part 1 study as well as in Table 2 of the present work. The relevant  $S_{\text{cloud}}(D_{\text{H}}, \kappa)$  range spans from  $\sim 0.18\%$  to  $\sim 0.34\%$  and, thus, overlaps with the interphase between low and intermediate  $S$  regimes. Note that the case study-specific CCN efficiency spectra in Fig. 10a allow an easy conversion into average CCN spectra by multiplication with the case study average  $N_{\text{CN}}$  results (Table 4). The resulting case study-specific CCN spectra are shown in Fig. S7.

Generally, the array of spectra in Fig. 10a spans a certain range of different shapes (see also Farmer et al., 2015). Within this range, the *NP* case study represents the lower limiting case with the ‘slowest’ increase in activated fractions (e.g., 50 % activation reached at  $S \sim 0.5\%$ ). In contrast, the *BB* and *LRT* case studies represent the upper limiting cases, reaching high activated fractions ‘quickly’ (50 % activation at  $S \sim 0.15\%$  for *BB* case and at  $0.09\%$  for *LRT* case, respectively). As a general observation, the trends among the case study spectra corresponds well with the trends among the seasonally averaged spectra (e.g., relationship between wet vs. dust seasons and *NP* vs. *LRT* case studies). However, certain features appear more emphasized in the case studies than in the seasonal averages (e.g., steeper slope at  $S < 0.05\%$  for *LRT* season than *LRT* case study) due to the fact that the case studies incorporate more defined aerosol plumes and/or populations. As an example, the *LRT season spectrum* includes several *LRT* pulses, however, also clean periods in between (see part 1 study), whereas the *LRT case study* spectrum includes one ‘pure’ *LRT* pulse (see Table 1).

Within the low  $S$  regime, which corresponds with the activation of accumulation mode particles, the following features stand out: The aerosol populations that act as CCN most efficiently – means at very low  $S < 0.05\%$  – are those with high  $\kappa$  levels, such as the sea salt-rich *LRT* and sulfate-rich *MixPol/high*  $\kappa$  populations. The aerosol population that acts as CCN least efficient is the *NP* case, which is characterized by a small fraction of accumulation mode particles with rather low  $\kappa$ . In between these extremes, the *BB* aerosol population is activated rapidly, once a threshold value of  $\sim 0.05\%$  is exceeded. Further note that all spectra have their largest slopes  $d(N_{\text{CCN}}(S)/N_{\text{CN},10})/dS$  within the low  $S$  regime, which means that the activated fractions of all aerosol populations are most sensitive to  $\Delta S$  in this range. In the intermediate  $S$  regime, corresponding to the activation of particles at the interphase of Aitken and accumulation modes (i.e., Hoppel minimum size range), the individual spectra show their highest divergence – means largest differences in CCN efficiency at a given  $S$ . In this range also the ATTO-relevant  $S_{\text{cloud}}(D_{\text{H}}, \kappa)$  levels are located. Thus, the important  $S_{\text{cloud}}(D_{\text{H}}, \kappa)$  range covers those  $S$  conditions that reveal the largest variability in activated fraction for the contrasting aerosol populations (e.g., *BB* vs. *NP* cases). In the high  $S$  range, all spectra show their smallest slopes and, thus, lowest sensitivity towards  $\Delta S$ .

Figure 10a may serve as a basis for dedicated cloud-microphysical studies on the characteristic differences between the aerosol/CCN populations and their impacts on cloud properties. As a particularly relevant aspect, the results obtained here (i.e.,  $N_{\text{CN}}$  concentrations and CCN efficiency spectra) can be used to investigate the sensitivity of clouds under *NP* conditions, as an approximation of a pre-industrial state of the atmosphere. There are evidently large differences between *NP* background conditions and perturbed atmospheric states related to anthropogenic (aged) *BB* smoke in terms of total aerosol concentration as well as the shape of the CCN efficiency spectra. Similarly, the differences between the *NP* and *LRT* case studies suggest that the frequent *LRT* pulses in the wet season are related to simultaneous changes in the cloud microphysical state, although changes in total aerosol concentration are small.



Since the size and composition of aerosol particles change dynamically due to atmospheric aging and processing, evidently, also the CCN spectra change accordingly. Figure 10b emphasizes the dynamic character of the CCN efficiency spectra's shape by means of different aging states of biomass burning plumes. Here we combined four biomass burning-related CCN efficiency spectra: (i) the *BB* case study spectrum, which represents smoke after ~2-3 days of atmospheric aging (see Fig. S4), (ii) the *MixPol/low*  $\kappa$  case study spectrum, which represents smoke after ~1 day of aging (see Fig. S6), (iii) "cloud-processed smoke" from biomass burning regions in southeast Brazil after hours to days of atmospheric aging according to Andreae et al. (2004), and (iv) "fresh smoke in the mixed layer", also from southeastern Brazil, which was sampled in the fire plumes and, thus, was aged for minutes to hours (Andreae et al., 2004). Clearly, the shape of the spectra in Fig. 10b is very different. The lowest activated fractions were observed for the fresh smoke (50 % activation at  $S \sim 0.96$  %; 90 % at  $S \sim 3.6$  %), followed by the "cloud-processed smoke" (50 % activation at  $S \sim 0.45$  %; converges against 86 %), then the *MixPol/low*  $\kappa$  case study spectrum (50 % activation at  $S \sim 0.28$  %; 90 % at  $S \sim 1.2$  %), and finally the *BB* case study spectrum (50 % activation at  $S \sim 0.15$  %; 90 % at  $S \sim 0.46$  %) with highest activated fractions as upper limiting case.

Atmospheric aging tends to increase the particle size through coagulation and condensational growth as well as enhances the particle's hygroscopicity through oxidation, aqueous phase chemistry, and reaction product deposition. In other words, aging tends to increase the strength of the accumulation at the expense of the Aitken mode and increases  $\kappa$ . Accordingly, it evolves the smoke's CCN efficiency spectra from the "fresh smoke" conditions – as the initial state – towards the *BB* case study conditions and presumably even further. This underlines the well-known trend that atmospheric aging increases the suitability of a given particle population to act as CCN (Andreae and Rosenfeld, 2008). Important to note in the context of this study is the following: The CCN efficiency spectra represent signatures of a given aerosol population in a given state of atmospheric aging. Accordingly, the atmospheric aerosol aging and the dynamic evolution of the CCN efficiency spectra's shape has to be kept in mind upon discussion and utilization of the spectra in follow-up studies.

25

#### 4 Summary and conclusions

In a recent synthesis paper on aerosol-cloud interaction and its highly uncertain representation in global climate models, Seinfeld et al. (2016) proposed that long-term and focused observations in "geographic areas that are critical in climate response" are necessary to obtain a detailed process understanding. Further, studies in "those regions of the present-day atmosphere that approximate preindustrial conditions" will help to "replicate preindustrial aerosol-cloud relationships". In these regions – such as the Amazon Basin – clouds are particularly sensitive to small changes in CCN concentrations (Carslaw et al., 2013). Accordingly, observations are needed here to obtain crucial knowledge on the man-made perturbation of preindustrial aerosol cycling and cloud properties. This work aims to help tackling this major scientific challenge by presenting detailed long-term aerosol and CCN data for characteristic atmospheric states at the Amazonian ATTO site, which is a unique, climate-relevant location with atmospheric conditions oscillation between near-pristine and anthropogenically strongly perturbed states.

The basis for this work are size-resolved measurements of atmospheric aerosol and cloud condensation nuclei (CCN) concentrations and hygroscopicity at the remote Amazon Tall Tower Observatory (ATTO) in the central Amazon Basin over a full seasonal cycle (Mar 2014 - Feb 2015). The results of these observations are presented in two papers: The recently published part 1 paper provides an in-depth analyses of the multi-month trends in the Amazonian CCN population as well as seasonal averages of the CCN key parameters (M. Pöhlker et



al., 2016). Further, part 1 compares and discusses different CCN parametrization schemes and their suitability to represent the Amazonian CCN cycling in modelling studies. The present part 2 study completes this picture by analyzing the CCN variability in original time resolution (4.5 h), which is sufficient to resolve its short-term variability in relation to air mass changes as well as aerosol emission and transformation processes.

5 A focal point of both studies is the concept of CCN efficiency spectra, which represent an instructive tool to visualize the different behaviors of contrasting aerosol populations in cloud formation and, thus can be regarded as ‘CCN signatures’. Analytically, the CCN efficiency spectra can be described precisely and in a physically correct way by single- or double-error functions (erf). In contrast to other common analytical functions, the erf approach describes the measurement results very accurately and allows to extrapolate CCN properties to experimentally hardly accessible supersaturations in the low and high  $S$  regimes.

10 Here, we zoom into the long-term CCN data in two steps: First, we discuss the aerosol and CCN variability for two 2-months periods that represent contrasting states in the aerosol, cloud microphysical, and precipitation seasonality in the central Amazon. The selected periods provide insights into the characteristic atmospheric cycling during the very clean wet season and the highly polluted dry season. Second, we focus on the following four selected case study periods, which represent particularly relevant atmospheric states:

15 *Near-pristine* (NP) and, thus, approximately preindustrial conditions are one of the scientifically most relevant atmospheric states at the ATTO site. Here, we defined NP conditions as the absence of detectable black carbon concentrations ( $<0.01 \mu\text{g m}^{-3}$ ) and found their predominant occurrence from March to May (peak at end of April/beginning of May with up to 30 % weekly abundance). Under NP conditions, aerosol concentrations were very low ( $270 \pm 100 \text{ cm}^{-3}$ ) and the aerosol population had a characteristic bimodal shape with a dominant Aitken and comparatively weak accumulation mode ( $D_{\text{Ait}} = 67 \text{ nm}$ ;  $N_{\text{Ait}} = \sim 200 \text{ cm}^{-3}$  vs.  $D_{\text{acc}} = 171 \text{ nm}$ ;  $N_{\text{acc}} = \sim 60 \text{ cm}^{-3}$ ). The aerosol particles comprise mostly organic matter with minor amounts of inorganic constituents (OA:  $0.64 \mu\text{g m}^{-3}$ ,  $\text{NO}_3^-$ :  $0.03 \mu\text{g m}^{-3}$ ,  $\text{SO}_4^{2-}$ :  $0.04 \mu\text{g m}^{-3}$ ,  $\text{Cl}^-$ :  $0.01 \mu\text{g m}^{-3}$ ). The observed low  $\kappa(S, D_a)$  levels agree with the particles’ composition and show a certain size dependence ( $\kappa_{\text{Ait}} = 0.12 \pm 0.01$  vs.  $\kappa_{\text{acc}} = 0.18 \pm 0.02$ ). The CCN efficiency spectrum shows a characteristic shape since it converges against full activation rather slowly (50 % activation at  $\sim 0.5$  %, 90 % activation at  $\sim 1.7$  %). Thus, the CCN population is sensitive towards  $\Delta S$  in both, the low and high  $S$  regime. Accordingly, the CCN population can be regarded as both, aerosol sensitive due to the low total aerosol concentrations and updraft sensitive according to the CCN efficiency spectrum with its sensitivity to  $\Delta S$  across a wide  $S$  range.

30 During *long-range transport* (LRT) episodes within the wet season, major amounts of aged Saharan dust, African biomass burning smoke, and Atlantic marine aerosols are advected pulse-wise into the Basin (mostly Feb - Apr). Total aerosol concentrations ( $440 \pm 100 \text{ cm}^{-3}$ ) are slightly enhanced relative to the NP state and the aerosol population has a bimodal shape with a minor Aitken and a stronger accumulation mode ( $D_{\text{Ait}} = 77 \text{ nm}$ ,  $N_{\text{Ait}} = \sim 120 \text{ cm}^{-3}$  vs.  $D_{\text{acc}} = 178 \text{ nm}$ ,  $N_{\text{acc}} = \sim 300 \text{ cm}^{-3}$ ). Beside the non-refractory fraction of organics and inorganics (OA:  $1.81 \mu\text{g m}^{-3}$ ,  $\text{NO}_3^-$ :  $0.08 \mu\text{g m}^{-3}$ ,  $\text{NH}_4^+$ :  $0.30 \mu\text{g m}^{-3}$ ,  $\text{SO}_4^{2-}$ :  $0.25 \mu\text{g m}^{-3}$ ,  $\text{Cl}^-$ :  $0.04 \mu\text{g m}^{-3}$ ), a larger refractory fraction of mineral dust and sea salts can be found in internally mixed particles. The observed  $\kappa(S, D_a)$  levels are increased compared to the NP state in agreement with the chemical composition ( $\kappa_{\text{Ait}} = 0.18 \pm 0.02$  vs.  $\kappa_{\text{acc}} = 0.34 \pm 0.04$ ). The CCN efficiency spectrum shows a steep increase – and thus high sensitivity to  $\Delta S$  – at low  $S$  and quickly converges against full activation towards high  $S$  (50 % activation at  $\sim 0.09$  %, 90 % activation at  $\sim 0.53$  %). Thus, the CCN regime under LRT influence can be regarded as aerosol limited.



*Biomass burning* (BB) is the predominant anthropogenic influence during the Amazonian dry season, which alters the atmospheric composition substantially. During the BB event analyzed here, we found strongly enhanced aerosol concentrations ( $3200 \pm 1040 \text{ cm}^{-3}$ ) and an accumulation mode dominated size distribution ( $D_{\text{Ait}} = 70 \text{ nm}$ ,  $N_{\text{Ait}} = \sim 140 \text{ cm}^{-3}$  vs.  $D_{\text{acc}} = 167 \text{ nm}$ ,  $N_{\text{acc}} = \sim 3440 \text{ cm}^{-3}$ ). The aged smoke particles comprise mostly organic matter (OA:  $19.1 \mu\text{g m}^{-3}$ ,  $\text{NO}_3^-$ :  $0.50 \mu\text{g m}^{-3}$ ,  $\text{NH}_4^+$ :  $0.54 \mu\text{g m}^{-3}$ ,  $\text{SO}_4^{2-}$ :  $0.79 \mu\text{g m}^{-3}$ ,  $\text{Cl}^-$ :  $0.03 \mu\text{g m}^{-3}$ ). The observed  $\kappa(S, D_a)$  levels were comparatively low and weakly size dependent ( $\kappa_{\text{Ait}} = 0.14 \pm 0.01$  vs.  $\kappa_{\text{acc}} = 0.17 \pm 0.02$ ). The corresponding CCN efficiency spectrum shows a rather steep increase at low  $S$  and converges against a threshold ( $\sim 93\%$ ) below full activation at high  $S$  ( $50\%$  activation at  $S \sim 0.15\%$ ). With respect to the large particle concentrations and the large sensitivity of the CCN efficiency spectrum to  $\Delta S$  in the low  $S$  regime, the BB case falls into the updraft limited regime.

During the dry season, the central Amazon often experiences superimposed aerosol populations from regional, continental, and even trans-continental sources. Here, we analyzed a characteristic example of such *mixed pollution* (MixPol) scenarios, in which a mixture of African volcanic emissions and nearby Amazonian fires impacted the ATTO site: Under conditions with a predominant influence of the African volcanic emissions, we found a broad monomodal size distribution ( $D_{\text{mode}} = 135 \text{ nm}$ ,  $N_{\text{mode}} = \sim 1300 \text{ cm}^{-3}$ ), strongly enhanced sulfate levels (OA:  $5.48 \mu\text{g m}^{-3}$ ,  $\text{SO}_4^{2-}$ :  $1.76 \mu\text{g m}^{-3}$ ), and correspondingly high hygroscopicities ( $\kappa_{<100\text{nm}} = 0.14 \pm 0.01$  vs.  $\kappa_{>100\text{nm}} = 0.22 \pm 0.03$ ). Under conditions with predominant influence by the nearby fires, we found high concentrations in a monomodal distribution ( $D_{\text{mode}} = 113 \text{ nm}$ ,  $N_{\text{mode}} = \sim 2800 \text{ cm}^{-3}$ ), an enhancement of organic matter on top of the sulfate background (OA:  $8.08 \mu\text{g m}^{-3}$ ,  $\text{SO}_4^{2-}$ :  $2.05 \mu\text{g m}^{-3}$ ), and low hygroscopicities ( $\kappa_{<150\text{nm}} = 0.10 \pm 0.01$  vs.  $\kappa_{>150\text{nm}} = 0.20 \pm 0.04$ ). Accordingly, the interplay of the aged volcanic plume and the fresh smoke resulted in large variations of the total aerosol concentration, aerosol composition, and CCN properties. We suppose that the highly variable CCN population yields associated (microphysical) variations in cloud properties.

Finally, the CCN efficiency spectra for all analyzed cases are discussed in an overview, which emphasizes the following differences, similarities and trends: (i) The array of all spectra span a range of variability, which represents the scope and diversity of CCN conditions in the central Amazon as a function of relevant  $S$  levels. (ii) Within this range, the estimated peak supersaturations at cloud base,  $S_{\text{cloud}}(D_{\text{H}}, \kappa)$ , are collocated with the intermediate  $S$  range (i.e.,  $0.2 - 0.5\%$ ), in which the CCN efficiency spectra shows their highest variability and, thus underlines the impact of changing aerosol populations on cloud properties. (iii) The sensitivity of the CCN populations to changes in  $S$  was highest within a low  $S$  regime ( $S < 0.2\%$ ), whereas the lowest susceptibilities occurred in the high  $S$  regime ( $S > 0.5\%$ ). (iv) The combination of CCN efficiency spectra for different, particularly contrasting, aerosol populations provides a basis for follow-up studies on the aerosol-related differences in cloud properties in the Amazon region and beyond. (v) Finally, the atmospheric aging of aerosol particles in the atmosphere is reflected into a corresponding evolution of the CCN efficiency spectra's shape and has to be kept in mind upon their utilization.



## 5 Data availability

The data of the key results presented here (i.e., aerosol size distributions,  $\kappa$  levels, CCN efficiency spectra) has been deposited in supplementary tables for use in follow-up studies. For specific data requests or detailed information on the deposited data, please refer to the corresponding authors.

5

## Acknowledgements

This work has been supported by the Max Planck Society (MPG) and the Max Planck Graduate Center with the Johannes Gutenberg University Mainz (MPGC). For the operation of the ATTO site, we acknowledge the support by the German Federal Ministry of Education and Research (BMBF contract 01LB1001A) and the Brazilian Ministério da Ciência, Tecnologia e Inovação (MCTI/FINEP contract 01.11.01248.00) as well as the Amazon State University (UEA), FAPEAM, LBA/INPA and SDS/CEUC/RDS-Uatumã. This work has been financial support from the German Research Foundation (DFG grant KA 2280/2); the St. Petersburg state University, Russia (project 11.37.220.2016) as well as the EU FP7 project BACCHUS (project no. 603445); the Sao Paulo Research Foundation (FAPESP grants 13/05014-0 and 13/50510-5); and the Atmospheric System Research program, US Department of Energy. This paper contains results of research conducted under the Technical/Scientific Cooperation Agreement between the National Institute for Amazonian Research, the State University of Amazonas, and the Max-Planck-Gesellschaft e.V.; the opinions expressed are the entire responsibility of the authors and not of the participating institutions. We highly acknowledge the support by the Instituto Nacional de Pesquisas da Amazônia (INPA). The Office of Biological and Environmental Research of the Office of Science is acknowledged for funding, specifically the Atmospheric Radiation Measurement (ARM) Climate Research Facility and the Atmospheric System Research (ASR) Program. We would like to especially thank all the people involved in the technical, logistical, and scientific support of the ATTO project, in particular Susan Trumbore, Carlos Alberto Quesada, Matthias Sörgel, Thomas Disper, Andrew Crozier, Bettina Weber, Nina Ruckteschler, Uwe Schulz, Steffen Schmidt, Antonio Ocimar Manzi, Alcides Camargo Ribeiro, Hermes Braga Xavier, Elton Mendes da Silva, Nagib Alberto de Castro Souza, Adir Vasconcelos Brandão, Amauri Rodrigues Perreira, Antonio Huxley Melo Nascimento, Thiago de Lima Xavier, Josué Ferreira de Souza, Roberta Pereira de Souza, Bruno Takeshi, and Wallace Rabelo Costa. We acknowledge the use of FIRMS data and imagery from the Land, Atmosphere Near real-time Capability for EOS (LANCE) system operated by the NASA/GSFC/Earth Science Data and Information System (ESDIS) with funding provided by NASA/HQ. Satellite product analyses and visualizations used in this paper were produced with the Giovanni online data system, developed and maintained by the NASA GES DISC. We also acknowledge the MODIS and OMI mission scientists and associated NASA personnel for the production of the data used in this research effort. Further, we thank the GoAmazon2014/5 team for the fruitful collaboration and discussions. Moreover, we thank Qiaoqiao Wang, Bruna Holanda, Oliver Lauer, Ovid O. Krüger, Maria Praß, Kathrin Reinmuth-Selzle, Daniel Rosenfeld, and J. Alex Huffman for support and stimulating discussions.

10  
15  
20  
25  
30  
35



## References

- Abouchami, W., Nathe, K., Kumar, A., Galer, S. J. G., Jochum, K. P., Williams, E., Horbe, A. M. C., Rosa, J. W. C., Balsam, W., Adams, D., Mezger, K., and Andreae, M. O.: Geochemical and isotopic characterization of the Bodele Depression dust source and implications for transatlantic dust transport to the Amazon Basin, *Earth Planet. Sci. Lett.*, 380, 112-123, 10.1016/j.epsl.2013.08.028, 2013.
- Acker, J. G., and Leptoukh, G.: Online analysis enhances use of NASA Earth science data, *Eos, Transactions American Geophysical Union*, 88, 14-17, 10.1029/2007EO020003, 2007.
- Andreae, M. O.: Aerosols before pollution, *Science*, 315, 50-51, 10.1126/science.1136529, 2007.
- Andreae, M. O., Acevedo, O. C., Araújo, A., Artaxo, P., Barbosa, C. G. G., Barbosa, H. M. J., Brito, J., Carbone, S., Chi, X., Cintra, B. B. L., da Silva, N. F., Dias, N. L., Dias-Júnior, C. Q., Ditas, F., Ditz, R., Godoi, A. F. L., Godoi, R. H. M., Heimann, M., Hoffmann, T., Kesselmeier, J., Könemann, T., Krüger, M. L., Lavric, J. V., Manzi, A. O., Moran-Zuloaga, D., Nölscher, A. C., Santos Nogueira, D., Piedade, M. T. F., Pöhlker, C., Pöschl, U., Rizzo, L. V., Ro, C. U., Ruckteschler, N., Sá, L. D. A., Sá, M. D. O., Sales, C. B., Santos, R. M. N. D., Saturno, J., Schöngart, J., Sörgel, M., de Souza, C. M., de Souza, R. A. F., Su, H., Targhetta, N., Tóta, J., Trebs, I., Trumbore, S., van Eijck, A., Walter, D., Wang, Z., Weber, B., Williams, J., Winderlich, J., Wittmann, F., Wolff, S., and Yáñez-Serrano, A. M.: The Amazon Tall Tower Observatory (ATTO): overview of pilot measurements on ecosystem ecology, meteorology, trace gases, and aerosols, *Atmos. Chem. Phys.*, 15, 10723-10776, 10.5194/acp-15-10723-2015, 2015.
- Andreae, M. O., Afchine, A., Albrecht, R., Holanda, B. A., Artaxo, P., Barbosa, H. M. J., Bormann, S., Cecchini, M. A., Costa, A., Dollner, M., Fütterer, D., Järvinen, E., Jurkat, T., Klimach, T., Könemann, T., Knote, C., Krämer, M., Krisna, T., Machado, L. A. T., Mertes, S., Minikin, A., Pöhlker, C., Pöhlker, M. L., Pöschl, U., Rosenfeld, D., Sauer, D., Schlager, H., Schnaiter, M., Schneider, J., Schulz, C., Spanu, A., Sperling, V. B., Voigt, C., Walser, A., Wang, J., Weinzierl, B., Wendisch, M., and Ziereis, H.: Aerosol characteristics and particle production in the upper troposphere over the Amazon Basin, *Atmos. Chem. Phys. Discuss.*, 2017.
- Andreae, M. O., Anderson, B. E., Blake, D. R., Bradshaw, J. D., Collins, J. E., Gregory, G. L., Sachse, G. W., and Shipham, M. C.: INFLUENCE OF PLUMES FROM BIOMASS BURNING ON ATMOSPHERIC CHEMISTRY OVER THE EQUATORIAL AND TROPICAL SOUTH-ATLANTIC DURING CITE-3, *Journal of Geophysical Research-Atmospheres*, 99, 12793-12808, 10.1029/94jd00263, 1994.
- Andreae, M. O., Artaxo, P., Beck, V., Bela, M., Freitas, S., Gerbig, C., Longo, K., Munger, J. W., Wiedemann, K. T., and Wofsy, S. C.: Carbon monoxide and related trace gases and aerosols over the Amazon Basin during the wet and dry seasons, *Atmospheric Chemistry and Physics*, 12, 6041-6065, 10.5194/acp-12-6041-2012, 2012.
- Andreae, M. O., Charlson, R. J., Bruynseels, F., Storms, H., Vangrieken, R., and Maenhaut, W.: Internal Mixture of Sea Salt, Silicates, and Excess Sulfate in Marine Aerosols, *Science*, 232, 1620-1623, 10.1126/science.232.4758.1620, 1986.
- Andreae, M. O., and Rosenfeld, D.: Aerosol-cloud-precipitation interactions. Part 1. The nature and sources of cloud-active aerosols, *Earth-Sci. Rev.*, 89, 13-41, 10.1016/j.earscirev.2008.03.001, 2008.
- Andreae, M. O., Rosenfeld, D., Artaxo, P., Costa, A. A., Frank, G. P., Longo, K. M., and Silva-Dias, M. A. F.: Smoking rain clouds over the Amazon, *Science*, 303, 1337-1342, 10.1126/science.1092779, 2004.
- Artaxo, P., Rizzo, L. V., Brito, J. F., Barbosa, H. M. J., Arana, A., Sena, E. T., Cirino, G. G., Bastos, W., Martin, S. T., and Andreae, M. O.: Atmospheric aerosols in Amazonia and land use change: from natural biogenic to biomass burning conditions, *Faraday Discuss.*, 165, 203-235, 10.1039/c3fd00052d, 2013.
- Atwood, S. A., Reid, J. S., Kreidenweis, S. M., Blake, D. R., Jonsson, H. H., Lagrosas, N. D., Xian, P., Reid, E. A., Sessions, W. R., and Simpas, J. B.: Size-resolved aerosol and cloud condensation nuclei (CCN) properties in the remote marine South China Sea – Part 1: Observations and source classification, *Atmos. Chem. Phys.*, 17, 1105-1123, 10.5194/acp-17-1105-2017, 2017.
- Baars, H., Ansmann, A., Althausen, D., Engelmann, R., Artaxo, P., Pauliquevis, T., and Souza, R.: Further evidence for significant smoke transport from Africa to Amazonia, *Geophys. Res. Lett.*, 38, L20802, L20802  
10.1029/2011gl049200, 2011.
- Bony, S., Stevens, B., Frierson, D. M. W., Jakob, C., Kageyama, M., Pincus, R., Shepherd, T. G., Sherwood, S. C., Siebesma, A. P., Sobel, A. H., Watanabe, M., and Webb, M. J.: Clouds, circulation and climate sensitivity, *Nature Geoscience*, 8, 261-268, 10.1038/ngeo2398, 2015.
- Braga, R. C., Rosenfeld, D., Weigel, R., Jurkat, T., Andreae, M. O., Wendisch, M., Pöhlker, M. L., Klimach, T., Pöschl, U., Pöhlker, C., Voigt, C., Mahnke, C., Bormann, S., Albrecht, R. I., Molleker, S., Vila, D. A., Machado, L. A. T., and Artaxo, P.: Comparing parameterized versus measured microphysical properties of tropical convective cloud bases during the ACRIDICON-CHUVA campaign, *Atmos. Chem. Phys.*, 17, 7365-7386, 10.5194/acp-17-7365-2017, 2017.
- Bristow, C. S., Hudson-Edwards, K. A., and Chappell, A.: Fertilizing the Amazon and equatorial Atlantic with West African dust, *Geophys. Res. Lett.*, 37, 10.1029/2010gl043486, 2010.



- Carbone, S., Brito, J. F., Xu, L., Ng, N. L., Rizzo, L., Holanda, B. A., Wolff, S., Saturno, J., Chi, X., Souza, R. A. F., Pöhlker, M. L., Andreae, M. O., Pöhlker, C., Barbosa, H. M. J., and Artaxo, P.: Long-term chemical composition and source apportionment of submicron aerosol particles in the central Amazon basin (ATTO), Atmos. Chem. Phys., in prep., 2017.
- 5 Carlaw, K. S., Lee, L. A., Reddington, C. L., Pringle, K. J., Rap, A., Forster, P. M., Mann, G. W., Spracklen, D. V., Woodhouse, M. T., Regayre, L. A., and Pierce, J. R.: Large contribution of natural aerosols to uncertainty in indirect forcing, Nature, 503, 67–+, [10.1038/nature12674](https://doi.org/10.1038/nature12674), 2013.
- 10 Cecchini, M. A., Machado, L. A. T., Andreae, M. O., Martin, S. T., Albrecht, R. I., Artaxo, P., Barbosa, H. M. J., Borrmann, S., Fütterer, D., Jurkat, T., Mahnke, C., Minikin, A., Molleker, S., Pöhlker, M. L., Pöschl, U., Rosenfeld, D., Voigt, C., Wenzierl, B., and Wendisch, M.: Sensitivities of Amazonian clouds to aerosols and updraft speed, Atmos. Chem. Phys., 17, 10037–10050, <https://doi.org/10.5194/acp-17-10037-2017>, 2017a.
- 15 Cecchini, M. A., Machado, L. A. T., Wendisch, M., Costa, A., Krämer, M., Andreae, M. O., Afchine, A., Albrecht, R. I., Artaxo, P., Borrmann, S., Fütterer, D., Klimach, T., Mahnke, C., Martin, S. T., Minikin, A., Molleker, S., Pardo, L. H., Pöhlker, C., Pöhlker, M. L., Pöschl, U., Rosenfeld, D., and Weinzierl, B.: Illustration of microphysical processes in Amazonian deep convective clouds in the Gamma phase space: Introduction and potential applications, Atmos. Chem. Phys. Discuss., 2017, 1–49, [10.5194/acp-2017-185](https://doi.org/10.5194/acp-2017-185), 2017b.
- Chen, Q., Farmer, D. K., Schneider, J., Zorn, S. R., Heald, C. L., Karl, T. G., Guenther, A., Allan, J. D., Robinson, N., Coe, H., Kimmel, J. R., Pauliquevis, T., Borrmann, S., Pöschl, U., Andreae, M. O., Artaxo, P., Jimenez, J. L., and Martin, S. T.: Mass spectral characterization of submicron biogenic organic particles in the Amazon Basin, Geophys. Res. Lett., 36, L20806, [10.1029/2009gl039880](https://doi.org/10.1029/2009gl039880), 2009.
- 20 Davidson, E. A., de Araujo, A. C., Artaxo, P., Balch, J. K., Brown, I. F., Bustamante, M. M. C., Coe, M. T., DeFries, R. S., Keller, M., Longo, M., Munger, J. W., Schroeder, W., Soares-Filho, B. S., Souza, C. M., Jr., and Wofsy, S. C.: The Amazon basin in transition, Nature, 481, 321–328, [10.1038/nature10717](https://doi.org/10.1038/nature10717), 2012.
- Draxler, R. R., and Hess, G. D.: An overview of the HYSPLIT 4 modelling system for trajectories, dispersion and deposition, Australian Meteorological Magazine, 47, 295–308, 1998.
- 25 Ekman, A. M. L., Krejci, R., Engstrom, A., Strom, J., de Reus, M., Williams, J., and Andreae, M. O.: Do organics contribute to small particle formation in the Amazonian upper troposphere?, Geophys. Res. Lett., 35, L17810, [10.1029/2008gl034970](https://doi.org/10.1029/2008gl034970), 2008.
- Engstrom, A., Ekman, A. M. L., Krejci, R., Strom, J., de Reus, M., and Wang, C.: Observational and modelling evidence of tropical deep convective clouds as a source of mid-tropospheric accumulation mode aerosols, Geophys. Res. Lett., 35, L23813, [10.1029/2008gl035817](https://doi.org/10.1029/2008gl035817), 2008.
- 30 Ervens, B.: Modeling the Processing of Aerosol and Trace Gases in Clouds and Fogs, Chemical Reviews, 115, 4157–4198, [10.1021/cr5005887](https://doi.org/10.1021/cr5005887), 2015.
- Farmer, D. K., Cappa, C. D., and Kreidenweis, S. M.: Atmospheric Processes and Their Controlling Influence on Cloud Condensation Nuclei Activity, Chemical Reviews, 115, 4199–4217, [10.1021/cr5006292](https://doi.org/10.1021/cr5006292), 2015.
- 35 Fearnside, P. M.: Brazil's Cuiaba-Santarem (BR-163) Highway: The environmental cost of paving a soybean corridor through the amazon, Environmental Management, 39, 601–614, [10.1007/s00267-006-0149-2](https://doi.org/10.1007/s00267-006-0149-2), 2007.
- Fioletov, V. E., McLinden, C. A., Krotkov, N., Li, C., Joiner, J., Theys, N., Carn, S., and Moran, M. D.: A global catalogue of large SO<sub>2</sub> sources and emissions derived from the Ozone Monitoring Instrument, Atmospheric Chemistry and Physics, 16, 11497–11519, [10.5194/acp-16-11497-2016](https://doi.org/10.5194/acp-16-11497-2016), 2016.
- 40 Freitas, S. R., Longo, K. M., Dias, M., Dias, P. L. S., Chatfield, R., Prins, E., Artaxo, P., Grell, G. A., and Recuero, F. S.: Monitoring the transport of biomass burning emissions in South America, Environmental Fluid Mechanics, 5, 135–167, [10.1007/s10652-005-0243-7](https://doi.org/10.1007/s10652-005-0243-7), 2005.
- Freud, E., Rosenfeld, D., Andreae, M. O., Costa, A. A., and Artaxo, P.: Robust relations between CCN and the vertical evolution of cloud drop size distribution in deep convective clouds, Atmospheric Chemistry and Physics, 8, 1661–1675, 2008.
- 45 Fuzzi, S., Decesari, S., Facchini, M. C., Cavalli, F., Emblico, L., Mircea, M., Andreae, M. O., Trebs, I., Hoffer, A., Guyon, P., Artaxo, P., Rizzo, L. V., Lara, L. L., Pauliquevis, T., Maenhaut, W., Raes, N., Chi, X., Mayol-Bracero, O. L., Soto-Garcia, L. L., Claeys, M., Kourtev, I., Rissler, J., Swietlicki, E., Tagliavini, E., Schkolnik, G., Falkovich, A. H., Rudich, Y., Fisch, G., and Gatti, L. V.: Overview of the inorganic and organic composition of size-segregated aerosol in Rondonia, Brazil, from the biomass-burning period to the onset of the wet season, Journal of Geophysical Research-Atmospheres, 112, [10.1029/2005jd006741](https://doi.org/10.1029/2005jd006741), 2007.
- 50 Glaser, G., Wernli, H., Kerkweg, A., and Teubler, F.: The transatlantic dust transport from North Africa to the Americas-Its characteristics and source regions, Journal of Geophysical Research-Atmospheres, 120, 11231–11252, [10.1002/2015jd023792](https://doi.org/10.1002/2015jd023792), 2015.
- 55 Goncalves, W. A., Machado, L. A. T., and Kirstetter, P. E.: Influence of biomass aerosol on precipitation over the Central Amazon: an observational study, Atmospheric Chemistry and Physics, 15, 6789–6800, [10.5194/acp-15-6789-2015](https://doi.org/10.5194/acp-15-6789-2015), 2015.



- Gunthe, S. S., King, S. M., Rose, D., Chen, Q., Roldin, P., Farmer, D. K., Jimenez, J. L., Artaxo, P., Andreae, M. O., Martin, S. T., and Pöschl, U.: Cloud condensation nuclei in pristine tropical rainforest air of Amazonia: size-resolved measurements and modeling of atmospheric aerosol composition and CCN activity, *Atmospheric Chemistry and Physics*, 9, 7551-7575, 2009.
- 5 Hamilton, D. S., Lee, L. A., Pringle, K. J., Reddington, C. L., Spracklen, D. V., and Carslaw, K. S.: Occurrence of pristine aerosol environments on a polluted planet, *Proceedings of the National Academy of Sciences of the United States of America*, 111, 18466-18471, 10.1073/pnas.1415440111, 2014.
- Huffman, J. A., Sinha, B., Garland, R. M., Snee-Pollmann, A., Gunthe, S. S., Artaxo, P., Martin, S. T., Andreae, M. O., and Pöschl, U.: Biological aerosol particle concentrations and size distributions measured in pristine tropical rainforest air during AMAZE-08, *Atmos. Chem. Phys.*, 12, 25181-25236, 2012.
- 10 Janhaell, S., Andreae, M. O., and Pöschl, U.: Biomass burning aerosol emissions from vegetation fires: particle number and mass emission factors and size distributions, *Atmospheric Chemistry and Physics*, 10, 1427-1439, 2010.
- Jimenez, J. L., Canagaratna, M. R., Donahue, N. M., Prevot, A. S. H., Zhang, Q., Kroll, J. H., DeCarlo, P. F., Allan, J. D., Coe, H., Ng, N. L., Aiken, A. C., Docherty, K. S., Ulbrich, I. M., Grieshop, A. P., Robinson, A. L., Duplissy, J., Smith, J. D., Wilson, K. R., Lanz, V. A., Hueglin, C., Sun, Y. L., Tian, J., Laaksonen, A., Raatikainen, T., Rautiainen, J., Vaattovaara, P., Ehn, M., Kulmala, M., Tomlinson, J. M., Collins, D. R., Cubison, M. J., Dunlea, E. J., Huffman, J. A., Onasch, T. B., Alfarra, M. R., Williams, P. I., Bower, K., Kondo, Y., Schneider, J., Drewnick, F., Borrmann, S., Weimer, S., Demerjian, K., Salcedo, D., Cottrell, L., Griffin, R., Takami, A., Miyoshi, T., Hatakeyama, S., Shimono, A., Sun, J. Y., Zhang, Y. M., Dzepina, K., Kimmel, J. R., Sueper, D., Jayne, J. T., Herndon, S. C., Trimborn, A. M., Williams, L. R., Wood, E. C., Middlebrook, A. M., Kolb, C. E., Baltensperger, U., and Worsnop, D. R.: Evolution of Organic Aerosols in the Atmosphere, *Science*, 326, 1525-1529, 10.1126/science.1180353, 2009.
- 15 Justice, C., Giglio, L., Roy, D., Boschetti, L., Csiszar, I., Davies, D., Korontzi, S., Schroeder, W., O'Neal, K., and Morisette, J.: MODIS-Derived Global Fire Products, in: *Land Remote Sensing and Global Environmental Change*, edited by: Ramachandran, B., Justice, C. O., and Abrams, M. J., Remote Sensing and Digital Image Processing, Springer New York, 661-679, 2011.
- 25 Kandler, K., Lieke, K., Benker, N., Emmel, C., Kuepper, M., Mueller-Ebert, D., Ebert, M., Scheuven, D., Schladitz, A., Schuetz, L., and Weinbruch, S.: Electron microscopy of particles collected at Praia, Cape Verde, during the Saharan Mineral Dust Experiment: particle chemistry, shape, mixing state and complex refractive index, *Tellus Series B-Chemical and Physical Meteorology*, 63, 475-496, 10.1111/j.1600-0889.2011.00550.x, 2011.
- 30 King, M. D., Platnick, S., Menzel, W. P., Ackerman, S. A., and Hubanks, P. A.: Spatial and Temporal Distribution of Clouds Observed by MODIS Onboard the Terra and Aqua Satellites, *Ieee Transactions on Geoscience and Remote Sensing*, 51, 3826-3852, 10.1109/tgrs.2012.2227333, 2013.
- Koren, I., Kaufman, Y. J., Remer, L. A., and Martins, J. V.: Measurement of the effect of Amazon smoke on inhibition of cloud formation, *Science*, 303, 1342-1345, 10.1126/science.1089424, 2004.
- 35 Krüger, M. L., Mertes, S., Klimach, T., Cheng, Y. F., Su, H., Schneider, J., Andreae, M. O., Pöschl, U., and Rose, D.: Assessment of cloud supersaturation by size-resolved aerosol particle and cloud condensation nuclei (CCN) measurements, *Atmos. Meas. Tech.*, 7, 2615-2629, 10.5194/amt-7-2615-2014, 2014.
- Kuhn, U., Ganzeveld, L., Thielmann, A., Dindorf, T., Schebeske, G., Welling, M., Sciare, J., Roberts, G., Meixner, F. X., Kesselmeier, J., Lelieveld, J., Kolle, O., Ciccioli, P., Lloyd, J., Trentmann, J., Artaxo, P., and Andreae, M. O.: Impact of Manaus City on the Amazon Green Ocean atmosphere: ozone production, precursor sensitivity and aerosol load, *Atmospheric Chemistry and Physics*, 10, 9251-9282, 10.5194/acp-10-9251-2010, 2010.
- 40 Kulmala, M., Vehkamäki, H., Petaja, T., Dal Maso, M., Lauri, A., Kerminen, V. M., Birmili, W., and McMurry, P. H.: Formation and growth rates of ultrafine atmospheric particles: a review of observations, *Journal of Aerosol Science*, 35, 143-176, 10.1016/j.jaerosci.2003.10.003, 2004.
- 45 Latham, T. L., Beyersdorf, A. J., Thornhill, K. L., Winstead, E. L., Cubison, M. J., Hecobian, A., Jimenez, J. L., Weber, R. J., Anderson, B. E., and Nenes, A.: Analysis of CCN activity of Arctic aerosol and Canadian biomass burning during summer 2008, *Atmospheric Chemistry and Physics*, 13, 2735-2756, 10.5194/acp-13-2735-2013, 2013.
- Martin, S. T., Andreae, M. O., Althausen, D., Artaxo, P., Baars, H., Borrmann, S., Chen, Q., Farmer, D. K., Guenther, A., Gunthe, S. S., Jimenez, J. L., Karl, T., Longo, K., Manzi, A., Muller, T., Pauliquevis, T., Petters, M. D., Prenni, A. J., Pöschl, U., Rizzo, L. V., Schneider, J., Smith, J. N., Swietlicki, E., Tota, J., Wang, J., Wiedensohler, A., and Zorn, S. R.: An overview of the Amazonian Aerosol Characterization Experiment 2008 (AMAZE-08), *Atmospheric Chemistry and Physics*, 10, 11415-11438, 10.5194/acp-10-11415-2010, 2010a.
- 50 Martin, S. T., Andreae, M. O., Artaxo, P., Baumgardner, D., Chen, Q., Goldstein, A. H., Guenther, A., Heald, C. L., Mayol-Bracero, O. L., McMurry, P. H., Pauliquevis, T., Pöschl, U., Prather, K. A., Roberts, G. C., Saleska, S. R., Dias, M. A. S., Spracklen, D. V., Swietlicki, E., and Trebs, I.: Sources and properties of Amazonian aerosol particles, *Rev. Geophys.*, 48, RG2002, 10.1029/2008rg000280, 2010b.
- 55 Martin, S. T., Artaxo, P., Machado, L., Manzi, A. O., Souza, R. A. F., Schumacher, C., Wang, J., Biscaro, T., Brito, J., Calheiros, A., Jardine, K., Medeiros, A., Portela, B., Sá, S. S. d., Adachi, K., Aiken, A. C., Albrecht, R., Alexander, L.,



- 5 Andreae, M. O., Barbosa, H. M. J., Buseck, P., Chand, D., Comstock, J. M., Day, D. A., Dubey, M., Fan, J., Fast, J., Fisch, G., Fortner, E., Giangrande, S., Gilles, M., Goldstein, A. H., Guenther, A., Hubbe, J., Jensen, M., Jimenez, J. L., Keutsch, F. N., Kim, S., Kuang, C., Laskin, A., McKinney, K., Mei, F., Miller, M., Nascimento, R., Pauliquevis, T., Pekour, M., Peres, J., Petäjä, T., Pöhlker, C., Pöschl, U., Rizzo, L., Schmid, B., Shilling, J. E., Dias, M. A. S., Smith, J. N., Tomlinson, J. M., Tóta, J., and Wendisch, M.: The Green Ocean Amazon Experiment (GoAmazon2014/5) Observes Pollution Affecting Gases, Aerosols, Clouds, and Rainfall over the Rain Forest, *Bulletin of the American Meteorological Society*, 0, null, 10.1175/bams-d-15-00221.1, 2016a.
- 10 Martin, S. T., Artaxo, P., Machado, L. A. T., Manzi, A. O., Souza, R. A. F., Schumacher, C., Wang, J., Andreae, M. O., Barbosa, H. M. J., Fan, J., Fisch, G., Goldstein, A. H., Guenther, A., Jimenez, J. L., Pöschl, U., Silva Dias, M. A., Smith, J. N., and Wendisch, M.: Introduction: Observations and modeling of the Green Ocean Amazon (GoAmazon2014/5), *Atmospheric Chemistry and Physics*, 4785-4797, 10.5194/acp-16-4785-2016, 2016b.
- 15 Moran-Zuloaga, D., Ditas, F., Walter, D., Araújo, A., Brito, J., Carbone, S., Chi, X., Hrabě de Angelis, I., Lavric, J. V., Ming, J., Pöhlker, M. L., Ruckteschler, N., Saturno, J., Wang, Y., Wang, Q., Weber, B., Wolff, S., Artaxo, P., Andreae, M. O., and Pöhlker, C.: Coarse mode aerosols in the Amazon rain forest – A multi-year study on the frequent advection of African dust plumes *Atmos. Chem. Phys.*, 2017.
- 20 Nepstad, D., McGrath, D., Alencar, A., Barros, A. C., Carvalho, G., Santilli, M., and Diaz, M. D. V.: Environment - Frontier governance in Amazonia, *Science*, 295, 629–+, 10.1126/science.1067053, 2002.
- Ng, N. L., Herndon, S. C., Trimborn, A., Canagaratna, M. R., Croteau, P. L., Onasch, T. B., Sueper, D., Worsnop, D. R., Zhang, Q., Sun, Y. L., and Jayne, J. T.: An Aerosol Chemical Speciation Monitor (ACSM) for Routine Monitoring of the Composition and Mass Concentrations of Ambient Aerosol, *Aerosol Science and Technology*, 45, 780-794, 10.1080/02786826.2011.560211, 2011.
- Petzold, A., and Schonlinner, M.: Multi-angle absorption photometry - a new method for the measurement of aerosol light absorption and atmospheric black carbon, *Journal of Aerosol Science*, 35, 421-441, 10.1016/j.jaerosci.2003.09.005, 2004.
- 25 Pöhlker, C., Walter, D., Paulsen, H., Könemann, T., Moran-Zuloaga, D., Brito, J., Carbone, S., Degrendele, C., Després, V. R., Ditas, F., Holanda, B. A., Lammel, G., Lavrič, J. V., Jing, M., Pickersgill, D., Pöhlker, M. L., Rodríguez-Caballero, E., Ruckteschler, N., Saturno, J., Sörgel, M., Wang, Q., Weber, B., Wolff, S., Artaxo, P., Pöschl, U., and Andreae, M. O.: Systematic backward trajectory and land cover analyses within the footprint of the remote ATTO site in the central Amazon Basin *Atmos. Chem. Phys.*, to be submitted, 2017.
- 30 Pöhlker, M. L., Pöhlker, C., Klimach, T., Hrabě de Angelis, I., Barbosa, H. M. J., Brito, J., Carbone, S., Cheng, Y., Chi, X., Ditas, F., Ditz, R., Gunthe, S. S., Kesselmeier, J., Könemann, T., Lavrič, J. V., Martin, S. T., Moran-Zuloaga, D., Rose, D., Saturno, J., Su, H., Thalman, R., Walter, D., Wang, J., Wolff, S., Artaxo, P., Andreae, M. O., and Pöschl, U.: Long-term observations of cloud condensation nuclei in the Amazon rain forest – Part I: Aerosol size distribution, hygroscopicity, and new model parameterizations for CCN prediction, *Atmos. Chem. Phys.*, 16, 15709-15740, 10.5194/acp-2016-519, 2016.
- 35 Pöschl, U., Martin, S. T., Sinha, B., Chen, Q., Gunthe, S. S., Huffman, J. A., Borrmann, S., Farmer, D. K., Garland, R. M., Helas, G., Jimenez, J. L., King, S. M., Manzi, A., Mikhailov, E., Pauliquevis, T., Petters, M. D., Prenni, A. J., Roldin, P., Rose, D., Schneider, J., Su, H., Zorn, S. R., Artaxo, P., and Andreae, M. O.: Rainforest Aerosols as Biogenic Nuclei of Clouds and Precipitation in the Amazon, *Science*, 329, 1513-1516, 10.1126/science.1191056, 2010.
- 40 Reutter, P., Su, H., Trentmann, J., Simmel, M., Rose, D., Gunthe, S. S., Wernli, H., Andreae, M. O., and Pöschl, U.: Aerosol- and updraft-limited regimes of cloud droplet formation: influence of particle number, size and hygroscopicity on the activation of cloud condensation nuclei (CCN), *Atmospheric Chemistry and Physics*, 9, 7067-7080, 2009.
- Rissler, J., Swietlicki, E., Zhou, J., Roberts, G., Andreae, M. O., Gatti, L. V., and Artaxo, P.: Physical properties of the sub-micrometer aerosol over the Amazon rain forest during the wet-to-dry season transition - comparison of modeled and measured CCN concentrations, *Atmospheric Chemistry and Physics*, 4, 2119-2143, 2004.
- 45 Rizzolo, J. A., Barbosa, C. G. G., Borillo, G. C., Godoi, A. F. L., Souza, R. A. F., Andreoli, R. V., Manzi, A. O., Sá, M. O., Alves, E. G., Pöhlker, C., Angelis, I. H., Ditas, F., Saturno, J., Moran-Zuloaga, D., Rizzo, L. V., Rosário, N. E., Pauliquevis, T., Yamamoto, C. I., Andreae, M. O., Taylor, P. E., and Godoi, R. H. M.: Mineral nutrients in Saharan dust and their potential impact on Amazon rainforest ecology, *Atmos. Chem. Phys. Discuss.*, 2016, 1-43, 10.5194/acp-2016-557, 2016.
- 50 Roberts, G. C., Artaxo, P., Zhou, J. C., Swietlicki, E., and Andreae, M. O.: Sensitivity of CCN spectra on chemical and physical properties of aerosol: A case study from the Amazon Basin, *Journal of Geophysical Research-Atmospheres*, 107, 10.1029/2001jd000583, 2002.
- Roberts, G. C., Nenes, A., Seinfeld, J. H., and Andreae, M. O.: Impact of biomass burning on cloud properties in the Amazon Basin, *Journal of Geophysical Research-Atmospheres*, 108, 10.1029/2001jd000985, 2003.
- Roberts, M. C., Andreae, M. O., Zhou, J. C., and Artaxo, P.: Cloud condensation nuclei in the Amazon Basin: "Marine" conditions over a continent?, *Geophys. Res. Lett.*, 28, 2807-2810, 2001.
- 55 Rosario, N. E., Longo, K. M., Freitas, S. R., Yamasoe, M. A., and Fonseca, R. M.: Modeling the South American regional smoke plume: aerosol optical depth variability and surface shortwave flux perturbation, *Atmospheric Chemistry and Physics*, 13, 2923-2938, 10.5194/acp-13-2923-2013, 2013.



- Rose, D., Gunthe, S. S., Mikhailov, E., Frank, G. P., Dusek, U., Andreae, M. O., and Poeschl, U.: Calibration and measurement uncertainties of a continuous-flow cloud condensation nuclei counter (DMT-CCNC): CCN activation of ammonium sulfate and sodium chloride aerosol particles in theory and experiment, *Atmospheric Chemistry and Physics*, 8, 1153-1179, 2008.
- 5 Rosenfeld, D., Andreae, M. O., Asmi, A., Chin, M., de Leeuw, G., Donovan, D. P., Kahn, R., Kinne, S., Kivekas, N., Kulmala, M., Lau, W., Schmidt, K. S., Suni, T., Wagner, T., Wild, M., and Quaas, J.: Global observations of aerosol-cloud-precipitation-climate interactions, *Rev. Geophys.*, 52, 750-808, [10.1002/2013rg000441](https://doi.org/10.1002/2013rg000441), 2014.
- Rosenfeld, D., Lohmann, U., Raga, G. B., O'Dowd, C. D., Kulmala, M., Fuzzi, S., Reissell, A., and Andreae, M. O.: Flood or drought: How do aerosols affect precipitation?, *Science*, 321, 1309-1313, [10.1126/science.1160606](https://doi.org/10.1126/science.1160606), 2008.
- 10 Rosenfeld, D., Zheng, Y., Hashimshoni, E., Pöhlker, M. L., Jefferson, A., Pöhlker, C., Yu, X., Zhu, Y., Liu, G., Yue, Z., Fischman, B., Li, Z., Giguzin, D., Goren, T., Artaxo, P., Barbosa, H. M. J., Pöschl, U., and Andreae, M. O.: Satellite retrieval of cloud condensation nuclei concentrations by using clouds as CCN chambers, *Proceedings of the National Academy of Sciences*, 113, 5828-5834, [10.1073/pnas.1514044113](https://doi.org/10.1073/pnas.1514044113), 2016a.
- 15 Rosenfeld, D., Zheng, Y. T., Hashimshoni, E., Pöhlker, M. L., Jefferson, A., Pöhlker, C., Yu, X., Zhu, Y. N., Liu, G. H., Yue, Z. G., Fischman, B., Li, Z. Q., Giguzin, D., Goren, T., Artaxo, P., Barbosa, H. M. J., Pöschl, U., and Andreae, M. O.: Satellite retrieval of cloud condensation nuclei concentrations by using clouds as CCN chambers, *Proceedings of the National Academy of Sciences of the United States of America*, 113, 5828-5834, [10.1073/pnas.1514044113](https://doi.org/10.1073/pnas.1514044113), 2016b.
- 20 Saturno, J., Ditas, F., Pöhlker, M. L., Carbone, S., Brito, J., Holanda, B. A., Hrabě de Angelis, I., Morán-Zuloaga, D., Walter, D., Artaxo, P., Pöschl, U., Andreae, M. O., and Pöhlker, C.: African volcanic sulfur emissions as a contributor to atmospheric sulfate aerosol over the Amazon rain forest, *Atmos. Chem. Phys.*, to be submitted, 2017a.
- Saturno, J., Pöhlker, C., Massabò, D., Brito, J., Carbone, S., Cheng, Y., Chi, X., Ditas, F., Hrabě de Angelis, I., Morán-Zuloaga, D., Pöhlker, M. L., Rizzo, L. V., Walter, D., Wang, Q., Artaxo, P., Prati, P., and Andreae, M. O.: Comparison of different Aethalometer correction schemes and a reference multi-wavelength absorption technique for ambient aerosol data, *Atmospheric Measurement Techniques*, in prep., 2016.
- 25 Saturno, J., Pöhlker, C., Wang, Q., Ditas, F., Morán-Zuloaga, D., Brito, J., Carbone, S., Cheng, Y., Chi, X., Hoffmann, T., Holanda, B. A., Hrabě de Angelis, I., Könemann, T., Lavric, J. V., Jing, M., Pöhlker, M. L., Rizzo, L. V., Walter, D., Wolff, S., Artaxo, P., Pöschl, U., and Andreae, M. O.: Aerosol optical properties over central Amazonia: Long-term measurements at the ATTO site *Atmos. Chem. Phys.*, to be submitted, 2017b.
- 30 Seinfeld, J. H., Bretherton, C., Carslaw, K. S., Coe, H., DeMott, P. J., Dunlea, E. J., Feingold, G., Ghan, S., Guenther, A. B., Kahn, R., Kraucunas, I., Kreidenweis, S. M., Molina, M. J., Nenes, A., Penner, J. E., Prather, K. A., Ramanathan, V., Ramaswamy, V., Rasch, P. J., Ravishankara, A. R., Rosenfeld, D., Stephens, G., and Wood, R.: Improving our fundamental understanding of the role of aerosol-cloud interactions in the climate system, *Proceedings of the National Academy of Sciences of the United States of America*, 113, 5781-5790, [10.1073/pnas.1514043113](https://doi.org/10.1073/pnas.1514043113), 2016.
- 35 Stevens, B., and Feingold, G.: Untangling aerosol effects on clouds and precipitation in a buffered system, *Nature*, 461, 607-613, [10.1038/nature08281](https://doi.org/10.1038/nature08281), 2009.
- Swap, R., Garstang, M., Greco, S., Talbot, R., and Kallberg, P.: SAHARAN DUST IN THE AMAZON BASIN, *Tellus Series B-Chemical and Physical Meteorology*, 44, 133-149, [10.1034/j.1600-0889.1992.t01-1-00005.x](https://doi.org/10.1034/j.1600-0889.1992.t01-1-00005.x), 1992.
- 40 Talbot, R. W., Andreae, M. O., Berresheim, H., Artaxo, P., Garstang, M., Harriss, R. C., Beecher, K. M., and Li, S. M.: AEROSOL CHEMISTRY DURING THE WET SEASON IN CENTRAL AMAZONIA - THE INFLUENCE OF LONG-RANGE TRANSPORT, *Journal of Geophysical Research-Atmospheres*, 95, 16955-16969, [10.1029/JD095iD10p16955](https://doi.org/10.1029/JD095iD10p16955), 1990.
- Tao, W. K., Chen, J. P., Li, Z. Q., Wang, C., and Zhang, C. D.: IMPACT OF AEROSOLS ON CONVECTIVE CLOUDS AND PRECIPITATION, *Rev. Geophys.*, 50, [10.1029/2011rg000369](https://doi.org/10.1029/2011rg000369), 2012.
- 45 Thalman, R., de Sá, S. S., Palm, B. B., Barbosa, H. M. J., Pöhlker, M. L., Alexander, M. L., Brito, J., Carbone, S., Castillo, P., Day, D. A., Kuang, C., Manzi, A., Ng, N. L., Sedlacek III, A. J., Souza, R., Springston, S., Watson, T., Pöhlker, C., Pöschl, U., Andreae, M. O., Artaxo, P., Jimenez, J. L., Martin, S. T., and Wang, J.: CCN activity and organic hygroscopicity of aerosols downwind of an urban region in central Amazonia: Seasonal and diel variations and impact of anthropogenic emissions, *Atmos. Chem. Phys.*, accepted, 2017.
- 50 Wang, J., Krejci, R., Giangrande, S., Kuang, C., Barbosa, H. M. J., Brito, J., Carbone, S., Chi, X., Comstock, J., Ditas, F., Lavric, J., Manninen, H. E., Mei, F., Moran-Zuloaga, D., Pöhlker, C., Pöhlker, M. L., Saturno, J., Schmid, B., Souza, R. A. F., Springston, S. R., Tomlinson, J. M., Toto, T., Walter, D., Wimmer, D., Smith, J. N., Kulmala, M., Machado, L. A. T., Artaxo, P., Andreae, M. O., Petäjä, T., and Martin, S. T.: Amazon boundary layer aerosol concentration sustained by vertical transport during rainfall, *Nature*, 539, 416-419, [10.1038/nature19819](https://doi.org/10.1038/nature19819), 2016.
- 55 Wang, X., Zhang, L., and Moran, M. D.: Uncertainty assessment of current size-resolved parameterizations for below-cloud particle scavenging by rain, *Atmos. Chem. Phys.*, 10, 5685-5705, [10.5194/acp-10-5685-2010](https://doi.org/10.5194/acp-10-5685-2010), 2010.
- Wendisch, M., Pöschl, U., Andreae, M. O., Machado, L. A. T., Albrecht, R., Schlager, H., Rosenfeld, D., Martin, S. T., Abdelmonem, A., Afchine, A., Araújo, A. C., Artaxo, P., Aufmhoff, H., Barbosa, H. M. J., Borrmann, S., Braga, R.,



- 5 Buchholz, B., Cecchini, M. A., Costa, A., Curtius, J., Dollner, M., Dorf, M., Dreiling, V., Ebert, V., Ehrlich, A., Ewald, F., Fisch, G., Fix, A., Frank, F., Fütterer, D., Heckl, C., Heidelberg, F., Hüneke, T., Jäkel, E., Järvinen, E., Jurkat, T., Kanter, S., Kästner, U., Kenntner, M., Kesselmeier, J., Klimach, T., Knecht, M., Kohl, R., Kölling, T., Krämer, M., Krüger, M., Krisna, T. C., Lavric, J. V., Longo, K., Mahnke, C., Manzi, A. O., Mayer, B., Mertes, S., Minikin, A., Molleker, S., Münch, S., Nillius, B., Pfeilsticker, K., Pöhlker, C., Roiger, A., Rose, D., Rosenow, D., Sauer, D., Schnaiter, M., Schneider, J., Schulz, C., Souza, R. A. F. d., Spanu, A., Stock, P., Vila, D., Voigt, C., Walser, A., Walter, D., Weigel, R., Weinzierl, B., Werner, F., Yamasoe, M. A., Ziereis, H., Zinner, T., and Zöger, M.: ACRIDICON-CHUVA Campaign: Studying Tropical Deep Convective Clouds and Precipitation over Amazonia Using the New German Research Aircraft HALO, *Bulletin of the American Meteorological Society*, 97, 1885-1908, 10.1175/bams-d-14-00255.1, 2016.
- 10 Winderlich, J., Chen, H., Gerbig, C., Seifert, T., Kolle, O., Lavrič, J. V., Kaiser, C., Höfer, A., and Heimann, M.: Continuous low-maintenance CO<sub>2</sub>/CH<sub>4</sub>/H<sub>2</sub>O measurements at the Zotino Tall Tower Observatory (ZOTTO) in Central Siberia, *Atmos. Meas. Tech.*, 3, 1113-1128, 10.5194/amt-3-1113-2010, 2010.
- 15 Yanez-Serrano, A. M., Noelscher, A. C., Williams, J., Wolff, S., Alves, E., Martins, G. A., Bourtsoukidis, E., Brito, J., Jardine, K., Artaxo, P., and Kesselmeier, J.: Diel and seasonal changes of biogenic volatile organic compounds within and above an Amazonian rainforest, *Atmospheric Chemistry and Physics*, 15, 3359-3378, 10.5194/acp-15-3359-2015, 2015.
- Yu, H. B., Chin, M., Yuan, T. L., Bian, H. S., Remer, L. A., Prospero, J. M., Omar, A., Winker, D., Yang, Y. K., Zhang, Y., Zhang, Z. B., and Zhao, C.: The fertilizing role of African dust in the Amazon rainforest: A first multiyear assessment based on data from Cloud-Aerosol Lidar and Infrared Pathfinder Satellite Observations, *Geophys. Res. Lett.*, 42, 1984-1991, 10.1002/2015gl063040, 2015.
- 20 Zhou, J., Swietlicki, E., Hansson, H. C., and Artaxo, P.: Submicrometer aerosol particle size distribution and hygroscopic growth measured in the Amazon rain forest during the wet season, *J. Geophys. Res.*, 107, 8055, 10.1029/2000jd000203, 2002.
- Zikova, N., and Zdimal, V.: Precipitation scavenging of aerosol particles at a rural site in the Czech Republic, *Tellus Series B-Chemical and Physical Meteorology*, 68, 10.3402/tellusb.v68.27343, 2016.



Table A1. List of frequently used symbols.

Symbol	Quantity and Unit
$a_{mode}$ (mode =1, 2)	prefactor of single- and double erf fits
$D$	mobility equivalent particle diameter, nm
$D_a(S)$	midpoint activation diameter determined from CCN activation curve, nm
$D_{Ait}$	position of Aitken mode maximum, nm
$D_{Acc}$	position of accumulation mode maximum, nm
$D_H$	position of Hoppel minimum, nm
$D_{cut}$	cut-off diameter of aerosol impactor, nm
$\kappa$	hygroscopicity parameter
$\kappa(S, D_a)$	hygroscopicity parameter determined from CCN activation curve
$\kappa_{Acc}$	mean hygroscopicity parameter for accumulation mode particles
$\kappa_{Ait}$	mean hygroscopicity parameter for Aitken mode particles
$\kappa_p$	predicted hygroscopicity parameter based on ACSM results
$MAF(S)$	maximum activated fraction determined by CCN activation curve
$M_{Bec}$	mass concentration of $BC_e$ , $\mu\text{g m}^{-3}$
$M_{Bec}^*$	threshold $M_{Bec}$ level for definition of near-pristine periods, $\mu\text{g m}^{-3}$
$M_{Org}$	ACSM-derived organic mass concentration, $\mu\text{g m}^{-3}$
$M_{NO_3}$	ACSM-derived nitrate mass concentration, $\mu\text{g m}^{-3}$
$M_{NH_4}$	ACSM-derived ammonium mass concentration, $\mu\text{g m}^{-3}$
$M_{SO_4}$	ACSM-derived sulfate mass concentration, $\mu\text{g m}^{-3}$
$M_{Cl}$	ACSM-derived chloride mass concentration, $\mu\text{g m}^{-3}$
$N$	number of data points
$N_{CCN}(S)$	CCN number concentration at a certain $S$ , $\text{cm}^{-3}$
$N_{CCN}(S, D)$	CCN number concentration at a certain $S$ and $D$ , $\text{cm}^{-3}$
$N_{CCN}(S) / N_{CN,10}$	CCN efficiency
$N_{CN,Dcut}$	CN number concentration ( $>D_{cut}$ ), $\text{cm}^{-3}$
$N_{CN,10}$	CN number concentration ( $>10$ nm), $\text{cm}^{-3}$
$N_{CN,Acc}$	CN number concentration for accumulation mode particles, $\text{cm}^{-3}$
$N_{CN,Ait}$	CN number concentration for Aitken mode particles, $\text{cm}^{-3}$
$N_d$	Cloud droplet number concentration, $\text{cm}^{-3}$
$N_{db}$	Cloud droplet number concentration at cloud base, $\text{cm}^{-3}$
$P_{ATTO}$	precipitation rate at ATTO, $\text{mm h}^{-1}$
$P_{BT}$	cumulative precipitation from HYSPLIT BTs, $\text{mm h}^{-1}$
$P_{TRMM}$	precipitation from TRMM satellite mission, $\text{mm h}^{-1}$
$r_e$	cloud droplet effective radius, $\mu\text{m}$
$S$	water vapor supersaturation, %
$S_{cloud}(D_H, \kappa)$	average peak supersaturation in cloud, %
$S_{mode}$ (mode =1, 2)	midpoint activation supersaturation determined from CCN efficiency spectra, %
std	standard deviation
$SW_{in}$	incoming short-wave radiation, $\text{W m}^{-2}$
$\theta_e$	equivalent potential temperature, K
$U$	wind speed, $\text{m s}^{-1}$
$v_1$	offset of single- and double erf fits
$w$	updraft velocity, $\text{m s}^{-1}$
$w_b$	updraft velocity at cloud base, $\text{m s}^{-1}$
$w_{mode}$ (mode =1, 2)	width of CCN efficiency spectra
$\sigma$	width of log-normal fit in Aitken and accumulation mode fitting
$\sigma_{ap}$	aerosol absorption coefficient, $\text{Mm}^{-1}$
$x_0$	position of log-normal fit in Aitken and accumulation mode fitting, nm



Table A2. List of frequently used acronyms.

Acronym	Description
ACSM	aerosol chemical speciation monitor
ATTO	Amazon tall tower observatory
BB	biomass burning
BC	black carbon
BC <sub>e</sub>	equivalent black carbon
BL	boundary layer
BT	backward trajectory
BVOC	biogenic volatile organic compound
CCN	cloud condensation nuclei
CCNC	cloud condensation nuclei counter
CPC	condensation particle counter
CS	case study
DSD	droplet size distribution
erf	Gaussian error function
FIRMS	fire information for resource management system
GDAS	global data assimilation system
GoAmazon2014/5	green ocean Amazon 2014/5
HYSPLIT	hybrid single particle Lagrangian integrated trajectory model
IOP	intensive observation period
lpm	liters per minute
LRT	long-range transport
ITCZ	intertropical convergence zone
MAAP	multi-angle absorption photometer
MAC	mass absorption coefficient
MODIS	moderate resolution imaging spectroradiometer
NOAA	national oceanic and atmospheric administration
NP	near-pristine
NASA	National Aeronautics and Space Administration
NPF	new particle formation
OA	organic aerosol
PBAP	primary biological aerosol particles
rBC	refractory black carbon
RH	relative humidity
ROI <sub>ATTO</sub>	region of interest, covering ATTO region
SE	standard error
SMPS	scanning mobility particle counter
SOA	secondary organic aerosol
SP2	single particle soot photometer
UT	upper troposphere
UTC	coordinated universal time





Table 2. Properties (position  $x_0$ , integral number concentration  $N_{CN}$ , width  $\sigma$ ) of Aitken and accumulation modes from single or double log-normal fit (compare  $R^2$ ) of the total particle size distribution. Values are given as means of the case study periods, whereas corresponding seasonally averaged results can be found in the part 1 study. The errors represent the uncertainty of the fit parameters. No meaningful double log-normal fit was obtained for the monomodal *MixPol* case – thus, a single log-normal fit was conducted to describe the properties of the main peak. For the case studies *NP* and *LRT* with a clearly resolved bimodal size distribution, values for the position of the Hoppel minimum  $D_H$  as well as estimated average peak supersaturation in cloud  $S_{cloud}(D_H, \kappa)$  are listed. The errors in  $S_{cloud}(D_H, \kappa)$  is the experimentally derived error in  $S$ .

Time period	Mode or size range	$N_{CN}$ [cm <sup>-3</sup> ]	$\kappa$	$x_0$ [nm]	$\sigma$	$R^2$	$D_H$ [nm]	$S_{cloud}(D_H, \kappa)$ [%]
Case study: near-pristine ( <i>NP</i> )	Aitken	203 ± 6	0.12 ± 0.01	67 ± 1	0.60 ± 0.01	0.99	122 ± 2	0.20 ± 0.01
	accumulation	65 ± 4	0.18 ± 0.02	171 ± 2	0.34 ± 0.02			
Case study: long-range transport ( <i>LRT</i> )	Aitken	120 ± 10	0.18 ± 0.02	77 ± 2	0.58 ± 0.03	0.99	109 ± 2	0.18 ± 0.01
	accumulation	300 ± 6	0.34 ± 0.04	178 ± 2	0.52 ± 0.01			
Case study: biomass burning ( <i>BB</i> )	Aitken	140 ± 29	0.14 ± 0.01	70 ± 1	0.20 <sup>a</sup>	0.99	--	--
	accumulation	3439 ± 39	0.17 ± 0.02	167 ± 1	0.58 ± 0.01			
Case study: mixed pollution ( <i>MixPol</i> )	< 100 nm	---	0.14 ± 0.01	--	--	0.99	--	--
	> 100 nm	1272 ± 27	0.22 ± 0.03	135 ± 5	0.85 ± 0.01		--	--
	< 150 nm	---	0.10 ± 0.01	--	--	0.99	--	--
	> 150 nm	2764 ± 84	0.20 ± 0.04	113 ± 1	0.81 ± 0.01		--	--

<sup>a</sup> Width of Aitken mode in double log-normal fit of *BB* case was predefined.



Table 3. Aerosol chemical composition from ACSM measurements at ATTO, showing characteristic differences between case studies as well as seasonal conditions (for details see Carbone et al., 2017). ACSM data was available for time period from 01 Aug 2014 to 30 Sep 2016 and the averaged values are shown here as mean  $\pm$  std. Information on averaged time frames for the individual case studies can be found in Table 1. The shown ACSM  $3\sigma$  detection limits for 30 min averaging time were obtained from Ng et al. (2011). Note that  $M_{\text{NH}_4}$  ranged below the instruments detection limit in certain cases, which makes the corresponding results unreliable. Predicted average aerosol hygroscopicity parameter,  $\kappa_p$ , was calculated according to Gunthe et al. (2009) and is shown as mean  $\pm$  standard error. The  $\kappa(0.10\%)$  results are shown with the experimentally derived error.

Time period	OA	NO <sub>3</sub> <sup>-</sup>	NH <sub>4</sub> <sup>+</sup>	SO <sub>4</sub> <sup>2-</sup>	Cl	OA/SO <sub>4</sub> <sup>2-</sup>	$\kappa_p$	$\kappa(0.10\%)^b$
Case study: near-pristine (NP)	0.64 $\pm$ 0.56 (89)*	0.03 $\pm$ 0.03 (4)*	0.18 $\pm$ 0.19 <sup>a</sup> (-)*	0.04 $\pm$ 0.03 (6)*	0.01 $\pm$ 0.01 (1)*	~ 46	0.16 $\pm$ 0.05 *	0.19 $\pm$ 0.05
Case study: long-range transport (LRT)	1.81 $\pm$ 2.63 (73)	0.08 $\pm$ 0.09 (3)	0.30 $\pm$ 0.37 (12)	0.25 $\pm$ 0.19 (10)	0.04 $\pm$ 0.05 (2)	~ 24	0.24 $\pm$ 0.16	0.35 $\pm$ 0.04
Case study: biomass burning (BB)	19.10 $\pm$ 6.65 (91)	0.50 $\pm$ 0.19 (2)	0.54 $\pm$ 0.25 (3)	0.79 $\pm$ 0.21 (4)	0.03 $\pm$ 0.02 (0)	~ 24	0.14 $\pm$ 0.02	0.18 $\pm$ 0.01
Case study: mixed pollution (MixPol)	5.48 $\pm$ 1.07 (68)	0.22 $\pm$ 0.08 (3)	0.54 $\pm$ 0.25 (7)	1.76 $\pm$ 0.62 (22)	0.03 $\pm$ 0.02 (0)	~ 3	0.26 $\pm$ 0.04	0.26 $\pm$ 0.05
low $\kappa$	8.08 $\pm$ 1.34 (72)	0.36 $\pm$ 0.21 (3)	0.69 $\pm$ 0.26 (6)	2.05 $\pm$ 0.60 (18)	0.03 $\pm$ 0.01 (0)	~ 4	0.23 $\pm$ 0.03	0.24 $\pm$ 0.02
Wet season (Feb-May) <sup>b</sup>	1.02 $\pm$ 0.75 (83)*	0.05 $\pm$ 0.06 (4)*	0.20 $\pm$ 0.23 <sup>a</sup> (-)*	0.14 $\pm$ 0.18 (11)*	0.02 $\pm$ 0.03 (2)*	~ 23	0.19 $\pm$ 0.08 *	0.21 $\pm$ 0.05
Transition periods (Jun/Jul & Dec/Jan)	3.16 $\pm$ 4.11 (88)*	0.11 $\pm$ 0.12 (3)*	0.13 $\pm$ 0.29 <sup>a</sup> (-)*	0.30 $\pm$ 0.31 (8)*	0.02 $\pm$ 0.03 (1)*	~ 21	0.16 $\pm$ 0.08 *	0.24 $\pm$ 0.05
Dry season (Aug-Nov)	5.86 $\pm$ 5.46 (83)	0.19 $\pm$ 0.15 (3)	0.33 $\pm$ 0.24 (5)	0.64 $\pm$ 0.38 (9)	0.02 $\pm$ 0.03 (0)	~ 11	0.18 $\pm$ 0.07	0.21 $\pm$ 0.04
ACSM $3\sigma$ detection limits	0.148	0.012	0.284	0.024	0.011	--	--	--

<sup>a</sup> Here, measured  $M_{\text{NH}_4}$  ranged below the ACSM detection limit and the shown values are questionable. For NP case study as well as averages of wet season and transition periods, mass fractions and  $\kappa_p$  were calculated by omitting  $M_{\text{NH}_4}$  as outlined in Sect. 2.1. The corresponding results are marked by \*.

<sup>b</sup> The entirely averaged wet season includes NP and LRT conditions and, thus, concentrations represent an intermediate state of the NP and LRT cases.



**Table 4. Error function (erf) fit parameters describing CCN efficiency spectra  $N_{CCN}(S)/N_{CCN,10}$  vs.  $S$  as model input data representing case studies as defined in this part 2 paper (upper part of table). For comparison, the erf fit parameters, presenting the seasonal averages from the companion part 1 paper (M. Pöhlker et al. 2016) are shown in the lower part of the table. A reference concentration of  $N_{CCN,10}$  has been used in all cases. Corresponding formulas can be found in Sect. 2.2.**

Time period	$N_{CCN}$ [ $\text{cm}^{-3}$ ]	erf fit	mode	$y_{\text{mode}}$	$a_{\text{mode}}$	$S_{\text{mode}}$ [%]	$W_{\text{mode}}$	$R^2$	comment
Case study: near-pristine (NP)	271 ± 100	single	1	0.5	0.5	0.47 ± 0.01	1.69 ± 0.06	0.99	
		double	2	-	0.40 ± 0.03	0.65 ± 0.06	1.18 ± 0.14	0.99	
Case study: long-range transport (LRT)	438 ± 96	single	1	0.5	0.5	0.09 ± 0.01	1.99 ± 0.16	0.96	fit parameters for CCN efficiency spectra in case studies as defined in the present <b>part 2</b> study
		single	1	0.5	0.5	0.15 ± 0.01	1.16 ± 0.13	0.96	
Case study: biomass burning (BB)	3200 ± 1039	single	1	0.43 ± 0.1	0.5	0.13 ± 0.01	0.94 ± 0.05	0.99	
Case study: mixed pollution (MixPol)	1277 ± 267	single	1	0.5	0.5	0.16 ± 0.01	1.70 ± 0.08	0.99	
		single	1	0.5	0.5	0.28 ± 0.01	1.60 ± 0.04	0.99	
seasonal average: wet	340 ± 139	single	1	0.5	0.5	0.35 ± 0.01	1.80 ± 0.06	0.99	fit parameters for seasonally averaged CCN efficiency spectra taken from <b>part 1</b> study (M. Pöhlker et al. 2016) for comparison
seasonal average: LRT	438 ± 244	single	1	0.5	0.5	0.22 ± 0.01	2.39 ± 0.10	0.98	
seasonal average: trans	1074 ± 385	single	1	0.5	0.5	0.28 ± 0.01	1.70 ± 0.05	0.99	
seasonal average: dry	1511 ± 785	single	1	0.5	0.5	0.18 ± 0.01	1.57 ± 0.11	0.98	

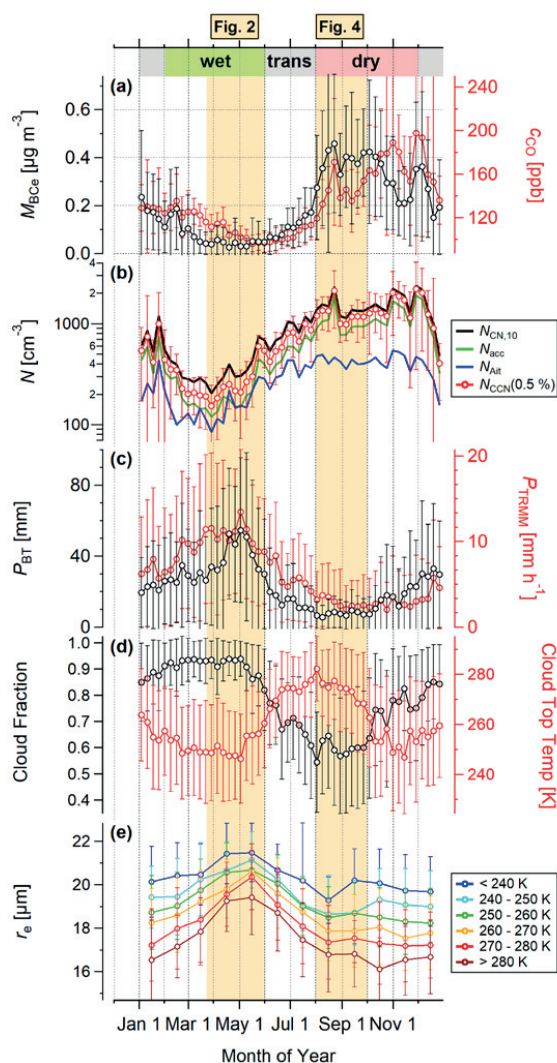


Figure 1. Seasonal cycle of selected trace gas, aerosol, and cloud microphysical parameters. (a) Pollution tracers  $M_{Bce}$  and  $c_{CO}$ . (b) Total aerosol number concentration  $N_{CN,10}$ . (c) Precipitation products  $P_{BT}$ , representing cumulative precipitation along BT tracks, and  $P_{TRMM}$ , representing TRMM-derived precipitation within the  $ROI_{ATTO}$  as defined in Fig. S1. (d) Satellite-derived cloud fraction and cloud top temperature within the  $ROI_{ATTO}$ . (e). Satellite-derived cloud droplet effective radius  $r_e$  within the  $ROI_{ATTO}$ . For a detailed characterization of the land use and recent land use change in the ATTO site footprint, including the  $ROI_{ATTO}$ , we refer the reader to a recent study on this topic (C. Pöhlker et al., 2017). Data in (a) to (d) is shown as weekly averages. Data in (e) is shown as monthly averages. Error bars represent one standard deviation. Vertical orange shading represents 2-month time frames of representative clean and polluted conditions as shown in detail in Fig. 2 and 4.

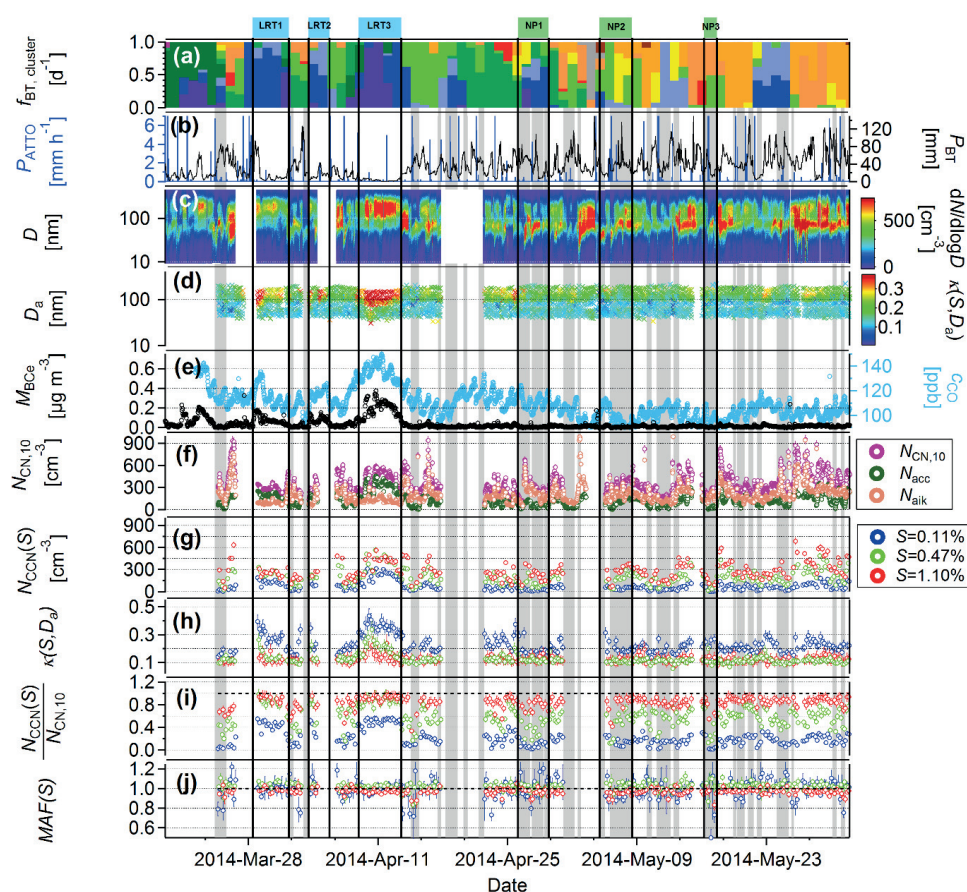
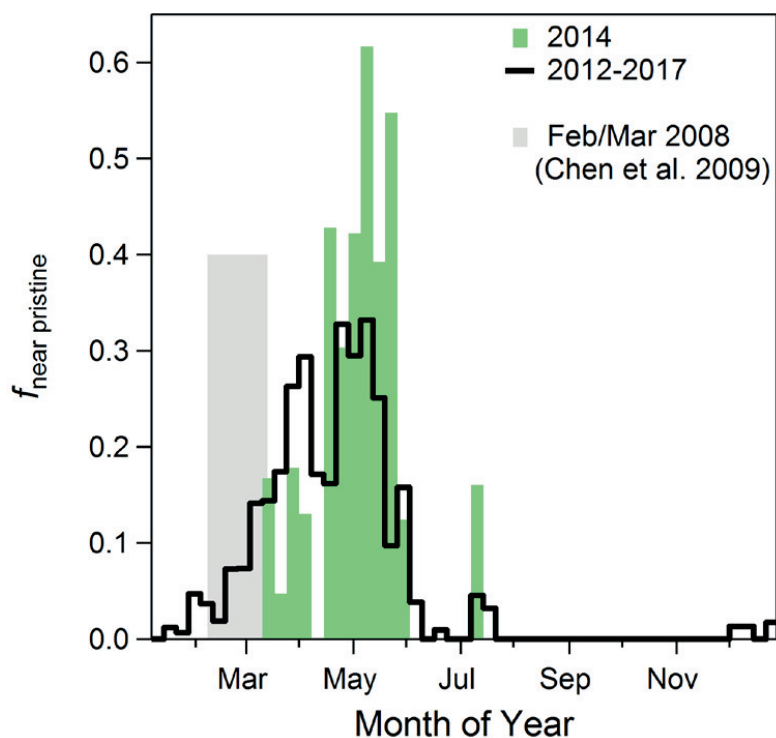


Figure 2. Overview plot illustrating selected meteorological, trace gas, aerosol, and CCN time series for representative wet season conditions in the central Amazon. Shown time period from 23 Mar until 31 May covers comparatively clean extended time frame throughout entire CCN measurement period. Individual panels represent: (a) Daily frequency of occurrence of 15 different BT clusters,  $f_{BT,cluster}$ , with color code corresponding to Fig. 1. (b) Precipitation rate  $P_{ATTO}$  measured locally at the ATTO site and cumulative precipitation from HYSPLIT trajectory analysis  $P_{BT}$  as measure for aerosol wet deposition. (c) SMPS-derived time series of number size distributions spanning nucleation, Aitken, and accumulation modes. (d) CCNC-derived time series of  $\kappa(S, D_a)$  size distributions. (e) Concentrations of biomass burning tracers CO mole fraction,  $c_{CO}$ , and BC<sub>e</sub> mass concentration,  $M_{BC_e}$ . (f) Total number concentrations of entire aerosol population  $N_{CN,10}$ , Aitken mode particles  $N_{Ait}$ , and accumulation mode particles  $N_{acc}$ . (g) CCN concentrations  $N_{CCN}(S)$  for selected supersaturations  $S$ . (h) Hygroscopicity parameter  $\kappa(S, D_a)$  for selected  $S$ , (i) CCN efficiencies  $N_{CCN}(S)/N_{CN,10}$  for selected  $S$ . (j) Maximum activated fraction  $MAF(S)$  for selected  $S$ . All CCN data is provided in original time resolution of about 4.5 h. Grey vertical shadings represent near-pristine periods according to definition in Sect. 2.3. Vertical markers  $NP1$ ,  $NP2$ , and  $NP3$  represent case studies on selected near-pristine (NP) episodes for detailed analysis in Sect. 3.4. Vertical markers  $LRT1$ ,  $LRT2$ , and  $LRT3$  represent case studies on African LRT influence for detailed analysis in Sect. 3.5.



5 Figure 3. Seasonality of relative fraction of near-pristine days,  $f_{near\ pristine}$ , in the ATTO region. Near-pristine episodes were defined in Sect. 2.3. Data is shown as weekly averages for time period from Mar 2012 until May 2017 (black line) and for 2014 only (green shading). Data shows that year 2014, which comprises most of the present CCN data, had highest fraction of near-pristine days in second half of the wet season (i.e., Apr and May) in agreement with multi-year trend. For comparison, the relative fraction of periods with dominant in-Basin processes accordingly to Chen et al. (2009) – interpreted here as similar to near-pristine conditions – is shown as grey shading and agrees with our data.

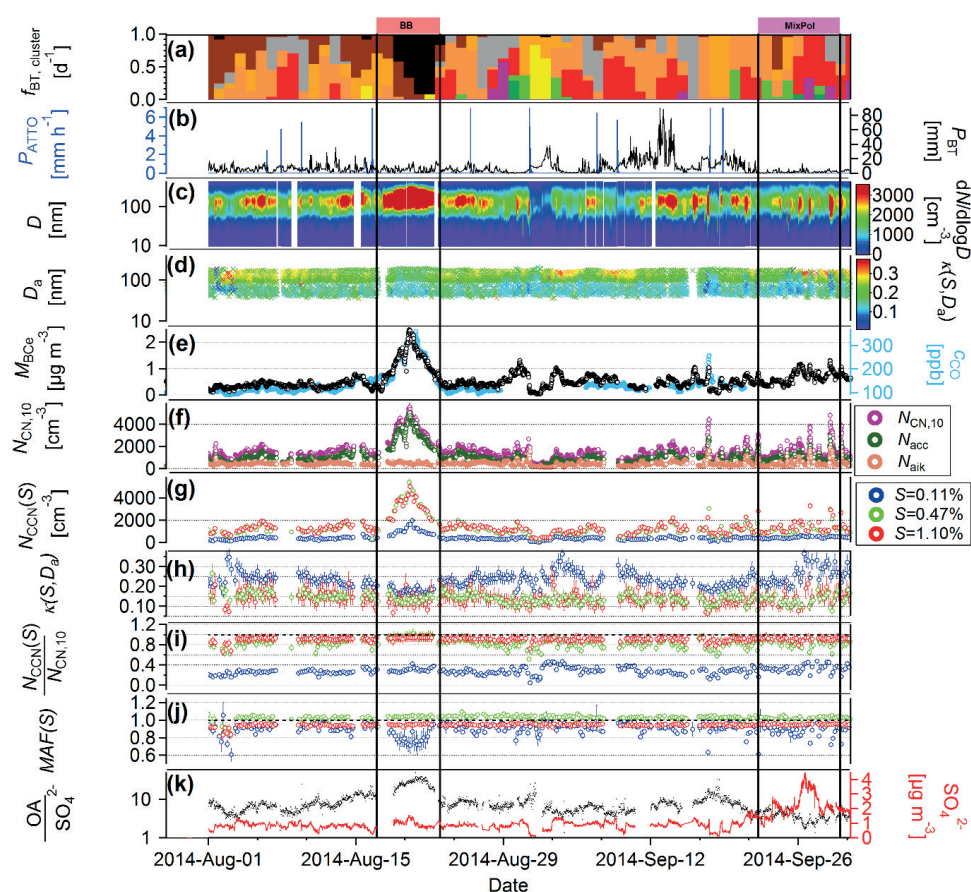


Figure 4. Overview plot illustrating selected meteorological, trace gas, aerosol, and CCN time series for representative dry season conditions in the central Amazon. Shown time period from 01 Aug until 31 Sep covers most polluted time frame throughout entire CCN measurement period. Individual panels represent: (a) Daily frequency of occurrence of 15 different BT clusters,  $f_{BT,cluster}$ , with color code corresponding to Fig. 1. (b) Precipitation rate  $P_{ATTO}$  measured locally at the ATTO site and cumulative precipitation from HYSPLIT trajectory analysis  $P_{BT}$  as measure for aerosol wet deposition. (c) SMPS-derived time series of number size distributions spanning nucleation, Aitken, and accumulation modes. (d) CCNC-derived time series of  $\kappa(S, D_a)$  size distributions. (e) Concentrations of biomass burning tracers CO mole fraction,  $c_{CO}$ , and  $BC_e$  mass concentration,  $M_{BC_e}$ . (f) Total number concentrations of entire aerosol population  $N_{CN,10}$ , Aitken mode particles  $N_{Ait}$ , and accumulation mode particles  $N_{acc}$ . (g) CCN concentrations  $N_{CCN(S)}$  for selected supersaturations  $S$ . (h) Hygroscopicity parameter  $\kappa(S, D_a)$  for selected  $S$ , (i) CCN efficiencies  $N_{CCN(S)}/N_{CN,10}$  for selected  $S$ . (j) Maximum activated fraction  $MAF(S)$  for selected  $S$ . (k) ACSM-derived sulfate mass concentration,  $m_{sulfate}$ , and organic-to-sulfate ratio,  $OA/SO_4^{2-}$ . All CCN data is provided in original time resolution of about 4.5 h. Vertical marker **BB** represent case studies on biomass burning episodes for detailed analysis in Sect. 3.6. Vertical marker **MixPol** represent case studies on mixed pollution conditions for detailed analysis in Sect. 3.7.

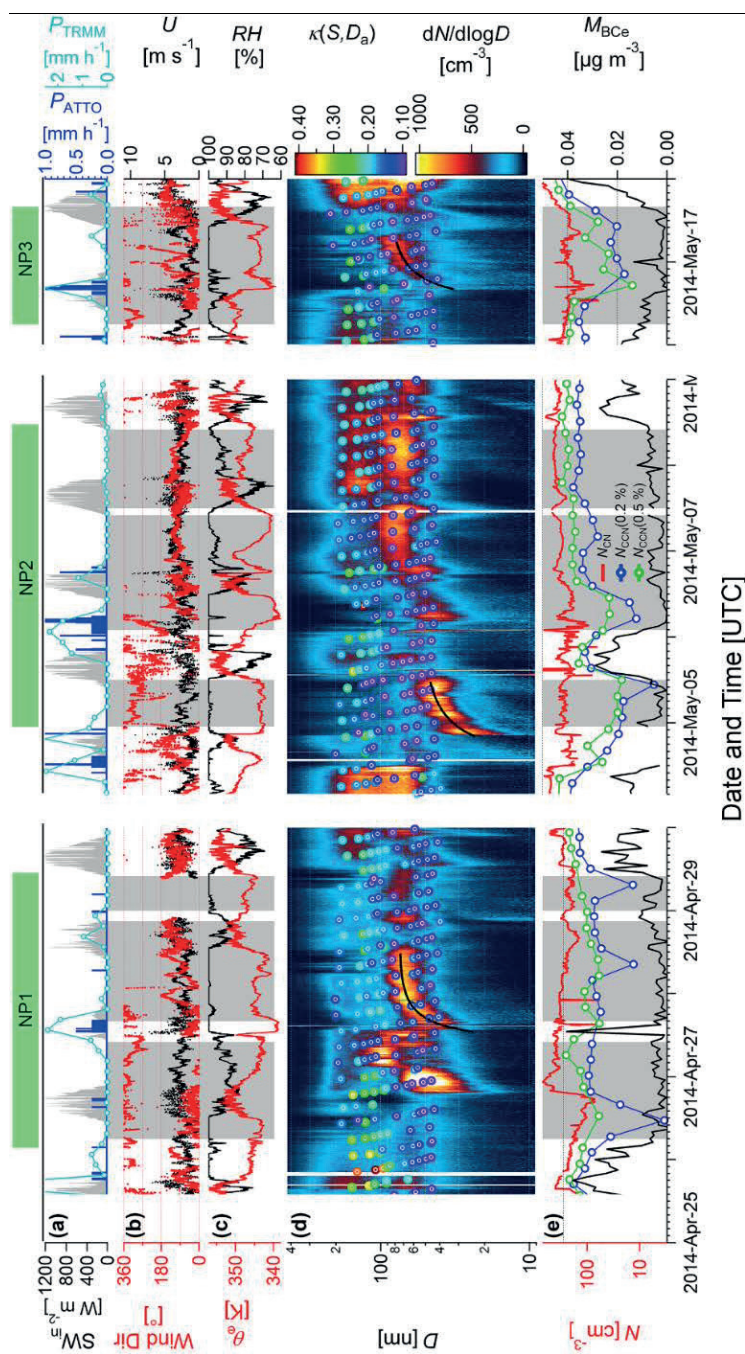


Figure 5. Selected meteorological, aerosol, and CCN time series from ground-based ATTO site measurements for near-pristine case study periods NP1, NP2, and NP3 (see Fig. 3). (a) Precipitation rates from TRMM satellite mission,  $P_{TRMM}$ , and *in situ* measurements at the ATTO site,  $P_{ATTO}$ . (b) Wind direction and wind speed,  $U$ , at the ATTO site. (c) Equivalent potential temperature,  $\theta_e$ , and relative humidity, RH, at the ATTO site. (d) Overlay of two data layers showing aerosol number size distribution contour plot ( $dN/d\log D$ ) as well as color coded markers, representing time series of  $\kappa(S, D_a)$  size distributions, and (e) CCN concentrations  $N_{CCN}(S)$  for two selected  $S$  levels, total aerosol number concentration  $N_{CN,0}$ , and  $BC_e$  mass concentration  $M_{BC_e}$ . Grey vertical shadings represent near-pristine periods according to definition in Sect. 2.3.

5

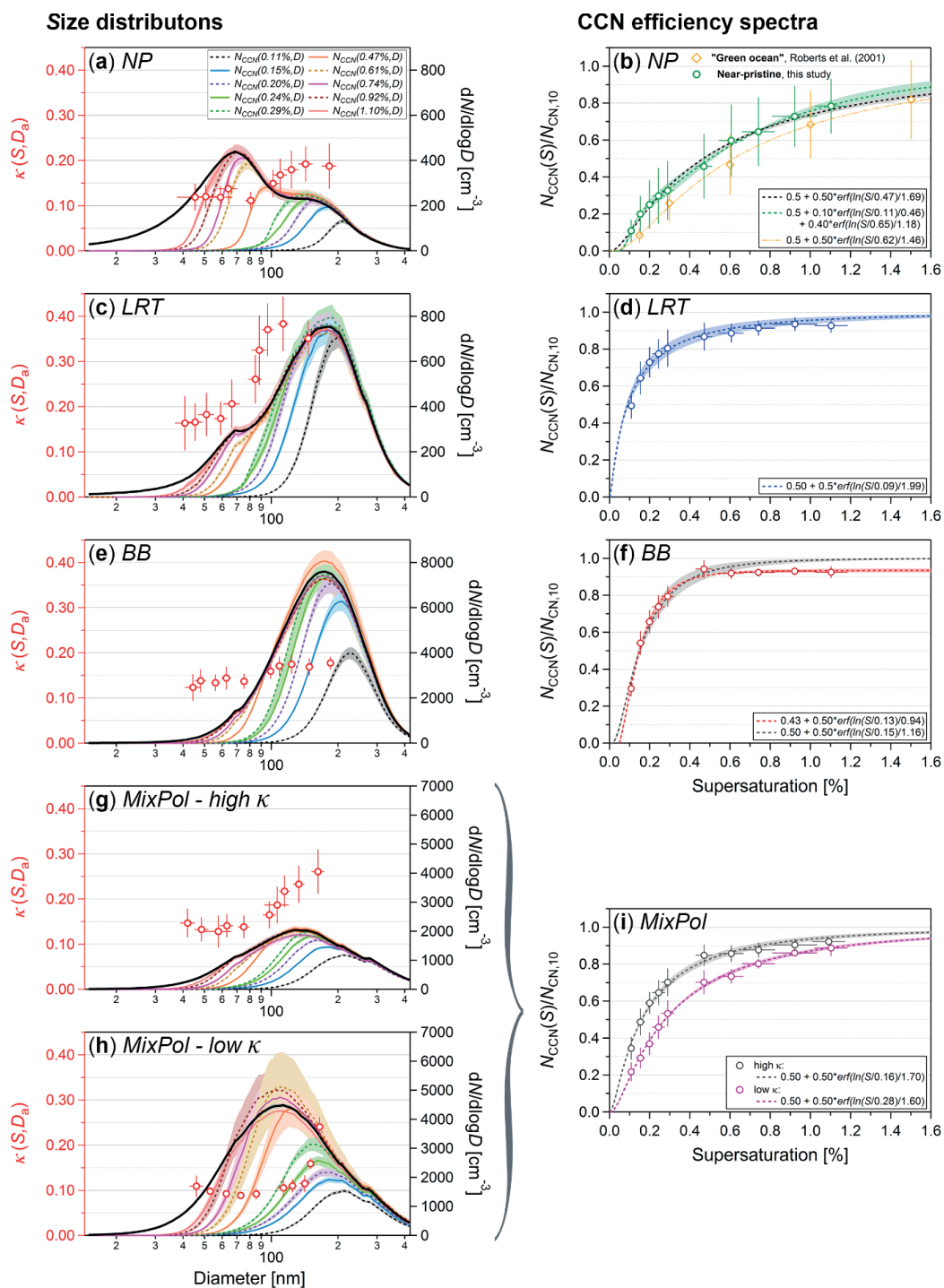
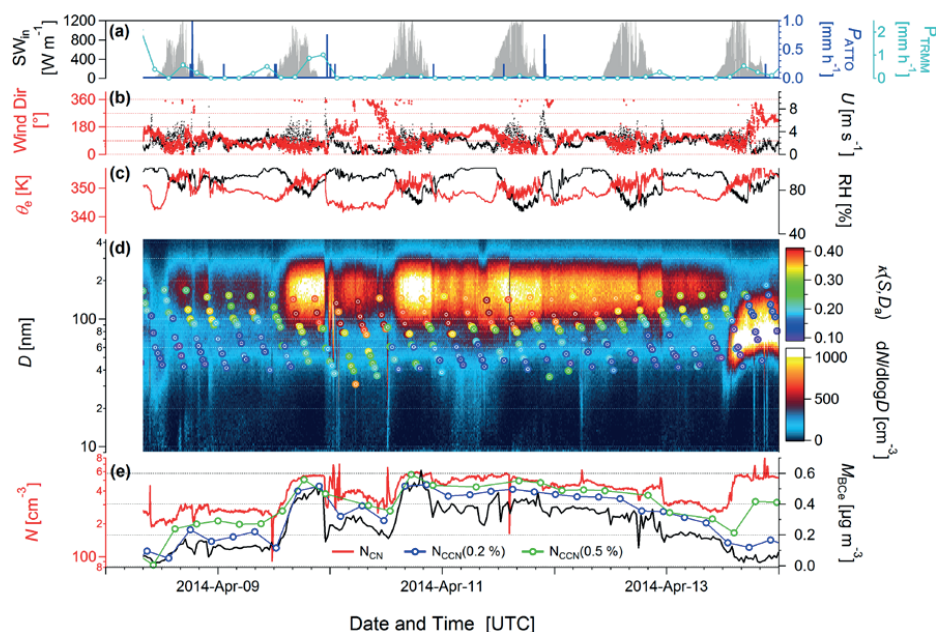
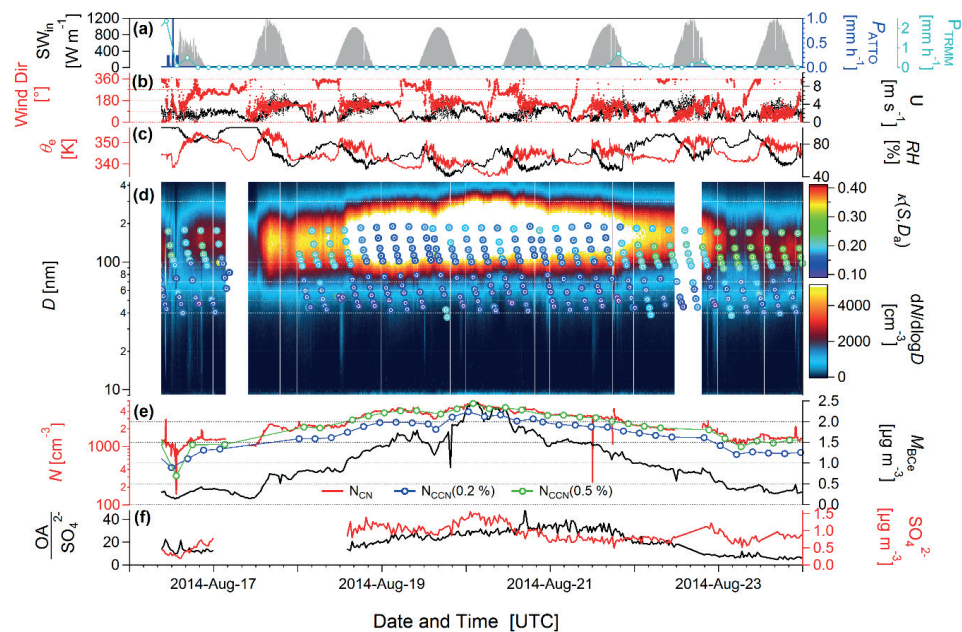




Figure 6. Overview of case studies conditions near-pristine (*NP*), long-range transport of African dust (*LRT*), biomass burning (*BB*), and mixed pollution of African and Amazonian sources (*MixPol*) showing: Size dependence of hygroscopicity parameter  $\kappa(S, D_a)$ , number size distributions of total aerosol particles  $N_{CN}(D)$ , and number size distributions of cloud condensation nuclei  $N_{CCN}(S, D)$  at all 10  $S$  levels ( $S = 0.11$ - $1.10$  %) (left column) and CCN efficiency spectra with erf fits (right column). For the size distributions (left): Values of  $\kappa(S, D_a)$  for every  $S$  level are plotted against their corresponding midpoint activation diameter  $D_a(S)$ . For  $\kappa(S, D_a)$ , the error bars represent 1 std. For  $D_a(S)$ , the experimentally derived error is shown. The standard errors of the number size distributions –  $N_{CN}(D)$  and  $N_{CCN}(S, D)$  – are indicated as shading of the individual lines. For the CCN efficiency spectra (right):  $N_{CN,10}$  was chosen as reference concentration. The experimental data was fitted with single- or double-erf fits (dashed lines with shading as uncertainty of the fits). The error bars at the markers represent the measurement error in  $S$  and 1 std in  $N_{CCN}(S)/N_{CN,10}$  dimension. The shading represents the uncertainty of the fits. An overview of the erf fits from all case studies can be found in Fig. 10. The parameters of all erf fits are summarized in Table 2. Data for *NP* conditions, shown in (a) and (b), represent averages of *all* near-pristine episodes during the entire CCN measurements as defined in Sect. 2.3. For the *NP* CCN efficiency spectra, the double-erf fit is the better representation, although the single-erf fit also works as a good approximation. The CCN efficiency spectrum representing “green ocean” condition according to Roberts et al., (2001) agrees well with the NP data. Data for *LRT* conditions, shown in (c) and (d), represent the *LRT3* period as shown in Fig. 2. A single-erf fit describes the experimental data accurately. Data for *BB* conditions, shown in (e) and (f), represent time period in Aug 2014 as shown in Fig. 4. For the *BB* case, the experimental data has been fitted with a single-erf fit in two modifications: (i) The ‘default’ fit with predefined variables  $v_1 = 0.5$  and  $a_1 = 0.5$  as utilized for all other case studies tends to overestimate  $N_{CCN}(S)/N_{CN,10}$  at high  $S$ . (ii) A corresponding fit with free variables  $v_1$  and  $a_1$  describes the experimental data more accurately. For comparison, CCN efficiency spectra representing rather fresh BB smoke according to Andreae et al., (2004) were added, which agree well with our data on aged BB smoke. Data for *MixPol* conditions, were separated into a *high*  $\kappa$  case (g), presenting sulfate-rich African aerosols and a *low*  $\kappa$  case (h), representing local fire plumes. *MixPol* CCN efficiency spectra are combined in (i) including single-erf fits.



5 **Figure 7.** Selected meteorological, aerosol, and CCN time series from ground-based ATTO site measurements for long-range transport study period *LRT3* (see Fig. 3). (a) Precipitation rates from TRMM satellite mission,  $P_{TRMM}$ , and *in situ* measurements at the ATTO site,  $P_{ATTO}$ . (b) Wind direction and wind speed,  $U$ , at the ATTO site. (c) Equivalent potential temperature,  $\theta_e$ , and relative humidity, RH, at the ATTO site, (d) Overlay of two data layers showing aerosol number size distribution contour plot ( $dN/d\log D$ ) as well as color coded markers, representing time series of  $\kappa(S, D_a)$  size distributions, and (e) CCN concentrations  $N_{CCN}(S)$  for two selected  $S$  levels, total aerosol number concentration  $N_{CN,10}$ , and  $BC_e$  mass concentration  $M_{BC_e}$ .



5 **Figure 8.** Selected meteorological, aerosol, and CCN time series from ground-based ATTO site measurements for biomass burning case study period *BB* (see Fig. 5). (a) Precipitation rates from TRMM satellite mission,  $P_{TRMM}$ , and *in situ* measurements at the ATTO site,  $P_{ATTO}$ . (b) Wind direction and wind speed,  $U$ , at the ATTO site. (c) Equivalent potential temperature,  $\theta_e$ , and relative humidity,  $RH$ , at the ATTO site, (d) Overlay of two data layers showing aerosol number size distribution contour plot ( $dN/d\log D$ ) as well as color coded markers, representing time series of  $\kappa(S, D_a)$  size distributions, and (e) CCN concentrations  $N_{CCN}(S)$  for two selected  $S$  levels, total aerosol number concentration  $N_{CN,10}$ , and  $BC_e$  mass concentration  $M_{BC_e}$ . (f) ACSM-derived sulfate mass concentrations and organic-to-sulfate mass ratio.

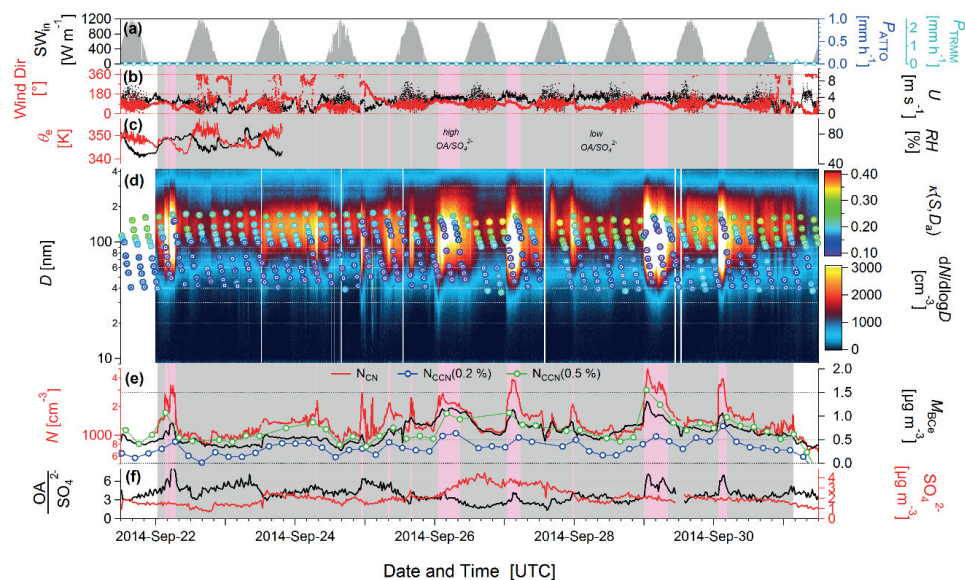
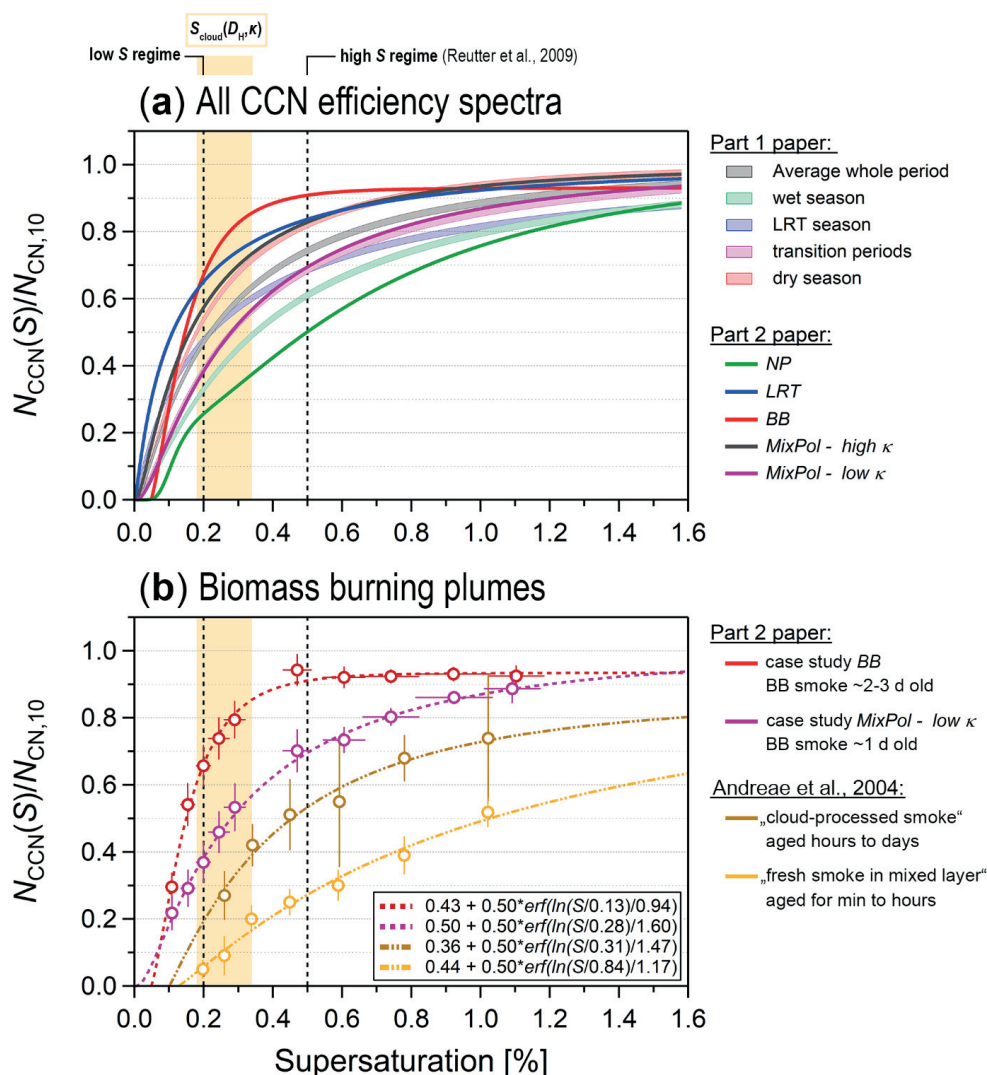


Figure 9. Selected meteorological, aerosol, and CCN time series from ground-based ATTO site measurements for mixed pollution case study period *MixPol* (see Fig. 5). (a) Precipitation rates from TRMM satellite mission,  $P_{TRMM}$ , and *in situ* measurements at the ATTO site,  $P_{ATTO}$ . (b) Wind direction and wind speed,  $U$ , at the ATTO site. (c) Equivalent potential temperature,  $\theta_e$ , and relative humidity,  $RH$ , at the ATTO site, (d) Overlay of two data layers showing aerosol number size distribution contour plot ( $dN/d\log D$ ) as well as color coded markers, representing time series of  $\kappa(S, D_a)$  size distributions, and (e) CCN concentrations  $N_{CCN}(S)$  for two selected  $S$  levels, total aerosol number concentration  $N_{CN,10}$ , and  $BC_e$  mass concentration  $M_{BC_e}$ . (f) ACSM-derived sulfate mass concentrations and organic-to-sulfate mass ratio. The vertical shading highlights episodes under the influence of local/regional fires (red) vs. periods that are dominated by background pollution (grey).



5 Figure 10. Concluding comparison of CCN efficiency spectra. (a) Combination of all case study spectra from present part 2 paper and seasonally averaged spectra from companion part 1 study (M. Pöhlker et al., 2016). (b) Combination of CCN efficiency spectra for biomass burning plumes in different states of atmospheric aging. Spectra originate from *BB* and *MixPol/low  $\kappa$*  case studies in present work as well as from previous study by Andreae et al. (2004). Vertical markers represent low *S* and high *S* regimes according to Reutter et al. (2009) (dashed lines) as well as estimated peak supersaturations at cloud base,  $S_{\text{cloud}}(D_H, \kappa)$  in the ATTO region according to Krüger et al., (2014) (orange shading).

*Supplement of*

**Long-term observations of cloud condensation nuclei in the Amazon rain forest – Part 2: Variability and characteristic differences under near-pristine, biomass burning, and long-range transport conditions**

**Mira L. Pöhlker et al.**

*Correspondence to:* Mira L. Pöhlker (m.pohlker@mpic.de) and C. Pöhlker (c.pohlker@mpic.de)

**This file includes:**

Supplementary Figs. S1 to S7

Supplementary Table S1

Data Tables

References

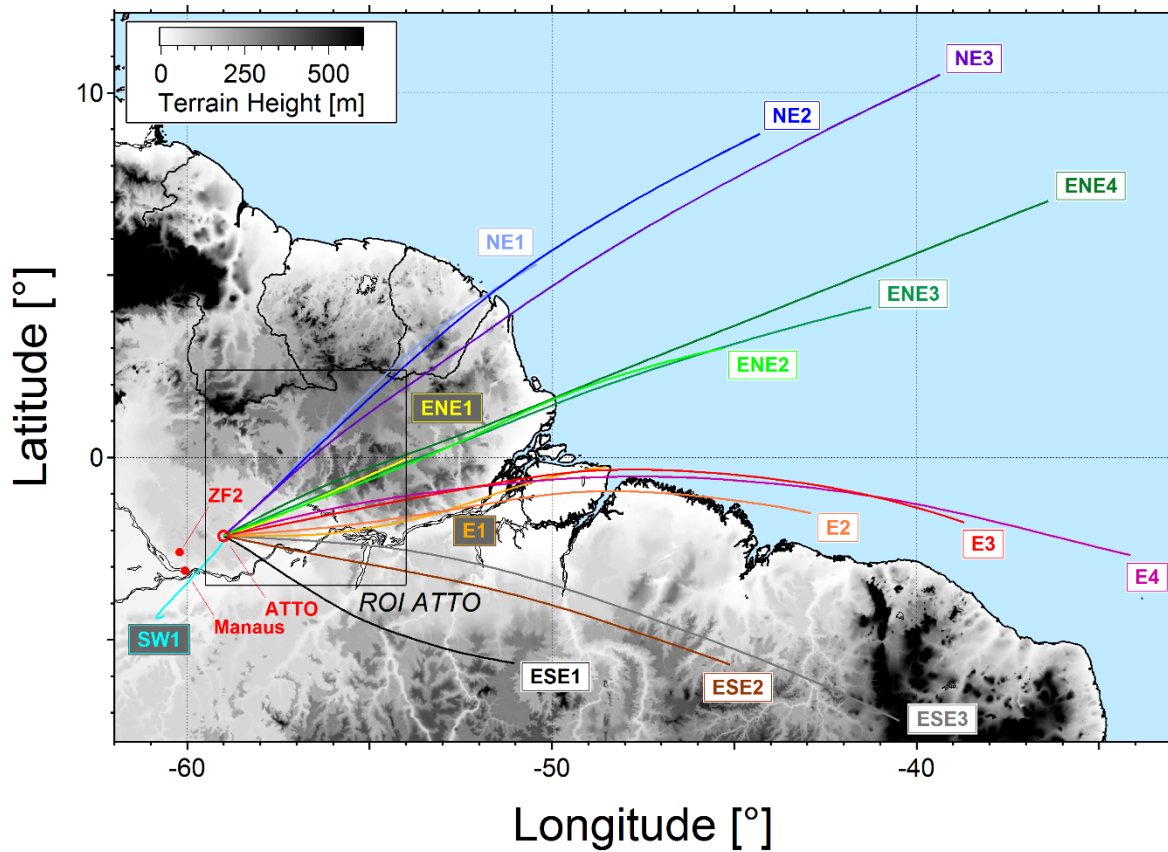
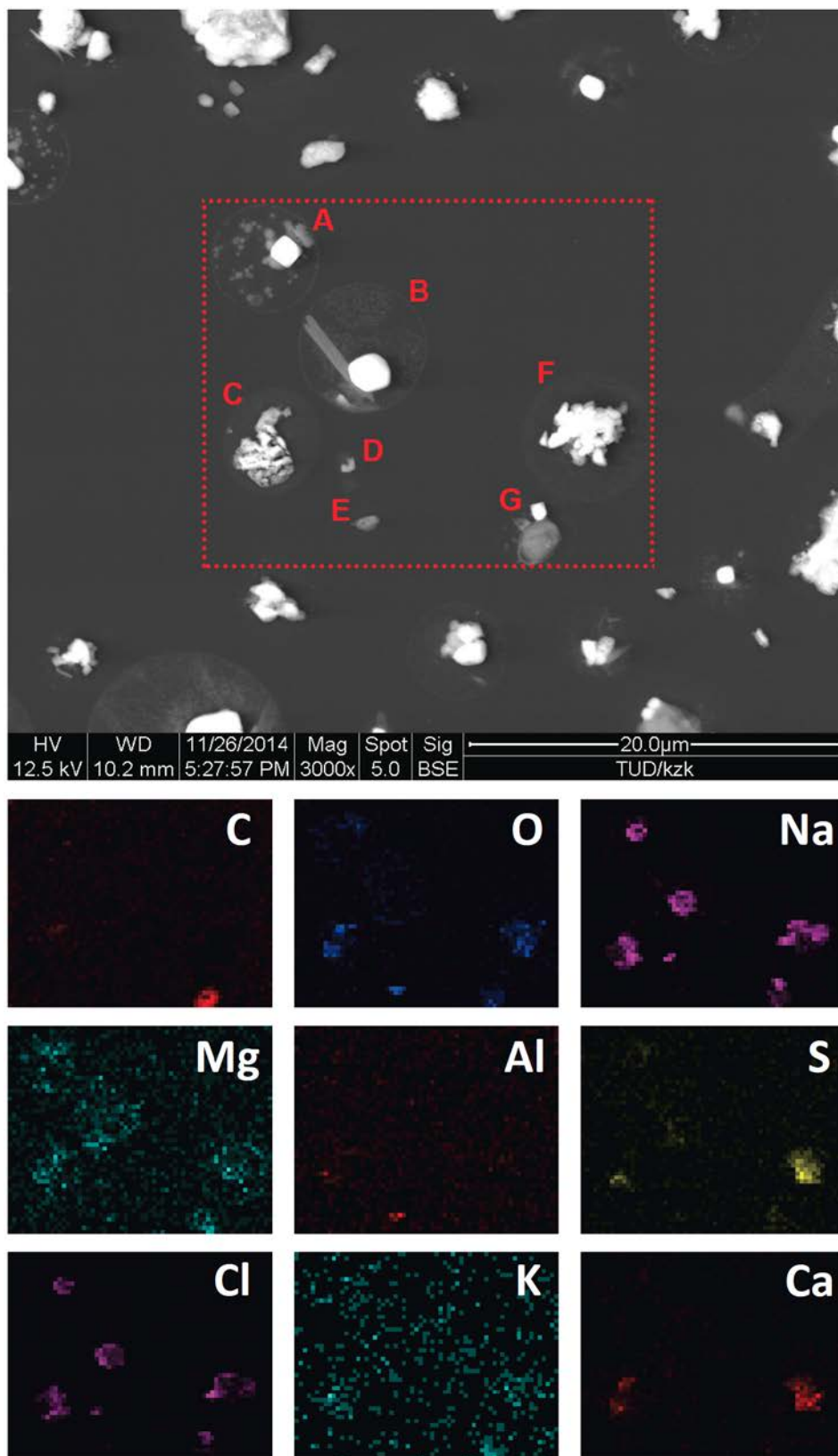


**Figure S1.** Map of northeast Amazon Basin with 15 final clusters from systematic BT cluster analysis based on multi-year BT data (for details see C. Pöhlker et al., 2017). The BT clusters show that air masses arrive at the ATTO site almost exclusively from northeastern to southeastern directions. Five major wind directions can be discriminated: (i) Northeastern clusters NE1, NE2, and NE3; (ii) east-northeastern clusters ENE1, ENE2, ENE3, and ENE4; (iii) eastern clusters E1, E2, E3, and E4; (iv) east-southeastern clusters ESE1, ESE2, and ESE3 and (v) one southwestern cluster SW1. Topographic map is represented by grey scale, which is capped at 600 m. Highlighted area represents region of interest ROI<sub>ATTO</sub>. Figure adapted from C. Pöhlker et al. (2017).



5 **Figure S2.** SEM images and EDX maps for selected aerosol sample showing typical appearance of LRT aerosol population at the ATTO site. Sample shows processed and internally mixed sea spray and dust particles. The results are based on an aerosol sample, collected on 15<sup>th</sup> Feb 2014 during LRT event

2014\_2 according to Moran-Zuloaga et al. (2017), which is comparable (i.e., transport patterns, physicochemical properties recorded by online measurements) to the event discussed as LRT case study in the present work. The particles A, B, and D resemble sea spray particles with a (large) cubic crystal of NaCl as well as weaker signals in Mg, O, and S (likely as MgSO<sub>4</sub>). Morphologically, the particles show similarities to examples of aged sea-salt particles in previous studies (e.g., Laskin et al., 2012). The needle-like structure in particle B could be a CaSO<sub>4</sub> crystal that appears to be too ‘thin’ to give a clear signal in the EDX maps. The particles C and F also show a strong NaCl signal. In addition, they reveal strong signals in S, O, and Ca. These particles resemble CaCO<sub>3</sub> particles from the Saharan dust plume, in which the CO<sub>3</sub><sup>2-</sup> anion was (partly) replaced by SO<sub>4</sub><sup>2-</sup> in the course of atmospheric processing. Similar particles have been described in Laskin et al. (2005). Upon processing, a certain amount of NaCl appears to be mixed in most particles. Particle G comprises a NaCl crystal that is attached to PBAP-like particle (based on morphology and strong C signal). Particle E shows signals in Al and O, which fit to an aluminosilicate particle.

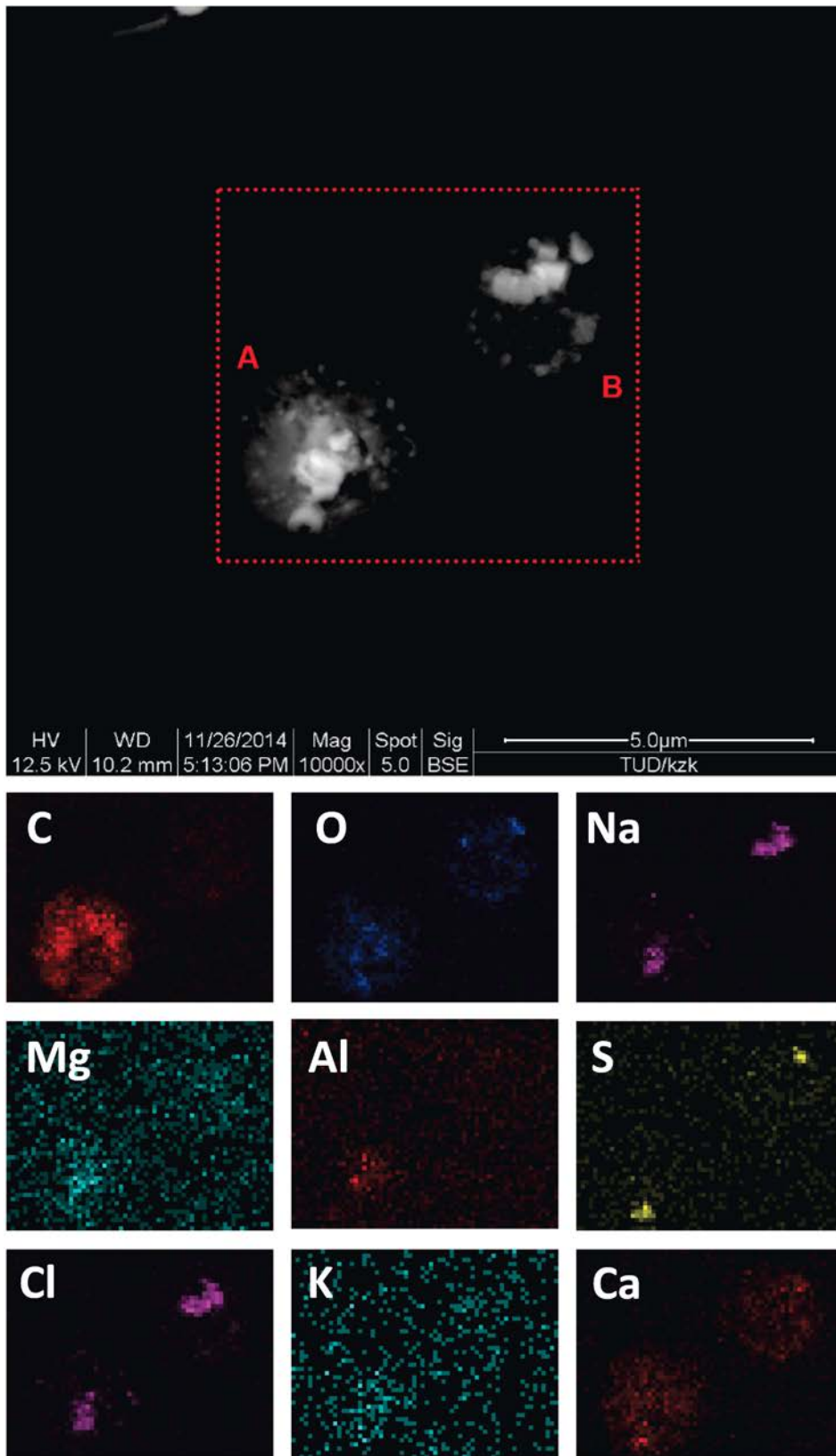


**Figure S3.** SEM images and EDX maps for selected aerosol sample showing a further example of the typical appearance of LRT aerosol population at the ATTO site. Sample shows processed and internally mixed sea spray and dust particles. For further relevant details, refer to caption on Fig. S2.

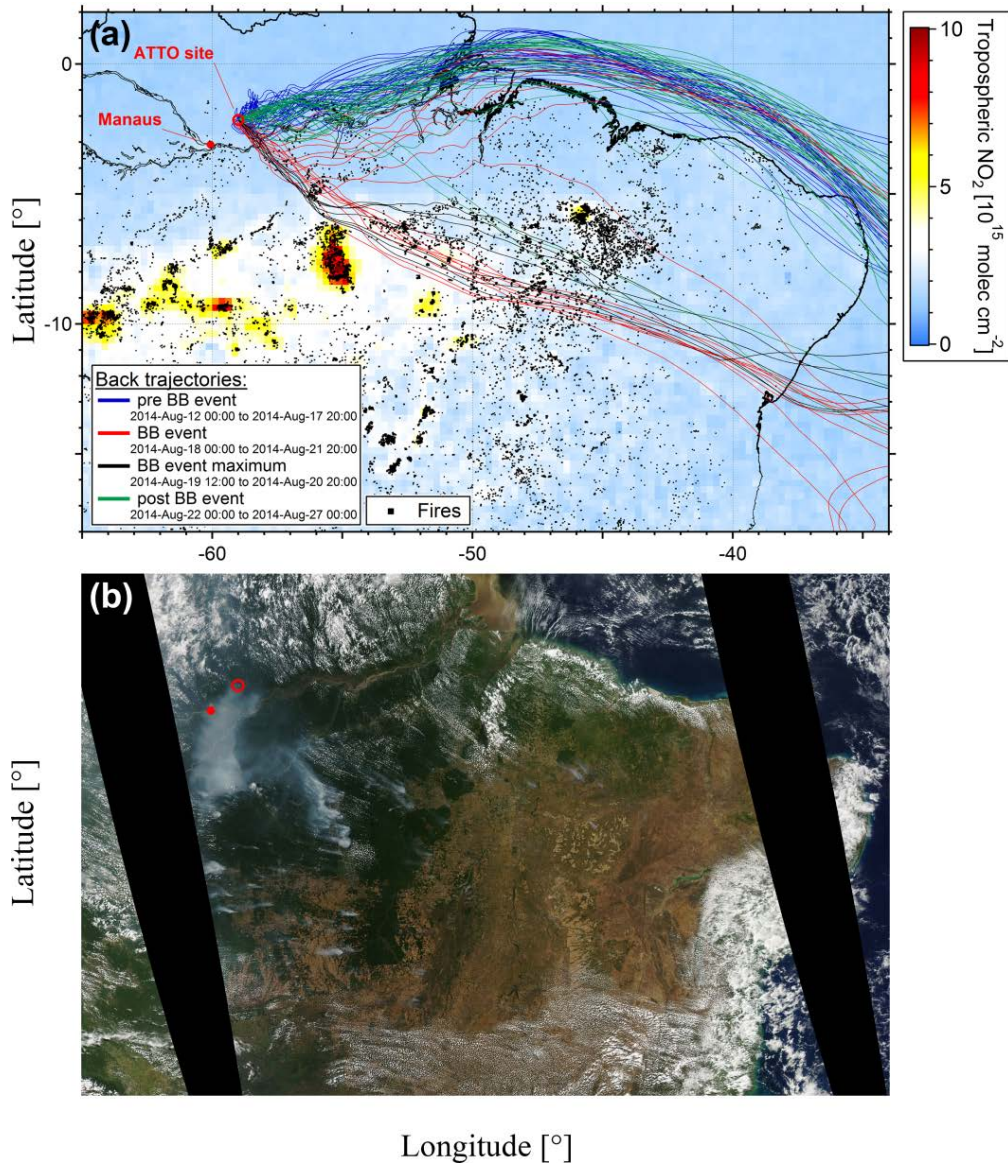


**Figure S4.** Composite maps illustrating origin of strong biomass burning (BB) plume that affected the ATTO site during BB case study period (17 to 23 Aug 2014). (a) Map combines BT ensembles for selected periods (HYSPLIT, NOAA-ARL, GDAS1, start height 200 m, BTs started every 4 h, Draxler and Hess, 1998) with satellite products for active fire counts (MODIS active fire detection extracted from MCD14ML distributed by NASA FIRMS, Justice et al. 2011) and NO<sub>2</sub> atmospheric column (OMI/Aura NO<sub>2</sub> Cloud-Screened Total and Tropospheric Column Daily L3 Global 0.25deg) during same period. BTs are color-coded for characteristic periods before, during, and after biomass burning event. BTs for pollution ‘peak’ at ATTO are color-coded as “BB event maximum”. Map indicates that the BTs’ main track temporarily swings from ‘coastal path’ to ‘inland path’ and back. Inland BTs intersect areas with strong fire activity, as visible in fire counts as well as in NO<sub>2</sub> map (i.e., 7° S, 55° W). The most intense fires are located along the highway BR-163, which is known to be a hotspot of recent deforestation activities (for details, see C. Pöhlker et al., 2017). (b) MODIS corrected reflectance image (taken during Aqua overflight on 19 August 2014 1700UT) confirms that major fires at about 7° S and 55° W have emitted clearly visible smoke plume that travels north-westwards and impacts the ATTO site.

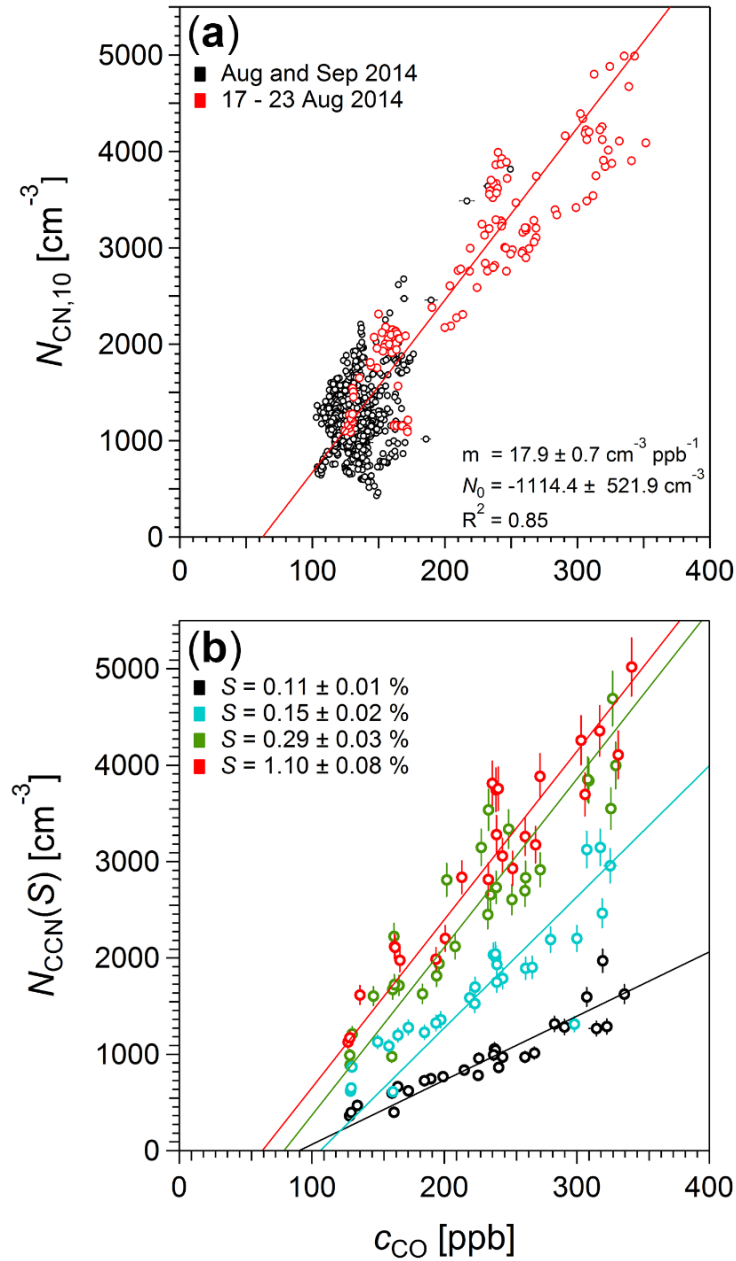


**Figure S5.** Scatter plots of total aerosol concentration  $N_{\text{CN},10}$  and CO mixing ratio  $c_{\text{CO}}$  (hourly average values) with bivariate regression fit in **(a)** and scatter plot of CCN concentrations  $N_{\text{CCN}}(S)$  and CO mixing ratio  $c_{\text{CO}}$  for four selected  $S$  with bivariate regression fit in **(b)**. Data in both cases covers peak period of the biomass burning case study *BB* (see Fig. 4). Error bars show standard errors.

5

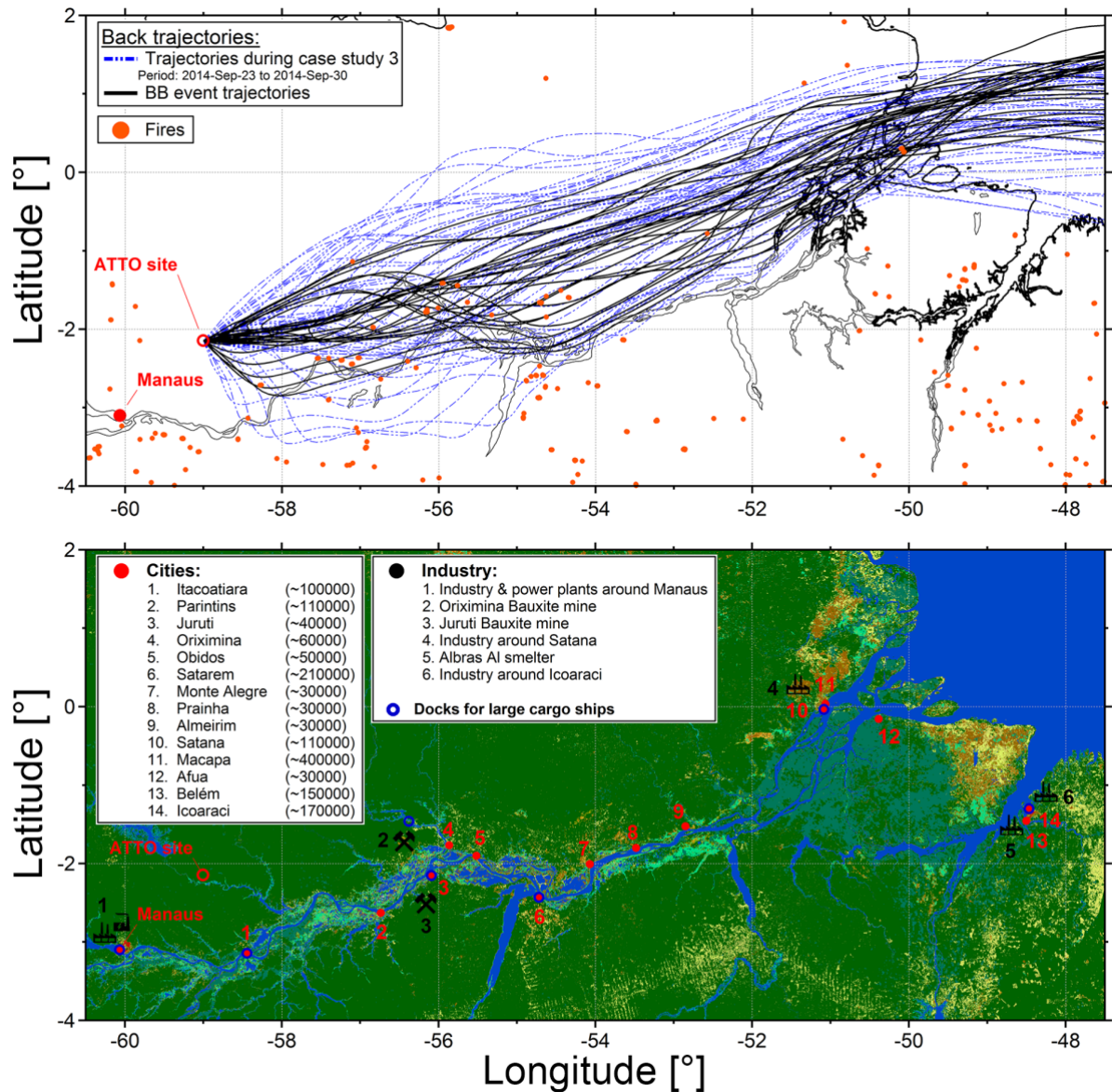


**Figure S6.** Composite maps illustrating conditions during *MixPol* case study (23 to 30 September 2014). Upper map combines back trajectories ensemble for selected periods (HYSPLIT, NOAA-ARL, GDAS1, start height 200 m, trajectories started every 4 h) (Draxler and Hess, 1998) with satellite products for active fire counts (MODIS active fire detection extracted from MCD14ML distributed by NASA FIRMS) (Justice et al., 2011) during same period. Blue trajectories represent ensemble during entire *MixPol* period. Black trajectories highlight episodes with can be attributed to biomass burning plumes (24 Sep 2014 2200UT – 26 Sep 0800UT, 27 Sep 0000UT – 27 Sep 0600UT, 29 Sep 0000UT – 29 Sep 1000UT). Main trajectory track follows westerly direction and passes several (smaller fires) along Amazon River. Lower map shows globcover 2009 data (Arino et al., 2008) and larger cities (population given in parenthesis) as well as larger industrial infrastructure along the Amazon River.

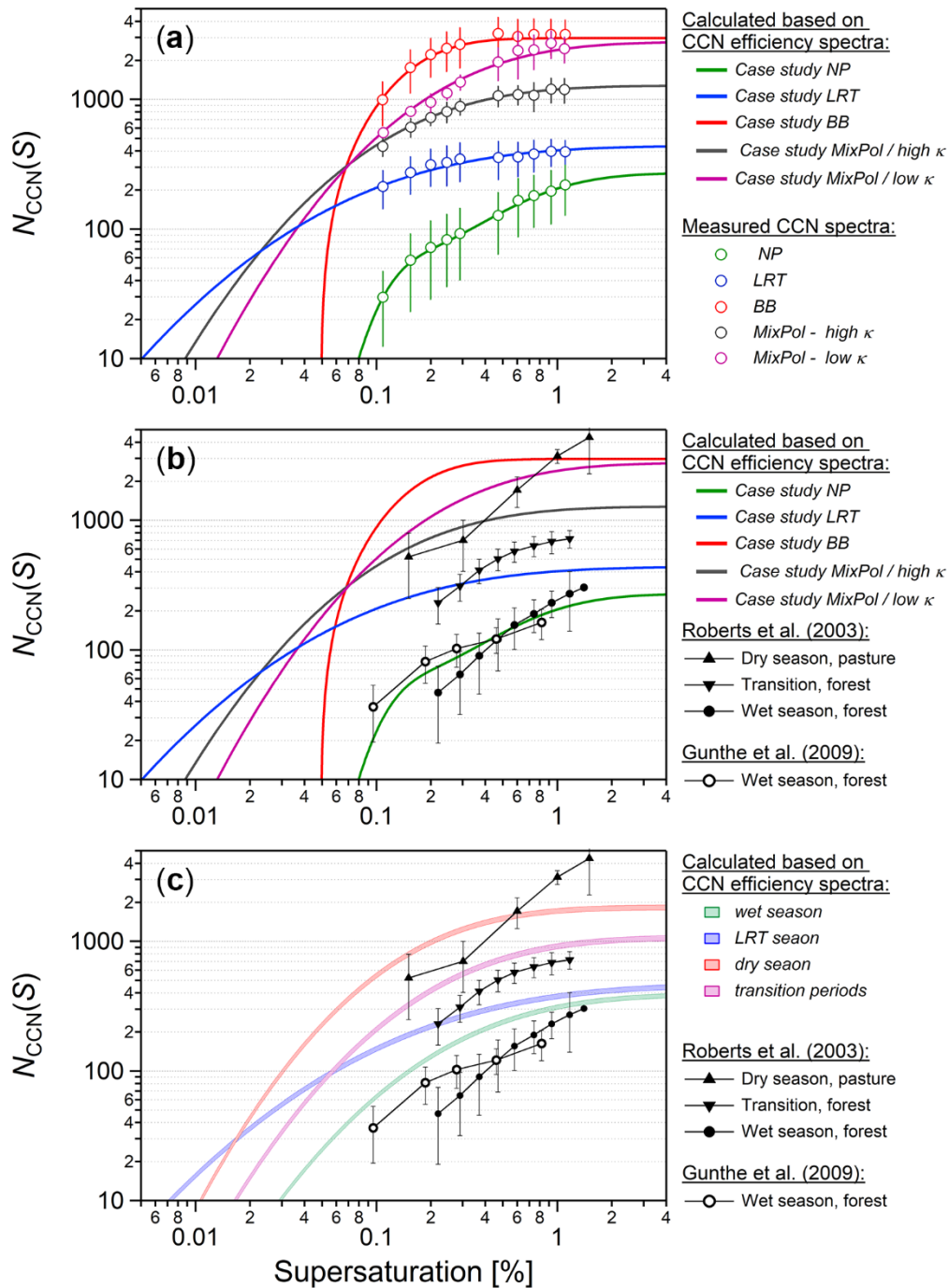


**Figure S7.** Comparison of CCN spectra. (a) Lines represent CCN spectra for case studies as defined in present part 2 paper. CCN spectra were obtained from multiplication of CCN efficiency spectra with average aerosol number concentrations for corresponding case studies. Markers represent measured average CCN concentrations for case study periods. Error bars at markers represent one std. Good agreement of CCN spectra and markers underlines reliability of CCN efficiency spectra in representation of CCN population. (b) Lines represent average CCN spectra for case study periods. Black markers shows CCN spectra from Amazon region as observed and reported by Roberts et al. (2003) based on several weeks of measurement data during the LBA-EUSTACH campaign in 1999 and Gunthe et al. (2009) based on several weeks of measurement data during the AMAZE-08 campaign in 2008. (c) Lines represent average CCN spectra for different seasons as reported in part 1 of this study (Pöhlker et al. 2016). Black markers shows CCN spectra as observed and reported by Roberts et al. (2003) and Gunthe et al. (2009).

## References

- Arino, O., Bicheron, P., Achard, F., Latham, J., Witt, R., and Weber, J.-L.: GLOBCOVER The most detailed portrait of Earth, *Esa Bulletin-European Space Agency*, 24-31, 2008.
- 5 Draxler, R. R., and Hess, G. D.: An overview of the HYSPLIT\_4 modelling system for trajectories, dispersion and deposition, *Australian Meteorological Magazine*, 47, 295-308, 1998.
- Gunthe, S. S., King, S. M., Rose, D., Chen, Q., Roldin, P., Farmer, D. K., Jimenez, J. L., Artaxo, P., Andreae, M. O., Martin, S. T., and Poschl, U.: Cloud condensation nuclei in pristine tropical rainforest air of Amazonia: size-resolved measurements and modeling of atmospheric aerosol composition and CCN activity, *Atmospheric Chemistry and Physics*, 9, 7551-7575, 2009.
- 10 Justice, C., Giglio, L., Roy, D., Boschetti, L., Csiszar, I., Davies, D., Korontzi, S., Schroeder, W., O'Neal, K., and Morisette, J.: MODIS-Derived Global Fire Products, in: *Land Remote Sensing and Global Environmental Change*, edited by: Ramachandran, B., Justice, C. O., and Abrams, M. J., Remote Sensing and Digital Image Processing, Springer New York, 661-679, 2011.
- 15 Laskin, A., Iedema, M. J., Ichkovich, A., Graber, E. R., Taraniuk, I., and Rudich, Y.: Direct observation of completely processed calcium carbonate dust particles, *Faraday Discuss.*, 130, 453-468, 10.1039/b417366j, 2005.
- Laskin, A., Moffet, R. C., Gilles, M. K., Fast, J. D., Zaveri, R. A., Wang, B., Nigge, P., and Shutthanandan, J.: Tropospheric chemistry of internally mixed sea salt and organic particles: Surprising reactivity of NaCl with weak organic acids, *Journal of Geophysical Research-Atmospheres*, 117, 10.1029/2012jd017743, 2012.
- 20 Moran-Zuloaga, D., Ditas, F., Walter, D., Araùjo, A., Brito, J., Carbone, S., Chi, X., Hrabce de Angelis, I., Lavric, J. V., Ming, J., Pöhlker, M. L., Ruckteschler, N., Saturno, J., Wang, Y., Wang, Q., Weber, B., Wolff, S., Artaxo, P., Andreae, M. O., and Pöhlker, C.: Coarse mode aerosols in the Amazon rain forest – A multi-year study on the frequent advection of African dust plumes *Atmos. Chem. Phys.*, 2017.
- 25 Pöhlker, C., Walter, D., Paulsen, H., Könemann, T., Moran-Zuloaga, D., Brito, J., Carbone, S., Degrendele, C., Després, V. R., Ditas, F., Holanda, B. A., Lammel, G., Lavrič, J. V., Jing, M., Pickersgill, D., Pöhlker, M. L., Rodríguez-Caballero, E., Ruckteschler, N., Saturno, J., Sörgel, M., Wang, Q., Weber, B., Wolff, S., Artaxo, P., Pöschl, U., and Andreae, M. O.: Systematic backward trajectory and land cover analyses within the footprint of the remote ATTO site in the central Amazon Basin *Atmos. Chem. Phys.*, to be submitted, 2017.
- 30 Roberts, G. C., Nenes, A., Seinfeld, J. H., and Andreae, M. O.: Impact of biomass burning on cloud properties in the Amazon Basin, *Journal of Geophysical Research-Atmospheres*, 108, 10.1029/2001jd000985, 2003.

**Aerosol characteristics and particle production in the upper troposphere  
over the Amazon Basin**

Meinrat O. Andreae<sup>1,12</sup>, Armin Afchine<sup>2</sup>, Rachel Albrecht<sup>3</sup>, Bruna Amorim Holanda<sup>1</sup>, Paulo Artaxo<sup>4</sup>, Henrique M. J. Barbosa<sup>4</sup>, Stephan Borrmann<sup>1</sup>, Micael A. Cecchini<sup>5,3</sup>, Anja Costa<sup>2</sup>, Maximilian Dollner<sup>6,9</sup>, Daniel Fütterer<sup>6</sup>, Emma Järvinen<sup>10</sup>, Tina Jurkat<sup>6</sup>, Thomas Klimach<sup>1</sup>, Tobias Konemann<sup>1</sup>, Christoph Knote<sup>9</sup>, Martina Krämer<sup>2</sup>, Trismono Krisna<sup>8</sup>, Luiz A. T. Machado<sup>5</sup>, Stephan Mertes<sup>7</sup>, Andreas Minikin<sup>6,16</sup>, Christopher Pöhlker<sup>1</sup>, Mira L. Pöhlker<sup>1</sup>, Ulrich Pöschl<sup>1</sup>, Daniel Rosenfeld<sup>14</sup>, Daniel Sauer<sup>6</sup>, Hans Schlager<sup>6</sup>, Martin Schnaiter<sup>10</sup>, Johannes Schneider<sup>1</sup>, Christiane Schulz<sup>1</sup>, Antonio Spanu<sup>6</sup>, Vicinius B. Sperling<sup>5</sup>, Christine Voigt<sup>6,15</sup>, Adrian Walser<sup>9,6</sup>, Jian Wang<sup>1,11</sup>, Bernadett Weinzierl<sup>6,13</sup>, Manfred Wendisch<sup>8</sup>, and Helmut Ziereis<sup>6</sup>

<sup>1</sup> *Multiphase Chemistry and Biogeochemistry Departments, Max Planck Institute for Chemistry, Mainz, Germany*

<sup>2</sup> *Forschungszentrum Jülich, Jülich, Germany*

<sup>3</sup> *Instituto de Astronomia, Geofísica e Ciências Atmosféricas, Universidade de São Paulo, São Paulo, Brazil*

<sup>4</sup> *Institute of Physics, University of São Paulo, São Paulo, Brazil*

<sup>5</sup> *National Institute for Space Research (INPE), São José dos Campos, Brazil*

<sup>6</sup> *German Aerospace Center (DLR), Institute of Atmospheric Physics (IPA), Weßling, Germany*

<sup>7</sup> *Leibniz Institute for Tropospheric Research, 04318 Leipzig, Germany*

<sup>8</sup> *Leipzig Institute for Meteorology, Leipzig University, Leipzig, Germany*

<sup>9</sup> *Meteorological Institute, Ludwig Maximilian University, Munich, Germany*

<sup>10</sup> *Institute for Meteorology and Climate Research, Karlsruhe Institute of Technology, Karlsruhe, Germany*

<sup>11</sup> *Brookhaven National Laboratory, Upton, New York, USA*

<sup>12</sup> *Scripps Institution of Oceanography, University of California San Diego, La Jolla, California, USA*

<sup>13</sup> *University of Vienna, Aerosol Physics and Environmental Physics, Wien, Austria*

<sup>14</sup> *Institute of Earth Sciences, The Hebrew University of Jerusalem, Israel*

<sup>15</sup> *Institute of Atmospheric Physics (IPA), Johannes Gutenberg University, Mainz, Germany*

<sup>16</sup> *German Aerospace Center (DLR), Flight Experiments, Oberpfaffenhofen, Germany*



1                   **Aerosol characteristics and particle production in the upper troposphere**  
2                   **over the Amazon Basin**

3 Meinrat O. Andreae<sup>1,12</sup>, Armin Afchine<sup>2</sup>, Rachel Albrecht<sup>3</sup>, Bruna Amorim Holanda<sup>1</sup>, Paulo Ar-  
4 taxo<sup>4</sup>, Henrique M. J. Barbosa<sup>4</sup>, Stephan Borrmann<sup>1</sup>, Micael A. Cecchini<sup>5,3</sup>, Anja Costa<sup>2</sup>, Maxi-  
5 milian Dollner<sup>6,9</sup>, Daniel Fütterer<sup>6</sup>, Emma Järvinen<sup>10</sup>, Tina Jurkat<sup>6</sup>, Thomas Klimach<sup>1</sup>, Tobias  
6 Konemann<sup>1</sup>, Christoph Knote<sup>9</sup>, Martina Krämer<sup>2</sup>, Trismono Krisna<sup>8</sup>, Luiz A. T. Machado<sup>5</sup>,  
7 Stephan Mertes<sup>7</sup>, Andreas Minikin<sup>6,16</sup>, Christopher Pöhlker<sup>1</sup>, Mira L. Pöhlker<sup>1</sup>, Ulrich Pöschl<sup>1</sup>,  
8 Daniel Rosenfeld<sup>14</sup>, Daniel Sauer<sup>6</sup>, Hans Schlager<sup>6</sup>, Martin Schnaiter<sup>10</sup>, Johannes Schneider<sup>1</sup>,  
9 Christiane Schulz<sup>1</sup>, Antonio Spanu<sup>6</sup>, Vicinius B. Sperling<sup>5</sup>, Christine Voigt<sup>6,15</sup>, Adrian Walser<sup>9,6</sup>,  
10 Jian Wang<sup>1,11</sup>, Bernadett Weinzierl<sup>6,13</sup>, Manfred Wendisch<sup>8</sup>, and Helmut Ziereis<sup>6</sup>

11

12 <sup>1</sup>Biogeochemistry, Multiphase Chemistry, and Particle Chemistry Departments, Max Planck Institute for Chemistry,  
13 Mainz, Germany

14 <sup>2</sup>Forschungszentrum Jülich, Jülich, Germany

15 <sup>3</sup>Instituto de Astronomia, Geofísica e Ciências Atmosféricas, Universidade de São Paulo, São Paulo, Brazil

16 <sup>4</sup>Institute of Physics, University of São Paulo, São Paulo, Brazil

17 <sup>5</sup>National Institute for Space Research (INPE), São José dos Campos, Brazil

18 <sup>6</sup>German Aerospace Center (DLR), Institute of Atmospheric Physics (IPA), Weßling, Germany

19 <sup>7</sup>Leibniz Institute for Tropospheric Research, 04318 Leipzig, Germany

20 <sup>8</sup>Leipzig Institute for Meteorology, Leipzig University, Leipzig, Germany

21 <sup>9</sup>Meteorological Institute, Ludwig Maximilian University, Munich, Germany

22 <sup>10</sup>Institute for Meteorology and Climate Research, Karlsruhe Institute of Technology, Karlsruhe, Germany

23 <sup>11</sup>Brookhaven National Laboratory, Upton, New York, USA

24 <sup>12</sup>Scripps Institution of Oceanography, University of California San Diego, La Jolla, California, USA

25 <sup>13</sup>University of Vienna, Aerosol Physics and Environmental Physics, Wien, Austria

26 <sup>14</sup>Institute of Earth Sciences, The Hebrew University of Jerusalem, Israel

27 <sup>15</sup>Institute of Atmospheric Physics (IPA), Johannes Gutenberg University, Mainz, Germany

28 <sup>16</sup>German Aerospace Center (DLR), Flight Experiments, Oberpfaffenhofen, Germany

29

30

31

32 **Abstract**

33           Airborne observations over the Amazon Basin showed high aerosol particle concentra-  
34 tions in the upper troposphere (UT) between 8 and 15 km altitude, with number densities (nor-  
35 malized to standard temperature and pressure) often exceeding those in the planetary boundary  
36 layer (PBL) by one or two orders of magnitude. The measurements were made during the Ger-  
37 man-Brazilian cooperative aircraft campaign ACRIDICON-CHUVA on the German High Alti-  
38 tude and Long Range Research Aircraft (HALO). The campaign took place in September/Octo-  
39 ber 2014, with the objective of studying tropical deep convective clouds over the Amazon rain-  
40 forest and their interactions with atmospheric trace gases, aerosol particles, and atmospheric radi-  
41 ation.



42 Aerosol enhancements were observed consistently on all flights during which the UT was  
43 probed, using several aerosol metrics, including condensation nuclei (CN) and cloud condensa-  
44 tion nuclei (CCN) number concentrations and chemical species mass concentrations. The UT  
45 particles differed in their chemical composition and size distribution from those in the PBL, rul-  
46 ing out convective transport of combustion-derived particles from the BL as a source. The air in  
47 the immediate outflow of deep convective clouds was depleted in aerosol particles, whereas  
48 strongly enhanced number concentrations of small particles (<90 nm diameter) were found in UT  
49 regions that had experienced outflow from deep convection in the preceding 5-72 hours. We also  
50 found elevated concentrations of larger (>90 nm) particles in the UT, which consisted mostly of  
51 organic matter and nitrate and were very effective CCN.

52 Our findings suggest a conceptual model, where production of new aerosol particles takes  
53 place in the UT from volatile material brought up by deep convection, which is converted to con-  
54 densable species in the UT. Subsequently, downward mixing and transport of upper tropospheric  
55 aerosol can be a source of particles to the PBL, where they increase in size by the condensation  
56 of biogenic volatile organic carbon (BVOC) oxidation products. This may be an important  
57 source of aerosol particles in the Amazonian PBL, where aerosol nucleation and new particle  
58 formation has not been observed. We propose that this may have been the dominant process sup-  
59 plying secondary aerosol particles in the pristine atmosphere, making clouds the dominant con-  
60 trol of both removal and production of atmospheric particles.

61

## 62 **1. Introduction**

63 Aircraft measurements in the upper troposphere (UT) have consistently shown large re-  
64 gions with very high aerosol particle number concentrations, typically in the tens of thousands of  
65 particles per cm<sup>3</sup>, with the strongest enhancements reported in tropical and subtropical regions  
66 (Clarke et al., 1999; Andreae et al., 2001; de Reus et al., 2001; Twohy et al., 2002; Krejci et al.,  
67 2003; Lee et al., 2003; Young et al., 2007; Ekman et al., 2008; Yu et al., 2008; Froyd et al.,  
68 2009; Weigelt et al., 2009; Borrmann et al., 2010; Clarke and Kapustin, 2010; Mirme et al.,  
69 2010; Weigel et al., 2011; Waddicor et al., 2012; Reddington et al., 2016; Rose et al., 2017). In  
70 most cases, these elevated aerosol concentrations were in the nucleation and Aitken mode size  
71 ranges, i.e., at particle diameters smaller than about 90 nm, with maxima typically between 20  
72 and 60 nm (e.g., de Reus et al., 2001; Lee et al., 2003; Weigel et al., 2011; Waddicor et al.,



73 2012). They generally occur as layers of a few hundred to thousand meters in thickness, often ex-  
74 tending over large horizontal distances, and are found over continents as well as over the most  
75 remote oceanic regions. The high concentrations of these aerosols in the UT are of great signifi-  
76 cance for the climate system, because they make this region an important reservoir of particles  
77 for the transport either downward into the planetary boundary layer (PBL) (Clarke et al., 1999;  
78 Clarke et al., 2013; Wang et al., 2016a) or upward into the Tropical Transition Layer (TTL) and  
79 the lower stratosphere (Weigel et al., 2011; Randel and Jensen, 2013), where they can grow into  
80 the optically and cloud-microphysically active size range.

81 Where enhanced particle concentrations in the accumulation mode (larger than about 90  
82 nm) have been observed, the enrichment was frequently attributed to sources of sulfur dioxide  
83 (SO<sub>2</sub>) and other combustion emissions, especially biomass burning, based on correlations with  
84 combustion tracers, such as carbon monoxide (CO), and air mass trajectories (e.g., Andreae et al.,  
85 2001; Clarke and Kapustin, 2010; Weigel et al., 2011; Clarke et al., 2013). After having been  
86 lofted to the UT by deep convection, particles in this size range can be transported over hemi-  
87 spheric distances, because removal processes are very inefficient at these altitudes (Andreae et  
88 al., 2001; Clarke and Kapustin, 2010).

89 The enhanced particle concentrations in the ultrafine (UF) size range (here defined as parti-  
90 cles smaller than 90 nm), on the other hand, cannot be explained by transport from the lower  
91 troposphere, since they far exceed typical concentrations in the PBL and generally are too short-  
92 lived to survive deep convection and long-range transport. Therefore, nucleation and new parti-  
93 cle formation (NPF) from gas phase precursors brought into the UT by the outflow from deep  
94 convection have been proposed as the source of these enhanced particle concentrations (Clarke et  
95 al., 1999; Twohy et al., 2002; Krejci et al., 2003; Lee et al., 2003; Young et al., 2007; Froyd et  
96 al., 2009; Merikanto et al., 2009; Weigel et al., 2011; Waddicor et al., 2012; Carslaw et al.,  
97 2017). High actinic flux, low preexisting aerosol surface area, and low temperatures make the  
98 UT an environment that is highly conducive to nucleation and NPF.

99 The nature of the gaseous species involved in particle nucleation and growth has been the  
100 subject of some debate (Kulmala et al., 2006). Most of the earlier papers attributed the nucleation  
101 to H<sub>2</sub>SO<sub>4</sub> in combination with H<sub>2</sub>O and NH<sub>3</sub>, especially in marine and anthropogenically influ-  
102 enced regions, where a sufficient supply of sulfur gases from either DMS oxidation or pollution



103 sources is available (e.g., Clarke et al., 1999; Twohy et al., 2002; Lee et al., 2003; Merikanto et  
104 al., 2009). However, there is growing evidence that, in most cases, there is not enough H<sub>2</sub>SO<sub>4</sub>  
105 available to explain the observed rates of growth. Therefore, the condensation of organics has  
106 been proposed to dominate particle growth after nucleation, especially over unpolluted vegetated  
107 areas such as the Amazon Basin (Ekman et al., 2008; Weigel et al., 2011; Waddicor et al., 2012;  
108 Murphy et al., 2015).

109 In fact, H<sub>2</sub>SO<sub>4</sub> may not always be required even to be the initially nucleating species. Re-  
110 cent studies conducted as part of the Cosmics Leaving OUtdoor Droplets (CLOUD) project have  
111 shown that organic vapors alone can produce particle nucleation (Kirkby et al., 2016) and that  
112 nearly all nucleation throughout the present-day atmosphere involves ammonia or biogenic or-  
113 ganic compounds (Dunne et al., 2016). Highly oxygenated multifunctional organic compounds  
114 (HOMs) formed by ozonolysis of  $\alpha$ -pinene were found to nucleate aerosol particles, especially  
115 when aided by ions. Extremely low volatility organic compounds (ELVOCs, which may be at  
116 least in part identical to HOMs) are also produced from the O<sub>3</sub>- or OH-initiated oxidation of bio-  
117 genic volatile organic compounds (BVOCs) (Jokinen et al., 2015). Following nucleation by the  
118 lowest-volatility species, with increasing particle size the condensation of progressively more  
119 volatile compounds is facilitated by the decrease in the Kelvin effect (Tröstl et al., 2016). These  
120 laboratory studies were confirmed by field observations at a mountain site in the free tropo-  
121 sphere, where NPF was found to take place through condensation of HOMs, albeit from anthro-  
122 pogenic precursor VOCs, within 1-2 days after being lofted from the PBL (Bianchi et al., 2016).

123 The production of particles in the UT may be a key component of the atmospheric budget  
124 of optically and cloud-microphysically active aerosols, especially in pristine or relatively unpol-  
125 luted regions, as was suggested in a modeling study by Merikanto et al. (2009). Studies in the  
126 Amazon have shown that NPF almost never takes place under clean conditions in the PBL over  
127 the Amazon Forest (Zhou et al., 2001; Martin et al., 2010; Andreae et al., 2015) and rarely oc-  
128 curs over the taiga forest in remote Siberia (Heintzenberg et al., 2011). Over the Amazon, down-  
129 ward transport of aerosols from the free troposphere (FT) has been identified as an important, if  
130 not dominant, source of particles to the lower troposphere (LT) (Zhou et al., 2001; Roberts and  
131 Andreae, 2003; Wang et al., 2016a). In turn, the concentrations of aerosols in the PBL have a  
132 pronounced influence on the characteristics of convection and thereby influence cloud radiative



133 forcing and atmospheric dynamics (Sherwood, 2002; Rosenfeld et al., 2008; Fan et al., 2012;  
134 Rosenfeld et al., 2014; Stolz et al., 2015; Cecchini et al., 2017).

135 Understanding the processes that control the aerosol burden in the pristine atmosphere is  
136 an essential prerequisite for assessing the magnitude of the climate forcing by anthropogenic aer-  
137 osols, since it forms the baseline from which anthropogenic forcing is derived. Because of the  
138 strong non-linearity of the relationship between particle number concentration and cloud-medi-  
139 ated aerosol effects, the uncertainty regarding the aerosol burden of the pristine atmosphere is the  
140 largest contributor to the uncertainty in estimates of anthropogenic aerosol climate forcing  
141 (Carslaw et al., 2013; Carslaw et al., 2017). For example, model calculations suggest that the in-  
142 clusion of ion-induced particle formation from biogenic HOMs in the natural atmosphere reduces  
143 the cloud-albedo radiative forcing by about one-third because of the higher albedo calculated for  
144 the clouds in the pre-industrial atmosphere (Gordon et al., 2016).

145 In this paper, we present the results of aerosol measurements made in the upper tropo-  
146 sphere across the Amazon Basin during the ACRIDICON-CHUVA campaign on the German  
147 HALO aircraft during September and October 2014 (Wendisch et al., 2016). ACRIDICON  
148 stands for “Aerosol, Cloud, Precipitation, and Radiation Interactions and Dynamics of Convec-  
149 tive Cloud Systems”; CHUVA is the acronym for “Cloud Processes of the Main Precipitation  
150 Systems in Brazil: A Contribution to Cloud Resolving Modeling and to the GPM (Global Precip-  
151 itation Measurement)”. We characterize these UT aerosol particles in terms of their microphysi-  
152 cal and chemical properties, and contrast them with the LT aerosols. From their spatial distribu-  
153 tion and their relationship to deep convection and convective outflow, we derive hypotheses  
154 about their mode of formation. Finally, we discuss the role of upper tropospheric aerosol for-  
155 mation in the life cycle of the atmospheric aerosol.

156

## 157 **2. Methods**

158 The observations discussed in this paper were collected aboard the HALO aircraft  
159 (<http://www.halo.dlr.de/>), a modified Ultra Long Range Business Jet G 550 (manufactured by  
160 Gulfstream, Savannah, USA). Because of its high ceiling altitude (up to 15 km) and long endur-  
161 ance (up to eight hours with a scientific payload), HALO is capable of collecting airborne meas-  
162 urements of cloud microphysical and radiative properties, aerosol characteristics, and chemical



163 tracer compounds in the upper troposphere, in and around tropical deep convective clouds. The  
164 aircraft and its instrumentation are described in the ACRIDICON-CHUVA overview paper by  
165 Wendisch et al. (2016).

166 In-situ meteorological and avionics data were obtained at 1 Hz from the Basic HALO  
167 Measurement And Sensor System (BAHAMAS). This data set includes pressure, temperature,  
168 wind direction and speed, humidity, water vapor mixing ratio, aircraft position, and altitude. All  
169 concentration data have been normalized to standard temperature and pressure ( $T = 273.15$  K  
170 and  $p = 1000$  hPa).

### 171 **2.1. The HALO aerosol submicrometer inlet (HASI)**

172 All aerosol sampling was conducted using the HALO aerosol submicrometer inlet  
173 (HASI), designed for HALO by the German Aerospace Center (DLR) in collaboration with en-  
174 viscope GmbH (Frankfurt, Germany) with the aim of providing up to  $30 \text{ l min}^{-1}$  sample air flow  
175 (divided over four sample lines) to aerosol instruments mounted inside the aircraft cabin. HASI  
176 samples the air on top of the fuselage outside of the aircraft boundary layer. The air stream is  
177 aligned in the inlet using a front shroud and decelerated by a factor of approximately 15. Four  
178 sample tubes with 6.2 mm outer diameter and frontal diffusers protrude into the decelerated air  
179 stream. The design goal is to allow regulating the sample airflow in each of the four sample lines  
180 to achieve isokinetic sampling conditions according to the actual speed of the aircraft. Since the  
181 automatic adjustment had not been implemented at the time of the field experiment, the flow was  
182 fixed to values providing near-isokinetic sampling for typical flight conditions based on geomet-  
183 ric considerations and preliminary flow simulations for the initial design of the inlet. The geo-  
184 metric design should prevent large cloud droplets and ice crystals from entering the sample lines  
185 directly. The inlet position is located in the shadow zone for larger ice crystals, which precludes  
186 artifacts by shattering and break-up of larger ice particles at the inlet tip (Witte, 2008). Judging  
187 from the first measurements with HASI, it appears that measurements of interstitial aerosol in  
188 liquid clouds are affected by artifacts, while in ice clouds there is no indication for such artifacts.  
189 The data selection procedures to exclude artifacts are discussed in section 2.2.



## 190 2.2. Condensation nuclei

191 Condensation nuclei (CN) number concentrations ( $N_{CN}$ ) were measured using the Aerosol  
192 Measurement System (AMETYST). This system was designed to provide an instrument package  
193 for HALO to measure basic microphysical properties of the ambient atmospheric aerosol (inte-  
194 gral number concentration, sub-micrometer size distribution, fraction of non-volatile particles,  
195 and particle absorption coefficient). AMETYST includes four butanol-based condensation parti-  
196 cle counters (CPCs, modified Grimm CPC 5.410 by Grimm Aerosol Technik, Ainring, Ger-  
197 many) with flow rates of 0.6 and 0.3 l min<sup>-1</sup>, configured with different nominal lower cutoff di-  
198 ameters at 4 nm and 10 nm (set via the temperature difference between saturator and condenser).  
199 In addition, two differential mobility analyzers (Grimm M-DMA) with a nominal size range be-  
200 tween 5.5 and 350 nm using <sup>241</sup>Am radioactive sources as aerosol neutralizers are part of the sys-  
201 tem.

202 Two of the four CPCs are generally set to measure the integral particle concentrations,  
203 while for the two other CPCs the configuration is selectable depending on measurement priori-  
204 ties. They can be used either as detectors for the DMAs or for additional integral concentration  
205 measurements. The DMAs can either be set to select specific diameters or operated as a DMPS  
206 (differential mobility particle sizer) system scanning the size distribution at predefined diameter  
207 steps. The integration times at each step have to be chosen such that meaningful statistics can be  
208 achieved depending on the measurement strategy. AMETYST also includes an optional ther-  
209 modenuder, which heats a section of the sample line to 250°C for the measurement of the non-  
210 volatile particle fraction.

211 The raw CPC data are corrected using an empirical, pressure-dependent flow correction  
212 to account for changes in the volume flow at different flight altitudes (D. Fütterer, PhD thesis, in  
213 preparation). Particle losses in the sampling lines have been estimated with the particle loss cal-  
214 culator by von der Weiden et al. (2009). Accounting for these effects leads to an increase of the  
215 effective cutoff diameter for all CPCs. The effective cutoffs are calculated as a convolution of  
216 the pressure-dependent CPC counting efficiency and the size-dependent transmission efficiency  
217 of the sample lines. The data reported here were taken by the CPC operated at 0.6 l min<sup>-1</sup>, with a  
218 nominal cutoff of 4 nm. Due to inlet losses, the effective cutoff diameter increases to 9.2 nm at  
219 1000 hPa, 11.2 nm at 500 hPa, and 18.5 nm at 150 hPa. This implies that the present setup of



220 AMETYST essentially does not detect nucleation mode particles below 10 nm at low altitudes  
221 and below 20 nm in the UT. Typical uncertainties of CPC number concentration measurements  
222 are estimated to be of the order of 5 to 10% (Petzold et al., 2011).

223 To eliminate artifacts from cloud hydrometeors and bias from local pollution, we ex-  
224 cluded measurements using the following criteria: (1) All cloud passages below 6 km were re-  
225 moved. During passages through water clouds, the CPCs showed erratic, unreasonably high  
226 number concentrations that are probably caused by droplet shattering at the probe tip. Cloud pas-  
227 sages were identified from the observation of elevated concentrations of particles  $>3 \mu\text{m}$  using  
228 the hydrometeor probes (see below). (2) In the mixed phase and ice phase regimes, all cloud pas-  
229 sages were inspected for possible shattering artifacts, and suspect data were rejected. Cloud pas-  
230 sages through pure ice clouds did not show evidence of hydrometeor shattering. (3) The flight  
231 segments during departure and approach to Manaus airport were removed to avoid pollution  
232 from the airport and its surroundings. (4) Flights segments through the Manaus urban plume,  
233 which was sampled during joint flight experiments with the DOE G1 aircraft and in the course of  
234 tracer studies in the PBL, were excluded in order to provide a sampling representative of the dry  
235 season atmosphere over the Amazon Basin away from local pollution. (5) Fire plumes that were  
236 sampled deliberately to study fresh emissions were not analyzed for this paper. (6) Segments  
237 where the aircraft passed through its own exhaust were also excluded from the data analysis.

### 238 **2.3. Aitken mode aerosol size spectra**

239 To obtain aerosol size spectra for particle sizes up to 300 nm, the DMAs within  
240 AMETYST were connected to two of the CPCs and operated in scanning mode for selected  
241 flight sequences (especially during longer flight legs, where relatively homogeneous conditions  
242 can be assumed). The size range covered by the scans was typically between 20 and 300 nm di-  
243 ameter in nine steps. To improve the time resolution, the two DMPS were usually set to scan the  
244 same sequence in opposite direction. The DMPS data are then analyzed taking into account a  
245 correction for multiple charges following Wiedensohler (1988) after correcting the measured  
246 concentrations to standard atmospheric conditions. To derive modal parameters for the particle  
247 size distribution, a bi-modal log-normal fit to the data points was computed.



#### 248 **2.4. Accumulation mode aerosol particles**

249 For the purposes of this paper, we define the accumulation mode as the particle size range  
250 from 90 nm to 600 nm and the total number concentration in this size class as the accumulation  
251 mode number concentration,  $N_{acc}$ . The particle concentrations in this range were measured with  
252 an optical particle counter (OPC), the Ultra High Sensitivity Aerosol Spectrometer (UHSAS;  
253 Droplet Measurement Technologies, Inc., Longmont, CO) (Cai et al., 2008; Brock et al., 2011).  
254 The UHSAS combines a high-power infrared laser ( $\lambda=1054$  nm) and a large solid angle range in  
255 sideways direction for the detection of light scattered by individual particles. Due to the resulting  
256 almost monotonic increase of instrument response with particle size, the UHSAS enables high-  
257 resolution measurements (100 selectable channels). The high laser intensity enables the detection  
258 of particle diameters down to about 60 nm, with the upper limit being approximately 1  $\mu\text{m}$ . Parti-  
259 cle concentrations of up to 3000  $\text{cm}^{-3}$  are recorded without significant counting coincidence  
260 losses (Cai et al., 2008). The airborne instrument version is mounted in an under-wing canister  
261 and equipped with a forward facing diffusor inlet. The slowed airflow is subsampled by a second  
262 inlet at approximately isokinetic conditions. The sample is not actively dried before the measure-  
263 ment, but due to combined heating effects the measured diameters can be assumed to be close to  
264 their dry diameters (Chubb et al., 2016). The UHSAS was calibrated with monodisperse polysty-  
265 rene latex (PSL) spheres of known refractive index and size. The evaluation of the OPC calibra-  
266 tion results and the derivation of realistic uncertainty estimates for the OPC size distributions is  
267 outlined in a recent study by Walser et al. (2017). Due to changes in the laser and instrument pa-  
268 rameter settings during the campaign, only the size range from  $\sim 90$  nm to  $\sim 600$  nm is considered  
269 here.

#### 270 **2.5. Cloud condensation nuclei**

271 The number concentration of CCN ( $N_{CCN}$ ) was measured with a continuous-flow stream-  
272 wise thermal gradient CCN counter (CCNC, model CCN-200, DMT, Longmont, CO, USA)  
273 (Roberts and Nenes, 2005; Rose et al., 2008). The CCN-200 consists of two columns, in which  
274 particles with critical supersaturations ( $S$ ) above a preselected value are activated and form water  
275 droplets. Droplets with diameters  $\geq 1$   $\mu\text{m}$  are detected by an optical particle counter (OPC) at the  
276 exit of the column. The inlet flow rate of the column used was 0.5  $\text{L min}^{-1}$  with a sheath-to-aero-  
277 sol flow ratio of 10. The water pump was operated at the CCNC setting of “high” liquid flow.



278 Variations in ambient pressure have a strong influence on the  $S$  inside the CCNC. For this pur-  
279 pose, a novel constant pressure inlet without significant particle losses was deployed on HALO.  
280 The instrument was calibrated before, during, and after the campaign at different pressures and  
281 flow rates according to Rose et al. (2008). For the data used in this study, we sampled from the  
282 HASI inlet and measured at  $S = 0.52 \pm 0.05\%$  and a time resolution of 1 Hz.

283 Since the flow in the instrument was kept constant for the data used here, the error in  $S$   
284 resulted from the calibration uncertainty, as described by M. Pöhlker et al. (2016); it is estimated  
285 to be in the range of 10%. According to Krüger et al. (2014), the error in  $N_{CCN}$  is based on the  
286 counting error of the measured particle number and is 10% of  $N_{CCN}$  for large concentrations; given  
287 that mostly low concentrations prevailed, the mean error was about 20% of  $N_{CCN}$ .

## 288 2.6. Cloud droplet and ice particle measurements

289 While measurements of liquid water and ice hydrometeor concentrations are not a subject  
290 of this paper, they were used to determine whether the aircraft was sampling inside clouds and if  
291 so, whether the cloud particles were liquid or frozen. For this purpose, we used data from the  
292 Cloud Droplet Probe (CDP) and the Cloud and Aerosol Spectrometer (CAS-DPOL), both of  
293 which are based on the principle of forward scattering detection. The CDP detects particles with  
294 sizes from 3  $\mu\text{m}$  to 50  $\mu\text{m}$ , and classifies them into size histograms of bin widths between 1 and  
295 2  $\mu\text{m}$ . The CAS-DPOL covers the size range of 0.6-50  $\mu\text{m}$  in 17 bins of varying width. The  
296 probes are described in Voigt et al. (2017) and probes and data correction techniques in Weigel  
297 et al. (2016).

298 Information regarding the ice particle properties was obtained from the Particle Habit Im-  
299 aging and Polar Scattering Probe (PHIPS-HALO), a single-particle cloud probe that measures  
300 microphysical and angular light scattering properties of individual particles (Abdelmonem et al.,  
301 2016). The instrument is composed of a stereoscopic imager that takes two brightfield images  
302 from the particles under a viewing angle difference of  $120^\circ$ . Simultaneously to collecting the im-  
303 ages, the scattering part of the instrument measures the angular scattering function of the parti-  
304 cles from  $18^\circ$  to  $170^\circ$  with an angular resolution of  $8^\circ$ . The optical resolution of the imager is  
305 about 2.5  $\mu\text{m}$ .



## 306 **2.7. Aerosol mass spectrometer**

307 For in-situ chemical analysis of submicrometer aerosol particles a compact time-of-flight  
308 aerosol mass spectrometer (C-ToF-AMS) (Drewnick et al., 2005; Schmale et al., 2010) was op-  
309 erated onboard HALO. The C-ToF-AMS was sampling through the HASI inlet for ambient aero-  
310 sol measurements. The aerosol particles enter the instrument via a pressure-controlled inlet and  
311 are focused into a narrow beam by an aerodynamic lens. In the vacuum chamber, the particles  
312 are flash-vaporized and the resulting gas-phase molecules are ionized by electron impact. The  
313 ions are guided into the Time-of-Flight mass spectrometer, separated by their mass-to-charge ra-  
314 tio, and detected by a microchannel plate detector. The C-ToF-AMS was operated with a time  
315 resolution of 30 seconds, providing mass concentrations of particulate organics, nitrate, sulfate,  
316 chloride, and ammonium.

## 317 **2.8. Refractory black carbon**

318 An eight-channel Single Particle Soot Photometer (SP2) was used to detect and quantify  
319 refractory black carbon (rBC) particles using laser-induced incandescence (Stephens et al., 2003;  
320 Schwarz et al., 2006). The instrument measures the time-dependent scattering and incandescence  
321 signals produced by individual aerosol particles when crossing a Gaussian-shaped laser beam  
322 (Nd:YAG;  $\lambda = 1064$  nm). The particles containing rBC cores absorb the laser light and evaporate  
323 within the optical chamber emitting thermal radiation (incandescence). The peak intensity of the  
324 incandescence signal, recorded by two photomultiplier tubes over two different wavelength inter-  
325 vals, is linearly proportional to the mass of the rBC in the particle (Laborde et al., 2013). The in-  
326 strument is sensitive to rBC cores in the nominal size range of 70 - 500 nm mass-equivalent di-  
327 ameter, assuming a density of  $1.8 \text{ g cm}^{-3}$ . The SP2 also detects the intensity of the light scattered  
328 by the particles using an avalanche photo-detector in order to determine the optical size of purely  
329 scattering particles in the diameter range of 200 - 400 nm.

330 The SP2 incandescence signal was calibrated several times (at the beginning, during, and  
331 at the end of the campaign) using size-selected fullerene soot particles. The scattering signal was  
332 calibrated using either spherical polystyrene latex size standards (208, 244, and 288 nm) or am-  
333 monium sulfate particles of different diameters selected by a differential mobility analyzer  
334 (DMA).



## 335 **2.9. Trace gases**

336 Ozone ( $O_3$ ) was measured by a dual-cell ultraviolet (UV) absorption detector (TE49C,  
337 Thermo Scientific) operating at a wavelength of 254 nm. Signal differences from a cell with the  
338 sample air and a parallel cell with ozone-scrubbed air are used to infer the concentration of  $O_3$ .  
339 Sample air was drawn into the instruments through the standard HALO gas inlet via a Teflon  
340 PFA line using an external pump at a nominal flow rate of  $1 \text{ l min}^{-1}$ . The calibration of the instru-  
341 ment is traceable to the  $O_3$  standard of the Global Atmosphere Watch station at Hohenpeißen-  
342 berg, Germany. The data output of the instrument is corrected for the temperature and pressure in  
343 the absorption cells. The precision of the  $O_3$  measurements is 2% or 1 ppb, whichever is larger,  
344 the accuracy is 5%. Details on the use of this instrument can be found in Huntrieser et al. (2016).

345 Carbon monoxide (CO) was detected with a fast-response fluorescence instrument  
346 (AL5002, Aerolaser, Garmisch, Germany) (Gerbig et al., 1999). The detection of CO is based on  
347 the excitation of CO at 150 nm using a  $CO_2$  resonance UV lamp. The fluorescence light is de-  
348 tected by a UV-sensitive photomultiplier. The CO detector was calibrated in-flight using onboard  
349 calibration and zero gas sources. Data are recorded at 1 Hz. The precision and accuracy are 3 ppb  
350 and 5%, respectively.

351 Nitrogen monoxide (NO) and total reactive nitrogen ( $NO_y$ ) were measured by a dual-  
352 channel chemiluminescence detector (CLD-SR, Eco Physics). For the  $NO_y$  channel, the chemilu-  
353 minescence detector is combined with a custom-built Au converter which reduces all oxidized  
354 reactive nitrogen species to NO (Ziereis et al., 2000). Detection of ambient NO is performed via  
355 reaction with  $O_3$  in a chamber and the luminescence signal of the excited  $NO_2$  produced by this  
356 reaction. Both detector channels are equipped with a pre-reaction chamber for determination of  
357 cross-reactions of  $O_3$  with interfering species. Sampling of ambient air is conducted via a stand-  
358 ard HALO gas inlet using a Teflon line. The precision and accuracy of the measurements depend  
359 on the ambient concentrations, typical values are 5% and 7% (NO) and 10% and 15% ( $NO_y$ ), re-  
360 spectively.

## 361 **2.10. Trajectories and air mass history analysis**

362 Backtrajectories were calculated for each minute, starting at the location of the HALO  
363 aircraft and using the FLEXPART (“FLEXible PARTicle”) Lagrangian Particle Dispersion



364 Model version 9.02 (Stohl et al., 1998; Stohl and Thomson, 1999; Seibert and Frank, 2004; Stohl  
365 et al., 2005). Trajectories were driven by six-hourly analyses, interlaced with the three-hour fore-  
366 casts, from the Global Forecast System (GFS) of the National Centers for Environmental Predic-  
367 tion (NCEP), provided on a 0.5 x 0.5 degree horizontal grid  
368 (<http://www.nco.ncep.noaa.gov/pmb/products/gfs/>, last accessed 8 Sep 2016). For each trajec-  
369 tory, 10,000 ‘particles’ (infinitesimally small air parcels) are released and followed back in time  
370 for 10 days. Sub-grid-scale processes like convection and turbulence act stochastically on each  
371 ‘particle’, resulting in a trajectory location probability distribution at each point in time. For con-  
372 venience, the location probability distribution is simplified using a clustering algorithm, calculat-  
373 ing five cluster centers of most probable trajectory locations (Stohl et al., 2002). Additional tra-  
374 jectory calculations were performed using the HYSPLIT model (Stein et al., 2015) with NCEP  
375 GDAS1 data and model vertical velocities.

376 We examined the history of the sampled airmasses for interactions with deep convection  
377 using the FLEXPART trajectories and GOES (Geostationary Operational Environmental Satel-  
378 lite) imagery. Every one-minute flight position was traced back in time in one-hour steps up to  
379 120 hours. Each position was then matched in time to the closest GOES-13 (Geostationary Oper-  
380 ational Environmental Satellite) infrared brightness temperature ( $T_b$ ). As a proxy for deep con-  
381 vection, we searched for cloud top  $T_b$  below  $-30\text{ }^\circ\text{C}$  and looked up the minimum  $T_b$  in a  $1^\circ \times 1^\circ$   
382 box around the center of the back-traced parcel. An example of this procedure is available in the  
383 Supplement (Figs. S1-S3). From these data, we recorded the time difference between the mo-  
384 ment that HALO was sampling the airmass and its encounter with deep convection, possibly in-  
385 cluding multiple contacts with deep convection. We also noted the “deepest convection” (mini-  
386 mum  $T_b$ ) encountered by the parcels and their height at the time of the encounter, as well as the  
387 number of hours that the parcel was within boxes with deep convection ( $T_b < -30\text{ }^\circ\text{C}$ ).

### 388 **3. Results and Discussion**

#### 389 **3.1. The ACRIDICON-CHUVA campaign**

390 The ACRIDICON-CHUVA flights covered most of the Amazon Basin, reaching from the  
391 Atlantic coastal waters in the east to near the Colombian border in the west, and from the Guy-



392 anas border in the north to the arc of deforestation in the south. The flight tracks of the flights an-  
393 alyzed in this paper are shown in Fig. 1, where the flight segments at altitudes >8 km are shown  
394 as heavier lines.

### 395 **3.2. Synoptic situation and chemical context**

#### 396 3.2.1. Meteorological overview

397 During boreal summer, the Intertropical Convergence Zone (ITCZ) undergoes a seasonal  
398 northward shift towards the northernmost part of South America, so that almost all of the Ama-  
399 zon Basin is in the meteorological Southern Hemisphere. Examination of cloud top height and  
400 precipitation images showed that the ITCZ was located between about 4 and 12 °N during the  
401 campaign (6 Sep to 1 Oct 2014), but was often not very well defined over South America  
402 ([worldview.earthdata.nasa.gov](http://worldview.earthdata.nasa.gov), accessed 13 Jan 2017). This seasonal shift establishes the large-  
403 scale thermodynamic conditions that define the dry season over the Amazon Basin, characterized  
404 by synoptic-scale subsidence, a relatively dry planetary boundary layer (PBL) and mid-tropo-  
405 sphere, and warm temperatures at the top of the PBL, resulting in elevated convective inhibition  
406 energy (CINE) (Fu et al., 1999; Wang and Fu, 2007; Collow et al., 2016). During the dry season,  
407 there is less shallow convection, cloud cover, and rainfall than in the wet season, but the convec-  
408 tion that does occur is more organized with pronounced vertical development because of the sim-  
409 ultaneous presence of high convective available potential energy (CAPE) and high CINE  
410 (Machado et al., 2004; Collow et al., 2016; Giangrande et al., 2017; Zhuang et al., 2017). The  
411 deep convective cloud fraction peaks in the late afternoon and evening (1600LT to 2400LT) with  
412 a cloud fraction maximum between 9 and 13 km altitude and a minimum near and above the  
413 freezing level between 4 and 7 km (Collow et al., 2016; Zhuang et al., 2017).

414 During the ACRIDICON-CHUVA campaign, the intense warm sea-surface temperature  
415 (SST) anomaly that had earlier prevailed in the southern South Atlantic and a less intense cold  
416 SST anomaly in the northern South Atlantic and near the Equator were strongly reduced, and a  
417 warm SST anomaly in the equatorial Pacific was building to form the 2015 El Nino (see also  
418 Martin et al., 2016). Consequently, the pattern of wind and omega (vertical motion) field anoma-  
419 lies decreased to nearly normal conditions. However, during the campaign there was a clear  
420 northeast-southwest contrast with drier conditions in the northeast and wetter ones in the south-  
421 west, as seen in the columnar precipitable water anomaly data from the NCEP Climate Forecast



422 System Version 2 Reanalysis (Fig. 2) (Saha et al., accessed 20 March 2017). The majority of  
423 HALO flights were over the drier anomaly or the neutral region. As a consequence of this drier  
424 anomaly, these regions presented warmer temperatures and lower relative humidity than the nor-  
425 mal climatology. The synoptic pattern during the campaign resulted in a spatial rainfall distribu-  
426 tion with a meridional pattern, with more intense rainfall in the west, around 300 mm in Septem-  
427 ber, and less than 100 mm in the eastern Amazon (Fig. 3). Nine cold fronts penetrated into Brazil  
428 during September, however, only two moved northward and they had little interaction with Ama-  
429 zon convection. Only the cold front on 20 to 23 September was able to organize convection in  
430 the south of the Amazon Basin.

431 Figures 4a and 4b show the low (850 hPa) and high (200 hPa) level wind fields during  
432 September 2014. The mean low-level flow at 850 hPa shows the typical easterly winds through-  
433 out the Amazon Basin (Fig. 4a), decelerating near the Andes and curving to the subtropics. At  
434 high levels (Fig. 4b), there is a weak anticyclonic circulation over the southern basin, featuring  
435 the initial increased deep convection in the transition from the dry to the wet season (September)  
436 and the development of the Bolivian High during the onset of the wet season (December to  
437 March) (Virji, 1981; Zhou and Lau, 1998).

438 During the research flights, HALO reached maximum altitudes of 12.6 to 14.4 km a.s.l.,  
439 corresponding to potential temperatures between 352 and 360 K (Fig. 5), i.e., the bottom of the  
440 tropical tropopause layer (TTL). The vertical profiles of temperature and potential temperature  
441 were remarkably consistent between the flights, showing a fairly stable stratification up to about  
442 8 km and a slightly weaker gradient in potential temperature above this altitude. Relative humid-  
443 ity shows a broad minimum in the region between 6 and 10 km. For comparison, the data from  
444 radiosonde soundings at Manacapuru (a site southwest of Manaus) are provided in the supple-  
445 ment (Fig. S4).

446 Based on the soundings, the mean height of the thermal tropopause during the campaign  
447 was  $16.9 \pm 0.6$  km, corresponding to a potential temperature of about 380 K. During September  
448 2014, the mean CAPE was  $1536 \text{ J kg}^{-1}$  and the mean CINE value was  $37 \text{ J kg}^{-1}$ , the precipitable  
449 water was 42 mm, the lifting condensation level 919 hPa, and the bulk shear  $4.8 \text{ m s}^{-1}$  (difference  
450 between the mean wind speed in the first 6 km and 500 meters). These values give a clear idea



451 about the typical cloud base expected, the high instability, the need of a forcing due to the CINE,  
452 the high shear, and the amount of integrated water vapor.

453 In this paper, we use the following terminology to describe the different layers of the  
454 tropical atmosphere: The region from the surface to the convective cloud base (typically about  
455 1.2 to 1.7 km during mid-day) is the planetary boundary layer (PBL), above which is the convec-  
456 tive cloud layer (CCL), which typically reached to altitudes of about 4-5 km during our cam-  
457 paign. The region between the CCL and the TTL is the free troposphere (FT), which we subdivi-  
458 de into the middle troposphere (MT) between about 5 km and 9 km and the and the upper tropo-  
459 sphere (UT) above ca. 9 km.

#### 460 3.2.2. Airmass origins and history

461 For an overview of airmass movement in the UT over the central Amazon during the  
462 campaign, we obtained trajectory frequency statistics for airmasses arriving at altitudes between  
463 10 and 14 km over the central Amazon Basin. The frequency analysis indicated that airmass  
464 movement in the upper troposphere was generally relatively slow and tended to follow anticy-  
465 clonic patterns (Fig. 6), consistent with the 200 hPa streamlines shown in Fig. 4b. The frequency  
466 diagram for the 72-h trajectories initialized at 12 km altitude (Fig. 6a) shows that most airmasses  
467 had remained over the basin for the preceding three days (only about 1% of the endpoints fall  
468 outside of the basin). The 10 and 14 km statistics show essentially the same patterns (Supplement  
469 Figs. S5-S6), as do the individual trajectories calculated from the aircraft positions along the  
470 flight tracks (not shown).

471 The 120-h trajectory statistics (Fig. 6b) and the examination of the individual trajectories  
472 along the flight tracks indicate that the air sampled in the UT had followed a number of different  
473 general flow patterns before being sampled by HALO: 1) flow from the Pacific with an anticy-  
474 clonic loop of variable extent over the basin, ranging from almost zonal west-to-east flow to a  
475 huge loop going as far south as Argentina and as far east as the Atlantic, and then returning to the  
476 basin (types A and B in Table 1), 2) flow from the Atlantic, often almost zonal (type C), 3) inter-  
477 nal circulation within the basin, usually along anticyclonic loops, but sometimes erratic (type D),  
478 and 4) flow from the Caribbean, often following an anticyclonic pattern (type E). The flow pat-  
479 terns of the UT airmasses that were enriched in aerosol particles are given in Table 1.



480 3.2.3. Atmospheric chemical environment

481 The atmospheric chemical environment over the Amazon Basin shows a pronounced sea-  
482 sonal variation (Talbot et al., 1988; Andreae et al., 1990b; Talbot et al., 1990; Andreae et al.,  
483 2002; Artaxo et al., 2002; Martin et al., 2010; Andreae et al., 2012; Artaxo et al., 2013; Andreae  
484 et al., 2015). During the rainy season, regional biomass burning is at a minimum and biological  
485 sources dominate trace gas and aerosol emissions in the basin, resulting in often near-pristine  
486 conditions. The most significant pollution input during this season is long-range transport from  
487 North and West Africa, which brings in a mixture of mineral dust and emissions from biomass  
488 and fossil fuel burning (Talbot et al., 1990; Wang et al., 2016b). In contrast, ACRIDICON-  
489 CHUVA took place during the dry season, when the Amazon Basin is impacted by a mixture of  
490 pollution from regional and remote sources (Andreae et al., 1988; Talbot et al., 1988; Artaxo et  
491 al., 2013). Deforestation and pasture-maintenance burning occurs throughout the basin, with the  
492 highest intensity along the southern periphery, the so called “arc of deforestation”. This creates a  
493 steep gradient of pollutant concentrations from the relatively moist and less densely developed  
494 northern and western basin to the drier and highly deforested and developed southern basin  
495 (Andreae et al., 2012).

496 Long-range transport from Africa affects pollution levels over the Amazon, in addition to  
497 regional sources. In the northern part of the basin, part of the 10-day backtrajectories arriving at  
498 the aircraft positions in the lower troposphere reach West Africa, where biomass burning and  
499 fossil-fuel emissions are prevalent, while other trajectories follow the northeastern coast of Bra-  
500 zil, which is densely populated. As one moves south, the influence of long-range transport from  
501 Southern Africa becomes more prevalent. This was clearly observed during flight AC19, which  
502 extended over the Atlantic east of the Brazilian coast. On this flight, an extended, 300-m thick  
503 layer of pollution at 4 km altitude was identified over the Atlantic with elevated rBC concentra-  
504 tions up to  $2 \mu\text{g m}^{-3}$  (see section 3.4.4). The backtrajectories from the Amazon south of the Equa-  
505 tor very frequently end in the central and eastern tropical Atlantic (see Fig. 3 in Andreae et al.,  
506 2015), where high levels of ozone, aerosols, and other pollutants from biomass burning have  
507 been documented by in-situ and satellite observations starting in the 1980s (Watson et al., 1990;  
508 Fishman et al., 1991; Andreae et al., 1994; Browell et al., 1996; Fishman et al., 1996).



### 509 3.3. Vertical distribution of aerosol particle number concentrations over the Amazon Basin

510 Figure 7a shows a statistical summary of all CN number concentrations ( $N_{\text{CN}}$ ) observed  
511 during the campaign. Data affected by local pollution and cloud artifacts have been removed as  
512 discussed in section 2.2. (Additional information about the flight segments on which elevated  
513  $N_{\text{CN}}$  were encountered is provided in Table 1.) In the PBL, which typically reached heights of 1.4  
514 to 1.8 km during the afternoon, mean  $N_{\text{CN}}$  ranged from  $\sim 750 \text{ cm}^{-3}$  on the least polluted flights to  
515  $\sim 4500 \text{ cm}^{-3}$  in the most polluted regions over the southern part of the basin. Above the PBL, CN  
516 concentrations typically remained relatively high within the lower troposphere up to about 3–4  
517 km, and then declined with altitude.  $N_{\text{CN}}$  reached a minimum of  $\sim 700 \text{ cm}^{-3}$  at about 4–5 km alti-  
518 tude everywhere over the basin. This aerosol minimum coincides with the minimum in cloud  
519 cover that has been observed at and above the freezing level, which has been suggested to be as-  
520 sociated with rain development by the Wegener-Findeisen-Bergeron process at this level  
521 (Collow et al., 2016).

522 Above this level, we found a general increase in particle concentrations, such that above 8  
523 km,  $N_{\text{CN}}$  were typically in the range of 2000 to  $10,000 \text{ cm}^{-3}$ . This altitude corresponds approxi-  
524 mately to the 340 K potential temperature level, above which elevated CN concentrations had  
525 also been found in previous studies (Borrmann et al., 2010; Weigel et al., 2011).

526 While the statistical plot in Fig. 7a shows a general particle enrichment in the UT, indi-  
527 vidual vertical profiles show more complex structures (Fig. 7b). The highest  $N_{\text{CN}}$ , sometimes  
528 reaching up to  $65,000 \text{ cm}^{-3}$ , were encountered in thin layers often only a few hundreds of meters  
529 thick. A distinct example for such a layer is seen in the descent profile (segment A2) from flight  
530 AC09 (Fig. 4b), with peak CN concentrations of ca.  $35,000 \text{ cm}^{-3}$ . Other profiles, e.g., the descent  
531 profile from flight AC07 (segment G), show enhancements over a layer about 3 km thick, with  
532  $N_{\text{CN}}$  of  $10,000 - 20,000 \text{ cm}^{-3}$ .

533 The CN enrichments in the UT consist predominantly of ultrafine particles in the size  
534 range below 90 nm. In contrast to  $N_{\text{CN}}$ , the enhancement of accumulation mode particles ( $N_{\text{acc}}$ ,  
535 defined here as the particles in the size range 90 to 600 nm) in the UT is much less pronounced.  
536 The concentration of accumulation mode particles in the LT typically ranged from  $\sim 500$  to  
537  $\sim 3000 \text{ cm}^{-3}$ , depending on the level of pollution (Fig. 8a). Like the vertical profile of  $N_{\text{CN}}$ , the  
538 profile of  $N_{\text{acc}}$  also shows a decrease above the LT to a minimum around 4–5 km, followed by an



539 increase towards the upper troposphere. Over the more polluted regions in the southern basin,  
540  $N_{acc}$  in the UT was often considerably lower than in the LT.

541 Figure 8b illustrates the different behavior of CN and accumulation mode particle number  
542 concentrations at the example of a sounding in the central Amazon Basin from flight AC19. In  
543 the LT,  $N_{CN}$  and  $N_{acc}$  have similar values and decline to a minimum at about 4.7 km. Above this  
544 altitude,  $N_{CN}$  shows several sharp concentration peaks, with one at about 7.4 km reaching con-  
545 centrations around  $65,000 \text{ cm}^{-3}$ . These peaks are only weakly, if at all, reflected in  $N_{acc}$ , which  
546 shows a broad enhancement in the UT to values around  $1000 \text{ cm}^{-3}$ . Consequently, we find two  
547 types of aerosol enrichments in the UT: at one extreme, thin layers with extremely high  $N_{CN}$  val-  
548 ues but no significant increase in particles larger than 90 nm, at the other, broad overall particle  
549 enrichments with modest values of both  $N_{CN}$  and  $N_{acc}$ .

### 550 **3.4. Differences between UT and LT aerosols**

551 The high concentrations of particles in the UT over the Amazon Basin beg the question of  
552 their origin. Three different mechanisms can be considered: vertical transport of particles from  
553 the PBL by deep convection, horizontal long-range transport from remote source regions, and in-  
554 situ new particle formation. To assess these possibilities, we discuss in the following sections the  
555 chemical and physical properties of the UT aerosols and contrast them with the LT aerosol.

556 A first argument against vertical transport as the dominant source mechanism for the  
557 large particle concentrations in the UT comes simply from the observed CN concentrations.  
558 Since we are using concentrations normalized to standard temperature and pressure,  $N_{CN}$  should  
559 not change with vertical transport alone, and the values measured in the UT should not exceed  
560 those measured in the PBL. The fact that CN concentrations in the UT across the entire Amazon  
561 Basin are higher than the PBL values we measured anywhere in the basin, often by very large  
562 factors, rules out vertical transport of particles from the Amazon PBL as the dominant source of  
563 UT particles.

#### 564 **3.4.1. Particle size**

565 The particles in the UT have a very different size distribution from those in the LT, which  
566 also shows that they could not have originated from upward transport of PBL aerosols by deep  
567 convection. Unfortunately, a detailed analysis of the size distribution of the particles in the UT is



568 hampered by the significant losses of small particles in our inlet system. As discussed in section  
569 2.2, the particle losses increase with altitude such that in the UT most of the particles below ca.  
570 20 nm are lost in the inlet system before reaching the CPC. Because of a longer inlet tubing con-  
571 nection and lower sample flow, the losses were even more significant for the DMPS, and as a re-  
572 sult of this and other operational limitations, valid particle size distributions are only available  
573 from the LT.

574 The DMPS measurements in the LT showed that the aerosol size distribution was domi-  
575 nated by an accumulation mode centered at about 190 nm, flanked by an Aitken mode with a  
576 maximum at about 80 nm (Fig. 9), in good agreement with the size distributions measured previ-  
577 ously at ground level in the Amazon (Zhou et al., 2002; Rissler et al., 2006; Andreae et al., 2015;  
578 Pöhlker et al., 2016) and those obtained over the Amazon on the G1 aircraft during the GoAma-  
579 zon 2014 campaign (Martin et al., 2016; Wang et al., 2016a). For comparison, we show size  
580 spectra from GoAmazon 2014 from Wang et al. (2016a), the only published size spectra from the  
581 FT over central Amazonia. Unfortunately, even these data reach only up to 5.8 km, the ceiling  
582 altitude of the G1 aircraft. In the PBL, these spectra were similar to our measurements from the  
583 LT. With increasing altitude, total particle concentrations increased and the size spectrum be-  
584 came dominated by an Aitken mode at ca. 50 nm (Wang et al., 2016a). A previous study over the  
585 northern Amazon in Suriname had also found a decrease in the modal diameter of the Aitken  
586 mode from ~70 nm in the LT to ~30 nm in the UT above 10 km (Krejci et al., 2003). Assuming  
587 that similar size distributions prevailed in the UT during ACRIDICON-CHUVA and given the  
588 fact that inlet losses limited our measurements to particle diameters >20-30 nm, it seems justified  
589 to conclude that our  $N_{CN}$  concentrations in the UT are actually lower limits and that the true con-  
590 centrations might have been significantly higher.

591 In the absence of full size spectra, we use the ultrafine fraction [UFF, defined as the frac-  
592 tion of particles with diameters between 90 nm (the lower cutoff of the UHSAS) and ~20 nm  
593 (the lower cutoff of the CPC), i.e.,  $UFF = (N_{CN} - N_{acc})/N_{CN}$ ] as a metric for the contribution of the  
594 Aitken and nucleation modes to the total observed particle concentration. The summary profile  
595 plot (Fig. 10a) shows the dramatic difference between the UFF in the LT and UT: In the LT, the  
596 mean UFF is about 0.05 to 0.2, showing the dominance of the accumulation mode. The share of  
597 ultrafine particles increases throughout the middle troposphere, and in the UT they account for  
598 the vast majority of particles, with UFF values around 0.7 in regions where both  $N_{acc}$  and  $N_{CN}$  are



599 moderately enriched, and values approaching 1.0 in the layers with very high  $N_{CN}$ . This shows  
600 up more clearly in individual profiles, e.g., the soundings in Fig 10b from flight AC18. The  
601 highly enriched layers are represented by UFF peaks in the range of 0.7 to 1.0, whereas the back-  
602 ground UT enrichment exhibits UFF values of 0.5 to 0.8. The highest UFF values were measured  
603 in the very young aerosol layer in segment E2 at 13.5 km (Fig. 10b), with an estimated particle  
604 age of about 1-5 hours (more on this layer in section 3.5.2).

### 605 3.4.2. Cloud nucleating properties

606 The cloud nucleating ability of aerosol particles depends both on their size and their  
607 chemical composition. Here we focus on CCN concentrations at 0.52% supersaturation ( $N_{CCN0.5}$ ),  
608 which are dominated by the particles in the accumulation mode size range, but also include a  
609 fraction of the Aitken mode. A full discussion of the CCN measurements during ACRIDICON-  
610 CHUVA will be presented elsewhere (M. Pöhlker et al., 2017, in preparation).

611 Figure 11a shows the vertical distribution of CCN for the entire campaign, indicating  
612 strong variability in the LT, a minimum at ca. 5 km, and elevated concentrations in the UT. The  
613  $N_{CCN0.5}$  variability in the LT was related to the variable level of pollution, mostly from biomass  
614 burning, which was much higher in the southern part of the basin than in the north. In contrast,  
615 there was no systematic difference between the CCN concentrations in the UT above polluted  
616 and relatively clean regions. Therefore, depending on the level of pollution in the lower tropo-  
617 sphere, the  $N_{CCN0.5}$  in the UT during our campaign were higher or lower than those in the LT.  
618 This is illustrated at the example of  $N_{CCN0.5}$  profiles from Flights AC09 and AC12+13, from a  
619 clean region (AC09) and one polluted by biomass burning emissions (AC12+13), respectively  
620 (Fig. 11b). While there was a large difference in the CCN concentrations in the LT, the values in  
621 the UT were very similar between these flights, indicating that the CCN enrichments in the UT  
622 are independent of the pollution levels in the LT.

623 The CCN concentrations at a supersaturation  $S=0.52\%$  in the UT were consistently  
624 greater than the corresponding values of accumulation particle number concentrations,  $N_{acc}$ , re-  
625 sulting in a median  $N_{CCN0.5}/N_{acc}$  ratio of 1.66 (quartile range 1.32 – 2.32,  $N=53,382$ ) above 8 km.  
626 This implies that some of the particles smaller than 90 nm are also able to nucleate cloud drops at  
627  $S=0.52\%$ . Because size-selective CCN measurements were not performed during ACRIDICON-  
628 CHUVA, it was not possible to derive the actual critical diameters and hygroscopicity factors ( $\kappa$ ,



629 Petters and Kreidenweis, 2007) for the CCN on this campaign. However, a consistency check  
630 can be made using the measured chemical composition. As will be discussed in detail in section  
631 3.4.4, the UT particles consist predominantly of organic material, with minor amounts of nitrate  
632 and very small fractions of sulfate. The hygroscopicity of particles consisting completely of or-  
633 ganic matter can vary greatly, with  $\kappa$  between near 0 and about 0.3 (Jimenez et al., 2009). Our  
634 AMS measurements (see section 3.4.4) showed that the UT secondary organic aerosol (SOA)  
635 contains a substantial fraction of organics derived from the oxidation of isoprene (IEPOX-SOA)  
636 (Schulz et al., 2017), which has relatively high hygroscopicity ( $\kappa \geq 0.1$ ) (Engelhart et al., 2011;  
637 Thalman et al., 2017). Assuming a conservative value of  $\kappa_{\text{org}} \cong 0.1$ , which had been found previ-  
638 ously for the Amazon PBL (Gunthe et al., 2009; Pöhlker et al., 2016), pure SOA particles would  
639 have to have diameters of  $\geq 80$  nm to act as CCN at 0.52% supersaturation, whereas for pure am-  
640 monium sulfate particles ( $\kappa \cong 0.6$ ), the critical diameter would be ca. 45 nm (Petters and  
641 Kreidenweis, 2007). At a typical organic mass fraction of 0.8 for the UT aerosol (see section  
642 3.4.4), an effective  $\kappa$  of ca. 0.2, corresponding to a critical diameter of  $\sim 65$  nm, is likely. Given  
643 the expected steep increase in particle concentration between the  $N_{\text{acc}}$  cutoff of 90 nm and the es-  
644 timated critical diameter of 65 nm, a  $N_{\text{CCN}0.5}/N_{\text{acc}}$  ratio of the observed magnitude appears thus  
645 quite reasonable.

646 The vertical distribution of the CCN fraction, i.e., the ratio  $N_{\text{CCN}0.5}/N_{\text{CN}}$ , shows a pro-  
647 nounced decrease with altitude (Fig. 12a), reflecting the smaller particle size in the UT. It also  
648 exhibits a strong inverse relation to the total particle concentration,  $N_{\text{CN}}$ . This is illustrated at the  
649 example of flight AC18 (Fig. 12b), where the data from different flight segments are plotted.  
650 Segments A and F (yellow and orange) are from soundings in the somewhat more polluted cen-  
651 tral part of the Amazon Basin, while B and C (green) are from the cleaner westernmost part and  
652 show the lowest CCN concentrations and the highest CCN fractions. Both soundings have high-  
653 CN layers at altitudes between 7 and 13 km, with  $N_{\text{CN}}$  up to almost  $23,000 \text{ cm}^{-3}$ , and correspond-  
654 ingly low  $N_{\text{CCN}0.5}/N_{\text{CN}}$ . Segment E2 (red) is from a layer that was intercepted downwind of a  
655 massive convective complex, with a transport time of 1-5 hours between the anvil and the air-  
656 craft (see section 3.5.2). This layer had  $N_{\text{CN}}$  values up to  $45,000 \text{ cm}^{-3}$ , CCN fractions down to  
657 0.01, and  $\text{UFF} \cong 0.98$ , suggesting that these recently formed particles were too small to act as  
658 CCN. This layer was embedded in a region of moderately elevated CN (segment E1 at 13-14 km;  
659 lilac), which had much higher  $N_{\text{CCN}0.5}/N_{\text{CN}}$  (0.2-0.5) and lower UFF (0.6-0.8), indicating larger



660 particle sizes and likely a more aged aerosol. Segment D (blue), at 11-12 km altitude, had similar  
661 properties to E1. These observations point to the presence of two distinct aerosol populations in  
662 the UT. At one extreme are aerosols with very high  $N_{CN}$  and ultrafine fractions and low CCN  
663 fractions (e.g., E2), presumably representing newly formed particles with sizes too small to act as  
664 CCN. At the other extreme are populations with modest  $N_{CN}$ , but high UFF and CCN fractions,  
665 indicating a more aged aerosol with larger particles (e.g., E1 and D).

666 The existence of these two populations is confirmed in plots of  $N_{CCN0.5}$  and  $N_{CCN0.5}/N_{CN}$   
667 against supersaturation. Examples are shown in Fig. 13a and 13b, with AC18-DD representing a  
668 segment dominated by larger and aged particles, AC07-F a region with high concentrations of  
669 small and younger particles, and AC09-AA a mixed case with short periods of very high  $N_{CN}$   
670 over a background of moderately elevated particle concentrations. Even though the mean CN  
671 concentration exceeds  $8900\text{ cm}^{-3}$  in AC07-F, the mean  $N_{CCN0.5}$  in the same region is only  $13\text{ cm}^{-3}$   
672 and therefore the  $N_{CCN0.5}/N_{CN}$  vs. S plot falls essentially on the baseline. In contrast, AC18-DD  
673 presents a fairly “classical” supersaturation spectrum, and AC09-AA is a mixed case with the  
674 measurements made during the  $N_{CN}$  peaks showing very low  $N_{CCN0.5}/N_{CN}$ .

675 In Fig. 13c and 13d, we compare the mean supersaturation spectra from the lower, middle  
676 and upper troposphere obtained on flights AC12 and AC13, which were taken on successive  
677 days over the same region and where the LT was influenced by biomass burning pollution. In the  
678 LT, the CCN fraction is in the range observed at ground level at the Amazon Tall Tower Obser-  
679 vatory (ATTO) site (Pöhlker et al., 2016) and in close agreement with measurements in the  
680 southern Amazon during the biomass burning season (Vestin et al., 2007). In the UT, we ob-  
681 served low CCN fractions representing the regions with high  $N_{CN}$  and UFF, mostly at altitudes of  
682 10-11 km, and higher CCN fractions at 12 km and above corresponding to a region with elevated  
683 CCN (cf. Fig. 11b, which shows the CCN concentrations from these flights). In the middle tropo-  
684 sphere (5-8 km) we found intermediate CCN fractions, consistent with a mixture of LT and UT  
685 aerosols.

### 686 3.4.3. Volatility

687 On several flights (AC16, 18, 19, and 20), a second CPC was operated behind a ther-  
688 modenunder at a temperature of  $250\text{ }^{\circ}\text{C}$ , in parallel to the regular CPC. The results of these meas-  
689 urements are shown in Fig. 14a in the form of the volatile fraction (VF), i.e.,  $(N_{CN} - N_{\text{nonvol}})/N_{CN}$ ,



690 plotted against altitude. In the LT, most particles are nonvolatile and the VF is typically between  
691 10 and 20%. This is consistent with the behavior described by Clarke and Kapustin (2010) and  
692 Thornberry et al. (2010), who found that aged combustion aerosols (from biomass of fossil-fuel  
693 burning) are non-volatile and mostly in the accumulation mode size fraction. With increasing al-  
694 titude, the VF increases, closely resembling the profile of the UFF. In the UT, the mean VF  
695 reaches about 80%, and approaches 100% in the most highly enriched layers (e.g., segment E2).  
696 In previous campaigns, high volatile fractions had also been observed in the tropical UT and  
697 TTL, with the highest VF in the region between 340 and 360 K potential temperature, corre-  
698 sponding to about 9-15 km (Borrmann et al., 2010; Weigel et al., 2011).

699 More detail can be seen when looking at data from an individual flight. In Fig. 14b we  
700 show the profiles from AC18, which we had already discussed in the context of CCN concentra-  
701 tions in the previous section. The profiles (segments A, B, C, and F) show the overall increase in  
702 VF with height, with peak values at embedded high-CN layers. The freshest layer (E2), which  
703 had the highest UFF, also has the highest VF. In contrast, segments D and E1, representing larger  
704 UT regions with moderate CN enrichments, larger particles, and higher CCN fraction also have  
705 lower VFs, between 0.4 and 0.7. A contribution from aged combustion aerosols can be ruled out  
706 as source for the non-volatile particles in these layers, because the rBC concentrations are close  
707 to zero (see below). As we will show in the next section, it appears that these low-volatility parti-  
708 cles represent a more aged organic aerosol.

#### 709 3.4.4. Chemical composition

710 As discussed above, the LT aerosol over the Amazon during the dry season is dominated  
711 by the products of biomass burning, with increasing concentrations from north to south. This is  
712 clearly reflected in its chemical composition, which is dominated by carbonaceous matter (or-  
713 ganic and elemental carbon) and only contains minor fractions of inorganic species, such as po-  
714 tassium, sulfate, and nitrate. Elemental or black carbon is a unique tracer of combustion emis-  
715 sions and was measured on HALO in the form of refractory black carbon (rBC).

716 The vertical profile of rBC shows a sharp separation between LT and FT (Fig. 15). The  
717 average rBC concentration in the region below 5 km was  $0.31 \pm 0.29 \mu\text{g m}^{-3}$ , whereas in the FT  
718 above 6 km it was  $0.0026 \pm 0.0069 \mu\text{g m}^{-3}$  in terms of mass concentrations, and  $99 \pm 92 \text{ cm}^{-3}$  vs.  
719  $1.5 \pm 2.5 \text{ cm}^{-3}$  in number concentrations of rBC particles. Interestingly, these concentrations over



720 the Amazon Basin are only slightly higher than the values measured over the tropical Western  
721 Atlantic during the Saharan Aerosol Long-range Transport and Aerosol-Cloud-Interaction Ex-  
722 periment (SALTRACE), June/July 2013: ca.  $0.2 \mu\text{g m}^{-3}$  in the LT and ca.  $0.001 \mu\text{g m}^{-3}$  in the FT  
723 (Schwarz et al., 2017), which suggests that a significant fraction of the rBC is entering the basin  
724 by long-range transport from Africa.

725 In 14 instances, elevated rBC concentrations were seen for short durations (usually less  
726 than 30 sec) in the UT. Most of the time, they occurred during cloud penetrations in the course of  
727 vertical cloud microphysics profiling. In the case of the flights over the northern half of the Ama-  
728 zon Basin, they could likely be attributed to sampling of HALO's own exhaust, based on the  
729 flight track and the presence of associated NO enhancements in the absence of strong enhance-  
730 ments of CO and other aerosol species ( $\text{CCN}$ ,  $N_{\text{acc}}$ ,  $N_{\text{CN}}$ ). On flights over the southern Amazon  
731 (AC07, AC12, AC13, and AC20), where the PBL was more polluted and active fires were pre-  
732 sent, there were a few instances when elevated rBC coincided with peaks in CO and accumula-  
733 tion mode particles, which suggests upward transport of biomass smoke aerosols. In view of the  
734 scarcity of such events during our campaign and their modest rBC concentrations, it is clear that  
735 they do not represent a major source of combustion aerosol for the UT during our campaign. No  
736 elevated rBC concentrations were observed during the extensive outflow sampling legs on any of  
737 the flights. A detailed discussion of the rBC measurements during the campaign will be pre-  
738 sented in a companion paper (Holanda et al., 2017).

739 The drop in rBC concentration by two orders of magnitude between LT and FT implies  
740 that rBC, and by extension other aerosols (which are likely even more prone to being removed  
741 by nucleation scavenging), are efficiently removed during deep convection and consequently that  
742 there is little transport of LT aerosols into the FT. Consequently, enrichments in  $N_{\text{CN}}$  and  $N_{\text{acc}}$   
743 in the FT cannot be explained by vertical transport of particles from the FT.

744 The AMS measurements also show pronounced differences in the composition of the LT  
745 and UT aerosols (Fig. 16). In Table 2 we present a detailed analysis of the results from three  
746 flights, AC07 from a polluted region in the southern Amazon, and AC09 and AC18 from rela-  
747 tively clean regions in the northern and northwestern parts of the Basin, respectively. Organic  
748 aerosol (OA) is the dominant aerosol species in all three regions at all altitudes, as expected in an



749 area where biomass burning and secondary organic aerosol (SOA) production are the dominant  
750 sources.

751 In the LT, (ammonium) sulfates (SO<sub>4</sub>) are together with rBC the next most important  
752 species. Here, we see a clear difference between the BB-dominated region in the south (with  
753 high OA, ammonium [NH<sub>4</sub>], and rBC, and relatively low SO<sub>4</sub>) versus the northern basin, where  
754 SO<sub>4</sub>, likely from long-range transport, plays a more important role. The ratio OA/rBC in the LT  
755 is in the range 3-11, consistent with values from BB aerosols. The biomass burning marker, f<sub>60</sub>  
756 (Schneider et al., 2006; Alfarrá et al., 2007), is present in all the measurements from the LT, but  
757 always mixed with oxidized secondary organics. It should also be noted that the f<sub>60</sub> marker is not  
758 an inert tracer but decays with time, and an observed background level of the f<sub>60</sub> tracer is 0.3% of  
759 OA (Cubison et al., 2011).

760 In the UT, SO<sub>4</sub> shows lower concentrations than in the LT, with the most pronounced  
761 difference on flights AC07 and AC18. The latter flights also show a large difference in the  
762 OA/SO<sub>4</sub> ratio, which is around 10 in the UT and around 2 in the LT. Because of the high BB  
763 component in flight AC07, this ratio is also high in the LT on this flight. The most pronounced  
764 differences between UT and LT are seen in the nitrogen species. Ammonium is usually present  
765 in the BL, sometimes at considerable levels (e.g., on AC07), but always below the detection limit  
766 in the UT. In contrast, nitrate (NO<sub>3</sub>) is a minor species in the LT, whereas in the UT it is com-  
767 parable or greater than SO<sub>4</sub>, so that the ratio NO<sub>3</sub>/SO<sub>4</sub> is about an order of magnitude higher in the  
768 UT than in the LT. High concentrations of organics, especially oxidized organics, and nitrate had  
769 been seen previously in the UT by Froyd et al. (2009).

770 The nature of the nitrate signal in the UT cannot be definitely identified from our data.  
771 The absence of NH<sub>4</sub> and the ratio of the peaks associated with ammonium nitrate make it un-  
772 likely that the NO<sub>3</sub> signal represents ammonium nitrate (Fry et al., 2009; Bruns et al., 2010). It  
773 may be, at least to a large part, indicative of organonitrates, which have been shown to account  
774 for 15-40% of SOA mass in laboratory experiments (Berkemeier et al., 2016) and whose for-  
775 mation is enhanced at low temperatures (Lee et al., 2014).

776 A closer look at the aerosol-enriched layers in the UT from these flights reinforces these  
777 conclusions (Table 2). In these layers, the ratios OA/SO<sub>4</sub> and NO<sub>3</sub>/SO<sub>4</sub> can reach very high val-  
778 ues, especially in the SO<sub>4</sub>-poor UT of flight AC07. On flights AC09 and AC18, we encountered



779 extended periods when  $N_{acc}$  and  $N_{CCN0.5}$  were elevated, while  $N_{CN}$  did not show extremely high  
780 values (AC09-AA, AC18-AA, and AC18-DD). The AMS data from these segments were gener-  
781 ally similar to the UT averages, suggesting that they are representative of the ambient UT aero-  
782 sols. The layers with very high  $N_{CN}$  on these flights (AC09-BB, AC09-EE, AC09-A1+A2, and  
783 AC18-A1, AC18-A2, AC18-E2, AC18-F) also did not show significant differences from the UT  
784 means on these flights, likely because the numerous, but very small CN in these layers did not  
785 contain enough mass to influence the measurements in a detectable way.

786 We attempted to examine this hypothesis further by investigating the size dependence of  
787 the AMS signals, but because of the small aerosol mass concentrations in the UT, size infor-  
788 mation from the AMS data required extended integration periods, which precluded obtaining size  
789 data from the relatively short segments with very high  $N_{CN}$ . The most robust size data were from  
790 the segments where relative high  $N_{acc}$  concentrations prevailed over extended periods of time,  
791 e.g., segment DD (Table 2) on flight AC18. Here, the organic aerosol (OA) showed a broad  
792 mode between 80 and 250 nm, with a modal diameter at 150 nm. This confirms that the AMS  
793 compositional data are dominated by the accumulation mode, while the particles that make up  
794 most of the UF fraction in the UT do not have enough mass to provide a clear AMS signal. An  
795 exception may be some segments on AC09 (BB and EE), where OA and NO<sub>3</sub> data suggest a  
796 mass mode between 60 and 120 nm. Here, the UFF is quite high (0.85 and 0.92, compared to  
797 segment DD on flight AC18, where it was 0.61) suggesting a smaller and therefore younger aer-  
798 osol population.

799 More detailed information on the origin of the organics in the UT aerosol can be obtained  
800 from specific markers. In the UT, the BB marker  $f_{60}$  is typically not detectable, which in combi-  
801 nation with the fact that the ratio OA/rBC is of the order of 1000, precludes a significant contri-  
802 bution of aerosols from biomass burning or other primary combustion aerosols to the OA in the  
803 UT. In contrast, the marker  $f_{82}$ , which is indicative of IEPOX-SOA formed by the photooxidation  
804 of isoprene (Robinson et al., 2011; Hu et al., 2015), is found in the aerosol-enriched layers in the  
805 UT, suggesting oxidation of isoprene and other biogenic volatile organic compounds (BVOC) as  
806 source of the OA (Schulz et al., 2017). The plot  $f_{43}$  vs.  $f_{44}$  is frequently used to represent the ag-  
807 ing of organic aerosols (Ng et al., 2011). In Fig. 17, we show the median locations of the LT and  
808 UT aerosol in this plot, which indicates that both are fairly well aged and oxidized, with the UT  
809 data plotting slightly towards less oxidized and younger values. This may reflect an overall



810 younger aerosol, or the admixture of recent material either by condensation on the accumulation  
811 mode particles or in the form of an external mixture of larger aged particles with small younger  
812 ones. The individual segments from flight AC18, which had the lowest OA/SO<sub>4</sub> and NO<sub>3</sub>/SO<sub>4</sub>  
813 ratios, also plot in this region, showing that they are dominated by a relatively well-aged aerosol.  
814 In contrast, segments AC09-AA, and AC07-AA1, AC07-AA2, and AC07-GG, which have the  
815 highest OA/SO<sub>4</sub> and NO<sub>3</sub>/SO<sub>4</sub> ratios and much higher N<sub>CN</sub>, plot much further to the lower right  
816 indicating a less oxidized, fresher aerosol. On this flight, the concentrations of accumulation  
817 mode aerosols in the UT were relatively low, so that freshly formed aerosol could be more evi-  
818 dent because of a lower background of aged aerosol.

819 In summary, the chemical composition data show that, while both LT and UT aerosols  
820 are dominated by aged organics, their sources must be different because the UT aerosol is essen-  
821 tially devoid of the combustion tracers, rBC and f<sub>60</sub>, whereas the OA/rBC ratios in the LT are  
822 consistent with combustion aerosols. Nitrate is strongly elevated in the UT, and may consist to a  
823 large extent of organonitrates. NH<sub>4</sub> is a significant component in the LT, whereas it is below the  
824 detection limit in the UT. Size-selective chemical analysis is difficult because of the low aerosol  
825 mass concentrations, but the available data suggest that the AMS measurements are dominated  
826 by the accumulation mode, and the strong N<sub>CN</sub> enhancements are not distinctly seen in the AMS  
827 data. Chemical marker analysis shows the general absence of BB tracers in the UT, while the  
828 marker f<sub>82</sub> indicates production of IEPOX-SOA from isoprene. Most of the UT organics are aged  
829 and oxidized, but in some of the CN-enriched layers, younger and less oxidized OA was evi-  
830 denced by much lower f<sub>44</sub>/f<sub>43</sub> ratios. A detailed discussion of the AMS measurements during  
831 ACRIDICON-CHUVA will be presented in Schulz et al. (2017).

### 832 3.5. Relationship to Deep Convection

833 In the preceding section, we have documented the differences between the aerosols in the  
834 LT and the UT, which rule out the possibility that convective transport of PBL aerosols can be an  
835 important source for the UT aerosols. This opens the question about the source of these particles:  
836 are they the result of long-range transport from remote sources or do they originate over the Am-  
837 azon Basin? In the latter case, are they directly released in the outflow from the convective  
838 clouds or are they produced by subsequent nucleation and growth in the UT?



839 For the larger particles in the accumulation mode, represented by elevated  $N_{acc}$  and  
840  $N_{CCN0.5}$  in the UT, long-range transport cannot be excluded, because such particles can have long  
841 lifetimes in the upper troposphere (Williams et al., 2002). While the absence of detectable rBC  
842 still rules out an origin from pollution aerosols lofted from the LT, they may have formed days or  
843 weeks ago by gas-to-particle formation mechanisms anywhere in the free troposphere. In con-  
844 trast, the high concentrations of small UF particles that we observed with high frequency in the  
845 UT cannot come from distant sources, as they persist only for hours to a few days before grow-  
846 ing to larger sizes and decreasing in concentration due to coagulation and dilution processes  
847 (Williams et al., 2002; Krejci et al., 2003; Ekman et al., 2006).

#### 848 3.5.1. Aerosols in cloud tops, anvils and outflows

849 First, we consider the possibility of these particles having been produced already inside  
850 the clouds and released by outflow into the UT. In earlier studies, NPF had been shown to occur  
851 in ice clouds in the tropical/subtropical UT, especially in conditions where the available surface  
852 area of ice particles was relatively low (e.g., Lee et al., 2004; Frey et al., 2011). To look for this  
853 phenomenon, we examined the particle concentrations during passages through the upper levels  
854 of deep convective clouds and in the anvils directly attached to active cumulonimbus clouds  
855 (Cb). Our measurements during these passages consistently show lower CN and CCN concentra-  
856 tions than in the surrounding UT air, as exemplified in Fig. 18a by data from flight AC18. Dur-  
857 ing this flight segment we performed multiple penetrations of the tops of growing Cb at altitudes  
858 between 10.7 and 12.0 km and temperatures in the range of 225 to 236 K. During each cloud  
859 passage (indicated in Fig. 18a by the ice particle concentrations) the aerosol concentrations de-  
860 creased sharply, to values of  $N_{CN}$  around  $800\text{ cm}^{-3}$  and  $N_{CCN0.5}$  around  $250\text{ cm}^{-3}$  during the longer  
861 cloud passages. (Here, we use  $N_{CCN0.5}$  as proxy for the accumulation mode particles, since the  
862  $N_{acc}$  measurements in clouds were perturbed by shattering at the probe tip, whereas the  $N_{CN}$  and  
863  $N_{CCN0.5}$  measurements showed no artifacts in ice clouds.) In the case of  $N_{CN}$ , the values in the  
864 cloud tops are about the same as the PBL concentrations measured in the same region, while for  
865  $N_{CCN0.5}$  they are significantly lower than the PBL values of around  $400\text{ cm}^{-3}$ .

866 The same behavior was found for all cloud penetrations in the UT during the campaign.  
867 In particular, extensive cloud top and outflow sampling on AC09, AC15, and AC16 also showed



868  $N_{CCN0.5}$  values down to 160-250  $\text{cm}^{-3}$  and  $N_{CN}$  values down to 600-1000  $\text{cm}^{-3}$ . The lowest parti-  
869 cle concentrations were seen in a large outflow sampled on AC13 (20:08-20:30 UTC), when  
870 both  $N_{CN}$  and  $N_{CCN0.5}$  reached values below 50  $\text{cm}^{-3}$  (Fig. 18b). In this airmass, NO and  $\text{NO}_y$   
871 were strongly elevated indicating recent NO production by lightning in the large Cb from which  
872 this outflow originated.

873         Given that the air sampled during the cloud passages had already mixed in by lateral en-  
874 trainment some of the surrounding air with much higher particle concentrations (Bertram et al.,  
875 2007; Yang et al., 2015), these low particle concentrations in the cloud tops and outflows are  
876 clear evidence that in-cloud processes were a sink and not a source of particles in the size class  
877 measureable with our instrumentation. A rough estimate of the scavenging efficiency of the con-  
878 vective process can be gained by using CO as a conservative tracer. For example, on flight AC18  
879 the PBL concentrations of CO and  $N_{CN}$  averaged  $\sim 120$  ppb and 780  $\text{cm}^{-3}$ , and the UT during the  
880 cloud penetrations around 1900 UTC had CO  $\sim 95$  ppb and  $N_{CN} \sim 1500$   $\text{cm}^{-3}$ . In the cloud, CO  
881 rose to 108 ppb and  $N_{CN}$  dropped to 750  $\text{cm}^{-3}$ . Following the approach of Bertram et al. (2007),  
882 we can estimate that the fraction of PBL air in the center of the cloud was ca. 0.52, and that with-  
883 out scavenging,  $N_{CCN0.5}$  would be ca. 1130  $\text{cm}^{-3}$ . From these values, a scavenging loss of 90% or  
884 more of CCN can be estimated, in good agreement with previous studies (e.g., Andreae et al.,  
885 2001; Yang et al., 2015), and with the absence of detectable rBC.

886         Flight AC20 was the only exception to this behavior. Here, CN were strongly enhanced  
887 during cloud passages and even CCN were slightly elevated in some passages. The cloud that  
888 was sampled on this flight appears to have been a pyrocumulus that had been ingesting fresh bio-  
889 mass smoke, as suggested by the strongly elevated CO during the cloud passages. This flight will  
890 be discussed as a separate case study below (section 3.6.).

891         While these results show that the high particle concentrations we observed in the UT  
892 were not directly released from the cloud tops, they do not rule out the possibility that new parti-  
893 cle formation had already started in the clouds or anvils. This is because the newly formed parti-  
894 cles observed in the earlier studies were almost exclusively in the size range below 20 nm (Lee et  
895 al., 2004; Frey et al., 2011). Since our measurements are limited to particle sizes  $>20$  nm, we  
896 would not have been able to detect such freshly nucleated particles, and therefore the earliest  
897 phases of particle nucleation and NPF over Amazonia will have to be addressed in future studies.



898 Our data do show, however, that release of particles by hydrometeor evaporation following deep  
899 convection is not a net source of particles to the UT over Amazonia, in contrast to what was ob-  
900 served over the Indian Ocean region by Engström et al. (2008). Because the  $N_{CN}$  and  $N_{CCN0.5}$   
901 concentrations in the ambient air in the UT are actually higher than in the air detrained by the Cb  
902 clouds, the detrainment leads at least initially to a reduction in UT particle concentrations in the  
903 size class  $>20$  nm. Only through subsequent NPF can this be reversed and deep convection then  
904 become a net source of UT aerosols.

### 905 3.5.2. Relationship between aerosol enhancements and airmass history

906 Connections between the presence of aerosol enhancements and the outflow from con-  
907 vective systems had been observed in some previous studies (de Reus et al., 2001; Twohy et al.,  
908 2002; Benson et al., 2008; Weigelt et al., 2009). We examined the connection between deep con-  
909 vection (DC) and the presence of high CN concentrations by a combination of backtrajectory cal-  
910 culations and the analysis of cloud-top temperatures from GOES-13 weather satellite images,  
911 similar to the approach used in some previous studies (de Reus et al., 2001; Froyd et al., 2009;  
912 Weigelt et al., 2009). We analyzed backtrajectories initialized at the aircraft locations where we  
913 had observed elevated aerosol concentrations, as listed in Table 1. Then we checked for each  
914 hour along the backtrajectories whether the airmass had crossed a region with DC (cloud top  
915 temperatures below  $-30$  °C). The results show that in almost all cases, the aerosol enriched air-  
916 masses had encountered deep convection within the last 120 hours.

917 In Fig. 19 we present the results from two flights (AC09 and AC18) as examples. We  
918 find that for all flight segments that showed high aerosol concentrations in the UT (dark shad-  
919 ing), the airmasses had made contact with DC with cloud tops typically reaching about  $-80$  °C.  
920 Of course, given the abundance of convection over Amazonia, it is to be expected that most air-  
921 masses would have interacted with convection within 120 hours (such as the example shown in  
922 the Supplement Fig. S2). For comparison, over the northeastern United States during summer-  
923 time, Bertram et al. (2007) had found that more than 50% of UT air had encountered DC within  
924 the previous 2 days.

925 The cumulative plot of the time since the most recent DC contact (Fig. 20a) shows that on  
926 all flights (except AC19, the flight over the Atlantic) almost all aerosol-enhanced air masses had  
927 seen DC within the last 30-40 hours. The cloud tops during these encounters typically reached -



928 70 to -80 °C (Fig. 20b). In many cases, the airmass history analysis shows multiple contacts with  
929 deep convection within the preceding 72 hours. It must be noted, however, that the physical in-  
930 teraction between an UT airmass and a specific deep convective event is not represented in the  
931 trajectory model and that the trajectory history preceding the most recent such encounter be-  
932 comes much more uncertain.

933 In some cases, the airmasses could be tracked back to regions where the cold cloud en-  
934 countered by the tracked airmass looked more like cirrus than identifiable deep convective out-  
935 flow. The same favorable conditions for nucleation (low temperature, low pre-existing aerosol  
936 surface) as in the outflow regions prevail also in native cirrus, and Lee et al. (2004) had reported  
937 NPF in cirrus without immediate connection to DC. This might also have occurred in our cam-  
938 paign, but it is usually difficult to distinguish cirrus and very aged outflow.

939 More specific information about the time required for particle production and the evolu-  
940 tion of the aerosol populations in the UT can be derived from a close examination of the trajec-  
941 tories for individual flight segments. Flight AC18 provides some illustrative examples. The trajec-  
942 tories of the first particle plumes encountered (A1 and A2, Table 1) had passed close to areas of  
943 intense deep convection (-30 to -60 °C) about 17-21 hours before sampling. Because it is likely  
944 that the aerosol precursor substances are formed by photochemical reactions, we also looked at  
945 the amount of time that the airmass was exposed to sunlight (Lee et al., 2003). Since the convec-  
946 tive encounters occurred between 16LT and 00LT and the measurements were taken at about  
947 11LT, the airmass had only about 5-7 h of sun exposure. Assuming that the formation of the par-  
948 ticles required photochemical processes, this implies that about 5-7 h were sufficient to produce  
949 particle concentrations above 20,000 cm<sup>-3</sup> with sizes >20 nm. The enrichment in this case oc-  
950 curred only in the particles sizes <90 nm, with a UFF of about 0.98, while N<sub>acc</sub> remained at the  
951 same levels as in the surrounding background FT. Segment F, near the end of the flight, was  
952 sampling a similar region as A1, with a similar airmass trajectory. Since this segment was taken  
953 near the end of the day, the airmass had experienced about 11 hours of sunlight. There is some-  
954 what of a shift towards larger particles, but this might also be coincidental.

955 The air in segments B and C had traveled along similar trajectories as A1 and A2, but un-  
956 fortunately there are no GOES images available for the time when they crossed the convective



957 region encountered by A1 and A2, and so no conclusions can be drawn for these segments. Seg-  
958 ments D and E1 represent airmasses that had made multiple and extended convection encounters  
959 over the central and western Amazon during the past 3 days. Here, we find only weak enhance-  
960 ments in  $N_{CN}$ , but significantly elevated  $N_{CCN0.5}$  and  $N_{acc}$ , with a UFF of 0.73 and 0.82, respec-  
961 tively, suggesting that coagulation and growth had taken place over this time period.

962 Some of the highest  $N_{CN}$  (up to ca.  $45,000 \text{ cm}^{-3}$ ) and UFF (0.98) were found in Segment  
963 AC18-E2, which was sampling the air just a few hours downwind of a massive convective sys-  
964 tem that reached well above our flight altitude of almost 14 km. The air sampled here had trav-  
965 eled for about one hour after leaving the convective complex before being encountered by  
966 HALO and had been interacting with this complex for up to 5 h, all of them in daylight. As in  
967 A1, A2, and F, there was no detectable enhancement in aerosol mass, as represented by  $N_{acc}$  and  
968  $N_{CCN0.5}$ . The strongest enhancement in aerosol mass, on the other hand, was seen in the early part  
969 of segment E1, which didn't show a strong increase in number concentration. The air during this  
970 segment had made its last contact with a convective system about 65-72 hours before sampling.

971 Another illustrative case is flight AC09 over a clean region in the northern Amazon. Seg-  
972 ments A1-A3 sampled clear air that had DC contact about 16 and 60 hours ago and the UFF  
973 around 0.94 indicated a moderately aged aerosol. Segments B1 and B2 were taken in air immedi-  
974 ately surrounding a Cb anvil, with previous DC contacts at about 14, 80, and 120 hours before.  
975 Here, the relatively low UFF of  $\sim 0.92$  signaled no influence from the freshly outflowing air. Seg-  
976 ments C, D, and E were in air close to a Cb, within its anvil, and in a large anvil/outflow, respec-  
977 tively. Otherwise, they had a DC contact history similar to B. Here also, the UFF remains fairly  
978 low, and there is no evidence of particle production directly in the anvil/outflow.

979 To summarize, our observations indicate that, while there is no evidence of immediate  
980 production of detectable particles (i.e.,  $>20 \text{ nm}$ ) in the actual anvil or outflow, a small number of  
981 daylight hours are sufficient to produce very large concentrations of particles with sizes larger  
982 than about 20 nm in the FT. This is consistent with the observations made in the outflow of a  
983 convective complex off Darwin, Australia, where maximum Aitken concentrations were reported  
984 after ca. 3 hours since the outflow (Waddicor et al., 2012). During NPF events in the FT on the  
985 Jungfrauoch, high concentrations of particles  $>20 \text{ nm}$  were observed about 4-6 hours after sun-  
986 rise (Bianchi et al., 2016). In the FT over other regions, growth may be considerably slower; for



987 example the measurements over oceanic regions by Weigelt et al. (2009) showed that it took  
988 about 12 hours for particles  $>12$  nm to reach their maximum concentrations.

989       Considerably longer times (a few days) are required, however, before increases are de-  
990 tectable in the size class  $>90$  nm. The development of significant amounts of particles in the ac-  
991 cumulation mode appears to take two days or more, in agreement with the observations of Froyd  
992 et al. (2009), who had found enhanced aerosol organic mass concentrations over the Caribbean in  
993 UT air originating from Amazonia after 2-4 days in the atmosphere. Since many, if not most of  
994 our trajectories remain over Amazonia for this amount of time, there is enough time available in  
995 the UT over the Amazon Basin to produce CCN-sized aerosols within the region, which can sub-  
996 sequently be transported downward or be exported to other regions.

### 997 3.5.3. Aerosol enhancements and chemical tracers

998       The relationship between new particle production and the input of boundary layer air is  
999 also reflected in a correlation between  $N_{CN}$  and CO. When taking all data above 8 km, this corre-  
1000 lation is highly significant given the large number of data points ( $N=68,360$ ) but not very close  
1001 ( $r^2=0.52$ ) because of the large variability of CO concentrations in the PBL and UT background  
1002 between flights (Fig. 21). Closer relationships are obtained when looking at individual flights  
1003 and especially at individual profiles within flights.

1004       Weigel et al. (2011) had seen a strong correlation between CO and nucleation mode parti-  
1005 cles over West Africa and interpreted it as indication of anthropogenic inputs. In contrast, over  
1006 Amazonia we have not seen any evidence that UT aerosol production shows any relationship to  
1007 boundary layer pollution, and we interpret the correlation between  $N_{CN}$  and CO simply as reflect-  
1008 ing the input of air from the PBL, which generally has higher CO concentrations than the UT, by  
1009 the cloud outflow. An opposite relationship is generally seen between  $N_{CN}$  and  $O_3$ , which tends  
1010 to be lower in the particle-enriched layer. We also see this as an indication of injection of air  
1011 from the PBL, which generally has lower  $O_3$  concentrations than the UT.

1012       The nitrogen oxides show a complex relationship with the particle enhancements in the  
1013 UT, as illustrated at the example of a flight segment from AC07 (Fig. 22). The highest NO con-  
1014 centrations are found in the Cb anvils or freshest outflows, as identified by significant concentra-  
1015 tions of ice particles (e.g., at 2056, 2119, and 2154 UTC). In these regions, we typically observed  
1016 particle minima, as discussed above. In these airmasses, NO has been formed very recently by



1017 lightning, and the NO to NO<sub>y</sub> ratios are usually still very high. Here, the particles are still de-  
1018 pleted by convection scavenging and there has not been enough time for new particles to form, at  
1019 least not in the size range detectable by our instrumentation. On the other hand, there is a strong  
1020 positive relationship between NO<sub>y</sub> and N<sub>CN</sub>, as seen in Fig. 22 during the entire period from 2051  
1021 to 2210 UTC. Regions with high concentrations of new particles generally show elevated NO<sub>y</sub>,  
1022 typically in the range of 1 to 3 ppb, indicating that photochemical reactions have taken place that  
1023 both produced new particles and converted NO to NO<sub>y</sub>.

### 1024 **3.6. Flight AC20: A special case with NPF from biomass smoke**

1025 On flight AC20, HALO performed detailed sampling of the anvil and outflow of a large  
1026 Cb over northern Rondonia, a state with a high incidence of deforestation burning. Numerous  
1027 outflow penetrations around this Cb were made, and the ice particles sampled here could be  
1028 clearly identified as freshly produced in the Cb top. The CN concentrations in the UT away from  
1029 the outflow were unimpressive, typically in the range 2000 to 10,000 cm<sup>-3</sup>. However, in sharp  
1030 contrast to the other flights, where the air in the outflow always had been depleted in aerosol par-  
1031 ticles, on this flight the outflow often showed much higher CN concentrations, between 10,000  
1032 and 20,000 cm<sup>-3</sup> (Fig. 23a). The concentrations of CCN and nonvolatile CN in the outflow were  
1033 either the same as in the surrounding air or slightly higher, also contrasting with the observations  
1034 on the other flights, where they had been depleted. Since the N<sub>CN</sub> in the outflow were also much  
1035 higher than in the PBL (~2000 cm<sup>-3</sup>), entrainment of PBL air cannot explain the CN enrichment.

1036 The mixing ratios of CO, NO, and NO<sub>y</sub> were also elevated in the outflow (Fig. 23b),  
1037 which in the case of CO and NO<sub>y</sub> might be explained by inputs from the PBL, where CO and  
1038 NO<sub>y</sub> levels were around 120-200 ppb and 2-3 ppb, respectively. The NO values in the PBL, on  
1039 the other hand, were only about 0.13 ppb, similar to the UT values, requiring an additional NO  
1040 source for the outflow.

1041 The explanation for this unusual behavior may be found in the layer between 11.5 and  
1042 12.5 km that was penetrated during both ascent and descent (Fig. 23c). In this layer, N<sub>CN</sub> reached  
1043 30,000 cm<sup>-3</sup>, CO was elevated to ~140 ppb, N<sub>acc</sub> to 850 cm<sup>-3</sup>, and NO<sub>y</sub> to ~1.6 ppb. The data also  
1044 suggest a slight enrichment in rBC, but this is close to the limit of detection. These values sug-  
1045 gest that this is a detrainment layer polluted with biomass smoke, as we have often seen on previ-  
1046 ous campaigns over the burning regions in southern Amazonia (Andreae et al., 2004). An urban



1047 origin of this pollution is unlikely, since the only town in the region, Porto Velho, lies about 50-  
1048 100 km downwind of the sampling area. The enhancement ratios in this layer, however, differ  
1049 from fresh biomass smoke. The ratio  $\Delta N_{\text{acc}}/\Delta \text{CO}$  is  $\sim 6\text{--}12 \text{ cm}^{-3} \text{ ppb}^{-1}$  and the ratio  $\Delta \text{CCN}/\Delta \text{CO}$   
1050 about  $2.5 \text{ cm}^{-3} \text{ ppb}^{-1}$ , much lower than the typical ratios in fresh smoke, which are about 20-40  
1051  $\text{cm}^{-3} \text{ ppb}^{-1}$  (Janhäll et al., 2010), indicating removal of CCN-sized particles during the upward  
1052 transport. In contrast, the ratio  $\Delta \text{CN}/\Delta \text{CO}$  was about  $350 \text{ cm}^{-3} \text{ ppb}^{-1}$ , almost an order of magni-  
1053 tude above the values typical of fresh smoke. These results suggest that biomass smoke was  
1054 brought to the UT either from the strongly smoke-polluted PBL in this region or actually by a  
1055 pyro-Cb over an active fire, and that the concentration of the larger particles was strongly re-  
1056 duced by scavenging, which allowed new particle formation in this smoke layer. The enrich-  
1057 ments seen in the outflow penetrations at altitudes above the 12-km layer may be the result of en-  
1058 trainment of air from this layer or of rapid particle formation in situ. While we have this kind of  
1059 observations from only one flight, which took place over the most polluted region sampled dur-  
1060 ing this campaign, they are suggestive of the potential of rapid particle formation and growth in  
1061 smoke detrainment layers, an issue that merits further study in future campaigns.

### 1062 3.7. Conceptual model and role in aerosol life cycle

1063 The discussion in the preceding sections can be summarized in a conceptual model of the  
1064 aerosol life cycle over the Amazon Basin (Fig. 20). In the Amazon PBL, the classical nucleation  
1065 events characterized by the rapid appearance of large numbers of particles  $< 10 \text{ nm}$  and subse-  
1066 quent growth into an Aitken mode (e.g., Kulmala and Kerminen, 2008) has never been reported,  
1067 in spite of several years of observations by several teams (Martin et al., 2010; Rizzo et al., 2013;  
1068 Andreae et al., 2015). This has been attributed to the low emissions of gaseous sulfur species in  
1069 the basin (Andreae and Andreae, 1988; Andreae et al., 1990a), which result in  $\text{H}_2\text{SO}_4$  vapor con-  
1070 centrations that are too low to induce nucleation (Martin et al., 2010). Nucleation of particles  
1071 from organic vapors alone is not favored in the Amazonian PBL because of high temperatures  
1072 and humidity as well as the competition by the condensation sink on pre-existing particles, which  
1073 results in organic coatings on almost all primary and secondary particles in the Amazonian PBL  
1074 (Pöschl et al., 2010; Pöhlker et al., 2012).

1075 Cloud updrafts in deep convection bring air from the PBL into the middle and upper trop-  
1076 sphere, where it is released in the convective outflow (Krejci et al., 2003). During this process,



1077 most pre-existing aerosols are removed by precipitation scavenging, especially the larger parti-  
1078 cles that account for most of the condensation sink (Ekman et al., 2006). Most likely, VOCs with  
1079 low and very low volatilities are also removed by deposition on hydrometeors, which provide a  
1080 considerable amount of surface area inside the clouds (Murphy et al., 2015).

1081 The outflow regions in the UT present an ideal environment for particle nucleation, as  
1082 had already been suggested in some earlier studies (Twohy et al., 2002; Lee et al., 2004; Kulmala  
1083 et al., 2006; Weigelt et al., 2009). The temperatures are some 60-80 K lower than in the PBL,  
1084 which decreases the equilibrium vapor pressure of gaseous species (Murphy et al., 2015) and in-  
1085 creases the nucleation rate. Based on classical nucleation theory and molecular dynamics calcu-  
1086 lations, Yu et al. (2017) have estimated an increase in nucleation rate by one order of magnitude  
1087 per 10 K. Nucleation rate measurements in the CERN CLOUD chamber indicate a similar tem-  
1088 perature dependence (Dunne et al., 2016). Because the preexisting aerosol has been depleted dur-  
1089 ing the passage through convective clouds before being released into the UT from the cloud out-  
1090 flow, the low particle surface area in the UT presents very little competition to nucleation from a  
1091 condensation sink (Twohy et al., 2002; Lee et al., 2003; Lee et al., 2004; Young et al., 2007;  
1092 Benson et al., 2008).

1093 The rapid transport of PBL air to the UT inside deep convective clouds facilitates lofting  
1094 of reactive BVOCs from the Amazon boundary layer (Colomb et al., 2006; Apel et al., 2012).  
1095 Here, the initially O<sub>3</sub>- and NO<sub>x</sub>-poor boundary layer air is supplied with O<sub>3</sub> by mixing with UT  
1096 air and addition of NO from lightning, creating a highly reactive chemical environment. This  
1097 mixture is exposed to an extremely high actinic flux due to the high altitude and multiple scatter-  
1098 ing by ice particles. Because of the low air mass at UT altitudes, the actinic flux is already very  
1099 high shortly after sunrise. In this environment, rapid photooxidation of BVOCs and formation of  
1100 ELVOCs/HOMs is to be expected. In laboratory studies, HOMs have been shown to be rapidly  
1101 produced at fairly high yields both by ozonolysis of terpenes and by reactions with OH radicals  
1102 (Ehn et al., 2014; Jokinen et al., 2015; Berndt et al., 2016; Dunne et al., 2016).

1103 In the absence of measurements of the relevant gaseous sulfur species and the composi-  
1104 tion of the nucleating clusters, we cannot make firm conclusions about the actual nucleation  
1105 mechanism. Over marine regions and polluted continental regions, the particles observed in out-  
1106 flows and in the UT were mostly identified as sulfates (Clarke et al., 1999; Twohy et al., 2002;



1107 Kojima et al., 2004; Waddicor et al., 2012), and consequently H<sub>2</sub>SO<sub>4</sub> has been proposed as the  
1108 nucleating species. However, since in some cases this identification was based only on the vola-  
1109 tility of the particles, they could have also consisted of organics or mixtures of organics and  
1110 H<sub>2</sub>SO<sub>4</sub>. Over the Amazon, nucleation by H<sub>2</sub>SO<sub>4</sub> cannot be excluded based on our observations,  
1111 especially if there was already some SO<sub>2</sub> or H<sub>2</sub>SO<sub>4</sub> present in the UT before the injection of the  
1112 organic-rich PBL air. However, since the Amazonian BL contains very little SO<sub>2</sub>, the sulfur spe-  
1113 cies would have had to come from outside the region and thus they would have had the oppor-  
1114 tunity to be oxidized to H<sub>2</sub>SO<sub>4</sub> and nucleate into particles during its travel in the UT well before  
1115 entering Amazonia. It is therefore much more likely that the particles in the Amazon UT formed  
1116 by homogeneous nucleation of organics, as has been suggested by several authors (Kulmala et  
1117 al., 2006; Ekman et al., 2008; Murphy et al., 2015). Nucleation by formation of clusters contain-  
1118 ing both H<sub>2</sub>SO<sub>4</sub> and oxidized organic molecules is of course also a possibility that we cannot ex-  
1119 clude (Metzger et al., 2010; Riccobono et al., 2014). However, recent studies have shown that  
1120 HOM compounds can nucleate to form particles even in the absence of H<sub>2</sub>SO<sub>4</sub>, especially in the  
1121 UT (Bianchi et al., 2016; Kirkby et al., 2016), and nucleation of HOMs without involvement of  
1122 H<sub>2</sub>SO<sub>4</sub> has been suggested to be the dominant mode of new particle formation in the pre-indus-  
1123 trial atmosphere by the modeling study of Gordon et al. (2016). The importance of ions produced  
1124 from cosmic radiation in this nucleation process is still controversial (Lee et al., 2003; Yu et al.,  
1125 2008; Bianchi et al., 2016; Kirkby et al., 2016).

1126       Regardless of the actual nucleating species, H<sub>2</sub>SO<sub>4</sub> or HOMs/ELVOCs, the growth of the  
1127 particles observed in our campaign must have been dominated by organics, as shown by the  
1128 composition of the aerosol measured by the AMS. The dominance of organics in the growth of  
1129 aerosols in pristine environments has also been suggested on the basis of modeling studies, both  
1130 for the lower troposphere (Laaksonen et al., 2008; Riipinen et al., 2012; Öström et al., 2017) and  
1131 the UT (Ekman et al., 2008; Murphy et al., 2015). In particular, isoprene-derived SOA has been  
1132 suggested to be important in the growth of sub-CCN-size particles to CCN (Ekman et al., 2008;  
1133 Jokinen et al., 2015), which would be consistent with the prevalence of isoprene in the Amazo-  
1134 nian PBL and our observations of IEPOX-SOA in the UT aerosol. As the particles grow, the de-  
1135 crease of the Kelvin (curvature) effect with increasing size of the growing particles implies that  
1136 subsequently relatively more volatile organics can condense (Tröstl et al., 2016), in agreement  
1137 with the observed high volatile fraction we observed in the upper tropospheric CN.



1138 While in general the volatile fraction of the particles in the UT was very high, there were  
1139 also regions with a significant fraction of particles that did not evaporate at 250 °C (see section  
1140 3.4.3). These were dominated by relatively aged organics, which, based on the absence on de-  
1141 tectable rBC, must also be of secondary origin. Such thermally refractory organics may explain  
1142 the presence of non-volatile particles in the tropical UTLS, which had been observed in previous  
1143 campaigns especially in the region above 360 K (Borrmann et al., 2010).

1144 Once particles have nucleated in the UT and grown into the Aitken mode and in some  
1145 cases even into the accumulation mode size ranges, they can be transported downward towards  
1146 the lower troposphere both by general subsidence under the prevailing high pressure system over  
1147 Amazonia and by downdrafts associated with deep convective activity. Large-scale entrainment  
1148 of UT and MT air into the boundary layer has been suggested as the major source of new parti-  
1149 cles in marine regions (Raes, 1995; Katoshevski et al., 1999; Clarke et al., 2013). Over Amazo-  
1150 nia with its high degree of convective activity, downdrafts are likely to play a more important  
1151 role. Downward transport of UT air by downdrafts associated with deep convective activity has  
1152 been shown to inject air with lower moisture content, lower equivalent potential temperature, and  
1153 elevated O<sub>3</sub> into the PBL (Zipser, 1977; Betts et al., 2002; Sahu and Lal, 2006; Grant et al., 2008;  
1154 Hu et al., 2010; Gerken et al., 2016). It would follow that the same mechanism also brings down  
1155 aerosol-rich air from the UT into the PBL. Indeed, in a recent aircraft study over the central Am-  
1156 azon, this mechanism was shown to be an important source of atmospheric aerosols, predomi-  
1157 nantly in the Aitken mode, to the Amazonian PBL (Wang et al., 2016a). Here, they can continue  
1158 to grow by condensation of BVOC-derived organics into the accumulation mode and become  
1159 available as CCN, closing the aerosol cycle over Amazonia.

#### 1160 **4. Summary and Conclusions**

1161 As part of the ACRIDICON-CHUVA 2014 aircraft campaign, we investigated the char-  
1162 acteristics and sources of aerosols in the upper troposphere over the Amazon Basin. We observed  
1163 regions with high number concentrations of aerosol particles (tens of thousands per cm<sup>3</sup> STP) in  
1164 the UT on all flights that reached above 8 km. The aerosol enhancements were commonly in the  
1165 form of distinct layers with thicknesses of a few hundreds to a few thousands of meters. Such  
1166 layer structures are a common feature of the free troposphere and have been related to detrain-  
1167 ment from deep convection and large-scale subsidence (Newell et al., 1999).



1168 In other regions, upward transport of aerosols from the PBL had been suggested to be an  
1169 important source of UT aerosols, based on the abundance of low-volatility particles (Clarke and  
1170 Kapustin, 2010), TEM analysis of individual particles (Kojima et al., 2004), or modeling of  
1171 cloud processes (Yin et al., 2005). Over Amazonia, however, the UT aerosol was fundamentally  
1172 different from the aerosol in the LT, indicating that upward transport of PBL aerosols, especially  
1173 combustion aerosols from BB, is not an important source of aerosols to the Amazonian UT.

1174 The number concentrations of particles in the UT were often by several orders of magni-  
1175 tude higher than in the LT, and their size distribution was dominated by the Aitken rather than  
1176 the accumulation mode. In contrast to the LT, the particles in the UT were predominantly vola-  
1177 tile at 250 °C and had much higher organics and nitrate contents. The extremely low concentra-  
1178 tions of rBC in the MT and UT show that the aerosols above the LT are not combustion-derived  
1179 and indicate that the low-volatility fraction must be representing secondary organics of extremely  
1180 low volatility (ELVOCs/HOMs). Regarding the size class large enough to act as CCN (larger  
1181 than 60-80 nm), we can conclude based on the absence of rBC and the lack of BB indicators in  
1182 the AMS measurements that the enhanced CCN in the UT are not related to upward transport of  
1183 combustion products, in contrast to most previous studies (e.g., Krejci et al., 2003; Engström et  
1184 al., 2008; Clarke et al., 2013).

1185 By analyzing the history of the particle-enriched airmasses and comparing the transport  
1186 paths to GOES infrared imagery, we could show in almost all cases that these airmasses had  
1187 been in contact with deep convective outflow. Measurements inside the cloud tops and the out-  
1188 flow anvils close to the clouds showed that the pre-existing aerosols in the ascending air had  
1189 been almost completely scavenged by in-cloud processes, making the clouds initially a net aero-  
1190 sol sink. The near-complete scavenging is consistent with the hypothesized large water vapor su-  
1191 persaturation in pristine tropical deep convective clouds, which can nucleate particles that are  
1192 much smaller than the commonly defined CCN (Khain et al., 2012).

1193 Based on our measurements, we propose that BVOCs in the cloud outflow are rapidly ox-  
1194 idized to HOMs/ELVOCs, which because of the low temperatures and low condensation sink  
1195 can readily nucleate new particles and grow to sizes  $\geq 20$  nm within a few hours, making deep  
1196 convective clouds an indirect aerosol source. This had also been concluded based on a large sta-  
1197 tistical sampling of UT air in the Northern Hemisphere by the CARIBIC aircraft measurement



1198 program (Weigelt et al., 2009). The importance of NPF in the UT for the budget of CN and CCN  
1199 had been proposed previously on the basis of modeling studies (Yu et al., 2008; Merikanto et al.,  
1200 2009; Carslaw et al., 2017), and is evident in the global enhancement of CN in the UT, especially  
1201 in tropical regions, seen in compilations of data from numerous aircraft campaigns (Yu et al.,  
1202 2008; Reddington et al., 2016). In this way, aerosol production by BVOC oxidation in the UT  
1203 can provide the “missing source” of FT organic aerosol, which had been deduced from a mis-  
1204 match between models and observations (Heald et al., 2005).

1205         The high aerosol concentrations in the UT provide a reservoir of particles that are availa-  
1206 ble for downward transport into the PBL both by large-scale downward motion and by convec-  
1207 tive downdrafts. In a recent study, we have shown that transport of aerosols by downdrafts from  
1208 the free troposphere is an important, if not the dominant, source of particles to the lower tropo-  
1209 sphere (LT) over the Amazon (Wang et al., 2016a). The particles that are produced by this mech-  
1210 anism in the UT over the Amazon (and probably other tropical continents as well) can be trans-  
1211 ported globally due to their long lifetime in the UT (Williams et al., 2002; Clarke et al., 2013)  
1212 and affect the microstructure of low-level clouds after they eventually descend into the PBL,  
1213 possibly at very large distances from the source areas of their precursors.

1214         Our study and the results of some previous studies (Lee et al., 2003; Froyd et al., 2009)  
1215 suggest that UT aerosol production is especially important in the tropics because of the high rate  
1216 of BVOC production and the abundance of deep convection, but its relevance may also extend to  
1217 temperate and boreal regions. Our measurements both in the Amazon and at a remote site in cen-  
1218 tral Siberia, distant from SO<sub>2</sub> emission sources and thus experiencing very low H<sub>2</sub>SO<sub>4</sub> concentra-  
1219 tions, show that classical nucleation events are very rare to absent at such sites and may not pro-  
1220 vide a strong source of new particles (Heintzenberg et al., 2011; Andreae et al., 2015;  
1221 Wiedensohler et al., 2017). Consequently, the UT may be an important, possibly even the domi-  
1222 nant source of tropospheric aerosol particles in regions that are not strongly affected by anthro-  
1223 pogenic aerosols. This would assign clouds a central role in the aerosol life cycle, controlling  
1224 both source and sink of aerosol particles, at least in regions of low anthropogenic pollution. Fur-  
1225 thermore, the relevance of UT aerosol production may not be limited to the troposphere, because  
1226 the UT and the TTL are also important reservoirs for the transport of particles into the lower  
1227 stratosphere (Fueglistaler et al., 2009; Borrmann et al., 2010; Randel and Jensen, 2013). Organic



1228 aerosols in the lower stratosphere have been shown to have significant radiative effects (Yu et  
1229 al., 2016).

1230 The conceptual model proposed here implies a profound difference between the present-  
1231 day polluted atmosphere and the pristine pre-industrial situation, especially over the continents.  
1232 In the pristine atmosphere, the gradient of particle number concentrations may have been from  
1233 high values in the UT to low values in the PBL, as we have found in Amazonia. In polluted con-  
1234 tinental regions, on the other hand, nucleation and NPF occur predominantly in the lower tropo-  
1235 sphere, which thus has become the dominant source of atmospheric aerosols in today's atmos-  
1236 phere over much of the world. Consequently, in the anthropocene the aerosol concentration pro-  
1237 file has been turned upside down in polluted regions, since now the highest concentrations are  
1238 found in the PBL.

1239 This has important consequences for the Earth's climate system. The aerosol concentra-  
1240 tions in the PBL influence cloud microphysical properties and radiative energy fluxes, which af-  
1241 fect the characteristics of convection and thereby influence cloud radiative forcing, atmospheric  
1242 stability, precipitation, and atmospheric dynamics at all scales (Jiang et al., 2008; Koren et al.,  
1243 2008; Rosenfeld et al., 2008; Koren et al., 2010; Fan et al., 2012; Rosenfeld et al., 2014;  
1244 Gonçalves et al., 2015; Stolz et al., 2015; Dagan et al., 2016; Braga et al., 2017). By their radia-  
1245 tive and microphysical effects on convection dynamics, aerosols are also able to increase upper  
1246 tropospheric humidity, which plays an important role in the Earth's radiation budget (Sherwood,  
1247 2002; Kottayil and Satheesan, 2015; Riuttanen et al., 2016) and may also affect the potential for  
1248 aerosol nucleation in the UT, thus providing an additional feedback.

1249

## 1250 **5. Acknowledgments**

1251 We thank the entire ACRIDICON-CHUVA team for the great cooperation that made this  
1252 study possible. Our thanks go especially to the HALO pilots, Steffen Gemsa, Michael Gross-  
1253 rubatscher, and Stefan Grillenbeck, who always worked hard to put the aircraft at the right place  
1254 for our measurements, even under sometimes difficult conditions. We appreciate the support of  
1255 the colleagues from enviscope GmbH for their valuable help in certifying and installing the nu-  
1256 merous instruments for HALO and thank the HALO team of the DLR for their cooperation. We  
1257 acknowledge the generous support of the ACRIDICON-CHUVA campaign by the Max Planck



1258 Society, the German Aerospace Center (DLR), FAPESP (São Paulo Research Foundation), and  
1259 the German Science Foundation (Deutsche Forschungsgemeinschaft, DFG) within the DFG Pri-  
1260 ority Program (SPP 1294) “Atmospheric and Earth System Research with the Research Aircraft  
1261 HALO (High Altitude and Long Range Research Aircraft)”. This study was also supported by  
1262 EU Project HAIC under FP7-AAT-2012-3.5.1-1 and by the German Science Foundation within  
1263 DFG SPP 1294 HALO by contract no VO1504/4-1 and contract no JU 3059/1-1. C. Voigt  
1264 acknowledges financing by the Helmholtz Association under contract no. W2/W3-60. M. A.  
1265 Cecchini was funded by FAPESP grants number 2014/08615-7 and 2014/21189-7. The participa-  
1266 tion of D. Rosenfeld was supported by project BACCHUS, European Commission FP7-603445.  
1267 This study was also supported by the German Federal Ministry of Education and Research  
1268 (BMBF, grant No. 01LG1205E), and by the German Science Foundation within DFG SPP 1294  
1269 HALO by contract no VO1504/4-1, SCHN1138/1-2, and contract no JU 3059/1-1.  
1270



## 1271 **6. Figure Captions**

1272

1273 Figure 1: Tracks of the flights on which measurements at high altitude were made during  
1274 ACRIDICON-CHUVA. The flight segments at altitudes  $>8$  km are shown as heavier lines.

1275 Figure 2: Columnar precipitable water anomaly for September 2014 (based on the 1981-2010 av-  
1276 erage NCEP/NCAR Reanalysis).

1277 Figure 3: Total rainfall (mm per month,  $1^\circ$  resolution) for September 2014. Data from the Global  
1278 Precipitation Climatology Centre (GPCC).

1279 Figure 4: Mean wind speeds during September 2014 at a) 850 hPa and b) 200 hPa (Data from  
1280 NCEP/NCAR).

1281 Figure 5: Vertical profiles of potential temperature, static air temperature, and relative humidity  
1282 measured on HALO during the ACRIDICON-CHUVA flights over the Amazon Basin.

1283 Figure 6: Trajectory statistics based on (a) 72-hour and (b) 120-hour backtrajectory calculations  
1284 for September 2014, initialized at Manaus at an elevation of 12 km.

1285 Figure 7: Vertical profiles of CN concentrations,  $N_{CN}$ ; a) overall statistics from all flights, b) ex-  
1286 amples from individual profiles on flight AC07 (segment G) and AC09 (segments A1 and A2).

1287 Figure 8: Vertical profiles of accumulation mode particle concentrations,  $N_{acc}$ ; a) 1-min averaged  
1288 data from all flights, b)  $N_{acc}$  profile from flight AC19 together with the profile of  $N_{CN}$  from the  
1289 same flight (1-sec data).

1290 Figure 9: Size spectra: The black line shows the mean boundary layer DMPS size spectrum from  
1291 a segment in the PBL on flight AC13 (16:55 to 17:18 UTC). The square black symbols represent  
1292 the mean, the grey shaded area the standard deviation of the measurements. The line is a loga-  
1293 rithmic fit with modal diameters of 74 and 175 nm. The colored lines represent size distributions  
1294 from 0.65 to 5.8 km from a G1 flight during GoAmazon (Wang et al., 2016a).

1295 Figure 10: Vertical profiles of the ultrafine fraction (UFF); a) overall statistics from all flights, b)  
1296 examples from individual profiles on flight AC18.

1297 Figure 11: Vertical profiles of CCN concentrations at 0.52% supersaturation; a) overall statistics  
1298 from all flights (1-min averages), b) examples from individual profiles on flights AC09 (green)



1299 and AC12+13 (red). Flights AC12 and AC13 were conducted over the same region on successive  
1300 days.

1301 Figure 12: a) CCN fraction ( $N_{CCN0.5}/N_{CN}$ ) vs altitude, all data. b) CCN fraction vs. CN concentra-  
1302 tion for specific segments from flight AC18 (see text for discussion).

1303 Figure 13: a) CCN fractions ( $N_{CCN0.5}/N_{CN}$ ) and b) CCN concentrations ( $N_{CCN0.5}$ ) vs. supersatura-  
1304 tion from selected legs from flights AC09, AC10, and AC18; c,d) data from flights AC12 and  
1305 AC13 for the LT, MT, and UT.

1306 Figure 14: Volatile fraction. a) statistics from all flights; b) individual segments from flight  
1307 AC18 (see text for discussion).

1308 Figure 15: Refractory black carbon vs altitude, all flights, 30-second averages.

1309 Figure 16: Aerosol chemical composition as determined by AMS and SP2 measurements in the  
1310 lower, middle and upper troposphere.

1311 Figure 17: Plot of the AMS factors  $f_{44}$  vs.  $f_{43}$ , indicating the median values for the LT and UT  
1312 and values for some UT flight segments with elevated aerosol concentrations. With increasing  
1313 degree of oxidation, the measurements move to the upper left of the triangle

1314 Figure 18: Measurements during passages through cumulonimbus cloud tops and outflow anvils:  
1315 a) Several cloud top penetrations at 10.7 to 12 km altitude on flight AC18 showing reduced  $N_{CN}$   
1316 and  $N_{CCN0.5}$  inside the cloud top; b) Outflow from a large active cumulonimbus, showing strong  
1317 aerosol depletion and NO production by lightning.

1318 Fig. 19: Airmass contacts with deep convection. The colors indicate the cloud top temperature of  
1319 the convective system with which the trajectory had the most recent contact. The aircraft altitude  
1320 at which the airmass was sampled is indicated by the red line. The colored dots are plotted at the  
1321 altitude at which the airmass crossed the grid cell with the convective system. The dots are only  
1322 plotted if this altitude is greater than 6 km and if it encountered a DC region (i.e.,  $T_b < -30$  °C).  
1323 The shaded areas correspond to the flight segments with elevated CN concentrations. a) flight  
1324 AC09, b) flight AC18.

1325 Figure 20: a) Number of hours since last contact with deep convection for flight segments with  
1326 elevated aerosol concentrations (cumulative frequency, all flights); b) frequency distribution of



- 1327 minimum GOES brightness temperature ( $T_b$ ) for selected flights legs (within 5-day backward tra-  
1328 jectories).
- 1329 Figure 21: CN vs CO concentrations in the upper troposphere above 8 km (15-second averages).
- 1330 Figure 22: CN, NO, and  $\text{NO}_y$  concentrations in a flight segment in the upper troposphere on  
1331 flight AC07.
- 1332 Figure 23: a) Measurements of  $N_{\text{CCN}0.5}$ ,  $N_{\text{CN}}$ ,  $N_{\text{nonvol}}$ , and ice particles during cloud top penetra-  
1333 tions on flight AC20. b) Concentrations of CO, NO, and  $\text{NO}_y$  on the same flight segments. c)  
1334 Measurements of  $N_{\text{acc}}$ ,  $N_{\text{CN}}$ , rBC, CO, and  $\text{O}_3$  during the climb from 11.0 to 13.5 km.
- 1335 Figure 24: Conceptual model of the aerosol life cycle over the Amazon Basin.

1336 **7. References**

1337

- 1338 Abdelmonem, A., Järvinen, E., Duft, D., Hirst, E., Vogt, S., Leisner, T., and Schnaiter, M.,  
1339 PHIPS–HALO: the airborne Particle Habit Imaging and Polar Scattering probe – Part 1:  
1340 Design and operation: *Atmos. Meas. Tech.*, 9, 3131-3144, doi:10.5194/amt-9-3131-2016,  
1341 2016.
- 1342 Alfarra, M. R., Prevot, A. S. H., Szidat, S., Sandradewi, J., Weimer, S., Lanz, V. A., Schreiber,  
1343 D., Mohr, M., and Baltensperger, U., Identification of the mass spectral signature of  
1344 organic aerosols from wood burning emissions: *Environ. Sci. Technol.*, 41, 5770-5777,  
1345 doi:10.1021/es062289b, 2007.
- 1346 Andreae, M. O., and Andreae, T. W., The cycle of biogenic sulfur compounds over the Amazon  
1347 Basin. I. Dry season: *J. Geophys. Res.*, 93, 1487-1497, 1988.
- 1348 Andreae, M. O., Browell, E. V., Garstang, M., Gregory, G. L., Harriss, R. C., Hill, G. F., Jacob,  
1349 D. J., Pereira, M. C., Sachse, G. W., Setzer, A. W., Dias, P. L. S., Talbot, R. W., Torres,  
1350 A. L., and Wofsy, S. C., Biomass-burning emissions and associated haze layers over  
1351 Amazonia: *J. Geophys. Res.*, 93, 1509-1527, 1988.
- 1352 Andreae, M. O., Berresheim, H., Bingemer, H., Jacob, D. J., Lewis, B. L., Li, S.-M., and Talbot,  
1353 R. W., The atmospheric sulfur cycle over the Amazon Basin, 2. Wet Season: *J. Geophys.*  
1354 *Res.*, 95, 16,813-16,824, 1990a.
- 1355 Andreae, M. O., Talbot, R. W., Berresheim, H., and Beecher, K. M., Precipitation chemistry in  
1356 central Amazonia: *J. Geophys. Res.*, 95, 16,987-16,999, 1990b.
- 1357 Andreae, M. O., Anderson, B. E., Blake, D. R., Bradshaw, J. D., Collins, J. E., Gregory, G. L.,  
1358 Sachse, G. W., and Shipham, M. C., Influence of plumes from biomass burning on  
1359 atmospheric chemistry over the equatorial Atlantic during CITE-3: *J. Geophys. Res.*, 99,  
1360 12,793-12,808, 1994.
- 1361 Andreae, M. O., Artaxo, P., Fischer, H., Freitas, S. R., Gregoire, J. M., Hansel, A., Hoor, P.,  
1362 Kormann, R., Krejci, R., Lange, L., Lelieveld, J., Lindinger, W., Longo, K., Peters, W.,  
1363 Reus, M. d., Scheeren, B., Silva Dias, M. A. F., Ström, J., van Velthoven, P. F. J., and  
1364 Williams, J., Transport of biomass burning smoke to the upper troposphere by deep  
1365 convection in the equatorial region: *Geophys. Res. Lett.*, 28, 951-954, 2001.
- 1366 Andreae, M. O., Artaxo, P., Brandão, C., Carswell, F. E., Ciccioli, P., da Costa, A. L., Culf, A.  
1367 D., Esteves, J. L., Gash, J. H. C., Grace, J., Kabat, P., Lelieveld, J., Malhi, Y., Manzi, A.  
1368 O., Meixner, F. X., Nobre, A. D., Nobre, C., Ruivo, M. d. L. P., Silva-Dias, M. A.,  
1369 Stefani, P., Valentini, R., von Jouanne, J., and Waterloo, M. J., Biogeochemical cycling  
1370 of carbon, water, energy, trace gases and aerosols in Amazonia: The LBA-EUSTACH  
1371 experiments: *J. Geophys. Res.*, 107, 8066, doi:10.1029/2001JD000524, 2002.
- 1372 Andreae, M. O., Rosenfeld, D., Artaxo, P., Costa, A. A., Frank, G. P., Longo, K. M., and Silva-  
1373 Dias, M. A. F., Smoking rain clouds over the Amazon: *Science*, 303, 1337-1342, 2004.
- 1374 Andreae, M. O., Artaxo, P., Beck, V., M. Bela, Gerbig, C., Longo, K., Munger, J. W.,  
1375 Wiedemann, K. T., and Wofsy, S. C., Carbon monoxide and related trace gases and



- 1376 aerosols over the Amazon Basin during the wet and dry seasons: Atmos. Chem. Phys.,  
1377 12, 6041–6065, 2012.
- 1378 Andreae, M. O., Acevedo, O. C., Araùjo, A., Artaxo, P., Barbosa, C. G. G., Barbosa, H. M. J.,  
1379 Brito, J., Carbone, S., Chi, X., Cintra, B. B. L., da Silva, N. F., Dias, N. L., Dias-Júnior,  
1380 C. Q., Ditas, F., Ditz, R., Godoi, A. F. L., Godoi, R. H. M., Heimann, M., Hoffmann, T.,  
1381 Kesselmeier, J., Könemann, T., Krüger, M. L., Lavric, J. V., Manzi, A. O., Lopes, A. P.,  
1382 Martins, D. L., Mikhailov, E. F., Moran-Zuloaga, D., Nelson, B. W., Nölscher, A. C.,  
1383 Santos Nogueira, D., Piedade, M. T. F., Pöhlker, C., Pöschl, U., Quesada, C. A., Rizzo,  
1384 L. V., Ro, C. U., Ruckteschler, N., Sá, L. D. A., de Oliveira Sá, M., Sales, C. B., dos  
1385 Santos, R. M. N., Saturno, J., Schöngart, J., Sörgel, M., de Souza, C. M., de Souza, R. A.  
1386 F., Su, H., Targhetta, N., Tóta, J., Trebs, I., Trumbore, S., van Eijck, A., Walter, D.,  
1387 Wang, Z., Weber, B., Williams, J., Winderlich, J., Wittmann, F., Wolff, S., and Yáñez-  
1388 Serrano, A. M., The Amazon Tall Tower Observatory (ATTO): overview of pilot  
1389 measurements on ecosystem ecology, meteorology, trace gases, and aerosols: Atmos.  
1390 Chem. Phys., 15, 10,723-10,776, doi:10.5194/acp-15-10723-2015, 2015.
- 1391 Apel, E. C., Olson, J. R., Crawford, J. H., Hornbrook, R. S., Hills, A. J., Cantrell, C. A.,  
1392 Emmons, L. K., Knapp, D. J., Hall, S., Mauldin, R. L., Weinheimer, A. J., Fried, A.,  
1393 Blake, D. R., Crouse, J. D., St Clair, J. M., Wennberg, P. O., Diskin, G. S., Fuelberg, H.  
1394 E., Wisthaler, A., Mikoviny, T., Brune, W., and Riemer, D. D., Impact of the deep  
1395 convection of isoprene and other reactive trace species on radicals and ozone in the upper  
1396 troposphere: Atmos. Chem. Phys., 12, 1135-1150, doi:10.5194/acp-12-1135-2012, 2012.
- 1397 Artaxo, P., Martins, J. V., Yamasoe, M. A., Procópio, A. S., Pauliquevis, T. M., Andreae, M. O.,  
1398 Guyon, P., Gatti, L. V., and Leal, A. M. C., Physical and chemical properties of aerosols  
1399 in the wet and dry season in Rondonia, Amazonia: J. Geophys. Res., 107, 8081,  
1400 doi:10.1029/2001JD000666, 2002.
- 1401 Artaxo, P., Rizzo, L. V., Brito, J. F., Barbosa, H. M. J., Arana, A., Sena, E. T., Cirino, G. G.,  
1402 Bastos, W., Martin, S. T., and Andreae, M. O., Atmospheric aerosols in Amazonia and  
1403 land use change: from natural biogenic to biomass burning conditions: Faraday  
1404 Discussions, 165, 203-235, doi:10.1039/C3FD00052D, 2013.
- 1405 Benson, D. R., Young, L. H., Lee, S. H., Campos, T. L., Rogers, D. C., and Jensen, J., The  
1406 effects of air mass history on new particle formation in the free troposphere: case studies:  
1407 Atmos. Chem. Phys., 8, 3015-3024, 2008.
- 1408 Berkemeier, T., Ammann, M., Mentel, T. F., Pöschl, U., and Shiraiwa, M., Organic nitrate  
1409 contribution to new particle formation and growth in secondary organic aerosols from  
1410 alpha-pinene ozonolysis: Environ. Sci. Technol., 50, 6334-6342,  
1411 doi:10.1021/acs.est.6b00961, 2016.
- 1412 Berndt, T., Richters, S., Jokinen, T., Hyttinen, N., Kurten, T., Otkjaer, R. V., Kjaergaard, H. G.,  
1413 Stratmann, F., Herrmann, H., Sipila, M., Kulmala, M., and Ehn, M., Hydroxyl radical-  
1414 induced formation of highly oxidized organic compounds: Nature Communications, 7,  
1415 13677, doi:10.1038/ncomms13677, 2016.
- 1416 Bertram, T. H., Perring, A. E., Wooldridge, P. J., Crouse, J. D., Kwan, A. J., Wennberg, P. O.,  
1417 Scheuer, E., Dibb, J., Avery, M., Sachse, G., Vay, S. A., Crawford, J. H., McNaughton,  
1418 C. S., Clarke, A., Pickering, K. E., Fuelberg, H., Huey, G., Blake, D. R., Singh, H. B.,



- 1419 Hall, S. R., Shetter, R. E., Fried, A., Heikes, B. G., and Cohen, R. C., Direct  
1420 measurements of the convective recycling of the upper troposphere: *Science* 315, 816-  
1421 820, 2007.
- 1422 Betts, A. K., Gatti, L. V., Cordova, A. M., Dias, M. A. F. S., and Fuentes, J. D., Transport of  
1423 ozone to the surface by convective downdrafts at night: *J. Geophys. Res.*, 107, 8046,  
1424 doi:10.1029/2000JD000158, 2002.
- 1425 Bianchi, F., Tröstl, J., Junninen, H., Frege, C., Henne, S., Hoyle, C. R., Molteni, U., Herrmann,  
1426 E., Adamov, A., Bukowiecki, N., Chen, X., Duplissy, J., Gysel, M., Hutterli, M.,  
1427 Kangasluoma, J., Kontkanen, J., Kürten, A., Manninen, H. E., Münch, S., Peräkylä, O.,  
1428 Petäjä, T., Rondo, L., Williamson, C., Weingartner, E., Curtius, J., Worsnop, D. R.,  
1429 Kulmala, M., Dommen, J., and Baltensperger, U., New particle formation in the free  
1430 troposphere: A question of chemistry and timing: *Science*, 352, 1109-1112,  
1431 doi:10.1126/science.aad5456, 2016.
- 1432 Borrmann, S., Kunkel, D., Weigel, R., Minikin, A., Deshler, T., Wilson, J. C., Curtius, J., Volk,  
1433 C. M., Homan, C. D., Ulanovsky, A., Ravagnani, F., Viciani, S., Shur, G. N., Belyaev, G.  
1434 V., Law, K. S., and Cairo, F., Aerosols in the tropical and subtropical UT/LS: in-situ  
1435 measurements of submicron particle abundance and volatility: *Atmos. Chem. Phys.*, 10,  
1436 5573-5592, doi:10.5194/acp-10-5573-2010, 2010.
- 1437 Braga, R. C., Rosenfeld, D., Weigel, R., Jurkat, T., Andreae, M. O., Wendisch, M., Pöschl, U.,  
1438 Voigt, C., Mahnke, C., Borrmann, S., Albrecht, R. I., Molleker, S., Vila, D. A., Machado,  
1439 L. A. T., and Grulich, L., Aerosol concentrations determine the height of warm rain and  
1440 ice initiation in convective clouds over the Amazon basin: *Atmos. Chem. Phys. Discuss.*,  
1441 2017, 1-44, doi:10.5194/acp-2016-1155, 2017.
- 1442 Brock, C. A., Cozic, J., Bahreini, R., Froyd, K. D., Middlebrook, A. M., McComiskey, A.,  
1443 Brioude, J., Cooper, O. R., Stohl, A., Aikin, K. C., de Gouw, J. A., Fahey, D. W., Ferrare,  
1444 R. A., Gao, R. S., Gore, W., Holloway, J. S., Hubler, G., Jefferson, A., Lack, D. A.,  
1445 Lance, S., Moore, R. H., Murphy, D. M., Nenes, A., Novelli, P. C., Nowak, J. B., Ogren,  
1446 J. A., Peischl, J., Pierce, R. B., Pilewskie, P., Quinn, P. K., Ryerson, T. B., Schmidt, K.  
1447 S., Schwarz, J. P., Sodemann, H., Spackman, J. R., Stark, H., Thomson, D. S.,  
1448 Thornberry, T., Veres, P., Watts, L. A., Warneke, C., and Wollny, A. G., Characteristics,  
1449 sources, and transport of aerosols measured in spring 2008 during the aerosol, radiation,  
1450 and cloud processes affecting Arctic Climate (ARCPAC) Project: *Atmos. Chem. Phys.*,  
1451 11, 2423-2453, doi:10.5194/acp-11-2423-2011, 2011.
- 1452 Browell, E. V., Fenn, M. A., Butler, C. F., Grant, W. B., Clayton, M. E., Fishman, J., Bachmeier,  
1453 A. S., Anderson, B. E., Gregory, G. L., Fuelberg, H. E., Bradshaw, J. D., Sandholm, S.  
1454 T., Blake, D. R., Heikes, B. G., Sachse, G. W., Singh, H. B., and Talbot, R. W., Ozone  
1455 and aerosol distributions and air mass characteristics over the South Atlantic basin during  
1456 the burning season: *J. Geophys. Res.*, 101, 24,043-24,068, 1996.
- 1457 Bruns, E. A., Perraud, V., Zelenyuk, A., Ezell, M. J., Johnson, S. N., Yu, Y., Imre, D.,  
1458 Finlayson-Pitts, B. J., and Alexander, M. L., Comparison of FTIR and particle mass  
1459 spectrometry for the measurement of particulate organic nitrates: *Environ. Sci. Technol.*,  
1460 44, 1056-1061, doi:10.1021/es9029864, 2010.



- 1461 Cai, Y., Montague, D. C., Mooiweer-Bryan, W., and Deshler, T., Performance characteristics of  
1462 the ultra high sensitivity aerosol spectrometer for particles between 55 and 800 nm:  
1463 Laboratory and field studies: *J. Aerosol Sci.*, 39, 759-769,  
1464 doi:10.1016/j.jaerosci.2008.04.007, 2008.
- 1465 Carslaw, K. S., Lee, L. A., Reddington, C. L., Pringle, K. J., Rap, A., Forster, P. M., Mann, G.  
1466 W., Spracklen, D. V., Woodhouse, M. T., Regayre, L. A., and Pierce, J. R., Large  
1467 contribution of natural aerosols to uncertainty in indirect forcing: *Nature*, 503, 67-71,  
1468 doi:10.1038/nature12674, 2013.
- 1469 Carslaw, K. S., Gordon, H., Hamilton, D. S., Johnson, J. S., Regayre, L. A., Yoshioka, M., and  
1470 Pringle, K. J., Aerosols in the pre-industrial atmosphere: *Current Climate Change*  
1471 *Reports*, 3, 1-15, doi:10.1007/s40641-017-0061-2, 2017.
- 1472 Cecchini, M. A., Machado, L. A. T., Andreae, M. O., Martin, S. T., Albrecht, R. I., Artaxo, P.,  
1473 Barbosa, H. M. J., Borrmann, S., Fütterer, D., Jurkat, T., Mahnke, C., Minikin, A.,  
1474 Molleker, S., Pöhlker, M. L., Pöschl, U., Rosenfeld, D., Voigt, C., Wenzierl, B., and  
1475 Wendisch, M., Sensitivities of Amazonian clouds to aerosols and updraft speed: *Atmos.*  
1476 *Chem. Phys. Discuss.*, 2017, 1-23, doi:10.5194/acp-2017-89, 2017.
- 1477 Chubb, T., Huang, Y., Jensen, J., Campos, T., Siems, S., and Manton, M., Observations of high  
1478 droplet number concentrations in Southern Ocean boundary layer clouds: *Atmos. Chem.*  
1479 *Phys.*, 16, 971-987, doi:10.5194/acp-16-971-2016, 2016.
- 1480 Clarke, A., and Kapustin, V., Hemispheric aerosol vertical profiles: Anthropogenic impacts on  
1481 optical depth and cloud nuclei: *Science*, 329, 1488-1492, 2010.
- 1482 Clarke, A. D., Eisele, F., Kapustin, V. N., Moore, K., Tanner, D., Mauldin, L., Litchy, M.,  
1483 Lienert, B., Carroll, M. A., and Albercook, G., Nucleation in the equatorial free  
1484 troposphere: Favorable environments during PEM-Tropics: *J. Geophys. Res.*, 104, 5735-  
1485 5744, doi:10.1029/98JD02303, 1999.
- 1486 Clarke, A. D., Freitag, S., Simpson, R. M. C., Hudson, J. G., Howell, S. G., Brekhovskikh, V. L.,  
1487 Campos, T., Kapustin, V. N., and Zhou, J., Free troposphere as a major source of CCN  
1488 for the Equatorial Pacific boundary layer: long-range transport and teleconnections:  
1489 *Atmos. Chem. Phys.*, 13, 7511-7529, doi:10.5194/acp-13-7511-2013, 2013.
- 1490 Collow, A. B. M., Miller, M. A., and Trabachino, L. C., Cloudiness over the Amazon rainforest:  
1491 Meteorology and thermodynamics: *J. Geophys. Res.*, 121, 7990-8005,  
1492 doi:10.1002/2016JD024848, 2016.
- 1493 Colomb, A., Williams, J., Crowley, J., Gros, V., Hofmann, R., Salisbury, G., Klupfel, T.,  
1494 Kormann, R., Stickler, A., Forster, C., and Lelieveld, J., Airborne measurements of trace  
1495 organic species in the upper troposphere over Europe: the impact of deep convection:  
1496 *Environmental Chemistry*, 3, 244-259, doi:10.1071/en06020, 2006.
- 1497 Cubison, M. J., Ortega, A. M., Hayes, P. L., Farmer, D. K., Day, D., Lechner, M. J., Brune, W.  
1498 H., Apel, E., Diskin, G. S., Fisher, J. A., Fuelberg, H. E., Hecobian, A., Knapp, D. J.,  
1499 Mikoviny, T., Riemer, D., Sachse, G. W., Sessions, W., Weber, R. J., Weinheimer, A. J.,  
1500 Wisthaler, A., and Jimenez, J. L., Effects of aging on organic aerosol from open biomass  
1501 burning smoke in aircraft and laboratory studies: *Atmos. Chem. Phys.*, 11, 12,049-  
1502 12,064, doi:10.5194/acp-11-12049-2011, 2011.



- 1503 Dagan, G., Koren, I., Altaratz, O., and Heiblum, R. H., Aerosol effect on the evolution of the  
1504 thermodynamic properties of warm convective cloud fields: *Scientific Reports*, 6, 38769,  
1505 doi:10.1038/srep38769, 2016.
- 1506 de Reus, M., Krejci, R., Williams, J., Fischer, H., Scheele, R., and Strom, J., Vertical and  
1507 horizontal distributions of the aerosol number concentration and size distribution over the  
1508 northern Indian Ocean: *J. Geophys. Res.*, 106, 28,629-28,641, 2001.
- 1509 Drewnick, F., Hings, S. S., DeCarlo, P., Jayne, J. T., Gonin, M., Fuhrer, K., Weimer, S.,  
1510 Jimenez, J. L., Demerjian, K. L., Borrmann, S., and Worsnop, D. R., A new time-of-  
1511 flight aerosol mass spectrometer (TOF-AMS) - Instrument description and first field  
1512 deployment: *Aerosol Sci. Tech.*, 39, 637-658, 2005.
- 1513 Dunne, E. M., Gordon, H., Kürten, A., Almeida, J., Duplissy, J., Williamson, C., Ortega, I. K.,  
1514 Pringle, K. J., Adamov, A., Baltensperger, U., Barmet, P., Benduhn, F., Bianchi, F.,  
1515 Breitenlechner, M., Clarke, A., Curtius, J., Dommen, J., Donahue, N. M., Ehrhart, S.,  
1516 Flagan, R. C., Franchin, A., Guida, R., Hakala, J., Hansel, A., Heinritzi, M., Jokinen, T.,  
1517 Kangasluoma, J., Kirkby, J., Kulmala, M., Kupc, A., Lawler, M. J., Lehtipalo, K.,  
1518 Makhmutov, V., Mann, G., Mathot, S., Merikanto, J., Miettinen, P., Nenes, A., Onnela,  
1519 A., Rap, A., Reddington, C. L. S., Riccobono, F., Richards, N. A. D., Rissanen, M. P.,  
1520 Rondo, L., Sarnela, N., Schobesberger, S., Sengupta, K., Simon, M., Sipilä, M., Smith, J.  
1521 N., Stozkhov, Y., Tomé, A., Tröstl, J., Wagner, P. E., Wimmer, D., Winkler, P. M.,  
1522 Worsnop, D. R., and Carslaw, K. S., Global atmospheric particle formation from CERN  
1523 CLOUD measurements: *Science*, 354, 1119-1124, doi:10.1126/science.aaf2649, 2016.
- 1524 Ehn, M., Thornton, J. A., Kleist, E., Sipila, M., Junninen, H., Pullinen, I., Springer, M., Rubach,  
1525 F., Tillmann, R., Lee, B., Lopez-Hilfiker, F., Andres, S., Acir, I. H., Rissanen, M.,  
1526 Jokinen, T., Schobesberger, S., Kangasluoma, J., Kontkanen, J., Nieminen, T., Kurten,  
1527 T., Nielsen, L. B., Jorgensen, S., Kjaergaard, H. G., Canagaratna, M., Dal Maso, M.,  
1528 Berndt, T., Petaja, T., Wahner, A., Kerminen, V. M., Kulmala, M., Worsnop, D. R.,  
1529 Wildt, J., and Mentel, T. F., A large source of low-volatility secondary organic aerosol:  
1530 *Nature*, 506, 476-479, doi:10.1038/nature13032, 2014.
- 1531 Ekman, A. M. L., Wang, C., Strom, J., and Krejci, R., Explicit simulation of aerosol physics in a  
1532 cloud-resolving model: Aerosol transport and processing in the free troposphere: *J.*  
1533 *Atmos. Sci.*, 63, 682-696, 2006.
- 1534 Ekman, A. M. L., Krejci, R., Engström, A., Ström, J., de Reus, M., Williams, J., and Andreae,  
1535 M. O., Do organics contribute to small particle formation in the Amazonian upper  
1536 troposphere?: *Geophys. Res. Lett.*, 35, L17810, doi:10.1029/2008GL034970, 2008.
- 1537 Engelhart, G. J., Moore, R. H., Nenes, A., and Pandis, S. N., Cloud condensation nuclei activity  
1538 of isoprene secondary organic aerosol: *J. Geophys. Res.*, 116, D02207,  
1539 doi:10.1029/2010jd014706, 2011.
- 1540 Engström, A., Ekman, A. M. L., Krejci, R., Strom, J., de Reus, M., and Wang, C., Observational  
1541 and modelling evidence of tropical deep convective clouds as a source of mid-  
1542 tropospheric accumulation mode aerosols: *Geophys. Res. Lett.*, 35, L23813,  
1543 doi:10.1029/2008gl035817, 2008.



- 1544 Fan, J. W., Rosenfeld, D., Ding, Y. N., Leung, L. R., and Li, Z. Q., Potential aerosol indirect  
1545 effects on atmospheric circulation and radiative forcing through deep convection:  
1546 *Geophys. Res. Lett.*, 39, L09806, doi:10.1029/2012gl051851, 2012.
- 1547 Fishman, J., Fakhruzzaman, K., Cros, B., and Nganga, D., Identification of widespread pollution  
1548 in the southern hemisphere deduced from satellite analyses: *Science*, 252, 1693-1696,  
1549 1991.
- 1550 Fishman, J., Brackett, V. G., Browell, E. V., and Grant, W. B., Tropospheric ozone derived from  
1551 TOMS/SBUV measurements during TRACE-A: *J. Geophys. Res.*, 101, 24,069-24,082,  
1552 1996.
- 1553 Frey, W., Borrmann, S., Kunkel, D., Weigel, R., de Reus, M., Schlager, H., Roiger, A., Voigt,  
1554 C., Hoor, P., Curtius, J., Kraemer, M., Schiller, C., Volk, C. M., Homan, C. D., Fierli, F.,  
1555 Di Donfrancesco, G., Ulanovsky, A., Ravegnani, F., Sitnikov, N. M., Viciani, S.,  
1556 D'Amato, F., Shur, G. N., Belyaev, G. V., Law, K. S., and Cairo, F., In situ  
1557 measurements of tropical cloud properties in the West African Monsoon: upper  
1558 tropospheric ice clouds, Mesoscale Convective System outflow, and subvisual cirrus:  
1559 *Atmos. Chem. Phys.*, 11, 5569-5590, doi:10.5194/acp-11-5569-2011, 2011.
- 1560 Froyd, K. D., Murphy, D. M., Sanford, T. J., Thomson, D. S., Wilson, J. C., Pfister, L., and Lait,  
1561 L., Aerosol composition of the tropical upper troposphere: *Atmos. Chem. Phys.*, 9, 4363-  
1562 4385, 2009.
- 1563 Fry, J. L., Kiendler-Scharr, A., Rollins, A. W., Wooldridge, P. J., Brown, S. S., Fuchs, H., Dube,  
1564 W., Mensah, A., dal Maso, M., Tillmann, R., Dorn, H. P., Brauers, T., and Cohen, R. C.,  
1565 Organic nitrate and secondary organic aerosol yield from NO<sub>3</sub> oxidation of beta-pinene  
1566 evaluated using a gas-phase kinetics/aerosol partitioning model: *Atmos. Chem. Phys.*, 9,  
1567 1431-1449, 2009.
- 1568 Fu, R., Zhu, B., and Dickinson, R. E., How do atmosphere and land surface influence seasonal  
1569 changes of convection in the tropical Amazon?: *J. Clim.*, 12, 1306-1321, 1999.
- 1570 Fueglistaler, S., Dessler, A. E., Dunkerton, T. J., Folkins, I., Fu, Q., and Mote, P. W., Tropical  
1571 tropopause layer: *Rev. Geophys.*, 47, RG1004, doi:10.1029/2008rg000267, 2009.
- 1572 Gerbig, C., Schmitgen, S., Kley, D., Volz-Thomas, A., Dewey, K., and Haaks, D., An improved  
1573 fast-response vacuum-UV resonance fluorescence CO instrument: *J. Geophys. Res.*, 104,  
1574 1699-1704, doi:10.1029/1998jd100031, 1999.
- 1575 Gerken, T., Wei, D., Chase, R. J., Fuentes, J. D., Schumacher, C., Machado, L. A. T., Andreoli,  
1576 R. V., Chamecki, M., Ferreira de Souza, R. A., Freire, L. S., Jardine, A. B., Manzi, A. O.,  
1577 Nascimento dos Santos, R. M., von Randow, C., dos Santos Costa, P., Stoy, P. C., Tóta,  
1578 J., and Trowbridge, A. M., Downward transport of ozone rich air and implications for  
1579 atmospheric chemistry in the Amazon rainforest: *Atmospheric Environment*, 124, 64-76,  
1580 doi:10.1016/j.atmosenv.2015.11.014, 2016.
- 1581 Giangrande, S. E., Feng, Z., Jensen, M. P., Comstock, J., Johnson, K. L., Toto, T., Wang, M.,  
1582 Burleyson, C., Mei, F., Machado, L. A. T., Manzi, A., Xie, S., Tang, S., Silva Dias, M. A.  
1583 F., de Souza, R. A. F., Schumacher, C., and Martin, S. T., Cloud Characteristics,  
1584 Thermodynamic Controls and Radiative Impacts During the Observations and Modeling



- 1585 of the Green Ocean Amazon (GoAmazon2014/5) Experiment: Atmos. Chem. Phys.  
1586 Discuss., 2017, 1-41, doi:10.5194/acp-2017-452, 2017.
- 1587 Gonçalves, W. A., Machado, L. A. T., and Kirstetter, P. E., Influence of biomass aerosol on  
1588 precipitation over the Central Amazon: an observational study: Atmos. Chem. Phys., 15,  
1589 6789-6800, doi:10.5194/acp-15-6789-2015, 2015.
- 1590 Gordon, H., Sengupta, K., Rap, A., Duplissy, J., Frege, C., Williamson, C., Heinritzi, M., Simon,  
1591 M., Yan, C., Almeida, J., Tröstl, J., Nieminen, T., Ortega, I. K., Wagner, R., Dunne, E.  
1592 M., Adamov, A., Amorim, A., Bernhammer, A.-K., Bianchi, F., Breitenlechner, M.,  
1593 Brilke, S., Chen, X., Craven, J. S., Dias, A., Ehrhart, S., Fischer, L., Flagan, R. C.,  
1594 Franchin, A., Fuchs, C., Guida, R., Hakala, J., Hoyle, C. R., Jokinen, T., Junninen, H.,  
1595 Kangasluoma, J., Kim, J., Kirkby, J., Krapf, M., Kürten, A., Laaksonen, A., Lehtipalo,  
1596 K., Makhmutov, V., Mathot, S., Molteni, U., Monks, S. A., Onnela, A., Peräkylä, O.,  
1597 Piel, F., Petäjä, T., Praplan, A. P., Pringle, K. J., Richards, N. A. D., Rissanen, M. P.,  
1598 Rondo, L., Sarnela, N., Schobesberger, S., Scott, C. E., Seinfeld, J. H., Sharma, S., Sipilä,  
1599 M., Steiner, G., Stozhkov, Y., Stratmann, F., Tomé, A., Virtanen, A., Vogel, A. L.,  
1600 Wagner, A. C., Wagner, P. E., Weingartner, E., Wimmer, D., Winkler, P. M., Ye, P.,  
1601 Zhang, X., Hansel, A., Dommen, J., Donahue, N. M., Worsnop, D. R., Baltensperger, U.,  
1602 Kulmala, M., Curtius, J., and Carslaw, K. S., Reduced anthropogenic aerosol radiative  
1603 forcing caused by biogenic new particle formation: Proc. Natl. Acad. Sci., 113, 12,053-  
1604 12,058, doi:10.1073/pnas.1602360113, 2016.
- 1605 Grant, D. D., Fuentes, J. D., DeLonge, M. S., Chan, S., Joseph, E., Kucera, P., Ndiaye, S. A., and  
1606 Gaye, A. T., Ozone transport by mesoscale convective storms in western Senegal:  
1607 Atmospheric Environment, 42, 7104-7114, doi:10.1016/j.atmosenv.2008.05.044, 2008.
- 1608 Gunthe, S. S., King, S. M., Rose, D., Chen, Q., Roldin, P., Farmer, D. K., Jimenez, J. L., Artaxo,  
1609 P., Andreae, M. O., Martin, S. T., and Pöschl, U., Cloud condensation nuclei in pristine  
1610 tropical rainforest air of Amazonia: size-resolved measurements and modeling of  
1611 atmospheric aerosol composition and CCN activity: Atmos. Chem. Phys., 9, 7551-7575,  
1612 2009.
- 1613 Heald, C. L., Jacob, D. J., Park, R. J., Russell, L. M., Huebert, B. J., Seinfeld, J. H., Liao, H., and  
1614 Weber, R. J., A large organic aerosol source in the free troposphere missing from current  
1615 models: Geophys. Res. Lett., 32, L18809, doi:10.1029/2005GL023831, 2005.
- 1616 Heintzenberg, J., Birmili, W., Otto, R., Andreae, M. O., Mayer, J.-C., Chi, X., and Panov, A.,  
1617 Aerosol particle number size distributions and particulate light absorption at the ZOTTO  
1618 tall tower (Siberia), 2006-2009: Atmos. Chem. Phys., 11, 8703-8719, 2011.
- 1619 Holanda, B. A., Wang, Q., Saturno, J., Ditas, F., Ditas, J., Pöhlker, M., Klimach, T., Moran, D.,  
1620 Schulz, C., Ming, J., Cheng, Y., Su, H., Wendisch, M., Machado, L. A. T., Schneider, J.,  
1621 Pöhlker, C., Artaxo, P., Pöschl, U., and Andreae, M., Transatlantic transport of pollution  
1622 aerosol from Africa to the Amazon rain forest - Aircraft observations in the context of the  
1623 ACRIDICON-CHUVA campaign: Atmos. Chem. Phys. Discuss., 2017, in preparation.
- 1624 Hu, W. W., Campuzano-Jost, P., Palm, B. B., Day, D. A., Ortega, A. M., Hayes, P. L.,  
1625 Krechmer, J. E., Chen, Q., Kuwata, M., Liu, Y. J., de Sa, S. S., McKinney, K., Martin, S.  
1626 T., Hu, M., Budisulistiorini, S. H., Riva, M., Surratt, J. D., St Clair, J. M., Isaacman-Van  
1627 Wertz, G., Yee, L. D., Goldstein, A. H., Carbone, S., Brito, J., Artaxo, P., de Gouw, J. A.,



- 1628 Koss, A., Wisthaler, A., Mikoviny, T., Karl, T., Kaser, L., Jud, W., Hansel, A., Docherty,  
1629 K. S., Alexander, M. L., Robinson, N. H., Coe, H., Allan, J. D., Canagaratna, M. R.,  
1630 Paulot, F., and Jimenez, J. L., Characterization of a real-time tracer for isoprene  
1631 epoxydiols-derived secondary organic aerosol (IEPOX-SOA) from aerosol mass  
1632 spectrometer measurements: Atmos. Chem. Phys., 15, 11,807-11,833, doi:10.5194/acp-  
1633 15-11807-2015, 2015.
- 1634 Hu, X. M., Fuentes, J. D., and Zhang, F. Q., Downward transport and modification of  
1635 tropospheric ozone through moist convection: J. Atmos. Chem., 65, 13-35,  
1636 doi:10.1007/s10874-010-9179-5, 2010.
- 1637 Huntrieser, H., Lichtenstern, M., Scheibe, M., Aufmhoff, H., Schlager, H., Pucik, T., Minikin,  
1638 A., Weinzierl, B., Heimerl, K., Futterer, D., Rappengluck, B., Ackermann, L., Pickering,  
1639 K. E., Cummings, K. A., Biggerstaff, M. I., Betten, D. P., Honomichl, S., and Barth, M.  
1640 C., On the origin of pronounced O<sub>3</sub> gradients in the thunderstorm outflow region during  
1641 DC3: J. Geophys. Res., 121, 6600-6637, doi:10.1002/2015jd024279, 2016.
- 1642 Janhäll, S., Andreae, M. O., and Pöschl, U., Biomass burning aerosol emissions from vegetation  
1643 fires: particle number and mass emission factors and size distributions: Atmos. Chem.  
1644 Phys., 10, 1427-1439, 2010.
- 1645 Jiang, J. H., Su, H., Schoeberl, M. R., Massie, S. T., Colarco, P., Platnick, S., and Livesey, N. J.,  
1646 Clean and polluted clouds: Relationships among pollution, ice clouds, and precipitation  
1647 in South America: Geophys. Res. Lett., 35, L14804, doi:10.1029/2008GL034631, 2008.
- 1648 Jimenez, J. L., Canagaratna, M. R., Donahue, N. M., Prevot, A. S. H., Zhang, Q., Kroll, J. H.,  
1649 DeCarlo, P. F., Allan, J. D., Coe, H., Ng, N. L., Aiken, A. C., Docherty, K. D., Ulbrich, I.  
1650 M., Grieshop, A. P., Robinson, A. L., Duplissy, J., Smith, J. D., Wilson, K. R., Lanz, V.  
1651 A., Hueglin, C., Sun, Y. L., Tian, J., Laaksonen, A., Raatikainen, T., Rautiainen, J.,  
1652 Vaattovaara, P., Ehn, M., Kulmala, M., Tomlinson, J. M., Collins, D. R., Cubison, M. J.,  
1653 Dunlea, E. J., Huffman, J. A., Onasch, T. B., Alfarra, M. R., Williams, P. I., Bower, K.,  
1654 Kondo, Y., Schneider, J., Drewnick, F., Borrmann, S., Weimer, S., Demerjian, K.,  
1655 Salcedo, D., Cottrell, L., Griffin, R., Takami, A., Miyoshi, T., Hatakeyama, S., Shimono,  
1656 A., Sun, J. Y., Zhang, Y. M., Dzepina, K., Kimmel, J. R., Sueper, D., Jayne, J. T.,  
1657 Herndon, S. C., Trimborn, A. M., Williams, L. R., Wood, E. C., Kolb, C. E.,  
1658 Baltensperger, U., and Worsnop, D. R., Evolution of organic aerosols in the atmosphere:  
1659 Science, 326, 1525-529, doi:10.1126/science.1180353, 2009.
- 1660 Jokinen, T., Berndt, T., Makkonen, R., Kerminen, V.-M., Junninen, H., Paasonen, P., Stratmann,  
1661 F., Herrmann, H., Guenther, A. B., Worsnop, D. R., Kulmala, M., Ehn, M., and Sipilä,  
1662 M., Production of extremely low volatile organic compounds from biogenic emissions:  
1663 Measured yields and atmospheric implications: Proc. Natl. Acad. Sci., 112, 7123-7128,  
1664 doi:10.1073/pnas.1423977112, 2015.
- 1665 Katoshevski, D., Nenes, A., and Seinfeld, J. H., A study of processes that govern the  
1666 maintenance of aerosols in the marine boundary layer: J. Aerosol Sci., 30, 503-532, 1999.
- 1667 Khain, A. P., Phillips, V., Benmoshe, N., and Pokrovsky, A., The role of small soluble aerosols  
1668 in the microphysics of deep maritime clouds: J. Atmos. Sci., 69, 2787-2807,  
1669 doi:10.1175/2011jas3649.1, 2012.



- 1670 Kirkby, J., Duplissy, J., Sengupta, K., Frege, C., Gordon, H., Williamson, C., Heinritzi, M.,  
1671 Simon, M., Yan, C., Almeida, J., Tröstl, J., Nieminen, T., Ortega, I. K., Wagner, R.,  
1672 Adamov, A., Amorim, A., Bernhammer, A.-K., Bianchi, F., Breitenlechner, M., Brilke,  
1673 S., Chen, X., Craven, J., Dias, A., Ehrhart, S., Flagan, R. C., Franchin, A., Fuchs, C.,  
1674 Guida, R., Hakala, J., Hoyle, C. R., Jokinen, T., Junninen, H., Kangasluoma, J., Kim, J.,  
1675 Krapf, M., Kürten, A., Laaksonen, A., Lehtipalo, K., Makhmutov, V., Mathot, S.,  
1676 Molteni, U., Onnela, A., Peräkylä, O., Piel, F., Petäjä, T., Praplan, A. P., Pringle, K., Rap,  
1677 A., Richards, N. A. D., Riipinen, I., Rissanen, M. P., Rondo, L., Sarnela, N.,  
1678 Schobesberger, S., Scott, C. E., Seinfeld, J. H., Sipilä, M., Steiner, G., Stozhkov, Y.,  
1679 Stratmann, F., Tomé, A., Virtanen, A., Vogel, A. L., Wagner, A. C., Wagner, P. E.,  
1680 Weingartner, E., Wimmer, D., Winkler, P. M., Ye, P., Zhang, X., Hansel, A., Dommen,  
1681 J., Donahue, N. M., Worsnop, D. R., Baltensperger, U., Kulmala, M., Carslaw, K. S., and  
1682 Curtius, J., Ion-induced nucleation of pure biogenic particles: *Nature*, 533, 521-526,  
1683 doi:10.1038/nature17953, 2016.
- 1684 Kojima, T., Buseck, P. R., Wilson, J. C., Reeves, J. M., and Mahoney, M. J., Aerosol particles  
1685 from tropical convective systems: Cloud tops and cirrus anvils: *J. Geophys. Res.*, 109,  
1686 D12201, 2004.
- 1687 Koren, I., Martins, J. V., Remer, L. A., and Afargan, H., Smoke invigoration versus inhibition of  
1688 clouds over the Amazon: *Science* 321, 946-949, 2008.
- 1689 Koren, I., Remer, L. A., Altaratz, O., Martins, J. V., and Davidi, A., Aerosol-induced changes of  
1690 convective cloud anvils produce strong climate warming: *Atmos. Chem. Phys.*, 10, 5001-  
1691 5010, doi:10.5194/acp-10-5001-2010, 2010.
- 1692 Kottayil, A., and Satheesan, K., Enhancement in the upper tropospheric humidity associated with  
1693 aerosol loading over tropical Pacific: *Atmospheric Environment*, 122, 148-153,  
1694 doi:10.1016/j.atmosenv.2015.09.043, 2015.
- 1695 Krejci, R., Strom, J., de Reus, M., Hoor, P., Williams, J., Fischer, H., and Hansson, H. C.,  
1696 Evolution of aerosol properties over the rain forest in Surinam, South America, observed  
1697 from aircraft during the LBA-CLAIRE 98 experiment: *J. Geophys. Res.*, 108, 4561,  
1698 doi:10.1029/2001JD001375, 2003.
- 1699 Krüger, M. L., Mertes, S., Klimach, T., Cheng, Y., Su, H., Schneider, J., Andreae, M. O., Pöschl,  
1700 U., and Rose, D., Assessment of cloud supersaturation by size-resolved aerosol particle  
1701 and cloud condensation nuclei (CCN) measurements: *Atmos. Meas. Tech.*, 7, 2615-2629,  
1702 doi:10.5194/amt-7-2615-2014, 2014.
- 1703 Kulmala, M., Reissell, A., Sipilä, M., Bonn, B., Ruuskanen, T. M., Lehtinen, K. E. J., Kerminen,  
1704 V.-M., and Strom, J., Deep convective clouds as aerosol production engines: Role of  
1705 insoluble organics: *J. Geophys. Res.*, 111, D17202, doi:10.1029/2005jd006963, 2006.
- 1706 Kulmala, M., and Kerminen, V. M., On the formation and growth of atmospheric nanoparticles:  
1707 *Atmos. Res.*, 90, 132-150, doi:10.1016/j.atmosres.2008.01.005, 2008.
- 1708 Laaksonen, A., Kulmala, M., O'Dowd, C. D., Joutsensaari, J., Vaattovaara, P., Mikkonen, S.,  
1709 Lehtinen, K. E. J., Sogacheva, L., Dal Maso, M., Aalto, P., Petaja, T., Sogachev, A.,  
1710 Yoon, Y. J., Lihavainen, H., Nilsson, D., Facchini, M. C., Cavalli, F., Fuzzi, S.,  
1711 Hoffmann, T., Arnold, F., Hanke, M., Sellegri, K., Umann, B., Junkermann, W., Coe, H.,  
1712 Allan, J. D., Alfarra, M. R., Worsnop, D. R., Riekkola, M. L., Hyotylainen, T., and



- 1713 Viisanen, Y., The role of VOC oxidation products in continental new particle formation:  
1714 Atmos. Chem. Phys., 8, 2657-2665, 2008.
- 1715 Laborde, M., Crippa, M., Tritscher, T., Juranyi, Z., Decarlo, P. F., Temime-Roussel, B.,  
1716 Marchand, N., Eckhardt, S., Stohl, A., Baltensperger, U., Prevot, A. S. H., Weingartner,  
1717 E., and Gysel, M., Black carbon physical properties and mixing state in the European  
1718 megacity Paris: Atmos. Chem. Phys., 13, 5831-5856, doi:10.5194/acp-13-5831-2013,  
1719 2013.
- 1720 Lee, L., Wooldridge, P. J., Gilman, J. B., Warneke, C., de Gouw, J., and Cohen, R. C., Low  
1721 temperatures enhance organic nitrate formation: evidence from observations in the 2012  
1722 Uintah Basin Winter Ozone Study: Atmos. Chem. Phys., 14, 12,441-12,454,  
1723 doi:10.5194/acp-14-12441-2014, 2014.
- 1724 Lee, S. H., Reeves, J. M., Wilson, J. C., Hunton, D. E., Viggiano, A. A., Miller, T. M.,  
1725 Ballenthin, J. O., and Lait, L. R., Particle formation by ion nucleation in the upper  
1726 troposphere and lower stratosphere: Science, 301, 1886-1889,  
1727 doi:10.1126/science.1087236, 2003.
- 1728 Lee, S. H., Wilson, J. C., Baumgardner, D., Herman, R. L., Weinstock, E. M., LaFleur, B. G.,  
1729 Kok, G., Anderson, B., Lawson, P., Baker, B., Strawa, A., Pittman, J. V., Reeves, J. M.,  
1730 and Bui, T. P., New particle formation observed in the tropical/subtropical cirrus clouds:  
1731 J. Geophys. Res., 109, D20209, doi:10.1029/2004jd005033, 2004.
- 1732 Machado, L. A. T., Laurent, H., Dessay, N., and Miranda, I., Seasonal and diurnal variability of  
1733 convection over the Amazonia: A comparison of different vegetation types and large  
1734 scale forcing: Theoretical and Applied Climatology, 78, 61-77, doi:10.1007/s00704-004-  
1735 0044-9, 2004.
- 1736 Martin, S. T., Andreae, M. O., Artaxo, P., Baumgardner, D., Chen, Q., Goldstein, A. H.,  
1737 Guenther, A., Heald, C. L., Mayol-Bracero, O. L., McMurry, P. H., Pauliquevis, T.,  
1738 Pöschl, U., Prather, K. A., Roberts, G. C., Saleska, S. R., Dias, M. A. S., Spracklen, D.,  
1739 Swietlicki, E., and Trebs, I., Sources and properties of Amazonian aerosol particles: Rev.  
1740 Geophys., 48, RG2002, doi:10.1029/2008RG000280, 2010.
- 1741 Martin, S. T., Artaxo, P., Machado, L. A. T., Manzi, A. O., Souza, R. A. F., Schumacher, C.,  
1742 Wang, J., Andreae, M. O., Barbosa, H. M. J., Fan, J., Fisch, G., Goldstein, A. H.,  
1743 Guenther, A., Jimenez, J. L., Pöschl, U., Silva Dias, M. A., Smith, J. N., and Wendisch,  
1744 M., Introduction: Observations and modeling of the Green Ocean Amazon  
1745 (GoAmazon2014/5): Atmos. Chem. Phys., 16, 4785-4797, doi:10.5194/acp-16-4785-  
1746 2016, 2016.
- 1747 Merikanto, J., Spracklen, D. V., Mann, G. W., Pickering, S. J., and Carslaw, K. S., Impact of  
1748 nucleation on global CCN: Atmos. Chem. Phys., 9, 8601-8616, 2009.
- 1749 Metzger, A., Verheggen, B., Dommen, J., Duplissy, J., Prevot, A. S. H., Weingartner, E.,  
1750 Riipinen, I., Kulmala, M., Spracklen, D. V., Carslaw, K. S., and Baltensperger, U.,  
1751 Evidence for the role of organics in aerosol particle formation under atmospheric  
1752 conditions: Proc. Natl. Acad. Sci., doi:10.1073/pnas.0911330107, 2010.



- 1753 Mirme, S., Mirme, A., Minikin, A., Petzold, A., Horrak, U., Kerminen, V. M., and Kulmala, M.,  
1754 Atmospheric sub-3 nm particles at high altitudes: Atmos. Chem. Phys., 10, 437-451,  
1755 2010.
- 1756 Murphy, B. N., Julin, J., Riipinen, I., and Ekman, A. M. L., Organic aerosol processing in  
1757 tropical deep convective clouds: Development of a new model (CRM-ORG) and  
1758 implications for sources of particle number: J. Geophys. Res., 120, 10,441-10,464,  
1759 doi:10.1002/2015JD023551, 2015.
- 1760 Newell, R. E., Thouret, V., Cho, J. Y. N., Stoller, P., Marengo, A., and Smit, H. G., Ubiquity of  
1761 quasi-horizontal layers in the troposphere: Nature, 398, 316-319, 1999.
- 1762 Ng, N. L., Canagaratna, M. R., Jimenez, J. L., Chhabra, P. S., Seinfeld, J. H., and Worsnop, D.  
1763 R., Changes in organic aerosol composition with aging inferred from aerosol mass  
1764 spectra: Atmos. Chem. Phys., 11, 6465-6474, doi:10.5194/acp-11-6465-2011, 2011.
- 1765 Öström, E., Putian, Z., Schurgers, G., Mishurov, M., Kivekäs, N., Lihavainen, H., Ehn, M.,  
1766 Rissanen, M. P., Kurtén, T., Boy, M., Swietlicki, E., and Roldin, P., Modeling the role of  
1767 highly oxidized multifunctional organic molecules for the growth of new particles  
1768 over the boreal forest region: Atmos. Chem. Phys., 17, 8887-8901, doi:10.5194/acp-17-  
1769 8887-2017, 2017.
- 1770 Petters, M. D., and Kreidenweis, S. M., A single parameter representation of hygroscopic growth  
1771 and cloud condensation nucleus activity: Atmos. Chem. Phys., 7, 1961–1971, 2007.
- 1772 Petzold, A., Marsh, R., Johnson, M., Miller, M., Sevcenco, Y., Delhaye, D., Ibrahim, A.,  
1773 Williams, P., Bauer, H., Crayford, A., Bachalo, W. D., and Raper, D., Evaluation of  
1774 methods for measuring particulate matter emissions from gas turbines: Environ. Sci.  
1775 Technol., 45, 3562-3568, doi:10.1021/es103969v, 2011.
- 1776 Pöhlker, C., Wiedemann, K., Sinha, B., Shiraiwa, M., Gunthe, S., Smith, M., Su, H., Artaxo, P.,  
1777 Chen, Q., Cheng, Y., Elbert, W., Gilles, M. K., Kilcoyne, A. L. D., Moffet, R. C.,  
1778 Weigand, M., Martin, S. T., Pöschl, U., and Andreae, M. O., Biogenic potassium salt  
1779 particles as seeds for secondary organic aerosol in the Amazon: Science, 337, 1075-1078,  
1780 2012.
- 1781 Pöhlker, M. L., Pöhlker, C., Ditas, F., Klimach, T., Hrabe de Angelis, I., Araújo, A., Brito, J.,  
1782 Carbone, S., Cheng, Y., Chi, X., Ditz, R., Gunthe, S. S., Kesselmeier, J., Könemann, T.,  
1783 Lavrič, J. V., Martin, S. T., Mikhailov, E., Moran-Zuloaga, D., Rose, D., Saturno, J., Su,  
1784 H., Thalman, R., Walter, D., Wang, J., Wolff, S., Barbosa, H. M. J., Artaxo, P., Andreae,  
1785 M. O., and Pöschl, U., Long-term observations of cloud condensation nuclei in the  
1786 Amazon rain forest – Part I: Aerosol size distribution, hygroscopicity, and new model  
1787 parametrizations for CCN prediction: Atmos. Chem. Phys., 16, 15,709-15,740,  
1788 doi:10.5194/acp-16-15709-2016, 2016.
- 1789 Pöschl, U., Martin, S. T., Sinha, B., Chen, Q., Gunthe, S. S., Huffman, J. A., Borrmann, S.,  
1790 Farmer, D. K., Garland, R. M., Helas, G., Jimenez, J. L., King, S. M., Manzi, A.,  
1791 Mikhailov, E., Pauliquevis, T., Petters, M. D., Prenni, A. J., Roldin, P., Rose, D.,  
1792 Schneider, J., Su, H., Zorn, S. R., Artaxo, P., and Andreae, M. O., Rainforest aerosols as  
1793 biogenic nuclei of clouds and precipitation in the Amazon: Science, 329, 1513-1516,  
1794 2010.



- 1795 Raes, F., Entrainment of free tropospheric aerosols as a regulating mechanism for cloud  
1796 condensation nuclei in the remote marine boundary layer: *J. Geophys. Res.*, 100, 2893-  
1797 2903, 1995.
- 1798 Randel, W. J., and Jensen, E. J., Physical processes in the tropical tropopause layer and their  
1799 roles in a changing climate: *Nature Geoscience*, 6, 169-176, doi:10.1038/ngeo1733, 2013.
- 1800 Reddington, C. L., Carslaw, K. S., Stier, P., Schutgens, N., Coe, H., Liu, D., Allan, J., Browse,  
1801 J., Pringle, K. J., Lee, L. A., Yoshioka, M., Johnson, J. S., Regayre, L. A., Spracklen, D.  
1802 V., Mann, G. W., Clarke, A., Hermann, M., Henning, S., Wex, H., Kristensen, T. B.,  
1803 Leaitch, W. R., Pöschl, U., Rose, D., Andreae, M. O., Schmale, J., Kondo, Y., Oshima,  
1804 N., Schwarz, J. P., Nenes, A., Anderson, B., Roberts, G. C., Snider, J. R., Leck, C.,  
1805 Quinn, P. K., Chi, X., Ding, A., Jimenez, J. L., and Zhang, Q., The Global Aerosol  
1806 Synthesis and Science Project (GASSP) - Measurements and modelling to reduce  
1807 uncertainty: *Bull. Am. Meteorol. Soc.*, 2016, under review.
- 1808 Riccobono, F., Schobesberger, S., Scott, C. E., Dommen, J., Ortega, I. K., Rondo, L., Almeida,  
1809 J., Amorim, A., Bianchi, F., Breitenlechner, M., David, A., Downard, A., Dunne, E. M.,  
1810 Duplissy, J., Ehrhart, S., Flagan, R. C., Franchin, A., Hansel, A., Junninen, H., Kajos, M.,  
1811 Keskinen, H., Kupc, A., Kürten, A., Kvashin, A. N., Laaksonen, A., Lehtipalo, K.,  
1812 Makhmutov, V., Mathot, S., Nieminen, T., Onnela, A., Petäjä, T., Praplan, A. P., Santos,  
1813 F. D., Schallhart, S., Seinfeld, J. H., Sipilä, M., Spracklen, D. V., Stozhkov, Y.,  
1814 Stratmann, F., Tomé, A., Tsagkogeorgas, G., Vaattovaara, P., Viisanen, Y., Vrtala, A.,  
1815 Wagner, P. E., Weingartner, E., Wex, H., Wimmer, D., Carslaw, K. S., Curtius, J.,  
1816 Donahue, N. M., Kirkby, J., Kulmala, M., Worsnop, D. R., and Baltensperger, U.,  
1817 Oxidation products of biogenic emissions contribute to nucleation of atmospheric  
1818 particles: *Science*, 344, 717-721, doi:10.1126/science.1243527, 2014.
- 1819 Riipinen, I., Yli-Juuti, T., Pierce, J. R., Petaja, T., Worsnop, D. R., Kulmala, M., and Donahue,  
1820 N. M., The contribution of organics to atmospheric nanoparticle growth: *Nature*  
1821 *Geoscience*, 5, 453-458, doi:10.1038/ngeo1499, 2012.
- 1822 Rissler, J., Vestin, A., Swietlicki, E., Fisch, G., Zhou, J., Artaxo, P., and Andreae, M. O., Size  
1823 distribution and hygroscopic properties of aerosol particles from dry-season biomass  
1824 burning in Amazonia: *Atmos. Chem. Phys.*, 6, 471-491, 2006.
- 1825 Riuttanen, L., Bister, M., Kerminen, V. M., John, V. O., Sundstrom, A. M., Dal Maso, M.,  
1826 Raisanen, J., Sinclair, V. A., Makkonen, R., Xausa, F., de Leeuw, G., and Kulmala, M.,  
1827 Observational evidence for aerosols increasing upper tropospheric humidity: *Atmos.*  
1828 *Chem. Phys.*, 16, 14,331-14,342, doi:10.5194/acp-16-14331-2016, 2016.
- 1829 Rizzo, L. V., Artaxo, P., Müller, T., Wiedensohler, A., Paixão, M., Cirino, G. G., Arana, A.,  
1830 Swietlicki, E., Roldin, P., Fors, E. O., Wiedemann, K. T., Leal, L. S. M., and Kulmala,  
1831 M., Long term measurements of aerosol optical properties at a primary forest site in  
1832 Amazonia: *Atmos. Chem. Phys.*, 13, 2391-2413, doi:10.5194/acp-13-2391-2013, 2013.
- 1833 Roberts, G. C., and Andreae, M. O., Reply to "Comment on Cloud condensation nuclei in the  
1834 Amazon Basin: "Marine" conditions over a continent?" by P. J. Crutzen et al.: *Geophys.*  
1835 *Res. Lett.*, 30, doi:10.1029/2002GL015564, 2003.
- 1836 Roberts, G. C., and Nenes, A., A continuous-flow streamwise thermal-gradient CCN chamber  
1837 for atmospheric measurements: *Aerosol Sci. Tech.*, 39, 206-221, 2005.



- 1838 Robinson, N. H., Hamilton, J. F., Allan, J. D., Langford, B., Oram, D. E., Chen, Q., Docherty,  
1839 K., Farmer, D. K., Jimenez, J. L., Ward, M. W., Hewitt, C. N., Barley, M. H., Jenkin, M.  
1840 E., Rickard, A. R., Martin, S. T., McFiggans, G., and Coe, H., Evidence for a significant  
1841 proportion of Secondary Organic Aerosol from isoprene above a maritime tropical forest:  
1842 Atmos. Chem. Phys., 11, 1039-1050, 2011.
- 1843 Rose, C., Sellegri, K., Moreno, I., Velarde, F., Ramonet, M., Weinhold, K., Krejci, R., Andrade,  
1844 M., Wiedensohler, A., Ginot, P., and Laj, P., CCN production by new particle formation  
1845 in the free troposphere: Atmos. Chem. Phys., 17, 1529-1541, doi:10.5194/acp-17-1529-  
1846 2017, 2017.
- 1847 Rose, D., Gunthe, S. S., Mikhailov, E., Frank, G. P., Dusek, U., Andreae, M. O., and Pöschl, U.,  
1848 Calibration and measurement uncertainties of a continuous-flow cloud condensation  
1849 nuclei counter (DMT-CCNC): CCN activation of ammonium sulfate and sodium chloride  
1850 aerosol particles in theory and experiment: Atmos. Chem. Phys., 8, 1153-1179, 2008.
- 1851 Rosenfeld, D., Lohmann, U., Raga, G. B., O'Dowd, C. D., Kulmala, M., Fuzzi, S., Reissell, A.,  
1852 and Andreae, M. O., Flood or drought: How do aerosols affect precipitation?: Science,  
1853 321, 1309-1313, 2008.
- 1854 Rosenfeld, D., Andreae, M. O., Asmi, A., Chin, M., de Leeuw, G., Donovan, D. P., Kahn, R.,  
1855 Kinne, S., Kivekäs, N., Kulmala, M., Lau, W., Schmidt, K. S., Suni, T., Wagner, T.,  
1856 Wild, M., and Quaas, J., Global observations of aerosol-cloud-precipitation-climate  
1857 interactions: Rev. Geophys., 52, 750-808, doi:10.1002/2013RG000441, 2014.
- 1858 Saha, S., Moorthi, S., Wu, X., Wang, J., Nadiga, S., Tripp, P., Behringer, D., Hou, Y.-T.,  
1859 Chuang, H.-y., Iredell, M., Ek, M., Meng, J., Yang, R., Mendez, M. P., Dool, H. v. d.,  
1860 Zhang, Q., Wang, W., Chen, M., and Becker, E., NCEP Climate Forecast System Version  
1861 2 (CFSv2) 6-hourly Products. Research Data Archive at the National Center for  
1862 Atmospheric Research, Computational and Information Systems Laboratory. Accessed  
1863 20 March 2017, <https://rda.ucar.edu/datasets/ds094.0/> (2017).
- 1864 Sahu, L. K., and Lal, S., Changes in surface ozone levels due to convective downdrafts over the  
1865 Bay of Bengal: Geophys. Res. Lett., 33, L10807, doi:10.1029/2006gl025994, 2006.
- 1866 Schmale, J., Schneider, J., Jurkat, T., Voigt, C., Kalesse, H., Rautenhaus, M., Lichtenstern, M.,  
1867 Schlager, H., Ancellet, G., Arnold, F., Gerding, M., Mattis, I., Wendisch, M., and  
1868 Borrmann, S., Aerosol layers from the 2008 eruptions of Mount Okmok and Mount  
1869 Kasatochi: In situ upper troposphere and lower stratosphere measurements of sulfate and  
1870 organics over Europe: J. Geophys. Res., 115, D00107, doi:10.1029/2009jd013628, 2010.
- 1871 Schneider, J., Weimer, S., Drewnick, F., Borrmann, S., Helas, G., Gwaze, P., Schmid, O.,  
1872 Andreae, M. O., and Kirchner, U., Mass spectrometric analysis and aerodynamic  
1873 properties of various types of combustion-derived aerosol particles: Int. J. Mass Spec.,  
1874 258, 37-49, 2006.
- 1875 Schulz, C., Schneider, J., Weinzierl, B., Sauer, D., Fütterer, D., and Borrmann, S., Aircraft-based  
1876 observations of IEPOX-derived isoprene SOA formation in the tropical upper  
1877 troposphere: Atmos. Chem. Phys. Discuss., 2017.
- 1878 Schwarz, J. P., Gao, R. S., Fahey, D. W., Thomson, D. S., Watts, L. A., Wilson, J. C., Reeves, J.  
1879 M., Darbeheshti, M., Baumgardner, D. G., Kok, G. L., Chung, S. H., Schulz, M.,



- 1880 Hendricks, J., Lauer, A., Karcher, B., Slowik, J. G., Rosenlof, K. H., Thompson, T. L.,  
1881 Langford, A. O., Loewenstein, M., and Aikin, K. C., Single-particle measurements of  
1882 midlatitude black carbon and light-scattering aerosols from the boundary layer to the  
1883 lower stratosphere: *J. Geophys. Res.*, 111, D16207, doi:10.1029/2006JD007076, 2006.
- 1884 Schwarz, J. P., Weinzierl, B., Samset, B. H., Dollner, M., Heimerl, K., Markovic, M. Z., Perring,  
1885 A. E., and Ziemba, L., Aircraft measurements of black carbon vertical profiles show  
1886 upper tropospheric variability and stability: *Geophys. Res. Lett.*, 44, 1132-1140,  
1887 doi:10.1002/2016GL071241, 2017.
- 1888 Seibert, P., and Frank, A., Source-receptor matrix calculation with a Lagrangian particle  
1889 dispersion model in backward mode: *Atmos. Chem. Phys.*, 4, 51-63, 2004.
- 1890 Sherwood, S., A microphysical connection among biomass burning, cumulus clouds, and  
1891 stratospheric moisture: *Science*, 295, 1272-1275, 2002.
- 1892 Stein, A. F., Draxler, R. R., Rolph, G. D., Stunder, B. J. B., Cohen, M. D., and Ngan, F.,  
1893 NOAA's HYSPLIT atmospheric transport and dispersion modeling system: *Bull. Am.*  
1894 *Meteorol. Soc.*, 96, 2059-2077, doi:10.1175/BAMS-D-14-00110.1, 2015.
- 1895 Stephens, M., Turner, N., and Sandberg, J., Particle identification by laser-induced  
1896 incandescence in a solid-state laser cavity: *Applied Optics*, 42, 3726-3736,  
1897 doi:10.1364/ao.42.003726, 2003.
- 1898 Stohl, A., Hittenberger, M., and Wotawa, G., Validation of the Lagrangian particle dispersion  
1899 model FLEXPART against large-scale tracer experiment data: *Atmospheric*  
1900 *Environment*, 32, 4245-4264, doi:10.1016/s1352-2310(98)00184-8, 1998.
- 1901 Stohl, A., and Thomson, D. J., A density correction for Lagrangian particle dispersion models:  
1902 *Boundary-Layer Meteorology*, 90, 155-167, doi:10.1023/a:1001741110696, 1999.
- 1903 Stohl, A., Eckhardt, S., Forster, C., James, P., Spichtinger, N., and Seibert, P., A replacement for  
1904 simple back trajectory calculations in the interpretation of atmospheric trace substance  
1905 measurements: *Atmospheric Environment*, 36, 4635-4648, doi:10.1016/s1352-  
1906 2310(02)00416-8, 2002.
- 1907 Stohl, A., Forster, C., Frank, A., Seibert, P., and Wotawa, G., Technical note: The Lagrangian  
1908 particle dispersion model FLEXPART version 6.2: *Atmos. Chem. Phys.*, 5, 2461-2474,  
1909 2005.
- 1910 Stolz, D. C., Rutledge, S. A., and Pierce, J. R., Simultaneous influences of thermodynamics and  
1911 aerosols on deep convection and lightning in the tropics: *J. Geophys. Res.*, 120, 6207-  
1912 6231, doi:10.1002/2014jd023033, 2015.
- 1913 Talbot, R. W., Andreae, M. O., Andreae, T. W., and Harriss, R. C., Regional aerosol chemistry  
1914 of the Amazon Basin during the dry season: *J. Geophys. Res.*, 93, 1499-1508, 1988.
- 1915 Talbot, R. W., Andreae, M. O., Berresheim, H., Artaxo, P., Garstang, M., Harriss, R. C.,  
1916 Beecher, K. M., and Li, S. M., Aerosol chemistry during the wet season in Central  
1917 Amazonia: The influence of long-range transport: *J. Geophys. Res.*, 95, 16,955-16,969,  
1918 1990.
- 1919 Thalman, R., Thalman, R., de Sá, S. S., Palm, B. B., Barbosa, H. M. J., Pöhlker, M. L.,  
1920 Alexander, M. L., Brito, J., Carbone, S., Castillo, P., Day, D. A., Kuang, C., Manzi, A.,



- 1921 Ng, N. L., Sedlacek III, A. J., Souza, R., Springston, S., Watson, T., Pöhlker, C., Pöschl,  
1922 U., Andreae, M. O., Artaxo, P., Jimenez, J. L., Martin, S. T., and Wang, J., CCN activity  
1923 and organic hygroscopicity of aerosols downwind of an urban region in central  
1924 Amazonia: Seasonal and diel variations and impact of anthropogenic emissions: Atmos.  
1925 Chem. Phys. Discuss., doi:10.5194/acp-2017-251, 2017.
- 1926 Thornberry, T., Froyd, K. D., Murphy, D. M., Thomson, D. S., Anderson, B. E., Thornhill, K. L.,  
1927 and Winstead, E. L., Persistence of organic carbon in heated aerosol residuals measured  
1928 during Tropical Composition Cloud and Climate Coupling (TC4): J. Geophys. Res., 115,  
1929 D00J02, doi:10.1029/2009jd012721, 2010.
- 1930 Tröstl, J., Chuang, W. K., Gordon, H., Heinritzi, M., Yan, C., Molteni, U., Ahlm, L., Frege, C.,  
1931 Bianchi, F., Wagner, R., Simon, M., Lehtipalo, K., Williamson, C., Craven, J. S.,  
1932 Duplissy, J., Adamov, A., Almeida, J., Bernhammer, A.-K., Breitenlechner, M., Brilke,  
1933 S., Dias, A., Ehrhart, S., Flagan, R. C., Franchin, A., Fuchs, C., Guida, R., Gysel, M.,  
1934 Hansel, A., Hoyle, C. R., Jokinen, T., Junninen, H., Kangasluoma, J., Keskinen, H., Kim,  
1935 J., Krapf, M., Kürten, A., Laaksonen, A., Lawler, M., Leiminger, M., Mathot, S., Möhler,  
1936 O., Nieminen, T., Onnela, A., Petäjä, T., Piel, F. M., Miettinen, P., Rissanen, M. P.,  
1937 Rondo, L., Sarnela, N., Schobesberger, S., Sengupta, K., Sipilä, M., Smith, J. N., Steiner,  
1938 G., Tomè, A., Virtanen, A., Wagner, A. C., Weingartner, E., Wimmer, D., Winkler, P.  
1939 M., Ye, P., Carslaw, K. S., Curtius, J., Dommen, J., Kirkby, J., Kulmala, M., Riipinen, I.,  
1940 Worsnop, D. R., Donahue, N. M., and Baltensperger, U., The role of low-volatility  
1941 organic compounds in initial particle growth in the atmosphere: Nature, 533, 527-531,  
1942 doi:10.1038/nature18271, 2016.
- 1943 Twohy, C. H., Clement, C. F., Gandrud, B. W., Weinheimer, A. J., Campos, T. L., Baumgardner,  
1944 D., Brune, W. H., Faloona, I., Sachse, G. W., Vay, S. A., and Tan, D., Deep convection  
1945 as a source of new particles in the midlatitude upper troposphere: J. Geophys. Res., 107,  
1946 4560, doi:10.1029/2001JD000323, 2002.
- 1947 Vestin, A., Rissler, J., Swietlicki, E., Frank, G., and Andreae, M. O., Cloud nucleating properties  
1948 of the Amazonian biomass burning aerosol: Cloud condensation nuclei measurements  
1949 and modeling: J. Geophys. Res., 112, D14201, doi:10.1029/2006JD008104, 2007.
- 1950 Virji, H., A preliminary study of summertime tropospheric circulation patterns over South  
1951 America estimated from cloud winds: Mon. Weather Rev., 109, 599-610, 1981.
- 1952 Voigt, C., Schumann, U., Minikin, A., Abdelmonem, A., Afchine, A., Borrmann, S., Boettcher,  
1953 M., Bucuchholz, B., Bugliaro, L., Costa, A., Curtius, J., Dollner, M., Doernbrack, A.,  
1954 Dreiling, V., Ebert, V., Ehrlich, A., Fix, A., Forster, L., Frank, F., Fuetterer, D., Giez, A.,  
1955 Graf, K., Grooss, J.-U., Gross, S., Heimerl, K., Heinold, B., Hueneker, T., Jaervinen, E.,  
1956 Jurkat, T., Kaufmann, S., Kenntner, M., Klingebiel, M., Klimach, T., Kohl, R., Kraemer,  
1957 M., Krisna, T. C., Luebke, A., Mayer, B., Mertes, S., Molleker, S., Petzold, A.,  
1958 Pfeilsticker, K., Port, M., Rapp, M., Reutter, P., Rolf, C., Rose, D., Sauer, D., Schaefer,  
1959 A., Schlage, R., Schnaiter, M., Schneider, J., Spelten, N., Spichtinger, P., Stock, P.,  
1960 Walser, A., Weigel, R., Weinzierl, B., Wendisch, M., Werner, F., Wernli, H., Wirth, M.,  
1961 Zahn, A., Ziereis, H., and Zoger, M., ML-CIRRUS: The airborne experiment on natural  
1962 cirrus and contrail cirrus with the high-altitude long-range research aircraft HALO: Bull.  
1963 Am. Meteorol. Soc., 98, 271-288, doi:10.1175/bams-d-15-00213.1, 2017.



- 1964 von der Weiden, S. L., Drewnick, F., and Borrmann, S., Particle Loss Calculator – a new  
1965 software tool for the assessment of the performance of aerosol inlet systems: Atmos.  
1966 Meas. Tech., 2, 479-494, doi:10.5194/amt-2-479-2009, 2009.
- 1967 Waddicor, D. A., Vaughan, G., Choularton, T. W., Bower, K. N., Coe, H., Gallagher, M.,  
1968 Williams, P. I., Flynn, M., Volz-Thomas, A., Pätz, H. W., Isaac, P., Hacker, J., Arnold,  
1969 F., Schlager, H., and Whiteway, J. A., Aerosol observations and growth rates downwind  
1970 of the anvil of a deep tropical thunderstorm: Atmos. Chem. Phys., 12, 6157-6172,  
1971 doi:10.5194/acp-12-6157-2012, 2012.
- 1972 Walsler, A., Sauer, D., Spanu, A., Gasteiger, J., and Weinzierl, B., On the parametrization of  
1973 optical particle counter response including instrument-induced broadening of size spectra  
1974 and a self-consistent evaluation of calibration measurements: Atmos. Meas. Tech.  
1975 Discuss., 2017, 1-30, doi:10.5194/amt-2017-81, 2017.
- 1976 Wang, H., and Fu, R., The influence of Amazon rainfall on the Atlantic ITCZ through  
1977 convectively coupled Kelvin waves: J. Clim., 20, 1188-1201, doi:10.1175/jcli4061.1,  
1978 2007.
- 1979 Wang, J., Krejci, R., Giangrande, S., Kuang, C., Barbosa, H. M. J., Brito, J., Carbone, S., Chi,  
1980 X., Comstock, J., Ditas, F., Lavric, J., Manninen, H. E., Mei, F., Moran-Zuloaga, D.,  
1981 Pöhlker, C., Pöhlker, M. L., Saturno, J., Schmid, B., Souza, R. A. F., Springston, S. R.,  
1982 Tomlinson, J. M., Toto, T., Walter, D., Wimmer, D., Smith, J. N., Kulmala, M.,  
1983 Machado, L. A. T., Artaxo, P., Andreae, M. O., Petäjä, T., and Martin, S. T., Amazon  
1984 boundary layer aerosol concentration sustained by vertical transport during rainfall:  
1985 Nature, 539, 416-419, doi:10.1038/nature19819, 2016a.
- 1986 Wang, Q., Saturno, J., Chi, X., Walter, D., Lavric, J. V., Moran-Zuloaga, D., Ditas, F., Pöhlker,  
1987 C., Brito, J., Carbone, S., Artaxo, P., and Andreae, M. O., Modeling investigation of  
1988 light-absorbing aerosols in the Amazon Basin during the wet season: Atmos. Chem.  
1989 Phys., 16, 14,775-14,794, doi:10.5194/acp-16-14775-2016, 2016b.
- 1990 Watson, C. E., Fishman, J., and Reichle, H. G., The significance of biomass burning as a source  
1991 of carbon monoxide and ozone in the Southern Hemisphere tropics: A satellite analysis:  
1992 J. Geophys. Res., 95, 14,443-14,450, 1990.
- 1993 Weigel, R., Borrmann, S., Kazil, J., Minikin, A., Stohl, A., Wilson, J. C., Reeves, J. M., Kunkel,  
1994 D., de Reus, M., Frey, W., Lovejoy, E. R., Volk, C. M., Viciani, S., D'Amato, F.,  
1995 Schiller, C., Peter, T., Schlager, H., Cairo, F., Law, K. S., Shur, G. N., Belyaev, G. V.,  
1996 and Curtius, J., In situ observations of new particle formation in the tropical upper  
1997 troposphere: the role of clouds and the nucleation mechanism: Atmos. Chem. Phys., 11,  
1998 9983-10,010, doi:10.5194/acp-11-9983-2011, 2011.
- 1999 Weigel, R., Spichtinger, P., Mahnke, C., Klingebiel, M., Afchine, A., Petzold, A., Krämer, M.,  
2000 Costa, A., Molleker, S., Reutter, P., Szakáll, M., Port, M., Grulich, L., Jurkat, T.,  
2001 Minikin, A., and Borrmann, S., Thermodynamic correction of particle concentrations  
2002 measured by underwing probes on fast-flying aircraft: Atmos. Meas. Tech., 9, 5135-  
2003 5162, doi:10.5194/amt-9-5135-2016, 2016.
- 2004 Weigelt, A., Hermann, M., van Velthoven, P. F. J., Brenninkmeijer, C. A. M., Schlaf, G., Zahn,  
2005 A., and Wiedensohler, A., Influence of clouds on aerosol particle number concentrations



- 2006 in the upper troposphere: *J. Geophys. Res.*, 114, D01204, doi:10.1029/2008jd009805,  
2007 2009.
- 2008 Wendisch, M., Pöschl, U., Andreae, M. O., Machado, L. A. T., Albrecht, R., Schlager, H.,  
2009 Rosenfeld, D., Buchholz, B., Ebert, V., Fisch, G., Curtius, J., Frank, F., Kohl, R., Rose,  
2010 D., Hüneke, T., Knecht, M., Pfeilsticker, K., Longo, K., Afchine, A., Costa, A., Krämer,  
2011 M., Jaervinen, E., Schnaiter, M., Ehrlich, A., Jäkel, E., Krisna, T. C., Kanter, S.,  
2012 Rosenow, D., Werner, F., Mertes, S., Kästner, U., Dorf, M., Klimach, T., Krüger, M.,  
2013 Nillius, B., Pöhlker, C., Schneider, J., Schulz, C., Borrmann, S., Mahnke, C., Mollerker,  
2014 S., Weigel, R., Ewald, F., Kölling, T., Mayer, B., Zinner, T., Fix, A., Fütterer, D., Jurkat,  
2015 T., Kenntner, M., Sauer, D., Paul Stock, Voigt, C., Weinzierl, B., Ziereis, H., Barbosa,  
2016 H., Artaxo, P., Souza, R. A. F. d., and Yamasoe, M. A., The ACRIDICON-CHUVA  
2017 observational study of tropical convective clouds and precipitation using the new German  
2018 research aircraft HALO: *Bull. Am. Meteorol. Soc.*, 97, 1885-1908, doi:10.1175/BAMS-  
2019 D-14-00255, 2016.
- 2020 Wiedensohler, A., An approximation of the bipolar charge distribution for particles in the sub-  
2021 micron size range: *J. Aerosol Sci.*, 19, 387-389, 1988.
- 2022 Wiedensohler, A., Ma, N., Birmili, W., Heintzenberg, J., Ditas, F., Andreae, M. O., and Panov,  
2023 A., Rare natural new particle formation events in the boundary layer of a remote forested  
2024 area: *Nature*, 2017, to be submitted.
- 2025 Williams, J., de Reus, M., Krejci, R., Fischer, H., and Strom, J., Application of the variability-  
2026 size relationship to atmospheric aerosol studies: estimating aerosol lifetimes and ages:  
2027 *Atmos. Chem. Phys.*, 2, 133-145, 2002.
- 2028 Witte, K., HALO Technical Note: Top Fuselage Aperture Plates - Particle Enrichment. DLR  
2029 Flight Facility Oberpfaffenhofen, Wessling, Germany, 17 p. (2008).
- 2030 Yang, Q., Easter, R. C., Campuzano-Jost, P., Jimenez, J. L., Fast, J. D., Ghan, S. J., Wang, H.,  
2031 Berg, L. K., Barth, M. C., Liu, Y., Shrivastava, M. B., Singh, B., Morrison, H., Fan, J.,  
2032 Ziegler, C. L., Bela, M., Apel, E., Diskin, G. S., Mikoviny, T., and Wisthaler, A., Aerosol  
2033 transport and wet scavenging in deep convective clouds: A case study and model  
2034 evaluation using a multiple passive tracer analysis approach: *J. Geophys. Res.*, 120,  
2035 8448-8468, doi:10.1002/2015JD023647, 2015.
- 2036 Yin, Y., Carslaw, K. S., and Feingold, G., Vertical transport and processing of aerosols in a  
2037 mixed-phase convective cloud and the feedback on cloud development: *Q. J. R.*  
2038 *Meteorol. Soc.*, 131, 221-245, 2005.
- 2039 Young, L. H., Benson, D. R., Montanaro, W. M., Lee, S. H., Pan, L. L., Rogers, D. C., Jensen, J.,  
2040 Stith, J. L., Davis, C. A., Campos, T. L., Bowman, K. P., Cooper, W. A., and Lait, L. R.,  
2041 Enhanced new particle formation observed in the northern midlatitude tropopause region:  
2042 *J. Geophys. Res.*, 112, D10218, doi:10.1029/2006jd008109, 2007.
- 2043 Yu, F., Wang, Z., Luo, G., and Turco, R., Ion-mediated nucleation as an important global source  
2044 of tropospheric aerosols: *Atmos. Chem. Phys.*, 8, 2537-2554, 2008.
- 2045 Yu, F., Luo, G., Nadykto, A. B., and Herb, J., Impact of temperature dependence on the possible  
2046 contribution of organics to new particle formation in the atmosphere: *Atmos. Chem.*  
2047 *Phys.*, 17, 4997-5005, doi:10.5194/acp-17-4997-2017, 2017.



- 2048 Yu, P. F., Murphy, D. M., Portmann, R. W., Toon, O. B., Froyd, K. D., Rollins, A. W., Gao, R.  
2049 S., and Rosenlof, K. H., Radiative forcing from anthropogenic sulfur and organic  
2050 emissions reaching the stratosphere: *Geophys. Res. Lett.*, 43, 9361-9367,  
2051 doi:10.1002/2016gl070153, 2016.
- 2052 Zhou, J., Swietlicki, E., Hansson, H.-C., and Artaxo, P., Submicrometer aerosol particle size  
2053 distribution and hygroscopic growth measured in the Amazon rain forest during the wet  
2054 season: *J. Geophys. Res.*, 107, 8055, doi:10.129/2000JD000203, 2002.
- 2055 Zhou, J. C., Swietlicki, E., Berg, O. H., Aalto, P. P., Hameri, K., Nilsson, E. D., and Leck, C.,  
2056 Hygroscopic properties of aerosol particles over the central Arctic Ocean during summer:  
2057 *J. Geophys. Res.*, 106, 32111-32123, 2001.
- 2058 Zhou, J. Y., and Lau, K. M., Does a monsoon climate exist over South America?: *J. Clim.*, 11,  
2059 1020-1040, 1998.
- 2060 Zhuang, Y., Fu, R., Marengo, J. A., and Wang, H., Seasonal variation of shallow-to-deep  
2061 convection transition and its link to the environmental conditions over the Central  
2062 Amazon: *J. Geophys. Res.*, 122, 2649-2666, doi:10.1002/2016JD025993, 2017.
- 2063 Ziereis, H., Schlager, H., Schulte, P., van Velthoven, P. F. J., and Slemr, F., Distributions of NO,  
2064 NO<sub>x</sub>, and NO<sub>y</sub> in the upper troposphere and lower stratosphere between 28° and 61°N  
2065 during POLINAT 2: *J. Geophys. Res.*, 105, 3653-3664, doi:10.1029/1999jd900870,  
2066 2000.
- 2067 Zipser, E. J., Mesoscale and convective-scale downdrafts as distinct components of squall-line  
2068 structure: *Mon. Weather Rev.*, 105, 1568-1589, doi:10.1175/1520-  
2069 0493(1977)105<1568:macdad>2.0.co;2, 1977.
- 2070



Table 1: Properties of the flight legs on which elevated aerosol concentrations were measured during ACRIDICON-CHUVA.

Flight	Leg	Start UTC	End UTC	Altitude range m	N <sub>CN</sub> max. cm <sup>-3</sup>	N <sub>CN</sub> mean cm <sup>-3</sup>	N <sub>CCN0.5</sub> mean cm <sup>-3</sup>	N <sub>acc</sub> mean cm <sup>-3</sup>	Ultrafine fraction	Trajectory type	Min T <sub>b</sub> [min,max] <sup>h</sup> °C	Time since last DC [min,max] <sup>b</sup> hours	Time in DC [min,max] <sup>c</sup> hours	Sampling environment	
															0.95
AC07	A1	1622	1626	8300-9200	17200	9360	657	696	0.93	A	[-76,-65]	[0, 0]	[21,27]	in and near outflows	
AC07	AA1	1626	1627	9140	36100	19230	775	588	0.97	A	---	---	---	in and near outflows	
AC07	A2	1627	1633	8100-9100	38400	24250	471	499	0.98	A	[-77,-76]	[0, 0]	[19,26]	clear air	
AC07	AA2	1633	1637	6700-8200	26700	6450	708	565	0.91	A	---	---	---	clear air	
AC07	B	1714	1717	7000-8400	15900	7140	214	270	0.96	A	[-75,-68]	[0, 0]	[13,28]	clear air	
AC07	C	1923	1929	9000	22600	16480	272	389	0.98	A	[-78,-74]	[0, 0]	[27,40]	clear air	
AC07	D1	2024	2027	8500-10500	23200	14270	---	146	0.99	A	[-74,-68]	[0, 0]	[29,40]	clear air near outflow	
AC07	D2	2028	2112	11000	28200	15160	---	76	0.99	A	[-76,-68]	[0, 0]	[12,28]	outflow, mixed with cirrus	
AC07	E	2126	2129	13100	33500	15140	---	---	---	A	[-72,-67]	[0, 0]	[21,28]	pristine ice cirrus	
AC07	F	2130	2147	13200	25300	12030	13	---	---	A	[-72,-69]	[0, 5]	[24,32]	clear air	
AC07	G	2205	2211	13000-10000	20500	15470	284	---	---	A	[-76,-51]	[0, 0]	[24,31]	cirrus	
AC07	GG	2210	2212	10200-9500	19500	16840	-	869	0.95	A	---	[0, 0]	[24,31]	cirrus	
AC08	No useful high alt CN data. CCN moderately elevated at ca. 10 and 13 km, ca. 1200 /cc														
AC09	A1	1453	1455	11400	24100	10370	901	572	0.94	B	[-74,-71]	[16,16]	[22,41]	clear air	
AC09	A2	1455	1458	11900	27600	12970	1103	808	0.94	B	[-76,-72]	[16,17]	[34,41]	clear air	
AC09	A3	1501	1503	11000	35100	14470	629	697	0.95	B	[-72,-70]	[17,17]	[38,40]	clear air	
AC09	B1	1815	1820	11000	19100	10540	1393	954	0.91	B	[-76,-74]	[14,14]	[49,54]	around Cb anvil	
AC09	B2	1821	1827	11300-11600	28300	15370	1414	1012	0.93	B	[-78,-73]	[14,14]	[47,57]	around Cb anvil	
AC09	C	1830	1838	11600	31700	9130	1490	1127	0.88	B	[-79,-76]	[1,19]	[45,56]	clear air	
AC09	D	1838	1923	11300-11900	13000	5690	1012	869	0.85	B, C	[-80,-74]	[1, 1]	[34,57]	outflow region	
AC09	E	1929	1957	11300	24200	12790	891	856	0.93	B, C	[-76,-70]	[2,21]	[24,48]	outflow region	
AC10	A	1709	1714	6700-8600	27400	13040	355	389	0.94	C	[-66,-54]	[6, 7]	[9,32]	clear air	
AC10	B	1721	1728	9200	32500	12480	850	861	0.91	D	[-78,-72]	[4,10]	[34,56]	clear air	
AC10	C	1800	1808	9200	26000	13100	1020	937	0.91	B	[-79,-71]	[7,10]	[33,56]	clear air	
AC10	D	1811	1815	9200-10100	33000	20180	1130	684	0.95	B	[-77,-71]	[5, 5]	[23,51]	clear air	
AC10	E	1817	1833	10800-13600	33400	22210	712	289	0.98	E	[-84,-72]	[0,12]	[42,76]	thin cirrus	
AC10	F	1835	1906	13800	34700	16540	464	---	---	E	[-80,-68]	[0, 0]	[33,54]	cirrus layer	
AC10	G	1912	1919	10600-7500	24200	10220	1230	1160	0.83	B	[-80,-58]	[0,14]	[11,60]	clear air	



AC11	A	1603	1605	8700-9700	47400	26280	572	323	0.98	E	[-54,-32]	[3,44]	[1,18]	clear air
AC11	B	1613	1630	11800	4700	3850	1390	763	0.80	E, D	[-76,-58]	[0,6]	[14,41]	clear air
AC11	C	1633	1642	11800-10800	31700	6080	1436	937	0.78	D	[-80,-77]	[0,0]	[30,46]	around anvil
AC11	D	1831	1850	5200-6700	25000	14380	---	187	0.98	C	[-79,-79]	[0,0]	[18,19]	outflow region
AC11	E	1907	1930	9900-12200	36100	29280	---	330	0.99	D	[-85,-74]	[0,0]	[26,82]	outflow region
AC11	F1	1940	1942	12200	54900	22060	---	674	0.95	E, D	[-84,-84]	[0,0]	[55,55]	outflow region
AC11	F2	1942	1951	12200	32800	20720	---	549	0.97	E, D	[-84,-84]	[0,0]	[55,55]	outflow region
AC11	G	2005	2030	13700-14200	2830	10090	---	---	---	D	[-84,-84]	[0,0]	[55,55]	outflow region
AC11	H	2042	2057	12200-10400	47900	20240	---	663	0.96	A	[-84,-84]	[0,0]	[55,55]	outflow region
AC12	A	1512	1518	9800-11300	19300	8040	1130	341	0.95	E	[-79,-74]	[0,0]	[23,37]	clear
AC12	B	1524	1527	11300	24700	9290	1120	358	0.95	A	[-83,-71]	[0,0]	[26,66]	thin outflow
AC12	C	1537	1541	7300-5600	26200	7760	356	186	0.95	B	[-78,-57]	[1,1]	[7,16]	clear
AC12	D	1922	1925	8000-9700	17400	11980	650	132	0.99	B	[-71,-71]	[17,20]	[6,12]	clear
AC12	E	1928	1933	10800-12200	25300	15740	423	75	0.99	B	[-70,-57]	[20,24]	[8,18]	clear
AC12	F1	1936	1950	12200-13100	7020	5940	2010	698	0.88	D	[-80,-67]	[0,38]	[12,40]	clear
AC12	F2	1952	2015	13100	7300	5950	1190	594	0.90	B, D	[-82,-74]	[0,21]	[28,77]	aged outflow
AC12	G	2017	2020	13200-12800	19600	10930	661	422	0.96	E	[-79,-75]	[0,0]	[26,49]	outflow
AC12	H	2023	2027	11300-9600	23900	16930	849	372	0.98	C	[-80,-77]	[0,0]	[37,59]	mostly clear air
AC13	A	1520	1533	11000-11900	43500	13830	1054	---	---	C	[-78,-75]	[0,12]	[27,43]	mostly cirrus and old outflow
AC13	B	1550	1607	11900-6900	36300	11890	1012	476	0.95	A	[-83,-50]	[1,8]	[11,47]	mostly cirrus and old outflow
AC13	C	1901	1908	9500	25700	17870	687	---	---	A	[-72,-66]	[0,0]	[13,24]	clear air around anvils
AC13	D1	1909	1912	10700	26200	18600	910	---	---	A	[-70,-66]	[0,0]	[15,19]	'''
AC13	D2	1916	1919	10700	28200	19170	1017	---	---	A	[-73,-69]	[0,0]	[24,25]	'''
AC13	D3	1921	1926	10700	29500	19010	919	---	---	A	[-69,-68]	[0,0]	[15,26]	'''
AC13	D4	1930	1933	10700	21600	10890	727	---	---	A	[-68,-67]	[0,0]	[14,17]	'''
AC13	E	1939	1942	11900	22500	15100	770	---	---	A	[-57,-47]	[10,10]	[5,8]	'''
AC13	F	2036	2043	12200	18600	7840	912	---	---	A	[-78,-76]	[0,0]	[34,43]	clear air, some cirrus
AC14	no	uscable	high alt data											
AC15	A	1415	1419	10500-11700	58500	38170	687	453	0.98	D	[-81,-78]	[0,9]	[63,68]	air around a huge Cb anvil
AC15	B	1419	1424	11800-12900	67900	46970	701	405	0.98	D	[-81,-81]	[0,0]	[59,66]	mostly cirrus and old outflow
AC15	C	1431	1432	13200	49500	20900	1070	747	0.94	D	[-84,-84]	[0,0]	[55,55]	'''
AC15	D	1436	1437	13200	38300	15300	1009	633	0.92	D	[-84,-77]	[0,0]	[50,56]	'''



AC15	E	1448	1449	12500	44500	29220	603	718	0.97	D	[-81,-79]	[0,0]	[54,59]	""
AC15	F	1452	1455	12500	60500	45100	672	514	0.97	D	[-79,-75]	[0,0]	[52,56]	""
AC15	G	1456	1500	12500-11900	59200	38070	748	574	0.98	D	[-82,-72]	[0,0]	[53,62]	""
AC15	H	1502	1505	11900-11600	49800	16440	1114	750	0.94	D	[-76,-73]	[0,0]	[62,69]	""
AC15	I	1518	1519	11300	46800	22000	1848	931	0.93	D	[-79,-73]	[0,0]	[65,71]	""
AC15	J	1526	1528	10700	21700	8980	1292	817	0.86	D	[-76,-75]	[0,0]	[59,65]	""
AC16	A	1554	1600	10700-12200	40300	21210	606	223	0.98	B	[-75,-68]	[0,0]	[9,18]	clear air
AC16	B	1749	1757	10000-10300	28200	11350	926	282	0.97	B	[-68,-57]	[0,0]	[8,10]	air around a large Cb anvil
AC16	C	1803	1815	10300-10700	27200	15180	746	208	0.98	B	[-75,-60]	[0,0]	[9,12]	air around a large Cb anvil
AC16	D	1818	1820	10700-11300	23100	11540	789	356	0.97	B	[-75,-67]	[0,0]	[10,17]	air around a large Cb anvil
AC16	E	1824	1826	12000	26700	14070	488	354	0.97	B	[-75,-75]	[0,0]	[17,19]	air around a large Cb anvil
AC16	F	1857	1911	12600-11900	19500	11210	598	521	0.94	B	[-73,-66]	[0,0]	[22,28]	air around a large Cb anvil
AC16	G	1925	1935	11900	22700	12880	703	492	0.95	B	[-73,-70]	[0,0]	[22,30]	air around a large Cb anvil
AC16	H	1950	2000	11900-9600	27100	12670	806	444	0.96	B	[-75,-65]	[0,0]	[13,29]	air around a large Cb anvil
AC17														no high alt data
AC18	A1	1454	1456	8300-8600	20700	10698	-	219	0.98	B	[-60,-10]	[14,17]	[2,5]	clear air
AC18	A2	1520	1522	12900-8400	22500	14538	479	400	0.97	C	[-58,-38]	[14,18]	[1,5]	clear air
AC18	B	1753	1801	7100	10040	6255	400	312	0.95	C	[-30,-0]	[0,0]	[1,2]	clear air around anvils
AC18	C	1833	1834	7100-7400	14200	10713	404	280	0.97	C	[-52,-28]	[22,22]	[1,1]	clear air around anvils
AC18	D	1913	2005	11300-12000	4000	2367	916	640	0.73	A, D	[-75,-37]	[0,16]	[3,46]	clear air around anvils
AC18	E1	2017	2034	13000-13700	8170	4841	1481	892	0.82	A, D	[-84,-68]	[0,44]	[21,45]	clear air
AC18	E2	2040	2043	13700-13200	44700	13679	469	283	0.98	D	[-77,-71]	[0,0]	[28,42]	clear air downwind of large Cb
AC18	F	2053	2057	9500-8100	15800	8778	444	318	0.96	C, D	[-68,-32]	[1,20]	[1,11]	clear air
AC19	A1	1518	1519	7300-7700	30600	28480	451	339	0.99	B	[-82,-65]	[14,43]	[7,14]	clear air
AC19	A2	1536	1601	12600	3600	2910	679	268	0.91	E	[-72,-58]	[43,94]	[6,19]	clear air, high alt leg
AC19	E1	2009	2010	8500-8900	14700	11470	642	271	0.98	B	[-75,-59]	[16,92]	[8,16]	clear air
AC19	E2	2023	2100	13800	3900	2690	1024	498	0.81	A	[-76,-29]	[0,105]	[1,22]	clear air
AC19	E3	2106	2119	13800	10200	2770	1073	950	0.65	B	[-73,-57]	[0,1]	[6,25]	outflow
AC19	E4	2127	2128	7500-6600	66000	16210	440	414	0.96	D	[-60,-59]	[3,22]	[4,7]	clear air
AC20	A	1654	1658	11700-12500	30300	21540	881	616	0.97	A, D	[-77,-53]	[1,1]	[7,28]	NPF at top of smoke layer
AC20	B	1901	1905	12300	21300	9340	614	381	0.95	A, D	[-78,-70]	[0,0]	[14,42]	NPF at top of smoke layer



- a) Minimum and maximum temperature at top of most recent deep convection in grid boxes through which the trajectories for the flight leg had passed.
- a) Trajectories were calculated for each minute of the leg, and for each trajectory the time between sampling and the most recent encounter with DC was determined. Given are the shortest and the longest of these time intervals.
- a) Minimum and maximum length of time that the trajectories from each leg had spent in grid boxes with DC.

Table 2: Composition of UT aerosols based on AMS and SP2 measurements

Flight	Time	N <sub>CN</sub>	N <sub>CCN0.5</sub>	N <sub>acc</sub>	OA	NO <sub>3</sub>	SO <sub>4</sub>	NH <sub>4</sub>	rBC	OA/SO <sub>4</sub>	NO <sub>3</sub> /SO <sub>4</sub>	Ultrafine fraction	CO
	UT	cm <sup>-3</sup>	cm <sup>-3</sup>	cm <sup>-3</sup>	µg m <sup>-3</sup>				ppb				
AC07													
<4 km	-	1620±680	1070±410	1363±651	1.15±0.82	0.057±0.031	0.14±0.07	0.21±0.16	0.40±0.21	8.1±5.8	0.40±0.29	0.19±0.16	-
>7 km	-	9300±7420	300±210	278±232	0.43±0.36	0.052±0.036	0.038±0.032	0.07±0.47	0.003±0.007	11.3±13.5	1.4±1.5	0.92±0.008	-
AA1	16:24-16:29	19200	650	588	1.03	0.097	<0.005	-	0.002	>200	>20	0.97	-
AA2	16:33-16:37	6450	710	565	0.90	0.086	0.011	-	0.002	82	7.8	0.89	-
GG	22:09-22:11	16800	-	921	1.72	0.143	<0.005	-	0.002	>350	>30	-	-
AC09													
<5 km	-	920±490	290±95	395±189	0.42±0.29	0.020±0.027	0.26±0.12	0.02±0.13	0.085±0.095	2.2±1.8	0.14±0.13	0.51±0.26	-
>9 km	-	8020±5180	1090±430	861±338	2.53±0.60	0.31±0.17	0.24±0.19	0.02±0.17	0.001±0.003	13.4±6.3	1.6±1.1	0.86±0.07	-
AA	14:48-15:08	2280	1050	754	2.23	0.30	0.14	0.013	0.001	24.0	3.0	0.54	-
BB	18:18-19:23	8060	1200	922	2.63	0.32	0.27	0.023	0.001	10.7	1.3	0.85	-
EE	19:28-19:58	12000	950	892	2.75	0.31	0.23	0.018	0.001	12.8	1.4	0.92	-
A1+A2	14:53-14:58	12100	1040	724	2.50	0.36	0.15	0.039	<0.001	23.9	3.4	0.91	-
AC18													
<5 km	-	740±220	350±100	473±212	1.61±1.26	0.070±0.054	0.92±0.47	0.17±0.16	0.15±0.15	1.6±0.8	0.078±0.055	0.51±0.26	-
>10 km	-	2950±2640	920±310	560±145	2.66±0.98	0.32±0.15	0.40±0.12	<0.05	0.002±0.005	7.0±3.0	0.85±0.38	0.86±0.07	-
AA	15:06-15:16	(1740)	870	545	2.20	0.28	0.35	<0.05	0.001	6.9	0.89	1.50	-
DD	19:21-20:05	2360	910	639	2.75	0.31	0.39	<0.05	0.002	7.8	0.88	0.61	-
A1	14:54-14:56	87000	-	203	0.52	0.099	0.27	<0.05	0.002	2.5	0.44	-	-
A2	15:20-15:22	17400	500	433	1.36	0.157	0.27	<0.05	0.002	5.1	0.62	0.97	-
E2	20:40-20:43	15900	360	-	1.28	0.157	0.35	<0.05	-	3.9	0.44	0.98	-
F	20:54-20:56	11600	460	361	1.37	0.164	0.42	<0.05	0.002	3.3	0.39	0.96	-
UT	9-15 km	7700±8000	840±440	568±313	2.57±1.12	0.273±0.165	0.32±0.23	0.21±0.22	0.003±0.003	8.1±6.7	0.86±0.78	0.86±0.11	116±39
MT	5-8 km	2130±3100	410±150	284±169	1.07±0.80	0.075±0.103	0.35±0.22	0.22±0.16	0.007±0.015	3.0±3.0	0.21±0.32	0.79±0.15	97±22
PBL	0-4 km	1650±980	950±700	1261±876	4.71±3.65	0.189±0.212	0.82±0.61	0.43±0.59	0.39±0.26	5.8±6.2	0.23±0.31	0.28±0.23	157±54



Figure 1: Tracks of the flights on which measurements at high altitude were made during ACRIDICON-CHUVA. The flight segments at altitudes  $>8$  km are shown as heavier lines.

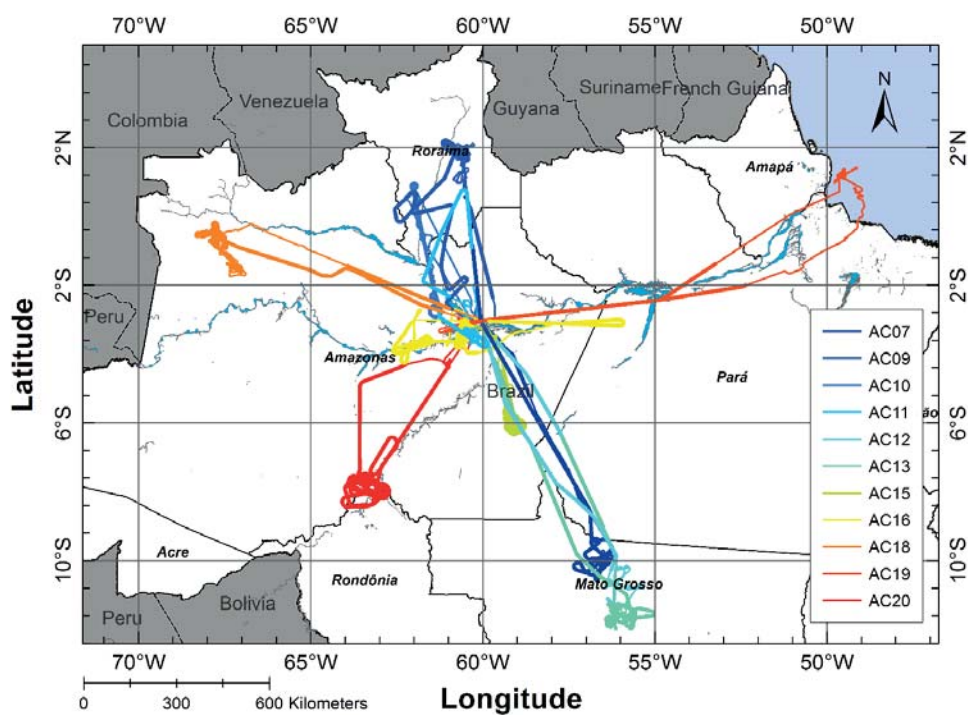




Figure 2: Columnar precipitable water anomaly for September 2014 (based on the 1981-2010 average NCEP/NCAR Reanalysis).

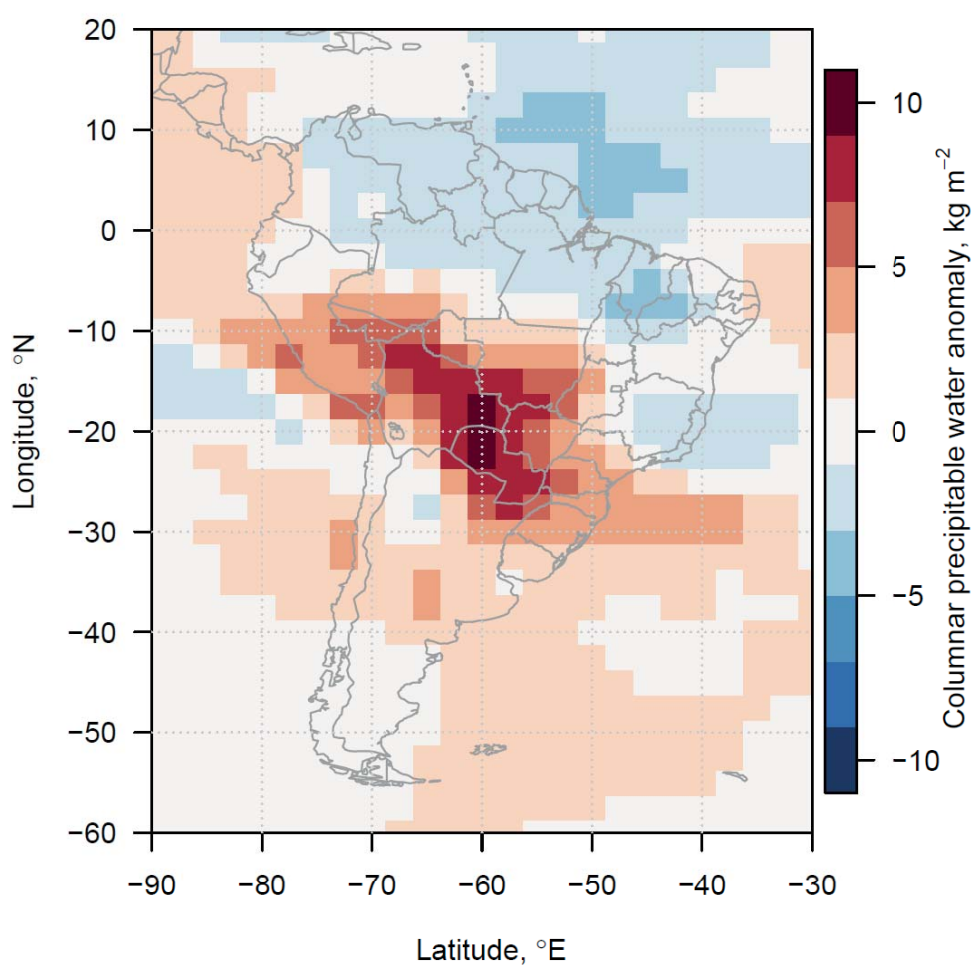




Figure 3: Total rainfall (mm per month, 1° resolution) for September 2014. Data from Global Precipitation Climatology Centre (GPCC).

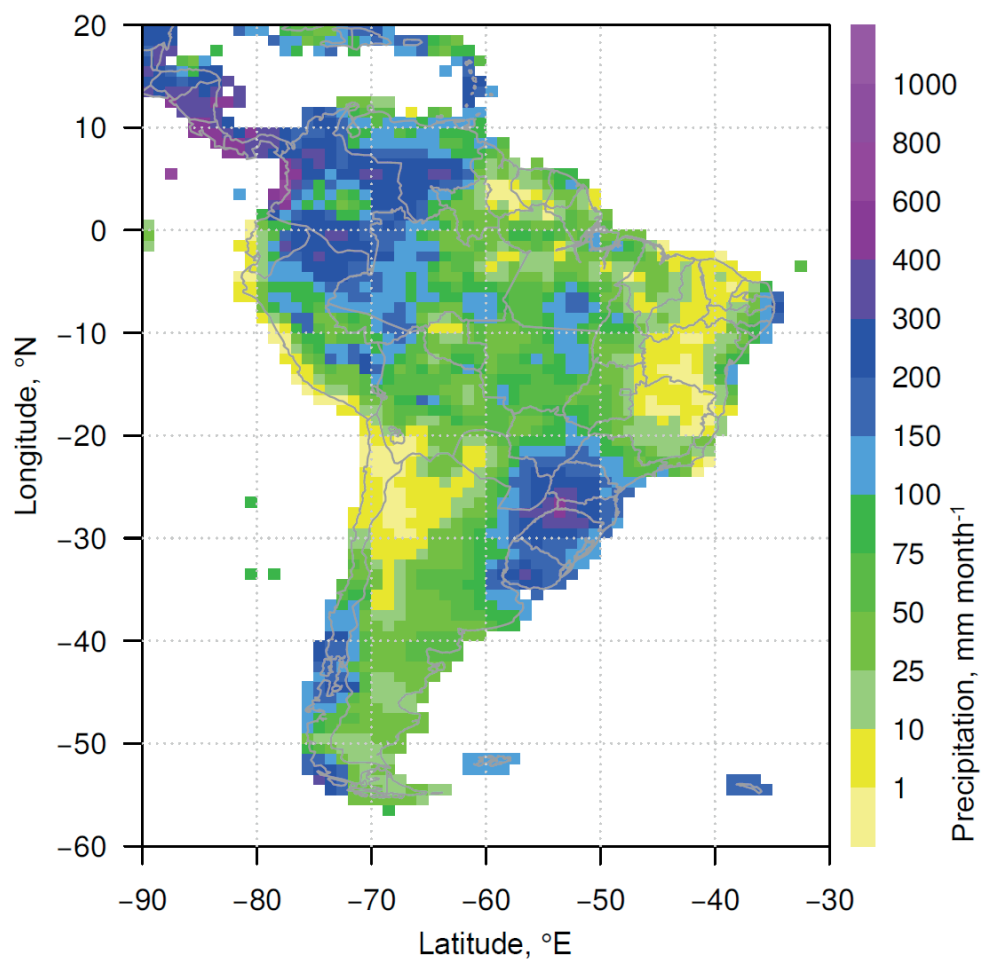




Figure 4: Mean wind speeds during September 2014 at a) 850 hPa and b) 200 hPa (Data from NCEP/NCAR).

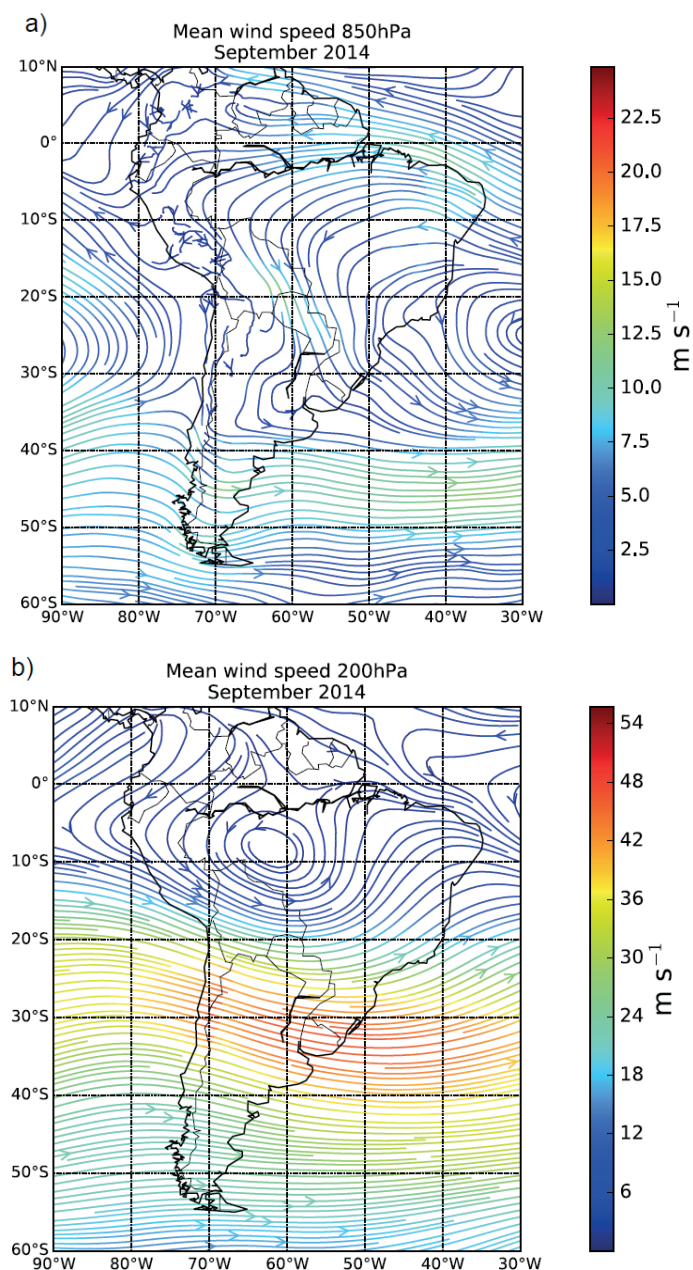




Figure 5: Vertical profiles of potential temperature, static air temperature and relative humidity measured on HALO during the ACRIDICON-CHUVA flights over the Amazon Basin.

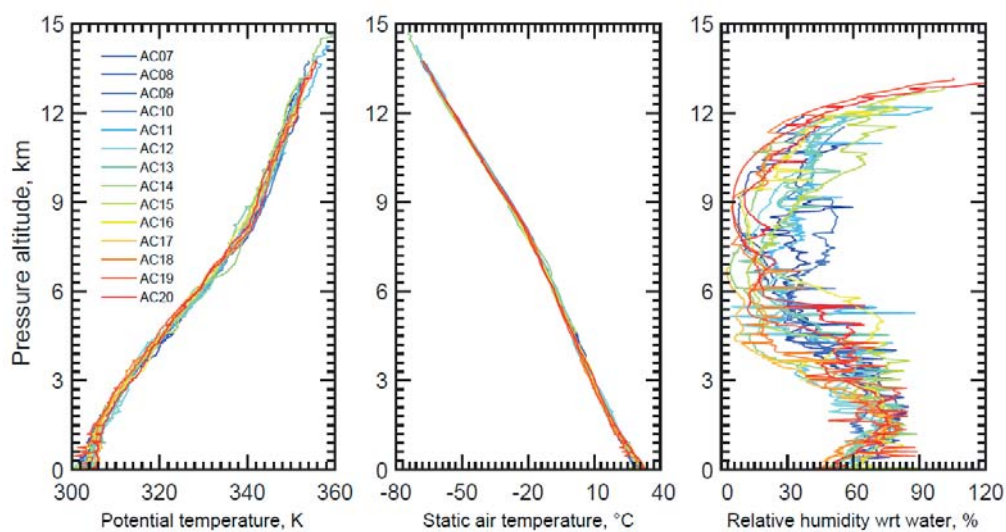




Figure 6: Trajectory statistics based on (a) 72-hour and (b) 120-hour backtrajectory calculations for September 2014, initialized at Manaus at an elevation of 12 km.

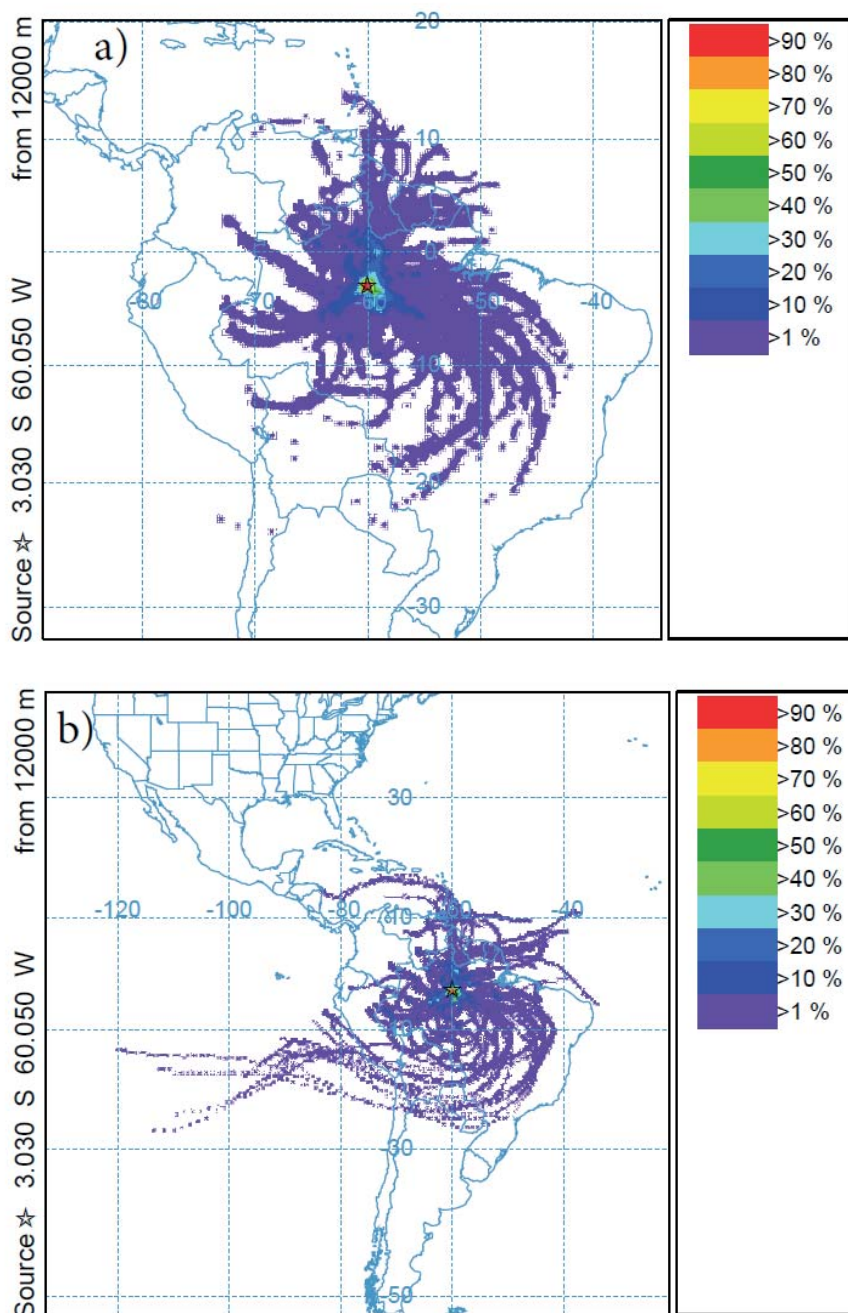




Figure 7: Vertical profiles of CN concentrations,  $N_{CN}$ ; a) overall statistics from all flights, b) examples from individual profiles on flight AC07 (segment G) and AC09 (segments A1 and A2).

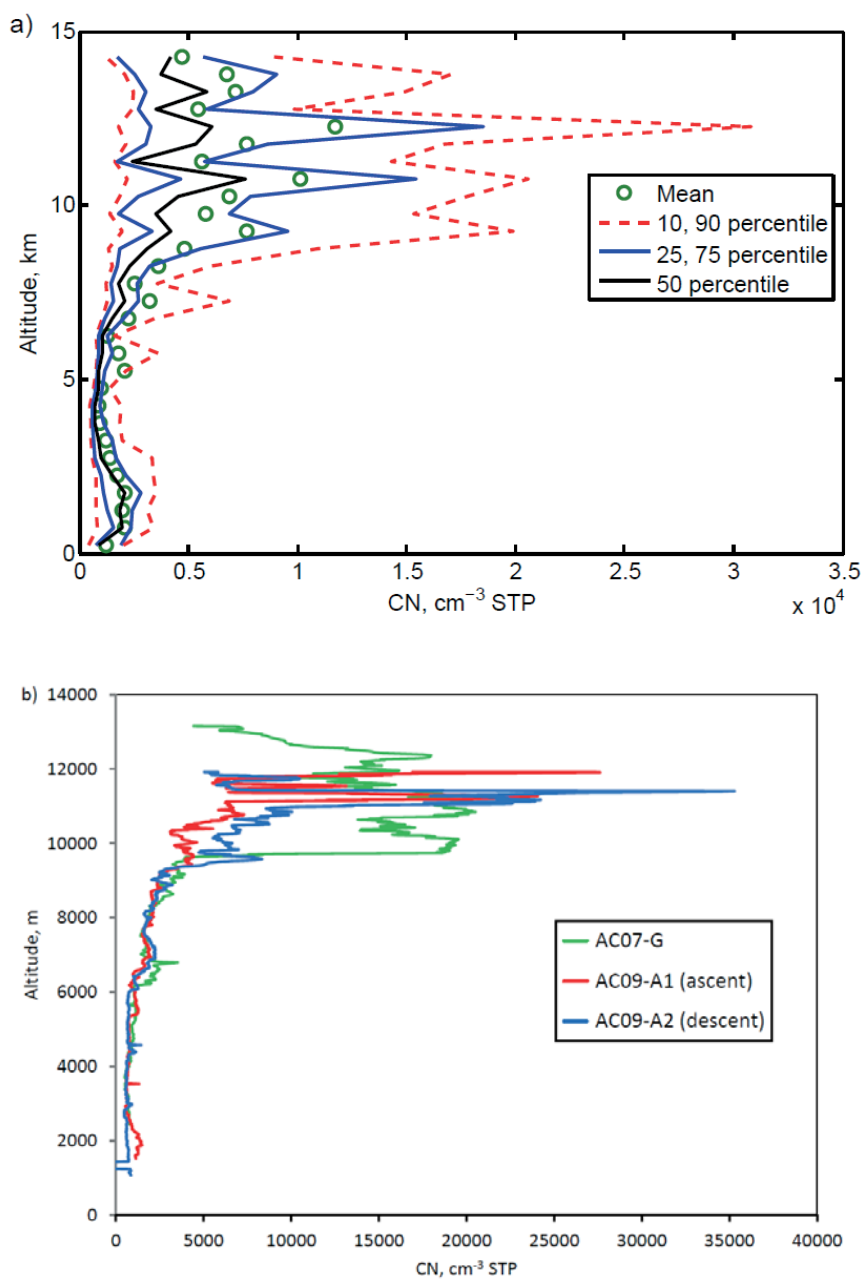




Figure 8: Vertical profiles of accumulation mode particle concentrations,  $N_{acc}$ ; a) 1-min averaged data from all flights, b)  $N_{acc}$  profile from flight AC19 together with the profile of  $N_{CN}$  from the same flight (1-sec data).

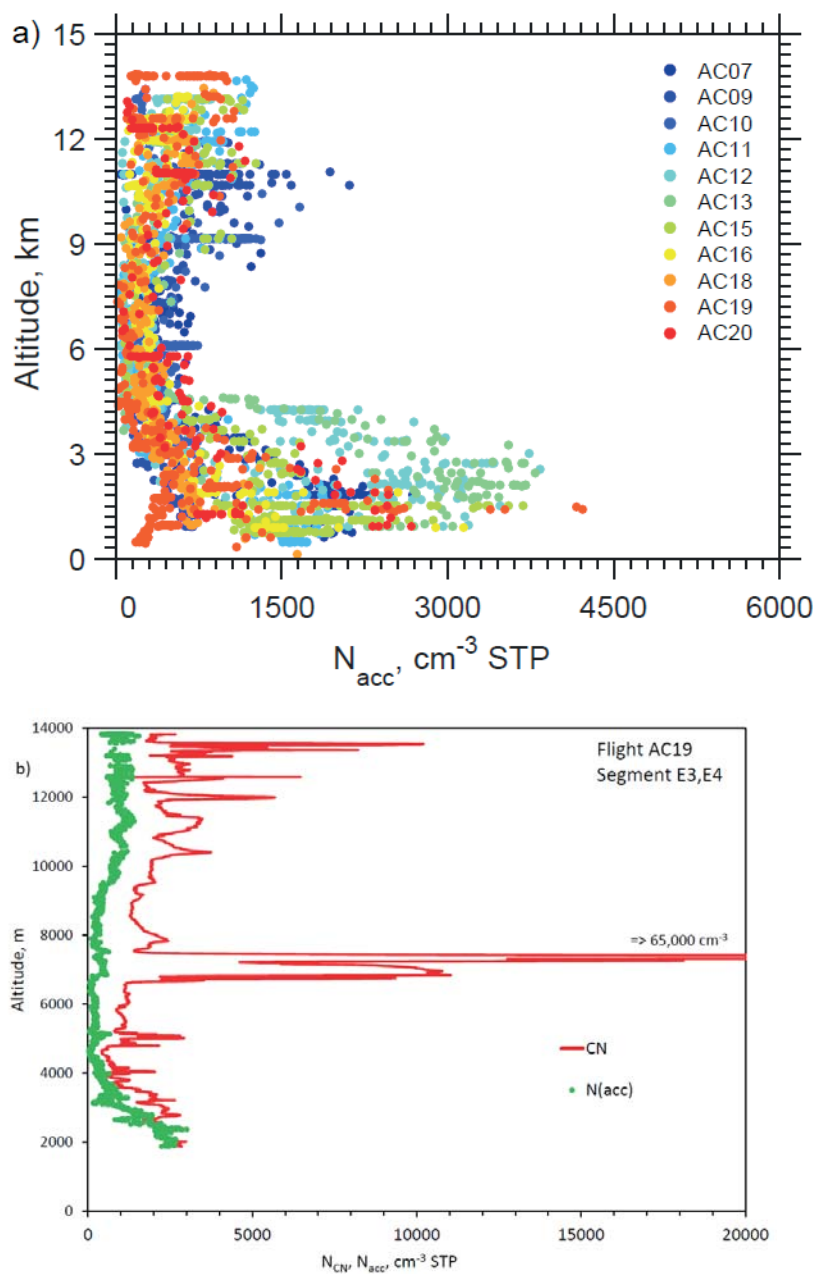




Figure 9: Size spectra: The black line shows the mean boundary layer DMPS size spectrum from a segment in the PBL on flight AC13 (16:55 to 17:18UT). The square black symbols represent the mean, the grey shaded area the standard deviation of the measurements. The line is a logarithmic fit with modal diameters of 74 and 175 nm. The colored lines represent size distributions from 0.65 to 5.8 km from a G1 flight during GoAmazon (Wang et al., 2016a).

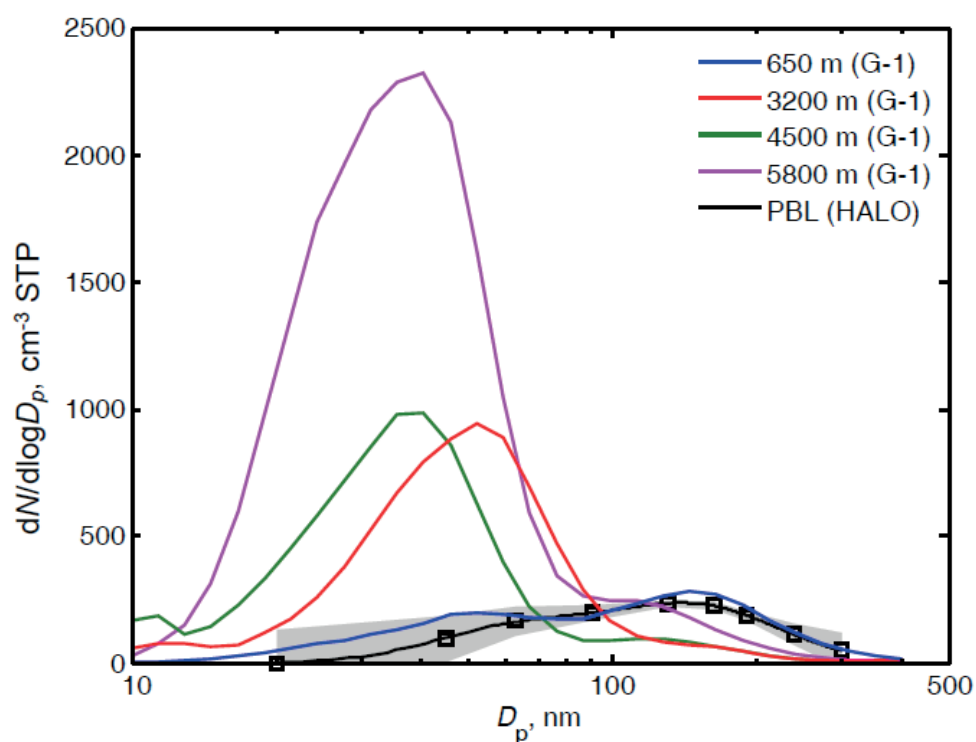




Figure 10: Vertical profiles of the ultrafine fraction (UFF); a) overall statistics from all flights, b) examples from individual profiles on flight AC18.

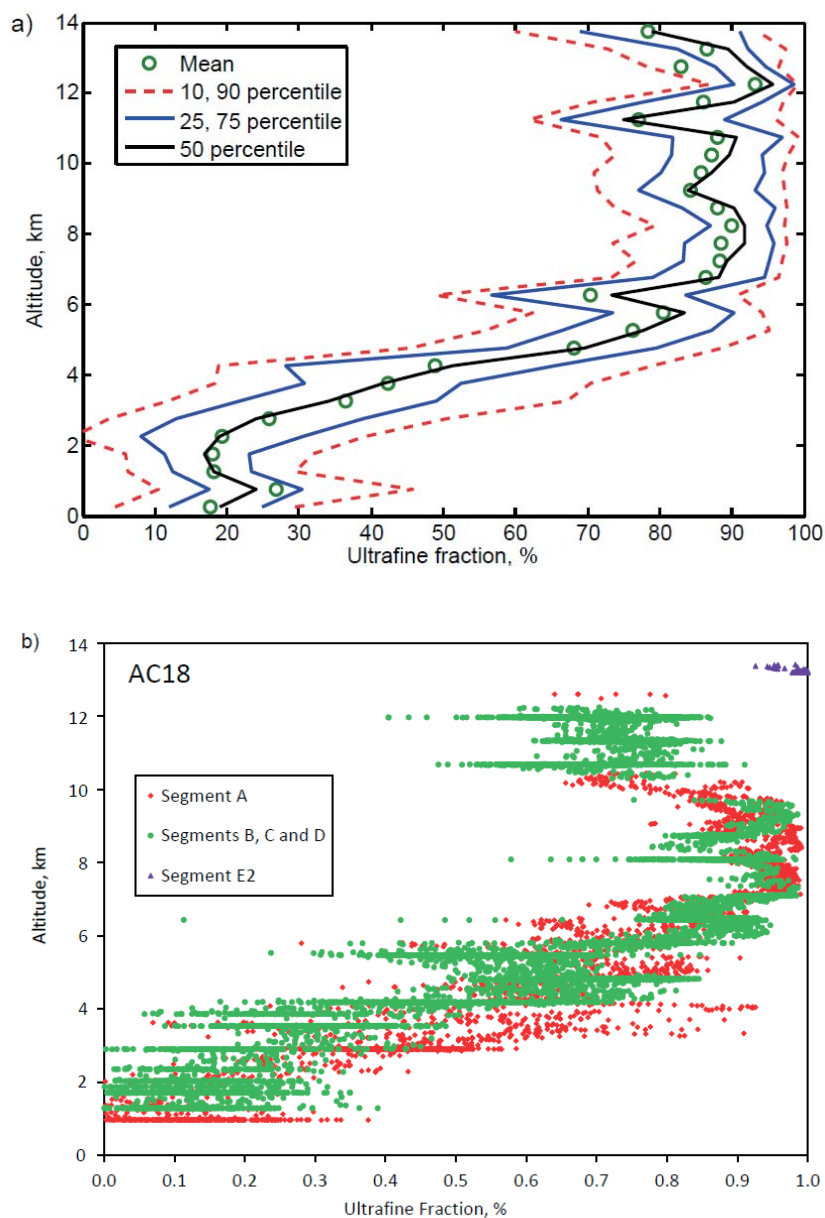




Figure 11: Vertical profiles of CCN concentrations at 0.52% supersaturation; a) overall statistics from all flights (1-min averages), b) examples from individual profiles on flights AC09 (green) and AC12+13 (red). Flights AC12 and AC13 were conducted over the same region on successive days.

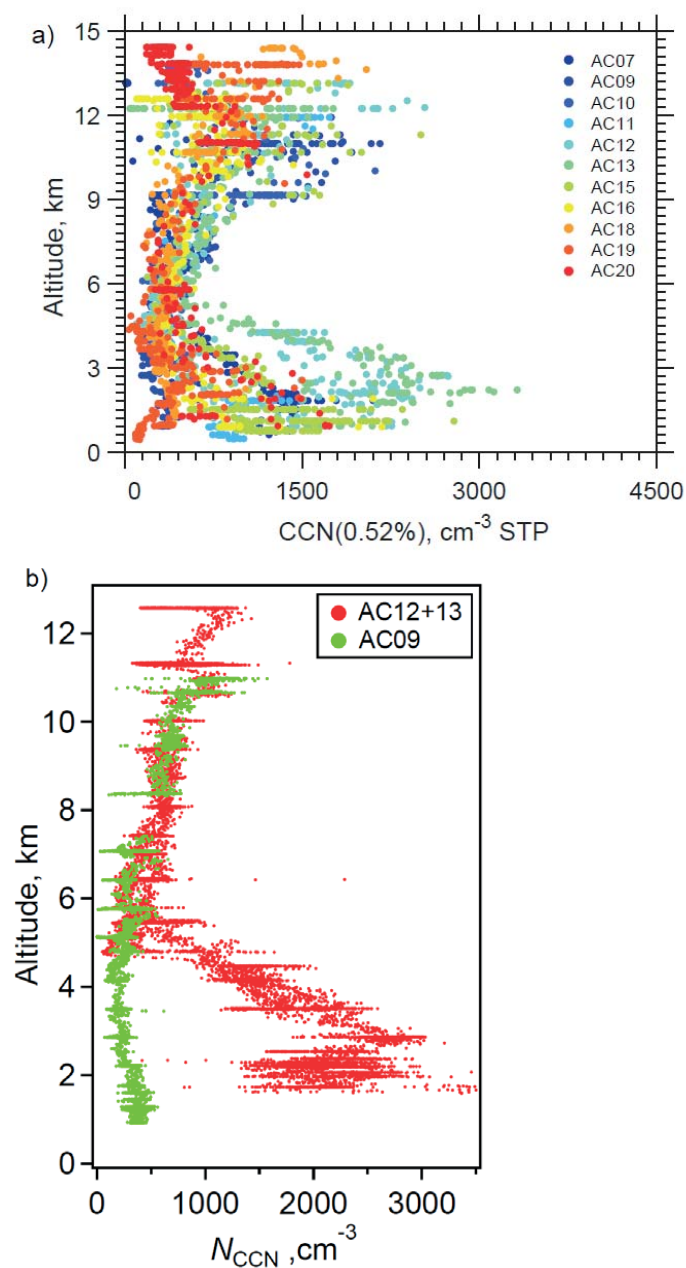




Figure 12: a) CCN fraction vs altitude, all data. b) CCN fraction vs. CN concentration for specific segments from flight AC18 (see text).

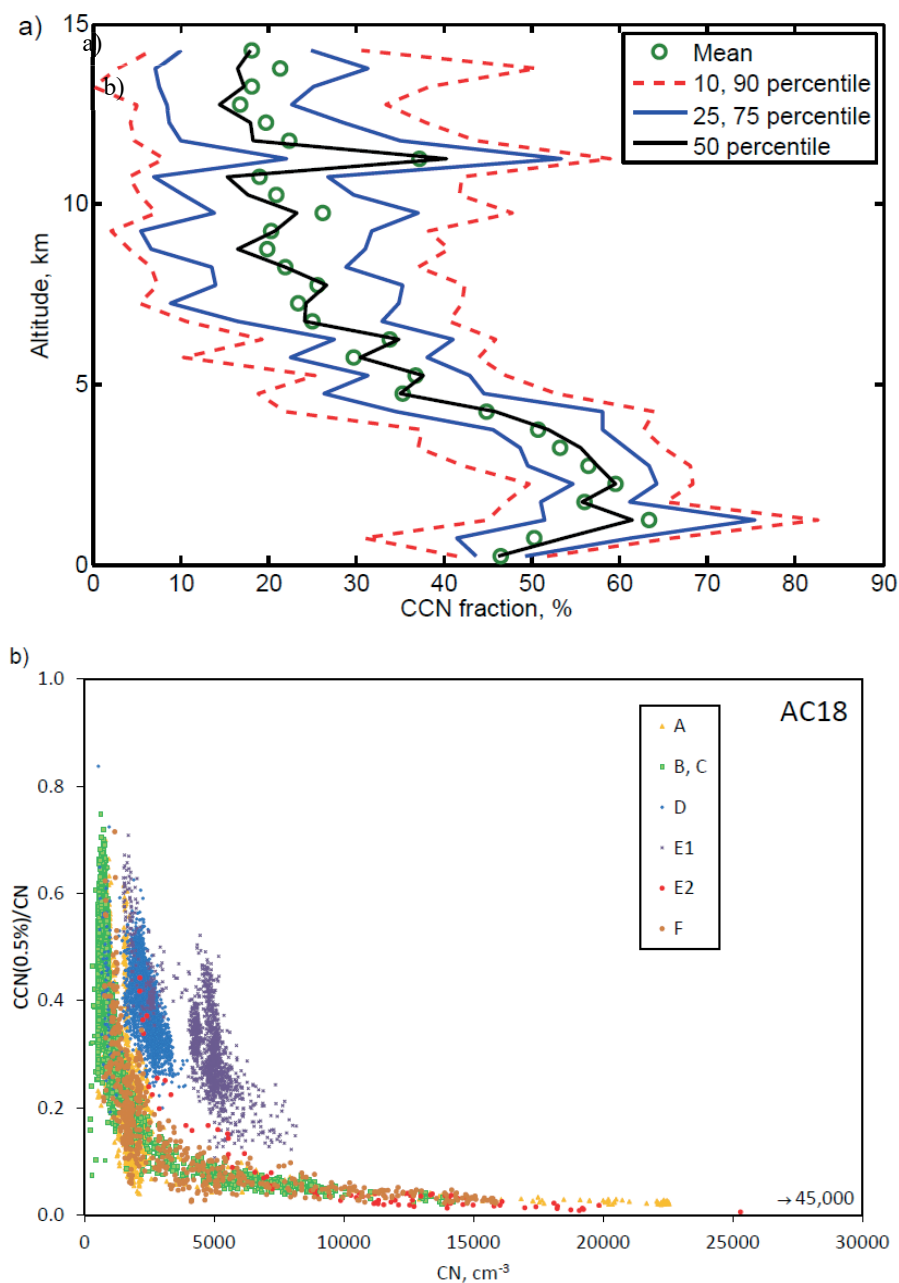
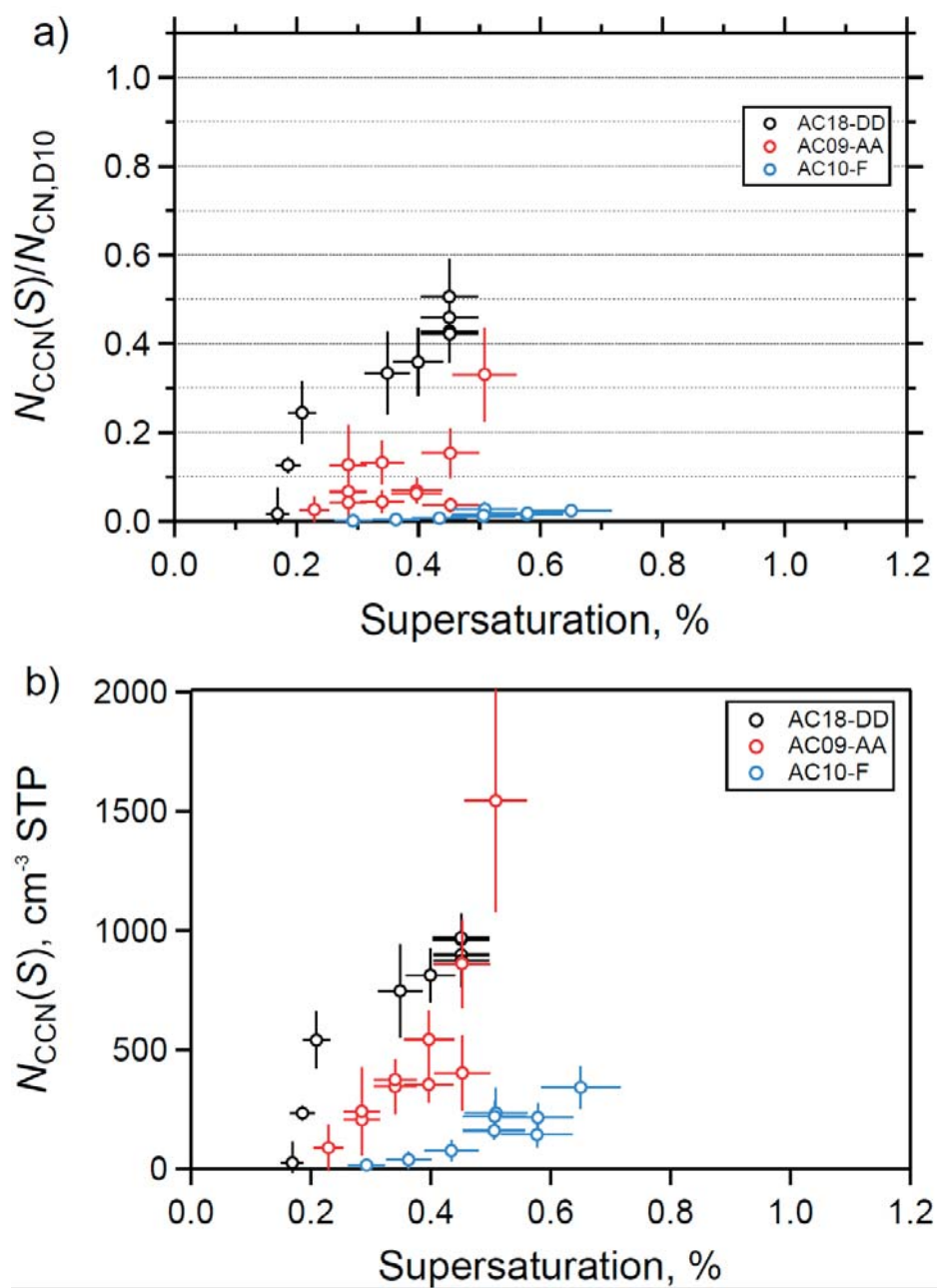




Figure 13: a) CCN fractions ( $N_{CCN0.5}/N_{CN}$ ) and b) CCN concentrations ( $N_{CCN0.5}$ ) vs. supersaturation from selected legs from flights AC09, AC10, and AC18; c,d) data from flights AC12 and AC13 for the LT, MT, and UT.



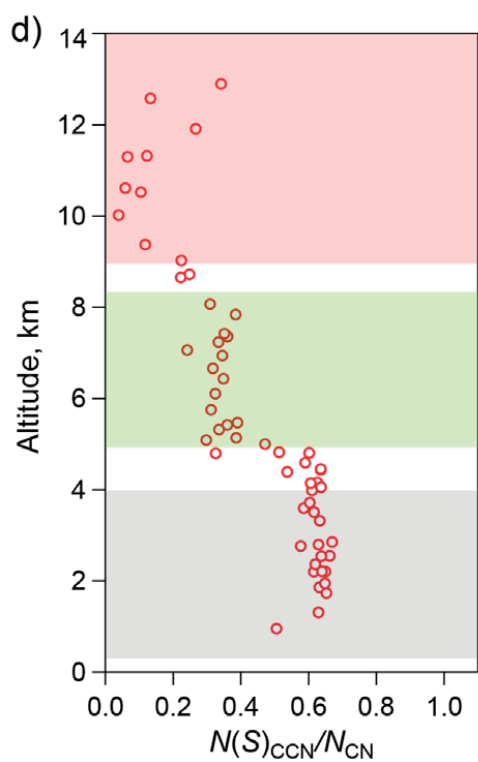
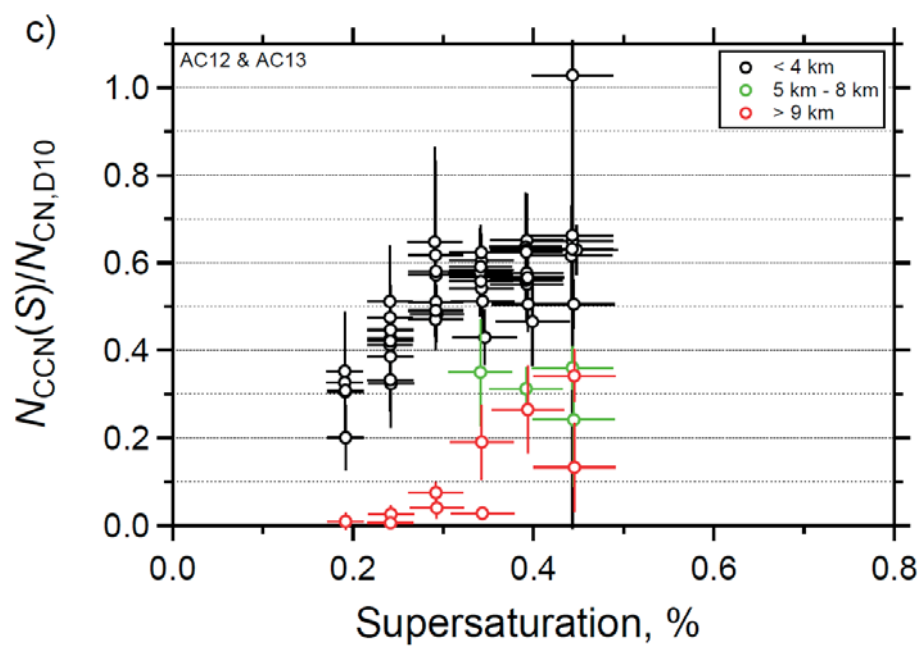




Figure 14: Volatile fraction. a) statistics from all flights; b) individual segments from flight AC18 (see text)

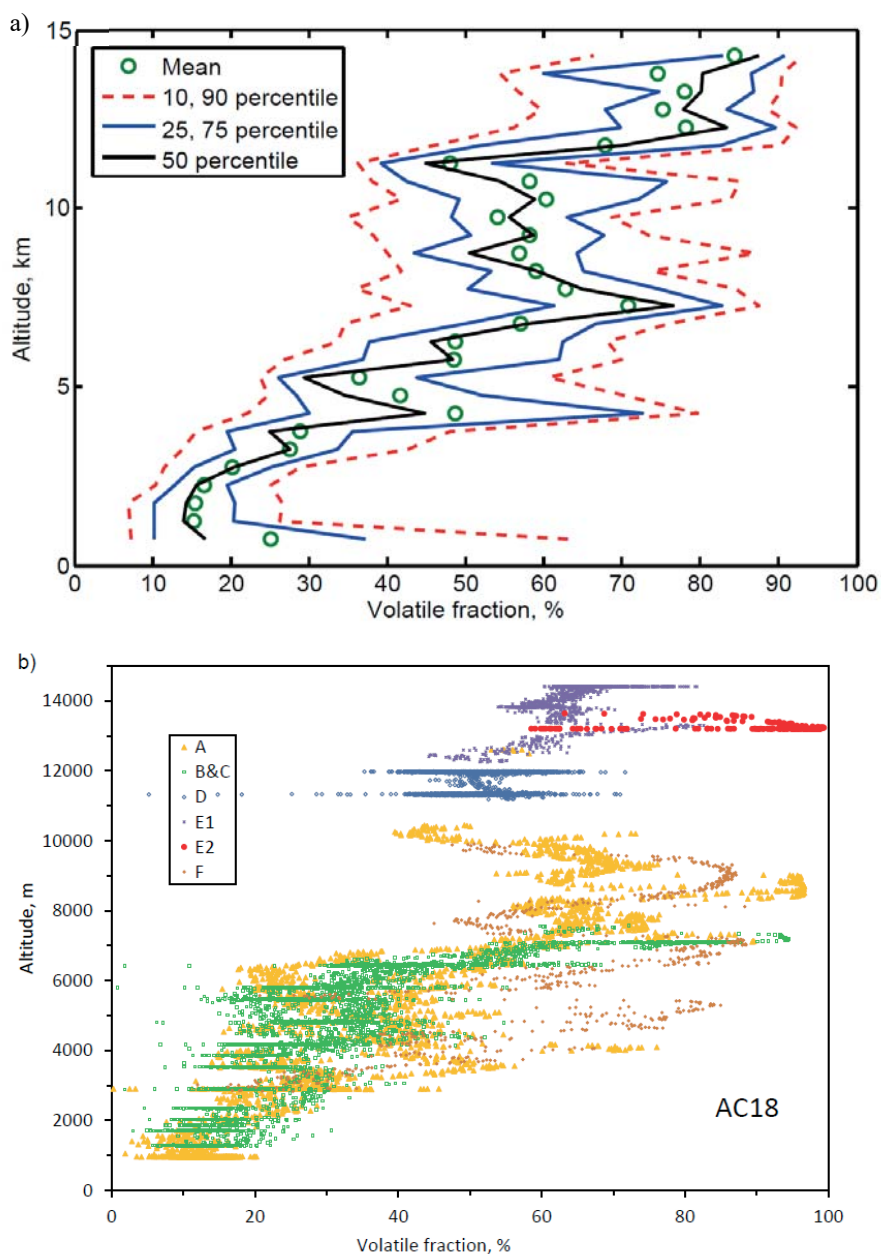




Figure 15: Refractory black carbon vs altitude, all flights, 30-second averages.

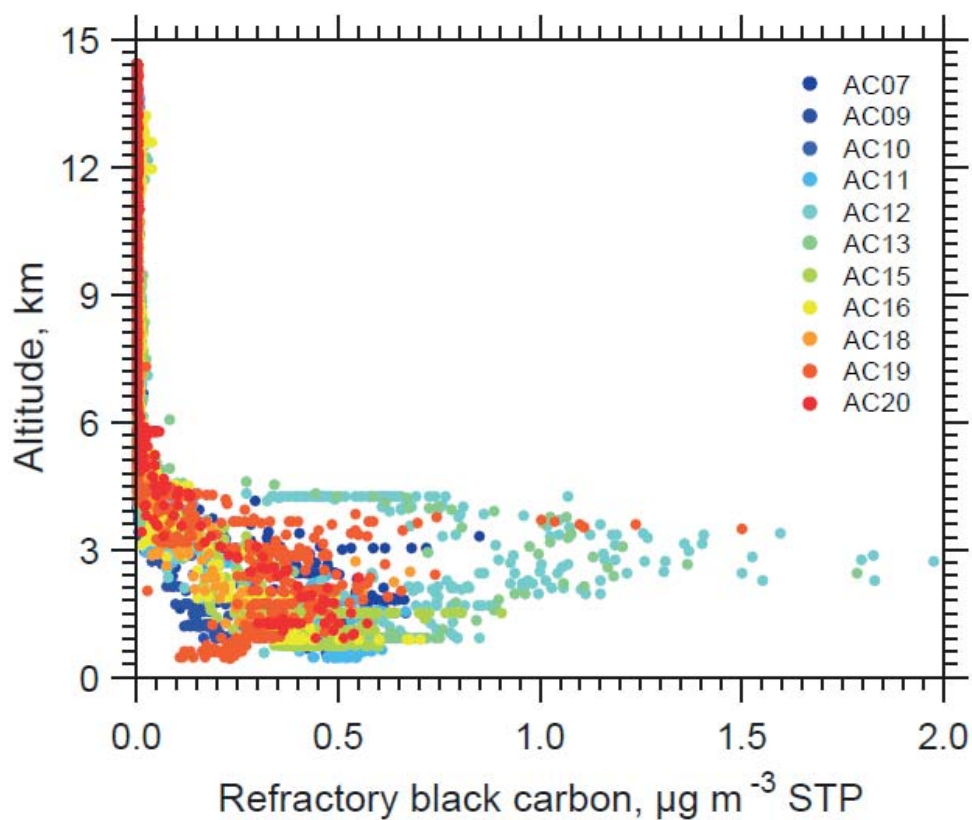




Figure 16: Aerosol chemical composition as determined by AMS and SP2 measurements in the lower, middle and upper troposphere.

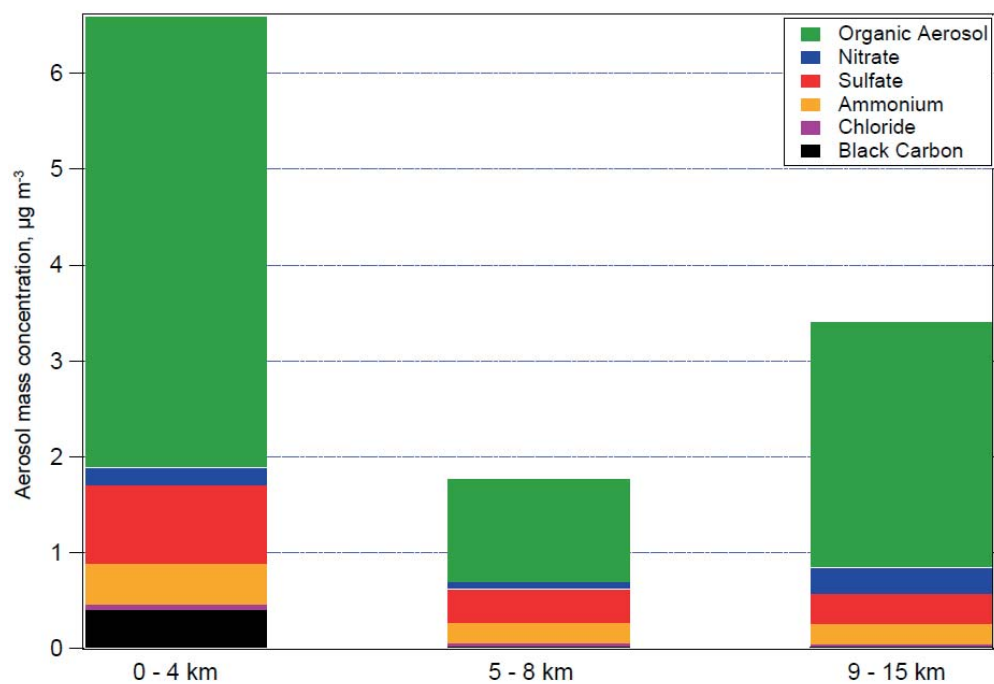




Figure 17: Plot of the AMS factors  $f_{44}$  vs.  $f_{43}$ , indicating the median values for the LT and UT and values for some UT flight segments with elevated aerosol concentrations. With increasing degree of oxidation, the measurements move to the upper left of the triangle

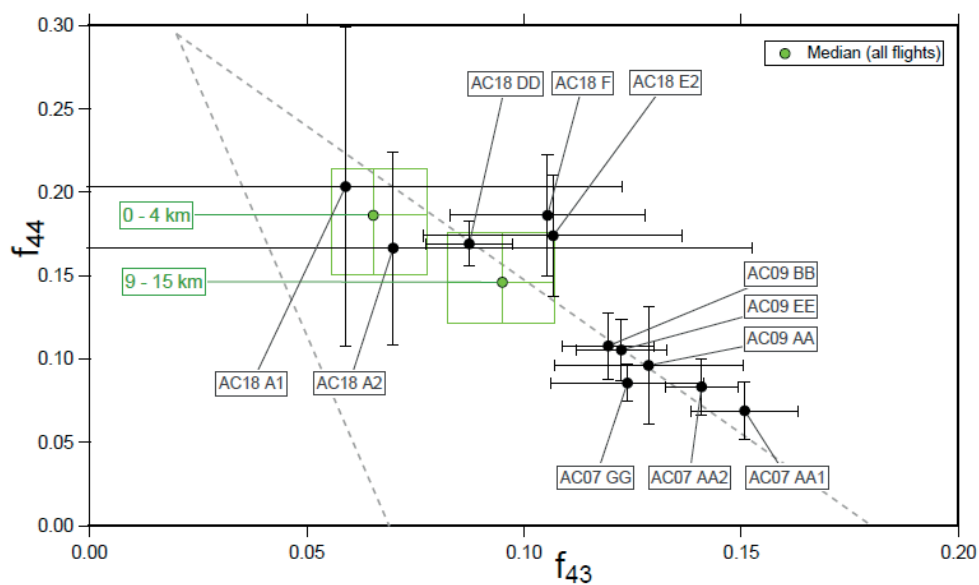




Figure 18: Measurements during passages through cumulonimbus cloud tops and outflow anvils: a) Several cloud top penetrations at 10.7 to 12 km altitude on flight AC18 showing reduced  $N_{CN}$  and  $N_{CCN0.5}$  inside the cloud top; b) Outflow from a large active cumulonimbus, showing strong aerosol depletion and NO production by lightning.

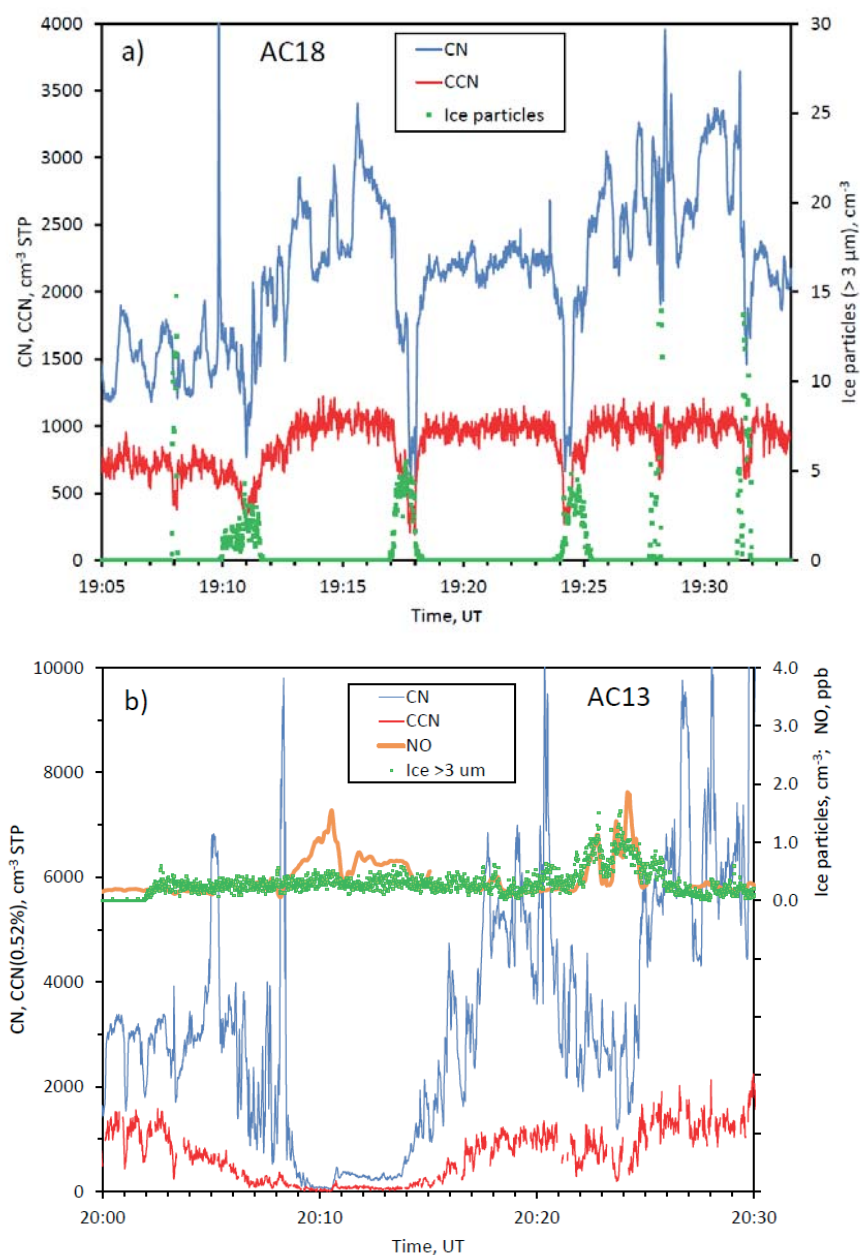




Fig. 19: Airmass contacts with deep convection. The colors indicate the cloud top temperature of the convective system with which the trajectory had the most recent contact. The aircraft altitude at which the airmass was sampled is indicated by the red line. The colored dots are plotted at the altitude at which the airmass crossed the grid cell with the convective system. The dots are only plotted if this altitude is greater than 6 km and if it encountered a DC (i.e.,  $T_b < -30$  °C). The shaded areas correspond to the flight segments with elevated CN concentrations. a) flight AC09, b) flight AC18.

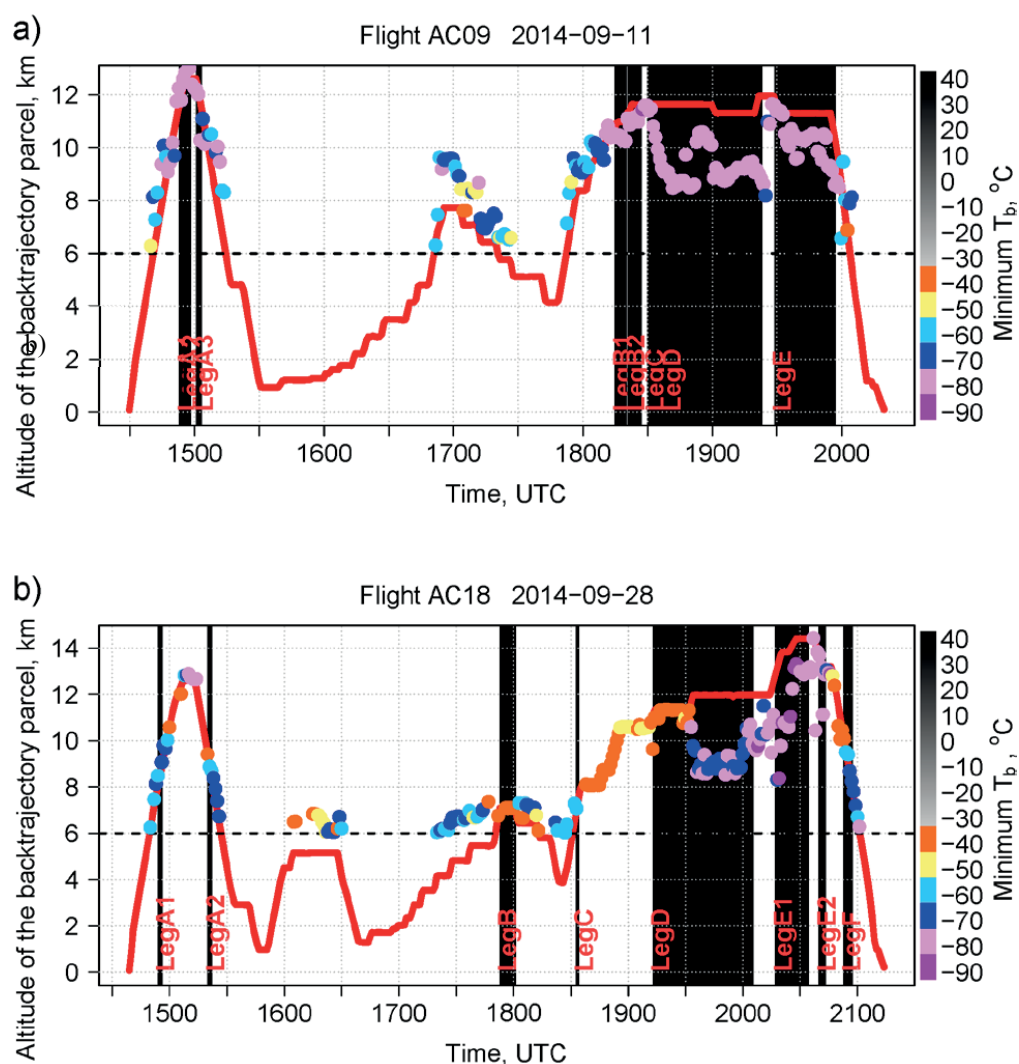




Figure 20: a) Number of hours since last contact with deep convection for flight segments with elevated aerosol concentrations (cumulative frequency, all flights); b) frequency distribution of minimum GOES brightness temperature ( $T_b$ ) for selected flights legs (within -5 days backward trajectories).

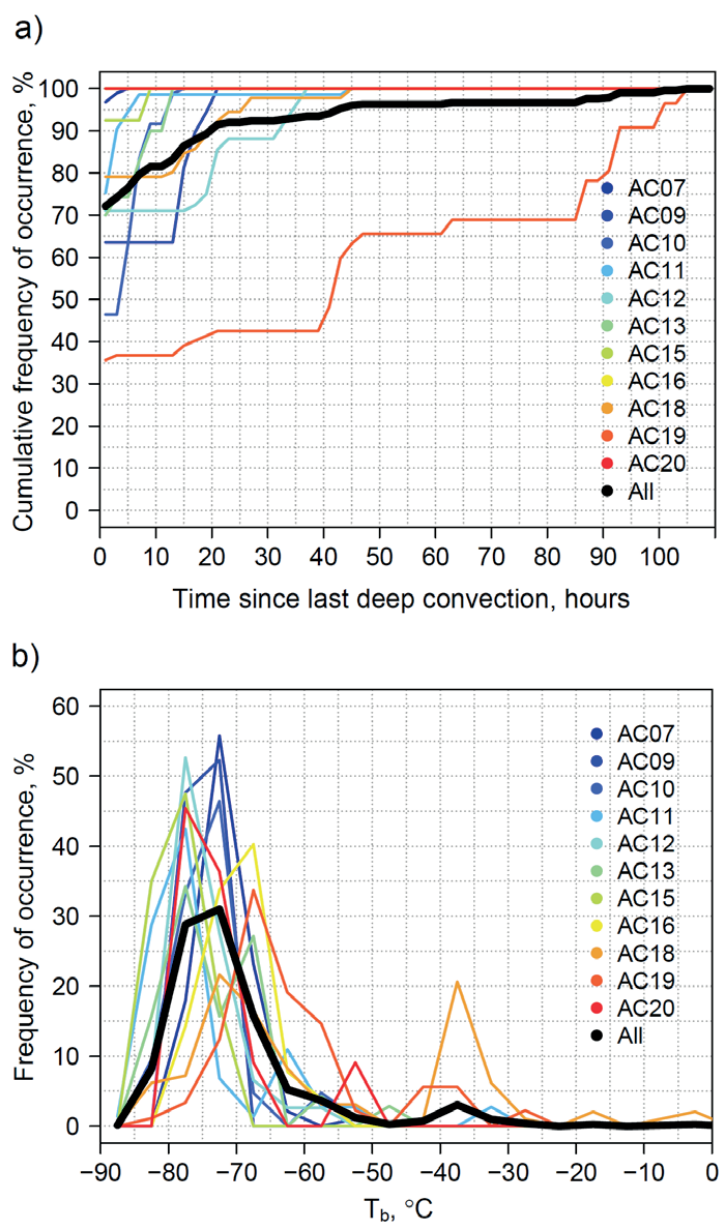




Figure 21: CN vs CO in the upper troposphere above 8 km (15-second averages).

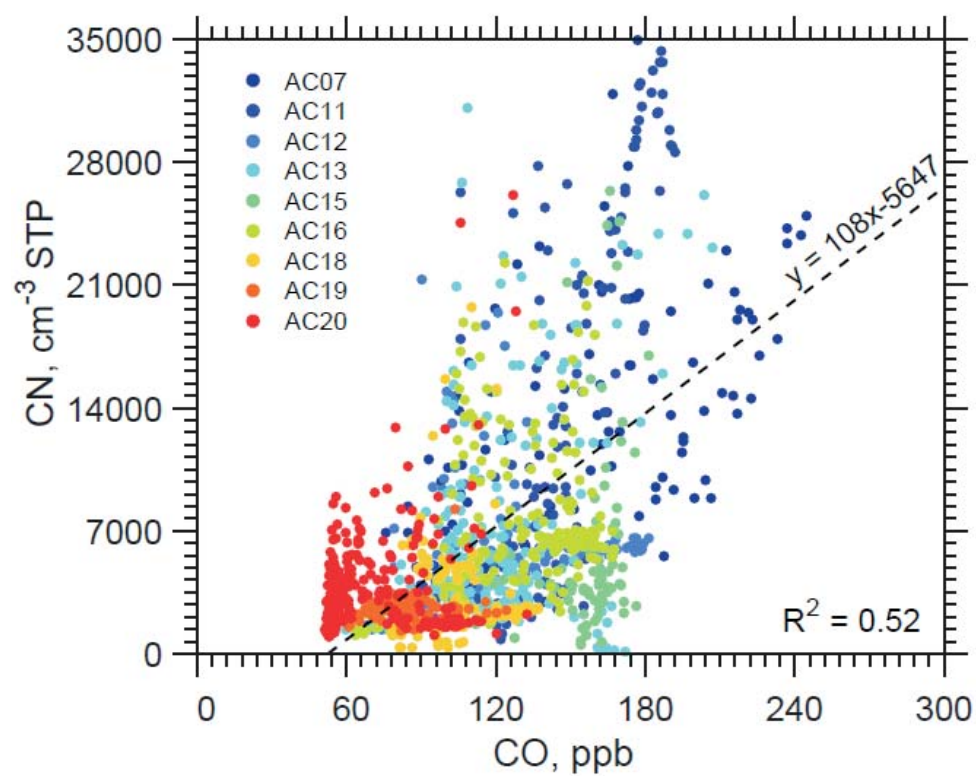




Figure 22: CN, NO and NO<sub>y</sub> in a flight segment in the upper troposphere on flight AC07.

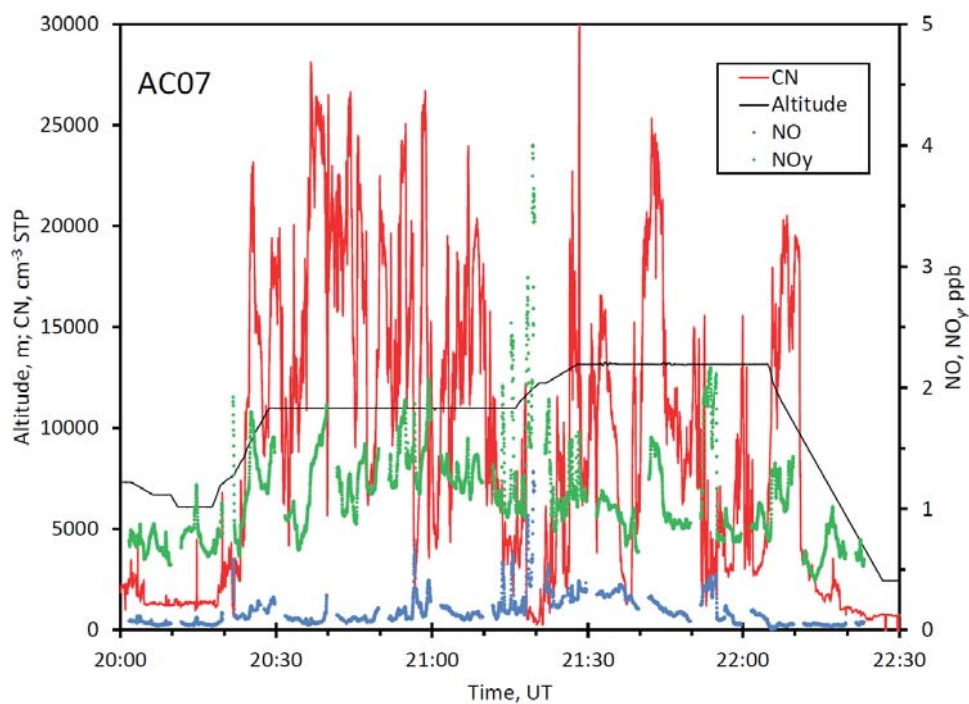
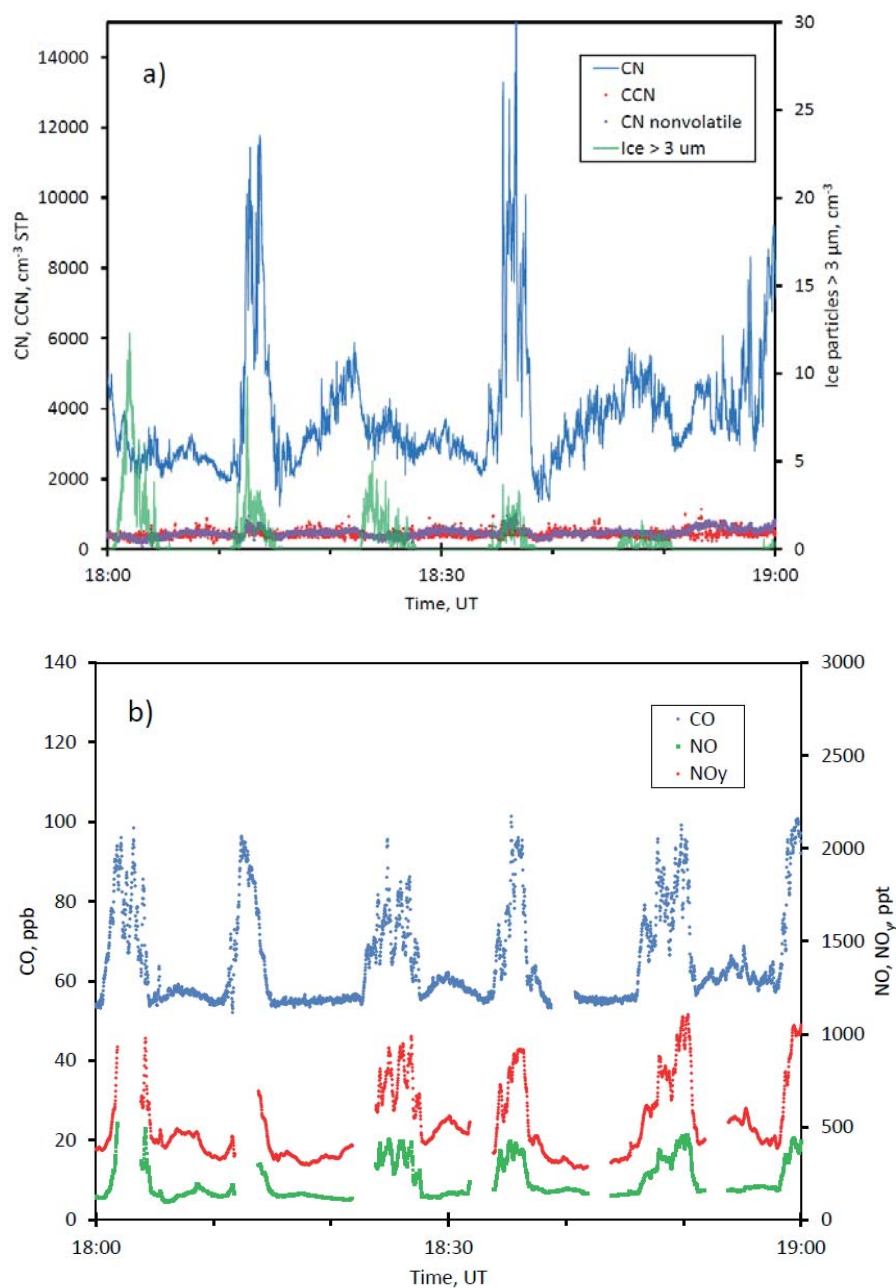




Figure 23: a) Measurements of  $N_{CCN0.5}$ ,  $N_{CN}$ ,  $N_{nonvol}$ , and ice particles during cloud top penetrations on flight AC20. b) Concentrations of CO, NO, and  $NO_y$  on the same flight segments. c) Measurements of  $N_{acc}$ ,  $N_{CN}$ , rBC, CO, and  $O_3$  during the climb from 11.0 to 13.5 km.



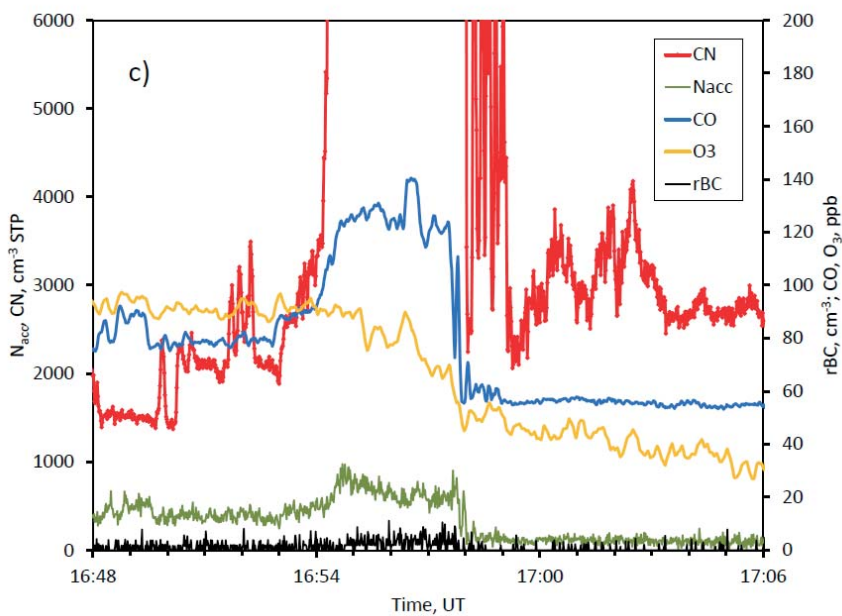




Figure 24: Conceptual model of the aerosol life cycle over the Amazon Basin

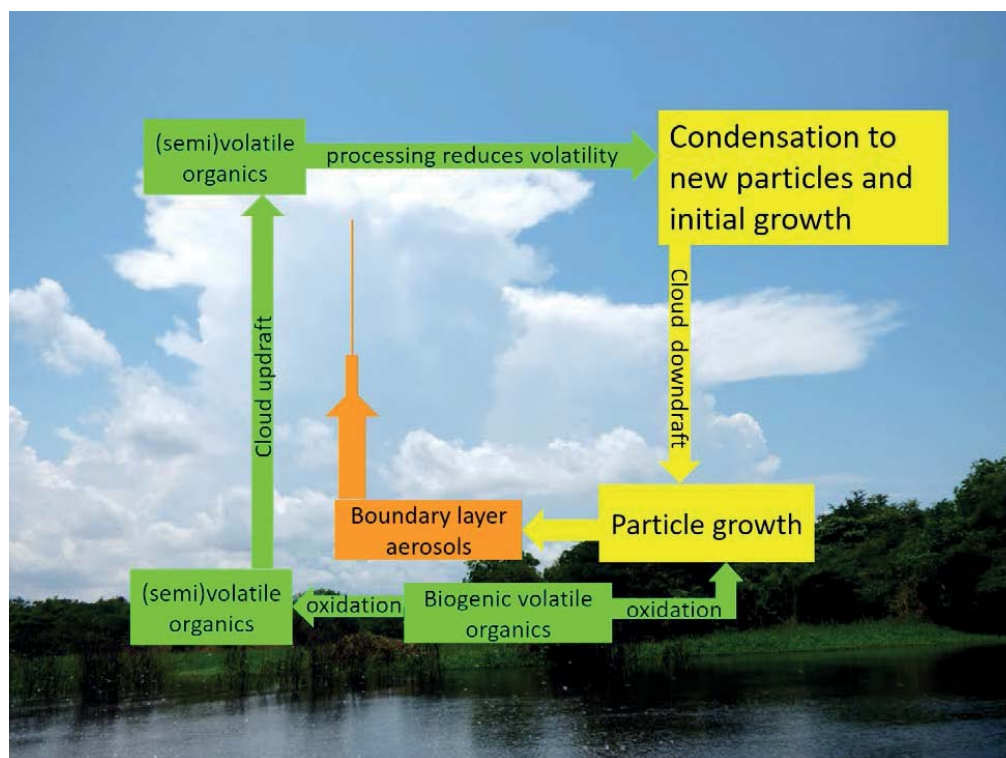


Figure S1: Example of a back-tracked parcel starting at the location of the HALO aircraft during flight AC18. This parcel started at 2014-09-28 20:34:53 UTC and was traced back in time in one-hour steps up to 120 hours, as shown in the time color scale on the right. The solid gray line is the full flight AC18 track.

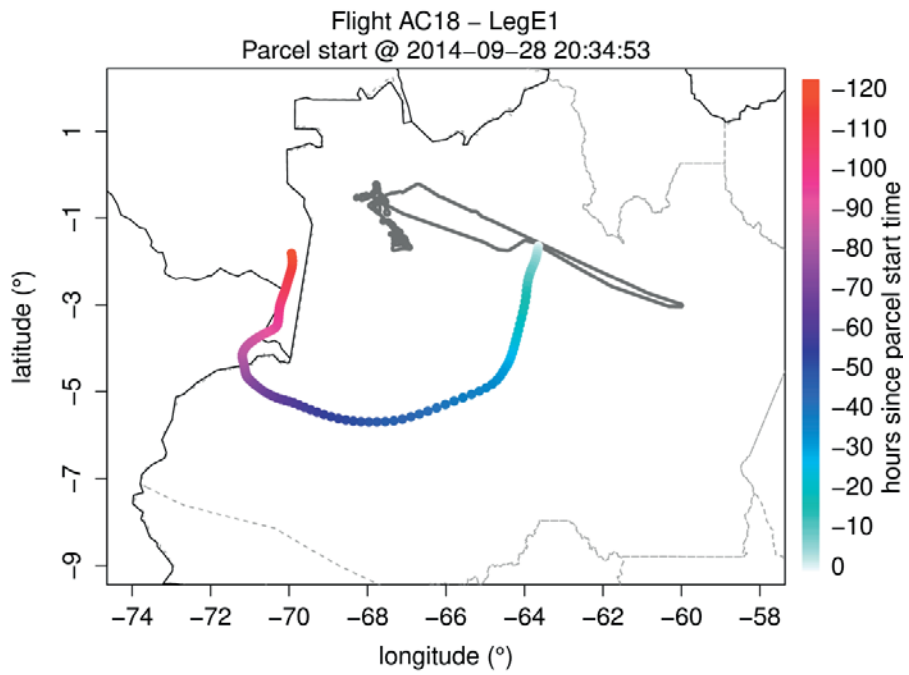


Figure S2: Examples of snapshots of the back-tracked parcel shown in Figure S1 matched in time to the closest GOES-13 infrared brightness temperature ( $T_b$ ). Color dots are the same ones as in Figure S1, representing the position and backward time (in hours). Here the snapshots are zoomed in a  $3^\circ \times 3^\circ$  box centered at the parcel location at the time shown on the top the snapshots. Dashed boxes show the  $1^\circ \times 1^\circ$  box centered in the back-tracked parcel within which we looked up the minimum  $T_b$ . This value is shown at the left corner of each snapshot as well as the parcel altitude and GOES-13 infrared (IR) time.

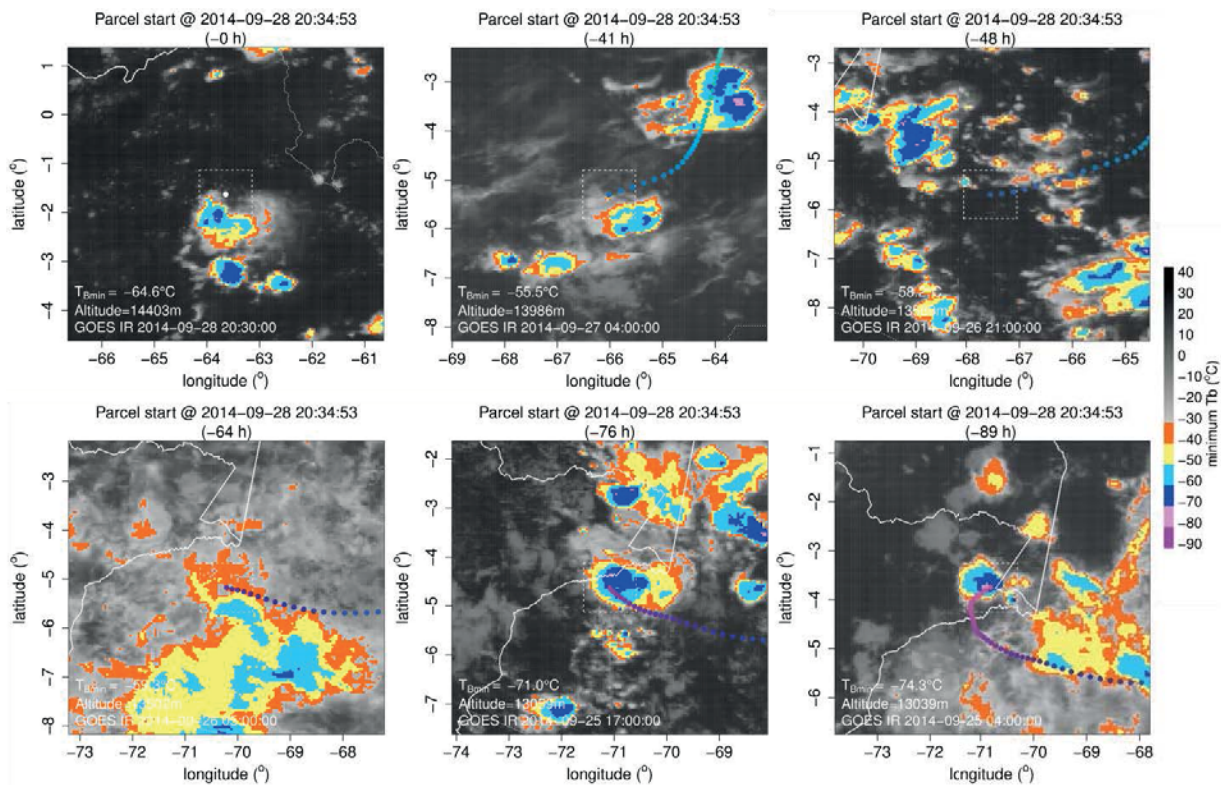


Figure S3: Summary of the back-tracked parcel positions (as in Fig. S1) with the minimum  $T_b$  tracked as shown in the snapshot examples of Figure S2. Here the back-track parcel position is colored with the value of minimum  $T_b$  found in the  $1^\circ \times 1^\circ$  box.

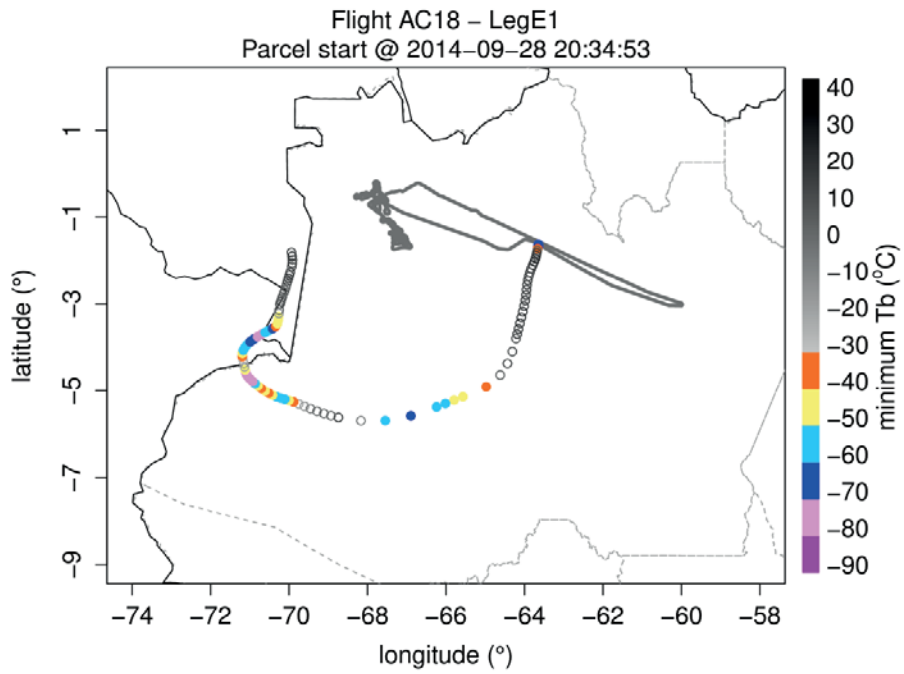


Figure S4. Mean vertical profiles of temperature, relative humidity and potential temperature ( $\theta$ ) from radiosoundings at Manacapuru.

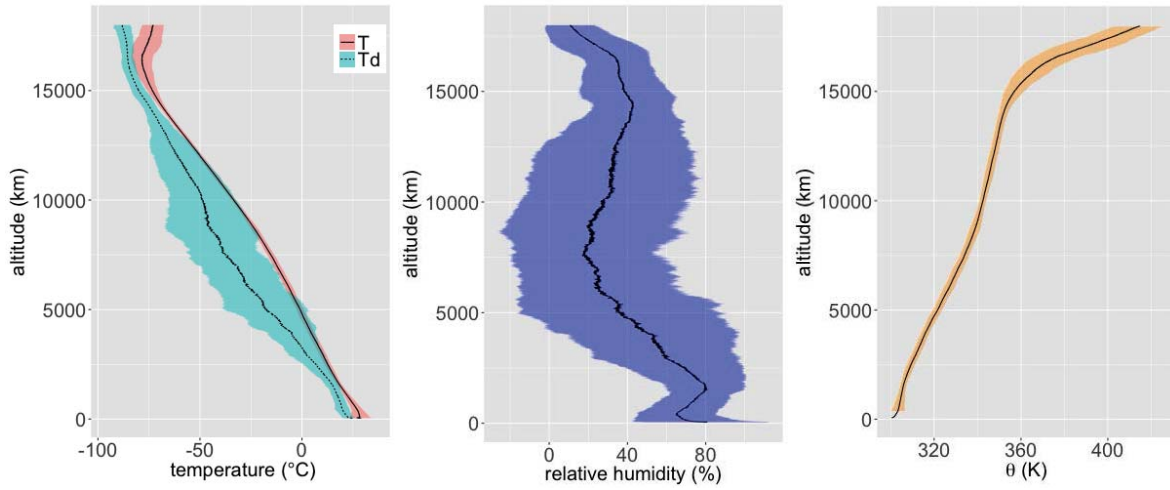


Figure S5: Trajectory statistics based on 120-hour backtrajectory calculations for September 2014, initialized at Manaus at an elevation of 10 km.

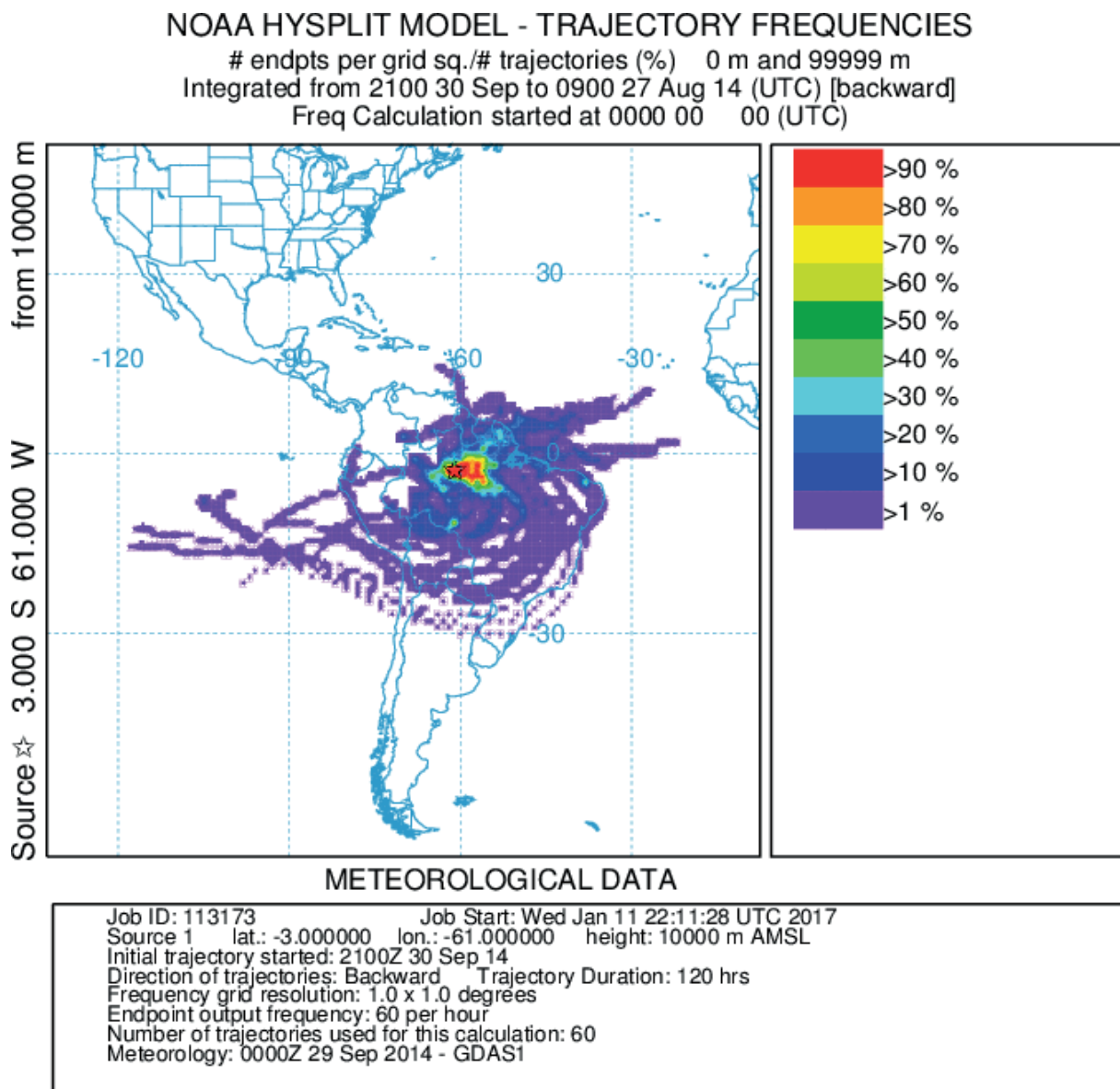
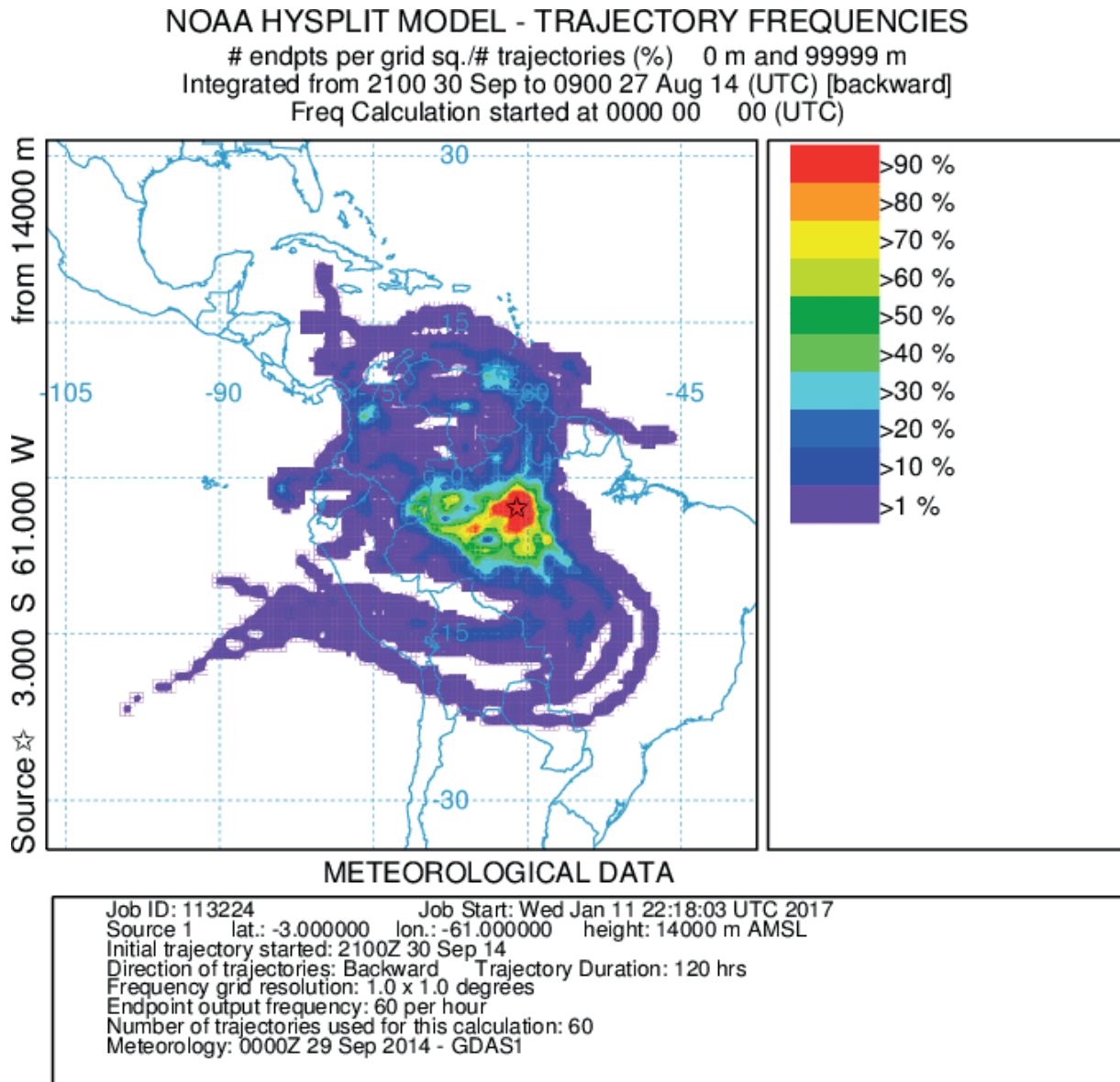


Figure S6: Trajectory statistics based on 120-hour backtrajectory calculations for September 2014, initialized at Manaus at an elevation of 14 km.



**B4. Krüger et al., Atmos. Meas. Tech., 2014**

**Assessment of cloud supersaturation by size-resolved aerosol particle and cloud condensation nuclei (CCN) measurements**

M. L. Krüger<sup>1</sup>, S. Mertes<sup>2</sup>, T. Klimach<sup>1</sup>, Y. F. Cheng<sup>1</sup>, H. Su<sup>1</sup>, J. Schneider<sup>1</sup>, M. O. Andreae<sup>1</sup>, U. Pöschl<sup>1</sup>,  
and D. Rose<sup>1,a</sup>

<sup>1</sup> *Multiphase Chemistry and Biogeochemistry Departments, Max Planck Institute for Chemistry, Mainz, Germany*

<sup>2</sup> *Leibniz Institute for Tropospheric Research, Leipzig, Germany*

<sup>a</sup> *now at Institute for Atmospheric and Environmental Sciences, Goethe University of Frankfurt, Frankfurt, Germany*

**Atmospheric Measurement Techniques, 7, 2615–2629, 2014**



# Assessment of cloud supersaturation by size-resolved aerosol particle and cloud condensation nuclei (CCN) measurements

M. L. Krüger<sup>1</sup>, S. Mertes<sup>2</sup>, T. Klimach<sup>1</sup>, Y. F. Cheng<sup>1</sup>, H. Su<sup>1</sup>, J. Schneider<sup>1</sup>, M. O. Andreae<sup>1</sup>, U. Pöschl<sup>1</sup>, and D. Rose<sup>1,\*</sup>

<sup>1</sup>Multiphase Chemistry, Biogeochemistry, and Particle Chemistry Departments, Max Planck Institute for Chemistry, P.O. Box 3060, 55020 Mainz, Germany

<sup>2</sup>Leibniz Institute for Tropospheric Research, Permoserstraße 15, 04318 Leipzig, Germany

\* now at: Institute for Atmospheric and Environmental Sciences, Goethe University of Frankfurt am Main, Altenhöferallee 1, 60438 Frankfurt am Main, Germany

Correspondence to: D. Rose (rose@iauw.uni-frankfurt.de)

Received: 19 September 2013 – Published in Atmos. Meas. Tech. Discuss.: 15 November 2013

Revised: 15 June 2014 – Accepted: 24 June 2014 – Published: 19 August 2014

**Abstract.** In this study we show how size-resolved measurements of aerosol particles and cloud condensation nuclei (CCN) can be used to characterize the supersaturation of water vapor in a cloud. The method was developed and applied during the ACRIDICON-Zugspitze campaign (17 September to 4 October 2012) at the high-Alpine research station Schneefernerhaus (German Alps, 2650 m a.s.l.). Number size distributions of total and interstitial aerosol particles were measured with a scanning mobility particle sizer (SMPS), and size-resolved CCN efficiency spectra were recorded with a CCN counter system operated at different supersaturation levels.

During the evolution of a cloud, aerosol particles are exposed to different supersaturation levels. We outline and compare different estimates for the lower and upper bounds ( $S_{\text{low}}$ ,  $S_{\text{high}}$ ) and the average value ( $S_{\text{avg}}$ ) of peak supersaturation encountered by the particles in the cloud. A major advantage of the derivation of  $S_{\text{low}}$  and  $S_{\text{avg}}$  from size-resolved CCN efficiency spectra is that it does not require the specific knowledge or assumptions about aerosol hygroscopicity that are needed to derive estimates of  $S_{\text{low}}$ ,  $S_{\text{high}}$ , and  $S_{\text{avg}}$  from aerosol size distribution data. For the investigated cloud event, we derived  $S_{\text{low}} \approx 0.07\text{--}0.25\%$ ,  $S_{\text{high}} \approx 0.86\text{--}1.31\%$  and  $S_{\text{avg}} \approx 0.42\text{--}0.68\%$ .

## 1 Introduction

Atmospheric aerosols consist of particles spanning a wide range of size and chemical composition from various natural and anthropogenic sources (Pöschl, 2005). They can act as cloud condensation nuclei (CCN) and affect climate by influencing the properties of clouds and precipitation (Lohmann and Feichter, 2005; Solomon et al., 2007; Rosenfeld et al., 2008). Depending on particle size, composition, and mixing state, aerosol particles are activated as CCN at different water vapor supersaturations (e.g., Köhler, 1936; Dusek et al., 2006; McFiggans et al., 2006; Andreae and Rosenfeld, 2008; Su et al., 2010).

As a result of long-term efforts and recent advances in atmospheric research, the CCN activity of atmospheric aerosol particles can be fairly well constrained by measurements and models (e.g., Petters and Kreidenweis, 2007, 2008; Gunthe et al., 2009; Kinne, 2009; Moore and Nenes, 2009; Pöschl et al., 2009; Juranyi et al., 2010; Pringle et al., 2010; Rose et al., 2010; Wex et al., 2010; Gunthe et al., 2011; Kim et al., 2011; Kulmala et al., 2011; Rose et al., 2011; Spracklen et al., 2011; Anttila et al., 2012; Christensen and Petters, 2012; Engelhart et al., 2012; Padró et al., 2012; Jurányi et al., 2013; Lance et al., 2013; Mikhailov et al., 2013; Petters and Kreidenweis, 2013). To fully describe the process of CCN activation and cloud droplet growth in the atmosphere, however, the supersaturation of water vapor in the cloud also needs to be known (e.g., Reutter et al., 2009; Pruppacher and Klett, 2010; Rosenfeld et al., 2012; Renno et al., 2013).

Upon cloud formation, the decrease of temperature in an ascending air parcel resulting from the expansion of air with decreasing pressure (adiabatic cooling) or the decrease of temperature in an air parcel moving horizontally over a colder surface or air mass (isobaric cooling) induces water vapor supersaturation (Pruppacher and Klett, 2010). At the point where the increase of supersaturation by cooling is compensated by the condensational sink of water vapor, the supersaturation reaches a maximum or peak value. Following Hammer et al. (2014) we use the expression “peak” rather than “maximum” supersaturation. Particles with a critical supersaturation equal to or lower than the peak supersaturation are activated and grow into cloud droplets. The peak supersaturation is a major determinant for the cloud droplet number and the regime of CCN activation (aerosol- vs. up-draft limited; Reutter et al., 2009; Rosenfeld et al., 2012). Due to inhomogeneities of the atmospheric aerosol load and air flow pattern (turbulence, entrainment), the peak supersaturations of different air parcels in a cloud can be temporally and spatially heterogeneous.

Techniques for the direct measurement of cloud supersaturation are not available. Thus, indirect methods have been developed to estimate the value of water vapor supersaturation in a cloud, which determines the fraction of particles that are activated and form cloud droplets.

An early approach to deduce the cloud supersaturation was presented by Hoppel et al. (1996). They commonly observed a double-peaked structure of the aerosol size distribution in the marine boundary layer, which is a result of processing aerosol through nonprecipitating cloud cycles. The authors suggest that the mode that peaks at 20 to 80 nm consists of particles that are too small to be activated during the cloud processing, and the mode that peaks at 160 to 400 nm represents the residue of evaporated cloud droplets that have been enlarged mainly as a result of liquid-phase conversion of soluble trace gases to nonvolatile compounds. Therefore, they could relate the diameter at which the minimum occurs (the so-called Hoppel minimum) to the supersaturation of the cloud, assuming the particles to consist of a mixture of ammonium sulfate and sulfuric acid.

Another method to derive the supersaturation of a cloud was used by, for example, Hammer et al. (2014), Ditas et al. (2012), Asmi et al. (2012), and Anttila et al. (2009). In these studies the fraction of activated particles in a cloud was deduced from the comparison of the number size distribution of interstitial particles (i.e., particles not taken up into cloud droplets) and total aerosol particles (i.e., cloud residuals plus interstitial particles). Through Köhler theory and with the assumption of an average particle hygroscopicity, the diameter at which 50 % of all particles activated was related to the particles' critical supersaturation, which was then regarded as the supersaturation at which ambient clouds had formed.

In a recent study, Russell et al. (2013) measured the CCN activation of cloud residuals, which were sampled behind a counterflow virtual impactor (CVI) and compared it to the

measured cloud droplet number concentration (CDNC). The supersaturation at which the CDNC was equal to the CCN concentration of the cloud residuals was assumed to be the cloud supersaturation.

Most likely the particles of a cloud are processed through a number of nonprecipitating cloud cycles (typically on the order of 10 or more; Hoppel et al., 1996). Thus, different particles may have been exposed to different peak supersaturations, at which they were activated into cloud droplets. For that reason the activation of aerosol particles in the cloud cannot be described or reproduced with the activation at one single supersaturation level.

In this study we derive and compare different estimates for an effective average value ( $S_{\text{avg}}$ ) and the lower and upper bounds ( $S_{\text{low}}$ ,  $S_{\text{high}}$ ) of the peak supersaturation encountered by the particles in a cloud. Estimates of  $S_{\text{avg}}$  (Sects. 3.2.1 and 3.2.2),  $S_{\text{low}}$  (Sect. 3.2.3), and  $S_{\text{high}}$  (Sect. 3.2.4) based on aerosol size distribution data require specific assumptions or measurements of aerosol hygroscopicity; these are not required for the derivation of  $S_{\text{low}}$  (Sect. 3.1.1) and  $S_{\text{avg}}$  (Sect. 3.1.2) from size-resolved CCN efficiency spectra.

## 2 Experimental methods and data analysis

### 2.1 Measurement site

Measurements were performed during the ACRIDICON-Zugspitze campaign (17 September to 4 October 2012) at the research station Schneefernerhaus, a mountain site in the German Alps (47.42° N, 10.97° E; 2650 m a.s.l.; www.schneefernerhaus.de). The aim of this campaign was the investigation of liquid water clouds. For the analysis in this paper we chose one exemplary cloud event, which occurred on 19 September 2012.

### 2.2 Inlet system

We used an inlet that segregated hydrometeors by means of a cyclone with a 2.5  $\mu\text{m}$  cut-off (PM<sub>2.5</sub>). During out-of-cloud conditions the inlet samples all aerosol particles with diameter < 2.5  $\mu\text{m}$  (total aerosol). During in-cloud conditions particles that have been activated to cloud droplets are removed because they are larger than the inlet cut-off diameter (Mertes et al., 2005). Therefore the sampled aerosol can be regarded as interstitial.

### 2.3 Liquid water content (LWC)

To distinguish between in-cloud and out-of-cloud conditions, we utilized measurements of the liquid water content (LWC), which were performed by a particle volume monitor (Gerber, 1991). As suggested also by Henning et al. (2002) we defined a period of CCN measurements as in cloud when the LWC was > 0.02 g m<sup>-3</sup> for 85 % of the time and as out of cloud when the LWC was < 0.02 g m<sup>-3</sup> for 85 % of the time.

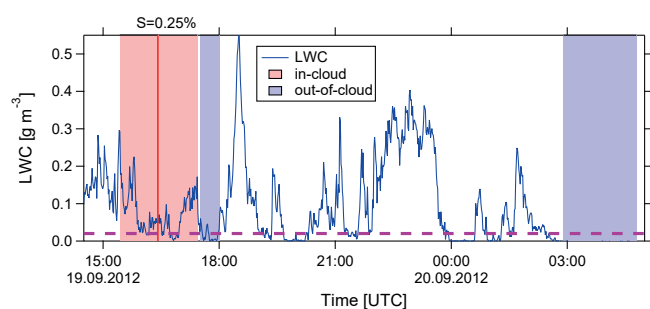


**Figure 1.** Time series of the liquid water content (LWC) measured by a particle volume monitor permitting distinction between in-cloud and out-of-cloud conditions. The time period for in-cloud conditions, during which the cloud supersaturation was investigated, is marked in red (19 September 2012, 15:26–17:17 UTC). The red vertical line indicates the time when the CCN scan at  $S = 0.25\%$  was finished. Out-of-cloud conditions are marked in blue, in which the first small time period was used to apply the SMPS method (19 September 2012, 17:30–18:00 UTC). The second larger period (20 September 2012, 02:54–04:47 UTC) was used for the CCN method, because a longer time interval without cloud was needed to get a full CCN spectrum.

For the analysis in this paper we chose one exemplary cloud event, which occurred on 19 September 2012. During this event the LWC was on average  $0.073 \text{ g m}^{-3}$ . Figure 1 shows the time series of the LWC for a certain time before, during, and after the analyzed cloud event with in-cloud and out-of-cloud conditions highlighted.

## 2.4 Size-resolved CCN measurements

The number concentration of CCN was measured using a continuous-flow streamwise thermal gradient CCN counter (CCNC), commercially available from Droplet Measurement Technologies Inc. (DMT, CCN-100). The operation principle of the CCNC is based on the fact that diffusion of heat in air is slower than diffusion of water vapor. This allows for the generation of a supersaturated area inside a flow tube by combining a temperature gradient with water vapor from a continuously wetted porous inner surface (Roberts and Nenes, 2005). The inlet flow rate of the CCNC was  $0.5 \text{ L min}^{-1}$ , with a sheath-to-aerosol flow ratio of 10. The water pump was operated at a rate of  $4 \text{ mL h}^{-1}$ , corresponding to the CCNC setting of “low” liquid flow. By changing the temperature gradient, the supersaturation of the CCNC was set to different values between 0.06 and 0.60%. Particles with a critical supersaturation equal to or smaller than the prescribed supersaturation ( $S_{\text{presc}}$ ) were activated and formed water droplets. An optical particle counter (OPC) at the exit of the flow tube determined the concentration of droplets larger than  $1 \mu\text{m}$ , which were considered to be activated CCN.

Combining the CCNC described above with a differential mobility analyzer (DMA) and a condensation particle counter (CPC), size-resolved CCN efficiency spectra at a given  $S_{\text{presc}}$  were measured as follows (Frank et al., 2006): first, aerosol particles were brought to charge equilibrium with an X-ray source (TSI 3087). Then the DMA selected monodisperse particles of 10 different diameters in the size range of 23 to 321 nm, which were passed on to the CCNC and the CPC (TSI 3762) measuring in parallel. At each diameter ( $D$ ), the CPC measured the number concentration of all aerosol particles ( $N_{\text{CN}}$ ), and the CCNC measured the number concentration of CCN ( $N_{\text{CCN}}$ ) for the given supersaturation. The CCN efficiency spectrum is the size-resolved fraction of all activated particles as a function of  $S_{\text{presc}}$ . The recording of a CCN efficiency spectrum at a given  $S_{\text{presc}}$  took  $\sim 23$  min, including  $\sim 90$  s integration time for each measurement data point,  $\sim 30$  s adjustment time for each new particle size, and  $\sim 4$  min for adjustment to the next supersaturation level. The completion of a full measurement cycle comprising CCN efficiency spectra at five different supersaturation levels took  $\sim 2$  h (including additional 5 min of adjustment time between the highest and the lowest  $S_{\text{presc}}$  level).

The measurement data of the CCN efficiency spectra were corrected for differences in the CCNC and CPC counting efficiencies as described in Rose et al. (2010), using a constant correction factor of 1.03. Moreover, a correction for multiply charged particles was performed according to Frank et al. (2006).

The supersaturation in the CCNC was calibrated using ammonium sulfate particles before, during, and after the campaign. We used the calibration method described in Rose et al. (2008), applying the activity parameterization Köhler model AP3 to derive the corresponding critical supersaturation from the critical dry diameter of CCN activation of the ammonium sulfate particles.

To relate the activation of aerosol particles in the CCNC to the activation at ambient conditions, the supersaturation levels prescribed in the CCNC at a sample temperature of approximately 298 K ( $S_{\text{presc}}$ ) were scaled to an equivalent supersaturation at an average ambient air temperature during the cloud event of  $\sim 273$  K ( $S_{\text{CCNC}}$ ) as described in Appendix C.

## 2.5 Error analysis

During a cloud event the number concentration measured for large monodisperse interstitial aerosol particles is generally very low. Therefore the possible sources of errors are particularly important. One potential source of systematic errors is false counts of the instruments. However, during frequently performed zero filter tests, our instruments showed no false counts, so the systematic error initiated from false counts could be neglected. The random error of the particle concentration measured by the CCNC ( $\Delta N_{\text{CCN}}$ ) and by the CPC ( $\Delta N_{\text{CN}}$ ), as well as the random error of the activated

fraction ( $\Delta(N_{CCN}/N_{CN})$ ) were derived through Gaussian error propagation.

Hence, the error of the activated fraction is given by

$$\Delta\left(\frac{N_{CCN}}{N_{CN}}\right) = \sqrt{\left(\frac{\Delta N_{CCN}}{N_{CN}}\right)^2 + \left(\frac{N_{CCN} \cdot \Delta N_{CN}}{N_{CN}^2}\right)^2}, \quad (1)$$

in which  $N_{CCN}$  and  $N_{CN}$  are the concentrations per size bin measured during the integration interval by the CCNC and the CPC, respectively. The number concentration of particles is the number of measured particles ( $c$ ) divided by the sample volume:  $N = c / (Q \cdot t)$ , where  $Q$  is the volumetric flow rate and  $t$  is the integration time. From this, the errors of the particle concentrations ( $\Delta N_{CCN}$  and  $\Delta N_{CN}$ ) are given by

$$\Delta N = \sqrt{\left(\frac{\Delta c}{Q \cdot t}\right)^2 + \left(\frac{c \cdot \Delta Q}{Q^2 \cdot t}\right)^2 + \left(\frac{c \cdot \Delta t}{Q \cdot t^2}\right)^2}. \quad (2)$$

Note that for the volumetric flow rate in the CCNC we had to insert the value for the measured actual aerosol flow ( $\sim 0.045 \text{ L min}^{-1}$ ) through the flow tube. This is only 1/11 of the CCNC inlet flow since the inlet flow is split into a filtered sheath and an aerosol flow with a ratio of 10. For the measurement time  $t$  we used the integration time for  $N_{CCN}$  and  $N_{CN}$  at a given  $D$  and  $S_{CCNC}$  ( $\sim 90 \text{ s}$ ). The error of the flow rate ( $\Delta Q$ ) was the standard deviation of the mean aerosol flow rate (of the CCNC or CPC) during time  $t$ , and the error of the time ( $\Delta t$ ) we assumed to be 1 s.

The error of the measured particle number ( $c$ ) we assumed to be the standard counting error of  $c$  plus 1 because one particle is the smallest countable value of the CCNC and the CPC:

$$\Delta c = \sqrt{c + 1}. \quad (3)$$

The analysis showed that the error of the interstitial CCN to CN ratio ( $N_{CCN}/N_{CN}$ ) measured during a cloud event was rather large. The reason was the very small aerosol flow through the CCNC ( $\sim 0.045 \text{ L min}^{-1}$ ), which required relatively long integration times.

During out-of-cloud conditions we have not encountered problems with counting statistics since the particle concentrations per size bin were at least 1 order of magnitude higher than during in-cloud conditions. We conclude that, in future studies measuring the size-resolved CCN fraction of interstitial particles in a cloud, it is necessary to increase the actual measured number of particles either by measuring over a longer time interval or by increasing the aerosol flow through the CCNC.

## 2.6 Calculation of CCN size distribution and integral CCN efficiency

Parallel to the CCN measurements, a scanning mobility particle sizer (SMPS, TSI 3080, using a DMA 3081, a CPC

3025A, and a neutralizer 3087 – operating with standard TSI software) was operated to measure the aerosol particle number (CN) size distribution over the size range of 16 to 600 nm (26 logarithmically equidistant size bins). Integral CN concentrations,  $N_{CN,int}$ , were calculated by integrating the CN size distributions.

CCN size distributions were calculated by multiplying the best-fit cumulative Gaussian distribution function (cf. Rose et al., 2008) of CCN efficiency spectra with the respective total aerosol size distributions, which were interpolated on a grid of 250 size steps (Rose et al., 2010). Integral CCN concentrations,  $N_{CCN,int}$ , were calculated by integrating the CCN size distributions. Integral CCN efficiencies ( $N_{CCN,int}/N_{CN,int}$ ) were calculated as the ratio of integral CCN concentration at a certain  $S_{CCNC}$  to integral CN concentration.

A list of frequently used symbols is given in Table A1 at the end of the manuscript.

## 3 Results and discussion

### 3.1 Derivation of cloud supersaturation from CCN measurements (CCNC method)

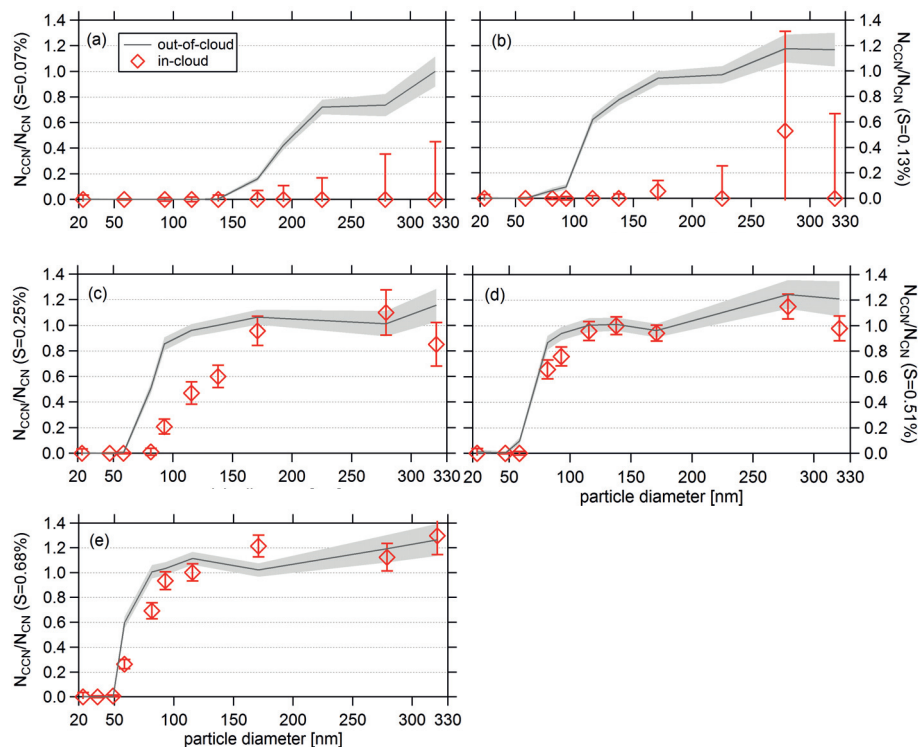
#### 3.1.1 Lower bound of peak supersaturation based on CCN efficiency spectra, $S_{low}$ (CCNC)

Figure 2 shows the size-resolved CCN efficiency spectra measured at five different supersaturation levels ( $S_{CCNC}$ ) for interstitial aerosol particles in cloud (red data points) and for total aerosol particles out of cloud (grey lines).

Out of cloud, the measured CCN efficiencies ( $N_{CCN}/N_{CN}$ ) exhibited the expected S-shaped increase from 0 for small particles to about 1 for large particles. The midpoint activation diameter ( $D_a$ , at  $N_{CCN}/N_{CN} = 0.5$ ) can be regarded as the average critical diameter of CCN activation at the given supersaturation. As expected,  $D_a$  exhibited a gradual decrease with increasing  $S_{CCNC}$ , i.e., the threshold diameter for the CCN activation of aerosol particles is lower for higher supersaturation.

In cloud, the CCN efficiency spectra of the interstitial aerosol observed at medium to high supersaturations were similar to those observed out of cloud ( $S_{CCNC} \geq 0.25 \%$ , Fig. 2c–e). At low supersaturations, however, they looked very different, and the CCN efficiency of the interstitial aerosol particles remained close to zero throughout the investigated diameter range ( $S_{CCNC} = 0.07$  and  $0.13 \%$ , Fig. 2a and b).

From this difference we derive a lower bound for the peak supersaturation at which particles have been activated to cloud droplets ( $S_{low}$ ). We take  $S_{low}(\text{CCNC})$  to be the mean value between the highest  $S_{CCNC}$  level at which no significant activation of interstitial particles is observed ( $(N_{CCN}/N_{CN} - \text{statistical error}) \leq 0$ ) and the lowest  $S_{CCNC}$  level at which significant activation of



**Figure 2.** Size-resolved CCN efficiency spectra measured for different  $S_{CCNC}$ . The red squares represent one example measurement during the cloud event (19 September 2012, 15:26–17:17 UTC) and the error bars correspond to the individual statistical errors calculated as described in Sect. 2.5. The grey shaded area represents the range of the measured data points  $\pm$  statistical error for one example CCN measurement performed during out-of-cloud conditions (20 September 2012, 02:54–04:47 UTC).

interstitial particles is observed ( $(N_{CCN}/N_{CN} - \text{statistical error}) > 0$ ). For the investigated cloud, we thus obtained  $S_{low}(CCNC) = 0.19 \pm 0.06\%$  (arithmetic mean  $\pm$  standard deviation). Particles exhibiting critical supersaturations smaller than or equal to  $S_{low}$  (CCNC) had formed cloud droplets and were therefore not sampled by the interstitial inlet. Hence, we did not measure activated particles in the CCNC as long as  $S_{CCNC} \leq S_{low}$  (CCNC). Interstitial particles could be activated in the CCNC only if  $S_{CCNC}$  exceeded  $S_{low}$  (CCNC).

Figure 3 displays integral CCN efficiencies ( $N_{CCN,int}/N_{CN,int}$ ) plotted against water vapor supersaturation. It shows that  $S_{low}(CCNC)$  can be derived not only from size-resolved measurement data but also from integral measurements of CCN and CN concentrations using a combination of CCNC and CPC without DMA. In fact, even a stand-alone CCNC instrument and plot of  $N_{CCN,int}$  vs.  $S_{CCNC}$  would suffice for the determination of  $S_{low}$ , provided that counting statistics are properly taken into account. The definition of  $S_{low}$  is the same as for the size-resolved CCN measurements:  $S_{low}$  (CCNC) is the mean value between the highest  $S_{CCNC}$  level at which no significant activation of interstitial particles is observed and the lowest  $S_{CCNC}$  level at which significant activation of interstitial particles is observed.

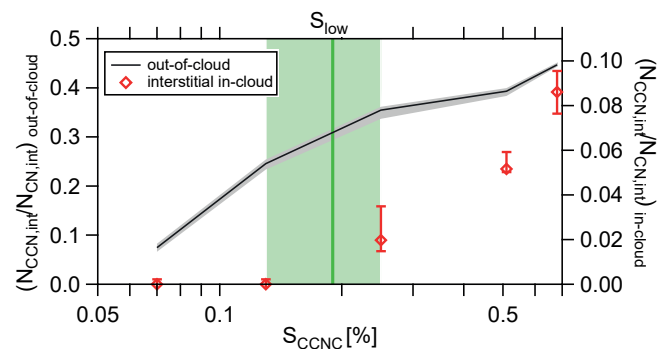


**Figure 3.** Integral CCN efficiency measured for total aerosol during out-of-cloud conditions (grey shaded area, range of measured data points  $\pm$  statistical error) and for interstitial aerosol in one example measurement during in-cloud conditions (red data points; error bars correspond to the individual statistical errors) plotted as a function of  $S_{CCNC}$ . The measurement times are the same as in Fig. 2. The vertical green line and shaded area represent the arithmetic mean and standard deviation range of  $S_{low}$  (CCNC). Since the activated fraction is much lower for in-cloud conditions,  $N_{CCN,int}$  is illustrated on the right axis with a smaller scale.

### 3.1.2 Average peak supersaturation based on CCN size distributions, $S_{\text{avg}}$ (CCNC)

The effective average peak supersaturation ( $S_{\text{avg}}$ ), at which the activation curve at the CCNC represents the activation that happened in the cloud event, can best be derived by comparison of the CCN size distributions measured for total aerosol at different supersaturation levels with the size distribution of aerosol particles actually activated in the cloud. The number size distribution of activated particles in a cloud is given by the difference between the size distributions of total and interstitial aerosol. In principle, the particle fraction activated at a given supersaturation in the cloud should also be activated at an equivalent supersaturation level in the CCNC instrument, taking into account the influence of different ambient conditions (in particular the influence of temperature on the Kelvin effect as described in Appendix C). Consequently, the number size distribution of activated particles in a cloud should be approximately equal to the CCN size distribution measured with the CCNC for total aerosol at a supersaturation level equivalent to the effective average peak supersaturation in the cloud.

In this study we had no opportunity to measure total aerosol properties under in-cloud conditions. For the investigated cloud event, however, the in-cloud and out-of-cloud measurement periods immediately followed each other without apparent changes in the regional atmospheric conditions. Thus, we assumed the total aerosol properties measured out of cloud to be approximately representative of the total aerosol properties in cloud.

Figure 4 shows aerosol particle size distributions measured by SMPS during the investigated cloud event on 19 September 2012. For the total aerosol out of cloud, we observed a bimodal distribution with a minimum at  $\sim 60$  nm. The Aitken and accumulation mode peaked at  $\sim 34$  nm with a maximum of  $\sim 2000 \text{ cm}^{-3}$  ( $\text{dN}/\text{dlog } D$ ) and at  $\sim 124$  nm with a maximum of  $\sim 1000 \text{ cm}^{-3}$  ( $\text{dN}/\text{dlog } D$ ), respectively. For the interstitial aerosol in cloud, the Aitken mode was only slightly shifted with a maximum of  $\sim 2200 \text{ cm}^{-3}$  ( $\text{dN}/\text{dlog } D$ ) at  $\sim 29$  nm, whereas the accumulation mode almost disappeared because most of the larger particles had been activated into cloud droplets and could therefore not be sampled by the interstitial inlet. Figure 5 shows the size distribution of aerosol particles activated in the cloud in comparison to CCN size distributions at  $S_{\text{CCNC}} = 0.25, 0.51$  and  $0.68\%$ . The size distribution of aerosol particles activated in the cloud was calculated by subtraction of the interstitial aerosol size distribution measured in cloud from the total aerosol size distribution measured out of cloud. The number size distribution of activated particles exhibited a large peak at  $\sim 124$  nm with a maximum of  $\sim 1000 \text{ cm}^{-3}$  ( $\text{dN}/\text{dlog } D$ ) and a shoulder at  $\sim 40$  nm with  $\sim 350 \text{ cm}^{-3}$  ( $\text{dN}/\text{dlog } D$ ), whereby the shoulder is mainly in the range of the error bars. On the one hand, the shoulder may result from a slight shift of the CN size distribution between in-cloud and out-of-cloud conditions,

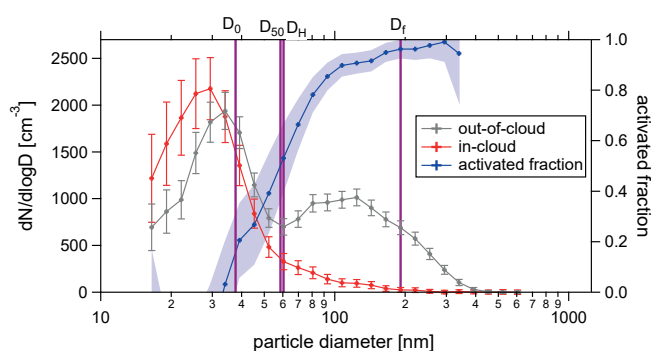


**Figure 4.** Average number size distribution of total aerosol particles (grey crosses, out of cloud) and of interstitial aerosol particles (red crosses, in cloud). The error bars correspond to the individual statistical errors calculated as described in Sect. 2.5. The activated fraction (blue crosses represent grey minus red, divided by grey; shaded area is the range of the statistical error of the data points) is plotted on the right axis. To assure comparability of the size distributions, their averaging times were chosen to be unambiguous with respect to LWC for in-cloud (mean LWC =  $0.089 \text{ g m}^{-3}$ ) and out-of-cloud conditions (mean LWC =  $0.016 \text{ g m}^{-3}$ ) within a short time interval (in cloud: 19 September 2012, 15:26–16:25 UTC; out of cloud: 19 September 2012, 17:30–18:00 UTC). The vertical lines indicate the diameters of zero activation ( $D_0$ ), 50 % activation ( $D_{50}$ ), Hopel minimum ( $D_H$ ), and full activation ( $D_f$ ).

which is likely due to aging processes such as condensational growth or coagulation, which are usually more pronounced for the Aitken mode than for the accumulation mode. On the other hand, it may result from a locally higher supersaturation during the cloud event ( $S_{\text{high}}$ ).

As shown in Fig. 5, the right-hand side of the size distribution of activated particles ( $D > 100$  nm) is in good agreement with each of the displayed CCN size distributions. In the diameter range of 34–120 nm, however, the CCN size distribution at  $S_{\text{CCNC}} = 0.25\%$  is much lower, with an average relative deviation of the error bars of about 9.0%. The CCN size distribution at  $S_{\text{CCNC}} = 0.51\%$  provides a fairly good match (average relative deviation 6.3%), and the deviation at  $S_{\text{CCNC}} = 0.68\%$  is only slightly higher (average relative deviation 6.8%). Thus, we take  $S_{\text{avg}}$  (CCNC)  $\approx 0.51 \pm 0.06\%$  as an estimate for the effective average peak supersaturation around which most particles had been activated and most cloud droplets had been formed.

## 3.2 Derivation of cloud supersaturation from SMPS measurements (SMPS method)

### 3.2.1 Average peak supersaturation based on 50 % activation, $S_{\text{avg}}$ ( $D_{50}, \kappa$ )

A common approach to derive an effective average peak supersaturation at which ambient clouds are formed is to compare the particle number or CN size distributions of total and interstitial aerosol (e.g., Anttila et al., 2009; Asmi et

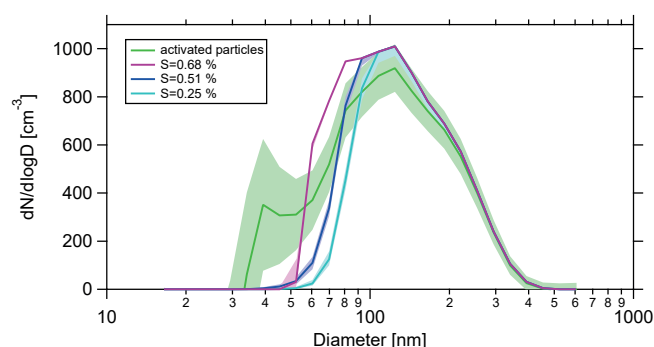


**Figure 5.** Average number size distribution of activated particles in the cloud (green) and CCN size distributions at  $S_{\text{CCNC}} = 0.25$ , 0.51, and 0.68 % (magenta, blue, and cyan). The shaded areas represent the range of the statistical error of the individual data points.

al., 2012; Ditas et al., 2012; Hammer et al., 2014). We also used this method, which will be referred to as the “SMPS method”, to calculate  $S_{\text{avg}}$  from our aerosol size distribution measurement results.

In our study it was not possible to measure the particle size distribution of both interstitial and total aerosol inside the investigated cloud. As outlined above, however, we have good reasons to assume that the total aerosol size distribution measured out of cloud was approximately representative of the total aerosol in cloud. A crucial point of the SMPS method is that it builds on Köhler theory calculations and requires an assumption on the hygroscopicity of the activated particles, which depends on their chemical composition. Appendix B describes how the hygroscopicity parameter,  $\kappa$ , relates the dry activation diameter of an aerosol particle to its critical supersaturation, which is the minimum supersaturation required to form a stable cloud droplet.

Figure 4 shows the CN size distribution of interstitial aerosol (red, in cloud) and total aerosol (grey, out of cloud). The activated fraction (blue) was calculated by dividing the number size distribution of activated particles (out of cloud minus in cloud) by the CN size distribution of the total aerosol. The diameter at which the activated fraction reached a value of 50 %,  $D_{50} = 59$  nm, can be regarded as an effective critical dry diameter of particle activation in the cloud. By Köhler theory this diameter can be converted into a critical supersaturation, which in turn can be regarded as an effective average peak supersaturation of the cloud (Hammer et al., 2014).

As mentioned above, the Köhler theory calculations require specific knowledge or assumptions about the hygroscopicity of the aerosol particles. Thus, we tested a range of relevant hygroscopicity parameters ( $\kappa$ ) as specified in Appendices A and B and Table 1: (1)  $\kappa_{\text{a}}$  as determined from the measured CCN efficiency spectra during out-of-cloud conditions ( $\kappa_{\text{a}} = 0.19$ ), (2)  $\kappa_{\text{cut}}$  as determined from the observed total CCN concentration and the CN size distribution

**Table 1.** Different combinations of hygroscopicity parameters ( $\kappa_{\text{a}}$ ,  $\kappa_{\text{cut}}$ ,  $\kappa_{\text{mean}}$ ,  $\kappa_{\text{AMS}}$ ) and activation threshold diameters ( $D_{\text{f}}$ ,  $D_{50}$ ,  $D_{\text{H}}$ ,  $D_0$ ) used to determine the cloud peak supersaturations reported in Table 2 by Köhler theory calculations as detailed in Appendices A and B.

	$D_{\text{f}} = 191$ nm	$D_{50} = 59$ nm	$D_{\text{H}} = 60$ nm	$D_0 = 38$ nm
$\kappa_{\text{a}}$	0.51	0.19	0.19	0.19
$\kappa_{\text{cut}}$	0.48	0.20	0.20	0.20
$\kappa_{\text{mean}}$	0.3	0.3	0.3	0.3
$\kappa_{\text{AMS}}$	0.45	0.45	0.45	0.45

during out-of-cloud conditions ( $\kappa_{\text{cut}} = 0.20$ ), (3) a global average  $\kappa$  value for continental aerosol of  $\kappa_{\text{mean}} = 0.3$  (Pringle et al., 2010), and (4)  $\kappa_{\text{AMS}}$  as derived from the aerosol chemical composition ( $\kappa_{\text{AMS}} = 0.45$ ). The large difference between  $\kappa_{\text{AMS}}$  and  $\kappa_{\text{a}}$  or  $\kappa_{\text{cut}}$  can be attributed to a size dependence of particle hygroscopicity with an enhanced organic mass fraction for sub-100 nm particles, as observed in earlier studies (e.g., Gunthe et al., 2009, 2011; Rose et al., 2011). The parameter  $\kappa_{\text{AMS}}$  reflects the mass-weighted average hygroscopicity of the total aerosol, which is dominated by large accumulation-mode particles with an enhanced inorganic fraction (typically around 300 nm). Depending on the prescribed  $\kappa$  value, the effective average peak supersaturation derived from the SMPS-based activation curve,  $S_{\text{avg}}(D_{50}, \kappa)$ , was calculated to be in the range of 0.44 to 0.68 % (arithmetic mean  $\pm$  standard deviation  $0.58 \pm 0.10$ , Table 2). This range is in agreement with the estimate derived above from the CCN measurement data without any assumption on particle hygroscopicity:  $S_{\text{avg}}(\text{CCNC}) \approx 0.51 \pm 0.06$  % (Sect. 3.1.2).

### 3.2.2 Average peak supersaturation based on the Hoppel minimum, $S_{\text{avg}}(D_{\text{H}}\kappa)$

An earlier approach by Hoppel et al. (1996) derived the average cloud peak supersaturation from the shape of the aerosol size distributions typically observed in remote marine boundary layer air. The authors proposed that the double-peaked structure of the aerosol size distribution is the result of particle processing through nonprecipitating cloud cycles. Thus, the diameter at which the minimum in a double-peaked particle number size distribution of total aerosol occurs (“Hoppel minimum”) can be regarded as an average critical diameter of particle activation related to the average cloud peak supersaturation.

As shown in Fig. 4, the total aerosol size distribution observed out of cloud exhibited a very pronounced double-peaked structure with a minimum at  $D_{\text{H}} = 60$  nm. As described above (Sect. 3.2.1) and in Appendix B, we performed Köhler theory calculations to also convert  $D_{\text{H}}$  into a critical supersaturation that can be regarded as an effective average cloud peak supersaturation, assuming appropriate hygroscopicity parameter values (Table 1).

**Table 2.** Lower bounds, average values, and upper bounds of cloud peak supersaturation ( $S_{\text{low}}$ ,  $S_{\text{avg}}$ ,  $S_{\text{high}}$ ) obtained by Köhler theory calculations assuming different types of hygroscopicity parameter ( $\kappa_a$ ,  $\kappa_{\text{cut}}$ ,  $\kappa_{\text{mean}}$ ,  $\kappa_{\text{AMS}}$ ) as reported in Table 1 (SMPS method, Sect. 3.2). The values displayed in the second-last line represent the arithmetic mean  $\pm$  standard deviation of the preceding four lines (SMPS method average). The supersaturation values displayed in the last line were obtained without assumptions about particle hygroscopicity (arithmetic mean  $\pm$  standard deviation; CCNC method, Sect. 3.1).

	$S_{\text{low}}(D = D_f, \kappa)$ [%]	$S_{\text{avg}}(D = D_{50}, \kappa)$ [%]	$S_{\text{avg}}(D = D_H, \kappa)$ [%]	$S_{\text{high}}(D = D_0, \kappa)$ [%]
$S(D, \kappa = \kappa_a)$	0.07	0.68	0.65	1.31
$S(D, \kappa = \kappa_{\text{cut}})$	0.07	0.66	0.63	1.28
$S(D, \kappa = \kappa_{\text{mean}})$	0.09	0.54	0.52	1.05
$S(D, \kappa = \kappa_{\text{AMS}})$	0.08	0.44	0.42	0.86
$S$ (SMPS)	$0.08 \pm 0.008$	$0.58 \pm 0.10$	$0.56 \pm 0.09$	$1.13 \pm 0.18$
$S$ (CCNC)	$0.19 \pm 0.06$	$0.51 \pm 0.06$	$0.51 \pm 0.06$	–

Depending on the prescribed  $\kappa$  value, the effective average peak supersaturation derived from the Hoppel minimum diameter,  $S_{\text{avg}}(D_H, \kappa)$ , was calculated to be in the range of 0.42 to 0.65 % (arithmetic mean  $\pm$  standard deviation:  $0.56 \pm 0.09$  %; Table 2). This range is again in agreement with the estimate derived from the CCN measurement data ( $S_{\text{avg}}(\text{CCNC}) \approx 0.51 \pm 0.06$  %, Sect. 3.1.2).

### 3.2.3 Lower bound of peak supersaturation based on full activation, $S_{\text{low}}(D_f, \kappa)$

To derive a lower bound of cloud peak supersaturation,  $S_{\text{low}}$ , from the activated particle fraction based on aerosol size distribution data, we determine an effective threshold diameter of full activation ( $D_f$ ). For  $D_f$  we take the mean value between the largest diameter at which the activated fraction is significantly below unity ((activated fraction + statistical error)  $< 1$ ) and the smallest diameter at which practically full activation is observed ((activated fraction + statistical error)  $\geq 1$ ). From Fig. 4 (blue data points) we obtained  $D_f = 191$  nm. As described above and in Appendix B, we performed Köhler theory calculations to also convert  $D_f$  into a critical supersaturation, which can be regarded as a lower bound of cloud peak supersaturation, assuming relevant hygroscopicity parameter values (Table 1). Depending on the prescribed  $\kappa$  values,  $S_{\text{low}}(D_f, \kappa)$  was calculated to be between 0.07 and 0.09 % (arithmetic mean  $\pm$  standard deviation:  $0.08 \pm 0.008$  %; Table 2). This range disagrees with the estimate derived from the CCN approach ( $S_{\text{low}}(\text{CCNC}) = 0.19 \pm 0.06$  %). A reason could be that the definition of  $S_{\text{low}}$  from the SMPS method strongly depends on uncertainties of the SMPS measurement. On the other hand, the SMPS approach tells more about the cloud history and not about the actual supersaturation at the inlet, which is accessible by the CCNC method. Therefore, the discrepancy can be traced back to the fact that SMPS and CCNC methods measure the supersaturation reached in the air parcel at different times in its history.

### 3.2.4 Upper bound of peak supersaturation based on zero activated fraction, $S_{\text{high}}(D_0, \kappa)$

To derive an upper bound of cloud peak supersaturation,  $S_{\text{high}}$ , from the activated particle fraction based on aerosol size distribution data, we determine an effective threshold diameter of zero activation ( $D_0$ ). For  $D_0$  we take the mean value between the largest diameter at which no significant activation is observed ((activated fraction – statistical error)  $\leq 0$ ) and the smallest diameter at which the activated fraction is significantly above zero ((activated fraction – statistical error)  $> 0$ ). From Fig. 4 (blue data points) we obtained  $D_0 = 38$  nm. As described above and in Appendix B, we performed Köhler theory calculations to also convert  $D_0$  into a critical supersaturation that can be regarded as an upper bound of cloud peak supersaturation, assuming relevant hygroscopicity parameter values (Table 1). Depending on the prescribed  $\kappa$  values,  $S_{\text{high}}(D_0, \kappa)$  was calculated to be between 0.86 and 1.31 % (arithmetic mean  $\pm$  standard deviation:  $1.13 \pm 0.18$  %; Table 2).

## 4 Conclusions and outlook

In this study we showed how size-resolved measurements of aerosol particles and CCN in cloud and out of cloud can be used to derive effective average values as well as lower and upper bounds of cloud peak supersaturation. For the investigated cloud event, the different estimates of the average peak supersaturation ( $S_{\text{avg}}$ ) obtained from CCNC and SMPS measurement data of total and interstitial aerosol particles are largely consistent with each other (Table 2). The main goal of this study, however, is to present an alternative method to estimate the cloud supersaturation. Thus, the numbers that we obtained for  $S_{\text{cloud}}$  are not necessarily generally representative values.

The lower bound of cloud peak supersaturation ( $S_{\text{low}}$ ) calculated by the CCNC method is significantly higher than the  $S_{\text{low}}$  calculated by the SMPS method. The following two

effects may explain this discrepancy: (i) SMPS data analysis requires integration over a certain time period to reduce uncertainties. This has an influence on the error, which is particularly important for the  $S_{\text{low}}$  estimation. (ii) All supersaturation estimates based on the SMPS method reflect the full history of supersaturation experienced by the aerosol particles during cloud evolution. Thus, particles that have been activated once into cloud droplets will be counted, independent of the time when the activation actually occurred. In contrast, the CCNC method, in which particle activation takes place during the measurements, provides in situ measurements of the actual supersaturation in the probed cloud air parcel.

The uncertainties of the estimates of cloud peak supersaturation presented here are mostly due to limitations in the time resolution and counting statistics of the measurement devices used (CCNC, CPC, SMPS). Estimates derived from SMPS data only are also influenced by uncertainties in the determination or assumption of aerosol hygroscopicity parameters.

In future studies, some uncertainties can and should be reduced by optimizing the applied instrumentation and measurement procedures. Specific avenues for improvement are as follows:

1. Parallel operation of total and interstitial aerosol inlets and SMPS measurements will make the determination of the fraction of aerosol particles activated in cloud more reliable.
2. Parallel operation of multiple CCNCs at different supersaturation levels and/or faster scanning of supersaturation in the CCNC by varying the flow rate rather than the temperature gradient (Moore and Nenes, 2009) will increase the number of supersaturation levels that can be monitored and hence will increase the precision of the derived cloud peak supersaturations.
3. Increasing the aerosol-to-sheath flow ratio and/or the integration times of the CCNC and SMPS will help to improve the counting statistics.

We suggest that comprehensive measurements of the temporal and spatial variability of cloud peak supersaturation (average values as well as upper and lower bounds) may provide deeper insights into the evolution of clouds, including the interaction of aerosol and cloud particles, water vapor, and dynamical features like turbulence and entrainment.

### Appendix A: calculation of $\kappa$ from AMS measurements

During the ACRIDICON-Zugspitze campaign the chemical composition of submicron aerosol particles was measured with a C-ToF-AMS (compact time-of-flight aerosol mass spectrometer; Drewnick et al., 2005; Canagaratna et al., 2007). The C-ToF-AMS quantitatively determines the mass concentration of nonrefractory species like organics, sulfate, nitrate, ammonium, and chloride. For the analysis of the cloud event investigated in this study, the AMS mass concentrations were averaged over the time period of out-of-cloud conditions (19 September 2013, 19:56–20:43 UTC). The organic ( $f_{\text{org}}$ ) and inorganic mass fractions ( $f_{\text{inorg}}$ ) were calculated by dividing the organic and inorganic (sum of sulfate, nitrate, ammonium, and chloride) mass concentrations by the sum of the masses of all AMS measured components, respectively.

To describe the influence of chemical composition on the CCN activity of aerosol particles, Petters and Kreidenweis (2007) proposed to use the hygroscopicity parameter  $\kappa$ . The hygroscopicity parameter ( $\kappa_{\text{AMS}}$ ) was approximated from the AMS obtained mass fraction by a simple mixing rule as follows:

$$\kappa_{\text{AMS}} = f_{\text{org}} \cdot \kappa_{\text{org}} + f_{\text{inorg}} \cdot \kappa_{\text{inorg}}, \quad (\text{A1})$$

in which  $\kappa_{\text{org}}$  and  $\kappa_{\text{inorg}}$  are the hygroscopicity parameters for pure organic and inorganic substances ( $\kappa_{\text{org}} = 0.1$  and  $\kappa_{\text{inorg}} = 0.6$ ) (Gunthe et al., 2009; Dusek et al., 2010; Rose et al., 2011). For the average AMS-derived hygroscopicity parameter we obtained  $\kappa_{\text{AMS}} = 0.45$ . This value reflects the mass-weighted average hygroscopicity of the total aerosol, which is dominated by large accumulation-mode particles with an enhanced inorganic fraction (typically around 300 nm).

**Table A1.** Notation (frequently used symbols).

Symbol	Quantity, unit
$N_{\text{CCN}}$	monodisperse number concentration of cloud condensation nuclei (CCN), $\text{cm}^{-3}$
$N_{\text{CN}}$	monodisperse number concentration of condensation nuclei (CN), $\text{cm}^{-3}$
$N_{\text{CCN}}/N_{\text{CN}}$	CCN efficiency (size resolved)
$N_{\text{CCN,int}}$	integral CCN concentration, $\text{cm}^{-3}$
$N_{\text{CN,int}}$	integral CN concentration, $\text{cm}^{-3}$
$N_{\text{CCN,int}}/N_{\text{CN,int}}$	integral CCN efficiency
$S_{\text{prese}}$	water vapor supersaturation prescribed in the CCNC operated at room temperature ( $\sim 298$ K), %
$S_{\text{CCNC}}$	water vapor supersaturation in the CCNC scaled to cloud temperature ( $\sim 273$ K), %
$S_{\text{low}}$	lower bound of cloud peak supersaturation, %
$S_{\text{avg}}$	average value of cloud peak supersaturation, %
$S_{\text{high}}$	upper bound of cloud peak supersaturation, %
$D_0$	diameter of zero activation observed in the cloud, nm
$D_{50}$	diameter of 50 % activation observed in the cloud, nm
$D_{\text{H}}$	diameter of the Hoppel minimum, nm
$D_{\text{f}}$	diameter of full activation observed in the cloud, nm
$D_{\text{a}}$	midpoint activation diameter of CCN efficiency spectra (at $N_{\text{CCN}}/N_{\text{CN}} = 0.5$ ), nm
$D_{\text{cut}}$	cut-off diameter of CCN activation, nm
$\kappa$	effective hygroscopicity parameter
$\kappa_{\text{a}}$	hygroscopicity parameter derived from $D_{\text{a}}$ via Köhler theory
$\kappa_{\text{cut}}$	hygroscopicity parameter derived from $D_{\text{cut}}$ via Köhler theory
$\kappa_{\text{mean}}$	mean hygroscopicity parameter for continental aerosol ( $\kappa_{\text{mean}} = 0.3$ )
$\kappa_{\text{AMS}}$	hygroscopicity parameter derived from AMS data ( $\kappa_{\text{AMS}} = 0.45$ )

## Appendix B: calculation of $\kappa$ from CCN measurements and Köhler theory

The Köhler theory relates the dry diameter of an aerosol particle to its critical water vapor supersaturation, i.e., to the minimum supersaturation that is required to form a stable cloud droplet (Köhler, 1936). The following  $\kappa$ -Köhler equation (equivalent to Eq. (6) of Petters and Kreidenweis, 2007) enables calculation of the critical supersaturation ( $S_{\text{crit}}$ ) for a given pair of dry particle diameters,  $D$ , and hygroscopicity parameters,  $\kappa$ , or the  $\kappa$  parameter for a given pair of critical supersaturations and activation diameters:

$$S = \left( \frac{D_{\text{wet}}^3 - D^3}{D_{\text{wet}}^3 - D^3 (1 - \kappa)} \exp \left( \frac{4\sigma M_w}{RT \rho_w D_{\text{wet}}} \right) - 1 \right) \cdot 100 \%, \quad (\text{B1})$$

where  $D_{\text{wet}}$  is the diameter of the droplet,  $\sigma$  is the surface tension of the droplet (approximated by that of water,  $\sigma = 0.072 \text{ J m}^{-2}$ ),  $M_w$  is the molar mass of water ( $M_w = 0.018015 \text{ kg mol}^{-1}$ ),  $R$  is the universal gas constant ( $R = 8.315 \text{ J K}^{-1} \text{ mol}^{-1}$ ), and  $\rho_w$  is the density of water ( $\rho_w = 997.1 \text{ kg m}^{-3}$ ).

In this study, two approaches were tested to derive  $\kappa$  from the CCN measurement results. Firstly, the hygroscopicity parameter  $\kappa$  was determined from Eq. (B1) by inserting the activation diameter  $D_a$  (Sect. 3.1.1) derived from the CCN efficiency spectra measured out of cloud (Fig. 1) for  $D$  and varying both  $\kappa$  and the droplet diameter  $D_{\text{wet}}$  until  $S$  was at the same time equal to the prescribed supersaturation  $S_{\text{presc}}$  and to the maximum of Eq. (B1) (cf. Rose et al., 2010). The temperature,  $T$ , used in Eq. (B1) was set to the value at which the particles were activated in the CCN ( $\sim 298 \text{ K}$ ).

A range of  $\kappa_a$  values between 0.14 and 0.59 were obtained for the different combinations of  $S_{\text{presc}}$  and  $D_a$  (highest values for low  $S_{\text{presc}}$ , i.e., large  $D_a$ ). The parameter  $\kappa_a$  characterizes the average hygroscopicity of CCN-active particles in the size range around  $D_a$ . Thus, for the calculations performed in this study we assumed  $\kappa_a = 0.51$  for  $D \sim 190 \text{ nm}$  and  $\kappa_a = 0.19$  for  $D \leq 60 \text{ nm}$  (Table 1).

Alternatively, the activation diameter and corresponding hygroscopicity parameter were derived from the integral CCN concentration and the CN size distribution out of cloud (cf. Sect. 2.6). The apparent cut-off diameter of CCN activation ( $D_{\text{cut}}$ ) is the diameter above which the integral CN number concentration equals the observed integral CCN concentration ( $N_{\text{CCN,int}}$ ). This is equivalent to the activation diameter obtained typically from integral CCN measurements (without size resolution), which was also used, for example, by Hammer et al. (2014).

The hygroscopicity parameter  $\kappa_{\text{cut}}$  was determined from Eq. (B1) by inserting the activation diameter  $D_{\text{cut}}$  for  $D$  and varying both  $\kappa$  and the droplet diameter  $D_{\text{wet}}$  until  $S$  was at the same time equal to the prescribed supersaturation  $S_{\text{presc}}$  and to the maximum of Eq. (B1). The temperature  $T$  used in Eq. (B1) was set to 298 K. For the measurement period of our study, a range of  $\kappa_{\text{cut}}$  values between 0.19 and 0.54 were

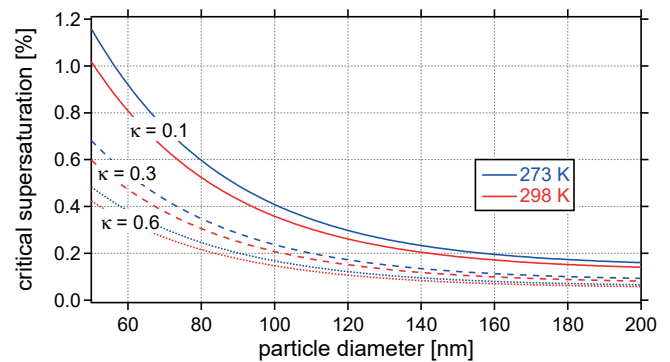


**Figure C1.** Critical supersaturation as a function of dry particle diameter calculated from Köhler theory (Appendix B) using different hygroscopicity parameters and temperatures as input parameters.

obtained for the different combinations of  $S_{\text{presc}}$  and  $D_{\text{cut}}$  (highest values for low  $S_{\text{presc}}$ , i.e., large  $D_{\text{cut}}$ ). The parameter  $\kappa_{\text{cut}}$  characterizes the average hygroscopicity of CCN-active particles in the size range around  $D_{\text{cut}}$ . Differences between  $\kappa_a$  and  $\kappa_{\text{cut}}$  mainly result from the shape of the particle number size distribution and from the heterogeneity of the particle composition, and have been discussed in detail by Rose et al. (2010). For the calculations performed in this study, we assumed  $\kappa_{\text{cut}} = 0.48$  for  $D \sim 190 \text{ nm}$  and  $\kappa_{\text{cut}} = 0.20$  for  $D \leq 60 \text{ nm}$  (Table 1).

In Sect. 3.2 of this paper, the critical supersaturation ( $S_{\text{crit}}$ ) as calculated from different pairs of observed dry activation diameters and prescribed  $\kappa$  values was related to the cloud supersaturation. It was determined from Eq. (B1) by inserting the above-mentioned  $\kappa$  values ( $\kappa_a$ ,  $\kappa_{\text{cut}}$ ,  $\kappa_{\text{AMS}}$ , and  $\kappa_{\text{mean}} = 0.3$ ) and varying both  $S$  and the droplet diameter  $D_{\text{wet}}$  until  $D$  was at the same time equal to the observed activation diameter and to the maximum of Eq. (B1). The temperature  $T$  used in Eq. (B1) had to be set to the value at which the cloud was formed in the ambient air. It was assumed to be  $\sim 273 \text{ K}$ , which was the average ambient air temperature during the cloud event.

## Appendix C: temperature scaling of supersaturation

Due to the temperature dependence of the Kelvin effect, the critical supersaturation ( $S_{\text{crit}}$ ) for the CCN activation of an aerosol particle depends not only on its size and composition but also on the temperature at which the activation occurs. Thus, the supersaturation level at which a particle is activated at ambient temperature in a cloud is not necessarily the same as the supersaturation level at which the particle is activated at the instrument temperature in a CCNC.

To compensate for this effect, the supersaturation levels prescribed in the CCNC at a sample temperature of approximately 298 K ( $S_{\text{presc}}$ ) were scaled to an equivalent

supersaturation at an average ambient air temperature during the cloud event of  $\sim 273$  K ( $S_{\text{CCNC}}$ ).

For this purpose we performed Köhler theory calculations of  $S_{\text{crit}}$  as a function of dry particle diameter for different hygroscopicity parameter values and temperatures (Fig. C1). For a given particle diameter, the relative difference of  $S_{\text{crit}}$  at 273 vs. 298 K was +14 %, independent of the other variables ( $S = 0.06$ – $0.7$  %;  $D = 50$ – $200$  nm,  $\kappa = 0.1$ – $0.6$ ). Thus, we multiplied the supersaturation levels prescribed in the CCNC at  $\sim 298$  K ( $S_{\text{presc}} = 0.06, 0.11, 0.22, 0.45,$  and  $0.60$  %) by a factor of 1.14 to obtain the equivalent supersaturation levels for CCN activation in a cloud at  $\sim 273$  K ( $S_{\text{CCNC}} = 0.07, 0.13, 0.25, 0.51,$  and  $0.68$  %), which were used for the derivation of the cloud peak supersaturation as specified in Sect. 3.1.

**Acknowledgements.** This work has been supported by the Max Planck Society (MPG), the Max Planck Graduate Center with the Johannes Gutenberg University Mainz (MPGC), and the German Research Foundation (DFG-SPP 1294-HALO, grant PO 1013/2, grant SCHN 1138/1, grant ME 3534/1-2). We thank D. Rosenow, M. Wendisch, and the ACRIDICON-Zugspitze team for collaboration and support. The team of the Environmental Research Station Schneefernerhaus (UFS) is acknowledged for logistical support and access to the Schneefernerhaus field site. The authors wish to thank K. Selzle, C. Pöhlker, S. S. Gunthe, E. Mikhailov, L. M. Russell, M. Gysel, E. Hammer, F. Ditas, A. Wiedensohler, and M. Schäfer for support and stimulating discussions.

The service charges for this open access publication have been covered by the Max Planck Society.

Edited by: P. Herckes

## References

- Andreae, M. O. and Rosenfeld, D.: Aerosol-cloud-precipitation interactions. Part 1. The nature and sources of cloud-active aerosols, *Earth-Sci. Rev.*, 89, 13–41, doi:10.1016/j.earscirev.2008.03.001, 2008.
- Anttila, T., Vaattovaara, P., Komppula, M., Hyvärinen, A.-P., Lihavainen, H., Kerminen, V.-M., and Laaksonen, A.: Size-dependent activation of aerosols into cloud droplets at a subarctic background site during the second Pallas Cloud Experiment (2nd PaCE): method development and data evaluation, *Atmos. Chem. Phys.*, 9, 4841–4854, doi:10.5194/acp-9-4841-2009, 2009.
- Anttila, T., Brus, D., Jaatinen, A., Hyvärinen, A.-P., Kivekäs, N., Romakkaniemi, S., Komppula, M., and Lihavainen, H.: Relationships between particles, cloud condensation nuclei and cloud droplet activation during the third Pallas Cloud Experiment, *Atmos. Chem. Phys.*, 12, 11435–11450, doi:10.5194/acp-12-11435-2012, 2012.
- Asmi, E., Freney, E., Hervo, M., Picard, D., Rose, C., Colomb, A., and Sellegri, K.: Aerosol cloud activation in summer and winter at puy-de-Dôme high altitude site in France, *Atmos. Chem. Phys.*, 12, 11589–11607, doi:10.5194/acp-12-11589-2012, 2012.
- Canagaratna, M. R., Jayne, J. T., Jimenez, J. L., Allan, J. D., Alfarra, M. R., Zhang, Q., Onasch, T. B., Drewnick, F., Coe, H., Middlebrook, A., Delia, A., Williams, L. R., Trimborn, A. M., Northway, M. J., DeCarlo, P. F., Kolb, C. E., Davidovits, P., and Worsnop, D. R.: Chemical and microphysical characterization of ambient aerosols with the aerodyne aerosol mass spectrometer, *Mass Spectr. Rev.*, 26, 185–222, 2007.
- Christensen, S. I. and Petters, M. D.: The Role of Temperature in Cloud Droplet Activation, *J. Phys. Chem. A*, 116, 9706–9717, doi:10.1021/jp3064454, 2012.
- Ditas, F., Shaw, R. A., Siebert, H., Simmel, M., Wehner, B., and Wiedensohler, A.: Aerosols-cloud microphysics-thermodynamics-turbulence: evaluating supersaturation in a marine stratocumulus cloud, *Atmos. Chem. Phys.*, 12, 2459–2468, doi:10.5194/acp-12-2459-2012, 2012.
- Drewnick, F., Hings, S. S., DeCarlo, P., Jayne, J. T., Gonin, M., Fuhrer, K., Weimer, S., Jimenez, J. L., Demerjian, K. L., Borrmann, S., and Worsnop, D. R.: A new time-of-flight aerosol mass spectrometer (TOF-AMS) – Instrument description and first field deployment, *Aerosol Sci. Technol.*, 39, 637–658, doi:10.1080/02786820500182040, 2005.
- Dusek, U., Frank, G. P., Hildebrandt, L., Curtius, J., Schneider, J., Walter, S., Chand, D., Drewnick, F., Hings, S., Jung, D., Borrmann, S., and Andreae, M. O.: Size matters more than chemistry for cloud-nucleating ability of aerosol particles, *Science*, 312, 1375–1378, doi:10.1126/science.1125261, 2006.
- Dusek, U., Frank, G. P., Curtius, J., Drewnick, F., Schneider, J., Kurten, A., Rose, D., Andreae, M. O., Borrmann, S., and Pöschl, U.: Enhanced organic mass fraction and decreased hygroscopicity of cloud condensation nuclei (CCN) during new particle formation events, *Geophys. Res. Lett.*, 37, L03804, doi:10.1029/2009gl040930, 2010.
- Engelhart, G. J., Hennigan, C. J., Miracolo, M. A., Robinson, A. L., and Pandis, S. N.: Cloud condensation nuclei activity of fresh primary and aged biomass burning aerosol, *Atmos. Chem. Phys.*, 12, 7285–7293, doi:10.5194/acp-12-7285-2012, 2012.
- Frank, G. P., Dusek, U., and Andreae, M. O.: Technical note: A method for measuring size-resolved CCN in the atmosphere, *Atmos. Chem. Phys. Discuss.*, 6, 4879–4895, doi:10.5194/acpd-6-4879-2006, 2006.
- Gerber, H.: Direct measurement of suspended particulate volume concentration and far-infrared extinction coefficient with a laser-diffraction instrument, *Appl. Opt.*, 30, 4824–4831, 1991.
- Gunthe, S. S., King, S. M., Rose, D., Chen, Q., Roldin, P., Farmer, D. K., Jimenez, J. L., Artaxo, P., Andreae, M. O., Martin, S. T., and Pöschl, U.: Cloud condensation nuclei in pristine tropical rainforest air of Amazonia: size-resolved measurements and modeling of atmospheric aerosol composition and CCN activity, *Atmos. Chem. Phys.*, 9, 7551–7575, doi:10.5194/acp-9-7551-2009, 2009.
- Gunthe, S. S., Rose, D., Su, H., Garland, R. M., Achtert, P., Nowak, A., Wiedensohler, A., Kuwata, M., Takegawa, N., Kondo, Y., Hu, M., Shao, M., Zhu, T., Andreae, M. O., and Pöschl, U.: Cloud condensation nuclei (CCN) from fresh and aged air pollution in the megacity region of Beijing, *Atmos. Chem. Phys.*, 11, 11023–11039, doi:10.5194/acp-11-11023-2011, 2011.
- Hammer, E., Bukowiecki, N., Gysel, M., Jurányi, Z., Hoyle, C. R., Vogt, R., Baltensperger, U., and Weingartner, E.: Investigation of the effective peak supersaturation for liquid-phase clouds at the high-alpine site Jungfraujoch, Switzerland (3580 m a.s.l.), *Atmos. Chem. Phys.*, 14, 1123–1139, doi:10.5194/acp-14-1123-2014, 2014.
- Henning, S., Weingartner, E., Schmidt, S., Wendisch, M., Gaggeler, H. W. and Baltensperger, U.: Size-dependent aerosol activation at the high-alpine site Jungfraujoch (3580 masl), *Tellus Ser. B-Chem. Phys. Meteorol.*, 54, 82–95, doi:10.1034/j.1600-0889.2002.00299.x, 2002.
- Hoppel, W. A., Frick, G. M. and Fitzgerald, J. W.: Deducing droplet concentration and supersaturation in marine boundary layer clouds from surface aerosol measurements, *J. Geophys. Res.-Atmos.*, 101, 26553–26565, doi:10.1029/96jd02243, 1996.
- Jurányi, Z., Gysel, M., Weingartner, E., DeCarlo, P. F., Kammermann, L., and Baltensperger, U.: Measured and modelled cloud condensation nuclei number concentration at the high alpine site Jungfraujoch, *Atmos. Chem. Phys.*, 10, 7891–7906, doi:10.5194/acp-10-7891-2010, 2010.
- Jurányi, Z., Tritscher, T., Gysel, M., Laborde, M., Gomes, L., Roberts, G., Baltensperger, U., and Weingartner, E.: Hy-

- grosopic mixing state of urban aerosol derived from size-resolved cloud condensation nuclei measurements during the MEGAPOLI campaign in Paris, *Atmos. Chem. Phys.*, 13, 6431–6446, doi:10.5194/acp-13-6431-2013, 2013.
- Kim, J. H., Yum, S. S., Shim, S., Yoon, S.-C., Hudson, J. G., Park, J., and Lee, S.-J.: On aerosol hygroscopicity, cloud condensation nuclei (CCN) spectra and critical supersaturation measured at two remote islands of Korea between 2006 and 2009, *Atmos. Chem. Phys.*, 11, 12627–12645, doi:10.5194/acp-11-12627-2011, 2011.
- Kinne, S.: Climatologies of Cloud-related Aerosol, Part 1: Particle Number and Size, in: *Clouds in the Perturbed Climate System: Their Relationship to Energy Balance, Atmospheric Dynamics, and Precipitation*, edited by: Heintzenberg, J. and Charlson, R. J., MIT Press, Cambridge, MA, USA, 37–57, 2009.
- Köhler, H.: The nucleus in and the growth of hygroscopic droplets, *Trans. Faraday Soc.*, 32, 1152–1161, doi:10.1039/tf9363201152, 1936.
- Kulmala, M., Asmi, A., Lappalainen, H. K., Baltensperger, U., Brenguier, J.-L., Facchini, M. C., Hansson, H.-C., Hov, Ø., O'Dowd, C. D., Pöschl, U., Wiedensohler, A., Boers, R., Boucher, O., de Leeuw, G., Denier van der Gon, H. A. C., Feichter, J., Krejci, R., Laj, P., Lihavainen, H., Lohmann, U., McFiggans, G., Mentel, T., Pilinis, C., Riipinen, I., Schulz, M., Stohl, A., Swietlicki, E., Vignati, E., Alves, C., Amann, M., Ammann, M., Arabas, S., Artaxo, P., Baars, H., Beddows, D. C. S., Bergström, R., Beukes, J. P., Bilde, M., Burkhardt, J. F., Canonaco, F., Clegg, S. L., Coe, H., Crumeyrolle, S., D'Anna, B., Decesari, S., Gilardoni, S., Fischer, M., Fjaeraa, A. M., Fountoukis, C., George, C., Gomes, L., Halloran, P., Hamburger, T., Harrison, R. M., Herrmann, H., Hoffmann, T., Hoose, C., Hu, M., Hyvärinen, A., Hörrak, U., Iinuma, Y., Iversen, T., Josipovic, M., Kanakidou, M., Kiendler-Scharr, A., Kirkevåg, A., Kiss, G., Klimont, Z., Kolmonen, P., Komppula, M., Kristjánsson, J.-E., Laakso, L., Laaksonen, A., Labonnote, L., Lanz, V. A., Lehtinen, K. E. J., Rizzo, L. V., Makkonen, R., Manninen, H. E., McMeeking, G., Merikanto, J., Minikin, A., Mirme, S., Morgan, W. T., Nemitz, E., O'Donnell, D., Panwar, T. S., Pawlowska, H., Petzold, A., Pienaar, J. J., Pio, C., Plass-Duelmer, C., Prévôt, A. S. H., Pryor, S., Reddington, C. L., Roberts, G., Rosenfeld, D., Schwarz, J., Seland, Ø., Sellegri, K., Shen, X. J., Shiraiwa, M., Siebert, H., Sierau, B., Simpson, D., Sun, J. Y., Topping, D., Tunved, P., Vaattovaara, P., Vakkari, V., Veefkind, J. P., Visschedijk, A., Vuollekoski, H., Vuolo, R., Wehner, B., Wildt, J., Woodward, S., Worsnop, D. R., van Zadelhoff, G.-J., Zardini, A. A., Zhang, K., van Zyl, P. G., Kerminen, V.-M., S Carslaw, K., and Pandis, S. N.: General overview: European Integrated project on Aerosol Cloud Climate and Air Quality interactions (EUCAARI) – integrating aerosol research from nano to global scales, *Atmos. Chem. Phys.*, 11, 13061–13143, doi:10.5194/acp-11-13061-2011, 2011.
- Lance, S., Raatikainen, T., Onasch, T. B., Worsnop, D. R., Yu, X.-Y., Alexander, M. L., Stolzenburg, M. R., McMurry, P. H., Smith, J. N., and Nenes, A.: Aerosol mixing state, hygroscopic growth and cloud activation efficiency during MIRAGE 2006, *Atmos. Chem. Phys.*, 13, 5049–5062, doi:10.5194/acp-13-5049-2013, 2013.
- Lohmann, U. and Feichter, J.: Global indirect aerosol effects: a review, *Atmos. Chem. Phys.*, 5, 715–737, doi:10.5194/acp-5-715-2005, 2005.
- McFiggans, G., Artaxo, P., Baltensperger, U., Coe, H., Facchini, M. C., Feingold, G., Fuzzi, S., Gysel, M., Laaksonen, A., Lohmann, U., Mentel, T. F., Murphy, D. M., O'Dowd, C. D., Snider, J. R., and Weingartner, E.: The effect of physical and chemical aerosol properties on warm cloud droplet activation, *Atmos. Chem. Phys.*, 6, 2593–2649, doi:10.5194/acp-6-2593-2006, 2006.
- Mertes, S., Lehmann, K., Nowak, A., Massling, A., and Wiedensohler, A.: Link between aerosol hygroscopic growth and droplet activation observed for hill-capped clouds at connected flow conditions during FEBUKO, *Atmos. Environ.*, 39, 4247–4256, doi:10.1016/j.atmosenv.2005.02.010, 2005.
- Mikhailov, E., Vlasenko, S., Rose, D., and Pöschl, U.: Mass-based hygroscopicity parameter interaction model and measurement of atmospheric aerosol water uptake, *Atmos. Chem. Phys.*, 13, 717–740, doi:10.5194/acp-13-717-2013, 2013.
- Moore, R. H. and Nenes, A.: Scanning Flow CCN Analysis-A Method for Fast Measurements of CCN Spectra, *Aerosol Sci. Technol.*, 43, 1192–1207, doi:10.1080/02786820903289780, 2009.
- Padró, L. T., Moore, R. H., Zhang, X., Rastogi, N., Weber, R. J., and Nenes, A.: Mixing state and compositional effects on CCN activity and droplet growth kinetics of size-resolved CCN in an urban environment, *Atmos. Chem. Phys.*, 12, 10239–10255, doi:10.5194/acp-12-10239-2012, 2012.
- Petters, M. D. and Kreidenweis, S. M.: A single parameter representation of hygroscopic growth and cloud condensation nucleus activity, *Atmos. Chem. Phys.*, 7, 1961–1971, 2007, <http://www.atmos-chem-phys.net/7/1961/2007/>.
- Petters, M. D. and Kreidenweis, S. M.: A single parameter representation of hygroscopic growth and cloud condensation nucleus activity – Part 2: Including solubility, *Atmos. Chem. Phys.*, 8, 6273–6279, doi:10.5194/acp-8-6273-2008, 2008.
- Petters, M. D. and Kreidenweis, S. M.: A single parameter representation of hygroscopic growth and cloud condensation nucleus activity – Part 3: Including surfactant partitioning, *Atmos. Chem. Phys.*, 13, 1081–1091, doi:10.5194/acp-13-1081-2013, 2013.
- Pöschl, U.: Atmospheric aerosols: Composition, transformation, climate and health effects, *Angewandte Chemie-International Edition*, 44, 7520–7540, doi:10.1002/anie.200501122, 2005.
- Pöschl, U., Rose, D., and Andreae, M. O.: Climatologies of cloud-related aerosols, Part 2: Particle hygroscopicity and cloud condensation nucleus activity, in: *Clouds in the Perturbed Climate System: Their Relationship to Energy Balance, Atmospheric Dynamics, and Precipitation*, edited by: Heintzenberg, J. and Charlson, R. J., MIT Press, Cambridge, MA, USA, 57–72, 2009.
- Pringle, K. J., Tost, H., Pozzer, A., Pöschl, U., and Lelieveld, J.: Global distribution of the effective aerosol hygroscopicity parameter for CCN activation, *Atmos. Chem. Phys.*, 10, 5241–5255, doi:10.5194/acp-10-5241-2010, 2010.
- Pruppacher, H. R. and Klett, J. D.: *Microphysics of Clouds and Precipitation*, Atmospheric and Oceanographic Sciences Library, 18, Springer Netherlands, 954 pp., 2010.
- Renn, N. O., Williams, E., Rosenfeld, D., Fischer, D. G., Fischer, J., Kremic, T., Agrawal, A., Andreae, M. O., Bierbaum, R., Blakeslee, R., Boerner, A., Bowles, N., Christian, H., Cox, A., Dunion, J., Horvath, A., Huang, X., Khain, A., Kinne, S., Lemos, M. C., Penner, J. E., Pöschl, U., and Quaas, J.: CHASER An Innovative Satellite Mission Concept to Measure the Effects of

- Aerosols on Clouds and Climate, *Bull. Am. Meteorol. Soc.*, 5, 685–694, doi:10.1175/bams-d-11-00239.1, 2013.
- Reutter, P., Su, H., Trentmann, J., Simmel, M., Rose, D., Gunthe, S. S., Wernli, H., Andreae, M. O., and Pöschl, U.: Aerosol- and updraft-limited regimes of cloud droplet formation: influence of particle number, size and hygroscopicity on the activation of cloud condensation nuclei (CCN), *Atmos. Chem. Phys.*, 9, 7067–7080, doi:10.5194/acp-9-7067-2009, 2009.
- Roberts, G. C. and Nenes, A.: A continuous-flow stream-wise thermal-gradient CCN chamber for atmospheric measurements, *Aerosol Sci. Technol.*, 39, 206–221, doi:10.1080/027868290913988, 2005.
- Rose, D., Gunthe, S. S., Mikhailov, E., Frank, G. P., Dusek, U., Andreae, M. O., and Pöschl, U.: Calibration and measurement uncertainties of a continuous-flow cloud condensation nuclei counter (DMT-CCNC): CCN activation of ammonium sulfate and sodium chloride aerosol particles in theory and experiment, *Atmos. Chem. Phys.*, 8, 1153–1179, doi:10.5194/acp-8-1153-2008, 2008.
- Rose, D., Nowak, A., Achtert, P., Wiedensohler, A., Hu, M., Shao, M., Zhang, Y., Andreae, M. O., and Pöschl, U.: Cloud condensation nuclei in polluted air and biomass burning smoke near the mega-city Guangzhou, China – Part 1: Size-resolved measurements and implications for the modeling of aerosol particle hygroscopicity and CCN activity, *Atmos. Chem. Phys.*, 10, 3365–3383, doi:10.5194/acp-10-3365-2010, 2010.
- Rose, D., Gunthe, S. S., Su, H., Garland, R. M., Yang, H., Berghof, M., Cheng, Y. F., Wehner, B., Achtert, P., Nowak, A., Wiedensohler, A., Takegawa, N., Kondo, Y., Hu, M., Zhang, Y., Andreae, M. O., and Pöschl, U.: Cloud condensation nuclei in polluted air and biomass burning smoke near the mega-city Guangzhou, China – Part 2: Size-resolved aerosol chemical composition, diurnal cycles, and externally mixed weakly CCN-active soot particles, *Atmos. Chem. Phys.*, 11, 2817–2836, doi:10.5194/acp-11-2817-2011, 2011.
- Rosenfeld, D., Lohmann, U., Raga, G. B., O’Dowd, C. D., Kulmala, M., Fuzzi, S., Reissell, A., and Andreae, M. O.: Flood or drought: How do aerosols affect precipitation?, *Science*, 321, 1309–1313, doi:10.1126/science.1160606, 2008.
- Rosenfeld, D., Williams, E., Andreae, M. O., Freud, E., Pöschl, U., and Rennó, N. O.: The scientific basis for a satellite mission to retrieve CCN concentrations and their impacts on convective clouds, *Atmos. Meas. Tech.*, 5, 2039–2055, doi:10.5194/amt-5-2039-2012, 2012.
- Russell, L. M., Sorooshian, A., Seinfeld, J. H., Albrecht, B. A., Nenes, A., Ahlm, L., Chen, Y. C., Coggon, M., Craven, J. S., Flagan, R. C., Frossard, A. A., Jonsson, H., Jung, E., Lin, J. J., Metcalf, A. R., Modini, R., Mulmenstadt, J., Roberts, G. C., Shingler, T., Song, S., Wang, Z., and Wonaschutz, A.: Eastern Pacific Emitted Aerosol Cloud Experiment, *Bull. Am. Meteorol. Soc.*, 94, 709–729, doi:10.1175/BAMS-D-12-00015.1, 2013.
- Solomon, S., Qin, D., Manning, Z., Chen, Z., Marquis, M., Avery, K. B., Tignor, M., and Miller, H. L. E.: IPCC 4th Assessment Report, Cambridge Univ. Press, Cambridge, 2007.
- Spracklen, D. V., Carslaw, K. S., Pöschl, U., Rap, A., and Forster, P. M.: Global cloud condensation nuclei influenced by carbonaceous combustion aerosol, *Atmos. Chem. Phys.*, 11, 9067–9087, doi:10.5194/acp-11-9067-2011, 2011.
- Su, H., Rose, D., Cheng, Y. F., Gunthe, S. S., Massling, A., Stock, M., Wiedensohler, A., Andreae, M. O., and Pöschl, U.: Hygroscopicity distribution concept for measurement data analysis and modeling of aerosol particle mixing state with regard to hygroscopic growth and CCN activation, *Atmos. Chem. Phys.*, 10, 7489–7503, doi:10.5194/acp-10-7489-2010, 2010.
- Wex, H., McFiggans, G., Henning, S., and Stratmann, F.: Influence of the external mixing state of atmospheric aerosol on derived CCN number concentrations, *Geophys. Res. Lett.*, 37, L10805, doi:10.1029/2010gl043337, 2010.

## **B5. Rosenfeld et al. PNAS, 2016**

### **Satellite retrieval of cloud condensation nuclei concentrations by using clouds as CCN chambers**

Daniel Rosenfeld<sup>1</sup>, Youtong Zheng<sup>2,3,4</sup>, Eyal Hashimshoni<sup>1</sup>, Mira L. Pöhlker<sup>5,6</sup>, Anne Jefferson<sup>7</sup>, Christopher Pöhlker<sup>5</sup>, Xing Yu<sup>8</sup>, Yannian Zhu<sup>4,8</sup>, Guihua Liu<sup>8</sup>, Zhiguo Yue<sup>8</sup>, Baruch Fischman<sup>1</sup>, Zhanqing Li<sup>2,3,4</sup>, David Giguzin<sup>1</sup>, Tom Goren<sup>1</sup>, Paulo Artaxo<sup>9</sup>, Henrique M. J. Barbosa<sup>9</sup>, Ulrich Pöschl<sup>5,6</sup>, and Meinrat O. Andreae<sup>5</sup>

<sup>1</sup> *Institute of Earth Sciences, The Hebrew University of Jerusalem, Jerusalem, Israel*

<sup>2</sup> *Department of Atmospheric and Oceanic Science, University of Maryland, College Park, MD, USA*

<sup>3</sup> *Earth System Science Interdisciplinary Center, University of Maryland, College Park, MD, USA*

<sup>4</sup> *State Key Laboratory of Earth Surface Processes and Resource Ecology, Beijing Normal University, Beijing, China*

<sup>5</sup> *Biogeochemistry Department, Max Planck Institute for Chemistry, Mainz, Germany*

<sup>6</sup> *Multiphase Chemistry Department, Max Planck Institute for Chemistry, Mainz, Germany*

<sup>7</sup> *Earth System Research Laboratory, National Oceanic and Atmospheric Administration, Boulder, CO, USA*

<sup>8</sup> *Meteorological Institute of Shaanxi Province, Xi'an, China*

<sup>9</sup> *Physics Institute, University of Sao Paulo, Sao Paulo, Brazil*

# Satellite retrieval of cloud condensation nuclei concentrations by using clouds as CCN chambers

Daniel Rosenfeld<sup>a,1</sup>, Youtong Zheng<sup>b,c,d</sup>, Eyal Hashimshoni<sup>a</sup>, Mira L. Pöhlker<sup>e,f</sup>, Anne Jefferson<sup>g</sup>, Christopher Pöhlker<sup>e</sup>, Xing Yu<sup>h</sup>, Yannian Zhu<sup>d,h</sup>, Guihua Liu<sup>h</sup>, Zhiguo Yue<sup>h</sup>, Baruch Fischman<sup>a</sup>, Zhanqing Li<sup>b,c,d</sup>, David Giguzin<sup>a</sup>, Tom Goren<sup>a</sup>, Paulo Artaxo<sup>i</sup>, Henrique M. J. Barbosa<sup>i</sup>, Ulrich Pöschl<sup>e,f</sup>, and Meinrat O. Andreae<sup>e</sup>

<sup>a</sup>Institute of Earth Sciences, The Hebrew University of Jerusalem, Jerusalem 91904, Israel; <sup>b</sup>Department of Atmospheric and Oceanic Science, University of Maryland, College Park, MD 20740; <sup>c</sup>Earth System Science Interdisciplinary Center, University of Maryland, College Park, MD 20740; <sup>d</sup>State Key Laboratory of Earth Surface Processes and Resource Ecology, College of Global Change and Earth System Science, Beijing Normal University, Beijing 100875, China; <sup>e</sup>Biogeochemistry Department, Max Planck Institute for Chemistry, Mainz 55020, Germany; <sup>f</sup>Multiphase Chemistry Department, Max Planck Institute for Chemistry, Mainz 55020, Germany; <sup>g</sup>Earth System Research Laboratory, National Oceanic and Atmospheric Administration, Boulder, CO 80305; <sup>h</sup>Meteorological Institute of Shaanxi Province, Xi'an 710015, China; and <sup>i</sup>Physics Institute, University of Sao Paulo, Sao Paulo 05508-090, Brazil

Edited by John H. Seinfeld, California Institute of Technology, Pasadena, CA, and approved January 29, 2016 (received for review September 14, 2015)

**Quantifying the aerosol/cloud-mediated radiative effect at a global scale requires simultaneous satellite retrievals of cloud condensation nuclei (CCN) concentrations and cloud base updraft velocities ( $W_b$ ). Hitherto, the inability to do so has been a major cause of high uncertainty regarding anthropogenic aerosol/cloud-mediated radiative forcing. This can be addressed by the emerging capability of estimating CCN and  $W_b$  of boundary layer convective clouds from an operational polar orbiting weather satellite. Our methodology uses such clouds as an effective analog for CCN chambers. The cloud base supersaturation ( $S$ ) is determined by  $W_b$  and the satellite-retrieved cloud base drop concentrations ( $N_{db}$ ), which is the same as  $CCN(S)$ . Validation against ground-based CCN instruments at Oklahoma, at Manaus, and onboard a ship in the north-east Pacific showed a retrieval accuracy of  $\pm 25\%$  to  $\pm 30\%$  for individual satellite overpasses. The methodology is presently limited to boundary layer not raining convective clouds of at least 1 km depth that are not obscured by upper layer clouds, including semi-transparent cirrus. The limitation for small solar backscattering angles of  $< 25^\circ$  restricts the satellite coverage to  $\sim 25\%$  of the world area in a single day.**

CCN concentrations | satellite remote sensing | convective clouds | cloud–aerosol interactions

The Intergovernmental Panel on Climate Change (IPCC) report (1) states that the uncertainty in aerosol/cloud interactions dominates the uncertainty about the degree of influence that human activities have on climate. Because clouds form in ascending air currents, whereas cloud droplets nucleate on aerosols that serve as cloud condensation nuclei (CCN), we need accurate measurements of both updrafts and CCN supersaturation ( $S$ ) spectra before we can disentangle aerosol effects on cloud radiative forcing (CRF) from dynamical effects.

## Need for Global Measurements of Cloud Base Updrafts and $CCN(S)$

Tackling the global change problems as identified by the IPCC requires that these quantities be measured on a global scale. However, satellites have not been able to measure updraft speed of the air that forms the clouds or the concentrations of aerosols that are capable of forming cloud drops, which are ingested into the clouds as they grow. Lack of such fundamental quantities has greatly hindered our capability of disentangling the effects of meteorology and anthropogenic aerosol emissions on cloud properties (2). This situation is starting to change with our recently developed methodology to retrieve updrafts at cloud base (3, 4) using the Visible/Infrared Imager Radiometer Suite (VIIRS) instrument onboard the Suomi National Polar-orbiting Partnership (NPP) satellite. This satellite is sun-synchronous, with an overpass time near 13:30 solar time.

Missing such fundamental quantities as  $CCN(S)$  and cloud base updraft  $W_b$  has been preventing us from disentangling the effects of aerosols from atmospheric dynamics (i.e., meteorology). Their absence also has limited our ability to validate the hypothesized impacts of added aerosols on a large range of phenomena, including (i) maintaining full cloud cover in marine stratocumulus, thus incurring a strong cooling effect on the climate system (5); (ii) suppressing precipitation from shallow clouds (6–8); (iii) invigorating the convection in deep tropical clouds (9); (iv) enhancing cloud electrification (10, 11); (v) intensifying severe convective storms to produce more large hail and tornadoes (12); and (vi) decreasing the intensity of tropical cyclones (13). In addition to their intrinsic importance, these aerosol effects could induce radiative effects that change Earth's energy budget in a significant way (1).

Previous satellite-based studies related cloud properties mostly to the aerosol optical depth (AOD) and the Ångström coefficient (14–18). However, AOD as a proxy for CCN is a rather crude tool that is fraught with problems (19) due to a large number of reasons, including (i) aerosol swelling with high relative humidity (20, 21); (ii) uncertainty in solubility and size distribution (18); (iii) lack of a discernible optical signal from small CCN; (iv) cloud contamination (22); (v) AOD not representing aerosol concentrations near cloud base; (vi) cloud obscuration of the aerosols in the boundary layer; (vii) cloud detrainment of aerosols aloft (23, 24) yielding an increase in AOD for deeper and more extensive clouds without corresponding increase in cloud base aerosol concentrations; and (viii) lack of accurate AOD signal for the pristine boundary layer, where accuracy is most critical because clouds respond to the relative change in CCN concentrations, which can be a very small absolute change at very low absolute concentrations (25). These factors often explain a substantial part of the indicated associations of AOD with cloud top properties (18, 26), which has been erroneously ascribed to aerosol effects.

This paper results from the Arthur M. Sackler Colloquium of the National Academy of Sciences, "Improving Our Fundamental Understanding of the Role of Aerosol–Cloud Interactions in the Climate System," held June 23–24, 2015, at the Arnold and Mabel Beckman Center of the National Academies of Sciences and Engineering in Irvine, CA. The complete program and video recordings of most presentations are available on the NAS website at [www.nasonline.org/Aerosol\\_Cloud\\_Interactions](http://www.nasonline.org/Aerosol_Cloud_Interactions).

Author contributions: D.R. designed research; D.R., Y. Zheng, Y. Zhu, Z.L., and M.O.A. performed research; X.Y., G.L., Z.Y., B.F., P.A., H.M.J.B., and U.P. contributed new analytic tools; Y. Zheng, E.H., M.L.P., A.J., C.P., X.Y., Y. Zhu, D.G., and T.G. analyzed data; D.R., U.P., and M.O.A. wrote the paper; M.L.P., A.J., and C.P. provided CCN data; and P.A. and H.M.J.B. facilitated the measurements of CCN in Brazil.

The authors declare no conflict of interest.

This article is a PNAS Direct Submission.

<sup>1</sup>To whom correspondence should be addressed. Email: [daniel.rosenfeld@huji.ac.il](mailto:daniel.rosenfeld@huji.ac.il).

This article contains supporting information online at [www.pnas.org/lookup/suppl/doi:10.1073/pnas.1514044113/-DCSupplemental](http://www.pnas.org/lookup/suppl/doi:10.1073/pnas.1514044113/-DCSupplemental).

Aerosol optical properties are useful for measuring aerosol type and particle size, which can be identified by active sensor backscatter intensity, color ratio, and polarimetry, or by passive multi-angle intensity measurements even without polarimetry. Adding polarimetry to passive, multiangle imaging should improve the precision and range of conditions under which particle size, shape, and refractive indices can be retrieved. However, this still leaves most of the issues unresolved, especially issues *iii* and *v–viii*, as listed above. To overcome this conundrum, a complete shift in approach is needed. Instead of addressing the limited information content in the optical signal of the aerosols, we extract  $CCN(S)$  by using clouds as an analog for CCN counter (CCNC) chambers.

The structure of this paper is as follows: This section provides the importance and motivation for retrieving  $CCN(S)$ . *Methodology* provides a summary of the recent advancements which constitute a critical mass enabling satellite-only retrieval of  $CCN(S)$  and applies it while describing the essence of the methodology. An extensive validation effort is described in *Validation of the Satellite-Retrieved CCN(S)*, and its results are given in *Results*, along with error calculations. The possibilities that open up with the emerging capabilities for coincident satellite retrieval of convective cloud base updrafts and  $CCN(S)$  are discussed in *Applications of Satellite-Retrieved Updrafts*. Finally, the conclusions are given in *Conclusions*.

## Methodology

**Using Clouds as CCN Chambers.** The commonly used CCNCs measure the number concentration of aerosol particles in a sample air stream ( $N_a$ ), which at a given  $S$  can be activated into the same number of cloud droplets at its base ( $N_{db}$ ) (27). Alternatively, retrieving  $N_{db}$  and  $S$  in clouds can provide  $CCN(S)$ . The peak vapor supersaturation at an adiabatic cloud base,  $S$ , is determined by  $CCN(S)$  and  $W_b$ . Therefore, a good approximation of  $S$  can be calculated from the retrieved  $N_{db}$  and  $W_b$  according to

$$S = C(T_b, P_b) W_b^{3/4} N_{db}^{-1/2}, \quad [1]$$

where  $C$  is a coefficient that depends weakly on cloud base temperature ( $T_b$ ) and pressure ( $P_b$ ) (28). This is an analytical expression that was derived based on theoretical considerations. Recently, it has become possible to estimate  $N_{db}$  and  $W_b$  from satellite measurements, thus calculating also  $S$ . This constitutes the ability to calculate  $CCN(S)$  from satellite measurements only. The following subsections describe the methodology of satellite estimation of  $N_{db}$  and  $W_b$ .

**Estimation of Cloud Base Drop Concentrations.** Retrieving  $T_b$ ,  $P_b$ ,  $W_b$ , and  $N_{db}$  became possible with the advent of the Suomi NPP satellite, which was launched in October 2011. The VIIRS onboard this satellite has a moderate spatial resolution of 750 m. The VIIRS has an Imager with a subset of five channels with double resolution of 375 m at 0.64  $\mu\text{m}$ , 0.865  $\mu\text{m}$ , 1.61  $\mu\text{m}$ , 3.74  $\mu\text{m}$ , and 11.45  $\mu\text{m}$ . Although VIIRS Imager 375-m data were not designed for retrieving cloud properties, a methodology was developed for using it to retrieve cloud drop effective radius ( $r_e$ ) and cloud-top temperatures ( $T$ ). The retrieval of  $r_e$  was based on the methodology developed by Rosenfeld and Lensky (29) for the Advanced Very High Resolution Radiometer. It has been applied to VIIRS by Rosenfeld et al. (30). The ability to retrieve cloud properties at a resolution of 375 m is a breakthrough compared with the previous best available resolution of 1 km. This allows microphysical monitoring of cloud properties with unprecedented accuracy and makes it possible to obtain the microstructure of small clouds at the top of the boundary layer (30).

A VIIRS-retrieved  $T-r_e$  relationship, which is obtained from a convective cloud ensemble within an area of  $\sim 30 \times 30$  km (28), serves as the basis for retrieving  $T_b$ ,  $P_b$ , and  $N_{db}$ . This satellite method is based on extensive aircraft measurements of  $T-r_e$  relationships. It was demonstrated that  $r_e$  varies with altitude nearly as in an adiabatic cloud, and therefore adiabatic cloud drop number concentrations ( $N_{da}$ ) can be calculated at different altitudes in the cloud using the calculated adiabatic water content  $LWC_a$  and  $r_{ea}$ , which is assumed to vary adiabatically with altitude, thus marked as  $r_{ea}$  (31). Then,  $N_{da}$  approximates  $N_{db}$ , because the cloud can be assumed to be adiabatic at its base. The retrieved  $r_e$  is assumed to be  $r_{ea}$  based on the assumption that the measured  $r_e$  is adiabatic, which is the case for clouds with extreme inhomogeneous mixing and with all cloud drops nucleated at their base.

Deviations from the extreme inhomogeneous assumption lead to a reduction of the aircraft-based calculation of  $N_{da}$  by an average factor of 1.3 with respect to the value calculated under this assumption (31). The cloud base drop concentration is approximated by the adiabatic cloud drop concentration as calculated by Eq. 2 (32),

$$N_{da} = \alpha^3 LWC_a / r_{ea}^3, \quad [2]$$

$$\alpha = 62.03 r_e / r_v, \quad [3]$$

where  $r_v$  is the cloud drop mean volume radius, as calculated by equally distributing cloud water content between the cloud droplets. We used the value of  $r_e = 1.08 r_v$  (31). The adiabatic water is obtained from the VIIRS-measured  $T_b$ , which is simply the warmest cloudy pixel, based on a specially developed cloud mask (33). The  $LWC_a$  is calculated based on an adiabatic parcel that rises from cloud base at  $T_b$  and  $P_b$  to the isotherm  $T$ , where multiple pairs of  $T$  and  $r_{ea}$  are retrieved for different cloudy pixels of the same cloud cluster at different heights above cloud base. Here,  $P_b$  is obtained from the pressure at the isotherm of satellite-retrieved cloud base height ( $H_b$ ), which was computed from the European Center for Medium-range Weather Forecasting reanalysis data.  $H_b$  was calculated as the difference between reanalysis surface air temperature and  $T_b$  divided by the dry adiabatic lapse rate.  $T_b$  was validated at a root-mean-square (RMS) error of 1.1 K, as shown in Fig. 1 (33).  $H_b$  and  $T_b$  were calculated for conditions of convective clouds that developed from well-mixed boundary layer at the early afternoon satellite overpass time (33), before the peak of the convective rain and the resultant cooling and moistening of the boundary layer by evaporating precipitation.

**Estimation of Cloud Base Updrafts.** Until now, only lidar and radar measurements of  $W_b$  were used. This is expanded here to satellite-retrieved  $W_b$ . According to Eq. 1, knowing  $W_b$  and  $N_{db}$  at cloud base yields  $S$ . Then,  $N_{db}$  is numerically identical to  $CCN(S)$ . Rosenfeld et al. (32) used this method to retrieve  $CCN(S)$  over the Atmospheric Radiation Measurement (ARM) site of the Southern Great Plains (SGP), using  $N_{db}$  retrieved from a satellite and  $W_b$  measured by ARM's vertically pointing  $K_a$ -band radar. The  $W_b$  was calculated from all full Doppler statistics during a 2-h window centered at the satellite overpass time, where the  $W_b$  of each point in time was weighted by  $W_b$  itself, thus representing its relative contribution to building the cloud volume. More specifically, equation 5 in Rosenfeld et al. (32) (replicated as Eq. 4 here) shows that the radar or lidar updraft  $W$  was constructed from all of the  $N$  realizations  $W_i$  of single data points within the time window as follows:

$$W = \frac{\sum N_i W_i^2}{\sum N_i W_i} \Big|_{W_i > 0}. \quad [4]$$

According to Eq. 4,  $W$  is the cloud volume-weighted updraft. Good agreement was achieved by Rosenfeld et al. (32) between  $CCN(S)$  as

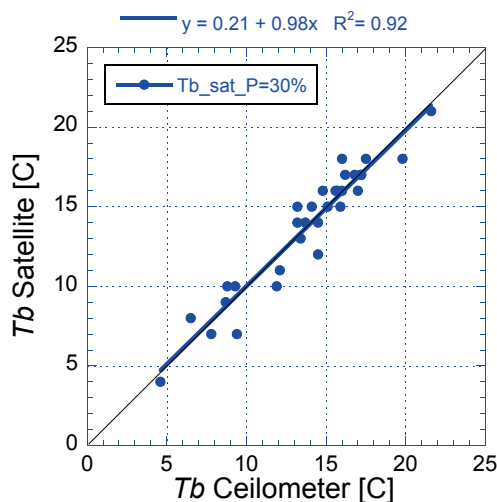


Fig. 1. The relationship between satellite-measured cloud base temperature and validation measurements by a combination of a ceilometer and soundings at the Department of Energy (DOE)/Atmospheric System Research (ASR) sites on the SGP in Oklahoma. Reproduced from ref. 33.

constructed by satellite-retrieved  $N_{db}$  and radar-retrieved  $W_b$  with the SGP ground base-measured  $CCN(S)$ , but the number of cases with useful clouds and data were rather small and served mainly to verify the methodology. The need for ground-based measurements of  $W_b$  limited severely the occasions where  $CCN$  could be retrieved to sites where cloud Doppler lidars or radars measurements are available. The present study is the first one, to our knowledge, to retrieve  $CCN(S)$  from satellite estimates of both  $N_{db}$  and  $W_b$ , thus becoming potentially very widely applicable, despite some limitations in the retrievals of  $N_{db}$  and  $W_b$ .

Retrieval of  $CCN$  solely from satellite data requires  $W_b$  to be retrieved from satellite. This was done by using satellite-retrieved components of the energy that propels the convection (3). Subsequently, Zheng and Rosenfeld (4) showed that  $W_b$  can be simply calculated by

$$W_b = AH_b, \quad [5]$$

where  $W_b$  is cloud base updraft in meters per second,  $A$  is a coefficient ( $0.0009 \text{ s}^{-1}$ ) obtained in a previous study (4), and  $H_b$  is the cloud base height above the ground in meters, which is determined by the difference between the surface air and cloud base temperatures, as explained at the end of *Estimation of Cloud Base Drop Concentrations*. This relationship was developed based on synchronous satellite and lidar measurements from the ARM SGP site and at the ARM Mobile Facility onboard a ship on a line between Los Angeles and Honolulu [Marine ARM GPCI Investigations of Clouds (MAGIC)]. The satellite-retrieved  $W_b$  was validated against the Doppler measurements, resulting in an RMS error of  $0.41 \text{ m}\cdot\text{s}^{-1}$  and a mean absolute percentage error (MAPE) of 24% and 21% by Zheng et al. (3) and Zheng and Rosenfeld (4), respectively. When forcing the relationships through zero (Eq. 5 and Fig. 2), the error becomes 27%. These results are consistent with the physical considerations of Williams and Stanfill (10). This means that the methodology is very likely to be universally applicable to boundary layer convective clouds.

Table 1 summarizes the methodology. It shows the satellite measurements, their combination with reanalysis data, and their propagation into the eventual  $W_b$  and  $CCN(S)$ , and the associated errors.

### Validation of the Satellite-Retrieved $CCN(S)$

Cloud base  $S$  was obtained from Eq. 1, with  $N_{db}$  calculated by Eq. 2 and  $W_b$  calculated using Eq. 5. The calculated  $N_{db}$  is by definition equal to  $CCN(S)$  at cloud base. To compare with surface-based measurements, the concentration is corrected for the difference between air density at cloud base and at the ground, and then validated against the  $CCN(S)$  as measured by the ground-based instrument. This assumes that the thermals bring the surface air to cloud base without much change in the mixing ratio and properties of aerosol particles. This is a widely accepted assumption for vapor mixing ratio at thermally driven cloud bases in a well-mixed

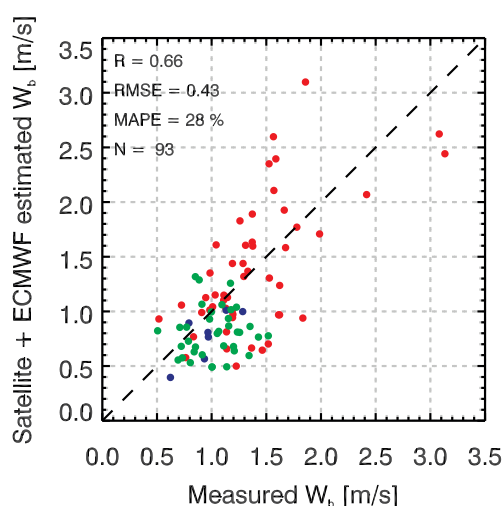


**Fig. 2.** Relationship between satellite-estimated  $W_b = 0.0009H_b$  and directly measured  $W_b$  by Doppler lidars at the SGP (red dots), Green Ocean Amazon (GOAmazon) (green), and MAGIC (blue). After Zheng and Rosenfeld (4). The satellite-retrieved  $T_b$  was converted to height using the European Centre for Medium-Range Weather Forecasts reanalysis data. RMSE is the estimation root mean square error.

boundary layer, where the lifting condensation level is usually very similar to the actual cloud base height.

An initial comparison of the satellite-retrieved  $CCN$  to the SGP instrumental validation data (assuming no error in the instrument measured  $CCN$ ) showed a slope of 0.74 for the regression line. A retrieval bias could be caused by a large number of factors, which are quantified in *Error Analysis*, but the largest potential source of error is inaccuracy in  $r_e$ . The observed 26% underestimate in  $CCN$  could have been caused by a 10% systematic overestimate in the retrieved  $r_e$ . This is quite probable, because MODIS-retrieved  $r_e$  was found to be larger by 10–15% than aircraft in situ measurements (34–36). An underestimate of satellite- versus surface-measured  $CCN$  can be also caused by a systematic decrease of  $CCN$  number concentration ( $N_{CCN}$ ) between the surface and cloud base heights. This bias has to be corrected before calculating  $S$  by Eq. 1, because, otherwise,  $S$  would be overestimated. To stay on the conservative side, we applied only half of the bias correction and used here a reduction factor of 1.15 instead of 1.3, as proposed by Freud et al. (31), and applied it to all of the validation sites.

Validation cases were selected over the sites of the ARM sites of the SGP in Oklahoma, at Manacapuru near Manaus in the Amazon, and over the northeastern Pacific onboard the MAGIC ship. In addition,  $CCN$  measurements were obtained from the Amazon Tall Tower Observatory (ATTO) site 150 km to the northeast of Manaus (37). Data were obtained from the start of availability of VIIRS data in 2012 until early 2015. The case selection criteria were as follows: (i) Satellite overpass has to occur at a zenith angle between  $0^\circ$  and  $45^\circ$  to the east of the ground track, which is the sunny side of the clouds. For a specific location, these satellite views occur once or twice every 6 d. (ii) Convective clouds must occur and possess a vertical development that spans at least 6 K of cloud temperature from base to top, limiting to clouds with thickness  $>1$  km. (iii) The clouds must not precipitate significantly (i.e., without a radar or lidar detectable rain shaft that reaches the ground). The precipitation causes cold pools that disconnect the continuity of the air between the surface and the cloud base. (iv) Cloud elements with indicated  $r_e > 18 \mu\text{m}$  are rejected automatically from the analysis that is likely to rain/drizzle heavily. (v) No obscuration from high clouds is allowed. An automatic detection of semitransparent clouds screens them from the selected area for analysis. (vi) Ground-based  $CCN$  data must be available.

The availability of  $CCN$  data from the ARM program at all of its three sites was severely limited due to data quality issues. Insufficient available time for stabilization of temperatures at low  $S$  caused the  $CCN$  readings at  $S \leq 0.25\%$  to be grossly underestimated or zero, and therefore they could not be used. The points with  $S > 0.25\%$  were fit with a second-order polynomial that was forced through the origin, because  $CCN$  must be zero for  $S = 0$ . By extrapolation with this polynomial, we could extend the use of the data down to  $S = 0.2\%$ . Cases with cloud base  $S < 0.2\%$  were rejected. The operation of the ARM CCNCs was changed after August 2014 to allow sufficient time for stabilization at low  $S$ . This correction was applied to Manacapuru only by April 2015, however. These limitations did not apply to ATTO, and valid data from this site were available from May 2014 until January 2015.

The results are shown in Fig. 3. Each point in the figure represents one satellite overpass over one ground-based CCNC. The  $CCN$  data from a time window of  $\pm 1$  h around the overpass are taken to include several  $CCN(S)$  spectra at all measured supersaturations. Because of the much slower scanning rate of  $S$  at ATTO, a larger time window of  $\pm 1.5$  h was taken there to include at least one full spectrum of  $CCN(S)$ . The satellite analyzes clouds over an area of about  $30 \times 30$  km around the ground measurement site, with some adjustments to incorporate the convective clouds in the vicinity. The satellite-retrieved  $CCN$  and  $S$  are compared with the instrument measurements as follows:

**Table 1. Propagation of the calculations from the satellite retrievals to the resultant  $CCN(S)$** 

Symbol	Parameter and unit	Source of calculation	Error
$r_e$	cloud drop effective radius, $\mu\text{m}$	satellite retrieval	8%
$T$	cloud surface temperature, $^{\circ}\text{C}$	satellite retrieval	0.2 $^{\circ}\text{C}$
$T_b$	cloud base temperature, $^{\circ}\text{C}$	satellite retrieval	1.1 $^{\circ}\text{C}$
$P_b$	cloud base pressure, hPa	$T_b$ + reanalysis	15 hPa
$r_v$	drop mean volume radius, $\mu\text{m}$	$r_e$ (Eq. 3)	8%
$LWC_a$	cloud adiabatic water, $\text{g}\cdot\text{kg}^{-1}$	$T + T_b + P_b$ (parcel)	15%
$N_d$	cloud base drop concentrations, $\text{cm}^{-3}$	$r_v(T) + LWC_a(T)$ (Eq. 2)	30%
$H_b$	cloud base height above surface, m	$T_b$ + reanalysis	150 m
$W_b$	cloud base updraft, $\text{m}\cdot\text{s}^{-1}$	$H_b$ (Eq. 5)	27%
$S$	cloud base max supersaturation, %	$T_b, P_b, W_b, N_d$ (Eq. 1)	25% of $S$ in percent
$N_{CCN}(S)$	CCN at cloud base, $\text{cm}^{-3}$	$N_d, S$ by definition	30%

(i) A scatter plot of the individual ground-based measurements of CCN concentrations ( $N_{CCN}$ ) is plotted as a function of  $S$ . (ii) A second-order polynomial curve is fit to the points. The function is forced through the origin, because zero  $S$  must correspond to zero  $N_{CCN}$ . (iii) The  $N_{CCN}$  is taken from the polynomial fit at the same  $S$  that is retrieved from satellite at cloud base. The  $\pm 95\%$  confidence interval of  $N_{CCN}$  at the value of satellite-retrieved  $S$  is calculated. (iv) The satellite-retrieved  $N_{CCN}$  is the satellite-retrieved  $N_{db}$ , corrected for the air density difference between cloud base and the surface.

### Results

Fig. 3 shows the relationships between the satellite retrievals of  $N_{CCN}$  and  $S$  at cloud base, and the ground-based measurements

of  $N_{CCN}$  at the same  $S$ . There are several points worth noting. (i) The figure covers a large dynamic range of  $S$  for both low and high values  $N_{CCN}$ . (ii) The value of  $R^2 = 0.76$  shows that the fit explains more than 3/4 of the variability between the satellite and ground-based measurements of  $CCN(S)$ . (iii) There is a systematic underestimate bias of 14% in the satellite-retrieved CCN. It follows that the estimation errors decrease almost linearly with smaller  $N_{CCN}$ . (iv) The variation of the satellite with respect to the ground-based measurements is within 20–25% of the ground-based measurements. This includes the 14% bias error. (v) The SD of the fit is similar to the expected magnitude from the error sources of the satellite uncertainties in  $W_b, T_b,$  and  $r_e$ .

The methodology was converted into a procedure that can be applied to any specified rectangle in the VIIRS imagery, which

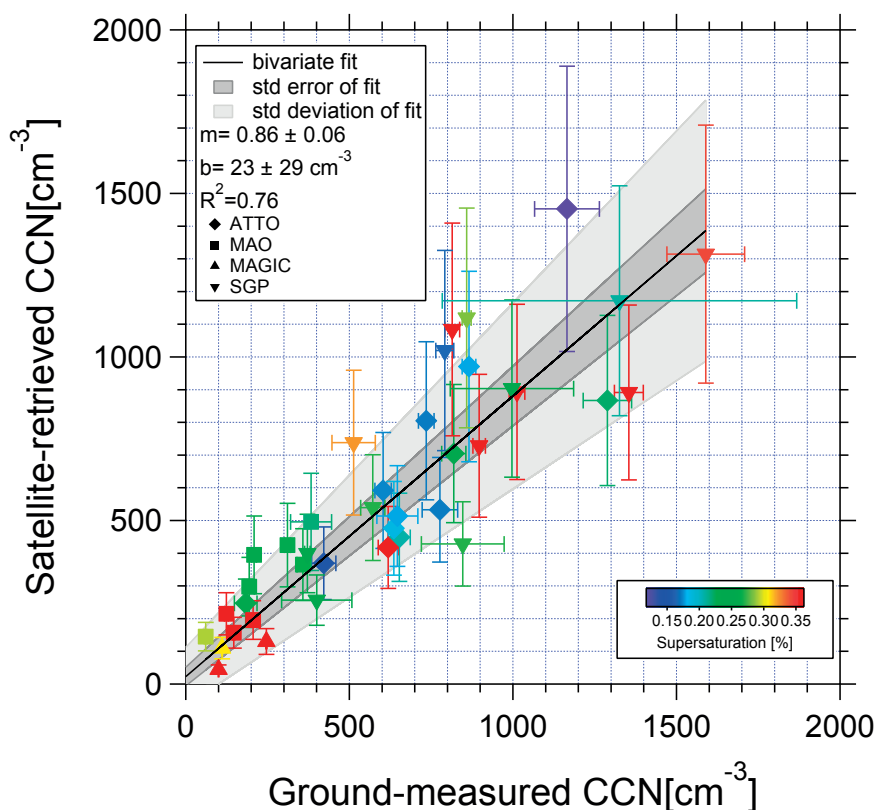


**Fig. 3.** The relationship between satellite-retrieved  $N_{CCN}$  and  $S$  at cloud base, and the ground-based instrument measurements of  $N_{CCN}$  at the same  $S$ . The slope and intercept of the best fit line are given in the key by  $m$  and  $b$ , respectively. The validation data are collected from the DOE/ASR sites on the SGP in Oklahoma and GOAmazon near Manaus, and over the northeast Pacific (MAGIC). In addition, data are obtained from the ATTO. The location is denoted by the marker shape, and  $S$  is shown by the color.

contains surface thermally driven convective clouds, and provides as output the following parameters:  $T_b$ ,  $P_b$ ,  $H_b$ ,  $W_b$ ,  $N_{db}$ , and  $S$ . The value of  $N_{db}$  is equal to the CCN concentrations at the retrieved  $S$  at cloud base, and this value of  $CCN(S)$  is also an output parameter. As an illustrative example, this procedure was applied to a regular grid of  $75 \times 75$  VIIRS Imager pixels ( $28 \times 28$  km at nadir) over the region of Houston during conditions of onshore flow of a tropical marine air mass. The results are shown in Fig. 4. The salient features are as follows: (i) There are very low CCN concentrations over the ocean. (ii) There is only a modest increase in CCN over the rural areas inland. (iii) The CCN concentrations more than triple over and downwind of the urban area compared with the cross-wind areas. (iv)  $S$  decreases over the urban area to less than half of the values over the rural areas. Therefore, CCN for the same  $S$  is enhanced by a factor much larger than 3. (v) The indicated CCN concentrations are similar in adjacent areas with similar conditions, indicating the robustness of the methodology.

### Applications of Satellite-Retrieved Updrafts and $CCN(S)$ to Reduced Climate Uncertainties

Here we showed the feasibility to retrieve  $CCN(S)$  from a single satellite passive sensor using clouds as CCN chambers, under certain conditions. There are still many challenges to overcome before it will be possible to do so for most cloud types. This requires the development of new satellite capabilities that will be

able to provide more direct measurements of updraft speeds, such as measuring vertical motions of cloud elements by tracking their evolution with time. Here we attempt to open a window to the potential applications of such capability, with a few examples.

The sensitivity of cloud properties to  $N_{CCN}$  is logarithmic (38). This means that a small absolute change in  $N_{CCN}$  has a much larger impact during pristine than polluted conditions. Carslaw et al. (25) argued that the main sensitivity to anthropogenic aerosols occurs in areas that had  $N_{CCN}$  of  $35\text{--}65\text{ cm}^{-3}$  during the preindustrial era. Satellite measurements show that an increase of more than  $100\text{ W}\cdot\text{m}^{-2}$  in cloud radiative effect (CRE) can occur when  $N_d$  of marine shallow boundary layer clouds increases from  $35\text{ cm}^{-3}$  to  $65\text{ cm}^{-3}$ , mainly due to increased cloud cover and cloud liquid water path. This is manifested as closing areas of open cellular convection (39). However, the satellite observed  $N_d$  is related to both  $W_b$  and  $CCN(S)$ , as shown by Eq. 1. Therefore, there is a possibility that measurements of the large enhancement of CRE that were associated with increased  $N_d$  could also result from changes in  $W_b$ , which could be caused by changes of meteorology (40). For separating the roles of  $W_b$  and  $N_{CCN}$  in the determination of  $N_{db}$ , both  $W_b$  and  $N_{CCN}$  should be measured. As already discussed in *Need for Global Measurements*, using AOD as a proxy for  $N_{CCN}$  in the marine boundary layer clouds has several shortcomings. Because, among other problems, the correlation between AOD and  $N_{CCN}$  is not very close and because a column property like AOD is not necessarily representative of the CCN

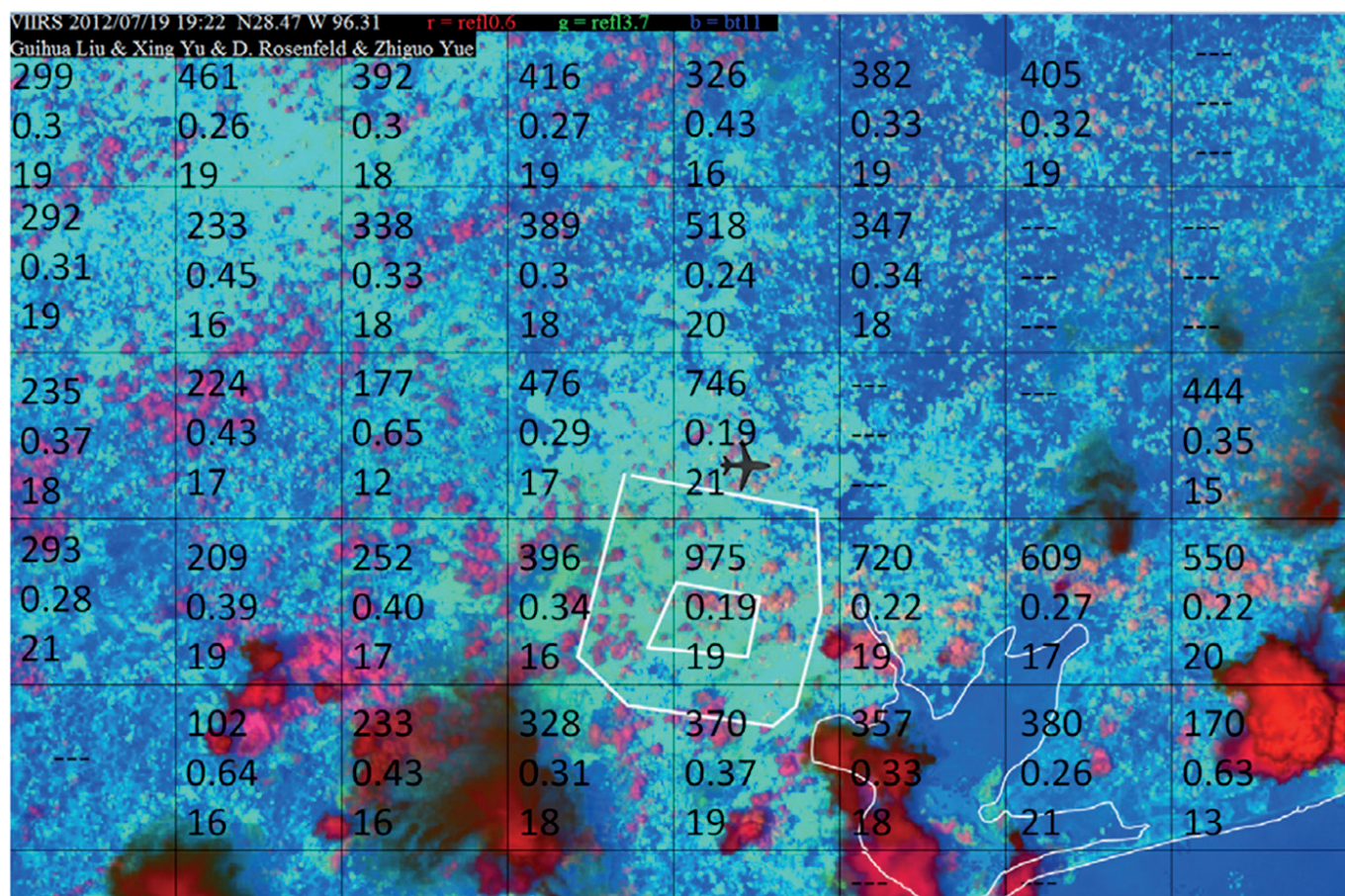


Fig. 4. Application of the methodology to the Houston area. The retrieval is done for a regular grid of  $75 \times 75$  375-m VIIRS/Imager pixels ( $\sim 28 \times 28$  km at nadir). The numbers in each area are: top, CCN (per cubic centimeter); middle,  $S$  (percent); and bottom, cloud base temperature (degrees Celsius). Unstable clean tropical air mass flows northward (upward in the image) from the Gulf of Mexico. The Houston urban effect is clearly visible by more than tripled CCN concentrations over Houston and the reduction of  $S$  to less than half. This represents an even larger factor in enhancing CCN for the same  $S$ . A smaller effect is seen over the urban and industrial areas to the east of Houston. The color composite is red, green, and blue for the visible reflectance,  $3.7\text{-}\mu\text{m}$  solar reflectance, and thermal temperature, respectively, as in Rosenfeld et al. (30). The Houston bay and beltways are marked by white lines.

concentrations that affect growing clouds, the AOD approach allows only an order-of-magnitude estimate of  $N_{CCN}$ . On the other hand, combining  $W_b$  with  $N_{db}$  can provide  $CCN(S)$  with an uncertainty that can be quantified and is far better than the AOD approach. Having both  $W_b$  and  $CCN(S)$  will allow disentangling of the roles of these two factors in determining  $N_d$  and in the attribution of the related changes in CRE to aerosols.

Having satellite retrievals of both  $W_b$  and  $N_{CCN}$  will allow disentangling of their respective roles on determining  $N_d$  and the related precipitation-forming processes, rainfall amounts, and distribution of vertical latent heating.  $CCN(S)$  ingested by deep convective clouds can be estimated by using adjacent shallower nonprecipitating convective clouds in their upwind side. Adding CCN to deep convective clouds can invigorate them and incur more extensive anvils and respective positive radiative forcing (41–43). This can be quantified observationally using long-term surface aerosol, cloud, and meteorological measurements made at a single location in the SGP (41, 42), and also using global A-Train satellite products (44). These estimates of CRF (the change in CRE due to anthropogenic causes) are associated with aerosol-induced changes in cloud properties that do not differentiate the respective roles of aerosol and dynamics or meteorology but their joint effects.

Having global coverage of  $CCN(S)$  where we need them most—in conjunction with the clouds that ingest them—will provide input for regional and global simulations. The coincident retrieved cloud properties will constrain these models and provide us with realistic assessments of the CRE. The retrieved  $CCN(S)$  can be used for constraining aerosol production and transport models. This will allow separating the aerosols into natural and anthropogenic components more accurately. The application of such classified  $CCN(S)$  will facilitate calculating the anthropogenic aerosol-induced CRF, which will constitute a major reduction of the uncertainty in anthropogenic climate forcing. Developing methodologies for retrieving updrafts at clouds with elevated bases will further enhance these possibilities.

## Conclusions

The feasibility of estimating  $CCN(S)$  and  $W_b$  of boundary layer clouds from the Suomi NPP polar-orbiting operational weather satellite was demonstrated with an accuracy of  $\pm 25\%$  to  $\pm 30\%$ , which is limited mostly by the accuracy in the retrieval of  $r_e$ . The validation was done in Oklahoma, the Amazon Basin, and the northeast Pacific Ocean. Our methodology is presently limited to boundary layer convective clouds of at least 1 km depth, which are not obscured by upper layer clouds, including semitransparent cirrus. This might limit its application in some regions of the world. Moreover, the limitation for small solar backscattering angles of  $< 25^\circ$  restricts the satellite coverage to 1/4 of the satellite swath width, or a view once every 4 d, on average. On the other hand, even for a regional coverage, it would be much more valuable to study the process of aerosol–cloud interactions rather than using single-point data as provided by ground-based observations.

A major advantage of using clouds as analog for CCN chambers relative to relying on the optical signal of the aerosols themselves is the fact that the optical signals (e.g., AOD and Ångström coefficient) vanish at very small aerosol concentrations, which is exactly where the relative changes in CCN concentrations matter most, or, in other words, where very small absolute changes in concentrations have very large impacts on clouds (16, 25). This is where the traditional remote sensing methods of aerosols break down, whereas the applicability of using clouds as CCN chambers remains intact, as evident by the lower left corner of Fig. 3. This has particular importance in the context of the quest for the significance of changes from the preindustrial era to the present background aerosols (25).

The retrieval of both  $CCN(S)$  and  $W_b$  allows, for the first time to our knowledge, disentangling of the roles of updrafts and

CCN on cloud microphysical, precipitation, and radiative properties over climatically meaningful areas. Previously, the inability to separate these factors has been a major impediment to our ability to quantify the aerosol/cloud-mediated effects on Earth's energy budget, thus keeping high the uncertainty of this effect (1). Application of the new capabilities offered by our methodology is expected to allow a breakthrough in quantifying these effects and to substantially reduce the uncertainty in anthropogenic aerosol climate forcing, at least for boundary layer convective clouds.

## Error Analysis

A direct comparison of the satellite- to ground-based CCN, assuming no errors in the CCNC measurements, shows a correlation coefficient of 0.88 and a slope of 0.9 (i.e., underestimate of 10%). The MAPE is  $\pm 30\%$ . However, both satellite retrievals and CCNC measurements are subject to errors. Therefore, a bivariate regression has to be used for fitting two parameters with associated errors for both (45). The associated error for the satellite-retrieved CCN for a given  $S$  was taken as  $\pm 30\%$ . The CCN instrument errors were taken as the  $\pm 95\%$  confidence interval (i.e.,  $\pm 2$  SDs) of  $N_{CCN}$  for the individual cases, as described at the end of *Estimation of Cloud Base Drop Concentrations*. Both sets of errors are shown as error bars in Fig. 3.

The largest sensitivity is to errors in  $r_e$ , because, according to Eq. 2, the error in  $N_a$  is the cube of the error in  $r_e$ . The accuracy of MODIS-retrieved  $r_e$  is best when the 3.7- $\mu\text{m}$  waveband is used (MODIS  $r_e$  is also available for 2.1- $\mu\text{m}$  and 1.6- $\mu\text{m}$  wavebands) in nondrizzling clouds; under these conditions, it showed the best agreement with aircraft measurements, with an uncertainty of 1  $\mu\text{m}$  (46). The 3.7- $\mu\text{m}$ -based  $r_e$  is also minimally affected by cloud inhomogeneities (47) because this band absorbs solar radiation much more strongly (48, 49). The VIIRS footprint area, which is sevenfold smaller than that of MODIS, further reduces the possibility of errors caused by cloud inhomogeneities. Our implementation to VIIRS is even more accurate than MODIS in the best of circumstances, because we use only pixels with visible reflectance  $> 0.4$  at backscattering angles (satellite zenith angle of 0–50 degrees). To avoid significant distortion of  $r_e$  by coalescence, we avoided heavily precipitating clouds at their tops ( $r_e > 18 \mu\text{m}$ ). MODIS  $r_e$  is larger than aircraft in situ measurements by 10–15% (34–36). This is probably not a problem for retrieved  $r_e$  based on the VIIRS Imager (30), because it is lower by a similar amount with respect to MODIS  $r_e$ . The retrieval uncertainty of  $r_e$  itself is roughly  $\pm 10\%$  (36). This translates to uncertainty of a factor of  $\pm 33\%$  in  $N_a$ . This error alone is larger than the measured validation error of  $\pm 30\%$  when assuming no errors in the ground-measured CCN, which includes many other error sources, as described next. This might serve as an indication that the error in the retrieved  $r_e$  from VIIRS is smaller than for MODIS, probably due to the much finer resolution.

The MAPE in cloud base temperature of  $\pm 1.1^\circ\text{C}$  propagates to a 5% error in  $N_a$  due to changing  $C(T_b, P_b)$  in Eq. 1. The error in  $W_b$  (Fig. 2) can be propagated to an error in  $N_a$  according to Twomey's approximation of

$$N_a = CCN(S = 1\%)^{2/(k+2)} W_b^{3k/(2k+4)}, \quad [6]$$

where  $k$  is the slope of the  $CCN(S)$  spectrum on a log–log scale (50). Accordingly, a  $W_b$  MAPE of  $\pm 27\%$  propagates to an error in  $N_a$  of only 7–13% for  $k = 0.5$  and 1, respectively. The overall combined error is  $\pm 36\%$ , as obtained by the calculation  $(0.33^2 + 0.05^2 + 0.13^2)^{0.5} = 0.36$ . This overall calculated error of  $\pm 35\%$ , even before adding the CCN instrument uncertainty, is larger than the measured validation error of  $\pm 30\%$  when assuming no errors in the ground-measured CCN. This discrepancy could be explained, for example, by reducing the  $r_e$  error from 10% to 8%.

**ACKNOWLEDGMENTS.** This study was made possible by merging the efforts of many researchers around the world, with a respective long list of acknowledgments. The study was supported by the US Department of Energy Office of Science Atmospheric System Research program (Grant DE-SC0006787), the State Basic Research Development Program of China (2013CB955804), and National Oceanographic and Atmospheric Administration Joint Polar Satellite System Proving Ground and Risk Reduction program. This study is also partially supported by project BACCHUS

European Commission FP7-603445. Measurements at Amazon Tall Tower Observatory are partially supported by FAPESP (Sao Paulo Research Foundation) Projects 13/50510-5 and 13/05014-0, by the Max Planck Society, and by the German Federal Ministry of Education and Research. We acknowledge the support from Instituto Nacional de Pesquisas da Amazonia and the LBA (The Large-Scale Biosphere-Atmosphere Experiment in Amazonia) central office for ATTO and GOAmazon (Green Ocean Amazon) logistical support and operation.

1. Boucher O, et al. (2013) Clouds and aerosols. *Climate Change 2013: The Physical Science Basis. Contribution of Working Group I to the Fifth Assessment Report of the Intergovernmental Panel on Climate Change* (Cambridge Univ Press, New York), pp 571–657.
2. Rosenfeld D, Sherwood S, Wood R, Donner L (2014) Atmospheric science. Climate effects of aerosol-cloud interactions. *Science* 343(6169):379–380.
3. Zheng Y, Rosenfeld D, Li Z (2015) Satellite inference of thermals and cloud base updraft speeds based on retrieved surface and cloud base temperatures. *J Atmos Sci* 72(6):2411–2428.
4. Zheng Y, Rosenfeld D (2015) Linear relation between convective cloud base height and updrafts and application to satellite retrievals. *Geophys Res Lett* 42(15):6485–6491.
5. Goren T, Rosenfeld D (2012) Satellite observations of ship emission induced transitions from broken to closed cell marine stratocumulus over large areas. *J Geophys Res* 117(D17):D17206.
6. Rosenfeld D (1999) TRMM observed first direct evidence of smoke from forest fires inhibiting rainfall. *Geophys Res Lett* 26(20):3105–3108.
7. Rosenfeld D (2000) Suppression of rain and snow by urban and industrial air pollution. *Science* 287(5459):1793–1796.
8. Andreae MO, et al. (2004) Smoking rain clouds over the Amazon. *Science* 303(5662):1337–1342.
9. Rosenfeld D, et al. (2008) Flood or drought: How do aerosols affect precipitation? *Science* 321(5894):1309–1313.
10. Williams E, Stanfill S (2002) The physical origin of the land–ocean contrast in lightning activity. *C R Phys* 3(10):1277–1292.
11. Bell TL, Rosenfeld D, Kim KM (2009) Weekly cycle of lightning: Evidence of storm invigoration by pollution. *Geophys Res Lett* 36(23):L23805.
12. Rosenfeld D, Bell TL (2011) Why do tornados and hailstorms rest on weekends? *J Geophys Res* 116(D20):D20211.
13. Rosenfeld D, et al. (2012) Aerosol effects on microstructure and intensity of tropical cyclones. *Bull Am Meteorol Soc* 93(7):987–1001.
14. Koren I, Kaufman YJ, Rosenfeld D, Remer LA, Rudich Y (2005) Aerosol invigoration and restructuring of Atlantic convective clouds. *Geophys Res Lett* 32(14):L14828.
15. Koren I, et al. (2012) Aerosol-induced intensification of rain from the tropics to the mid-latitudes. *Nat Geosci* 5(2):118–122.
16. Koren I, Dagan G, Altaratz O (2014) From aerosol-limited to invigoration of warm convective clouds. *Science* 344(6188):1143–1146.
17. Niu F, Li Z (2012) Systematic variations of cloud top temperature and precipitation rate with aerosols over the global tropics. *Atmos Chem Phys* 12(18):8491–8498.
18. Liu J, Li Z (2014) Estimation of cloud condensation nuclei concentration from aerosol optical quantities: Influential factors and uncertainties. *Atmos Chem Phys* 14(1):471–483.
19. Andreae MO (2009) Correlation between cloud condensation nuclei concentration and aerosol optical thickness in remote and polluted regions. *Atmos Chem Phys* 9(2):543–556.
20. Kapustin V, et al. (2006) On the determination of a cloud condensation nuclei from satellite: Challenges and possibilities. *J Geophys Res* 111(D4):D04202.
21. Boucher O, Quaas J (2013) Water vapour affects both rain and aerosol optical depth. *Nat Geosci* 6(1):4–5.
22. Koren I, Oreopoulos L, Feingold G, Remer L, Altaratz O (2008) How small is a small cloud? *Atmos Chem Phys* 8(14):3855–3864.
23. Chakraborty S, Fu R, Wright JS, Massie ST (2015) Relationships between convective structure and transport of aerosols to the upper troposphere deduced from satellite observations. *J Geophys Res* 120(13):6515–6536.
24. Zhu Y, Rosenfeld D, Yu X, Li Z (2015) Separating aerosol microphysical effects and satellite measurement artifacts of the relationships between warm rain onset height and aerosol optical depth. *J Geophys Res*, 120(15):7726–7736.
25. Carslaw KS, et al. (2013) Large contribution of natural aerosols to uncertainty in indirect forcing. *Nature* 503(7474):67–71.
26. Gryspeerd E, Stier P, Grandey B (2014) Cloud fraction mediates the aerosol optical depth–cloud top height relationship. *Geophys Res Lett* 41(10):3622–3627.
27. Roberts G, Nenes A (2005) A continuous-flow streamline thermal-gradient CCN chamber for atmospheric measurements. *Aerosol Sci Technol* 39(3):206–221.
28. Pinsky M, Khain A, Mazin I, Korolev A (2012) Analytical estimation of droplet concentration at cloud base. *J Geophys Res* 117(D18):D18211.
29. Rosenfeld D, Lensky IM (1998) Satellite-based insights into precipitation formation processes in continental and maritime convective clouds. *Bull Am Meteorol Soc* 79(11):2457–2476.
30. Rosenfeld D, et al. (2014) High-resolution (375 m) cloud microstructure as seen from the NPP/VIIRS satellite imager. *Atmos Chem Phys* 14(5):2479–2496.
31. Freud E, Rosenfeld D, Kulkarni J (2011) Resolving both entrainment-mixing and number of activated CCN in deep convective clouds. *Atmos Chem Phys* 11(24):12887–12900.
32. Rosenfeld D, Fischman B, Zheng Y, Goren T, Giguzin D (2014) Combined satellite and radar retrievals of drop concentration and CCN at convective cloud base. *Geophys Res Lett* 41(9):3259–3265.
33. Zhu Y, et al. (2014) Satellite retrieval of convective cloud base temperature based on the NPP/VIIRS Imager. *Geophys Res Lett* 41(4):1308–1313.
34. Painemal D, Zuidema P (2011) Assessment of MODIS cloud effective radius and optical thickness retrievals over the Southeast Pacific with VOCALS-REX in situ measurements. *J Geophys Res* 116(D24):D24206.
35. Min Q, et al. (2012) Comparison of MODIS cloud microphysical properties with in-situ measurements over the Southeast Pacific. *Atmos Chem Phys* 12(23):11261–11273.
36. Noble SR, Hudson JG (2015) MODIS comparisons with northeastern Pacific in situ stratocumulus microphysics. *J Geophys Res* 120(16):8332–8344.
37. Andreae M, et al. (2015) The Amazon Tall Tower Observatory (ATTO): overview of pilot measurements on ecosystem ecology, meteorology, trace gases, and aerosols. *Atmos Chem Phys* 15(18):10723–10776.
38. Koren I, Martins JV, Remer LA, Afargan H (2008) Smoke invigoration versus inhibition of clouds over the Amazon. *Science* 321(5891):946–949.
39. Goren T, Rosenfeld D (2014) Decomposing aerosol cloud radiative effects into cloud cover, liquid water path and Twomey components in marine stratocumulus. *Atmos Res* 138:378–393.
40. George RC, Wood R (2010) Subseasonal variability of low cloud radiative properties over the southeast Pacific Ocean. *Atmos Chem Phys* 10(8):4047–4063.
41. Li Z, et al. (2011) Long-term impacts of aerosols on the vertical development of clouds and precipitation. *Nat Geosci* 4(12):888–894.
42. Yan H, Li Z, Huang J, Cribb M, Liu J (2014) Long-term aerosol-mediated changes in cloud radiative forcing of deep clouds at the top and bottom of the atmosphere over the Southern Great Plains. *Atmos Chem Phys* 14(14):7113–7124.
43. Fan J, et al. (2013) Microphysical effects determine macrophysical response for aerosol impacts on deep convective clouds. *Proc Natl Acad Sci USA* 110(48):E4581–E4590.
44. Peng J, Li Z, Zhang H, Liu J, Cribb M (2015) Systematic changes in cloud radiative forcing with aerosol loading for deep clouds in the tropics. *J Atmos Sci* 73(1):231–249.
45. Cantrell C (2008) Technical Note: Review of methods for linear least-squares fitting of data and application to atmospheric chemistry problems. *Atmos Chem Phys* 8(17):5477–5487.
46. King N, Bower K, Crosier J, Crawford I (2013) Evaluating MODIS cloud retrievals with in situ observations from VOCALS-REX. *Atmos Chem Phys* 13(1):191–209.
47. Zhang Z, Platnick S (2011) An assessment of differences between cloud effective particle radius retrievals for marine water clouds from three MODIS spectral bands. *J Geophys Res Atmos* 116(D20):D20215.
48. Rosenfeld D, Cattani E, Melani S, Levizzani V (2004) Considerations on daylight operation of 1.6-versus 3.7- $\mu\text{m}$  channel on NOAA and METOP satellites. *Bull Am Meteorol Soc* 85(6):873–881.
49. Grosvenor D, Wood R (2014) The effect of solar zenith angle on MODIS cloud optical and microphysical retrievals within marine liquid water clouds. *Atmos Chem Phys* 14(14):7291–7321.
50. Twomey S (1959) The nuclei of natural cloud formation part II: The supersaturation in natural clouds and the variation of cloud droplet concentration. *Geofis Pura Appl* 43(1):243–249.





